Aqueous piperazine blend for CO_2 Capture

Quarterly Report for April 1 – June 30, 2014

by Yang Du

Supported by the Texas Carbon Management Program

McKetta Department of Chemical Engineering

The University of Texas at Austin

July 31, 2014

Abstract

Work completed this quarter is divided between this report and a manuscript that is attached. The manuscript describes a novel blend of piperazine (PZ) with triethylenediamine (TEDA) as a superior solvent for CO_2 capture from coal-fired flue gas. Blending PZ with TEDA can remediate the precipitation issue of concentrated PZ while maintaining its high CO_2 absorption capacity and rate, and high resistance to oxidative degradation. Although PZ/TEDA has a lower thermal stability than concentrated PZ, it is better than PZ/methyldiethanolamine (MDEA).

This report is divided into two sections: 1) a screening test for 16 new PZ blends for CO_2 capture; 2) characterization of PZ/imidazoles for CO_2 capture. The 16 amines in consideration include four amino-piperidines, four hindered amines, four tertiary amines, three hybrid amines, and 4-Hydroxypiperidine. Viscosity measurement shows that both the structure and size of a molecule affect its viscosity. The addition of $-CH_2/CH_3$ and $-NH_2/NH$ groups seems to have a more significant effect on viscosity, compared to the –OH/O group. A thermal degradation screening test shows that PZ/N-(2-Hydroxyethyl) morpholine (HE-Morph), PZ/N-(3-Aminopropyl)morpholine (AP-Morph), PZ/3-Aminomethyl-piperidine (3AM-PD), PZ/4-Aminomethyl-piperidine (4AM-PD), and PZ/4-Hydroxypiperidine (4H-PD) are thermally stable at 150 °C. The WWC test shows that PZ/H-Morph and PZ/AP-Morph have 45% and 30% lower CO_2 capacity, respectively, but a similar absorption rate to 8 m PZ.

8 m PZ/imidazoles (imidazole or simple imidazole derivatives) were tested this quarter for viscosity, solvent degradation, CO_2 absorption rate, and CO_2 absorption capacity. PZ/1-Methylimidazole (1-IMI), PZ/2-Methylimidazole (2M-IMI), PZ/1,2-Dimethylimidazole (DIMI), PZ/2-Ethylimidazole (2E-IMI), and PZ/2-Ethyl-4-Methylimidazole (2E-4M-IMI) were found to be thermally stable at 150 °C. Phase separation was observed for CO_2-loaded PZ/2E-IMI and 2E-4M-IMI, indicating a potential volatility issue. The normalized CO_2 capacity of 5 m PZ/5 m 2E-IMI is 10% lower than 8 m PZ, but its absorption rate is 20% higher. The solvent solubility of 5 m PZ/5 m imidazoles is comparable to 5 m PZ/5 m MDEA.

Introduction

Amine scrubbing has shown the most promise for effective capture of CO_2 from coal-fired flue gas. PZ-based amine blends, such as PZ/AMP, PZ/MDEA, PZ/2MPZ, and PZ/AEP, have gained

attention due to their superior overall performance for CO_2 capture by absorption/stripping (Li et al., 2013). However, these blended amines still have problems, such as the high volatility of AMP and high viscosity of 2MPZ, that limit their industrial application. To find a better amine to blend with PZ, a solvent screening project was started this quarter. 16 amines in consideration include four amino-piperidines, four hindered amines, four tertiary amines, three hybrid amines, and 4-Hydroxypiperidine.

Imidazole was proposed as a physical solvent for CO_2 capture, because of its good CO_2 solubility, as well as low viscosity and low partial pressure (Shannon et al., 2011). Although the pKa of imidazole itself (7.0) is too low to be used as a chemical solvent for CO_2 capture from flue gas, some simple imidazole derivative, such as 2E-4M-IMI, has a pKa as high as 8.7. Viscosity, solvent solubility, solvent degradation, CO_2 absorption rate, and CO_2 absorption capacity were tested this quarter for 8 new PZ/imidazoles.

Experimental Methods

Solution preparation

Aqueous PZ/second amine was prepared by melting anhydrous PZ in a mixture of water and the second amine, and gravimetrically sparging CO_2 (99.5%, Matheson Tri Gas, Basking Ridge, NJ) to achieve the desired CO_2 concentration. The concentration of CO_2 was determined by total inorganic carbon (TIC) analysis, described by Freeman (2011).

Viscosity measurement

Viscosity of PZ/second amine was measured using a Physica MCR 300 cone-and-plate rheometer (Anton Paar GmbH, Graz, Austria). The method was described by Freeman (2011). The average value and standard deviation calculated from 10 individual measurements for each sample was reported.

Thermal degradation

Thermal degradation was measured in 3/8'' 316 stainless steel Swagelok® cylinders with a volume of 4.5 ml and diameter of 0.95 cm. Cylinders were filled with 4 mL of amine solution with around 0.5 mL of headspace, sealed with two Swagelok® end caps, and placed in forced convection ovens maintained at the target temperature. Individual cylinders were removed from the ovens at each sampling point and then analyzed for degradation products, degradation rate, and CO_2 loading, using a Dionex ICS-2500 cation ion chromatograph, a Dionex ICS-3000 modular Dual Reagent-Free anion ion chromatograph (Dionex Corporation), and an infrared CO_2 analyzer (Horiba Instruments Inc., Spring, TX). The details of the experimental apparatus, procedure, and analytical methods are described by Freeman (2011).

Oxidative Degradation

Oxidative degradation experiments for PZ/second amine spiked with 0.05 mM Cr^{3+}, 0.1 mM Ni^{2+}, 0.4 mM Fe^{2+} and 0.1 mM Mn^{2+} were conducted in a low gas flow agitated reactor with 100 mL/min of a saturated 98%/2% O_2/CO_2 gas mixture fed into the reactor headspace. The duration of the experiment was 2 weeks and 3 ml samples were taken every two to three days. Water was added periodically to maintain the water balance of the reactor contents. The liquid samples were analyzed for amine loss and degradation products using ion chromatography. The details

of the experimental apparatus, procedure, and analytical methods were described by Sexton (2009).

CO_2 absorption rate and solubility

CO_2 absorption rate and equilibrium partial pressure in PZ/second amine were measured from 20 to 95 °C using a wetted wall column (WWC), which counter-currently contacted an aqueous PZ/second amine solution with a saturated N_2/CO_2 stream on the surface of a stainless steel rod with a known surface area to simulate the situation of CO_2 absorption in a absorber. The detailed description of wetted wall column measurement has been given by Chen (2011).

Safety considerations

For the screening test, the MSDS for each new amine should be read for proper solvent storage. Flammable amines should only be stored in the "flammables" cabinet.

Results and discussion of screening test

Viscosity result

Table 1 lists the 16 amines in consideration as well as PZ, AMP, and MDEA for comparison. The viscosity of 6 m PZ/2 m second amine with CO_2 loading of 0.4 mol/mol alkalinity at 40 °C is shown in Table 1. The viscosity of 6 m PZ/2 m 4-Aminopiperidine was not measured because it had an extremely low CO_2 solubility. The viscosity of 6 m PZ/2 m 2-(aminomethyl) piperidine was not measured because it precipitated at this loading at room temperature. The viscosity results show that both the structure and size of a molecule affect its viscosity. It seems that the addition of the $-CH_2/CH_3$ and $-NH_2/NH$ groups has a mre significant effect on viscosity than the -OH/O group. For example, PZ/amino-piperidines have high viscosity, while 3-morpholino-1, 2-propanediol, which has the largest MW, has very low viscosity among the amines studied. More effort is needed to confirm this observation.

Table 1: Viscosity (40°C, 0.4 loading) and thermal degradation for 6 m PZ/2 m second amine at 0.2 loading for 2 weeks at 150°C

No.	Amine	Structure	MW	Viscosity (cp)	Amine loss PZ	Amine loss X
1	4-Aminopiperidine	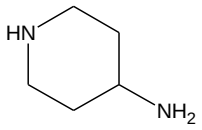	100.16	——	——	
2	4-(aminomethyl) piperidine	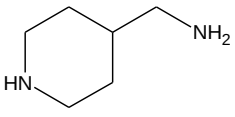	114.19	17.5	0.10	
3	3-aminomethyl-piperidine	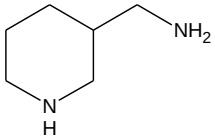	114.19	14.8	0.05	0.15

4	2-(aminomethyl) piperidine	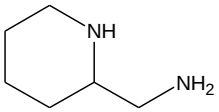	114.19	——	——	
5	AMP	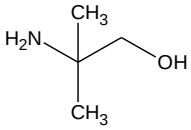	89.14	12.1	0.14	0.28
6	2-Amino-2-methyl-1,3-propanediol	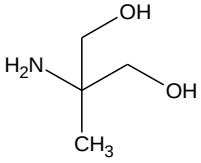	105.14	11.9	0.17	0.59
7	2-Amino-2-ethyl-1,3-propanediol	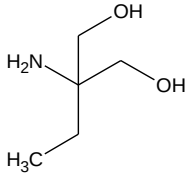	119.16	13.1	0.29	0.73
8	2-Amino-1-butanol	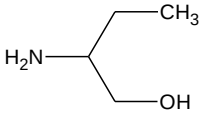	89.14	10.2	0.31	0.89
9	Diisopropanolamine	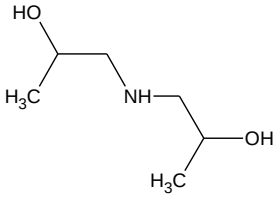	133.19	13.3	0.41	0.98
10	MDEA	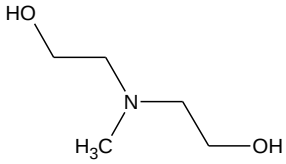	119.16	10.1	0.38	0.45
11	3-Diethylamino-1,2-propanediol	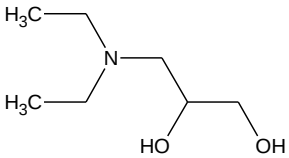	147.22	14.5	0.12	0.39
12	3-Morpholino-1,2-propanediol	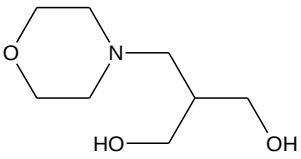	161.20	11.0	0.19	0.15
13	N-(2-Hydroxyethyl)morpholine	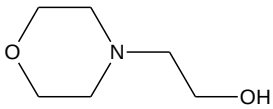	131.17	9.9	0.10	0.15

14	3-(Dimethylamino)-1,2-propanediol	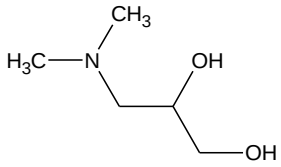	119.16	11.3	0.22	0.52
15	4-(2-Aminoethyl)morpholine	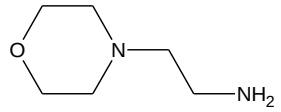	130.19	12.9	0.21	0.26
16	3-(4-Morpholinyl)propylamine	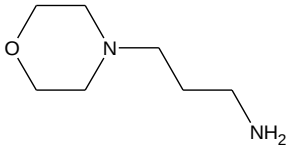	144.22	15.0	<0.05	<0.05
17	1-Ethylpiperazine	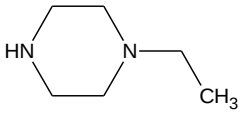	114.19	13.7	0.17	0.16
18	4-Hydroxypiperidine	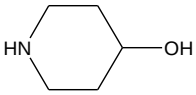	101.15	11.0	0.09	0.07
19	PZ	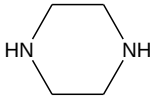	86.14	11.1	0.05	

Thermal degradation

The thermal degradation of 6 m PZ/2 m amine at CO_2 loading of 0.2 mol/mol alkalinity was measured at 150 °C. The loss of PZ and the blended amines after 2 weeks is shown in Table 1. As can be seen from Table 1, among the studied 16 PZ/second amines, only PZ/HE-Morph, PZ/ AP-Morph, PZ/3AM-PD, PZ/4AM-PD, and PZ/4H-PD are thermally stable at 150 °C (amine loss is less than 15%).

CO_2 solubility and rate

The CO_2 solubility in loaded 4 m PZ/4 m HE-Morph and 4 m PZ/4 m AP-Morph was measured from 20 to 95 °C using the WWC (Figures 1 and 2). CO_2 equilibrium partial pressure, P_{CO2} (Pa), was regressed using the following empirical model as a function of temperature, T (K), and CO_2 loading, α (mol CO_2/mol alkalinity), in the liquid phase.

$$\ln P_{CO2} = A - B*\frac{1}{T} - C*a + D*\frac{a}{T} - E*a^2 + F*\frac{a^2}{T}$$

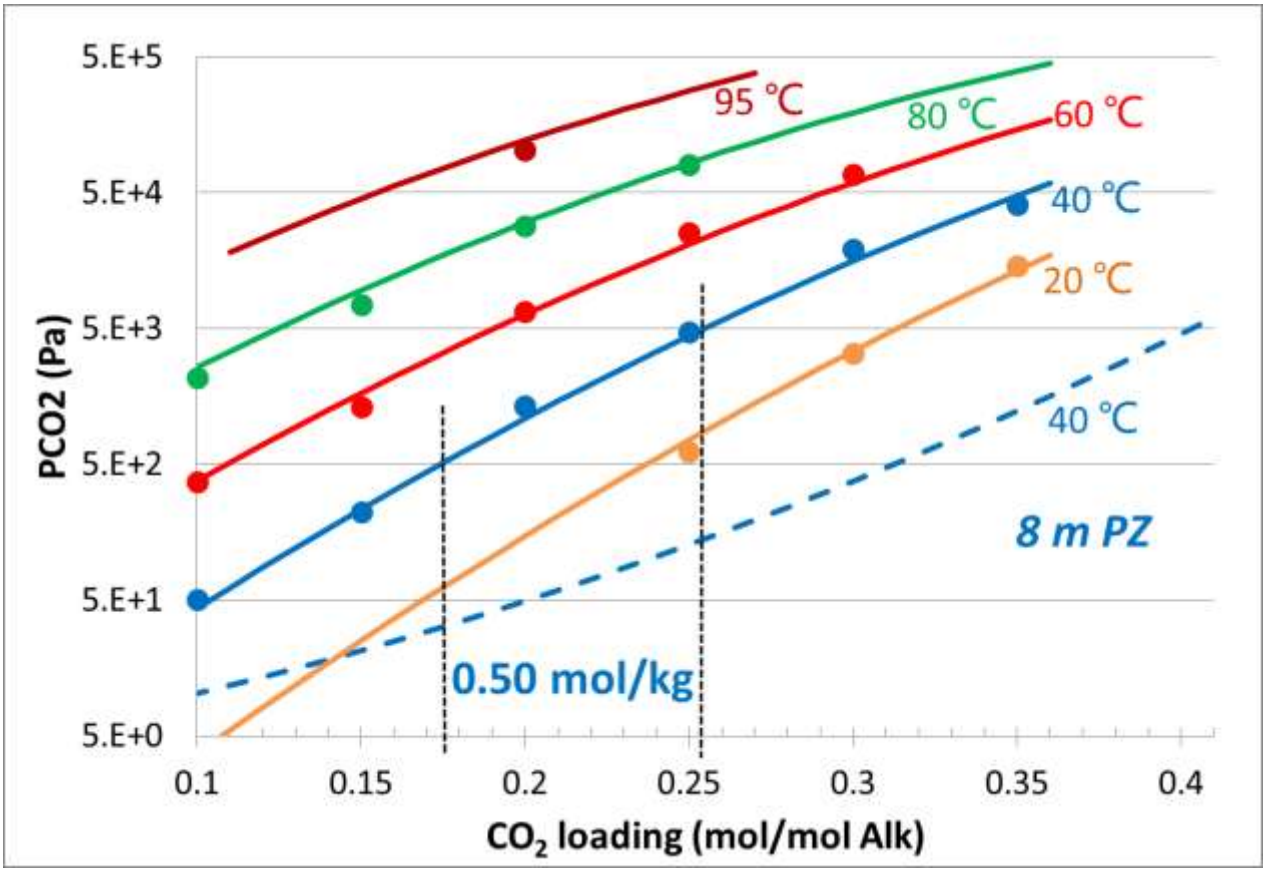

Figure 1: CO_2 solubility for 4 m PZ/4 m HE-Morph (Solid lines: 4 m PZ/4 m HE-Morph equation model; Solid circles: measured data for 4 m PZ/4 m HE-Morph using WWC; Dashed lines: 8 m PZ equation model at 40 °C from Xu (2011).

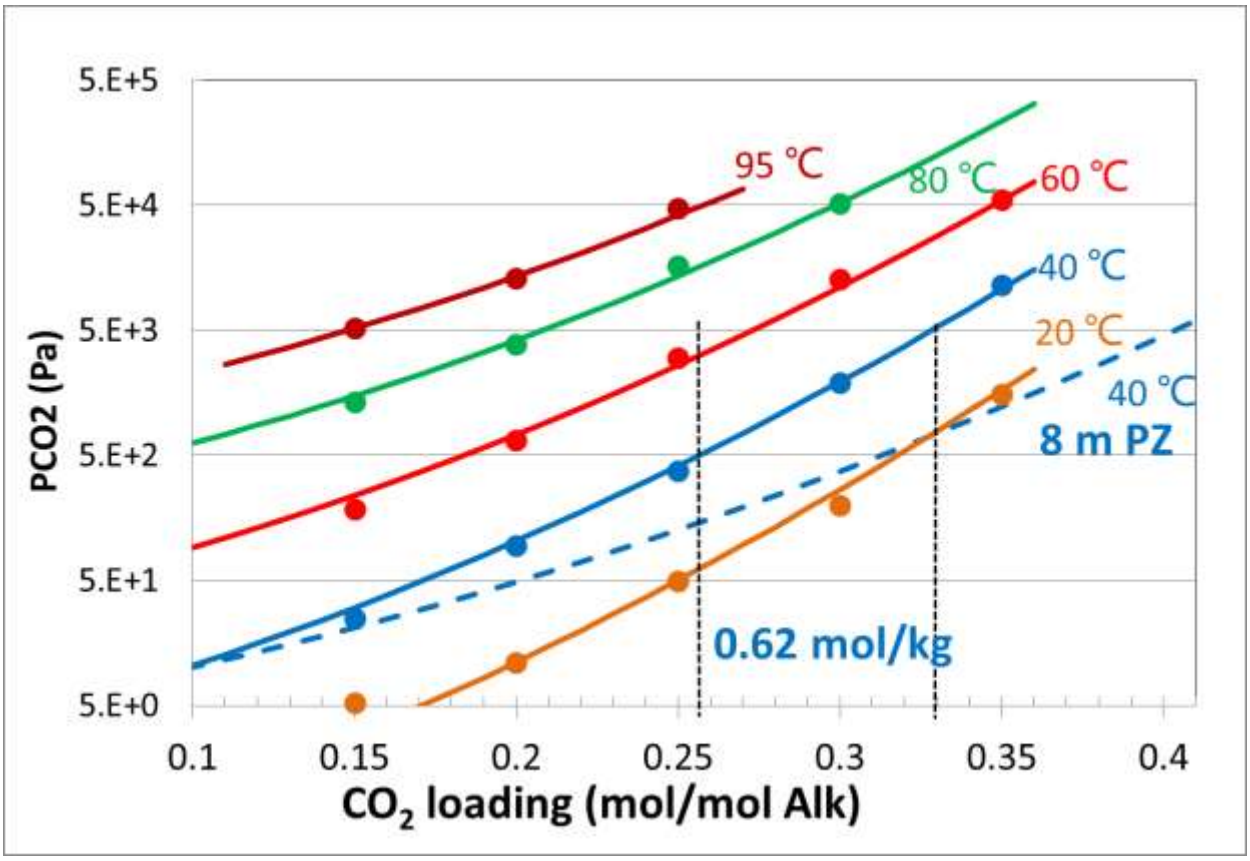

Figure 2: CO_2 solubility for 4 m PZ/4 m AP-Morph (Solid lines: 4 m PZ/4 m AP-Morph equation model; Solid circles: measured data for 4 m PZ/4 m AP-Morph using WWC; Dashed lines: 8 m PZ equation model at 40 °C from Xu (2011).

The CO_2 partial pressure of 8 m PZ is also given for comparison. Figures 1 and 2 show that CO_2 partial pressure of 4 m PZ/4 m HE-Morph and 4 m PZ/4 m AP-Morph at 40 °C is consistently higher than that of 8 m PZ at the same temperature, indicating a lower CO_2 solubility in these two PZ blends. Based on the difference in the equilibrium CO_2 partial pressure from 5 to 0.5 kPa at 40 °C, the working capacity of 4 m PZ/4 m HE-Morph (0.50 mole per kg amines + water) is lower than that of 8 m PZ (Li et al., 2013) (0.86 mole per kg amines + water), but still comparable to that of 7 m MEA (0.50 mole per kg amines + water) (Li et al., 2013). The working capacity of 4 m PZ/4 m AP-Morph (0.62 mole per kg amines + water) is 20% higher than that of 7 m MEA (Li et al., 2013).

CO_2 absorption rate (kg') into 4 m PZ/4 m HE-Morph and 4 m PZ/4 m AP-Morph is shown in Figure 3. To compare kg' of 4 m PZ/4 m HE-Morph and 4 m PZ/4 m AP-Morph to that of 8 m PZ on the same basis, the rate data are plotted against partial pressure of CO_2 instead of CO_2 loading. At 40 °C, the two blends have a similar absorption rate to 8 m PZ.

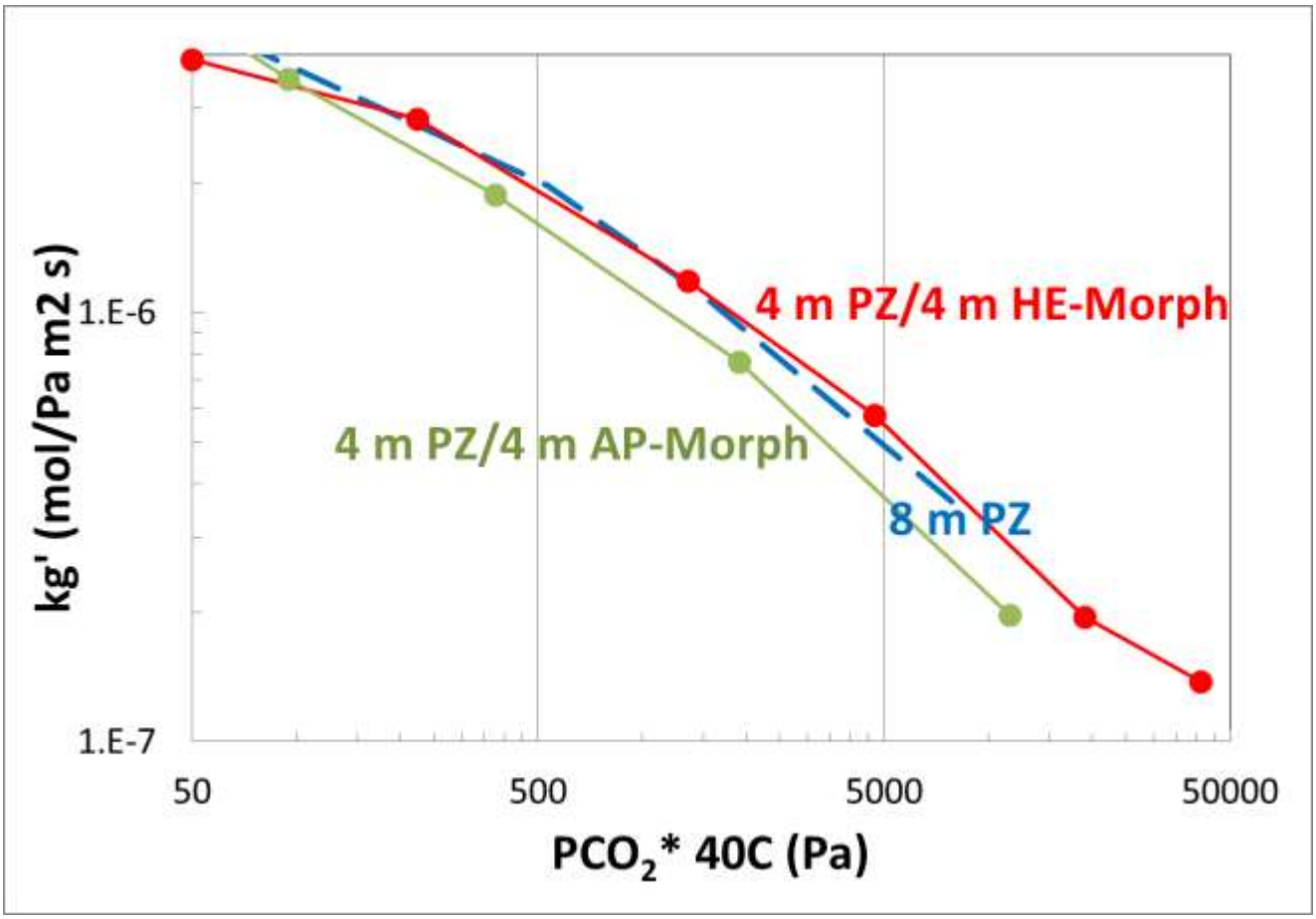

Figure 3: Mass transfer coefficients (kg') in 4 m PZ/4 m HE-Morph and 4 m PZ/4 m AP-Morph (solid lines) at 40 °C, compared to that in 8 m PZ (dashed line) at 40 °C.

Results and discussion of PZ/imidazoles

Viscosity

Table 2 lists the 8 imidazoles in consideration as well as PZ, MEA, and PZ/MDEA for comparison. The viscosity of 4 m PZ/4 m imidazoles with CO_2 loading of 0.2 mol/mol alkalinity at 40 °C is shown in Table 2. 4 m PZ/4 m imidazoles have a comparable or even lower viscosity than 7 m MEA, which is much lower than 8 m PZ and 2 m PZ/7 m MDEA.

Table 2: Viscosity and T_{max} of 4 m PZ/4 m imidazoles with 0.2 mol CO_2/mol alkalinity

Amine Name	Structure	pKa	Viscosity	T_{max}
Imidazole (IMI)	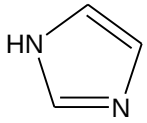	7.0	——	<138
1-Methylimidazole (1M-IMI)	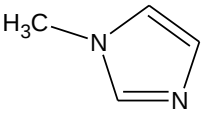	7.2	2.1	155
2-Methylimidazole (2M-IMI)	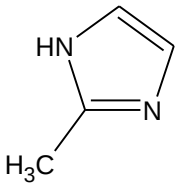	7.9	2.6	156
4(5)-Methylimidazole (4M-IMI)	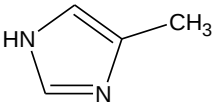	7.7	2.5	144
1,2-Dimethylimidazole (1,2-DIMI)	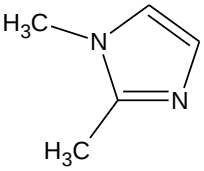	8.2	2.6	152
2-Ethylimidazole (2E-IMI)	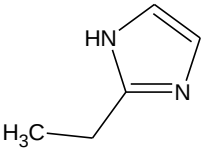	8.0	3.0	157
2-Ethyl 4-Methylimidazole (2E-4M-IMI)	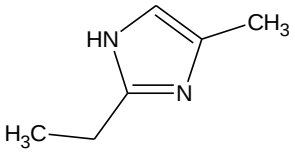	8.7	——	152
1-(3-Aminopropyl)imidazole (AP-IMI)	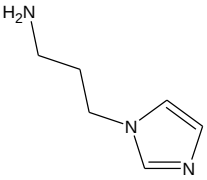	9.0/7.0	——	142
8 m PZ		9.7	10.8	163
2 m PZ/7 m MDEA		9.7/8.8	13.2	126
7 m MEA		9.6	3.0	122

Thermal degradation

Table 2 shows the T_{max} for the 4 m PZ/4 m imidazoles with 0.2 mol CO_2/mol alkalinity. For reference, T_{max} of 8 m PZ, 7 m MEA, and 2 m PZ/7 m MDEA under similar conditions is also shown in Table 2. The results show that PZ/1-IMI, PZ/2M-IMI, PZ/1, 2 DIMI, PZ/2E-IMI, and PZ/2E-4M-IMI are thermally stable at 150 °C.

CO_2 capacity and rate

The CO_2 solubility in loaded 5 m PZ/5 m 2E-IMI was measured at 40 °C (Figure 4). The CO_2 partial pressure of 8 m PZ is given for comparison. Figure 4 shows that CO_2 partial pressure of 5 m PZ/5 m 2E-IMI at 40 °C is consistently higher than that of 8 m PZ at the same temperature, indicating a lower CO_2 solubility in 5 m PZ/5 m 2E-IMI. Although CO_2 absorption rate into 5 m PZ/5 m 2E-IMI is higher than 8 m PZ during normal loading range (Figure 5), the working capacity of 5 m PZ/5 m 2E-IMI (0.64 mole per kg amines + water) is 25% lower than that of 8 m PZ (0.86 mole per kg amines + water) (Li et al., 2013). However, as 5 m PZ/5 m 2E-IMI has a much lower viscosity than 8 m PZ, its normalized CO_2 capacity is similar to that of 8 m PZ. The normalized CO_2 capacity and average absorption rate of 5 m PZ/5 m 2E-IMI is shown in Figure 6, with 8 m PZ, 7 m MEA, 5 m PZ/5 m MDEA, and 4 m PZ/4 m TEDA as comparison.

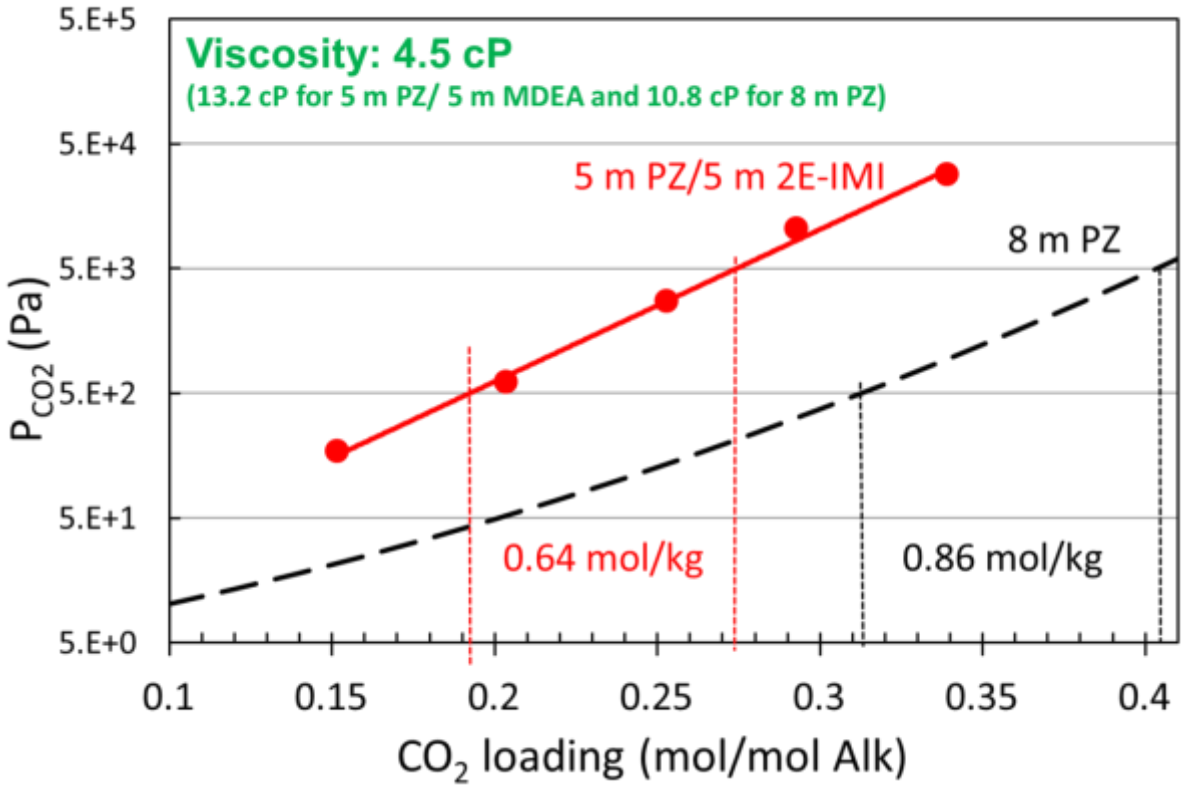

Figure 4: CO_2 solubility for 5 m PZ/5 m 2E-IMI (Dashed lines: 8 m PZ equation model at 40 °C from Xu (2011)).

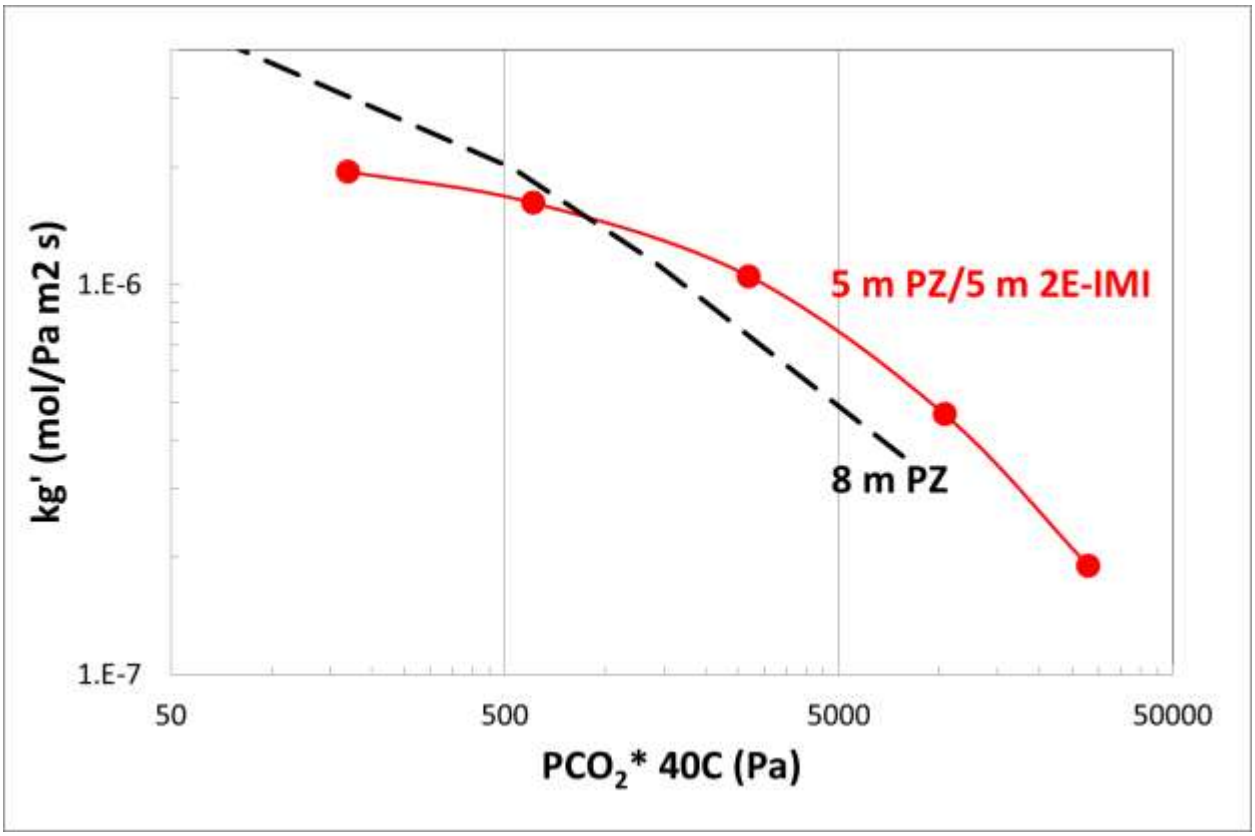

Figure 5: Mass transfer coefficients (kg') in 5 m PZ/5 m 2E-IMI (solid lines) at 40 °C, compared to that in 8 m PZ (dashed line) at 40 °C.

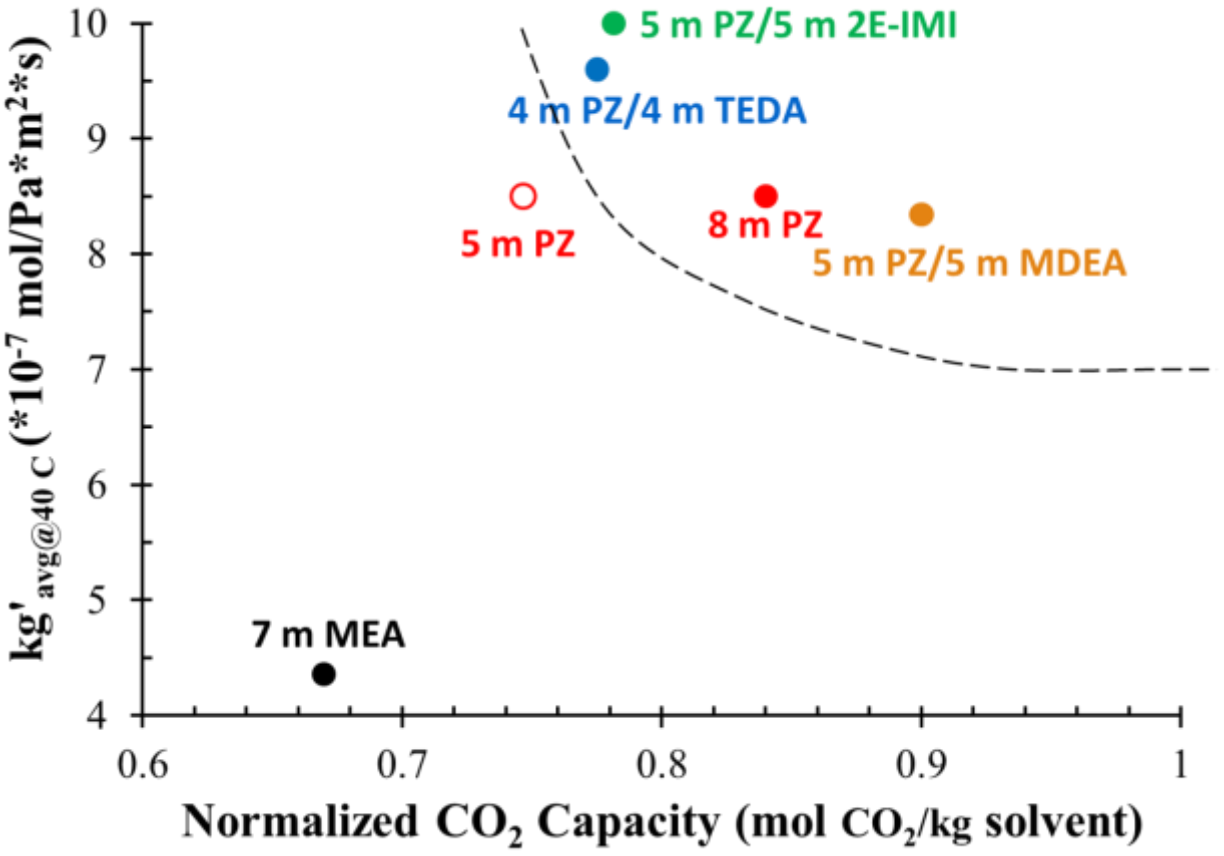

Figure 6: Normalized CO_2 capacity and average mass transfer coefficients (kg') for 5 m PZ/5 m 2E-IMI, compared to other common amines.

Oxidative degradation

Oxidation of 5 m PZ/5 m 2E-IMI at 70 °C in the presence of 0.1 mM Mn^{2+} and the typical SSM mixture (0.4 mM Fe^{2+}, 0.05 mM Cr^{3+}, and 0.1 mM Ni^{2+}), was investigated in the low flow gas apparatus for 2 weeks. The amine loss is shown in Figure 7. It can be seen from Figure 7 that both PZ and 2E-IMI in the blend are resistant to oxidation.

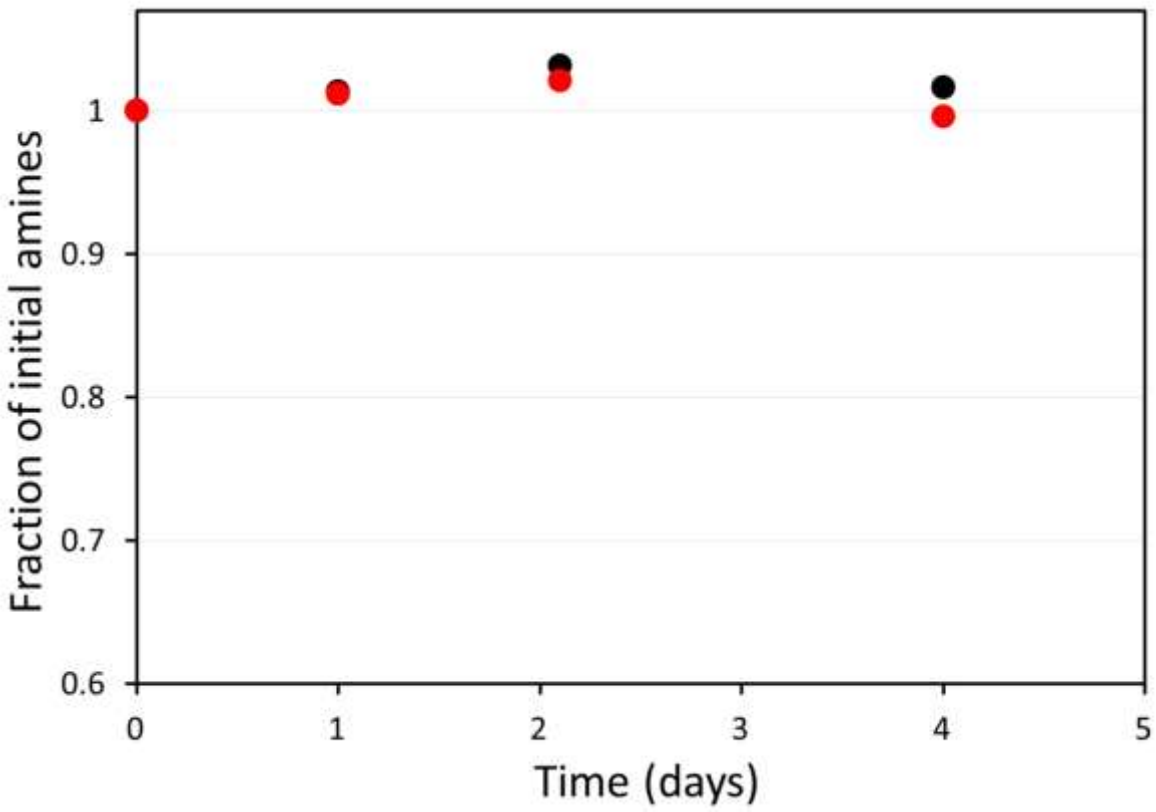

Figure 7: Amine loss for 5 m PZ/5 m 2E-IMI at 70 °C in the presence of O_2, as well as 0.1 mM Mn^{2+}, 0.4 mM Fe^{2+}, 0.05 mM Cr^{3+}, and 0.1 mM Ni^{2+}

Solvent solubility of PZ/imidazoles

The melting transition temperature of 5 m PZ/5 m 1M-IMI and 5 m PZ/5 m 2E-IMI over a range of CO_2 loading from 0 to 0.4 mol/mol alkalinity is shown in Figure 8. The transition temperature for 5 m PZ/5 m MDEA, and non-blended 8 m PZ from Freeman (2011) is shown for comparison. Unlike 8 m PZ, which also precipitates when CO_2 loading reaches 0.44 mol CO_2/mol alkalinity, no precipitate was observed for the three PZ blends at rich CO_2 loading. Also, compared to 8 m PZ, the three blends require a lower CO_2 loading to maintain a liquid solution without precipitation at room temperature (22 °C). The solvent solubility of 5 m PZ/5 m 1M-IMI and 5 m PZ/5 m 2E-IMI is comparable to 5 m PZ/5 m MDEA.

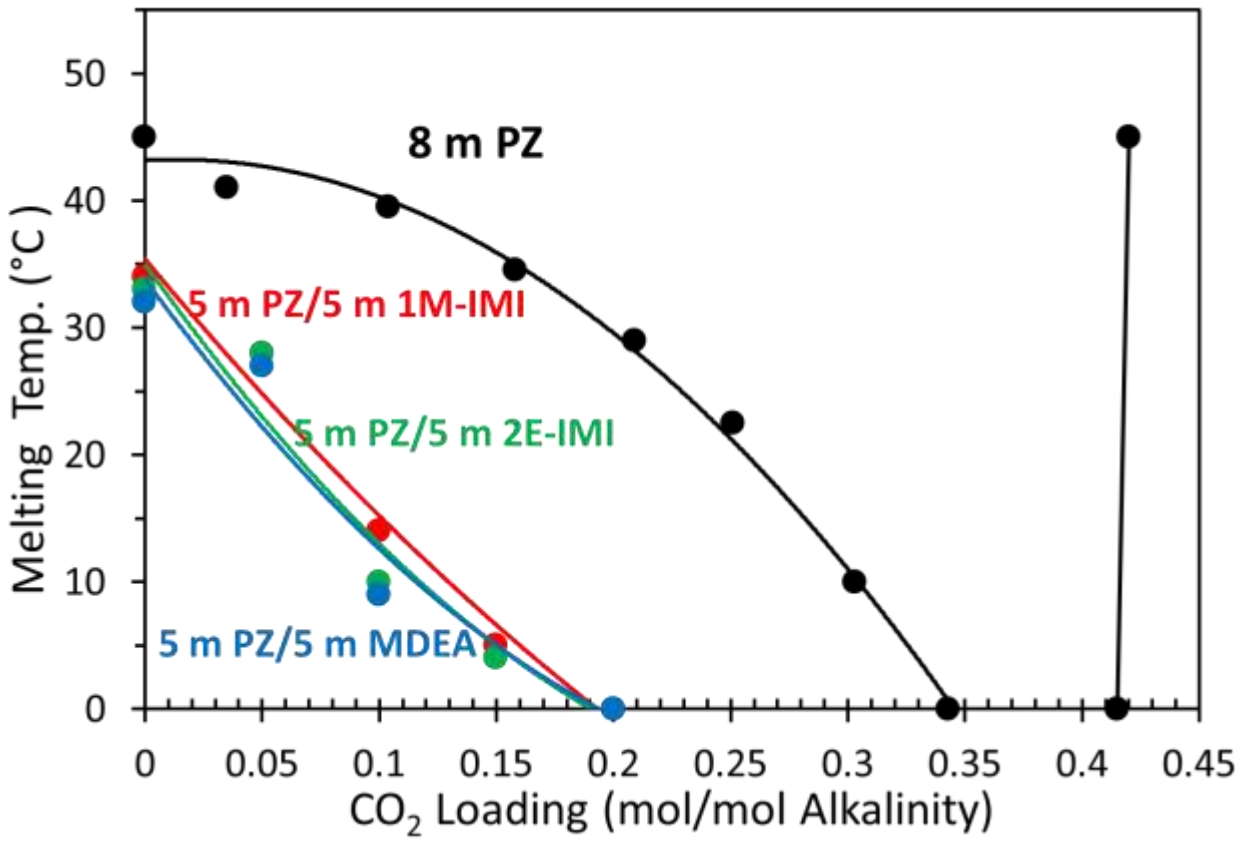

Figure 8: Liquid-Solid transition temperature for 5 m PZ/5 m 1M-IMI and 5 m PZ/5 m 2E-IMI, compared to 8 m PZ and 5 m PZ/5 m MDEA.

Conclusions

1. Both the structure and size of a molecule affect its viscosity. The addition of -CH_2/CH_3 and -NH_2/NH groups seems to have a more significant effect on viscosity than the OH/O group.
2. 6 m PZ/2 m HE-Morph, 6 m PZ/2 m AP-Morph, 6 m PZ/2 m 3AM-PD, 6 m PZ/2 m 4AM-PD, and 6 m PZ/2 m 4H-PD are thermally stable at 150 °C.
3. PZ/H-Morph and PZ/AP-Morph have 45% and 30% lower CO_2 capacity, respectively, but similar absorption rate to 8 m PZ.
4. The viscosity of 4 m PZ/4 m imidazoles is comparable to 7 m MEA under similar conditions, but much lower than 8 m PZ and 2 m PZ/7 m MDEA.
5. PZ/1-IMI, PZ/2M-IMI, PZ/1, 2 DIMI, PZ/2E-IMI, and PZ/2E-4M-IMI are thermally stable at 150 °C.
6. 5 m PZ/5 m 2E-IMI is resistant to oxidation.
7. The normalized CO_2 capacity of 5 m PZ/5 m 2E-IMI is 10% lower than 8 m PZ, but its absorption rate is 20% higher.
8. The solvent solubility of 5 m PZ/5 m 1M-IMI and 5 m PZ/5 m 2E-IMI is comparable to 5 m PZ/5 m MDEA.

Future Work

1. As phase-separation was observed for CO_2 loaded PZ/2E-IMI and 2E-4M-IMI, indicating a potential volatility issue, their volatility will be measured next quarter.
2. 5 m PZ/5 m 2M-IMI is believed to be a promising solvent. 2M-IMI has similar thermal stability and pKa to 2E-IMI, but probably much lower volatility. CO_2 solubility, CO_2 absorption rate, and volatility of PZ/2M-IMI will be tested next quarter.

References

Chen X. *Carbon dioxide thermodynamics, kinetics, and mass transfer in aqueous piperazine derivatives and other amines.* The University of Texas at Austin. Ph.D. Dissertation. 2011.

Freeman SA. *Thermal Degradation and Oxidation of Aqueous Piperazine for Carbon Dioxide Capture.* The University of Texas at Austin. Ph.D. Dissertation. 2011.

Li L, Voice AK, Li H, Namjoshi O, Nguyen T, Du Y, Rochelle GT. "Amine blends using concentrated piperazine." *Energy Proc.* 2013;**37**:353–369..Shannon MS, Bara JE. "Properties of Alkylimidazoles as Solvents for CO_2Capture and Comparisons to Imidazolium-Based Ionic Liquids." *Ind. Eng. Chem. Res.* 2011;50:8665–8677.

Sexton AJ, Rochelle GT. "Catalysts and inhibitors for oxidative degradation of monoethanolamine." *Int J Greenh Gas Con*. 2009;3(6):704–711.

Xu Q. *Thermodynamics of CO_2 Loaded Aqueous Amines.* The University of Texas at Austin. Ph.D. Dissertation. 2011.

Aqueous piperazine/Triethylenediamine for CO_2 capture

Yang Du, Gary T. Rochelle

Abstract

A novel blend of piperazine (PZ) with triethylenediamine (TEDA) has been proposed as a superior solvent for CO_2 capture from coal-fired flue gas. Blending PZ with TEDA can remediate the precipitation issue of concentrated PZ while maintaining its high CO_2 absorption capacity and rate, and high resistance to oxidative degradation. Although PZ/TEDA has a lower thermal stability than concentrated PZ, it is better than PZ/methyldiethanolamine (MDEA).

1. Introduction

Amine scrubbing has shown the most promise for effective capture of CO_2 from coal-fired flue gas [1]. Concentrated piperazine (PZ) has been proposed as a possible alternative to 30 wt % monoethanolamine (MEA), the current industrial standard, for CO_2 capture from coal-fired flue gas [2]. PZ has about twice the CO_2 absorption rate and CO_2 capacity of, and greater resistance to oxidative and thermal degradation than 30 wt % MEA, which can lower the heat duty for the stripper in amine scrubbing systems by approximately 5–10% [3]. In spite of desirable characteristics, the application of concentrated PZ in industry may be limited by solid precipitation at both lean and rich CO_2 loading [3]. Blending solvents already in use is one way to combine desirable characteristics. A novel PZ-based blend, piperazine/triethylenediamine (PZ/TEDA), was investigated in this study to remediate the precipitation of concentrated PZ without sacrificing its CO_2 capacity and absorption rate, resistance to degradation, and other desirable characteristics.

2. Materials and Methods

2.1. Solution preparation

Aqueous PZ/TEDA was prepared by dissolving anhydrous PZ (99%, Alfa Aesar, Ward Hill, MA) in a water and TEDA (99%, Alfa Aesar, Ward Hill, MA) mixture, and gravimetrically sparging CO_2 (99.5%, Matheson Tri Gas, Basking Ridge, NJ) to achieve the desired CO_2 concentration. The concentration of CO_2 was determined by total inorganic carbon (TIC) analysis, described by Hilliard [4].

2.2. Solvent solubility

The transition temperature of PZ/TEDA with variable amine concentration was measured in a water bath over a range of CO_2 loading from 0 to 0.4 mol/mol alkalinity. The solid solubility measurements were based on visual observations and the method was described in detail by Freeman [5]. Solutions with desired properties were heated to 50 °C in a water bath to melt precipitates in solution with lean CO_2 loading. While cooling slowly, the temperature at which the solution first began to crystallize or precipitate was regarded as the crystallizing transition temperature. The solution was heated again to carefully observe the temperature when the crystals fully melt and this was noted as the melting transition temperature. The difference between crystallizing and melting transition temperature, which is also called hysteresis, was

minimized to 1 °C or less for most of the measured points by giving enough equilibrium time and repeating the melting-crystallizing process at transition temperatures.

2.3. Viscosity measurements

Viscosity of 4 m PZ/4 m TEDA with 0.15–0.30 mol CO_2/mol alkalinity was measured at 40 °C using a Physica MCR 300 cone-and-plate rheometer (Anton Paar GmbH, Graz, Austria). The method was described by Freeman [5]. The average value and standard deviation calculated from 10 individual measurements for each sample was reported.

2.4. Thermal degradation

Thermal degradation was measured in 3/8'' 316 stainless steel Swagelok® cylinders with a volume of 4.5 ml and diameter of 0.95 cm. Cylinders were filled with 4 mL of amine solution with around 0.5 mL of headspace, sealed with two Swagelok® end caps, and placed in forced convection ovens maintained at the target temperature. Individual cylinders were removed from the ovens at each sampling point and then analyzed for degradation products, degradation rate, and CO_2 loading, using a Dionex ICS-2500 cation ion chromatograph, a Dionex ICS-3000 modular Dual Reagent-Free anion ion chromatograph (Dionex Corporation), and an infrared CO_2 analyzer (Horiba Instruments Inc., Spring, TX). The details of the experimental apparatus, procedure, and analytical methods are described by Freeman [5, 6].

2.5. Oxidation

Oxidative degradation experiments for 4 m PZ and 4 m TEDA, loaded with 0.2 mol CO_2/mol alkalinity and spiked with 0.05 mM Cr^{3+}, 01 mM Ni^{2+}, 0.4 mM Fe^{2+}, and 0.1 mM Mn^{2+}, were conducted in a low gas flow agitated reactor with 100 mL/min of a saturated 98%/2% O_2/CO_2 gas mixture fed into the reactor headspace. The duration of the experiment was 2 weeks. 3 ml samples were taken every two to three days, and water was added periodically to maintain the water balance of the reactor contents. The liquid samples were analyzed for PZ, TEDA, and degradation products using ion chromatography. The details of the experimental apparatus, procedure, and analytical methods are described by Sexton [7].

2.6. Volatility

Amine volatility was measured in a stirred reactor coupled with a hot gas FTIR analyzer (Fourier Transform Infrared Spectroscopy, Temet Gasmet Dx-4000). This was the same method and apparatus used by Nguyen to measure amine volatility and CO_2 partial pressure in loaded solutions [8].

2.7. CO_2 absorption rate and solubility

CO_2 absorption rate and equilibrium partial pressure in 4 m PZ/4 m TEDA were measured from 20 to 95 °C using a wetted wall column (WWC), which countercurrently contacted an aqueous 4 m PZ/4 m TEDA solution with a saturated N_2/CO_2 stream on the surface of a stainless steel rod with a known surface area to simulate the situation of CO_2 absorption in a absorber. The detailed description of wetted wall column measurement has been given by Li [9].

3. Results and Discussion

3.1. Solvent solubility of PZ/TEDA

The melting transition temperature of PZ/TEDA with variable amine concentration over a range of CO_2 loading from 0 to 0.4 mol/mol alkalinity is shown in Figure 1. The transition temperature for non-blended 8 m PZ from Freeman [5] is also shown for comparison. As the proportion of PZ in the blend decreases, the transition temperature decreases. Unlike 8 m PZ, which precipitates when CO_2 loading reaches 0.44 mol CO_2/mol alkalinity [1], no precipitate was observed for the three blends at rich CO_2 loading. Compared to 8 m PZ, the three blends require a lower CO_2 loading to maintain a liquid solution without precipitation at room temperature (22 °C). CO_2 loading has a lesser effect on the solubility of 2 m PZ/7 m TEDA. The precipitate in 2 m PZ/7 m TEDA at rich CO_2 loading is believed to be TEDA, which cannot form carbamate with CO_2.

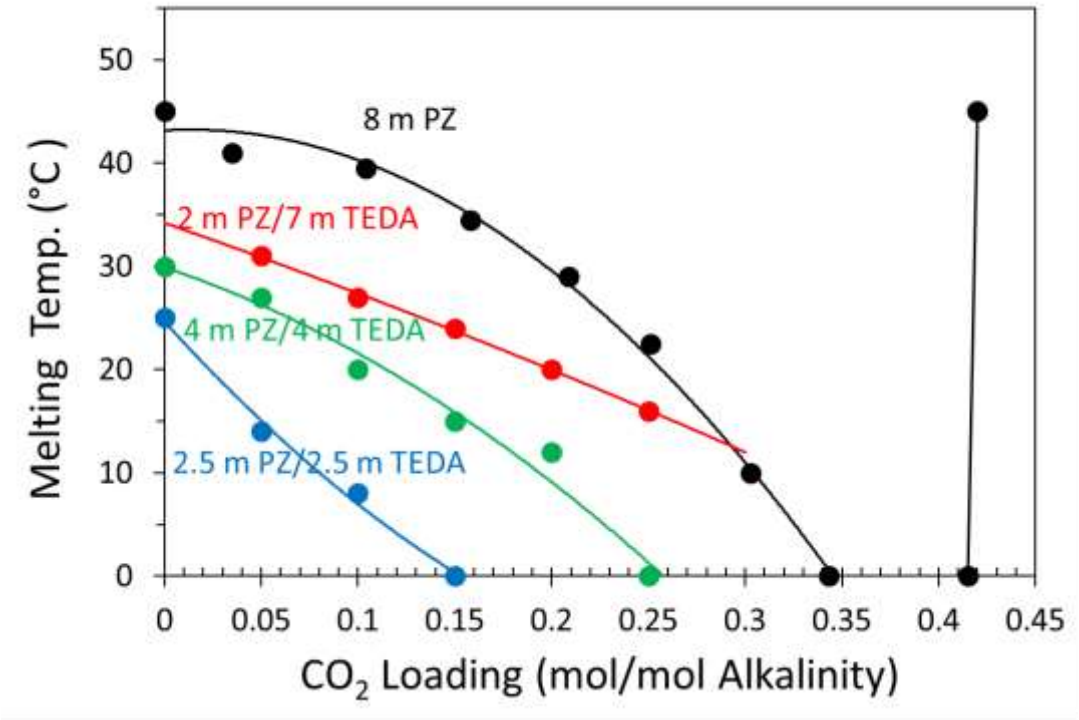

Fig. 1: Liquid-Solid transition temperature for PZ/TEDA with different amine ratios, ●: 8 m PZ [3]; ●: 2 m PZ/7 m TEDA; ●: 4 m PZ/4 m TEDA; ●: 2.5 m PZ/2.5 m TEDA.

3.2. Viscosity

Viscosity of 4 m PZ/4 m TEDA with 0.15–0.30 mol CO_2/mol alkalinity was measured at 40 °C (Table 1). The results suggests that the viscosity of this blend is comparable to that of 8 m PZ [5] (i.e., 12.1 cP for 4 m PZ/4 m TEDA compared to 10.0 cP for 8 m PZ at 0.30 mol CO_2/mol alkalinity and 40 °C). The data demonstrate the expected trend that viscosity increases with increasing CO_2 concentration.

Table 1. Viscosity of 4 m PZ/4 m TEDA at 40 °C

CO_2 Loading (mol/mol alkalinity)	Viscosity (cP)
0.15	9.9
0.20	10.9
0.25	11.2
0.30	12.1

3.3. Thermal Degradation

The thermal degradation of PZ/TEDA with variable amine concentration at CO_2 loading of 0.2 mol/mol alkalinity was measured at 150 °C, 165 °C, and 175 °C. At 175 °C and 165 °C excessive solidification occurred for all loaded solvents (2 m TEDA, 0.6 m PZ/3 m TEDA, 2 m PZ/4 m TEDA, 2.5 m PZ/2.5 m TEDA, 4 m PZ/4 m TEDA) after 1–3 days. Unloaded 2 m TEDA was free of solidification and was found to be stable at 165 °C. The solidification is believed to have been caused by the polymerization of TEDA itself or polymerization between PZ and TEDA. This could be due to the lack of protonated TEDA in the solution, which is likely to be the initiating species required for the initial reactions of thermal degradation [5, 6]. At 150 °C, solidification also occurred for loaded 2 m TEDA, 0.6 m PZ/3 m TEDA, and 4 m PZ/4 m TEDA after 3–5 days. However, loaded 2.5 m PZ/2.5 m TEDA was free of solidification until 10 days at 150 °C, though a small amount of precipitate was observed. In loaded 2.5 m PZ/2.5 m TEDA, the loss of PZ and TEDA at 150 °C was approximately 15% and 25%, respectively, after 10 days (Figure 2).

The thermal degradation of 2.5 m PZ/2.5 m TEDA is compared to that of 2 m PZ/7 m MDEA and 8 m PZ [10, 11], as well as their apparent first-order rate constants (k_1) for thermal degradation in Table 2. The TEDA in this blend degrades on the same scale as that of MDEA in 2 m PZ/7 m MDEA. However, the PZ in the blend degraded one order of magnitude slower than PZ in 2 m PZ/7 m MDEA, though it is still much faster than 8 m PZ. The relatively slow degradation of PZ in 2.5 m PZ/2.5 m TEDA is due to the lack of oxazolidone formation, which occurs in the degradation of 2 m PZ/7 m MDEA.

Table 2. Apparent first-order rate constant (k_1) at 150 ˚C for thermal degradation of PZ/TEDA and other related solvents

Amine	Components	Loading mol/mol alkalinity	$k_1 \times 10^{-9}$ (s^{-1})
PZ	2.5 m PZ/2.5 m TEDA	0.20	150
TEDA	2.5 m PZ/2.5 m TEDA	0.20	347
PZ	2 m PZ/7 m MDEA	0.25	2050
MDEA	2 m PZ/7 m MDEA	0.25	284
PZ	8 m PZ	0.30	6.1

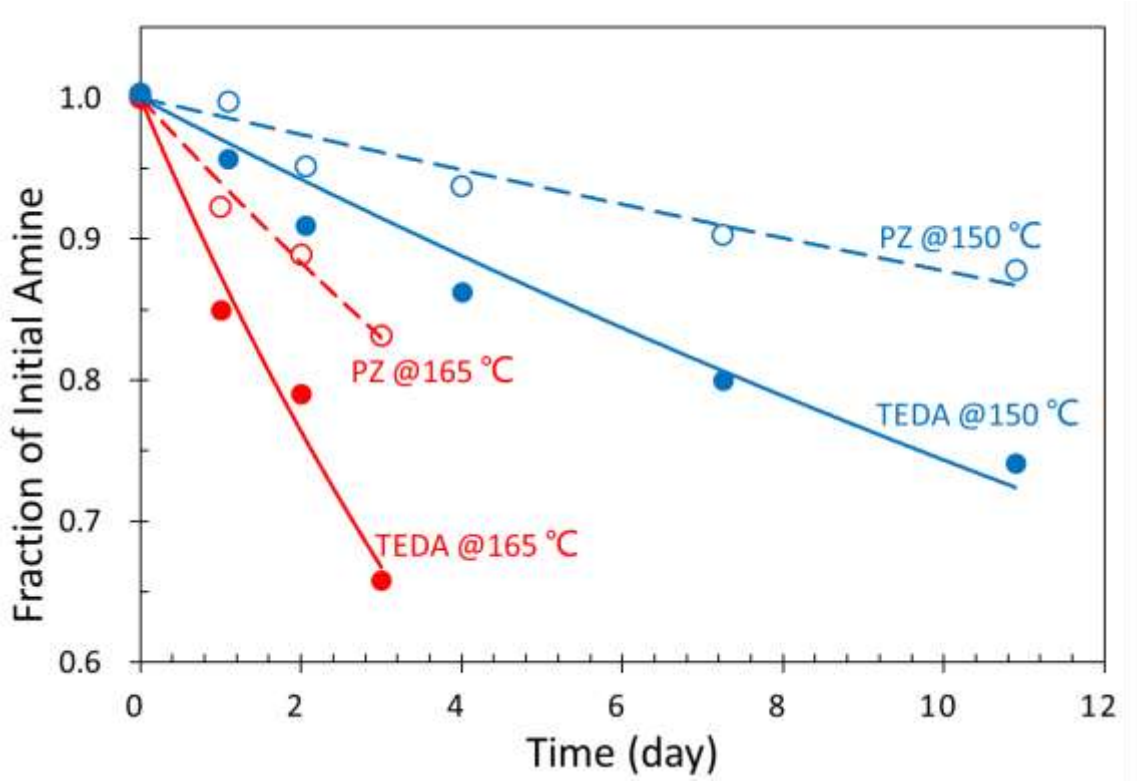

Fig. 2. Amine loss in 2.5 m PZ/2.5 m TEDA at 150 and 165 °C at 0.3 mol CO_2/mol alkalinity.

3.4. Oxidative degradation

Oxidation of 4 m PZ/4 m TEDA at 70 °C in the presence of 0.1 mM Mn^{2+} and the typical SSM mixture (0.4 mM Fe^{2+}, 0.05 mM Cr^{3+}, and 0.1 mM Ni^{2+}) was investigated in the low flow gas apparatus for 2 weeks. The amine loss is shown in Figure 3. Figure 3 sh that both PZ and TEDA in 4 m PZ/4 m TEDA are resistant to oxidation.

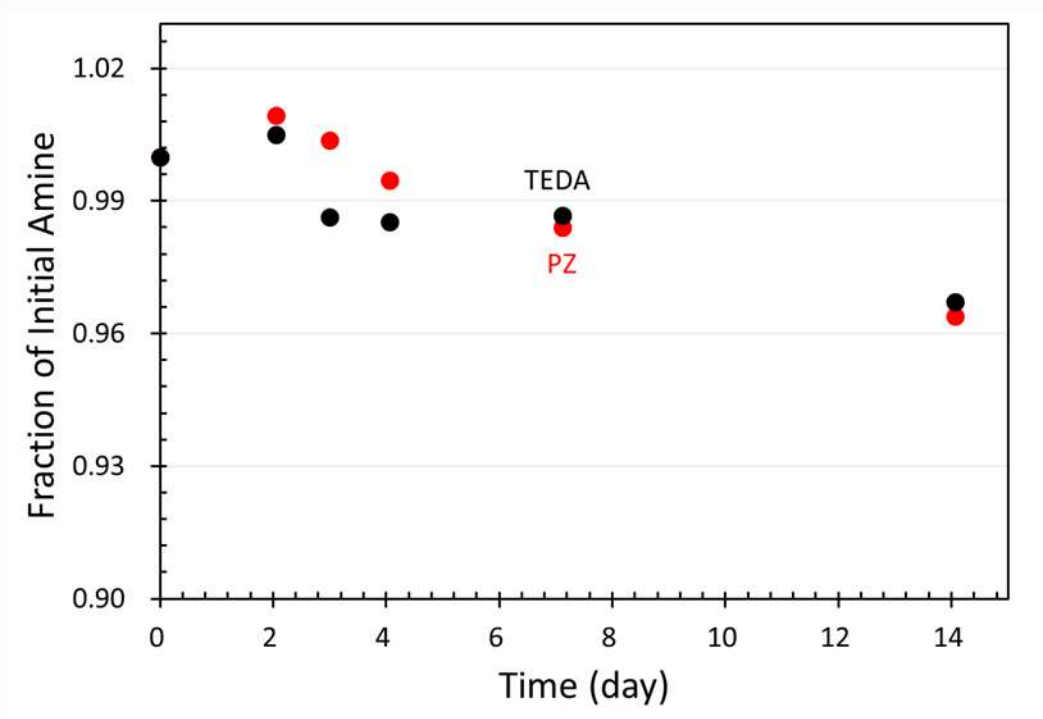

Fig. 3. Amine loss in 4 m PZ/4 m TEDA at 70 °C in the presence of O_2, as well as 0.1 mM Mn^{2+}, 0.4 mM Fe^{2+}, 0.05 mM Cr^{3+}, and 0.1 mM Ni^{2+}

3.5. Volatility

Figure 4 shows the partial pressure of unloaded 0.5 m and 2 m TEDA, and unloaded 2.5 m PZ/2.5 m TEDA. The partial pressure of unloaded 0.5 m PZ was shown for comparison [8]. The partial pressure of TEDA is comparable to PZ at the same concentration. The data demonstrate the expected trend that partial pressure of TEDA increases with increasing concentration and temperature. Unloaded PZ/TEDA, PZ, and TEDA show almost the same volatility.

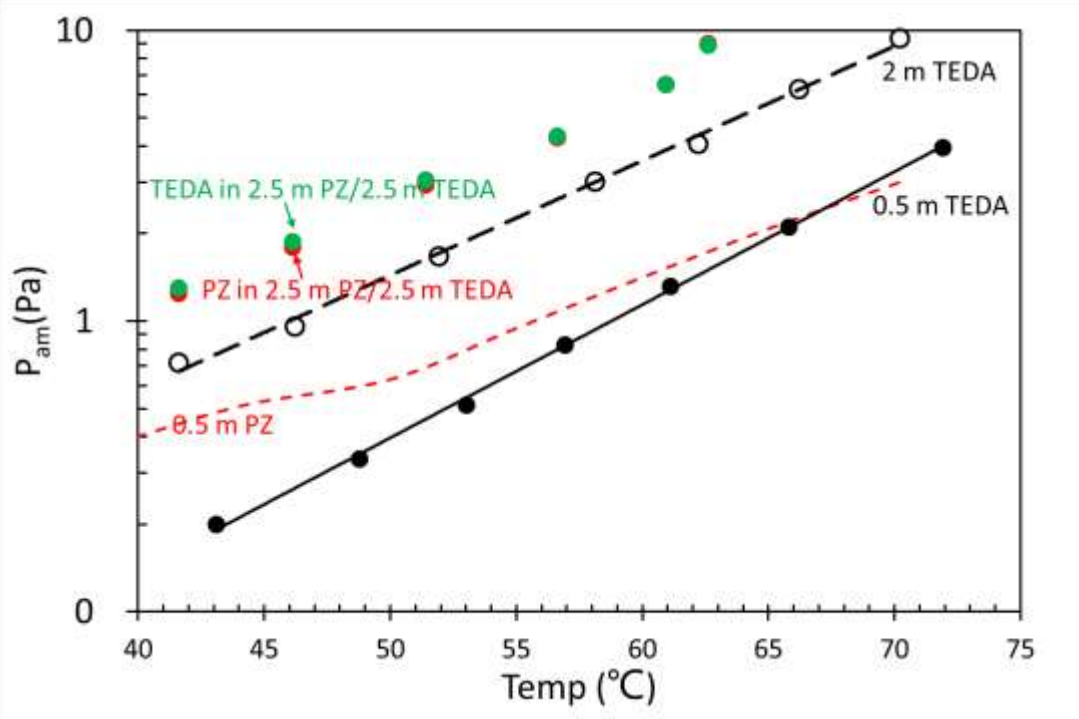

Fig. 4. Partial pressure of unloaded 0.5 m and 2 m TEDA, and unloaded 2.5 m PZ/2.5 m TEDA, compared to unloaded 0.5 m PZ.

Figure 5 shows the partial pressure of loaded 2.5 m PZ/2.5 m TEDA. The partial pressure of unloaded 2.5 m PZ/2.5 m TEDA was shown for comparison. In the loaded solution, the partial pressure of PZ is almost one order manganite lower than TEDA. The loading of CO_2 has no significant effect on the volatility of TEDA. PZ can react with CO_2 to form carbamate which has much lower volatility than free PZ, but TEDA, as a tertiary amine, cannot form carbamate.

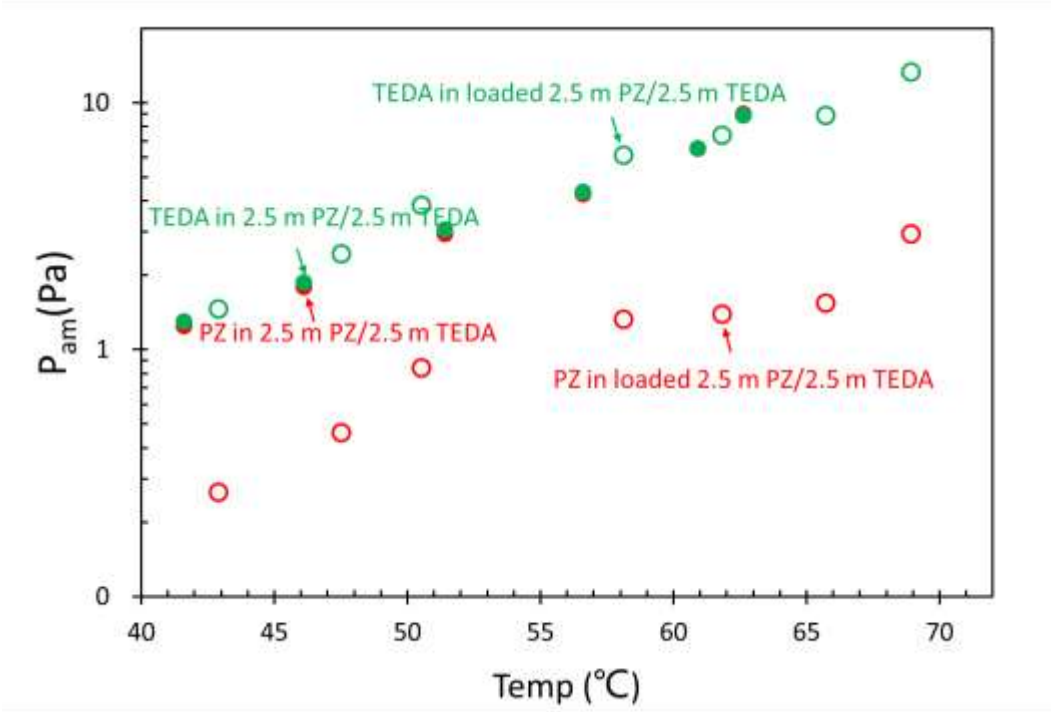

Fig. 5. Partial pressure of loaded 2.5 m PZ/2.5 m TEDA, compared to unloaded 2.5 m PZ/2.5 m TEDA.

3.6. CO_2 solubility

The CO_2 solubility in loaded 4 m PZ/4 m TEDA was measured from 20 to 95 °C. CO_2 equilibrium partial pressure, P_{CO2} (Pa), was regressed using the empirical model shown in Equation 1 as a function of temperature, T (K), and CO_2 loading, α (mol CO_2/mol alkalinity), in the liquid phase.

$$\ln P_{CO2} = 37.41 - 11029 * \frac{1}{T} - 19.21 * a + 11315 * \frac{a}{T} + 16.68 * a^2 + 667 * \frac{a^2}{T} \quad (1)$$

CO_2 partial pressure of 4 m PZ/4 m TEDA is higher than that of 8 m PZ at 40 °C, indicating a lower CO_2 solubility in this blend. Based on the difference in the equilibrium CO_2 partial pressure from 5 to 0.5 kPa at 40 °C, the working capacity of 4 m PZ/4 m TEDA (0.79 mole per kg amines + water) is 10% lower than that of 8 m PZ [9] (0.86 mole per kg amines + water), but still much higher than that of 7 m MEA (0.50 mole per kg amines + water) [9].

3.7. Absorption rate

CO_2 absorption rate into 4 m PZ/4 m TEDA was also studied in the wetted wall column. The liquid-film mass transfer coefficients (k_g') of CO_2 absorption into 4 m PZ/4 m TEDA are shown in Figure 7. To compare kg' in 4 m PZ/4 m TEDA to that in 8 m PZ on the same basis, the rate data are plotted against partial pressure of CO_2 instead of CO_2 loading. To compare kg' at variable temperature, the rate data of 4 m PZ/4 m TEDA at 40 to 95 °C are plotted as a function of the equilibrium partial pressure of CO_2 at 40 °C. Compared to 8 m PZ, at 40 °C the blend has a higher rate. Similar to other amines studied in CO_2 capture [8], temperature has a negative effect on CO_2 absorption rate into 4 m PZ/4 m TEDA.

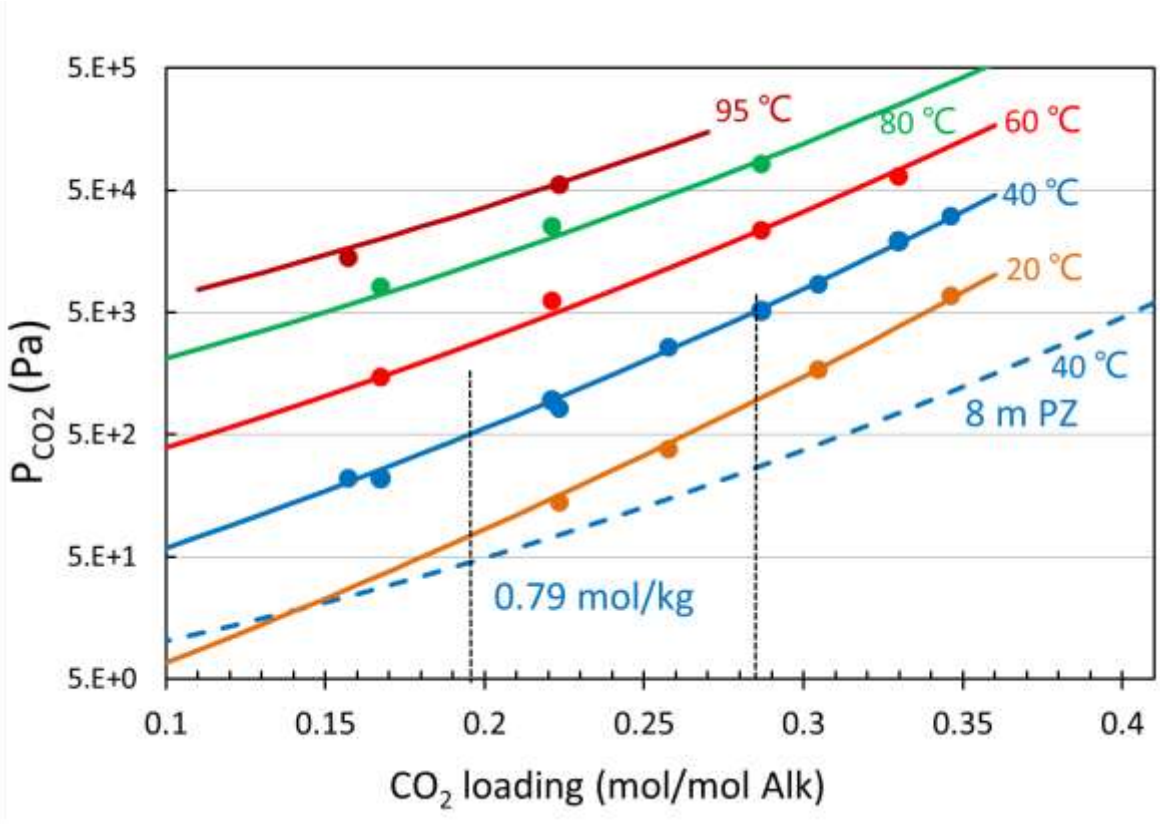

Fig. 6. CO_2 solubility for 4 m PZ/4 m TEDA (Solid lines: 4 m PZ/4 m TEDA equation model; Solid circles: measured data for 4 m PZ/4 m TEDA using WWC; Dashed lines: 8 m PZ equation model [9].

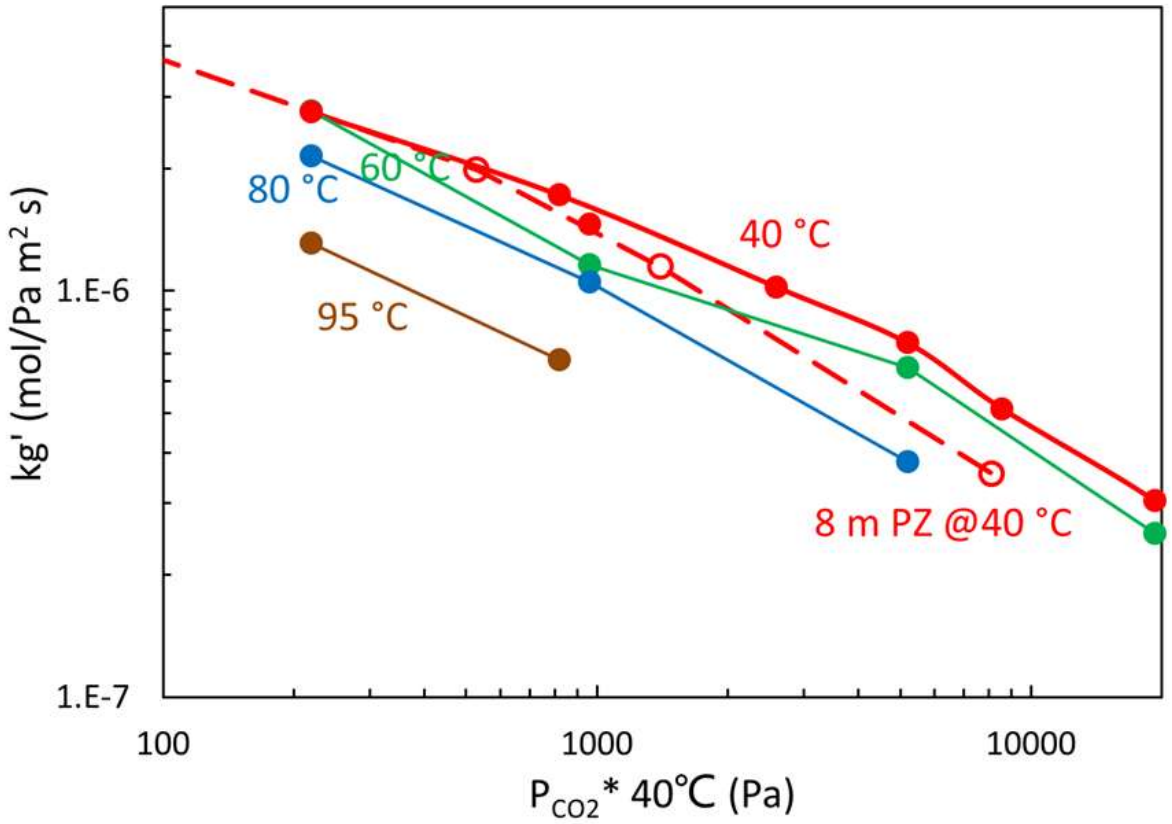

Fig. 7. Mass transfer coefficients (kg') in 4 m PZ/4 m TEDA (solid lines) from 40 to 95 °C, compared to that in 8 m PZ (dashed line) at 40 °C.

4. Conclusions

Blending PZ with TEDA can lower the solvent transition temperature. No precipitate was observed in PZ/TEDA at rich CO_2 loading.

The viscosity of 4 m PZ/4 m AEP is comparable to 8 m PZ.

4 m PZ/4 m TEDA is resistant to oxidative degradation, but it solidifies at high temperature (150 °C) after 4 days. 2.5 m PZ/2.5 m TEDA is free of solidification until 10 days at 150 °C, though some precipitate was observed. The thermal degradation of 2.5 m PZ/2.5 m TEDA is slower than 2 m PZ/7 m MDEA, but faster than 8 m PZ.

The working capacity of 4 m PZ/4 m TEDA (0.79 mole per kg amines + water) is 10% lower than that of 8 m PZ (0.86 mole per kg amines + water), but still much higher than that of 7 m MEA (0.50 mole per kg amines + water). Kinetics measurements have shown that compared to 8 m PZ, at 40 °C 4 m PZ/4 m TEDA has higher CO_2 absorption rates.

Compared to 8 m PZ, the greater solvent solubility and absorption rate, and comparable oxidation rate and viscosity, indicate that PZ/TEDA is a promising alternative solvent for CO_2 capture by absorption/stripping.

Acknowledgements

The authors acknowledge the financial support of the Texas Carbon Management Program in the performance of this work and preparation of the manuscript.

One author of this publication consults for Southern Company and for Neumann Systems Group on the development of amine scrubbing technology. The terms of this arrangement have been reviewed and approved by the University of Texas at Austin in accordance with its policy on objectivity in research.

References

1. Rochelle GT. Amine Scrubbing for CO_2 Capture. *Science.* 2009;**325**(5948):1652-4.

2. Rochelle GT, Chen E, Freeman SA, Van Wagener DH, Xu Q, Voice AK. Aqueous piperazine as the new standard for CO_2 capture technology. *Chem Eng J.* 2011;**171**(3):725-33.

3. Freeman SA, Dugas RE, Van Wagener DH, Nguyen T, Rochelle GT. Carbon dioxide capture with concentrated, aqueous piperazine. *Int J Greenh Gas Con.* 2010;**4**(2):119-24.

4. Hilliard MD. A Predictive Thermodynamic Model for an Aqueous Blend of Potassium Carbonate, Piperazine, and Monoethanolamine for Carbon Dioxide Capture from Flue Gas. Ph.D. Dissertation. The University of Texas at Austin, Austin, TX, 2008.

5. Freeman SA. Thermal Degradation and Oxidation of Aqueous Piperazine for Carbon Dioxide Capture. Ph.D. Dissertation. The University of Texas at Austin, Austin, TX, 2011.

6. Freeman SA, Rochelle GT. Thermal Degradation of Aqueous Piperazine for CO_2 Capture: 2. Product Types and Generation Rates. *Ind Eng Chem Res.* 2012;**51**(22):7726-35.

7. Sexton AJ. Amine oxidation in CO_2 capture processes. Ph.D. Dissertation. The University of Texas at Austin, Austin, TX, 2008.

8. Nguyen T. Amine Volatility in CO_2 Capture. Ph.D. Dissertation. Ph.D. Dissertation. The University of Texas at Austin, Austin, TX, 2013.

9. Li L, et al. Amine blends using concentrated piperazine. Presented at GHGT-11, Kyoto, Japan, November 18-22, 2012. *Energy Proc*. 2013.

10. Closmann FB. Oxidation and thermal degradation of methyldiethanolamine/piperazine in CO_2 capture. Ph.D. Dissertation. The University of Texas at Austin, Austin, TX, 2011.

11. Freeman SA, Rochelle GT. Thermal degradation of piperazine and its structural analogs. *Energy Proc.* 2011;**4**:43-50.

Simplified stoichiometric VLE model for CO_2/Amine/H_2O systems

Quarterly Report for April 1 – June 30, 2014

by Le Li

Supported by the Texas Carbon Management Program

McKetta Department of Chemical Engineering

The University of Texas at Austin

July 31, 2014

Abstract

A simplified stoichiometric VLE modeling framework is developed using MATLAB. The model equations use simplified chemical equilibrium relationships and mass balances to represent the CO_2/H_2O/amine system with five equations, two of which are nonlinear equations. The model contains two parts. The first is a nonlinear equation solver, which calculates the concentration of true molecular species in the liquid phase and the equilibrium partial pressure of CO_2 in the gas phase (P_{CO2}). The nonlinear equation solver also requires values for four parameters, which are to be specified by the user. The solver can be linked to the second part of the model, which is a parameter regression function. This second part adjusts the specified parameter values of the solver until the calculated output from the model matches experimental result.

The model setup was tested for CO_2/monoethanolamine/H_2O. Experimental CO_2 VLE data for MEA from four sources and ranges from 40–160 °C were included. The regressed model fit experimental P_{CO2}^* values well, and predicts the liquid phase speciation. The speciation predictions are well behaved and follow the same trend as Aspen Plus® results. Some slight deviation is observed between the MATLAB model and Aspen Plus® around the CO_2 loading of 0.5 mol/mol alkalinity, likely due to the significant reduction in complexity and total number of adjusted parameters in the simplified stoichiometric model.

Introduction

The absorption of CO_2 is thermodynamically limited by the solubility of gaseous CO_2 in the amine solvent. Thus, accurate prediction and characterization of CO_2 solubility are essential in the optimization and design of the process. Mainly, CO_2 solubility determines the CO_2 capacity of an amine solvent, which significantly affects the overall energy cost of the amine scrubbing process. Second, CO_2 solubility affects the CO_2 mass transfer driving force during absorption and the cost of the absorber column. Third, the temperature dependence of the CO_2 solubility is related to the heat of CO_2 absorption into the amine solvent, which also affects the energy cost of the process.

In the context of solvent selection, amines interact differently with CO_2 depending on the chemical properties and molecular structure of the amine, which affects CO_2 solubility.

Understanding the relationship between CO_2 solubility and the chemical and molecular properties of the amine is necessary for proper solvent selection.

CO_2/H_2O/amine vapor-liquid equilibrium

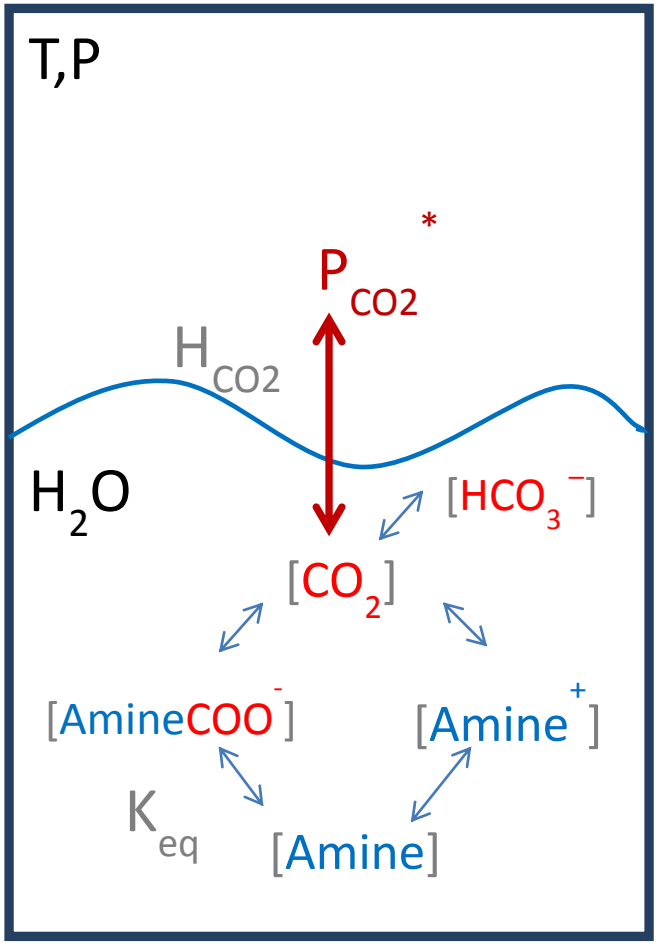

Figure 1: CO_2 VLE in aqueous amines

The CO_2 solubility in aqueous amines involves two equilibrium relationships (Figure 1). First, CO_2 in the gas phase is in equilibrium with the free CO_2 in the liquid phase. Second, the free CO_2 in the liquid phase is in chemical equilibrium with the amine and amine-CO_2 reaction products.

Thermodynamic modeling of CO_2 VLE

Experimentally, CO_2 VLE in aqueous amine is determined by measuring the equilibrium partial pressure of CO_2 (P_{CO2}^*), which is the CO_2 concentration in the gas phase, and the corresponding total CO_2 and amine concentrations in the liquid phase (Figure 2). Effective thermodynamic modeling of CO_2 VLE should: 1) represent the experimental data; 2) adequately interpolate between and extrapolate near experimental conditions; 3) describe the CO_2/H_2O/amine system with equations that are derived from thermodynamic and chemical first principles, such that the parameters carry physical significance.

Common methods of modeling CO_2 VLE fall into two categories. The first is the semi-empirical method, which relates to P_{CO2}^* with system temperature and total liquid phase CO_2 concentration and various combinations of the two independent variables in a linear expression. An example of a semi-empirical model is shown in Equation 1 (Xu, 2011).

$$\ln\left(P_{CO_2}{}^*\right) = a + \frac{b}{T} + c \cdot \alpha_{CO_2} + d \cdot \alpha_{CO_2}{}^2 + e \cdot \frac{\alpha_{CO_2}}{T} + f \cdot \frac{\alpha_{CO_2}{}^2}{T} \quad (1)$$

2 is the ratio of total moles of CO_2 species against the total moles of amine species in the liquid. The semi-empirical model typically fits experimental data well across most of the temperature and CO_2 concentration relevant to amine scrubbing. An example of a fit of semi-empirical model against experimental data is shown in Figure 2 with monoethanolamine (MEA). These simple models can be used to interpolate between and extrapolate near the experimental conditions. Also the model can capture 1st order temperature dependence of the VLE data, provided the appropriate temperature dependence terms are included in the model expression. The temperature dependence of the semi-empirical model can be used to estimate the heat of CO_2 absorption, as shown in Equation 2, which is important in the calculation of process energy cost.

$$-\Delta H_{ABS} = -R \cdot \frac{\partial \ln(P_{CO_2}{}^*)}{\partial {}^1/_T} = -R \cdot (b + e \cdot \alpha_{CO_2} + f \cdot \alpha_{CO_2}{}^2) \quad (2)$$

However, the semi-empirical model is not derived from thermodynamic first principles, and its parameters carry little physical meaning. More importantly, as the model relates P_{CO2}^* to apparent total CO_2 and amines in the liquid, it cannot be used to determine the chemical equilibrium between the CO_2 and amine species.

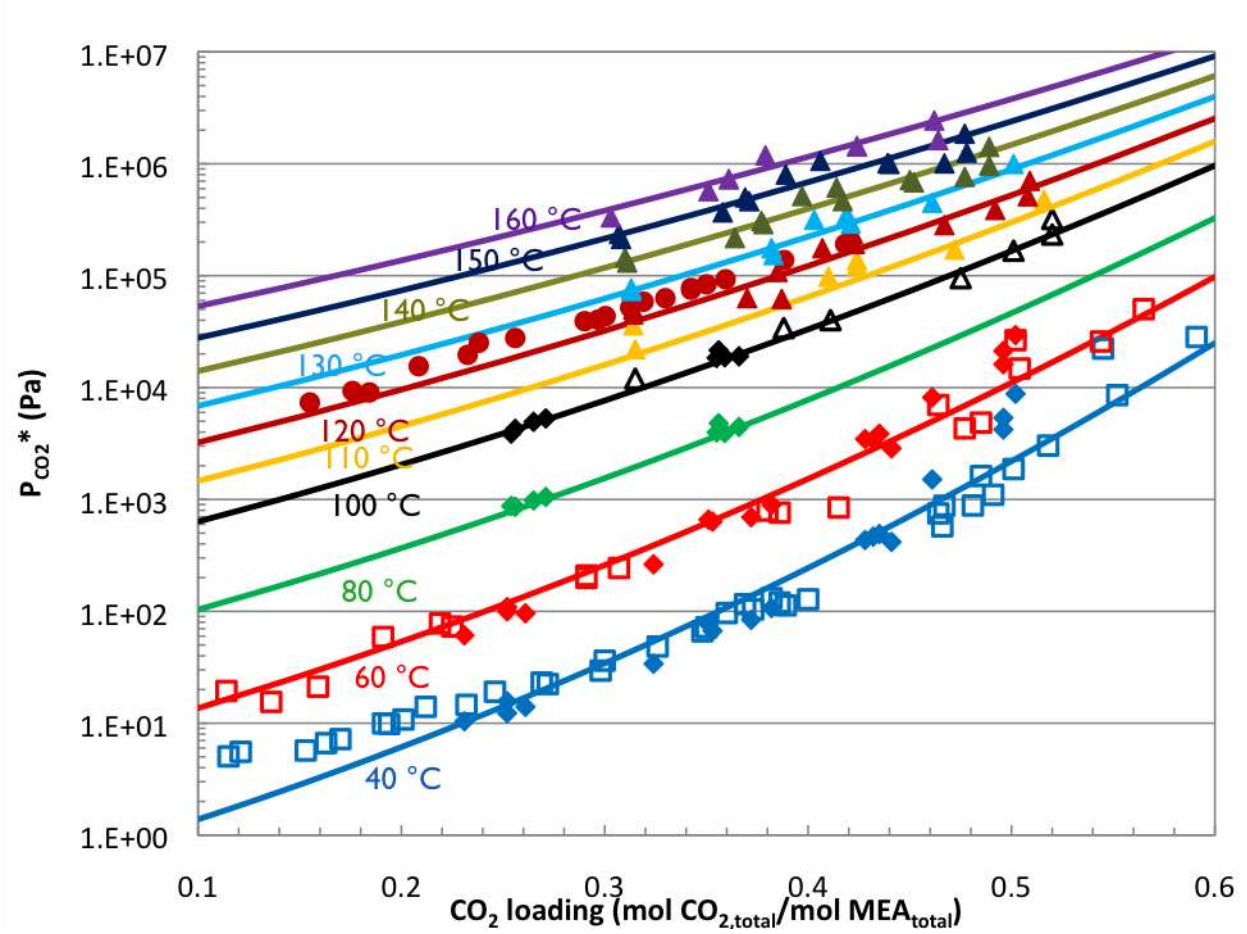

Figure 2: CO_2 solubility of monoethanolamine (MEA). Experimnetal data: □ - Hillard (2005); ♦-Dugas (2009); Δ-Xu (2011); ●-Ma'mun (2008). Semi-empirical model result: lines (Xu, 2011).

The other category of CO_2 VLE models is rigorous thermodynamic modeling. These models typically use an existing thermodynamic framework, such as electrolyte-NRTL in Aspen Plus®. These are complex models, which represent the physical system with first principle thermodynamic relationships, such as activity-based chemical equilibrium. However, rigorous thermodynamic modeling is significantly more involved in terms of model development as well as data requirement. In addition to the CO_2 VLE data, other thermodynamic data of the amine/H2O system is typically required.

The objective of this work is to develop a CO_2 VLE model with characteristics between the two common categories. First, this model needs to be able to fit experimental P_{CO2}^* data well. Second, only P_{CO2}^* data will be used to regress the model parameters which define the physical system. These parameters should represent some fundamental properties of the amine, which dictates the interaction between the amine and CO_2. Third, the model needs to predict liquid phase speciation across the relevant CO_2 loading range, which is to be achieved by using physically representative model equations.

Simplified Stoichiometric Model

Stoichiometric model equations

The physical solubility of a gas over a liquid can be approximated using Henry's law (Equation 3):

$$P_{CO_2}{}^{*} = H_{CO_2} \cdot \gamma_{CO_2} \cdot x_{CO_2} \tag{3}$$

The liquid phase non-ideality can be neglected as a first approximation, which eliminates the activity term in Equation 3.

For primary and secondary unhindered amines containing a single amine group, the chemical equilibrium between the species in the liquid phase can be described using the following equations (4–7):

$$K_1 = \frac{x_{Amine^+} \cdot x_{AmineCOO^-}}{x_{Amine}{}^2 \cdot x_{CO_2}} \tag{4}$$

$$K_2 = \frac{x_{Amine^+} \cdot x_{HCO_3^-}}{x_{AmineCOO^-} \cdot x_{H_2O}} \tag{5}$$

$$K_3 = \frac{x_{CO_3{}^{2-}} \cdot x_{H_3O^+}}{x_{HCO_3^-} \cdot x_{H_2O}} \tag{6}$$

$$K_4 = \frac{x_{H_3O^+} \cdot x_{OH^-}}{x_{H_2O}{}^2} \tag{7}$$

Equations 4–7 are concentration-based chemical equilibriums, which neglects liquid-phase non-idealities. The main interactions between amine and CO_2 can be described by Equations 4 and 5. Equation 6 describes the formation and dissociation of carbonate from bicarbonate. While carbonate does form in the CO_2/H_2O/amine system, its concentration is orders of magnitudes lower than other species so this equilibrium can be neglected. Equation 7 describes the protonation of water, which occurs but is not a significant reaction in the CO_2/H_2O/amine system relative to other chemical interactions. Thus, the water protonation equilibrium is neglected in this work.

Further simplifications can be made regarding the major chemical equilibrium described in Equations 4 and 5. First, the physical solubility equation (Equation 3) can be used to substitute x_{CO2} for $P_{CO2}{}^{*}$ in Equation 4, which becomes Equation 8. This combination of Equations 3 and 4 assumes the Henry's constant H_{CO2} does not change with CO_2 concentration in the liquid phase, and the liquid-phase non-ideality is also neglected.

$$K_1{}' = K_1 \cdot \frac{1}{H_{CO_2}} = \frac{x_{Amine^+} \cdot x_{AmineCOO^-}}{x_{Amine}{}^2 \cdot P_{CO_2}{}^{*}} \tag{8}$$

In Equation 5, the mole fraction of water (x_{H2O}) can be assumed to be constant with change in CO_2 concentration in the liquid phase. This is the same assumption used to eliminate the water protonation equilibrium (Equation 7). Thus, the x_{H2O} term can be combined into the equilibrium constant, as shown in Equation 9.

$$K_2{}' = K_2 \cdot x_{H_2O} = \frac{x_{Amine^+} \cdot x_{HCO_3^-}}{x_{AmineCOO^-}} \tag{9}$$

With the stated assumptions and simplifications, the physical solubility equation and four chemical equilibrium reactions can be reduced to two equilibrium expressions. Together with

the total species balance of CO_2 and amine, and a charge balance equation, this produces the model equation which describes the CO_2/H_2O/amine system (Equation 10).

The general model equation can be written for a specific amine. In this work, monoethanolamine (MEA) is the example used, and its system of model equation is shown in Equation 10. MEA is used in this work because there are available experimental results of P_{CO2}^* in MEA measured in published literature from many sources, making it an ideal test case for the model structure.

$$fun = \begin{cases} K_1{}' = \frac{x_{MEA} \cdot x_{MEACOO^-}}{x_{MEA}{}^2 \cdot P_{CO_2}{}^*} \\ K_2{}' = \frac{x_{MEA^+} \cdot x_{HCO_3{}^-}}{x_{MEACOO^-}} \\ x_{MEA^+} + x_{MEACOO^-} + x_{MEA} = x_{MEATotal} \\ x_{MEACOO^-} + x_{HCO_3{}^-} = x_{CO_2Total} \\ x_{MEA^+} = x_{MEACOO^-} + x_{HCO_3{}^-} \end{cases} \quad (10)$$

The equilibrium constants in Equation 10 also vary with temperature, and as a first-order approximation, a simple temperature dependence form is assumed (Equation 11):

$$fun = \begin{cases} K_1{}' = \frac{x_{MEA} \cdot x_{MEACOO^-}}{x_{MEA}{}^2 \cdot P_{CO_2}{}^*} \\ K_2{}' = \frac{x_{MEA^+} \cdot x_{HCO_3{}^-}}{x_{MEACOO^-}} \\ x_{MEA^+} + x_{MEACOO^-} + x_{MEA} = x_{MEATotal} \\ x_{MEACOO^-} + x_{HCO_3{}^-} = x_{CO_2Total} \\ x_{MEA^+} = x_{MEACOO^-} + x_{HCO_3{}^-} \end{cases} \quad (11)$$

For the system of model equations described in Equation 10, the independent (input) variables are the total amines and CO_2 in the liquid, and the temperature of the system (Equation 12):

$$Input = \begin{bmatrix} x_{AminesTotal} \\ x_{CO_2Total} \\ T \end{bmatrix} \quad (12)$$

The model equation (10) includes two specified parameters (four, if temperature dependence is considered). The values of the parameters are to be determined by matching the model results against experimental data.

$$Parameters = \begin{bmatrix} K_1{}' \\ K_2{}' \end{bmatrix} = \begin{bmatrix} c_1 \\ c_2 \\ c_3 \\ c_4 \end{bmatrix} \quad (13)$$

The results (output) of the model equations are the five unknown variables, which are the liquid-phase concentration of the reactants and products of the CO_2/amine reaction and the P_{CO2}^* (Equation 14):

$$Unknown = \begin{bmatrix} x_{MEA} \\ x_{MEA^+} \\ x_{MEACOO^-} \\ x_{HCO_3{}^-} \\ P_{CO_2}{}^* \end{bmatrix} \quad (14)$$

Equation 10 is a system of nonlinear algebraic equations, with variable values that differ by orders of magnitude. This property makes the system of equations a "stiff" system, which is difficult to solve numerically. Thus, the two equilibrium equations in the system are transformed by taking the natural log of both sides, which linearizes the equations and reduce each term in the equations to the same order of magnitude. With this transformation, the final system of model equations is shown in Equation 15.

$$fun = \begin{cases} K_1{}'' = \ln(x_{MEA}) + \ln(x_{MEACOO^-}) - 2 \cdot \ln(x_{MEA}) - \ln(P_{CO_2}{}^*) \\ K_2{}'' = \ln(x_{MEA^+}) + \ln(x_{HCO_3^-}) - ln(x_{MEACOO^-}) \\ x_{MEA^+} + x_{MEACOO^-} + x_{MEA} = x_{MEATotal} \\ x_{MEACOO^-} + x_{HCO_3^-} = x_{CO_2Total} \\ x_{MEA^+} = x_{MEACOO^-} + x_{HCO_3^-} \end{cases} \quad (15)$$

Calculation methods

Nonlinear equation solver

The parameters in the model equation are passed from the parameter regression step (or can be otherwise specified). Next, for one experimental data point, the system of nonlinear equations takes input values that correspond to a set of conditions (temperature, total CO_2 concentration, total amine concentration). Initial guess are required for each unknown variable (Equation 14) in the system of equations, which can then be solved using the 'fsolve' nonlinear equation solver in MATLAB. The solution (output) of the model equations includes the value for P_{CO2}*. This step is to be performed for conditions where experimental data were measured. The calculated P_{CO2}* values are to be compared against the corresponding measured P_{CO2}* which contributes to the total error of the model (Equation 16).

$$error = \sum_{i=1}^{n} \left(\frac{P_{CO_2}{}^*{}_{model} - P_{CO_2}{}^*{}_{data}}{P_{CO_2}{}^*{}_{data}} \right)^2 \quad (16)$$

This calculated error of the model is passed to the parameter regression function in MATLAB, as the objective function of the optimization calculation.

Parameter regression

The specified parameter values in the model equations are then adjusted to minimize the total error of the model (Equation 16). This step is an optimization problem, which can be described as:

$$\min_{(K)} error(K) = \sum_{i=1}^{n} \left(\frac{P_{CO_2}{}^*{}_{model}(K) - P_{CO_2}{}^*{}_{data}}{P_{CO_2}{}^*{}_{data}} \right)^2 \quad (17)$$

This optimization problem is solved using MATLAB function 'fmincon'.

Results and discussion

The convergence of the nonlinear equation solver is highly sensitive to the value of the adjustable parameters, as well as the initial guesses of the unknown variables. The values of the adjustable parameters are passed to the nonlinear solver function from the parameter regression

function. To obtain good initial guesses, the constant temperature model equation (11) was first used to regress data at the same temperatures. The estimated parameter values are summarized in Table 1. The estimation results show the parameter value for the first chemical equilibrium relationship (Equation 8) to have physically significant values over the entire range of temperatures. The parameter representing the second chemical equilibrium (Equation 9) has physically significant values at lower temperatures. At high temperatures, the parameter values for the second equilibrium are associated with large standard deviations, suggesting low physical significance of the parameter.

Table 1: Regressed parameter values at corresponding temperatures

T	$\ln(K_1')$		$\ln(K_2')$	
(◦C)	Value	St.Dev	Value	St.Dev
40	-4.47	0.11	-6.21	0.90
60	-6.41	0.42	-5.86	1.17
80	-8.34	0.68	-5.35	1.50
100	-10.09	0.99	-4.85	1.91
120	-11.72	1.28	-4.34	2.19
140	-13.26	1.85	-3.82	2.93
160	-14.75	2.69	-3.25	3.83

To estimate the temperature dependence parameter values, the parameters in the model equations are substituted into Equation 11. To obtain the best initial guess for the temperature dependent parameters, the parameter values from the constant temperature regressions (Table 1) are used. As shown in Figure 3, the estimated constant temperature parameter values are plotted against its corresponding temperatures, and a clear linear relationship is observed. The coefficients and slopes of the two linear curves in Figure 3 are used as the initial guess for the regression of the temperature dependent parameters.

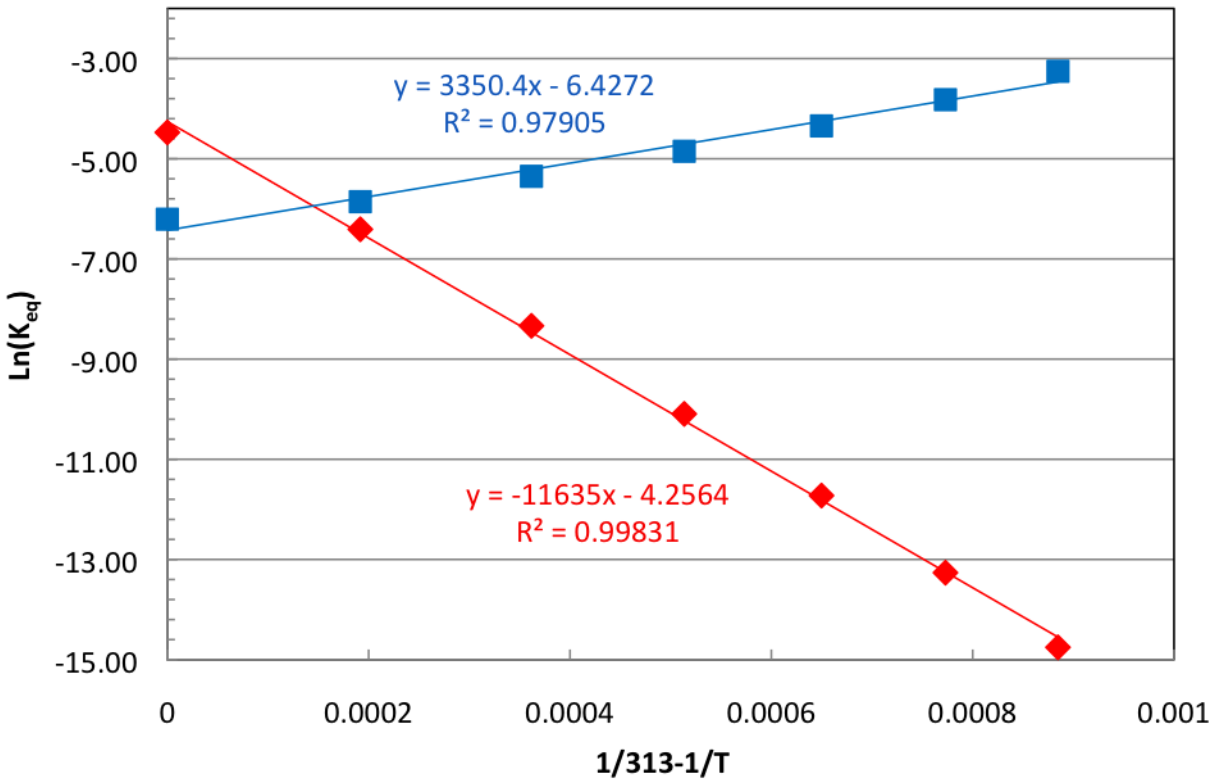

Figure 3: Temperature dependence of the regressed equilibrium constants

Using initial guesses evaluated from the constant temperature parameters, the temperature dependent model equations were used, and the regressed temperature dependent parameter values are summarized in Table 2. The corresponding standard deviation value suggests the parameters are physically significant for the first three parameters.

Table 2: Temperature dependent parameter values

	Parameter values	Standard Deviation
c_1	4.55	0.39
c_2	10.24	2.21
c_3	5.95	1.55
c_4	1.55	4.59

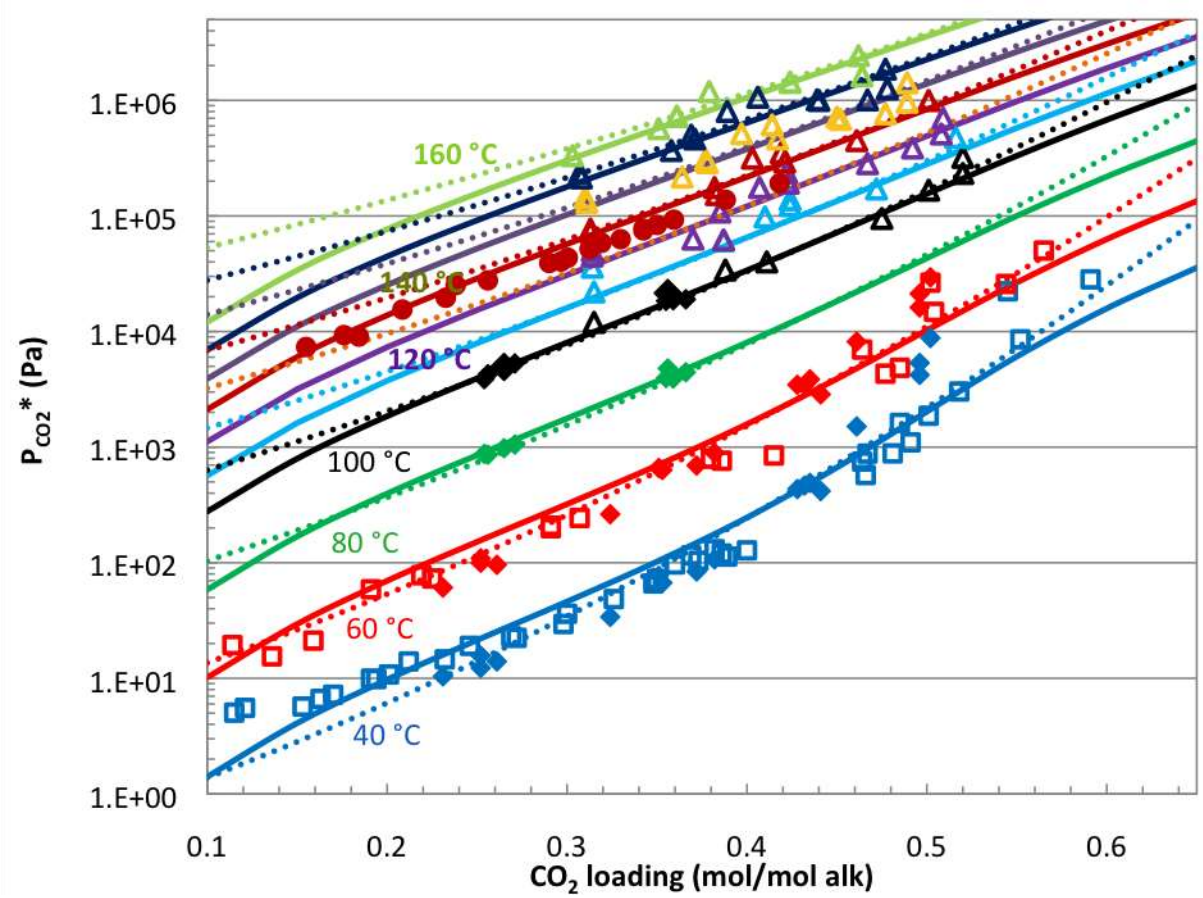

Figure 4: CO_2 VLE between 40–160 °C predicted by the simplified stoichiometric VLE model. "◦": experimental data. Solid lines: stoichiometric model prediction. Dashed lines: semi-empirical model prediction.

The regressed temperature dependent parameters are used in the model equation to predict P_{CO2}*, the result of which is plotted in Figure 4. The simplified speciation model fits the CO_2 loading dependency and temperature dependency of the measured P_{CO2}^{*} well. The VLE curves generated with the simplified speciation model have slightly different slopes from those by the semi-empirical fit, particularly at low and high loadings.

The overall fit of the simplified stoichiometric model to the experimental data can be better seen in a parity plot (Figure 5). The error between the model value and the experimental result shows little systematic trend with temperature or CO_2 loading. The calculated average absolute relative deviation (AARD) can be calculated using Equation 18:

$$AARD = \frac{1}{N}\sum_{i=1}^{N} \frac{\left|P^{*}_{CO_2\,model} - P^{*}_{CO_2\,data}\right|}{P^{*}_{CO_2\,data}}\% \qquad (18)$$

The AARD of the simplified speciation model for CO_2/MEA/H_2O is about 28%.

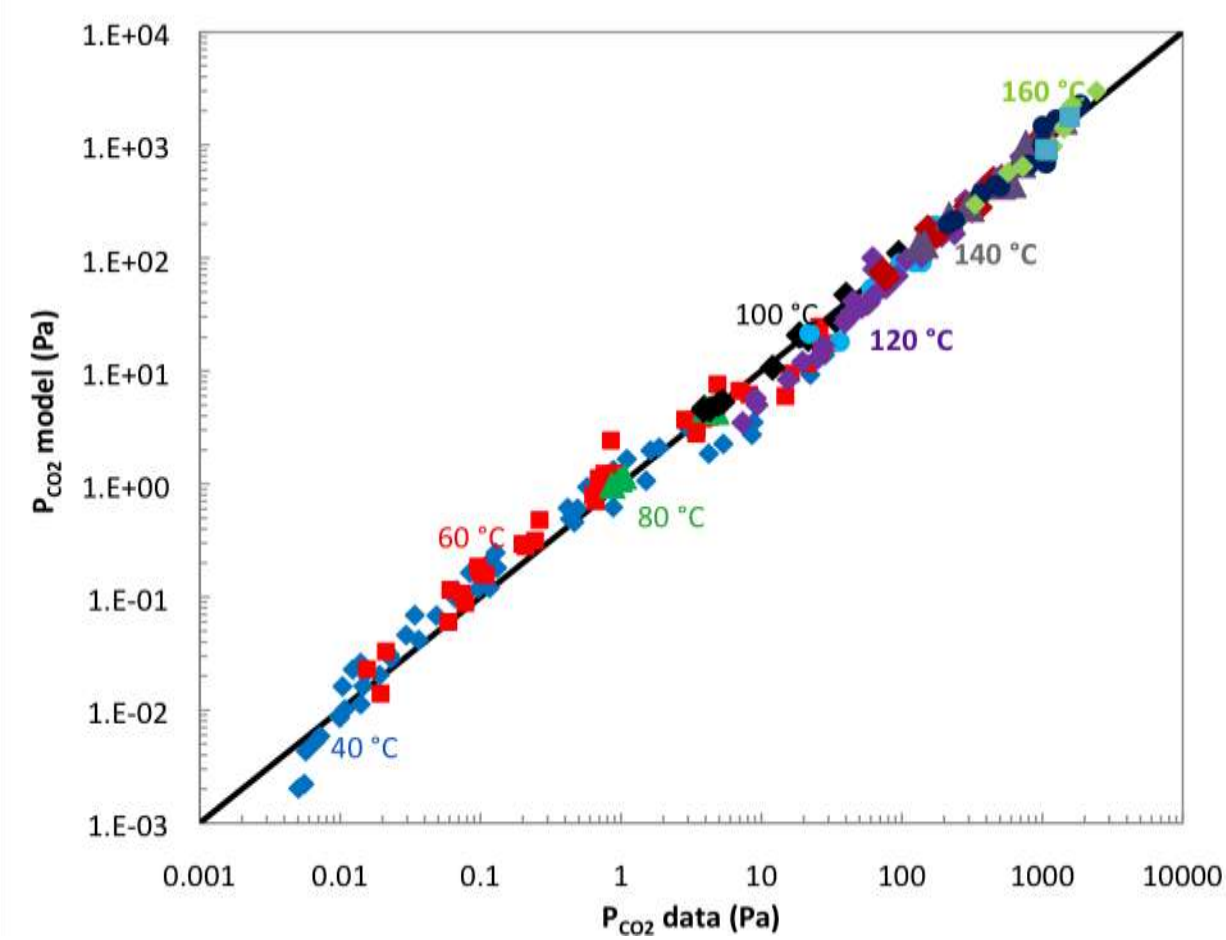

Figure 5: Parity plot of the model calculated P_{CO2}* compared to experimental values

The CO_2 VLE behavior at 40 °C is critical in the modeling and prediction of real process performance. Thus, the quality of the model result (goodness of fit) at 40 °C is important. The CO_2 VLE curves at 40 °C from three different models are compared to experimental data in Figure 6. The curves from the simplified stoichiometric model and the semi-empirical model are similar in shape for most of the loading range; and are both different from the Aspen Plus® result, which better fit the CO_2 loading trend observed in the data near CO_2 loading of 0.5 than the other two models. The better observed fit of the Aspen Plus® curve is likely because this model uses many more parameters than the other two models. The fit of the simplified stoichiometric model can be improved by including additional terms, specifically CO_2 loading dependent terms.

The simplified stoichiometric model can also be used to predict liquid phase speciation. The results at 40 °C are compared to Aspen Plus® results in Figure 7. The overall trend of the stoichiometric model matches Aspen Plus® results well, while differences are observed in the mid-CO_2 loading range, which can be attributed to the assumptions applied to simplify the model equations.

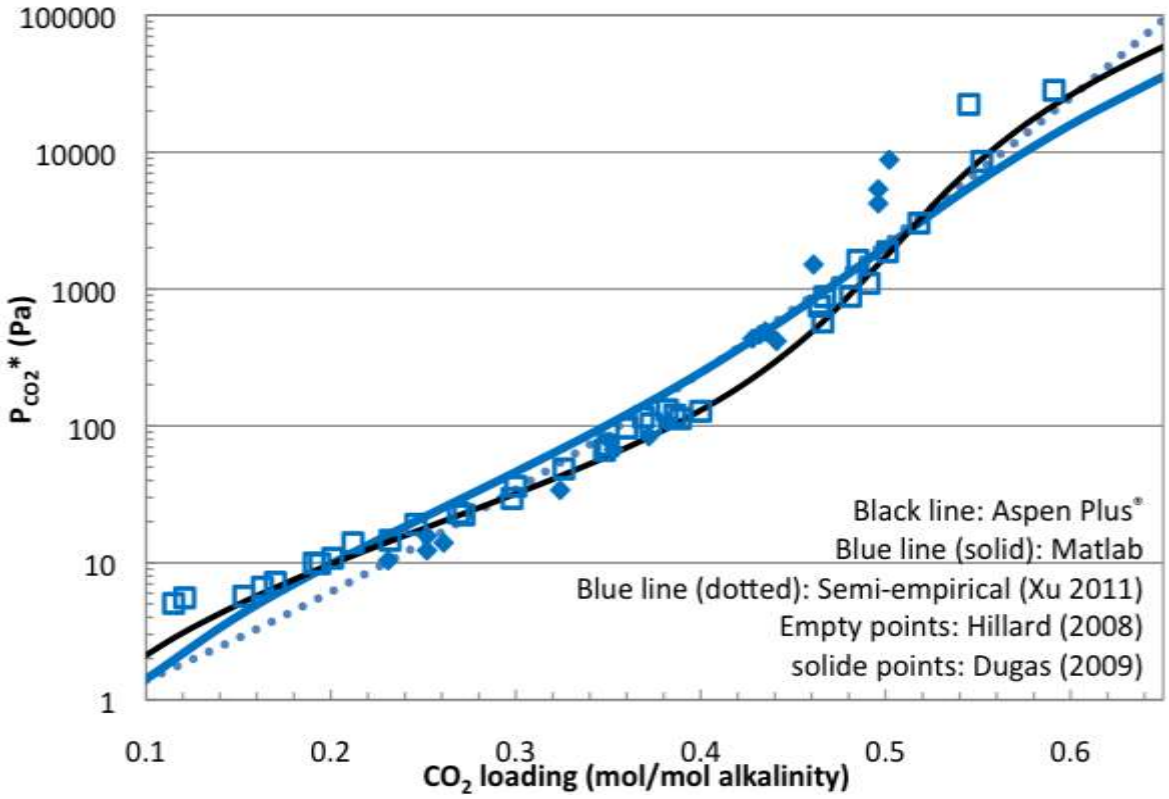

Figure 6: Result comparison of three model methods for CO_2 VLE at 40 °C

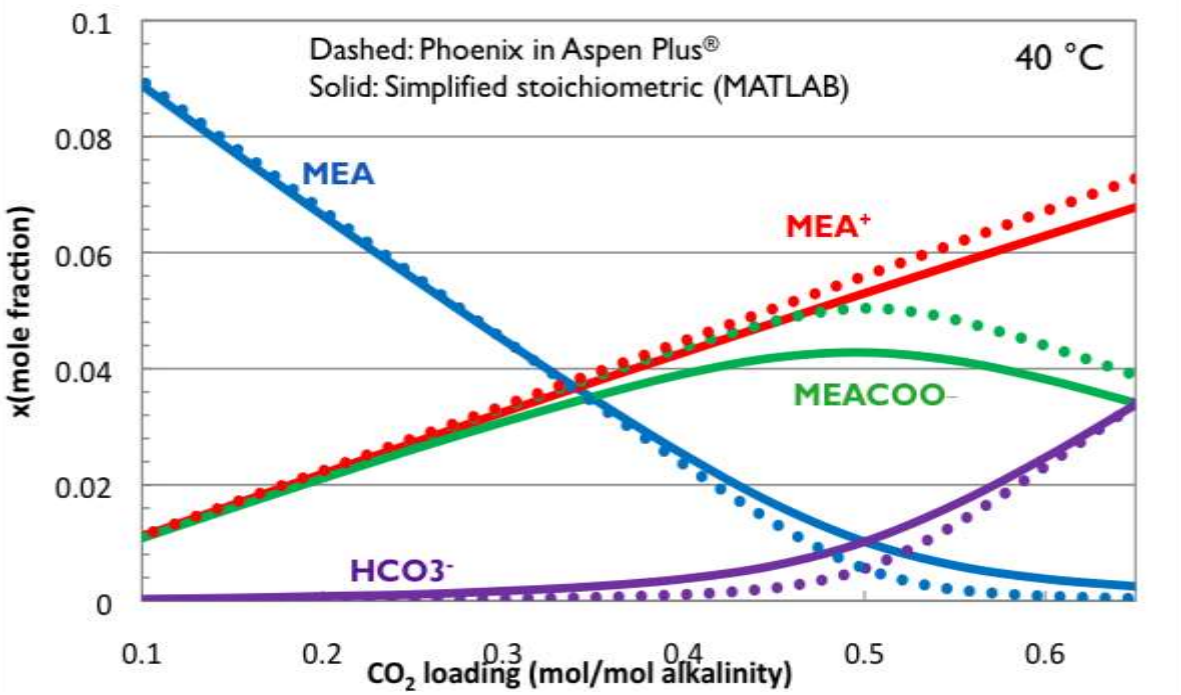

Figure 7: Liquid phase speciation of MEA at 40 °C predicted using the simplified stoichiometric VLE model (solid lines). Dashed lines: Aspen Plus® result using Phoenix V.1.

Table 3: Correlation matrix of the regressed parameters from the simplified stoichiometric model for CO_2/MEA/H_2O system

	c_1	c_2	c_3	c_4
c_1	1	-0.85	-0.92	-0.91
c_2		1	0.67	0.95
c_3			1	0.84
c_4				1

The correlation matrix of the regressed parameters shows a strong dependency between all parameter pairs.

Conclusions

A simplified stoichiometric CO_2 VLE model was tested for CO_2/MEA/H_2O using about 200 experimental data points from literature, which span 40–160 °C and a wide range of MEA concentration and CO_2 loading range. The model successfully fit the experimental data, with an average absolute relative deviation (AARD) of 28%. The CO_2 VLE curves generated by the model are well behaved and physically realistic across all experimental conditions. The liquid phase speciation at 40 °C predicted by the simplified stoichiometric model is well behaved, and shows good agreement in the trend of the curves against Aspen Plus®.

Future Work

The simplified stoichiometric model will be improved by including CO_2 loading dependent terms, in an effort to capture the ionic strength effect of the physical system. This improvement may result in better agreement between the simplified stoichiometric model and Aspen Plus®.

The final version of the simplified stoichiometric model will be used for other primary and secondary amines. The regressed parameters, which represent the equilibrium constants of the CO_2-amine chemical reactions will be used to generalize the performance of the amine with its structure.

References

Dugas RE. "Absorption and desorption rates of carbon dioxide with monoethanolamine and piperazine." *GHGT-9*, Washington D.C. 2008.

Hilliard MD. *A Predictive Thermodynamic Model for an Aqueous Blend of Potassium Carbonate, Piperazine, and Monoethanolamine for Carbon Dioxide Capture from Flue Gas.* The University of Texas at Austin. Ph.D. Dissertation. 2008.

Ma'mum S, Svendsen HF, Hoff KA, Juliussen O. (2006). "Selection of New Absorbents for Carbon Dioxide Capture." Energy Conversion and Management. 48 (1): 251-258.

Xu, Q. *Thermodynamics of CO_2 Loaded Aqueous Amines*. Department of Chemical Engineering, University of Texas at Austin, Ph.D. Dissertation. 2011.

Appendix

The model file included in calls the excel spreadsheet "Specmodeldata", where experimental data is stored. The file will be submitted electronically.

A. Constant temperature models

A.1. Nonlinear equation solver function

```
function [error] = SimpVLETranssolver( k )
% This is a simplified equation set which describes the CO2 VLE into primary
% or secondary (unhindered) amines

% The governing equations are transformed to improve convergence

% The governing equations does NOT consider temperature dependence

% This function takes the equilibrium parameter values and reads the
experimental
% conditions and calculates PCO2
%
%
%
% k=[-4.3354;
%   -6.2696];



%k(1) is the carbamate stability constant
%k(2) MEA protonation constant

% x are the experimental conditions: temperature, total CO2, total amine

T=xlsread('Specmodeldata','Data T','A2:A102');
xaminetotal=xlsread('Specmodeldata','Data T','B2:B102');
```

```
xCO2total=xlsread('Specmodeldata','Data T','C2:C102');
LnPCO2data=xlsread('Specmodeldata','Data T','F2:F102');

x=[T xaminetotal xCO2total];

% y are the outputs of the function VLE
% y(1): xMEA
% y(2): xMEA+
% y(3): xMEACOO-
% y(4): xHCO3-
% y(5): ln(PCO2)

[m,n]=size(T);

for i=1:m
    xi=x(i,:);

    VLE=@(y)[log(y(3))+log(y(2))-y(5)-2*log((y(1)))-k(1)
             log(y(4))+log(y(1))-log(y(3))-k(2)
             y(1)+y(2)+y(3)-xi(2)
             y(2)-y(3)-y(4)
             y(3)+y(4)-xi(3)];

    yo=[xi(2)-xi(3)*1.5
        xi(3)
        xi(3)
        xi(3)/10
        LnPCO2data(i)];
    [yi,fval]=fsolve(VLE,yo);
    LnPCO2calc(i)=yi(5);
    HCO3(i)=yi(4);


    %Y(i,:)=[yi(1) yi(2) yi(3) yi(4) yi(5)/1000];
    %F(i,:)=fval
end
```

```
CO2ldg=xCO2total./xaminetotal;
error=sum(((LnPCO2data-LnPCO2calc')./LnPCO2data).^2);

%plot(CO2ldg,HCO3)
%plot(CO2ldg,LnPCO2data,CO2ldg,LnPCO2calc')
```

A.2. Parameter regression m.file

```
% this script performs nonlinear parameter regression for CO2 VLE models
% this script calls the nonlinear solver function "SimpVLETranssolver"

clear all

ko=[-10;
    -4];

A=[];
b=[];
Aeq=[];
beq=[];

lb=[-30
    -20];
ub=[-1
    -1];


options = optimset('Disp','iter');
[k,error,EXITFLAG,OUTPUT,LAMBDA,GRAD,HESSIAN] =
fmincon(@SimpVLETranssolver,ko,A,b,Aeq,beq,lb,ub,[],options)

covar1=inv(HESSIAN)
Stdev1=sqrt(diag(covar1))
cor1=corr(covar1)
```

B. Temperature dependent model

B.1. Nonlinear equation solver function

```
function [error] = SimpVLEsolverT( c )
% This is a simplified equation set which describes the CO2 VLE into primary
% or secondary (unhindered) amines

% This function is to be used together with a parameter regression code
% ParamRegTransT

% The governing chemical equilibrium equations are transformed in order to
% improve convergence of the nonlinear solver

% The

% This function takes the equilibrium parameter values and reads the
experimental
% conditions and calculates PCO2 and liquid phase species (at the
% experimental conditions)

%
% c = [4.0224;
%     1.1201;
%     2.4212;
%     2.7189];

%k(1) is the carbamate stability constant
%k(2) MEA protonation constant

% x are the experimental conditions: temperature, total CO2, total amine

T=xlsread('Specmodeldata','Raw Data','A2:A198');
xaminetotal=xlsread('Specmodeldata','Raw Data','B2:B198');
```

```
xCO2total=xlsread('Specmodeldata','Raw Data','C2:C198');
LnPCO2data=xlsread('Specmodeldata','Raw Data','F2:F198');



size(T);
size(xaminetotal);
size(xCO2total);

x=[T xaminetotal xCO2total];

% y are the outputs of the function VLE
% y(1): xMEA
% y(2): xMEA+
% y(3): xMEACOO-
% y(4): xHCO3-
% y(5): ln(PCO2)

[m,n]=size(T);

for i=1:m
    xi=x(i,:);

    VLE=@(y)[log(y(3))+log(y(2))-y(5)-2*log(y(1))+c(1)*10-c(2)/T(i)*10000
             log(y(4))+log(y(1))-log(y(3))-c(3)*0.1+c(4)/T(i)*1000
             y(1)+y(2)+y(3)-xi(2)
             y(2)-y(3)-y(4)
             y(3)+y(4)-xi(3)];

    yo=[xi(2)-xi(3)*1.5
        xi(3)
        xi(3)
        xi(3)/10
        LnPCO2data(i)];

    [yi,fval]=fsolve(VLE,yo);
    LnPCO2calc(i)=yi(5);
```

```
%      xMEA(i)=yi(1);
%      xMEAp(i)=yi(2);
%      xMEACOO(i)=yi(3);
%      xHCO3(i)=yi(4);
%
    %Y(i,:)=[yi(1) yi(2) yi(3) yi(4) yi(5)/1000];
    %F(i,:)=fval
end
%CO2ldg=xCO2total(1:12)./xaminetotal(1:12);


%LnCalc=LnPCO2calc';


%plot(CO2ldg,LnCalc,CO2ldg,LnPCO2data)


%plot(CO2ldg,LnCalc(1:12),CO2ldg,LnCalc(13:24),CO2ldg,LnCalc(25:36),CO2ldg,Ln
Calc(37:48),CO2ldg,LnPCO2data(1:12),CO2ldg,LnPCO2data(13:24),CO2ldg,LnPCO2dat
a(25:36),CO2ldg,LnPCO2data(37:48))


%plot(CO2ldg,xMEA(1:12)',CO2ldg,xMEAp(1:12)',CO2ldg,xMEACOO(1:12)',CO2ldg,xHC
O3(1:12)')
error=sum(((LnPCO2data-LnPCO2calc')./LnPCO2data).^2);
```

B.2. Parameter estimation m.file

```
% this script performs nonlinear parameter regression for CO2 VLE models
% this script reads experimental data

clear all

co = [3.7692;
    1.0383;
    2;
    1.9143];
A=[];
b=[];
```

```
Aeq=[];
beq=[];


lb=[1
    0.5
    0.1
    0.5];
ub=[10
    5
    50
    5];



options = optimset('Disp','iter');
[c,error,EXITFLAG,OUTPUT,LAMBDA,GRAD,HESSIAN] =
fmincon(@SimpVLEsolverT,co,A,b,Aeq,beq,lb,ub,[],options)
%%
covar=inv(HESSIAN)
Stdev=sqrt(diag(covar))
c_1=corr(covar)
end
```

Absorber Intercooling Evaluation

Quarterly Report for April 1 – June 30, 2014

by Darshan Sachde

Supported by the Texas Carbon Management Program

McKetta Department of Chemical Engineering

The University of Texas at Austin

July 31, 2014

Abstract

The evaluation of intercooling benefits was expanded to include the packing requirements to approach maximum solvent capacity. Previously, minimum solvent rate analysis (L_{MIN}) identified conditions where intercooling would provide significant capacity (energy performance) benefits. Three flue gas sources were included for the evaluation with 8 m PZ: natural gas combined cycle (NGCC, 4.1% CO_2), coal-fired boiler (13.5% CO_2), and steel blast furnace (27.4% CO_2). Analysis of packing requirements for the NGCC and coal-fired boiler cases were completed to determine whether additional packing benefits were derived from intercooling, identify conditions where novel intercooling could be used to achieve packing benefits, and identify conditions where intercooling is not required (minimal packing and capacity benefits).

The results for the NGCC case showed that intercooling is not required at "over-stripped" conditions (0.15–0.21 mol CO_2/mol alkalinity) due to the large driving forces present throughout the absorber. Moderate packing reduction (0–25%) could be achieved with an intercooled absorber, but is not likely to justify added costs and complexity. The coal-fired boiler showed nearly identical behavior with no capacity benefits and minimal packing benefits (0–30%).

In intermediate to high loading ranges (0.22–0.30 mol CO_2/mol alkalinity), the NGCC application provides opportunities for novel intercooling. In this range, solvent capacity benefits (doubling of solvent capacity) over in-and-out intercooling may be possible and packing required to approach maximum capacity can also be reduced (25–50%).

The intermediate loading range for coal (0.19–0.30 mol CO_2/mol alkalinity) is best designed with in-and-out intercooling. The solvent rate in coal application is relatively large and makes in-and-out intercooling more effective in addressing temperature limitations. Minimal capacity improvement (–25%) and packing reduction (0–30%) can be achieved over in-and-out intercooling in this region.

Finally, for the high loading region for coal (>0.30 mol CO_2/mol alkalinity), intercooling is not required. The L/G in this region is high enough to moderate temperature effects on driving forces, limiting the capacity (5%) and packing (15%) improvements attainable with intercooling.

Introduction

Previous work used the minimum solvent rate (or maximum rich loading) to evaluate potential benefits of intercooling for a wide range of lean loadings for three CO_2 flue gas feed concentrations representative of potential capture applications (NGCC, coal-fired boiler, steel blast furnace). This analysis isolated conditions where intercooling could provide capacity (energy performance) benefits, but did not consider the packing required to approach maximum capacity of the solvent. The current work expands on the previous analysis by evaluating the packing requirement for several representative cases from the previous work. The detailed conditions for the analysis are summarized in subsequent sections. The goal of the analysis is to determine if intercooling can provide mass transfer benefits (reduced packing) in the approach to maximum capacity and to identify conditions where novel designs may be able to provide packing reduction. By considering capacity benefits and packing requirements, optimal absorber designs and operating conditions can be identified for all of the aforementioned capture applications.

Evaluating Intercooling Configurations: Approach to Maximum Capacity

In previous work, the minimum solvent flow rate (L_{MIN}) was used to assess potential benefits of intercooling configurations (Rochelle et al., 2014). L_{MIN} for any absorption process can be defined as the solvent rate required to achieve a specific solute removal (or specific gas inlet and outlet compositions) for a given inlet solvent composition (loading) with infinite mass transfer area available. L_{MIN} also corresponds to the maximum rich loading (maximum solvent capacity) achievable and serves as a proxy for the best energy performance that can be achieved with the design and operating conditions of a given absorber. Table 1 summarizes the conditions for the expanded analysis that was conducted using 8 m PZ with 90% CO_2 removal. The current work will focus on NGCC and coal-fired boiler results.

Table 1: Summary of L_{MIN} Analysis Design Conditions

Flue Gas Source	**CO_2** (mol%)	**Lean Loading** mols CO_2/mols alk.
Natural Gas Combined Cycle (NGCC)	4.1%	0.15–0.30
Coal-Fired Boiler	13.5%	0.15–0.36
Steel Blast Furnace	27.4%	0.1– 0.39

The following absorber configurations were modeled for the operating conditions outlined in Table 1:

1) Adiabatic (no intercooling);
2) In-and-out intercooling;
3) Isothermal absorber (operated at T = 40 °C).

For each operating condition, the isothermal absorber represents the best possible performance (lowest L_{MIN}) and the adiabatic absorber represents the worst case performance (highest L_{MIN}). Intercooled absorbers will fall between these limiting cases. The ratio of the adiabatic L_{MIN} to the isothermal L_{MIN} at each condition can serve as a screening tool for the conditions where intercooling will be beneficial for energy performance. High values of the preceding ratio

indicate large potential benefits of intercooling. A ratio equal to (or approaching) unity indicates that the benefits of intercooling are negligible or non-existent. Figures 1 and 2 summarize the L_{MIN} results for the NGCC and coal-fired boiler cases. Tables 2 and 3 provide the corresponding raw data for the minimum solvent rate analysis.

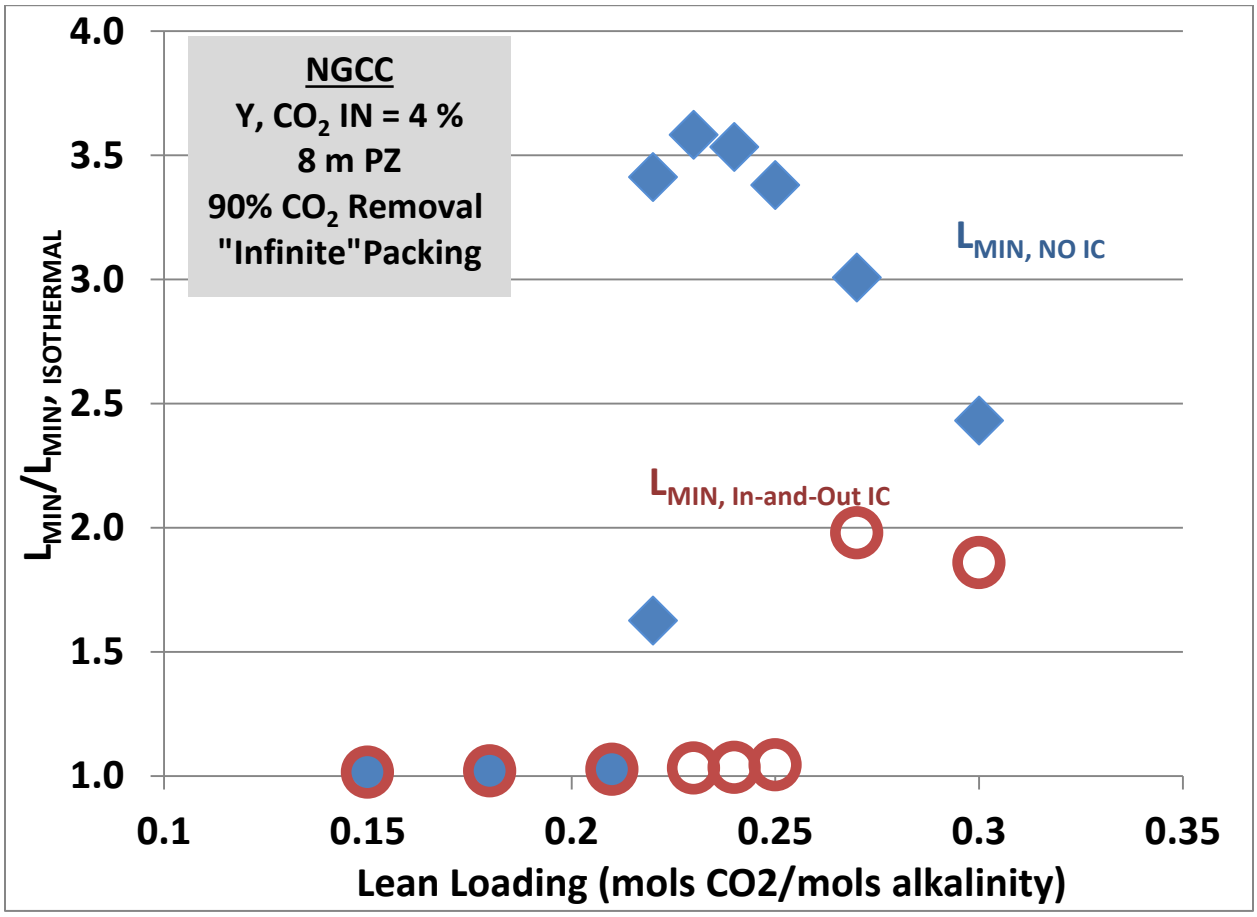

Figure 1: Ratio of the minimum solvent rate ("infinite" packing) for an adiabatic absorber (no intercooling) and intercooled absorber (in-and-out intercooling) to an isothermal absorber (40 °C) for 90% CO_2 capture from a natural gas combined cycle power plant (4.1% CO_2) using 8 m PZ.

Table 2: Minimum Solvent Rate (L_{MIN}) Data for NGCC Case

NGCC (4.1% CO_2, Gas Rate = 31.2 kmol/s)			
Lean Loading	L_{MIN} (kmol/s)		
mol CO_2/mol alk.	Isothermal	In-and-Out	Adiabatic
0.15	18.7	18.9	19.0
0.18	21.3	21.7	21.8
0.21	24.7	25.4	25.4
0.22	26.2	N/A	42.5
0.22	26.2	N/A	89.2
0.23	27.7	28.6	99.4
0.24	29.5	30.5	104.4
0.25	31.6	33.0	106.7
0.27	36.7	72.5	110.2
0.30	48.3	89.7	117.3

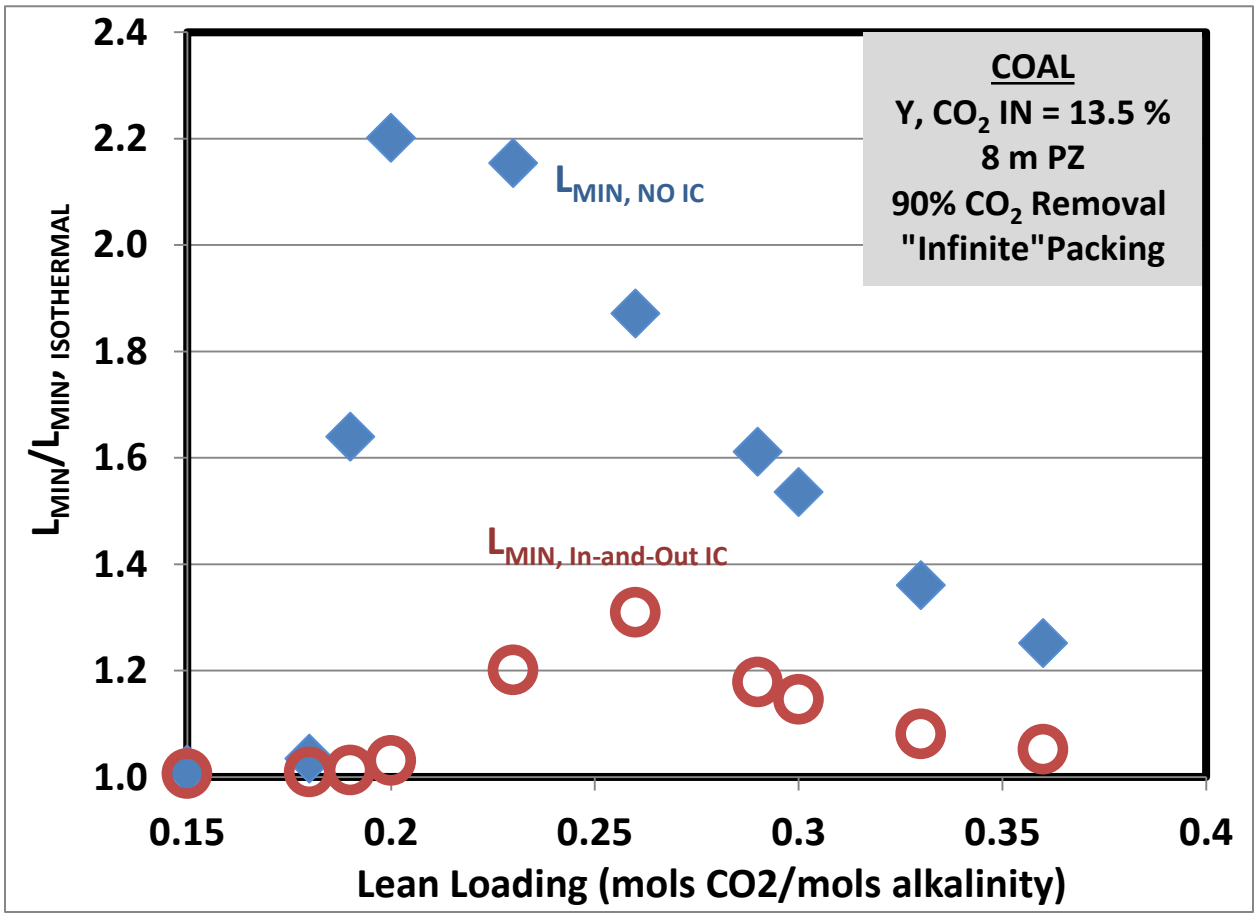

Figure 2: Ratio of the minimum solvent rate ("infinite" packing) for an adiabatic absorber (no intercooling) and intercooled absorber (in-and-out intercooling) to an isothermal absorber (40 °C) for 90% CO_2 capture from a coal-fired boiler (13.5% CO_2) using 8 m PZ.

Table 3: Minimum Solvent Rate (L_{MIN}) Data for Coal-Fired Boiler Case

Coal-Fired Boiler (13.5% CO_2, Gas Rate = 18.8 kmol/s)			
Lean Loading	L_{MIN} (kmol/s)		
mol CO_2/mol alk.	Isothermal	In-and-Out	Adiabatic
0.15	36.5	36.7	37.0
0.18	41.5	41.8	42.9
0.19	42.8	43.4	70.2
0.20	44.7	46.1	98.5
0.23	51.7	62.1	111.4
0.26	61.3	80.3	114.7
0.29	75.3	88.7	121.2
0.3	81.4	93.3	125.0
0.33	108.0	116.7	146.9
0.36	160.2	168.6	200.6

The intercooled absorber provides capacity benefits (denoted by lower ratios) compared to the adiabatic absorber for both cases across the entire loading range evaluated. Additionally, there is a range of loadings where in-and-out intercooling does not provide maximum capacity benefits (ratio > 1) and a novel design may be introduced to achieve additional capacity benefits. To evaluate the packing requirements necessary to achieve the capacity benefits, representative loadings were selected for further evaluation (see Table 4). These loadings can be broadly classified as follows:

1) "Over-stripped" Loading Range: Low lean loadings (large driving forces) mean intercooling is not required to provide capacity benefits in this region.
2) Simple Intercooling Range: Simple in-and-out intercooling provides maximum solvent capacity benefits.
3) Intermediate Loading Range: Simple intercooling does not achieve maximum capacity benefits in this range.
4) High L/G Range: Capacity benefits of intercooling diminish at high loadings due to high solvent rate limiting temperature effects in the absorber. This region only exists for coal-fired boiler.

Table 4: Summary of Loading Ranges and Representative Loadings used In Packing Evaluation

Loading Range	Loading Range (Representative Loading) mol CO_2/mol alkalinity	
	Natural Gas Combined Cycle (NGCC)	Coal-Fired Boiler
"Over-Stripped"	0.15–0.21 (0.18)	0.15–0.18 (0.15)
Simple Intercooling	0.22–0.26 (0.25)	0.19–0.21 (0.20)
Intermediate	> 0.26 (0.30)	0.22–0.30 (0.26)
High Solvent Rate	N/A	> 0.30 (0.36)

The packing requirement results for each case in Table 4 are summarized in the subsequent sections.

"Over-Stripped" Loading Range

Figures 3 and 4 provide the packing requirement as a function of solvent rate for the NGCC and coal cases. In each case, the curves approach a horizontal asymptote as the packing area is increased. This limit is the L_{MIN} as used in the solvent capacity analysis in Figures 1 and 2.

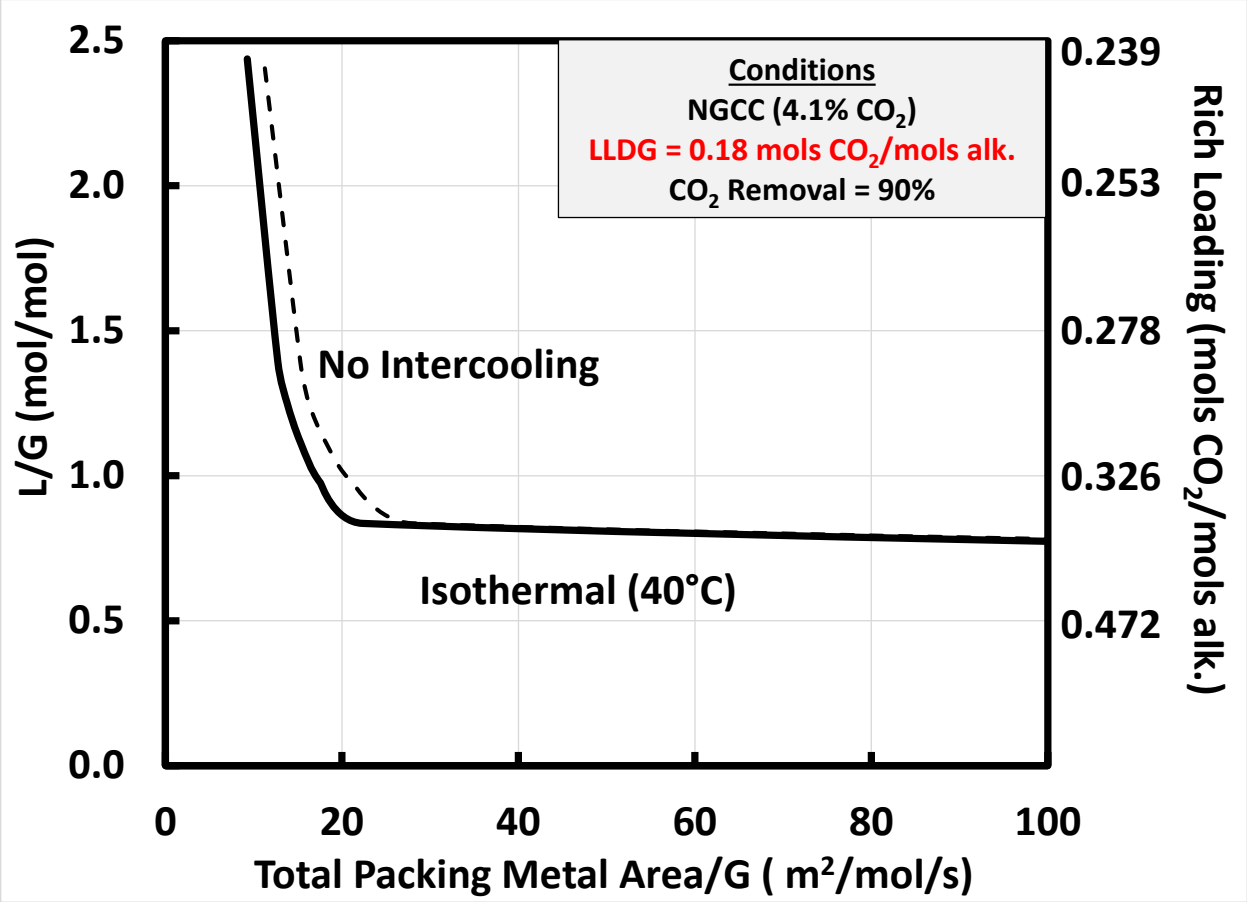

Figure 3: Design curves for adiabatic (dashed) and isothermal (solid) operation for NGCC application (4.1% CO_2) in the "over-stripped" loading range (0.18 mol CO_2/mol alkalinity). Each curve represents the packing requirement to achieve 90% CO_2 removal for a given liquid to gas ratio (L/G). For each point on the curve, the lean loading, removal, and solvent rates are fixed, so a unique rich loading exists (secondary y-axis).

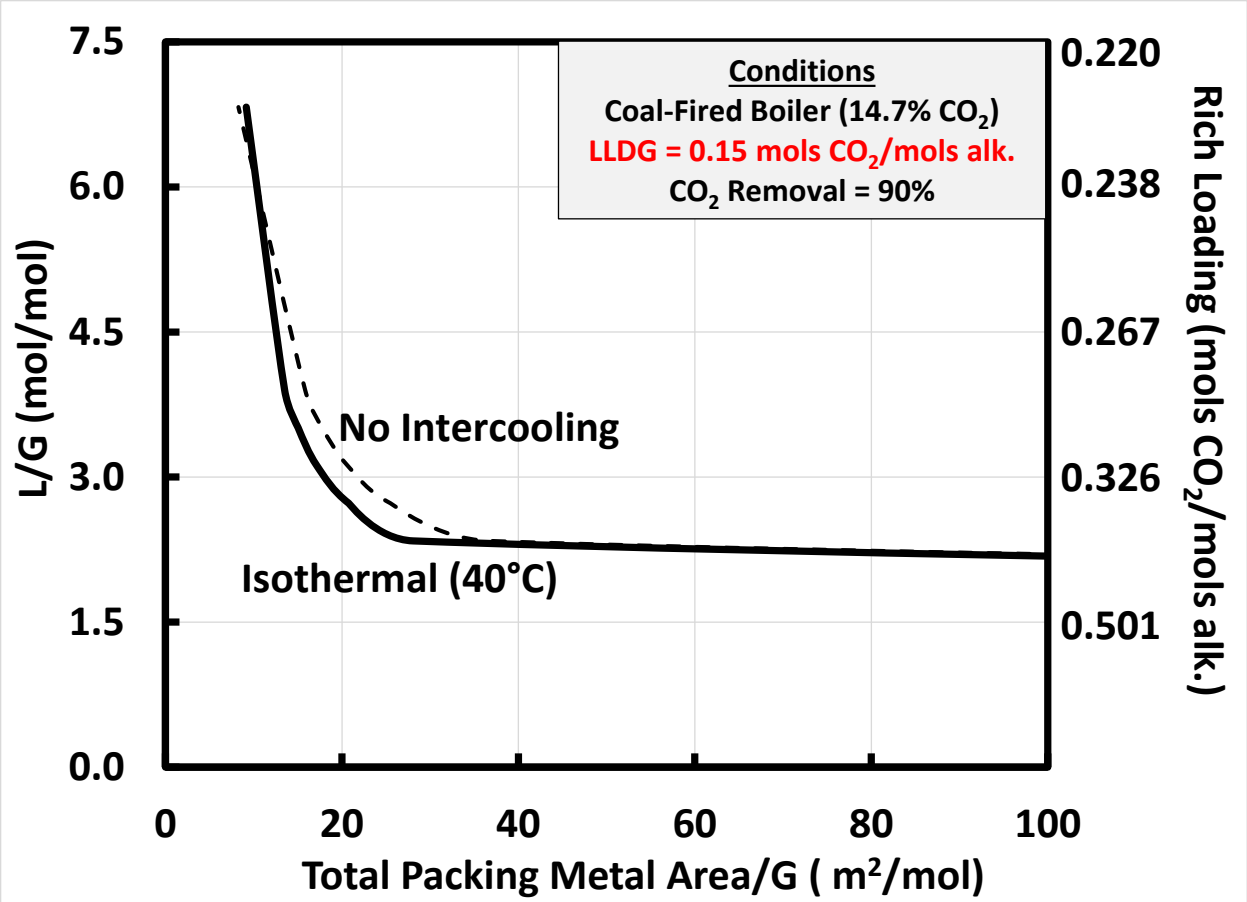

Figure 4: Design curves for adiabatic (dashed) and isothermal (solid) operation for coal-fired boiler application (14.7% CO_2) in the "over-stripped" loading range (0.15 mol CO_2/mol alkalinity). Each curve represents the packing requirement to achieve 90% CO_2 removal for a given liquid to gas ratio (L/G). For each point on the curve, the lean loading, removal, and solvent rates are fixed, so a unique rich loading exists (secondary y-axis).

For both applications, the adiabatic and isothermal curves nearly overlap. This indicates that there is minimal opportunity for packing or capacity benefits via intercooling. The large driving forces at the over-stripped condition combined with a relatively low L/G ratio (gas carrying heat out of the column) mitigate temperature-related equilibrium effects in the absorber. To quantify the packing benefits, the packing requirement for the adiabatic absorber can be compared to the requirement for the isothermal ("perfect" intercooling) absorber at each L/G across the operating range to identify the maximum packing reduction of intercooling. The maximum packing reduction for the NGCC case is 25% and for the coal case is 30% and occurs near the L_{MIN} asymptote in both cases. Therefore, the small packing reduction without accompanying capacity benefits is unlikely to justify implementation of intercooling at the over-stripped condition.

Simple Intercooling Loading Range

Figures 5 and 6 provide the packing requirements for loading conditions where simple in-and-out intercooling can achieve maximum solvent capacity.

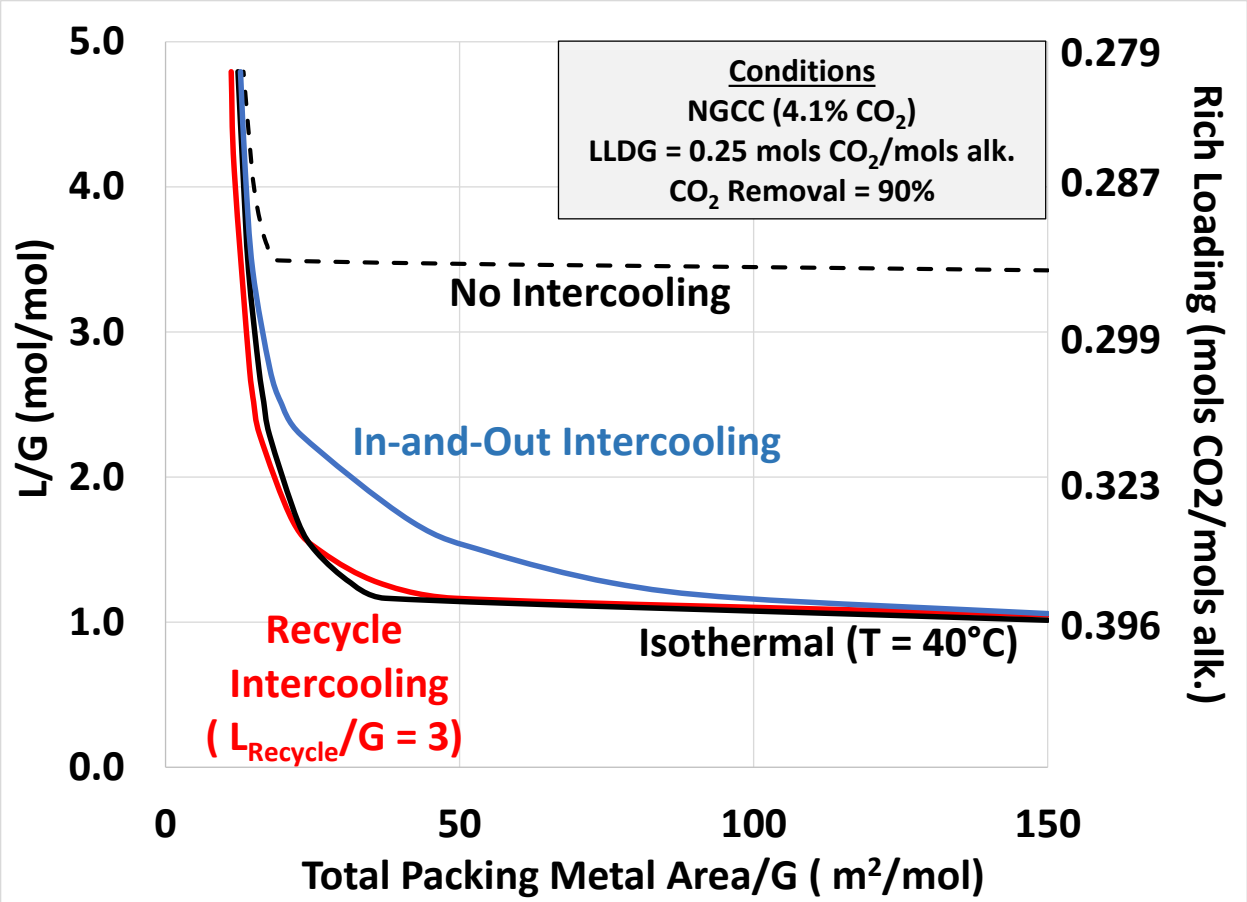

Figure 5: Design curves for adiabatic (dashed), in-and-out intercooling (Blue), recycle intercooling at $L_{Recycle}/G = 3$ (Red) and isothermal (solid) operation for NGCC application (4.1% CO_2) in the simple intercooling loading range (0.25 mol CO_2/mol alkalinity). Each curve represents the packing requirement to achieve 90% CO_2 removal for a given liquid to gas ratio (L/G). For each point on the curve, the lean loading, removal, and solvent rates are fixed, so a unique rich loading exists (secondary y-axis).

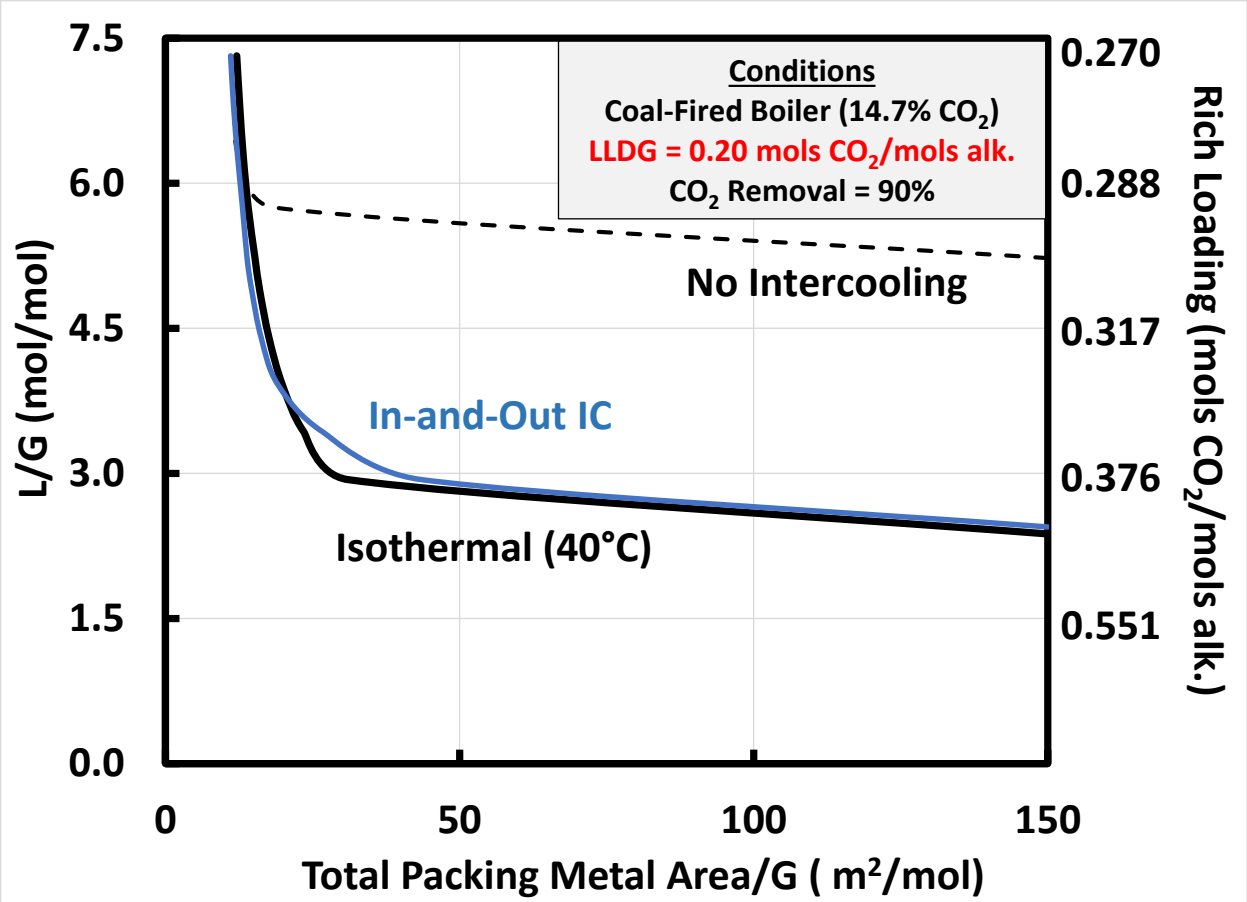

Figure 6: Design curves for adiabatic (dashed), in-and-out intercooling (Blue), and isothermal (solid) operation for coal-fired boiler application (14.7% CO_2) in the simple intercooling loading range (0.20 mol CO_2/mol alkalinity). Each curve represents the packing requirement to achieve 90% CO_2 removal for a given liquid to gas ratio (L/G). For each point on the curve, the lean loading, removal, and solvent rates are fixed, so a unique rich loading exists (secondary y-axis).

In this region, intercooling is necessary due to the large capacity benefits achieved over the adiabatic absorber. However, the intercooling design should also minimize the packing requirement to achieve the capacity benefit. For the NGCC case, simple in-and-out intercooling can achieve the maximum solvent capacity, but the slope of this curve in Figure 5 is relatively flat in its approach to L_{MIN}. The slope of the curve reflects the packing requirement for an incremental improvement in capacity (reduction in solvent rate); a flat curve indicates a large packing requirement to achieve capacity improvement. Therefore, a recycle intercooling design introduced in previous work (Rochelle et al., 2013) was included to achieve packing reduction while maintaining capacity benefits. The recycle intercooling design reduced the packing requirement by as much as 52% over the simple intercooling design to achieve the same solvent capacity.

In the coal-fired boiler case (Figure 6), in-and-out intercooling tracks closely to the isothermal curve over the entire range of conditions. The relatively large L/G ratios (solvent carries more of the heat) for the coal application make in-and-out intercooling more effective for addressing

temperature-related constraints. The maximum packing reduction achieved with isothermal operation in place of in-and-out intercooling is 29%, and is non-existent over most operating conditions. Therefore, simple intercooling is recommended in the operating range around 0.20 mol CO_2/ mol alkalinity for coal applications.

Intermediate Loading Range

Figures 7 and 8 provide the packing requirements for loading conditions where simple in-and-out intercooling is not sufficient to achieve maximum capacity of the solvent.

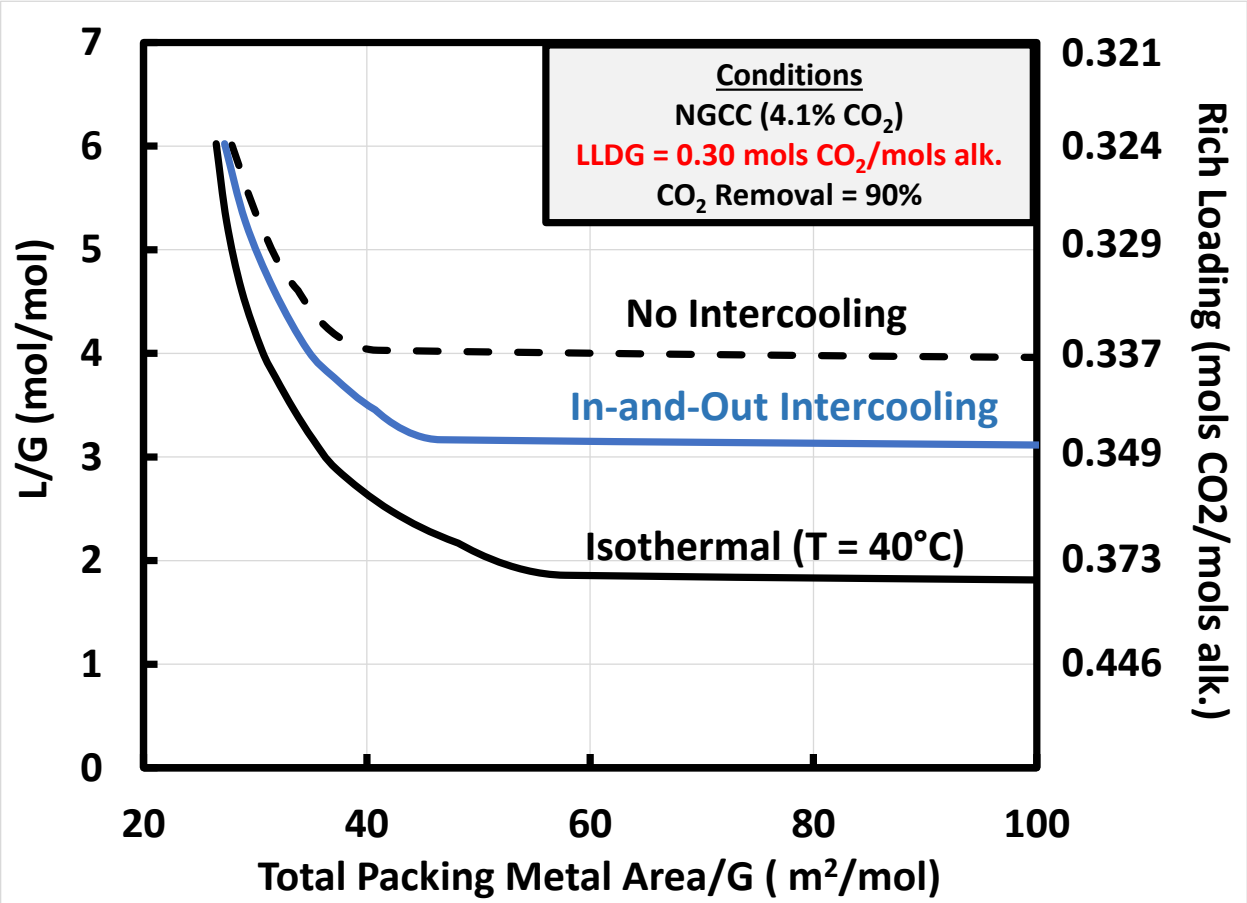

Figure 7: Design curves for adiabatic (dashed), in-and-out intercooling (Blue), and isothermal (solid) operation for NGCC application (4.1% CO_2) in the intermediate loading range (0.30 mol CO_2/mol alkalinity). Each curve represents the packing requirement to achieve 90% CO_2 removal for a given liquid to gas ratio (L/G). For each point on the curve, the lean loading, removal, and solvent rates are fixed, so a unique rich loading exists (secondary y-axis).

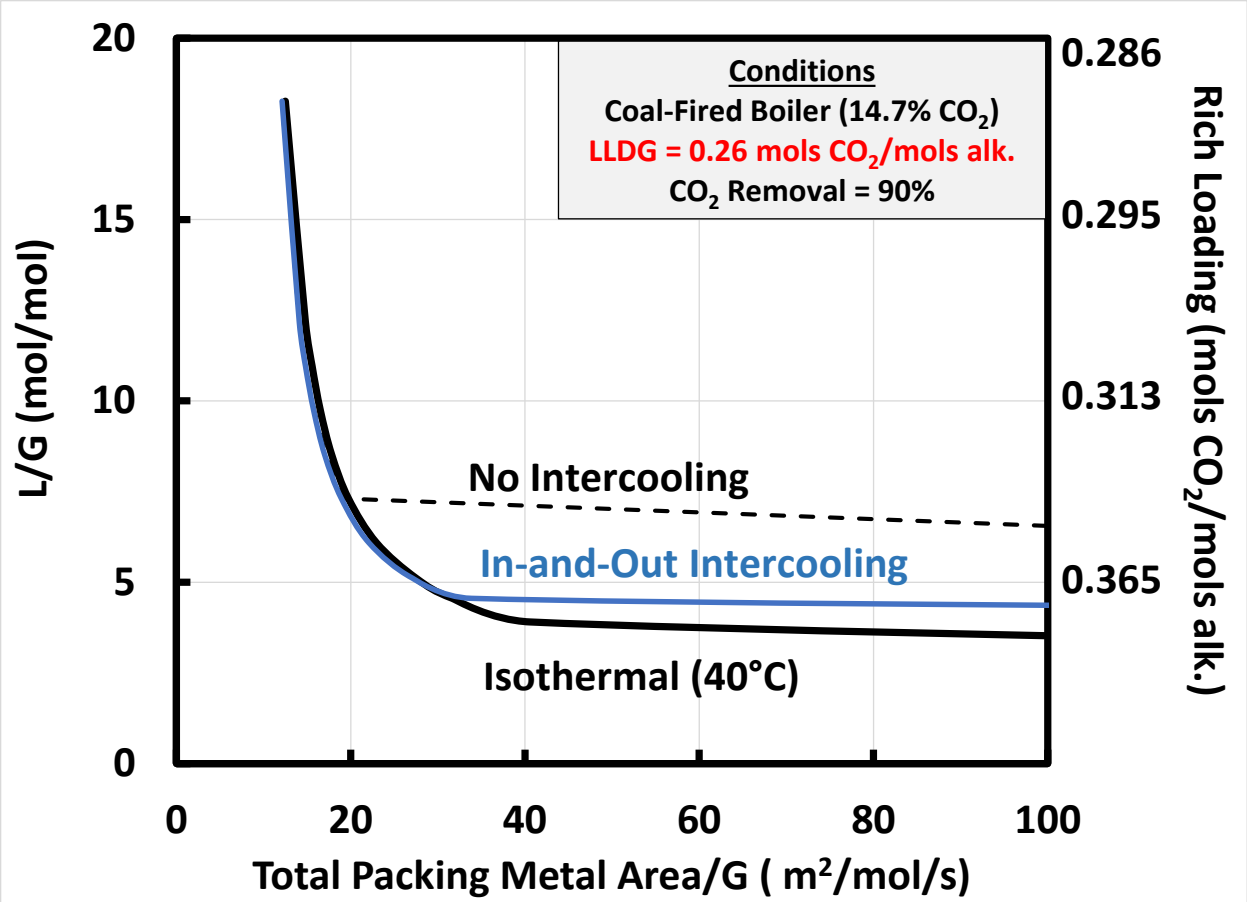

Figure 8: Design curves for adiabatic (dashed), in-and-out intercooling (Blue), and isothermal (solid) operation for coal-fired boiler application (14.7% CO_2) in the intermediate loading range (0.26 mol CO_2/mol alkalinity). Each curve represents the packing requirement to achieve 90% CO_2 removal for a given liquid to gas ratio (L/G). For each point on the curve, the lean loading, removal, and solvent rates are fixed, so a unique rich loading exists (secondary y-axis).

For the NGCC case (Figure 7), the gap between the in-and-out intercooling curve and isothermal curve clearly highlights the potential for improvement with a novel intercooling design (e.g., recycle intercooling). Simple intercooling does not achieve maximum solvent capacity (approximately 100% removed from maximum capacity) and exhibits a relatively flat slope in the approach to maximum capacity. Therefore, in addition to capacity benefits, significant packing reduction may also be possible with a novel intercooling design. Recycle intercooling will be considered for this operating condition as well.

The coal-fired boiler case exhibits different behavior in this region. As seen in Figure 8, in-and-intercooling provides a large capacity benefit over the adiabatic absorber and is within approximately 25% of the isothermal maximum capacity. Therefore, the capacity benefit of a novel design at this condition is not as large as the benefit realized in the NGCC case. Furthermore, the slope of the in-and-out intercooling curve tracks the isothermal curve in the approach to maximum capacity. This indicates that minimal packing benefits would be achieved from a novel design. For the coal-fired boiler case in this loading range, a novel intercooling

design must include minimal additional capital expenditure and operating complexity while achieving maximum solvent capacity to justify implementation over in-and-out intercooling.

High L/G Loading Range

For the coal-fired boiler application, an additional loading range exists where the solvent rate is sufficiently high to mitigate temperature related equilibrium constraints and the system can approach maximum capacity without intercooling. Figure 9 provides absorber design curves for this operating range.

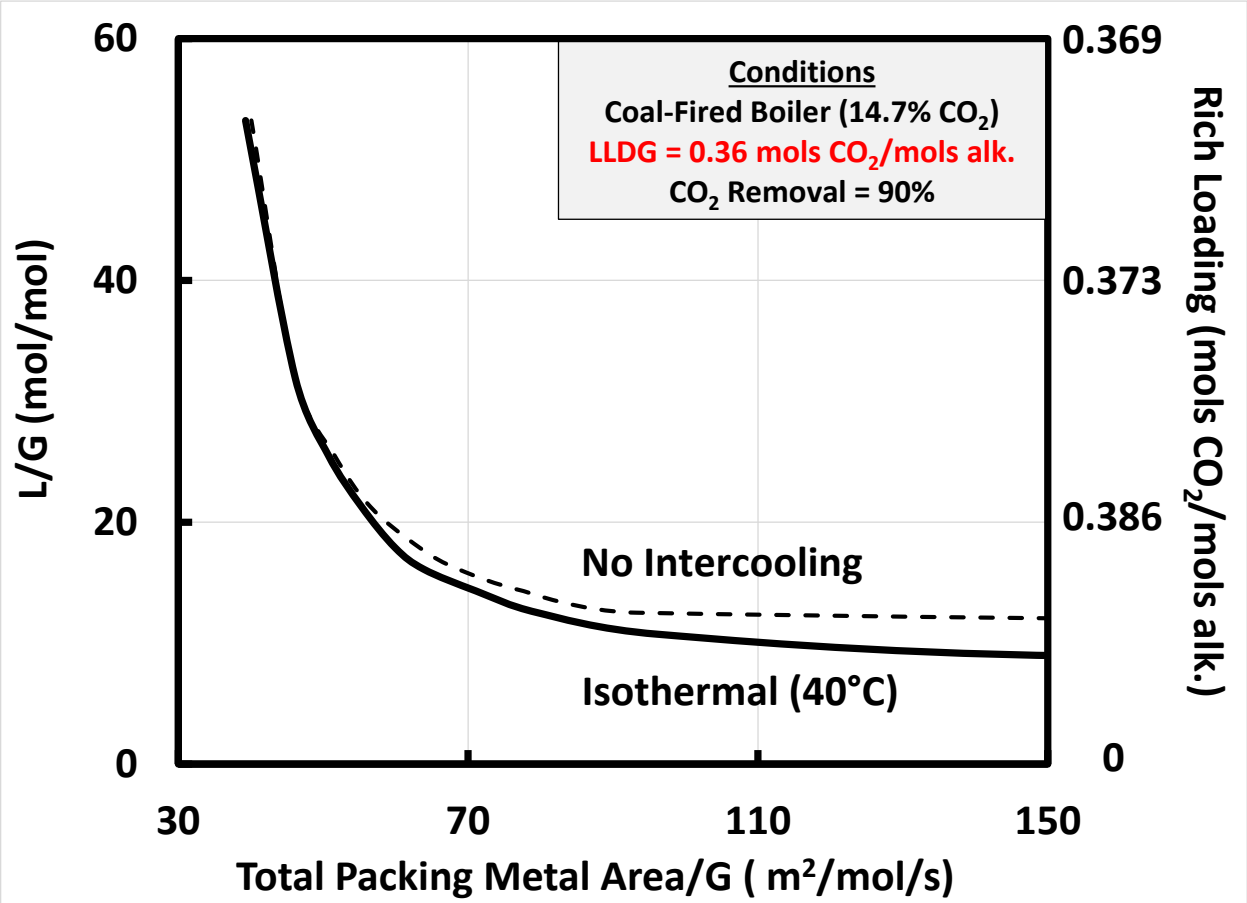

Figure 9: Design curves for adiabatic (dashed) and isothermal (solid) operation for coal-fired boiler application (14.7% CO_2) in the large solvent rate loading range (0.36 mol CO_2/mol alkalinity). Each curve represents the packing requirement to achieve 90% CO_2 removal for a given liquid to gas ratio (L/G). For each point on the curve, the lean loading, removal, and solvent rates are fixed, so a unique rich loading exists (secondary y-axis).

As expected, the high solvent rate dampens temperature effects in the column and the adiabatic absorber performs similarly to the isothermal absorber. The maximum solvent capacity is approximately 5% better with isothermal operation and the maximum packing reduction with isothermal operation over the range is 15%. These small improvements are unlikely to justify implementation of intercooling at this condition.

Conclusions

By introducing packing requirements to the minimum solvent rate (L_{MIN}) analysis developed previously, it is possible to make recommendations regarding intercooling design for NGCC (4.1% CO_2) coal-fired boiler applications (14.7% CO_2) without a detailed economic analysis. Representative loading ranges were identified for both applications and absorber design curves (solvent flow rate or capacity as a function of packing requirement) were developed for each operating range. The following conclusions regarding absorber design were developed for each application and loading range:

- "Over-stripped" Loading Range:
    - NGCC (0.15–0.21 mol CO_2/mol alkalinity): **No intercooling recommended.** An adiabatic absorber can achieve maximum (isothermal) capacity and the maximum packing reduction achieved by isothermal operation is 25%. Large driving forces making intercooling benefits marginal.
    - Coal (0.15–0.18 mol CO_2/mol alkalinity): **No intercooling recommended.** Similar behavior to NGCC case. Maximum packing reduction with isothermal operation is 30%.
- Simple Intercooling Loading Range:
    - NGCC (0.22–0.26 mol CO_2/mol alkalinity): **Recycle (or novel) intercooling recommended.** Intercooling provides significant capacity benefits over an adiabatic absorber. Simple in-and-out intercooling can achieve maximum solvent capacity, but the packing requirement is large. A novel design, such as recycle intercooling, can reduce the packing requirement by more than 50% while achieving the same capacity.
    - Coal (0.19–0.21 mol CO_2/mol alkalinity): **In-and-Out Intercooling recommended.** In-and-out intercooling can achieve maximum solvent capacity with packing requirements that are nearly identical to an isothermal column at most conditions. Isothermal operation can reduce packing requirements by up to 29% over in-and-out intercooling, providing moderate incentive for further intercooling development.
- Intermediate Loading Range:
    - NGCC (> 0.26 mol CO_2/mol alkalinity): **Novel Intercooling recommended.** In-and-out intercooling only achieves part of the capacity benefits possible with intercooling benefits (approximately half of isothermal capacity) and also requires more packing for the same capacity benefits (maximum packing reduction of 25%). The combination of capacity and packing benefits makes this a good condition for novel intercooling development.
    - Coal (0.22–0.30 mol CO_2/mol alkalinity): **In-and-Out Intercooling recommended.** Simple intercooling is within 25% of maximum isothermal capacity and has nearly identical packing requirements to an isothermal column.

Novel intercooling can only be justified by economic benefits of capacity improvement (requires stripper evaluation).

- High L/G Loading Range:
  - Coal (>0.30 mol CO_2/mol alkalinity): **No Intercooling recommended.** The high L/G dampens temperature effects in the column. An adiabatic absorber is within 5% of the maximum isothermal capacity and the maximum packing reduction that can be achieved with isothermal operation is 15%.

Future Work

The absorber design curve methodology in this work will be extended to the steel blast furnace application and recommendations for intercooling at high CO_2 concentrations will be developed. Theoretical explanations will be developed for the behavior observed across the full range of conditions studied, including generalization or development of dimensionless groups if possible. For conditions where novel intercooling design may provide significant benefits, several new design options will be developed and analyzed based on the operating conditions. Finally, economic analysis will be used to optimize and evaluate intercooling choices for all applications.

Safety

One of the primary safety issues associated with the absorber unit operation in an amine scrubbing facility is exposure to the amine. Amine leaks may occur from the equipment at joint or seal locations. In the absorber area, the intercooling loop provides multiple potential leak sources. The use of recycle intercooling creates an added risk since the equipment in this area will see the highest amine flow rates in the process (several times higher than the nominal amine circulation rate throughout the remainder of the plant). Any leak in this area will result in large amounts of solvent loss and significant exposure risk for plant employees. The intercooling exchanger is a potential leak source in this area. The heat exchanger is most susceptible to leaks at the gaskets (if the exchanger is not welded). The gaskets should be routinely inspected during preventative maintenance. Gaskets at risk of failure may be discolored, brittle, or display cracking or flaking, which indicate the integrity of the gasket material has been compromised. The gasket material should be thoroughly vetted or tested for compatibility with the solvent selected for operation and re-evaluated if changes are made (e.g., changes in amine concentration or amine type). Secondary containment (with proper drain specifications and leak detection sensors) should be used around the intercooling loop to provide early warning when leaks occur and to prevent amine from spreading throughout the facility.

References

Rochelle GT et al. "CO_2 Capture by Aqueous Absorption, First Quarterly Progress Report 2014." Texas Carbon Management Program. The University of Texas at Austin. 2014.

Rochelle GT et al. "CO_2 Capture by Aqueous Absorption, Third Quarterly Progress Report 2013." Texas Carbon Management Program. The University of Texas at Austin. 2013.

Modeling and Optimization of Advanced Stripper Configurations

Quarterly Report for April 1 – June 30, 2014

by Yu-Jeng Lin

Supported by the Texas Carbon Management Program

McKetta Department of Chemical Engineering

The University of Texas at Austin

July 31, 2014

Abstract

The compression work accounts for about 1/3 of total energy requirement with piperazine regenerated at 150°C in the advanced flash stripper. To determine the optimum lean loading, the energy and capital cost of compression have to be correctly evaluated. This work will update the multi-stage compressor configuration.

The updated configuration uses multi-stage compressors to compress CO_2 to above supercritical pressure and intercool to 40 °C between stages. The supercritical CO_2 is then aftercooled to 30 °C and pressurized to 150 bar using a supercritical pump. Three alternative multi-stage compressor configurations were investigated, including conventional compressor, supersonic compressor, and supersonic compressor with heat recovery. The updates include 86% compressor efficiency and the supercritical pump for the last stage. The simulation results show that the updated conventional multi-stage compressor requires 6–9 kJ/mol CO_2 with inlet pressure of 5–13 bar, which is about 1 kJ/mol CO_2 lower than the correlation developed by Van Wagener. The major differences come from the higher efficiency and aftercooling.

The supersonic compressor has been developed with a pressure ratio per stage of up to 10, but it has proved less efficient than the conventional compressor due to higher discharge temperature, although it can provide similar compression work after heat recovery.

The capital cost of the multi-stage compressor including the compressors, the intercoolers, the motor drive, and the supercritical pump was priced with varied inlet pressure. The annualized CAPEX is \$2–4/tonne CO_2 with 5–13 bar inlet pressure, which is about 1/3 of total compression cost. Combining the OPEX and CAPEX, the total compression cost is \$6–10/tonne CO_2 with 5-13 bar inlet pressure.

Introduction

In post-combustion CO_2 capture, steam usage for lean solvent regeneration in the stripper and CO_2 compression work are the main contributors to the energy requirement. Implementing CO_2 capture incurs a 20–30% penalty on electricity output for a typical coal-fired power plant

(Rochelle, 2009). Alternative stripper configurations could improve energy efficiency significantly compared to a simple stripper.

Several previous studies have been done to improve equivalent work by introducing alternative stripper configurations. Oyenekan (2007) proposed matrix, internal exchange, multi-pressure, and flashing feed stripper configurations. The best performance was obtained in a matrix with MDEA/PZ, improving energy savings by 22% over the simple stripper. Van Wagener (2011) emphasized the importance of increasing process reversibility by introducing more complex configurations including multi-stage flash, cold rich bypass, and an interheated column. Van Wagener showed that the interheated column with 8 m PZ offers the best energy savings. To improve capture efficiency, stripper modeling and optimization of novel configurations have been done using Aspen Plus® software.

Loss of steam heat from the stripper is one reason that CO_2 capture by amine scrubbing is inefficient. When the stripper is operated at 120–150 ^oC, water in the rich solvent is vaporized and emitted with CO_2 from the top of stripper. Flashing can be reduced using cold rich bypass. Another method is the rich exchanger bypass employing a heat exchanger to recover steam heat by bypassing the cold rich solvent.

The total equivalent work is used to evaluate the overall energy requirement of the process rather than relying only on reboiler duty.

Methods

Process specifications

Process specifications used in the simulations are shown in Table 1. A split flow sheet was used, with typical rich solvent conditions such as loading and temperature fixed as inputs. For the main heat exchanger, instead of a HeatX block, two-stage heater blocks were used to facilitate convergence. In the first stage where only liquid exists (i.e., flash is not allowed), the solvent was heated from 46 ^oC to its bubble point. In the second stage, the vapor-liquid condition was specified so flashing occurs. In this way, the calculated LMTD is closer to a real situation than using only one-stage heater blocks and specifying non-flashing.

Table 1: Process simulation specifications

Process modeling tool	Aspen Plus® v7.3
Thermodynamic model	Independence
Packing type	2 m Mellapak standard 250X
Regeneration temperature (^oC)	150
Rich loading (mol CO_2/mol alk)	0.4
Rich solvent temperature (^oC)	46
Main exchanger LMTD (^oC)	5
Rich exchanger LMTD (^oC)	20

Advanced Flash Stripper

Figure 1 shows the advanced flash stripper with warm rich bypass and rich exchanger bypass. In this configuration, the rich exchanger is used to preheat cold rich solvent by hot CO_2 vapor coming out of the stripper. A portion of the cold rich solvent obtains latent heat of steam from the stripped vapor. Warm rich bypass is extracted between two cross exchangers and fed to the top of the stripper after mixing with cold rich bypass. The temperature was selected as the bubble point temperature at the stripper operating pressure. The rest of the rich solvent is heated by a steam heater and fed into the bottom of the flash stripper. The reboiler found in a typical stripper is replaced by a steam heater and a flash vessel. Only part of the rich solvent countercurrently contacts with vapor in the flash stripper.

To reduce the inefficiency caused by stripping steam heat, either cold rich bypass or rich exchanger bypass can be used.

For both strategies, stripping steam heat can be recovered either in the cross exchanger or in the stripper, which serves as a direct contact cooler. In this configuration (Figure 1), both concepts are applied. Warm rich bypass condenses part of the steam in the stripper and the cold rich bypass recovers the rest. This works more efficiently than rich exchanger bypass and cold rich bypass. Since the convective steam heater has less solvent hold-up and residence time, it will minimize thermal degradation.

The temperature of the hot lean solvent is set to 150 ^{o}C at the bottom of the stripper. The hot rich solvent from the steam heater is mixed with the warm bypass solvent coming down from the stripper, which is colder than 150 ^{o}C. Either heating the hot rich solvent in the steam heater to higher than 150 ^{o}C or feeding the warm bypass solvent back to the steam heater can achieve 150 ^{o}C after mixing. The heat duty required is the same for both but the first needs higher equivalent work due to higher steam temperature.

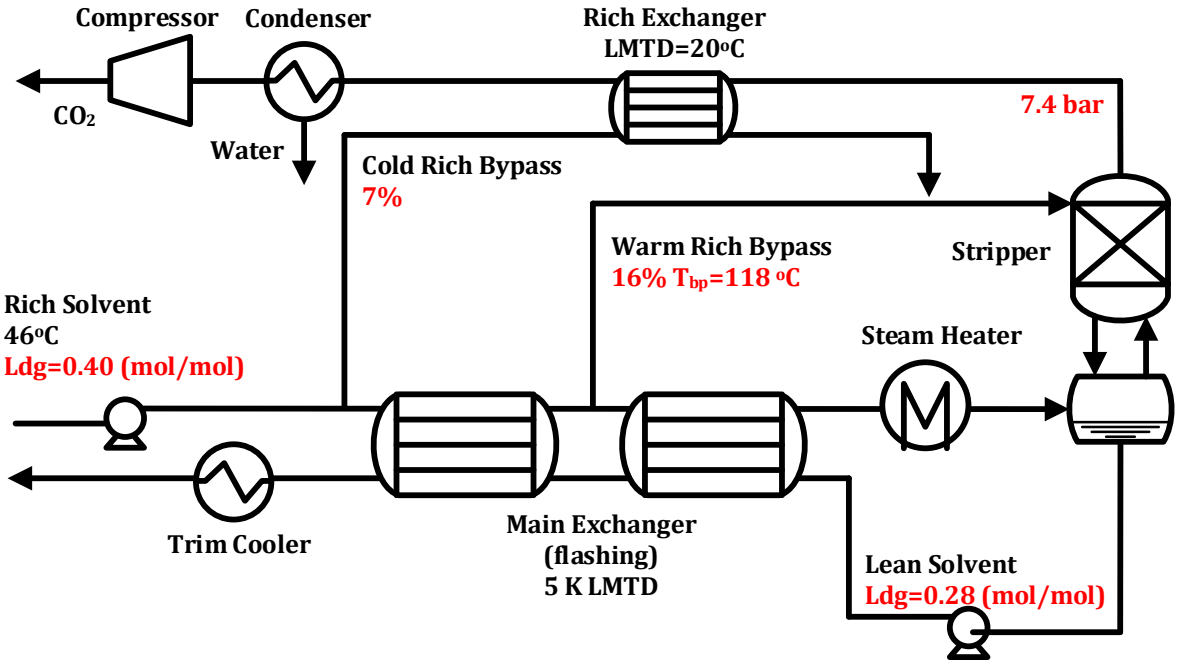

Figure 1: Advanced flash stripper using 8 m PZ at 0.28 lean loading

Equivalent Work Calculation

Equivalent work is a more useful metric of energy use than heat duty alone. As Equation 1 shows, equivalent work consists of pump work, compression work, and heat work. The pump is required to move the solvent from the absorber to the pressure and height of the stripper. Heat work is obtained from heat duty by Equation 2. The turbine efficiency is set to a typical value of 90%.

$$W_{eq}\left(\frac{kJ}{mol\ CO_2}\right) = W_{Heat} + W_{pump} + W_{comp} \tag{1}$$

$$W_{Heat} = 90\%\left(\frac{T_{source} + \Delta T - T_{sink}}{T_{source} + \Delta T}\right) Q_{reb} \tag{2}$$

Update of Multi-stage Compressor

Van Wagener (2011) proposed a correlation of compression work for CO_2 capture by regressing data from Aspen Plus®. The multi-stage compressor train employed the compressors with 72% polytropic efficiency, the intercoolers at 40 ^oC and water knock-out drums between stages. The compression work can be obtained by the input of stripper pressure as shown in Equation 3.

$$W_{comp}\left(\frac{kJ}{mol\ CO_2}\right) = \begin{cases} 4.572\ln\left(\frac{150}{P_{in}}\right) - 4.096 & P_{in} \le 4.56\ bar \\ 4.023\ln\left(\frac{150}{P_{in}}\right) - 2.181 & P_{in} > 4.56\ bar \end{cases} \tag{3}$$

In this work, the specifications of the multi-stage compressor are modified to improve the efficiency of compressors, and to introduce a supercritical pump for the last stage.

Characteristics of CO_2 compression

The inlet pressure of the compressor train is determined by the stripper pressure, which is dependent on the system lean loading and reboiler temperature. To sequester the CO_2 underground, the target pressure of the compressor has to be at least above its supercritical pressure, 74 bar. To replace the pressure loss during transportation, 0.4–0.5 bar/km is required. In this work, the target pressure is 150 bar. When the CO_2 is in the supercritical phase such that its density is similar to liquid, the difference between a pump and a compressor for the compression task disappears and becomes a question of density rather than phase. The supercritical pump is suggested for the last stage when the density is above 500 kg/m^3 (Bargamini, 2011).

To decrease the pipeline diameter, aftercooling can be applied to increase CO_2 density and reduce volume flow rate (Moore, 2008). In this work, the aftercooler that cools CO_2 is employed before the supercritical pump to attain a density suitable for pumping and to reduce the pump work from reduced volume flow rate. As shown in Figure 2, the density increases dramatically around the critical region. The aftercooling temperature is specified as 30 ^oC to obtain the major density increase.

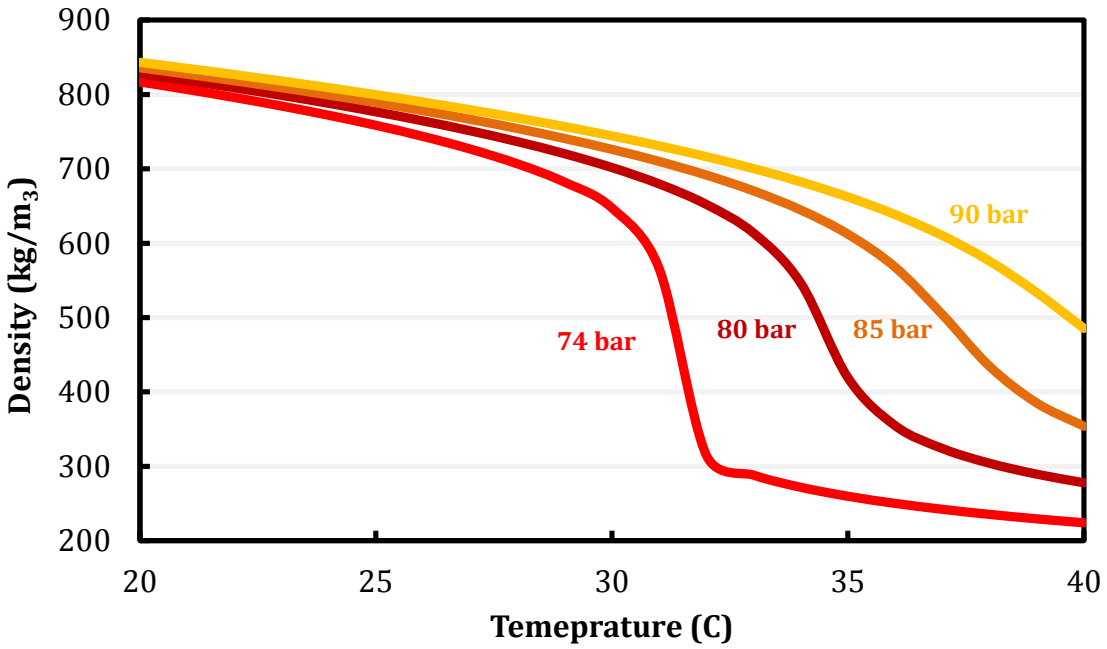

Figure 2: Density of supercritical CO_2 with varied temperature.

Conventional compressor

Three types of compressor are typically used in industry: reciprocating, axial, and centrifugal. The reciprocating compressor provides a wide range of pressure ratio but can only accommodate inlet volume flow rate up to 7000 ft^3/min. The axial compressor has high capacity but lower pressure ratio (1.05–1.2). The pressure ratio and capacity of a centrifugal compressor is between that of a reciprocating and axial compressor. For a coal-fired power plant with 593 MW gross output, the CO_2 volume flow rate is around 140,000 ft^3/min at 1 bar inlet pressure. A centrifugal compressor with intermediate pressure ratio and large capacity has been suggested for CO_2 capture (Suri, 2007). The maximum pressure ratio is specified as 2 due to high molecular weight.

Supersonic Shock Wave Compressor

The Ramgen Company has been developing the Supersonic Shock Wave Compressor with a blade tip not limited by Mach number, so the pressure ratio can be up to 10 per stage (Lawlor, 2005). The physical size of the compressor is smaller and only 1–2 stages are required. It has been claimed that the Supersonic Shock Wave Compressor can save 40–50% of capital cost and provide higher efficiency. Also, the higher discharge temperature makes heat recovery from the intercoolers easier to implement. The design allows the discharge temperature to be up to 260 ^oC compared to 120–140 ^oC for a conventional compressor. A single-stage supersonic compressor has been demonstrated with 7.7 pressure ratio, and a commercial size will be tested in the future.

The conventional and supersonic compressors will be simulated in Aspen Plus®. The multi-stage compressor will compress the CO_2 from the stripper pressure to 76 bar that includes 2 bar of net positive suction head (NPSH), and the supercritical pump will pressurize the supercritical CO_2 to

150 bar. The configurations of the conventional and supersonic compressor are shown in Figures 3 and 4, respectively.

Table 2: Multi-stage compressor specifications

	Conventional	Supersonic
Maximum pressure ratio/stage	2	10
Compressor polytropic efficiency (%)	86	90
Intercooling temperature (^{o}C)	40	
Aftercooling temperature (^{o}C)	30	
Supercritical pump efficiency (%)	65	
Multi-stage compressor outlet P (bar)	76	
Final target P (bar)	150	

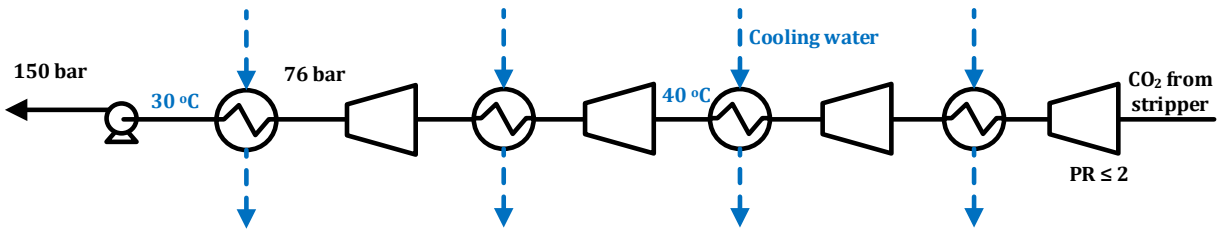

Figure 3: Configuration of conventional multi-stage compressor

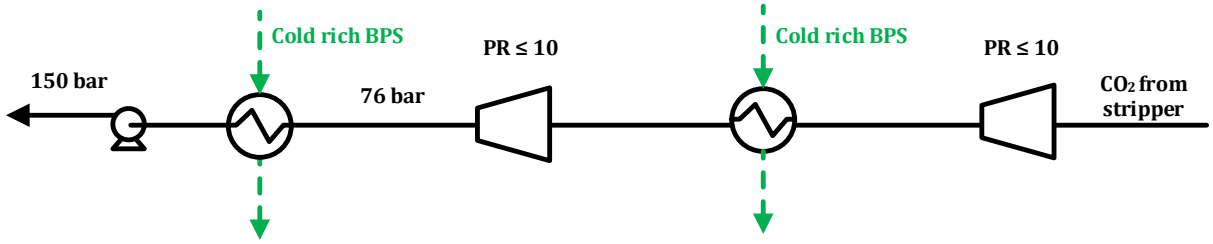

Figure 4: Configuration of supersonic multi-stage compressor with heat recovery

Capital Cost of Multi-stage Compressor

The capital cost of the multi-stage compressor is investigated in this work. The Aspen Icarus® software will be used to price the equipment based on the simulation results. The multi-stage compressor includes the compressors, the intercoolers, a motor drive, and a supercritical pump. The major inputs are the inlet pressure, CO_2 volume flow rate and compression work.

Process Safety

Compressor surge

Compressor surge occurs when the inlet flow rate is reduced too much from the design point. When the gas pressure after the compressor is actually higher than what the compressor itself can physically maintain, this causes the airflow in the compressor wheel to back up, build pressure, and sometimes stall. Compressor surge can cause the thrust bearings of the turbo to be destroyed, and will sometimes even lead to mechanical failure of the compressor wheel itself. To avoid surge, anti-surge control can be installed. A portion of the outlet gas will be recycled to the inlet to maintain minimum flow rate and avoid the surge region.

Results and Discussion

Compression work

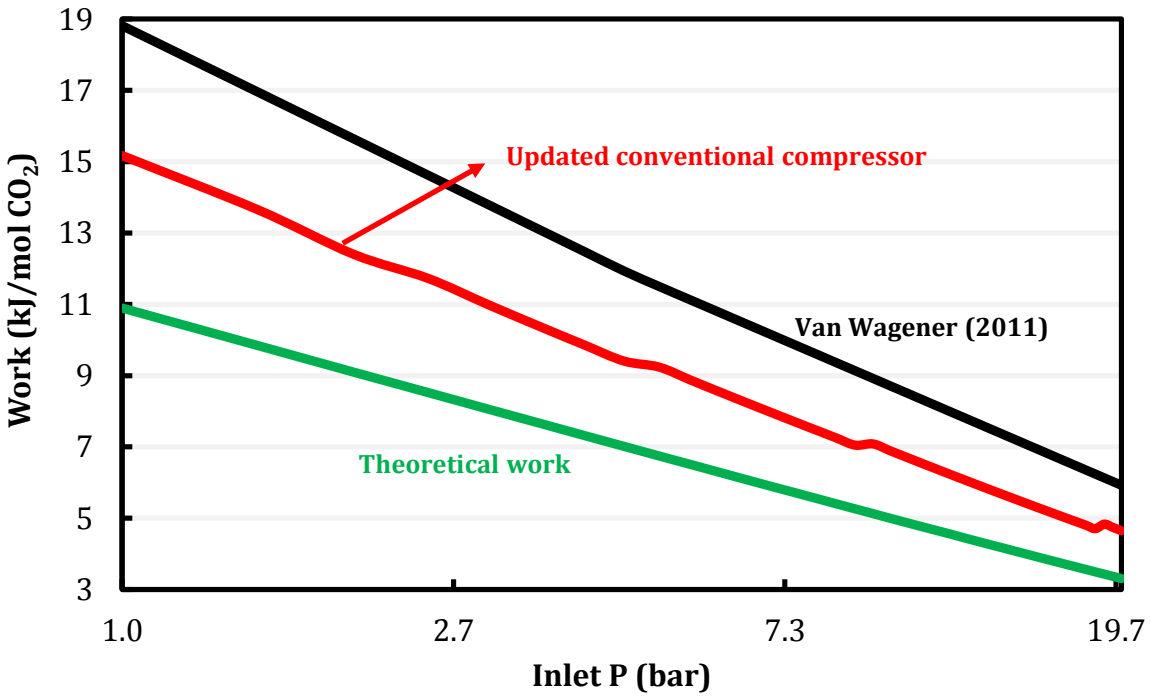

Figure 5: Compression work of conventional multi-stage compressor; the updated conventional compressor intercool to 40 ^{o}C, discharge at 76 bar, aftercool to 30 ^{o}C and pressurize to 150 bar using a supercritical pump; pressure ratio of compressor is less than 2 per stage.

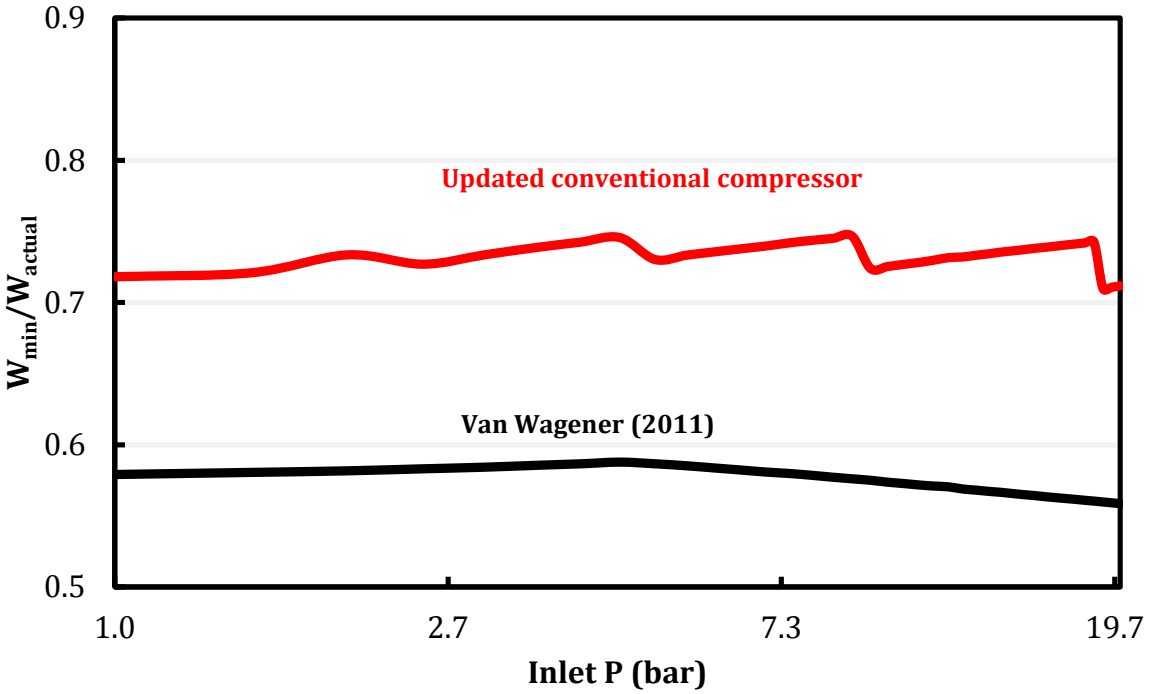

Figure 6: Ratio of minimum work to actual work of the multi-stage compressor; the updated conventional compressor intercool to 40 °C, discharge at 76 bar, aftercool to 30 °C, and pressurize to 150 bar using a supercritical pump; pressure ratio of compressor is less than 2 per stage.

Figure 5 compares work using a conventional multi-stage compressor regressed by Van Wagener (2011) and the updated results in this work. The updated compression work is about 1 kJ/mol CO_2 lower, mostly due to the higher compressor efficiency, 86% rather than 72%. Even though the supercritical pump is less efficient (65%), aftercooling that increases the CO_2 density compensates for the inefficiency. The updated compression work requirement can be regressed as Equation 4 over the range of inlet pressure from 1 to 20 bar. The theoretical work is calculated from the difference of Gibbs free energy between inlet pressure and 150 bar at 40 °C. Figure 6 shows the ratio of the minimum work to the actual work. The compression efficiency of the updated conventional compressor is above 70%.

$$W_{comp}\left(\frac{kJ}{mol\ CO_2}\right) = -3.48\ln(P_{in}) + 14.85 \quad (4)$$

Figure 7 shows the comparison of the conventional and supersonic compressors. In the loading range from 0.20 to 0.34 (5–13 bar), only one or two stages are required. A significant increase of compression work around 8 bar is due to the transition from two stages to one stage. The increase in pressure ratio causes the elevated discharge temperature and further departure from isothermal operation. Since the conventional compressor intercools more frequently, the more isothermal compression requires less work. The waste heat from the intercoolers of the supersonic compressor can be recovered by the process itself using the cold rich bypass. The dashed line in Figure 6 shows the compression work of the supersonic compressor with heat recovery using 8 m PZ. The cold rich bypass rates are adjusted to meet 20 K LMTD in the heat

exchanger. After heat recovery, the supersonic compressor performs similarly to the conventional compressor. The potential benefits of the supersonic compressor only come from the savings of capital and installation costs due to the compact design.

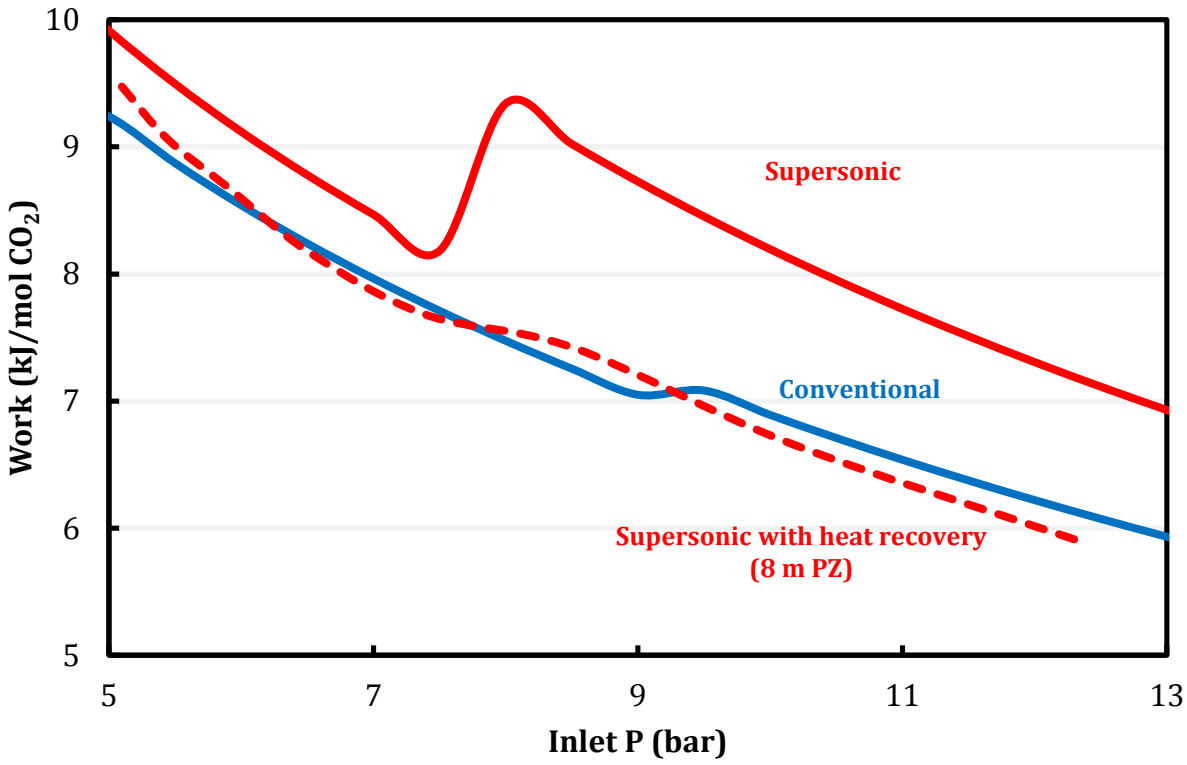

Figure 7: Compression work of supersonic multi-stage compressor; heat recovery with 8 m PZ; lean loading 0.20 to 0.34.

Compressor sizing and pricing

The capital cost of the multi-stage compressor consists of the compressors, the intercoolers, a motor drive, and a supercritical pump. The sizing uses the simulation results from Aspen Plus®. The PEC (purchased equipment cost) of the compressor and motor were obtained from Aspen Icarus®. The PEC of compressors is a function of inlet volume flow rate and pressure rating. The PEC of the motor drive is only a function of compression work.

The annualized capital cost ($/yr) is obtained from multiplying the PEC ($) by the scaling factor, α, and the annualized factor, β. The α includes the direct cost, the indirect cost, and the working capital. The β includes the income tax, the depreciation, and the 10% return on investment. The α and β are 5 and 2, respectively. The energy cost is calculated by the compression work required, 90% capacity and $100/MWh of the levelized electricity cost.

Figure 8 shows the annualized capital cost of the conventional multi-stage compressor with varied inlet pressure. The capital cost is mainly driven by the compressor cost. Step changes of compression work can be seen when number of stages varies. The MEA at 120 °C is typically operated between 1 to 4 bar and PZ at 150 °C is from 5 to 12 bar. Using PZ only requires 3 or 4

stages compared to MEA that needs 5–7 stages at the typical lean loading. This demonstrates the benefit of PZ with higher thermal stability that can be operated at elevated temperature providing higher stripper pressure.

Figure 9 shows the annualized energy and capital cost with varied inlet pressure. Both of these decrease with increasing inlet pressure. Compared to a conventional stripper using MEA and operated at low pressure, combining the capital and energy cost amplifies the benefits of a high pressure stripper using PZ. The total compressor cost is from \$6–10/tonne CO_2 with 5–13 bar stripper pressure. The total compression cost including capital and energy cost can be expressed by Equation 5 with varied inlet pressure.

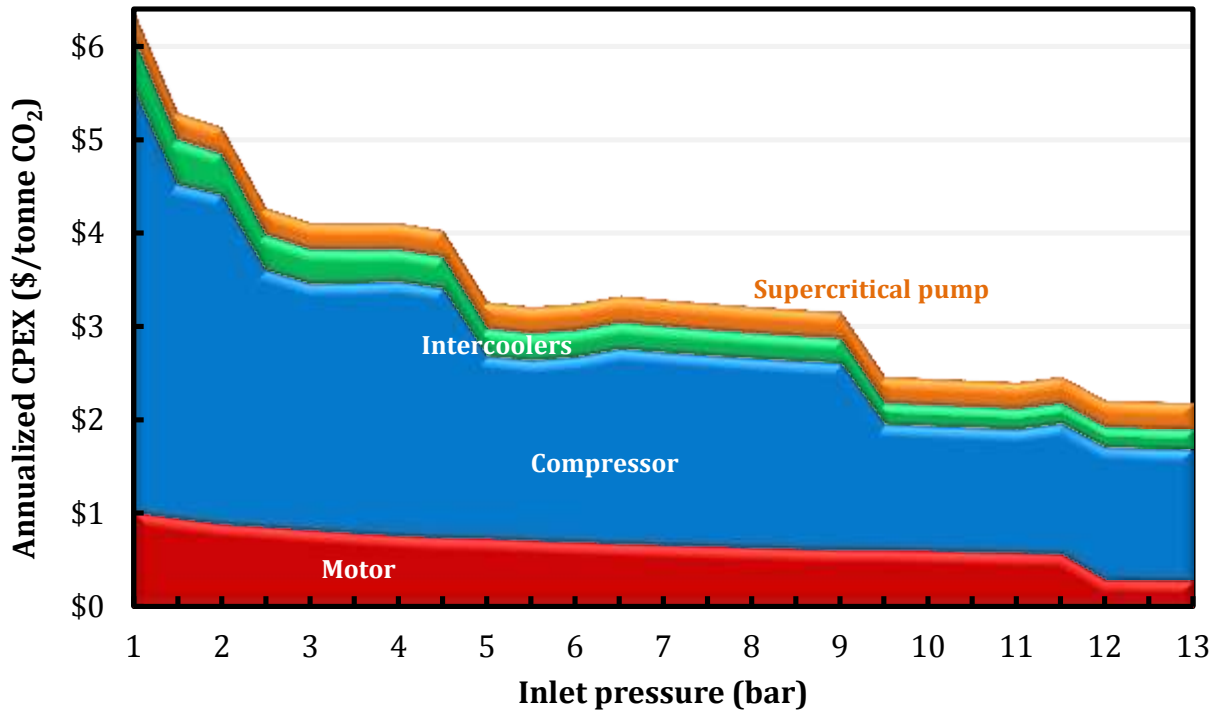

Figure 8: Capital cost of multi-stage compressor; CO_2 flow rate 115 kg/s; αβ = 1; CEPCI (2014) = 568.

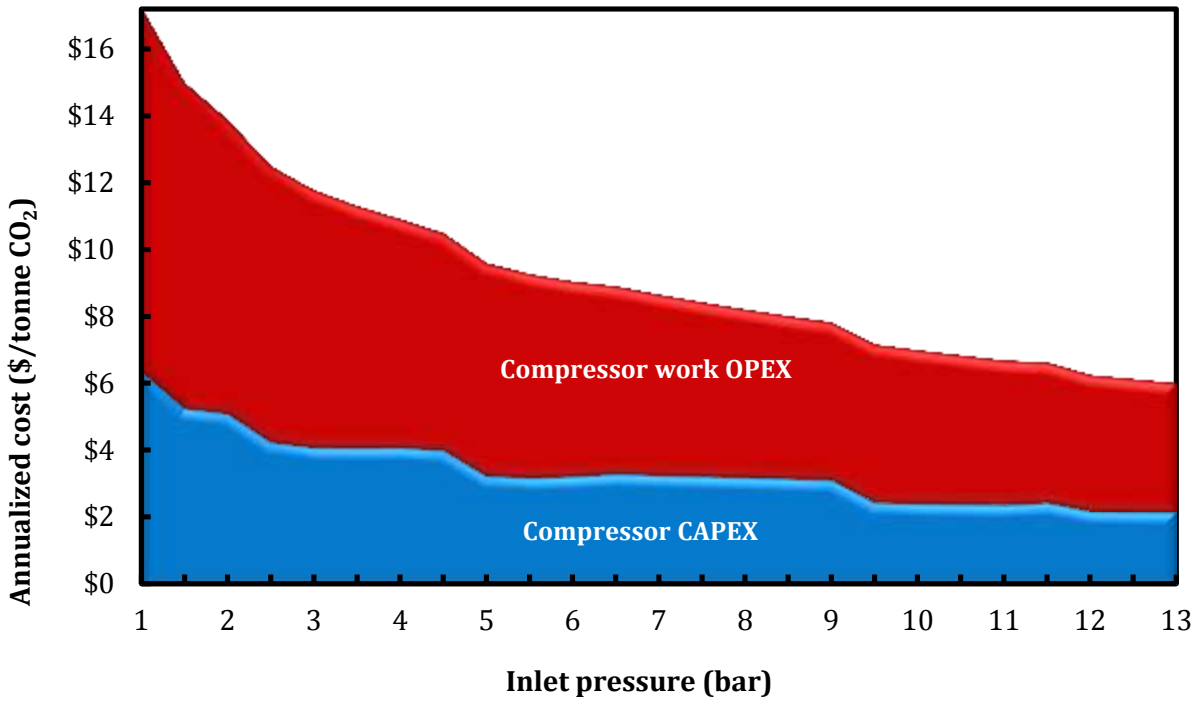

Figure 9: Capital cost and operating cost of multi-stage compressor; CO_2 flow rate 115 kg/s; αβ = 1; CEPCI (2014) = 568; COE $100/MWh

$$Compression\ Cost\left(\frac{\$}{tonne\ CO_2}\right) = -3.72\ln(P_{in}) + 15.46 \qquad (5)$$

Figure 10 shows the total equivalent work using the updated conventional compressor design. The optimum lean loading of the advanced flash stripper is at 0.28 with total equivalent work 30.4 kJ/mol CO_2, providing 10% improvement over the simple stripper.

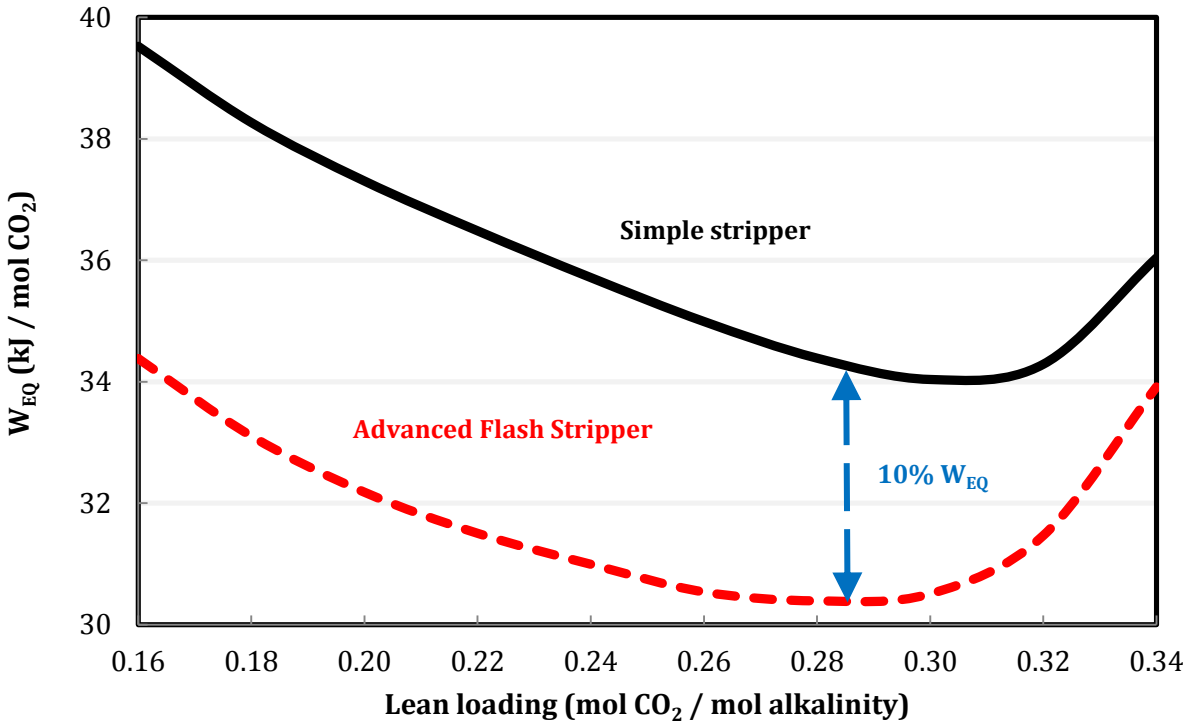

Figure 10: Total equivalent work of simple stripper and advanced flash stripper with updated conventional multi-stage compressor; 5 K LMTD; 8 m PZ; optimum bypass rates.

Conclusions

1. The conventional multi-stage compressor has been updated to include higher compressor efficiency (86%) and the supercritical pump for the last stage.

2. The supersonic compressor with a pressure ratio up to 10 per stage was investigated and found to be less efficient than the conventional compressor due to higher discharge temperature, although it provides similar compression work requirement after heat recovery.

3. The capital cost of the multi-stage compressor was evaluated with varied inlet pressure. The annualized CAPEX is \$2–4/tonne CO_2 and total compression cost is \$6–10/tonne CO_2 with 5–13 bar inlet pressure.

Future Work

1. Investigate the theoretical work and irreversibility of the simple stripper and the advanced flash stripper.

2. Investigate the sensitivity of packing height in the stripper and the temperature of warm rich bypass.

3. Develop the total regeneration cost analysis of the advanced flash stripper using 8 m and 5 m PZ

References

Bergamini L, Vescovo C, Milone F. "Centrifugal pumps for CO_2 applications". *Proceedings of the Twenty-Seventh International Pump User Symposium,Houston, Texas, September 12-15*. 2011.

Moore J, Lerche A, Delgado H, Allison T, Pacheco J. "Development of advanced centrifugal compressors and pumps for carbon capture and sequestration applicaitons". *Proceedings of the Fortieth Turbomachinery Symposium,Houston, Texas, September 12-15* . 2011.

Moore J, Nored M. "Novel concepts for the compression of large volumes of Carbon Dioxide". *Proceedings of ASME Turbo Expo: Power for Land, Sea and Air, Berlin, Germany, June 9-13*. 2008.

Suri R. *CO_2 Compression for Capture-Enabled Power Systems*. University of Waterloo. M.S. Thesis. 2007.

Lawlor S, Baldwin P. "Conceptual design of a supersonic CO_2 compressor". *Proceedings of ASME Turbo Expo: Power for Land, Sea and Air, Reno-Tahoe, Nevada, June 6-9*. 2005.

Oyenekan BA. *Modeling of Strippers for CO_2 Capture by Aqueous Amines*. The University of Texas at Austin. Ph.D. Dissertation. 2007.

Rochelle GT. "Amine scrubbing for CO_2 capture". *Science.* 2009;325:1652–24.

Van Wagener DH. *Stripper Modeling for CO_2 Removal Using Monoethanolamine and Piperazine Solvents.* The University of Texas at Austin. Ph.D. Dissertation. 2011.

Absorber performance with High CO_2

Quarterly Report for April 1 – June 30, 2014

by Yue Zhang

Supported by the

Howard A. Halff Endowed Graduate Fellowship in Chemical Engineering

and the Texas Carbon Management Program

McKetta Department of Chemical Engineering

The University of Texas at Austin

July 31, 2014

Acknowledgement: This material is based on work supported in part by the Department of Energy under Award Number DE-FE0013188.

Abstract

Previous studies of CO_2 absorption mainly focused on coal-fired flue gas with 12% CO_2. However, in a hybrid process combining amine scrubbing with membrane technology, the CO_2 concentration in the flue gas may be enriched to 20%. This work simulates absorber performance at 12 to 20% CO_2 with the Independence model for piperazine (PZ) in Aspen Plus®.

5 molal (m) PZ was chosen as the solvent with a solvent rate of $1.1*L_{min}$. There are three degrees of freedom: CO_2 concentration coming into the absorber, absorber CO_2 removal, and lean loading. To better understand and further estimate the absorber performance in this range, a factorial design has been used to define the model inputs. To improve the mass transfer rate, both in-and-out intercooling and pump-around intercooling have been simulated for the absorber. The model calculates the solvent rate, packing height, rich loading, and optimized position of intercooling for each case. The absorber performance with intercooling can be seen from the liquid/gas temperature profile and CO_2 composition profile in Aspen Plus®, and the intercooling loops of the absorber model can be further modified to minimize energy use.

Empirical correlations for normalized packing and rich loading have been derived. Normalized packing and rich loading can be predicted from CO_2 concentration, removal, and LLDG by interpolating.

The solvent blend 5 molal (m) MDEA/5 molal (m) PZ offers higher CO_2 capacity and the VLE curve of the solvent blend is flatter at the rich end than that of the PZ solvent. It is expected to result in greater delta loading and lower energy cost. Different intercooling configurations have also been tested to get better absorber performance and minimize energy use.

Introduction

Membrane Technology and Research, Inc. has proposed a hybrid system combining amine scrubbing with membrane technology to reduce energy cost. Previous studies of CO_2 absorption mainly focused on coal-fired flue gas with 12% CO_2. However, in the hybrid process, the CO_2 concentration in the flue gas may be enriched to 20%.

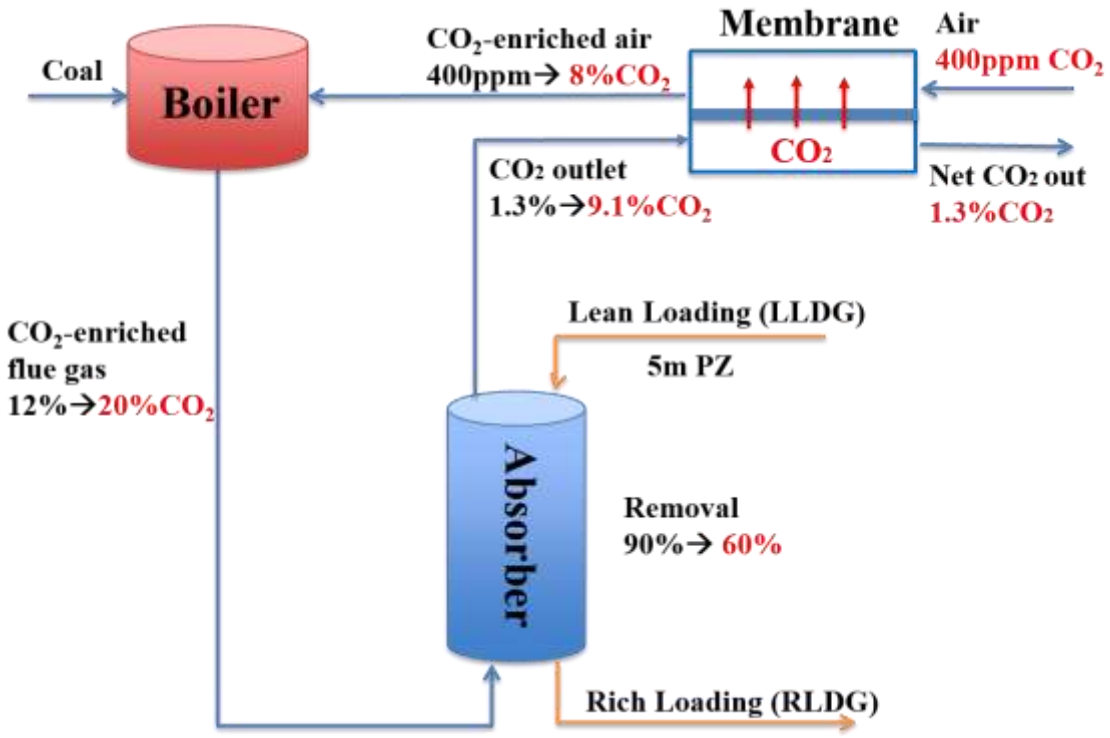

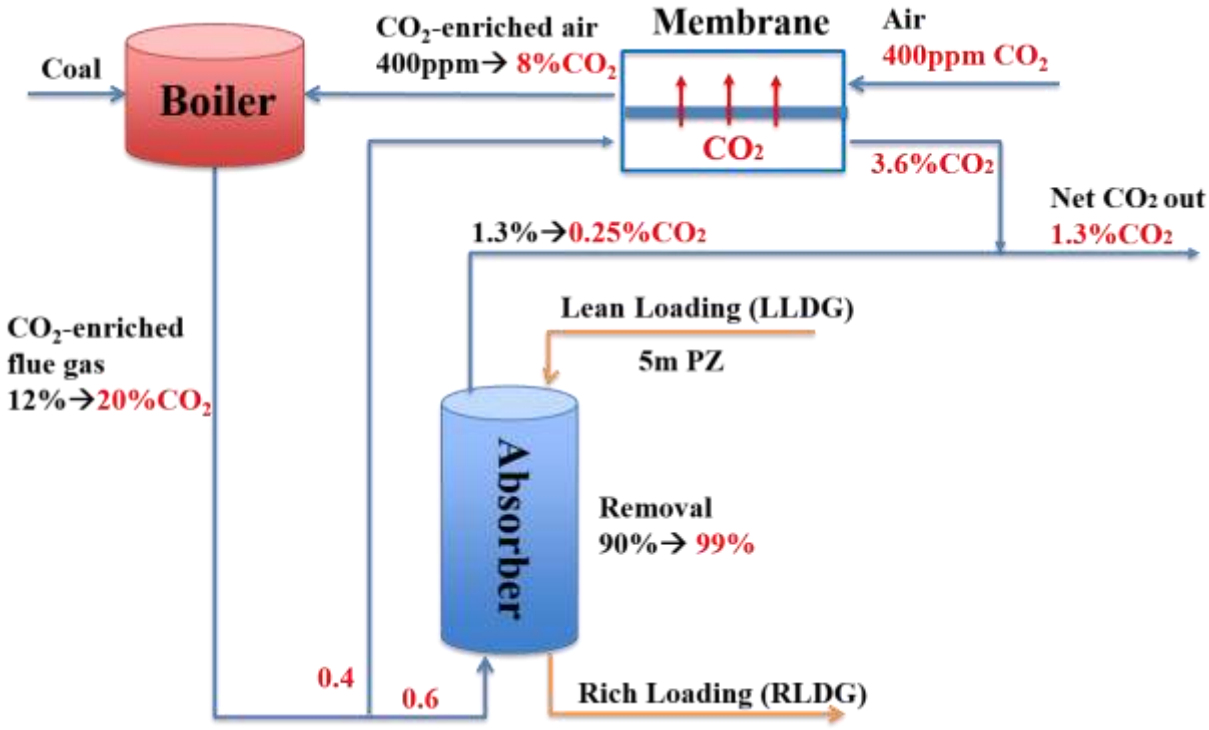

Figure 1: Hybrid-series and hybrid-parallel system combining amine scrubbing with membrane technology

In the hybrid-series arrangement (Figure 1), the outlet CO_2 concentration can be increased to 9.1% and removal can be reduced to 60%, which will result in smaller absorber packing height. With larger driving force at the top and bottom of the absorber, higher lean loading can be used to minimize energy use. In the hybrid-parallel arrangement, removal can be increased to 99%. Both the absorber and the membrane will deal with less CO_2, which will result in smaller diameter and smaller membrane area. This work simulates absorber performance at 12 to 20% CO_2 and 60 to 90% removal with the Independence model for PZ in Aspen Plus®.

To improve the mass transfer rate, both in-and-out intercooling and pump-around intercooling have been simulated for the absorber. In-and-out intercooling draws and returns the solvent to the same stage after cooling it. Pump-around intercooling draws the solvent out from the bottom of the absorber and sends it back to the middle after cooling.

In order to calculate the optimized position of intercooling, the absorber is considered in parts: top, middle, and bottom. In-and-out intercooling draws and returns the solvent to the first stage of the middle part. Pump-around intercooling draws the solvent out from the last stage of the bottom part, and sends it back to the first stage of the bottom part. Each case has been simulated to find the best position for intercooling.

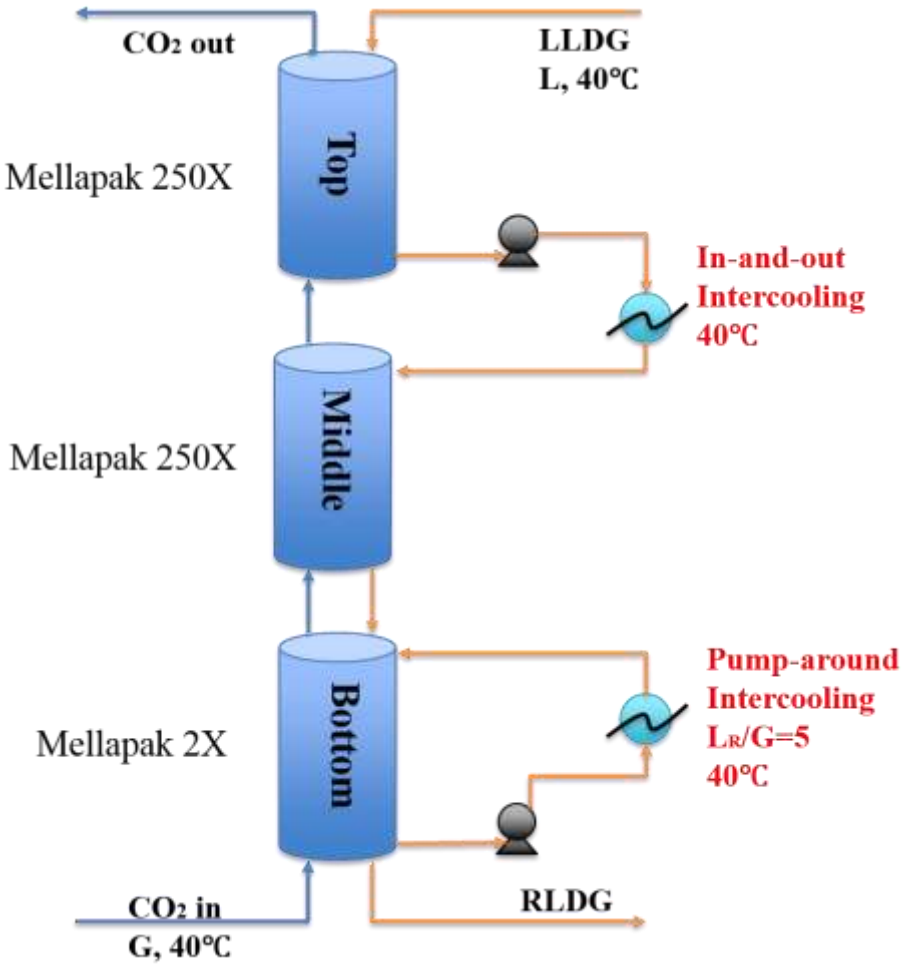

Figure 2: Two types of intercooling

Safety

In order to improve the mass transfer rate, both in-and-out intercooling and pump-around intercooling have been added to the absorber. However, this can result in gasket failure of the plate intercooling heat exchanger. Gasket failure will result in solvent splash and personnel exposure to amine. To avoid exposure, the plate heat exchanger should be put on ground level. If the heat exchanger is installed above ground level, solvent will splash over people when gasket fails. A splash protector should be added around the heat exchanger, and a spill containment system should be implemented to collect solvent.

Valves are very important in the operation process to allow quick shutdown of the solvent flowing through the heat exchanger if an accident occurs. Valves should be installed away from the heat exchanger to avoid personnel contact with the splashing solvent.

Factorial Design

In order to predict the absorber performance at 12 to 20% CO_2, factorial design was used to define the cases. There are three degrees of freedom: CO_2 concentration coming into the absorber, absorber CO_2 removal, and lean loading. The factorial design includes 18 cases: three

different CO_2 concentrations (coal-fired flue gas with 12% CO_2, and the hybrid process with 15% and 20% CO_2), three different removals (60%, 90%, and 99%), as well as two different lean loadings (over-stripping and normal lean loading is defined by the ratio of the partial pressure of CO_2 in the lean loading solvent and the partial pressure of CO_2 coming out of the absorber). With the results from the factorial design, a correlation between these factors will be developed to predict the rich loading and packing area from the CO_2 concentration, CO_2 removal, and lean loading. The top and middle sections of the absorber use Mellapak 250X. The bottom section uses Mellapak 2X. 5 m PZ was chosen as the solvent with a solvent rate of $1.1*L_{min}$.

Table 1: Factorial Design Cases

	Cases	CO_2 Conc (%)	Removal (%)	CO_2 out (%)	$P_{CO2}*/P_{(CO2\ out)}$	$P_{CO2}*$	Lean loading (molality)
1	no membrane	12	60	5.172	0.03704	0.19157	0.265
2	no membrane	12	60	5.172	0.37037	1.91571	0.36
3	no membrane	12	90	1.345	0.03704	0.04983	0.192
4	no membrane	12	90	1.345	0.37037	0.49826	0.307
5	no membrane	12	99	0.136	0.03704	0.00504	0.061
6	no membrane	12	99	0.136	0.37037	0.05044	0.192
7	with membrane	15	60	6.593	0.0370	0.2442	0.275
8	with membrane	15	60	6.593	0.3704	2.4420	0.368
9	with membrane	15	90	1.734	0.0370	0.0642	0.206
10	with membrane	15	90	1.734	0.3704	0.6423	0.318
11	with membrane	15	99	0.176	0.0370	0.0065	0.071
12	with membrane	15	99	0.176	0.3704	0.0652	0.208
13	with membrane	20	60	9.091	0.0370	0.3367	0.290
14	with membrane	20	60	9.091	0.3704	3.3670	0.378
15	with membrane	20	90	2.439	0.0370	0.0903	0.226
16	with membrane	20	90	2.439	0.3704	0.9033	0.332
17	with membrane	20	99	0.249	0.0370	0.0092	0.088
18	with membrane	20	99	0.249	0.3704	0.0924	0.227

L_{min} case

L_{min} is the minimum solvent rate required to achieve a specific value of removal. For each case L_{min} was determined by using excessive packing height in each section. It also shows the pinch behavior of the column at L_{min} for several cases.

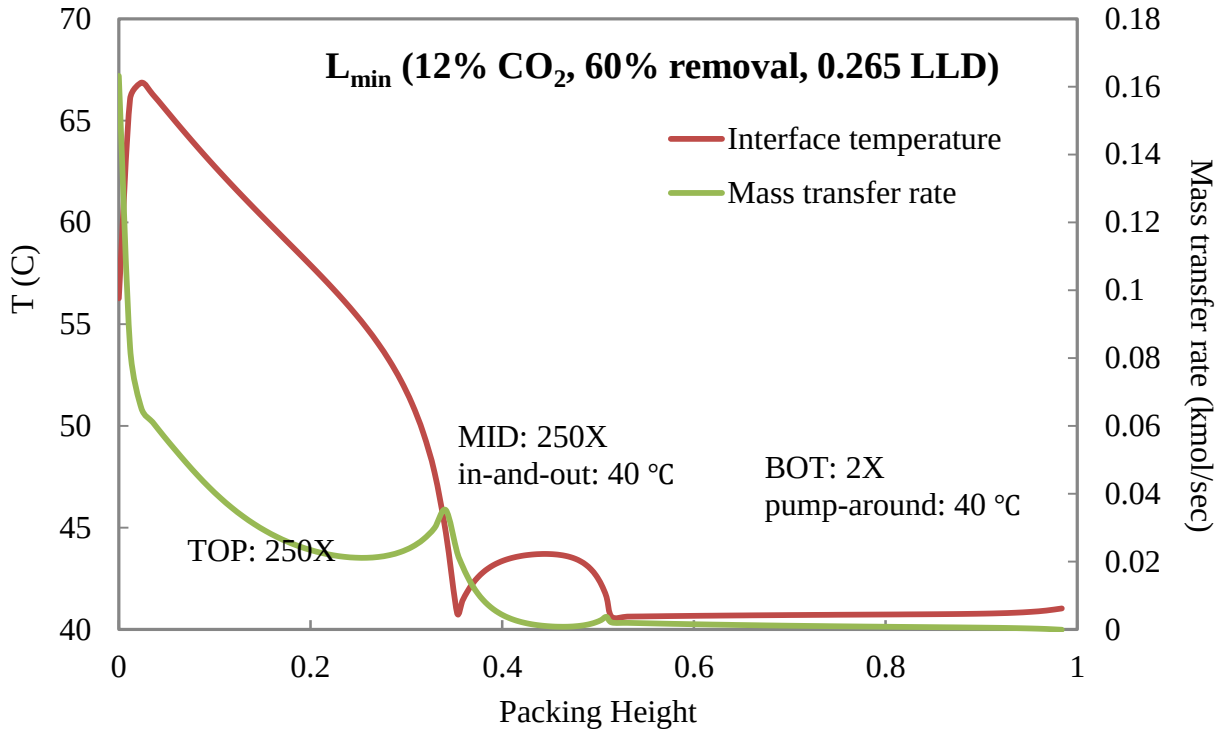

Figure 3: Interface temperature profile and mass transfer rate profile for L_{min} of Case 1

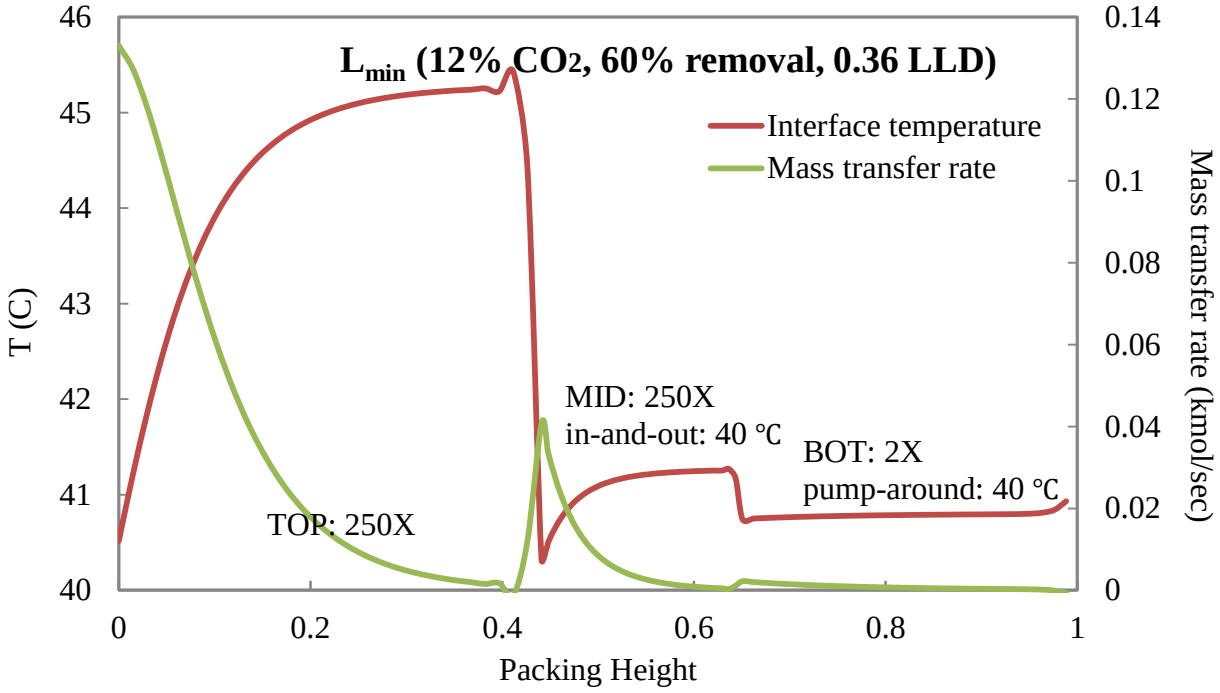

Figure 4: Interface temperature profile and mass transfer rate profile for L_{min} of Case 2

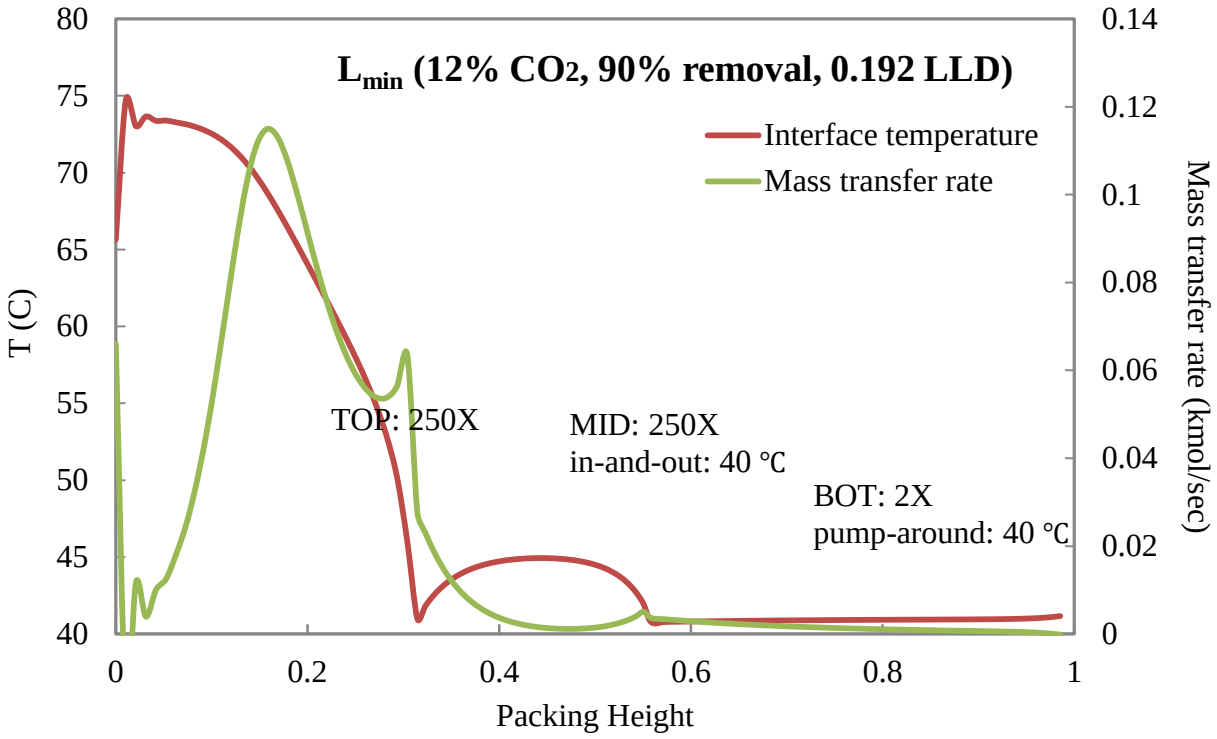

Figure 5: Interface temperature profile and mass transfer rate profile for L_{min} of Case 3

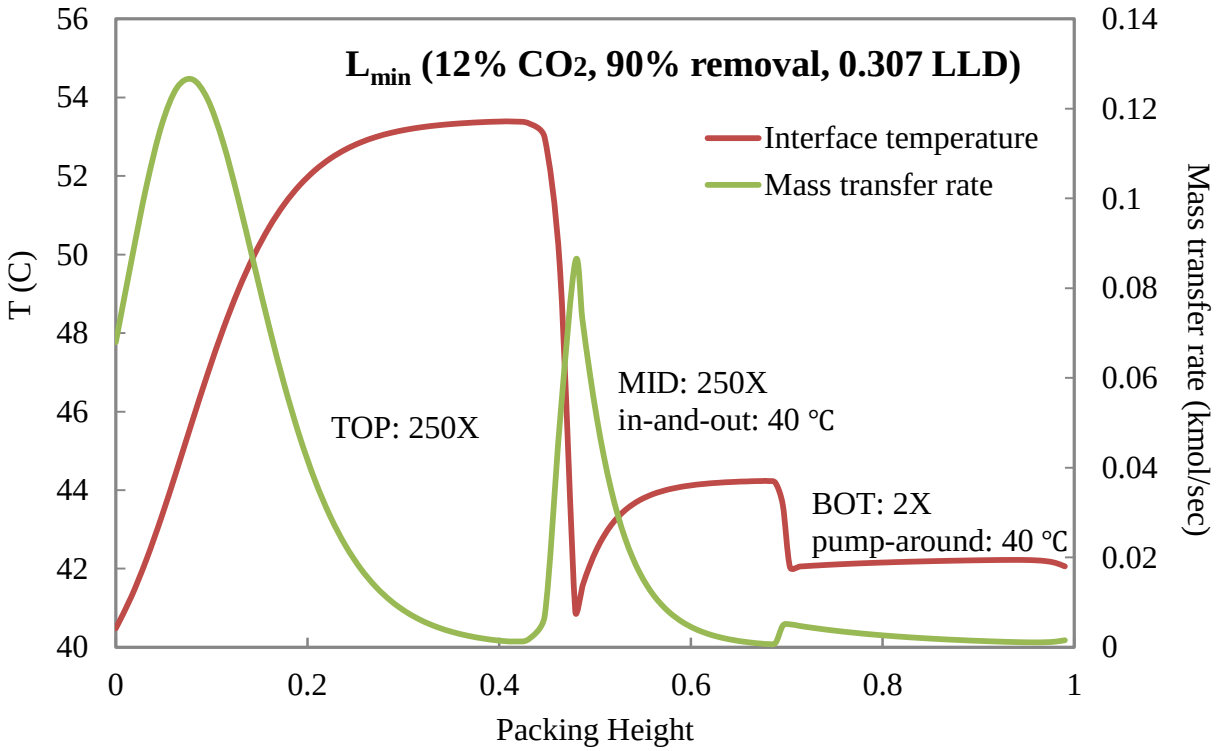

Figure 6: Interface temperature profile and mass transfer rate profile for L_{min} of Case 4

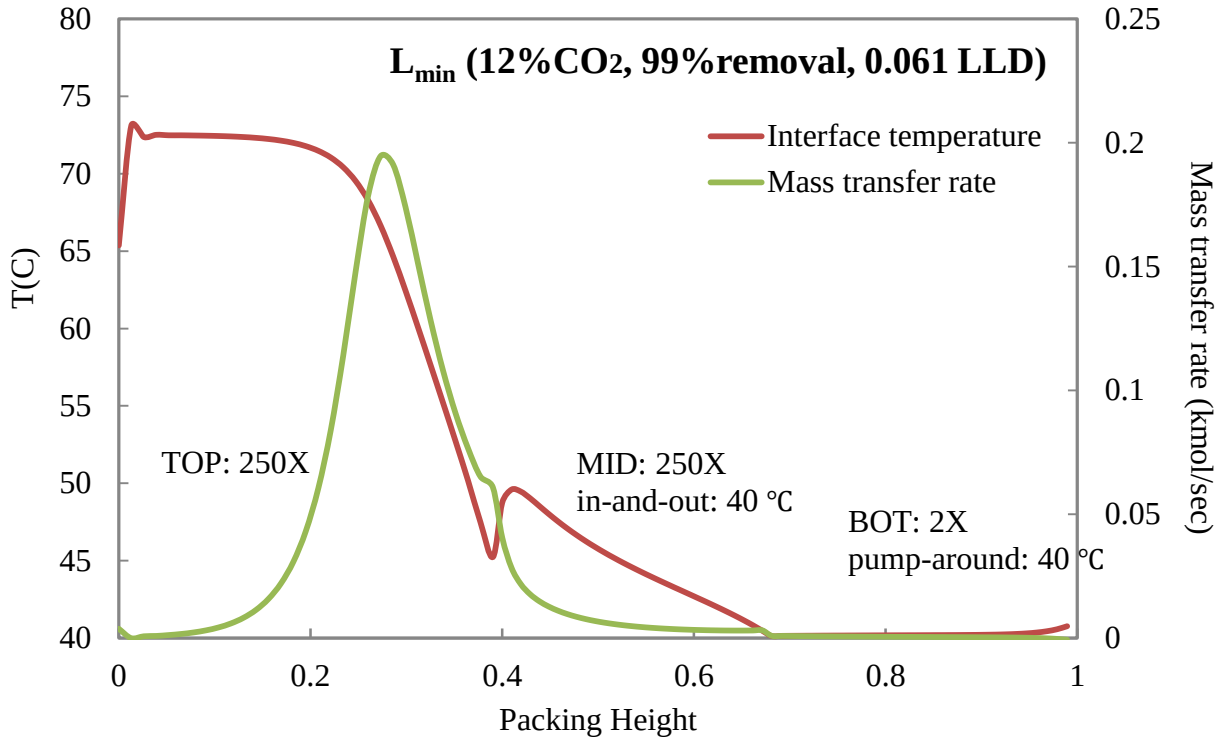

Figure 7: Interface temperature profile and mass transfer rate profile for L_{min} of Case 5

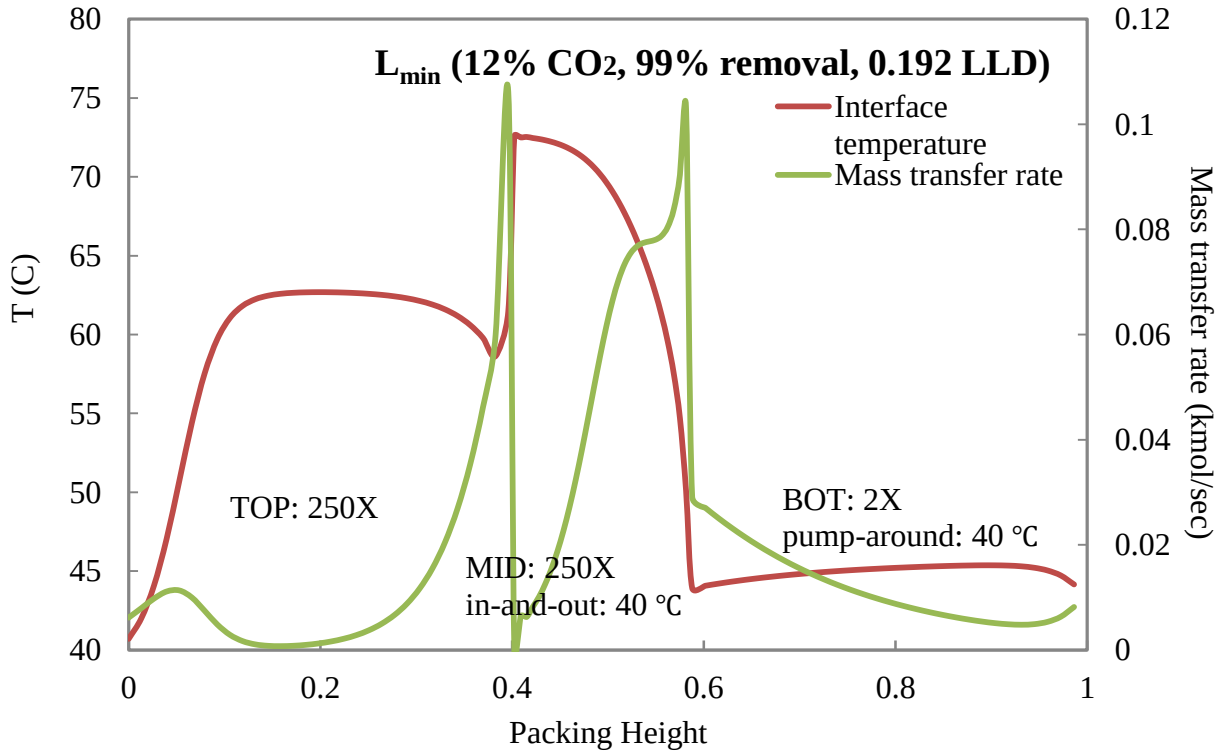

Figure 8: Interface temperature profile and mass transfer rate profile for L_{min} of Case 6

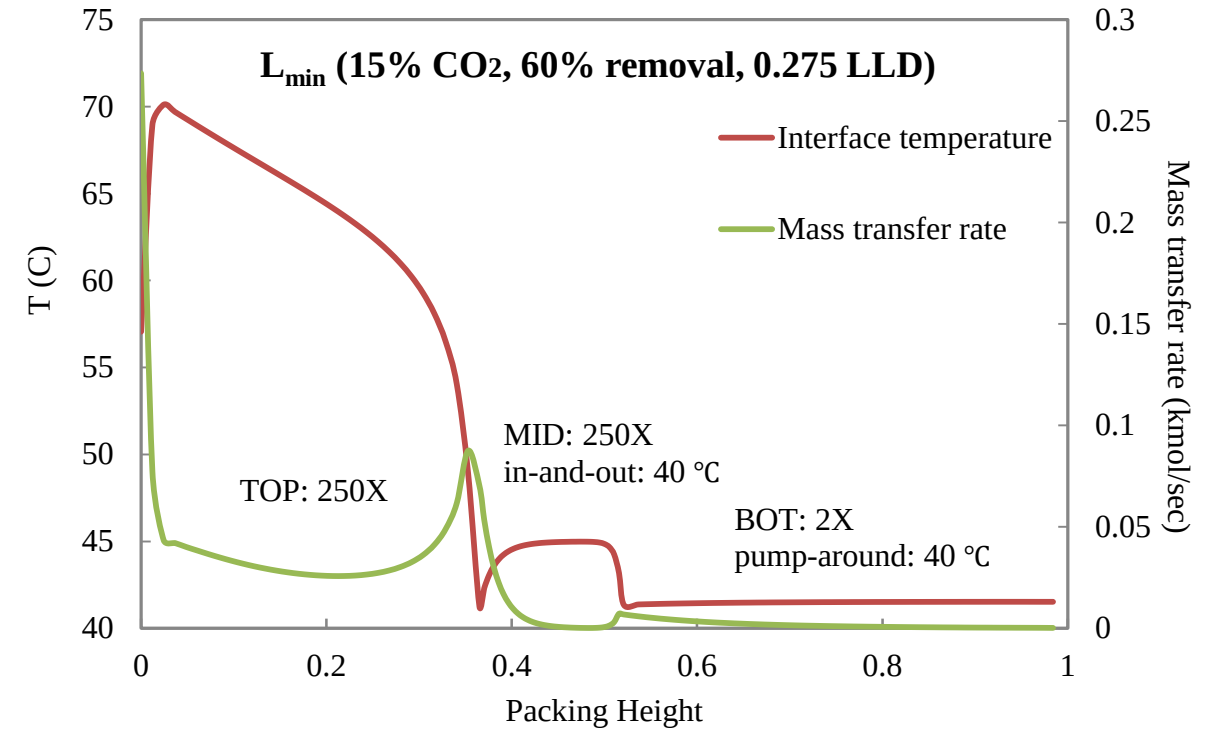

Figure 9: Interface temperature profile and mass transfer rate profile for L_{min} of Case 7

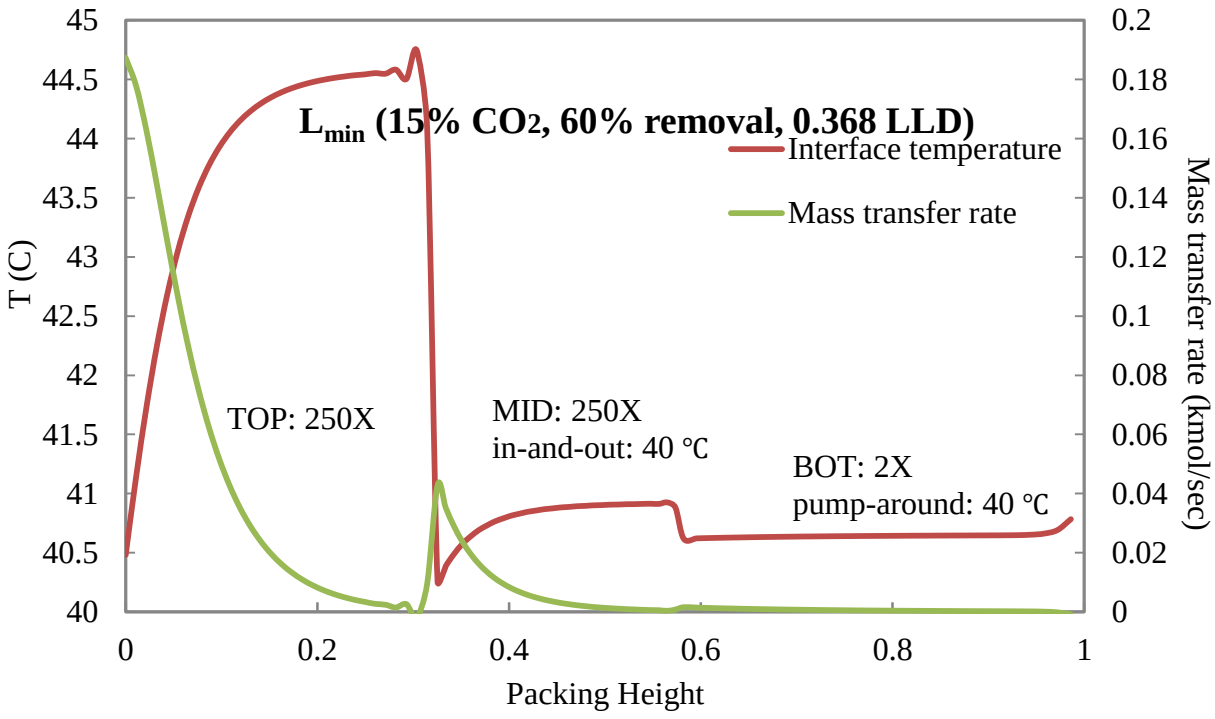

Figure 10: Interface temperature profile and mass transfer rate profile for L_{min} of Case 8

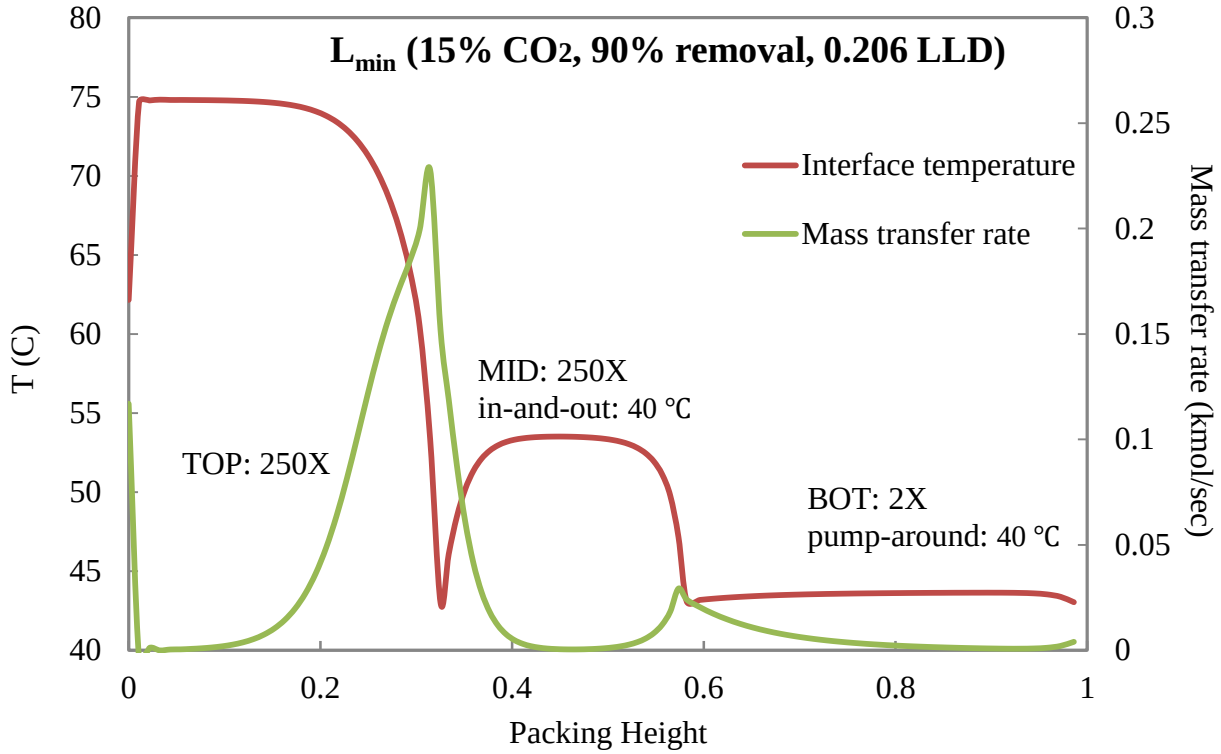

Figure 11: Interface temperature profile and mass transfer rate profile for L_{min} of Case 9

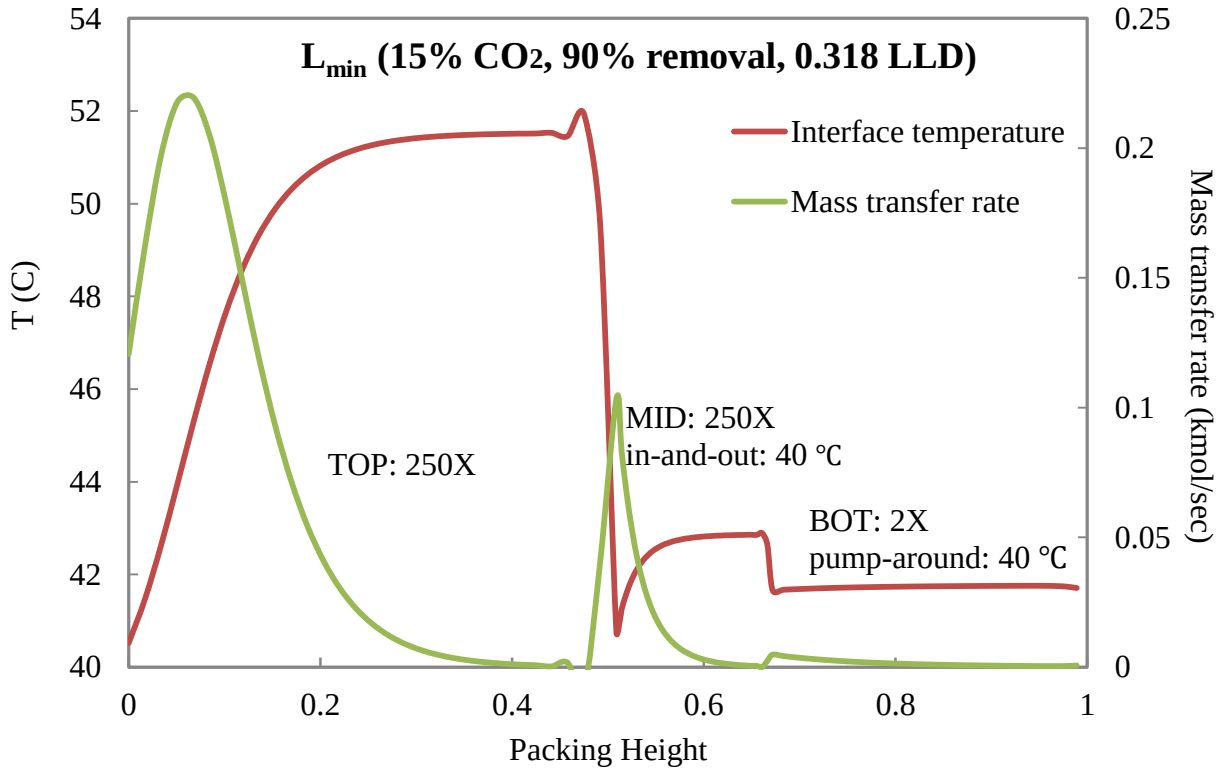

Figure 12: Interface temperature profile and mass transfer rate profile for L_{min} of Case 10

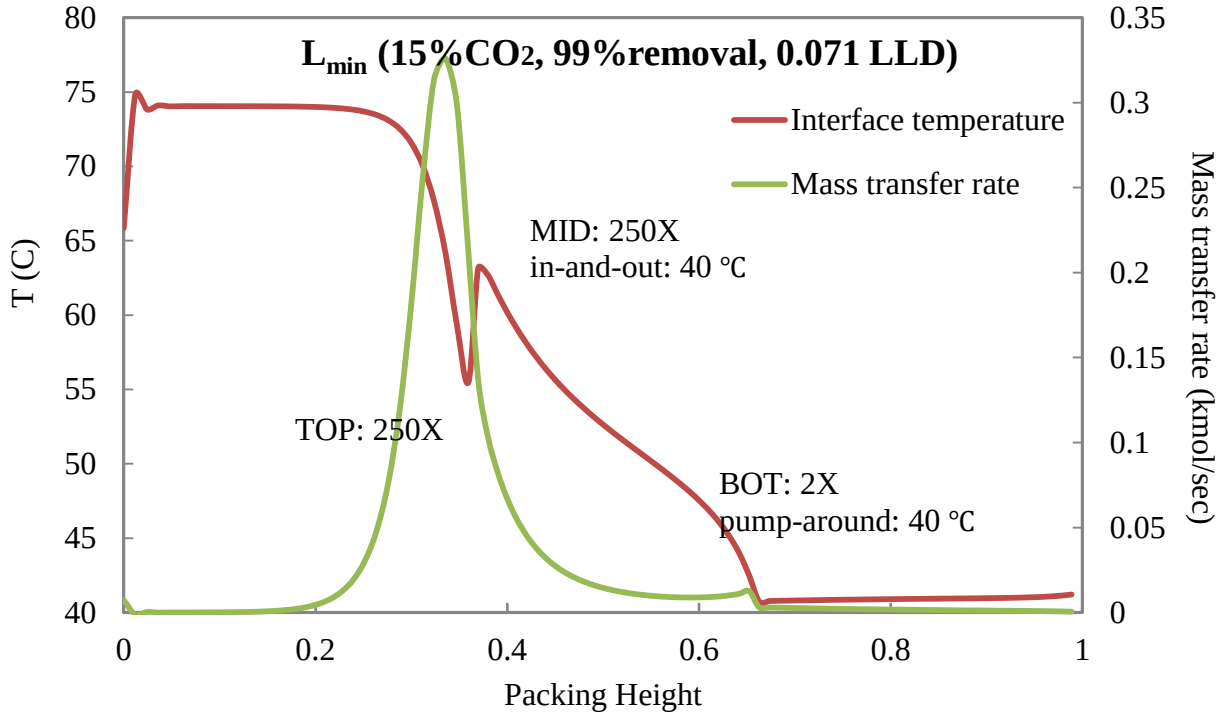

Figure 13: Interface temperature profile and mass transfer rate profile for L_{min} of Case 11

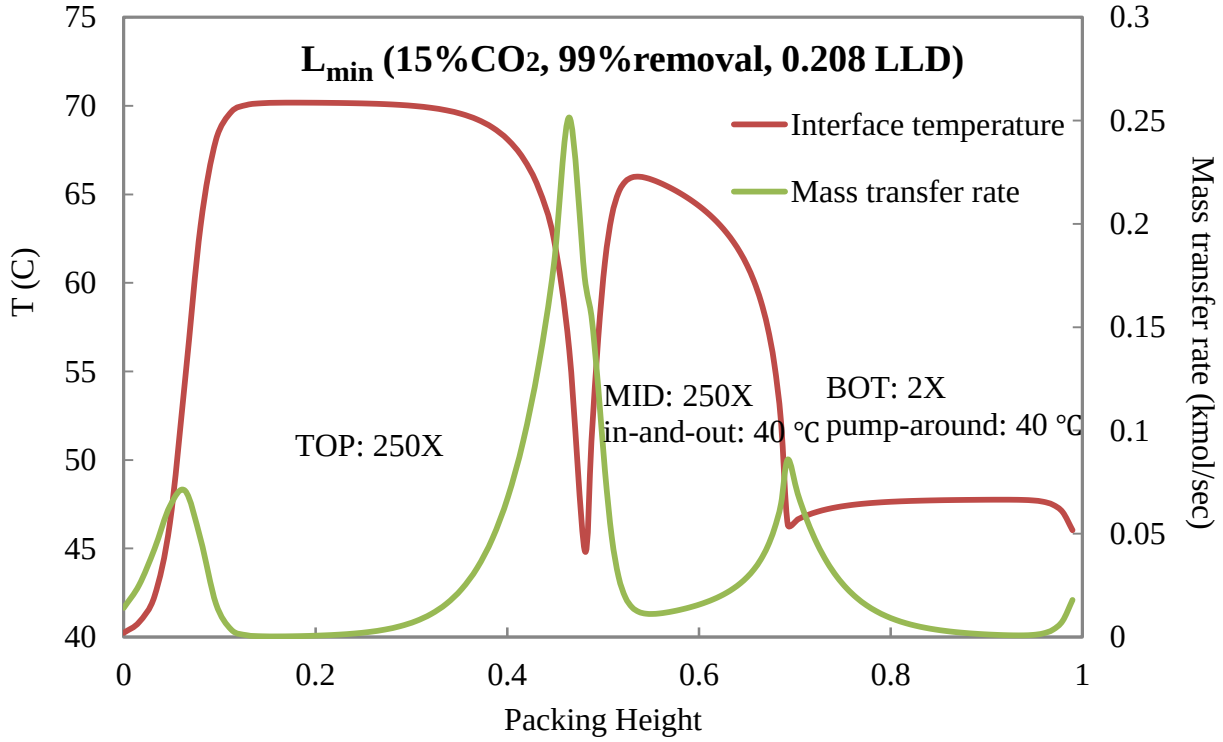

Figure 14: Interface temperature profile and mass transfer rate profile for L_{min} of Case 12

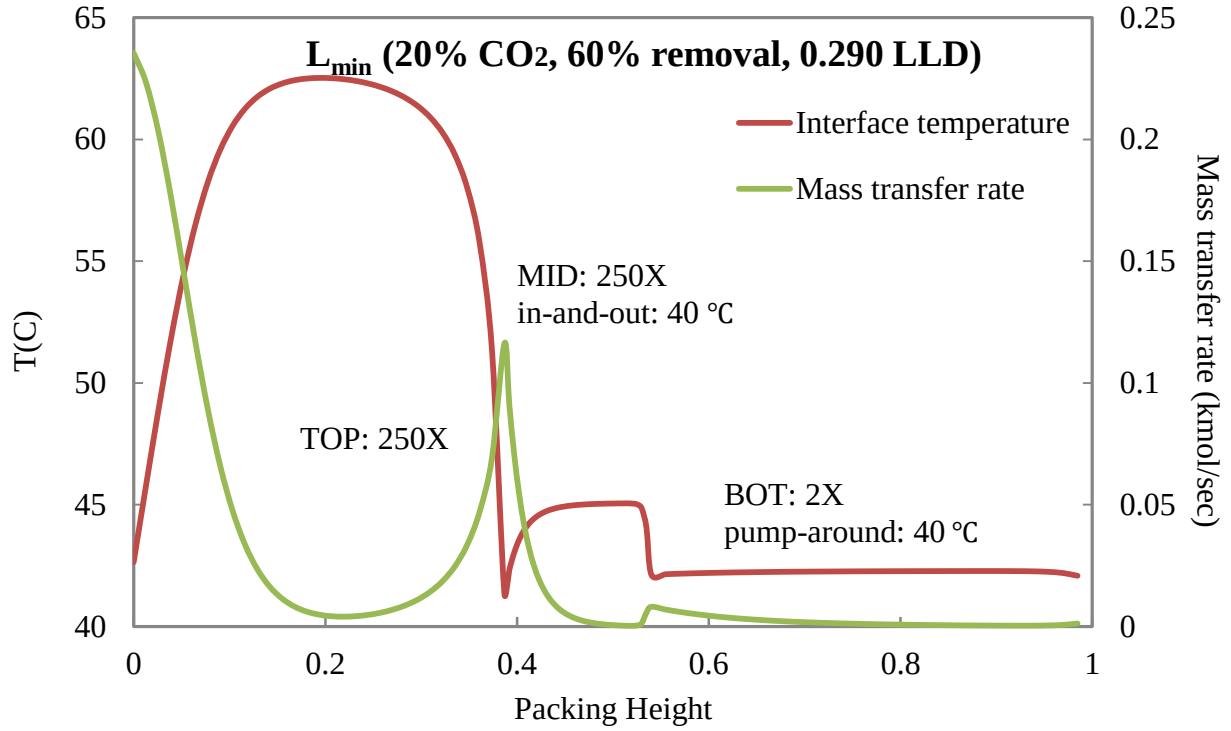

Figure 15: Interface temperature profile and mass transfer rate profile for L_{min} of Case 13

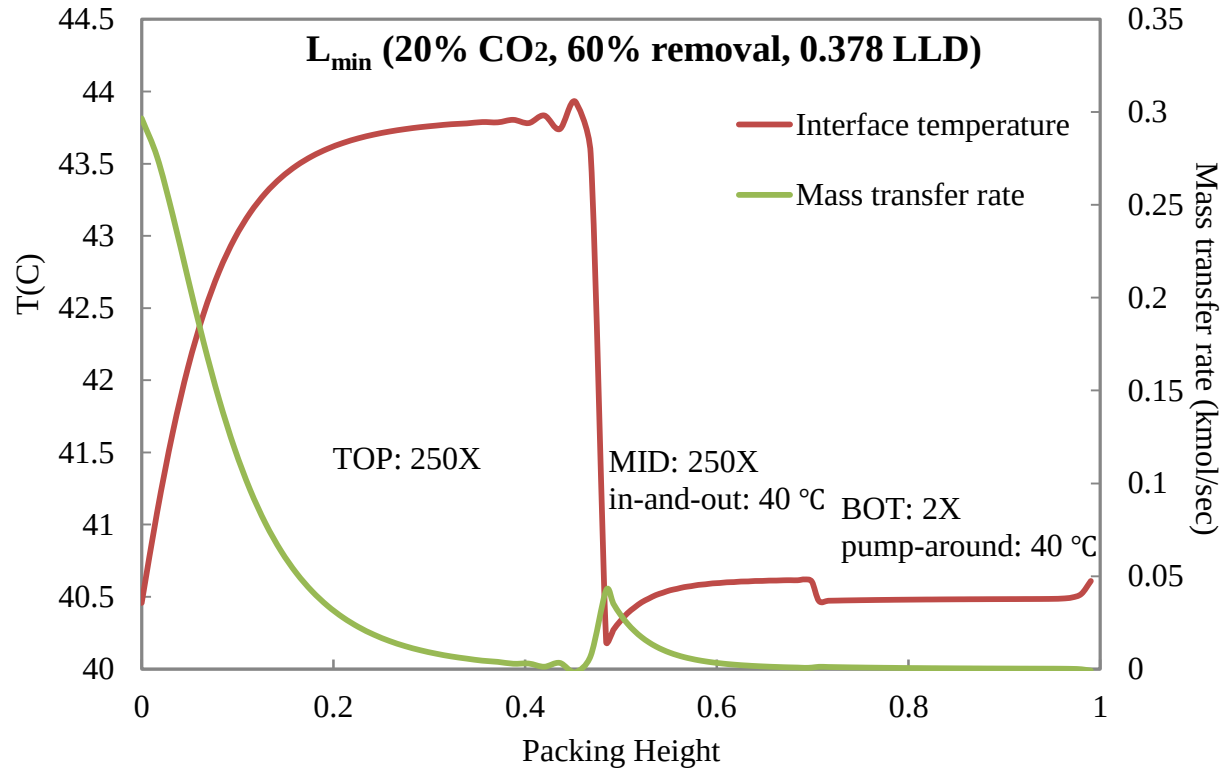

Figure 16: Interface temperature profile and mass transfer rate profile for L_{min} of Case 14

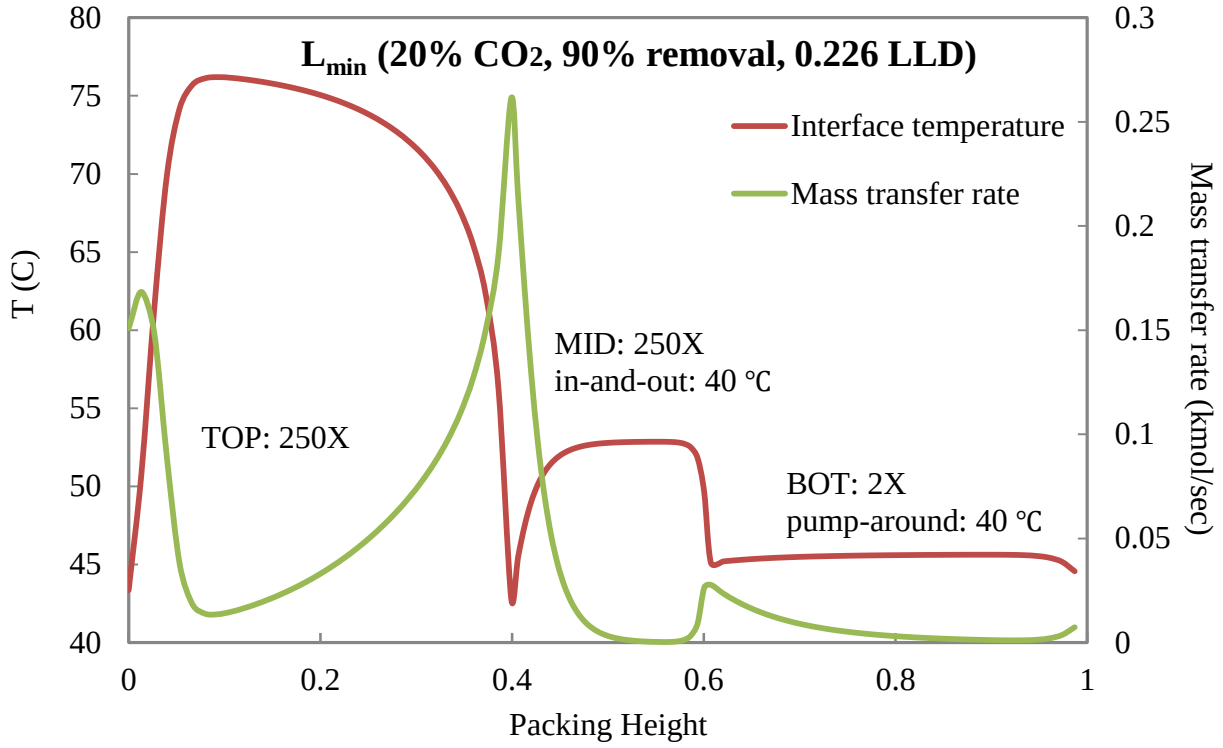

Figure 17: Interface temperature profile and mass transfer rate profile for L_{min} of Case 15

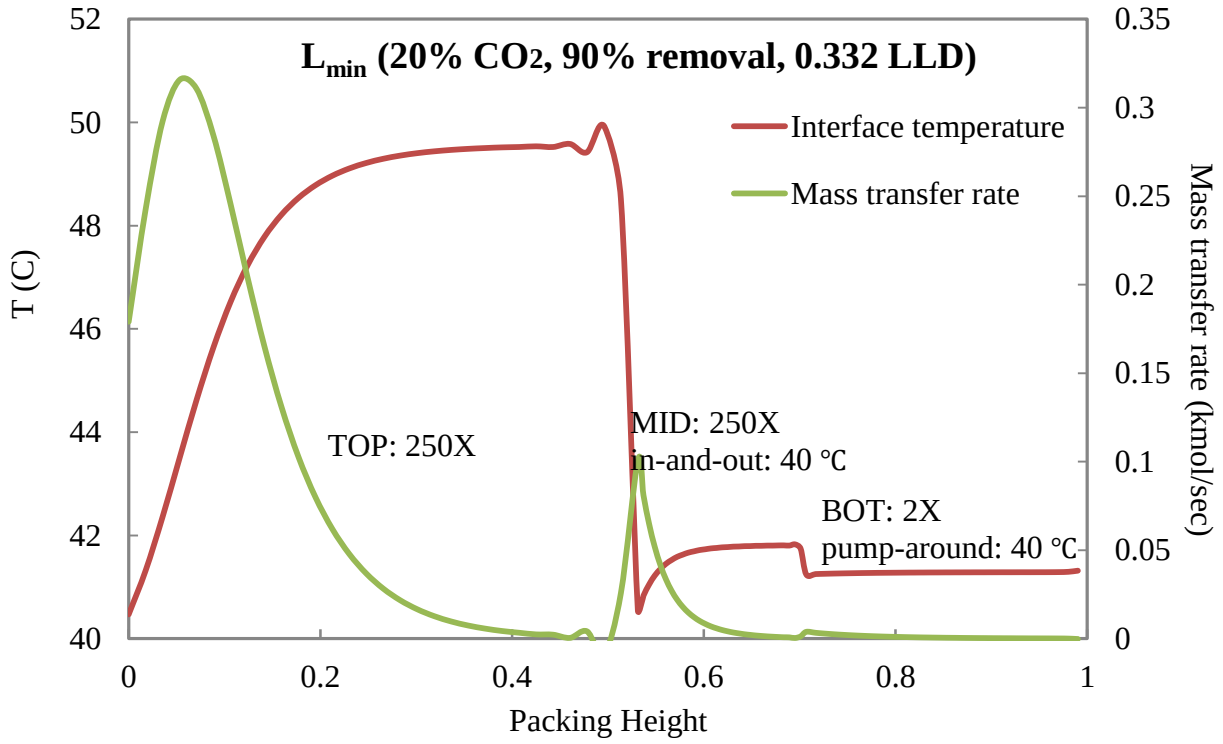

Figure 18: Interface temperature profile and mass transfer rate profile for L_{min} of Case 16

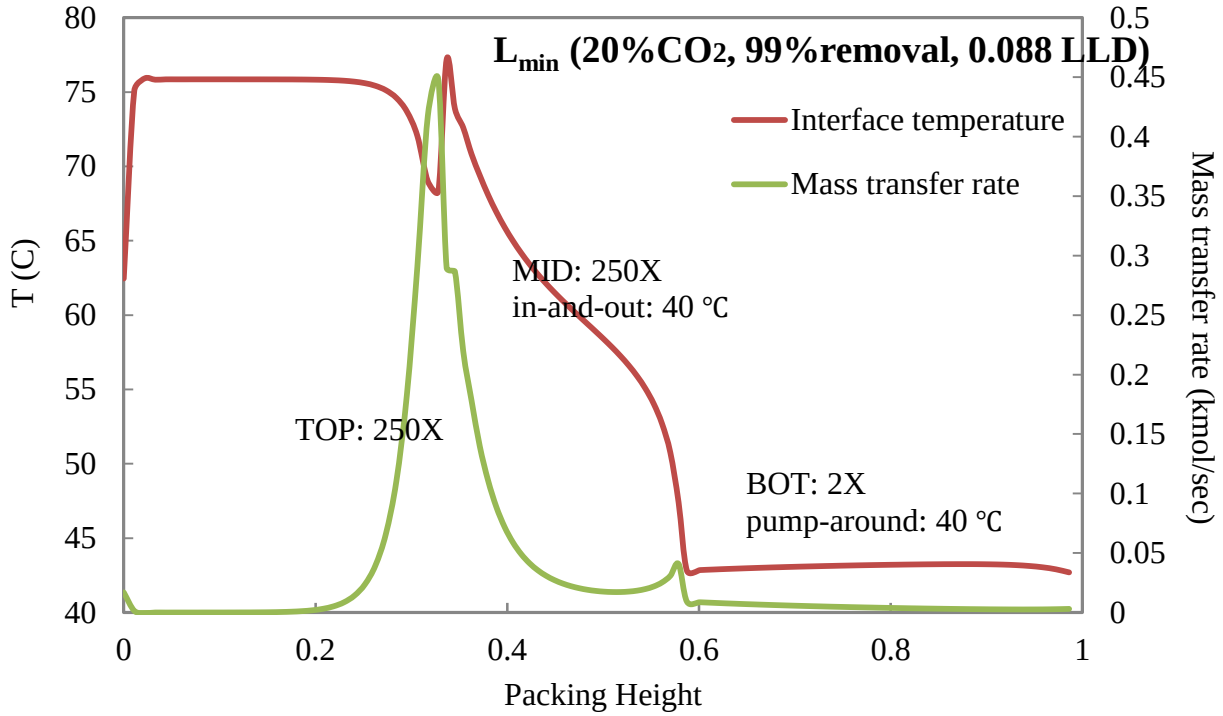

Figure 19: Interface temperature profile and mass transfer rate profile for L_{min} of Case 17

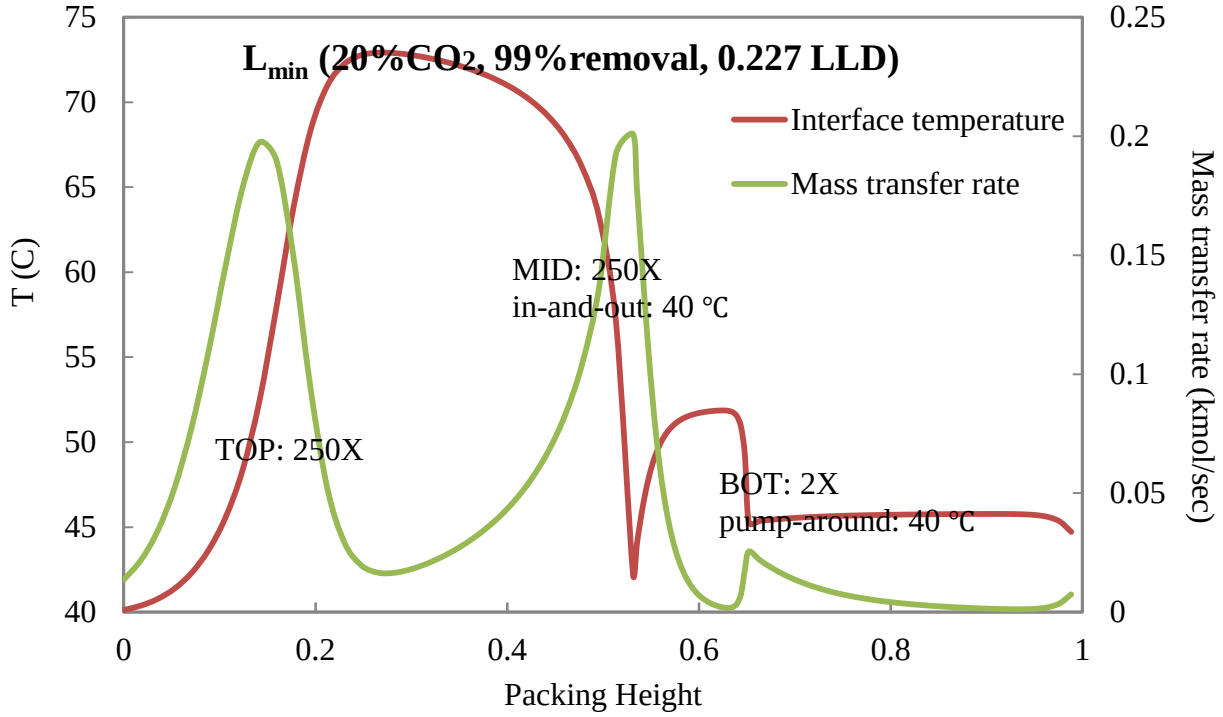

Figure 20: Interface temperature profile and mass transfer rate profile for L_{min} of Case 18

Pinch exists where the flux is zero. In all L_{min} cases, the pinch is reached at the middle, and bottom part of the absorber. For Cases 1 & 7, there is no real pinch in the top section. Table 2 shows T_{max} magnitude and position of each packing section.

Table 2: T_{max} magnitude and position summary

Cases	CO_2 Conc (%)	Removal (%)	Lean loading	Top		Middle		Bottom	
				T_{max}(℃)	T_{max} location	T_{max}(℃)	T_{max} location	T_{max}(℃)	T_{max} location
1	12	60	0.265	66.9	top	43.6	mid	41.0	bot
2	12	60	0.36	45.5	bot	41.3	bot	40.8	bot
3	12	90	0.192	75.0	top	45.0	mid	41.1	bot
4	12	90	0.307	53.3	bot	44.2	bot	42.2	bot
5	12	99	0.061	72.5	top	49.5	top	40.8	bot
6	12	99	0.192	62.2	mid	72.3	top	45.2	bot
7	15	60	0.275	70.1	top	44.2	bot	41.5	bot
8	15	60	0.368	44.7	bot	40.9	bot	40.8	bot
9	15	90	0.206	74.8	top	53.5	mid	43.5	bot
10	15	90	0.318	51.9	bot	42.9	bot	41.7	bot
11	15	99	0.071	74.8	top	62.7	top	41.2	bot
12	15	99	0.208	70.1	mid	66.0	mid	47.6	mid
13	20	60	0.29	62.5	mid	45.0	bot	42.3	bot
14	20	60	0.378	43.9	bot	40.6	bot	40.6	bot
15	20	90	0.226	76.1	mid	52.5	bot	45.5	bot
16	20	90	0.332	49.9	bot	41.7	bot	41.3	bot
17	20	99	0.088	75.8	top	77.2	top	43.3	bot
18	20	99	0.227	72.9	mid	51.9	bot	45.7	bot

Table 2 shows that for most cases T_{max} is in the top section (except for Cases 6 & 17). Due to excessive packing height of each section, the solvent rate is low, as a result of which vapor will carry most of the heat and push heat to the top of the absorber. For the same inlet CO_2 concentration and same CO_2 removal, T_{max} of over-stripping LLDG is higher than that of normal LLDG. Because L_{min} of over-stripping LLDG cases is lower, the in-and-out intercooling is not sufficient. The heat accumulates, resulting in higher T_{max}.

Figure 1 shows that most of CO_2 absorption occurs in the top section. Some CO_2 is removed in the middle section, and there is almost no CO_2 being removed in the bottom section. The heat duty of the in-and-out intercooling and pump-around intercooling are very low, suggesting that the intercoolers are not effective. The middle and bottom sections as well as the two intercoolers can be removed from the absorber. For every single case, the packing requirement and absorber configuration can be modified by looking at the mass transfer profile and intercooler heat duty in L_{min} cases.

Absorber performance with intercooling

To improve the mass transfer rate, both in-and-out intercooling and pump-around intercooling have been simulated for the absorber. The solvent rate is $1.1*L_{min}$. The pump-around intercooling L/G is 5 mol/mol. The model calculates the solvent rate, packing areas, rich loading, and optimized position of intercooling for each case.

Table 3: Factorial design cases for optimization

Cases	CO_2 Conc (%)	Removal (%)	Lean loading	L_{min} (kg/sec)	Flow rate (kg/sec)	Diameter (meter)
1	12	60	0.265	1455.8	1601.4	16.239
2	12	60	0.360	4374.3	4811.7	17.909
3	12	90	0.192	1419.9	1561.8	16.251
4	12	90	0.307	3190.4	3509.5	17.339
5	12	99	0.061	935.0	1028.5	16.035
6	12	99	0.192	1620.0	1782.0	16.534
7	15	60	0.275	1906.4	2097.0	16.566
8	15	60	0.368	5848.9	6433.8	18.442
9	15	90	0.206	1894.9	2084.3	16.750
10	15	90	0.318	4221.6	4643.8	17.144
11	15	99	0.071	1196.6	1316.2	16.446
12	15	99	0.208	2172.4	2389.7	17.025
13	20	60	0.290	2752.4	3027.6	17.065
14	20	60	0.378	8584.5	9443.0	19.625
15	20	90	0.226	2764.6	3041.1	17.290
16	20	90	0.332	6137.4	6751.2	18.802
17	20	99	0.088	1675.9	1843.5	17.004
18	20	99	0.227	3063.2	3369.5	17.548

Table 4: Optimization results of factorial design

Case	Lean loading	Rich loading	L/G	Surface Area ($1000*m^2$)				Surface Area Fraction			Normalized Packing ($sec*m^2/mol$)
				Top	Mid	Bot	Total	Top	Mid	Bot	
1	0.265	0.397	3.32	116.65	53.28	131.65	301.59	0.39	0.18	0.44	222.27
2	0.360	0.405	9.72	346.87	164.87	225.36	737.10	0.47	0.22	0.31	543.26
3	0.192	0.390	3.31	130.65	101.33	150.33	382.32	0.34	0.27	0.39	187.70
4	0.307	0.398	7.20	332.43	155.36	168.69	656.47	0.51	0.24	0.26	322.55
5	0.061	0.379	2.27	162.92	121.39	109.16	393.48	0.41	0.31	0.28	175.76
6	0.192	0.382	3.78	219.91	106.56	187.67	514.14	0.43	0.21	0.37	229.65
7	0.275	0.401	4.34	126.19	53.88	135.81	315.89	0.40	0.17	0.43	186.25
8	0.368	0.410	12.97	410.22	194.72	220.09	824.98	0.50	0.24	0.27	486.47
9	0.206	0.392	4.40	129.28	102.06	136.16	367.49	0.35	0.28	0.37	144.45
10	0.318	0.404	9.49	372.68	119.36	197.16	689.21	0.54	0.17	0.29	270.91
11	0.071	0.3820	2.89	154.16	129.93	118.55	402.64	0.38	0.32	0.29	143.88
12	0.208	0.3864	5.04	246.51	108.68	129.16	484.35	0.51	0.22	0.27	173.08
13	0.290	0.406	6.24	144.18	57.18	140.61	341.97	0.42	0.17	0.41	151.22
14	0.378	0.416	18.99	509.42	233.40	252.99	995.81	0.51	0.23	0.25	440.35

15	0.226	0.397	6.38	158.68	82.83	128.01	369.52	0.43	0.22	0.35	108.94
16	0.332	0.411	13.75	464.40	153.59	210.15	828.14	0.56	0.19	0.25	244.14
17	0.088	0.386	4.03	137.97	109.03	142.21	389.21	0.35	0.28	0.37	104.31
18	0.227	0.397	7.07	294.62	67.02	158.23	519.89	0.57	0.13	0.30	139.33

Normalized packing can reflect the absorber efficiency.

Normalized packing = Total surface area/(Total Gas flow rate*CO_2 Conc*Removal) (1)

In Case 1,

Normalized packing = 301.59/(18.8450876*0.12*0.99) = 222.27 sec*m^2/mol.

A lower value for normalized packing indicates better absorber performance, because the absorber needs less packing to capture the same amount of CO_2. The normalized packing is also the reciprocal of the average CO_2 flux. Cases with low lean loading and high removal have lower normalized packing, which indicates better absorber performance. When using intercooling, the rich loading increases as expected with the inlet CO_2. At a given inlet CO_2, rich loading does not vary significantly, which indicates that the solvent practically reaches equilibrium with the CO_2 at the bottom of the absorber.

The ratio between solvent flow rate and gas flow rate (L/G) has great influence on absorber performance. At high lean loading L/G is high. The absorber performance can be seen from the liquid/gas temperature profile and CO_2 composition profile in Aspen Plus®. The secondary y axis is normalized flux.

Normalized flux = (CO_2 vapor mass transfer rate/Area)/CO_2 vapor composition (2)

Normalized flux is the CO_2 vapor flux divided by CO_2 vapor composition. Because mass transfer flux will change with both vapor phase and liquid phase, divided by CO_2 vapor composition, it is only dependent on the liquid phase. Liquid phase mass transfer dependence is more important in this research.

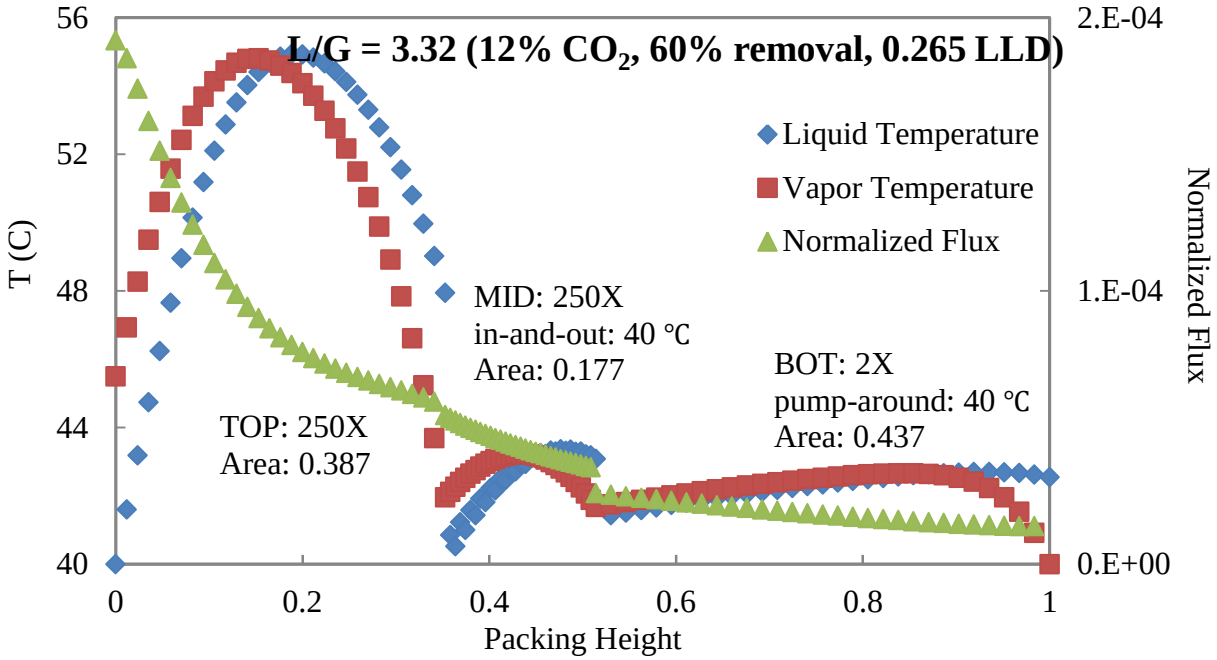

Figure 21: Absorber performance and interface temperature for Case 1

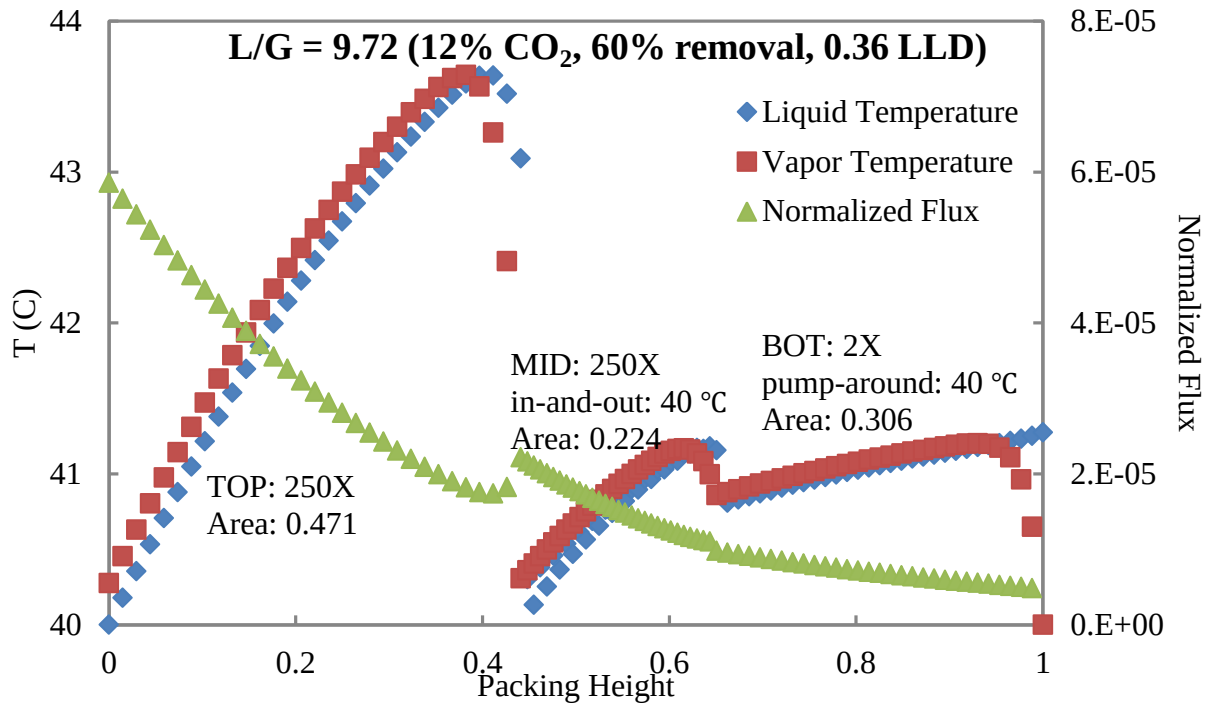

Figure 22: Absorber performance and interface temperature for Case 2

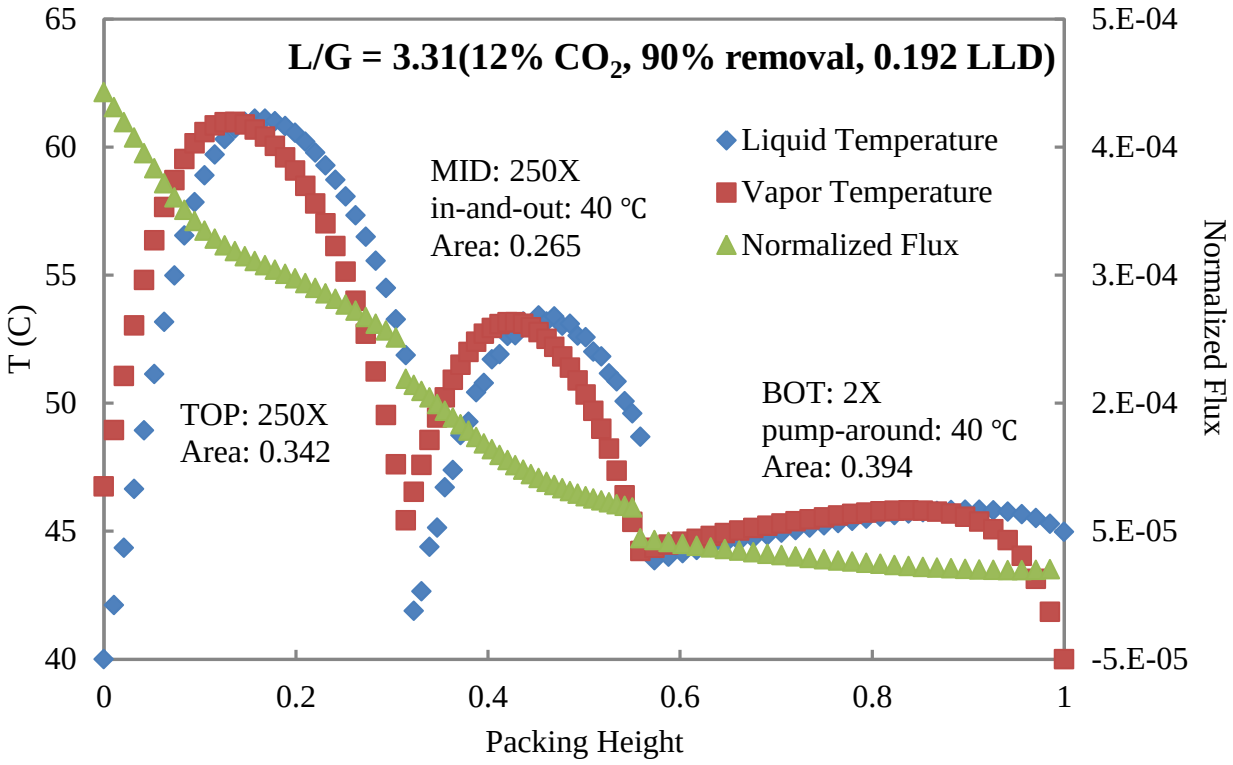

Figure 23: Absorber performance and interface temperature for Case 3

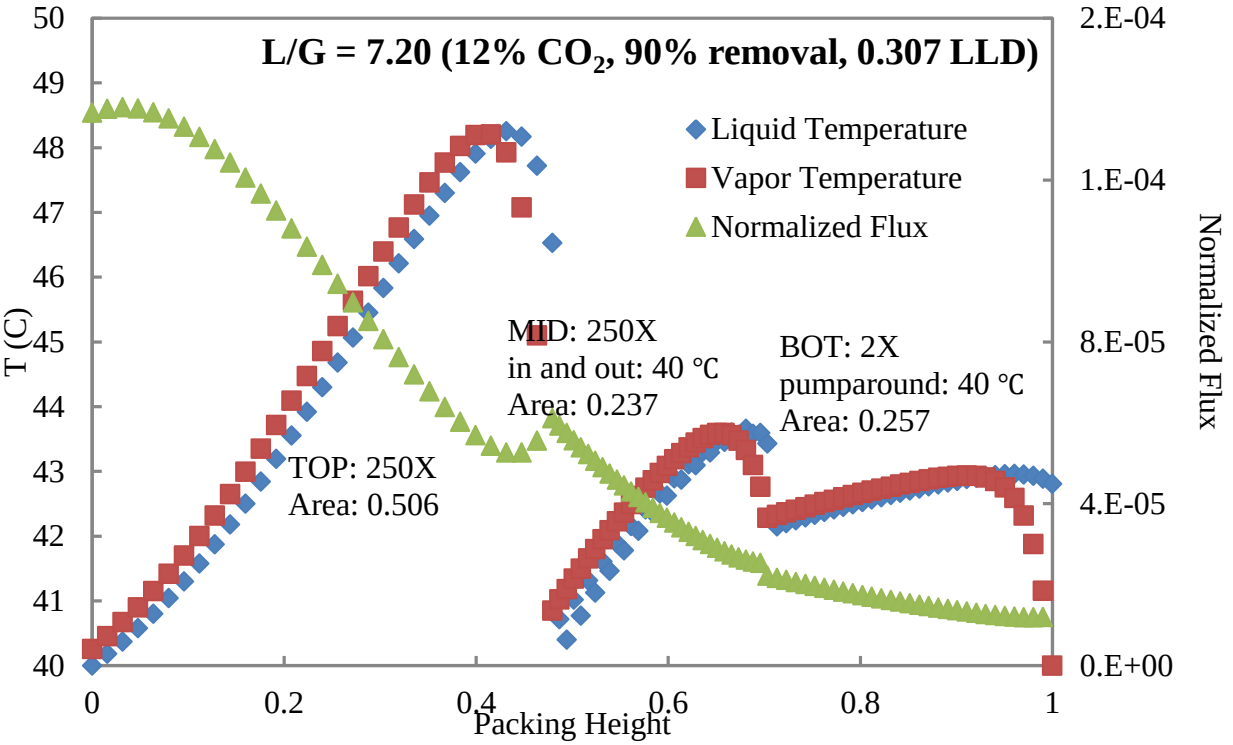

Figure 24: Absorber performance and interface temperature for Case 4

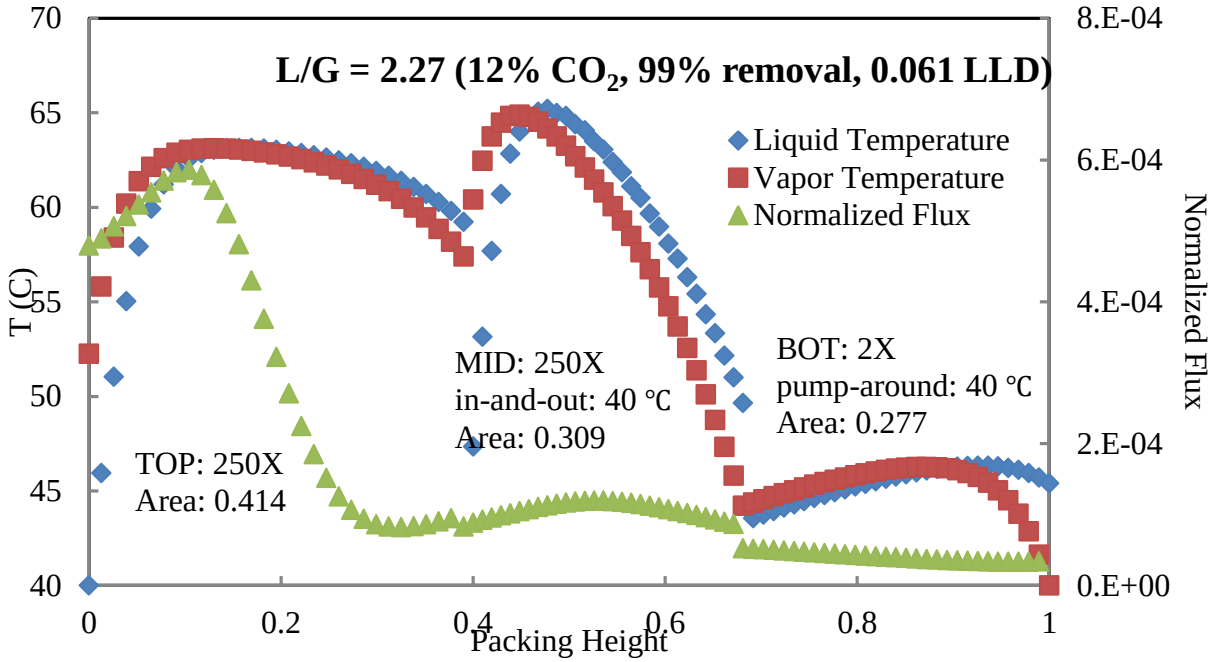

Figure 25: Absorber performance and interface temperature for Case 5

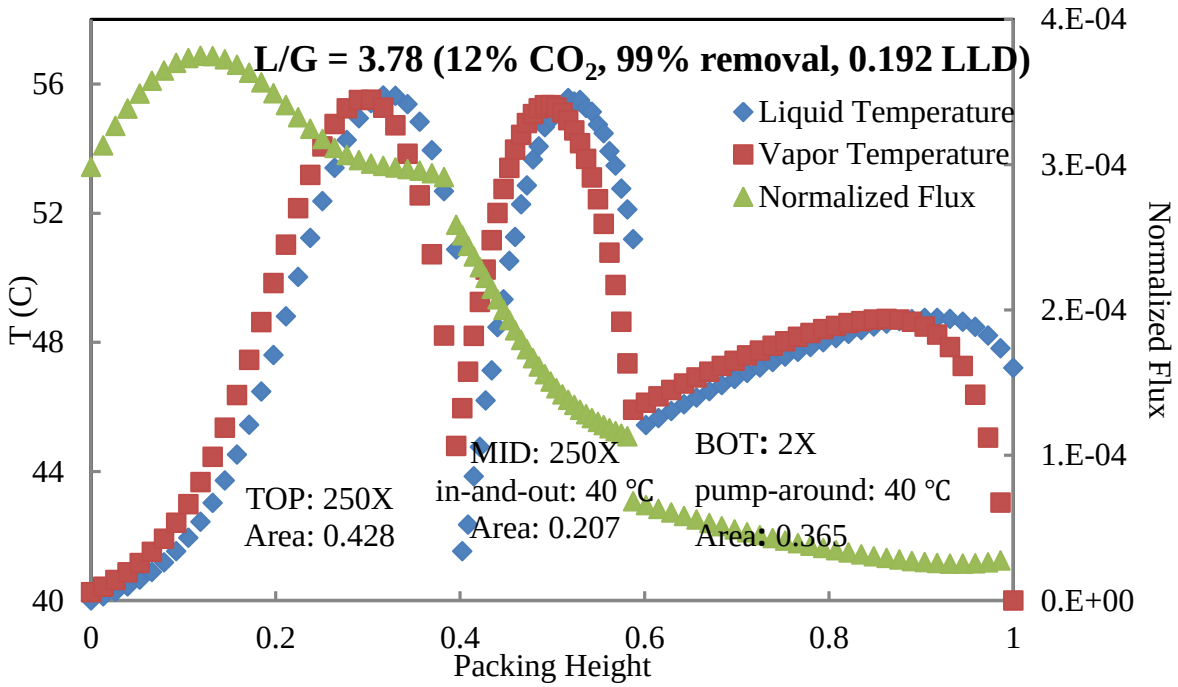

Figure 26: Absorber performance and interface temperature for Case 6

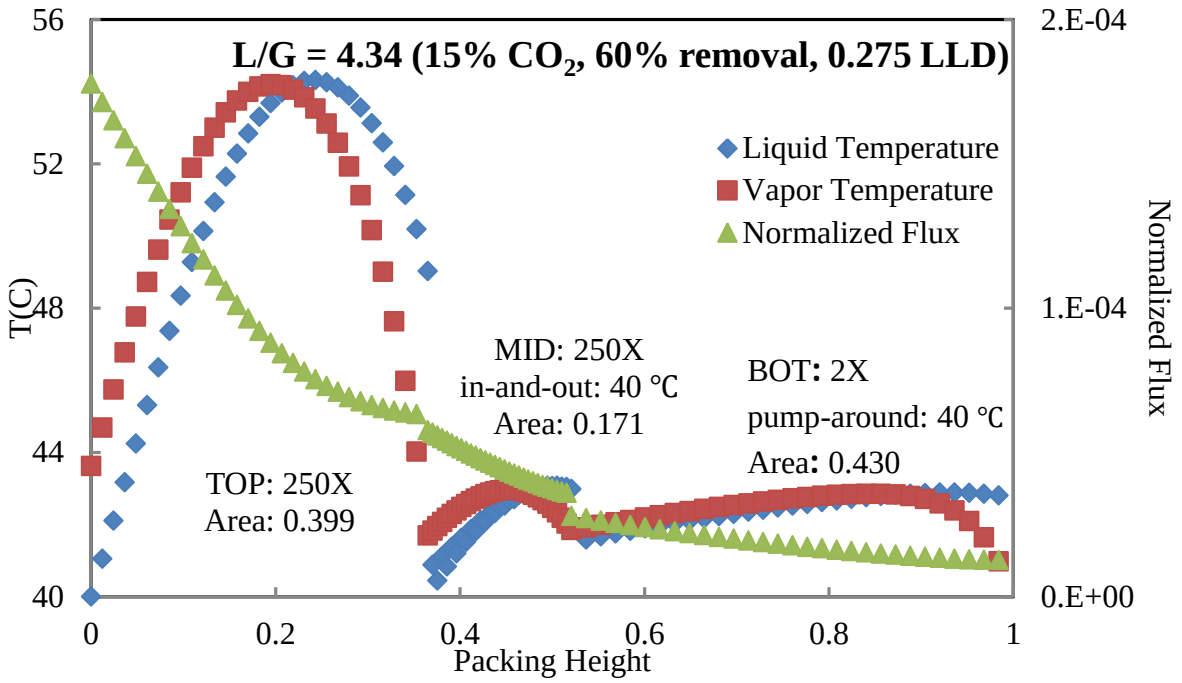

Figure 27: Absorber performance and interface temperature for Case 7

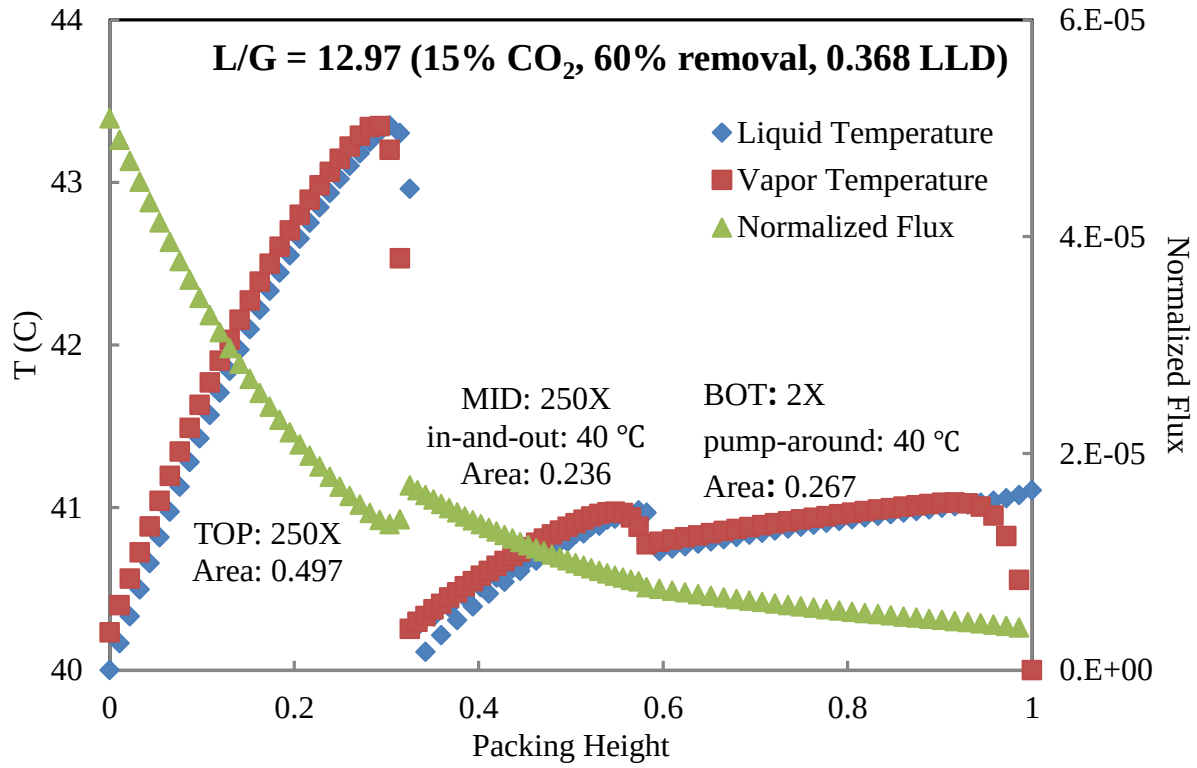

Figure 28: Absorber performance and interface temperature for Case 8

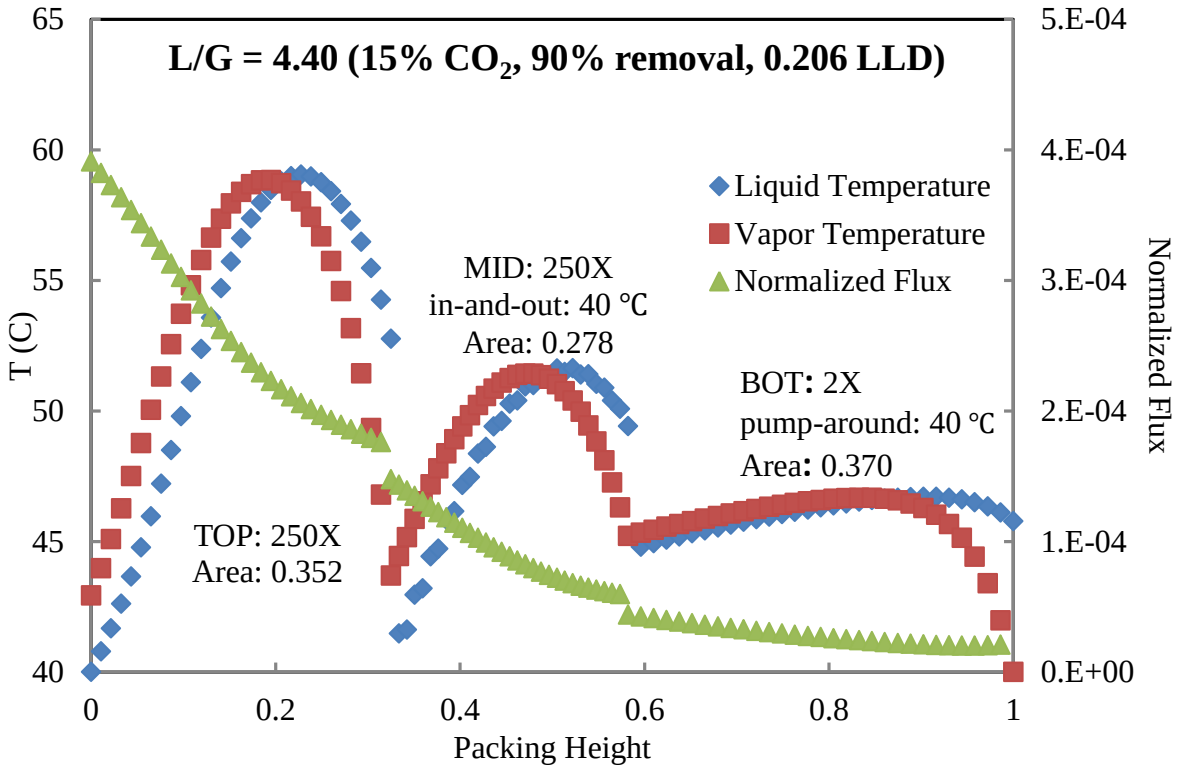

Figure 29: Absorber performance and interface temperature for Case 9

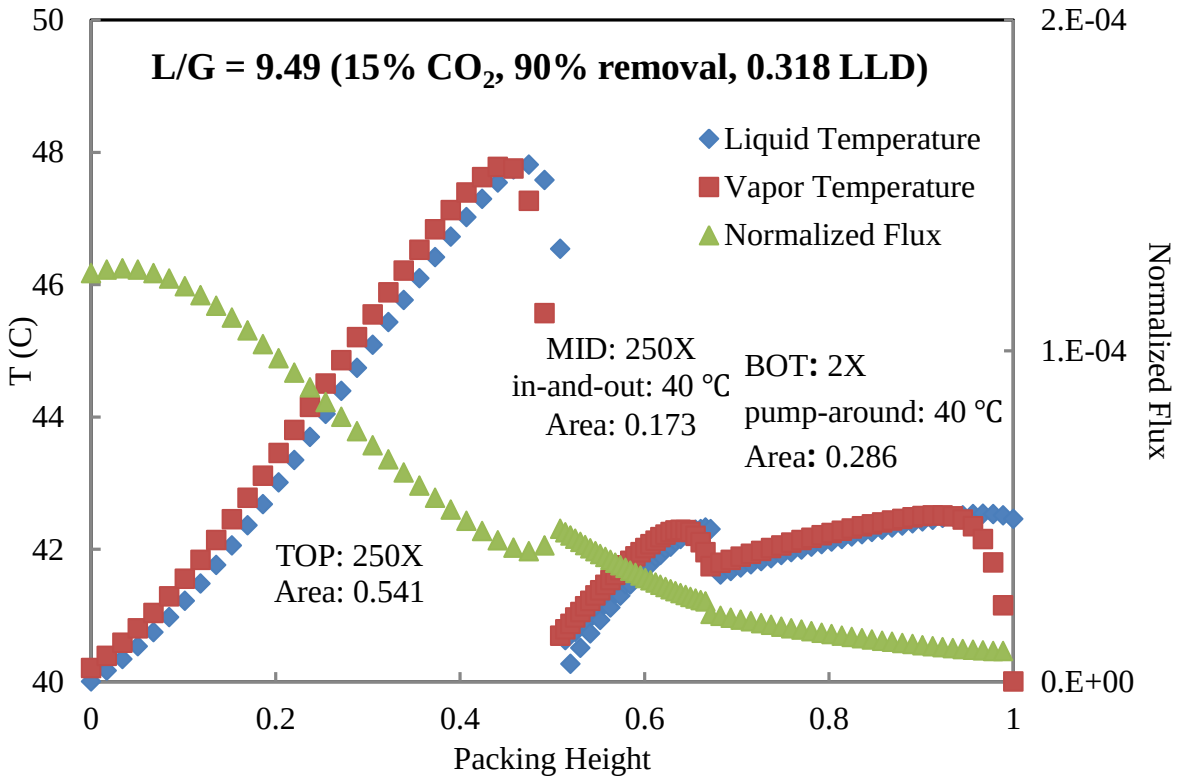

Figure 30: Absorber performance and interface temperature for Case 10

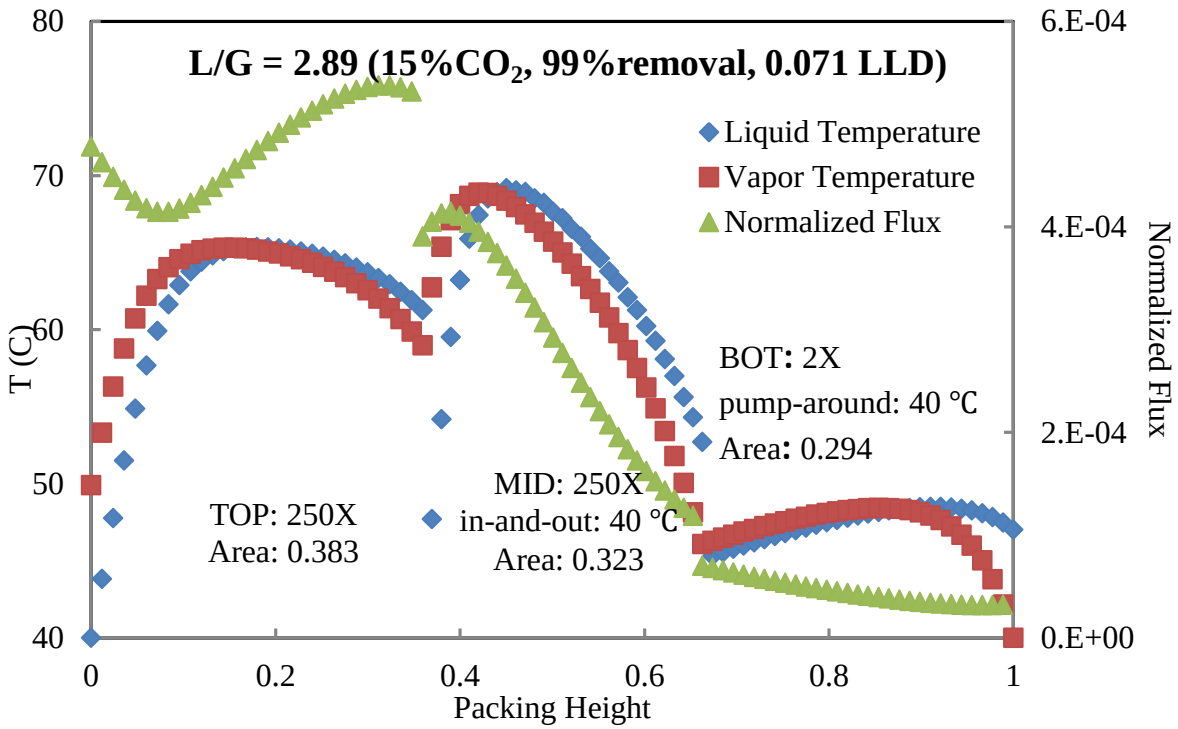

Figure 31: Absorber performance and interface temperature for Case 11

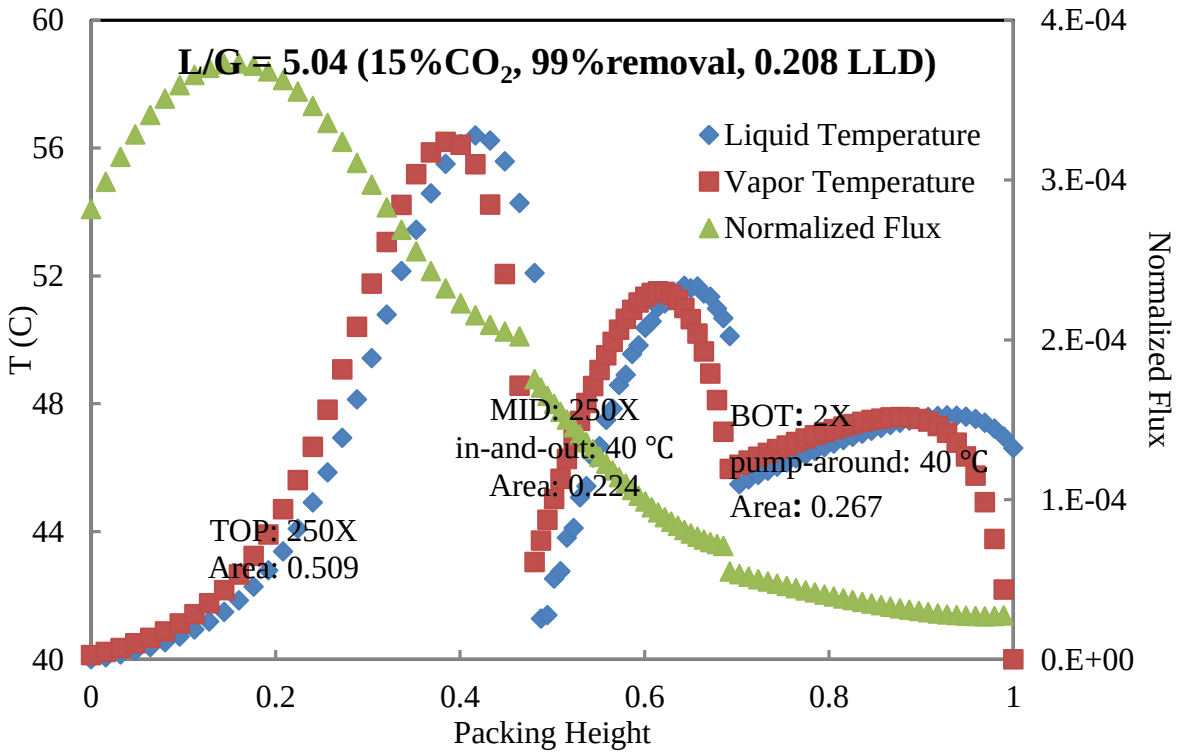

Figure 32: Absorber performance and interface temperature for Case 12

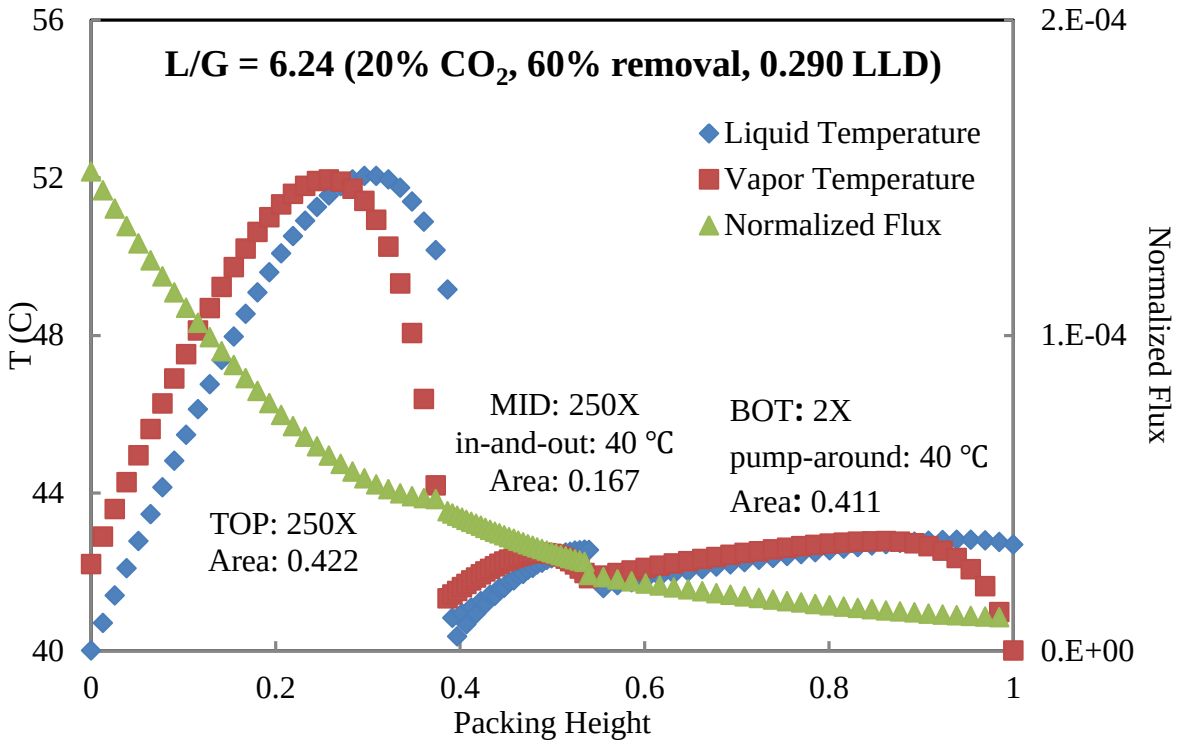

Figure 33: Absorber performance and interface temperature for Case 13

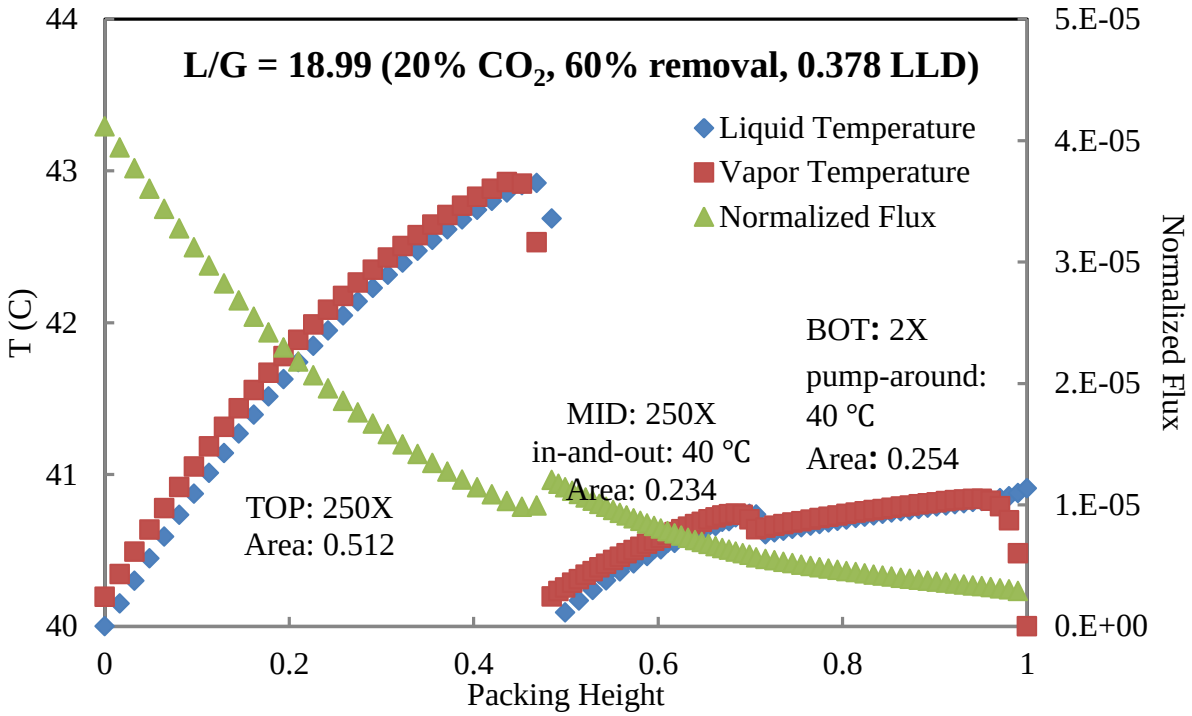

Figure 34: Absorber performance and interface temperature for Case 14

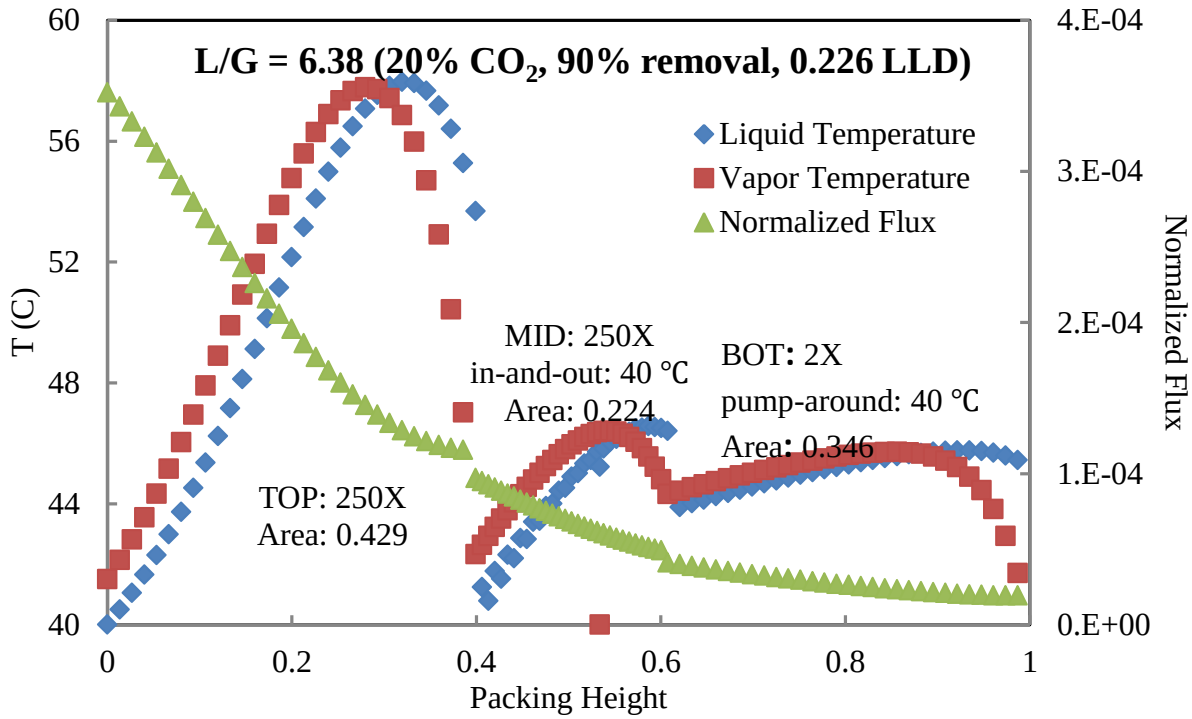

Figure 35: Absorber performance and interface temperature for Case 15

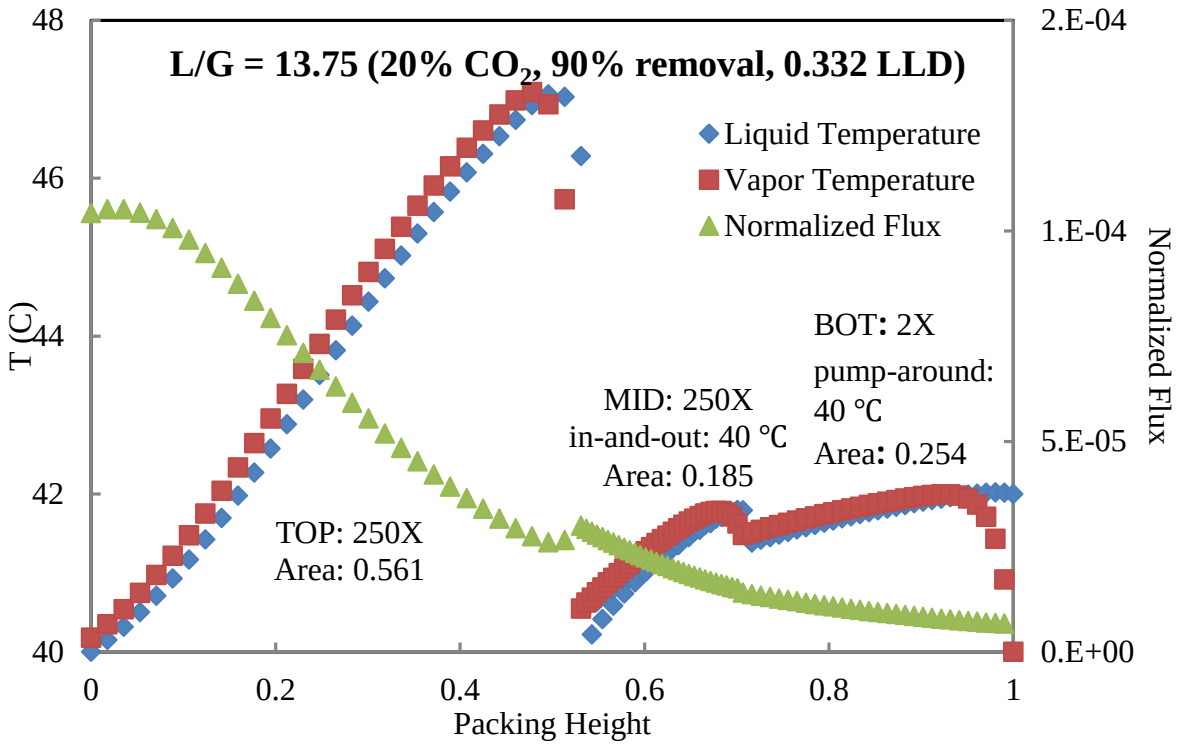

Figure 36: Absorber performance and interface temperature for Case 16

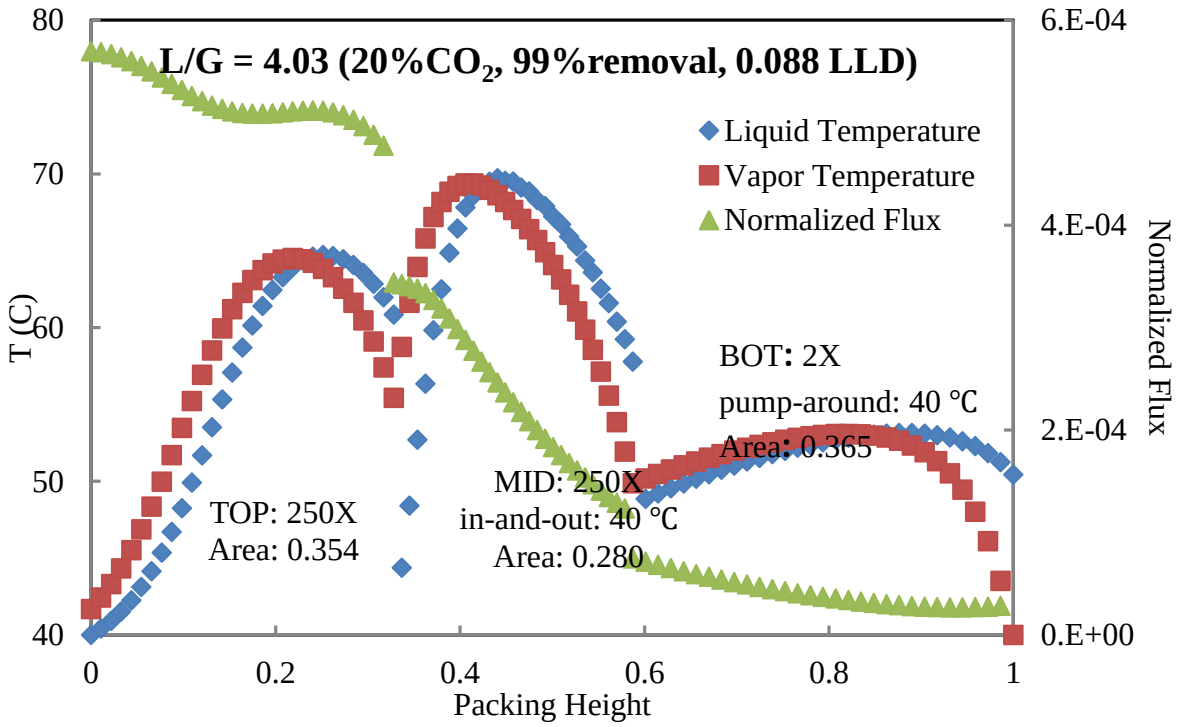

Figure 37: Absorber performance and interface temperature for Case 17

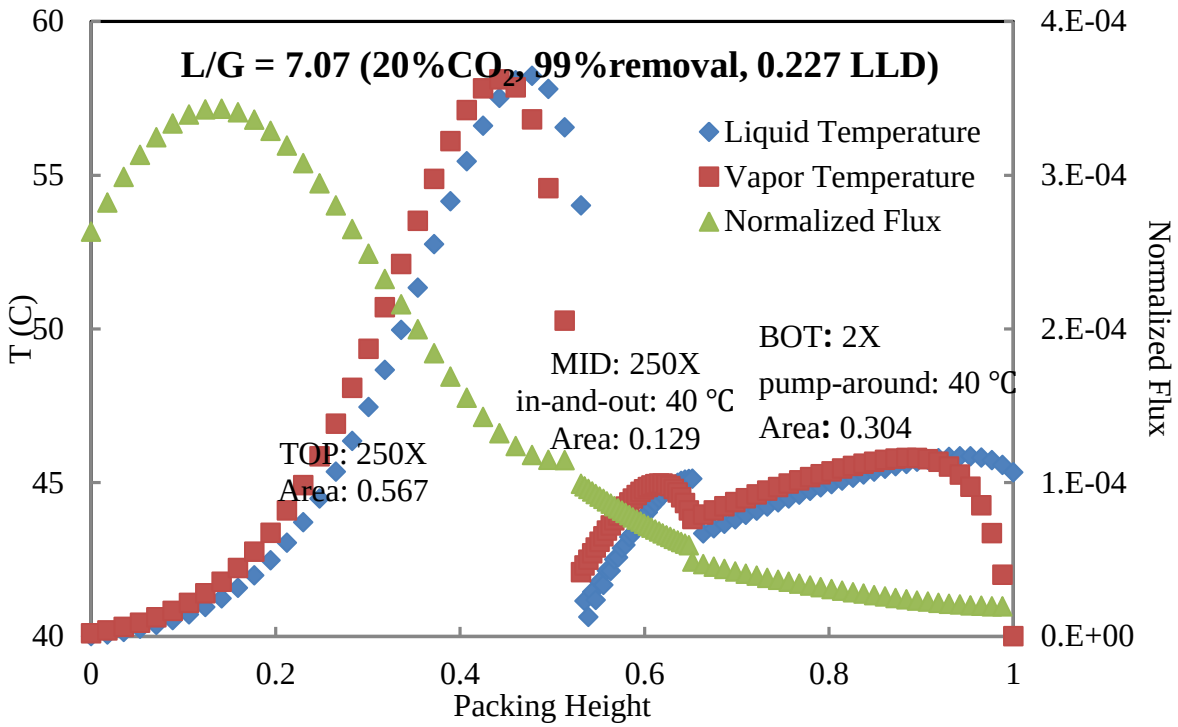

Figure 38: Absorber performance and interface temperature for Case 18

For all cases, when using intercooling the rich loading increases as expected with the inlet CO_2. At a given inlet CO_2 rich loading does not vary significantly, which indicates that the solvent practically reaches equilibrium with the CO_2 at the bottom of the absorber.

In high L/G cases, the in-and-out intercooling can sufficiently cool down the gas and liquid, and bring the heat down to the bottom of the absorber. The pump-around intercooling is not necessary, and in-and-out intercooling is necessary only in the middle of the absorber.

With low L/G, in-and-out intercooling is not effective and pump-around intercooling is desirable to cool down both the gas and the solvent. To minimize energy and capital cost, the in-and-out intercooling can be removed.

Intercooling modification

In Figure 21 (Case 1), the packing fraction of the middle part is 0.17, much lower than that of the two other sections. The middle section of packing can be removed.

In Figure 25 (Case 5), due to the low L/G value, the gas cannot be sufficiently cooled down. As a result, the in-and-out intercooling is not so effective. In Case 5-1 in-and-out intercooling has been removed and all the other operating conditions are the same as Case 5. The results are listed in Table 4.

Table 5: Intercooling modification of Case 5

Cases	Lean loading	Rich loading	L/G	Surface Area (1000*m^2)				Surface Area Fraction			Normalized Packing (sec*m^2/mol)
				Top	Mid	Bot	Total	Top	Mid	Bot	
5	0.061	0.379	2.27	162.92	121.39	109.16	393.48	0.41	0.31	0.28	175.76
5-1	0.061	0.372	2.32	280.70		152.68	433.38	0.65		0.35	193.58

In Case 5-1 there is a higher value for normalized packing, which indicates that the absorber needs more area to capture CO_2. However, due to the removal of the in-and-out intercooling, there is a substantial reduction in the capital cost.

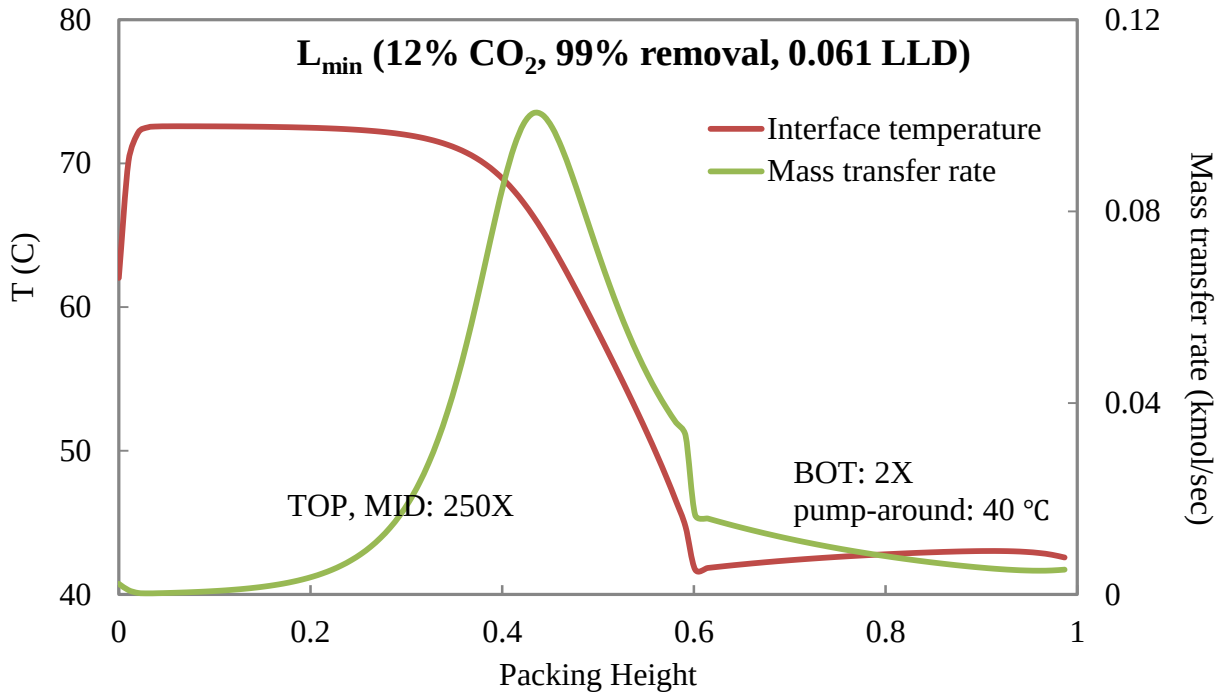

Figure 39: Interface temperature profile and mass transfer rate profile for L_{min} of Case 5-1

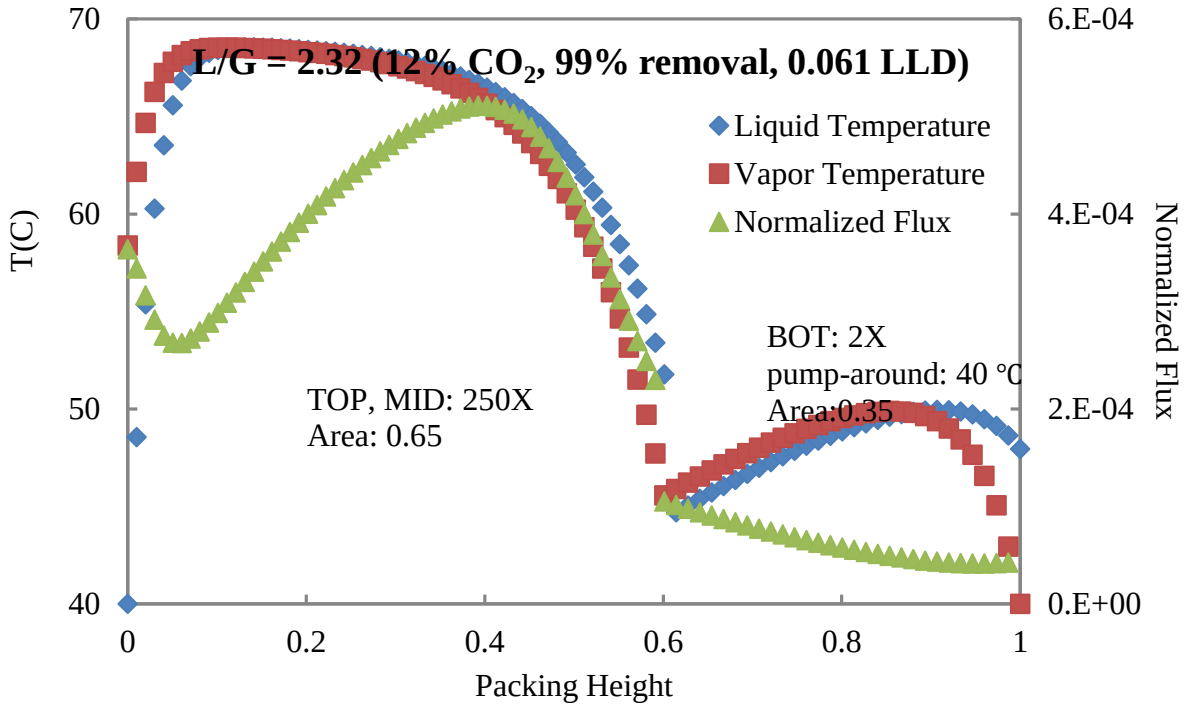

Figure 40: Absorber performance and interface temperature for Case 5-1

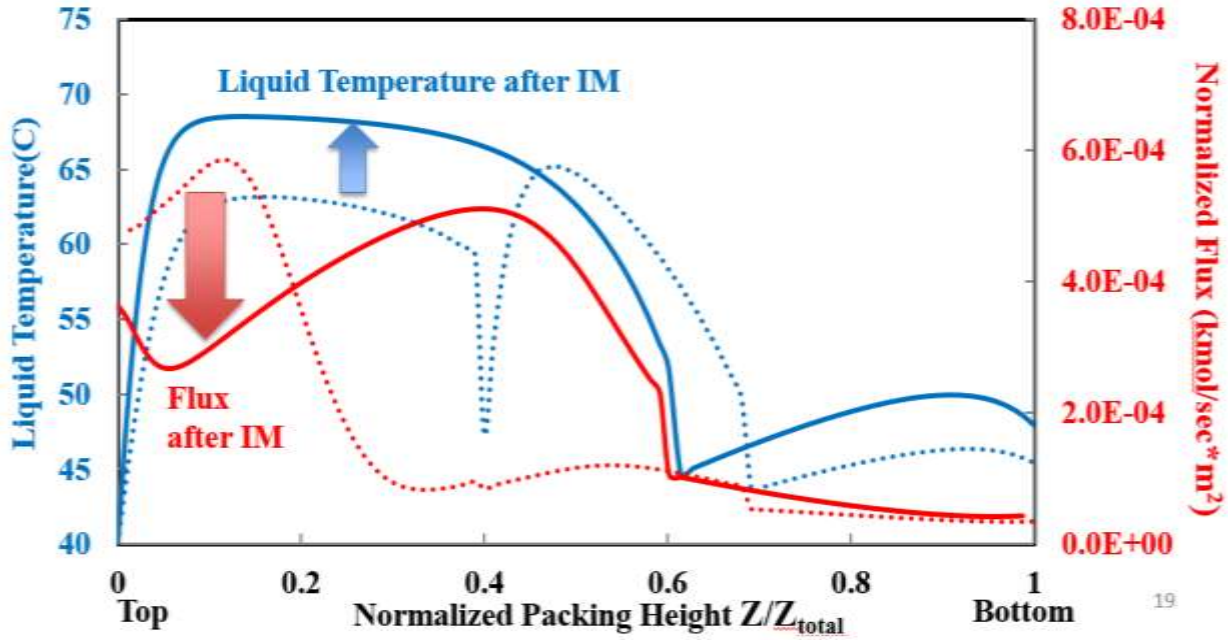

Figure 41: Comparison of absorber performance of Cases 5 & 5-1

Figure 41 shows that, after removing the in-and-out intercooling, the temperature of the top section is higher than that of Case 5, which limits the mass transfer rate in the top section. At the

same time, in Case 5-1, the packing fraction of the bottom section is higher than that of Case 5, which indicates that the bottom section removes more CO_2. As can been seen, by intercooling modification, although mass transfer rate may be sacrificed slightly, significant energy and capital costs can be saved.

Normalized packing and rich loading empirical correlations

There are three degrees of freedom: CO_2 Concentration (CO_2 Conc), Removal (f), and lean loading (LLDG). In order to derive the normalized packing and rich loading (RLDG) empirical correlation, further experiments are performed at different lean loadings.

Table 6: Empirical correlation data

Cases	CO_2 Conc	Removal (%)	LLDG	RLDG	Normalized Packing (sec*m^2/mol)
1	0.12	60	0.265	0.3967	222.269
2	0.12	60	0.360	0.4050	543.260
3	0.12	90	0.192	0.3896	187.704
3-1	0.12	90	0.231	0.3875	189.196
4	0.12	90	0.307	0.3979	322.548
4-1	0.12	90	0.327	0.4007	424.929
4-2	0.12	90	0.336	0.4019	505.139
5	0.12	99	0.061	0.3786	175.758
6	0.12	99	0.192	0.3820	229.652
7	0.15	60	0.275	0.4006	186.250
8	0.15	60	0.368	0.4100	486.470
9	0.15	90	0.206	0.3918	144.449
10	0.15	90	0.318	0.4040	270.905
11	0.15	99	0.071	0.3820	143.876
12	0.15	99	0.208	0.3864	173.076
13	0.2	60	0.290	0.4060	151.218
14	0.2	60	0.378	0.4160	440.348
15	0.2	90	0.226	0.3970	108.935
15-1	0.2	90	0.261	0.4022	132.827
16	0.2	90	0.332	0.4110	244.137
16-1	0.2	90	0.350	0.4133	321.727
16-2	0.2	90	0.358	0.4141	383.266
17	0.2	99	0.088	0.3856	104.307
18	0.2	99	0.227	0.3970	139.330
19	0.2	95	0.303	0.4079	197.445

Rich loading empirical correlation

In order to derive the rich loading empirical correlation, 25 experiments were performed at different lean loadings. Based on mass transfer theory, the original terms and logarithm terms were chosen as variables for linear regression.

Table 7: Rich loading empirical correlation data

CO_2 Conc	Ln(CO_2 Conc)	1-f	ln(1-f)	LLDG	Ln(LLDG)	RLDG
0.12	-2.120	0.4	-0.916	0.265	-1.328	0.397
0.12	-2.120	0.4	-0.916	0.360	-1.022	0.405
0.12	-2.120	0.1	-2.303	0.192	-1.650	0.390
0.12	-2.120	0.1	-2.303	0.231	-1.465	0.388
0.12	-2.120	0.1	-2.303	0.307	-1.181	0.398
0.12	-2.120	0.1	-2.303	0.327	-1.118	0.401
0.12	-2.120	0.1	-2.303	0.336	-1.091	0.402
0.12	-2.120	0.01	-4.605	0.061	-2.797	0.379
0.12	-2.120	0.01	-4.605	0.192	-1.650	0.382
0.15	-1.897	0.4	-0.916	0.275	-1.291	0.401
0.15	-1.897	0.4	-0.916	0.368	-1.000	0.410
0.15	-1.897	0.1	-2.303	0.206	-1.580	0.392
0.15	-1.897	0.1	-2.303	0.318	-1.146	0.404
0.15	-1.897	0.01	-4.605	0.071	-2.645	0.382
0.15	-1.897	0.01	-4.605	0.208	-1.570	0.386
0.2	-1.609	0.4	-0.916	0.290	-1.238	0.406
0.2	-1.609	0.4	-0.916	0.378	-0.973	0.416
0.2	-1.609	0.1	-2.303	0.226	-1.487	0.397
0.2	-1.609	0.1	-2.303	0.261	-1.343	0.402
0.2	-1.609	0.1	-2.303	0.332	-1.103	0.411
0.2	-1.609	0.1	-2.303	0.350	-1.050	0.413
0.2	-1.609	0.1	-2.303	0.358	-1.028	0.414
0.2	-1.609	0.01	-4.605	0.088	-2.430	0.386
0.2	-1.609	0.01	-4.605	0.227	-1.483	0.397
0.2	-1.609	0.05	-2.996	0.303	-1.194	0.408

When all these six terms were regressed, the regression statistics were as follows.

Table 8: Rich loading empirical correlation regression statistics

Variable Names	Coefficients	Standard Error	t Stat	P-value
Intercept	0.353	0.065	5.4	4.0E-05
1-f	-0.010	0.004	-1.5	1.5E-01
ln(1-f)	0.002	0.001	3.4	3.2E-03

CO_2 Conc	0.048	0.144	0.3	7.4E-01
ln(CO_2 Conc)	0.010	0.023	0.5	6.5E-01
LLDG	0.163	0.014	11.9	0.0E+00
ln(LLDG)	-0.02	0.002	-6.0	1.0E-05

Regression Statistics	
R Square	0.986
Observations	25

In statistical significance testing, the p-value is the probability of an observed result arising by chance. The null hypothesis will be rejected and the test hypothesis can be accepted as valid when the p-value is less than a certain significance level, often 0.05. The observed results would be highly likely and the regression model can be trusted.

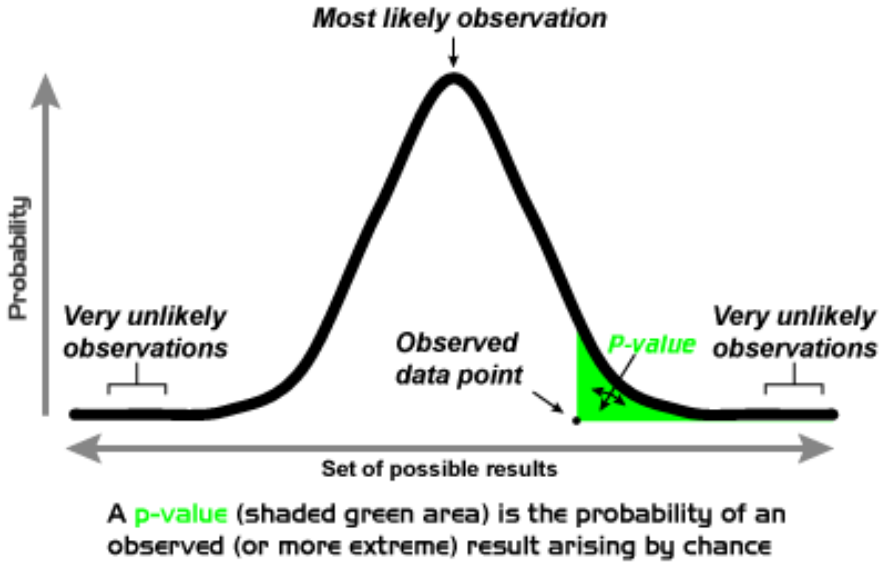

Figure 42: P-value in a statistical test (Repapetilto, 2012)

The term CO_2 Conc with p-value greater than 0.05 was removed. As a result, there were only five variables left: 1-f, Ln(1-f), ln(CO_2 Conc), LLDG, and Ln(LLDG). When the linear regression was repeated, the results are as follows.

Table 9: Rich loading empirical correlation regression statistics

Variable Names	Coefficients	Standard Error	t Stat	P-value
Intercept	0.374	0.007	50.1	1.2E-21
1-f	-0.007	0.004	-1.6	1.2E-01
ln(1-f)	0.002	0.001	3.5	2.2E-03

ln(CO_2 Conc)	0.018	0.001	13.5	3.3E-11
LLDG	0.163	0.013	12.3	1.7E-10
ln(LLDG)	-0.015	0.002	-6.2	6.4E-06

Regression Statistics	
R Square	0.984
Observations	25

The variables with p-value greater than 0.05 were removed. There were only four variables left: ln(1-f), ln(CO_2 Conc), LLDG, and ln(LLDG).

When the linear regression was repeated, the results are as follows.

Table 10: Rich loading empirical correlation regression statistics

Variable Names	Coefficients	Standard Error	t Stat	P-value
Intercept	0.374	0.008	48.2	3.7E-22
ln(1-f)	0.001	0.000	3.7	1.4E-03
ln(CO_2 Conc)	0.018	0.001	13.0	3.3E-11
LLDG	0.160	0.014	11.7	2.1E-10
ln(LLDG)	-0.014	0.002	-5.7	1.4E-05

Regression Statistics	
R Square	0.984
Observations	25

As can be seen, the p-values are all less than 0.01. This correlation can be trusted. The empirical correlation of rich loading is:

Rich loading = 0.374 + 0.001*ln(1-f) + 0.018*ln(CO_2 Conc) + 0.160*LLDG - 0.014*ln(LLDG) (3)

For 90% removal, rich loading is plotted against LLDG in MATLAB at 0.12, 0.15, and 0.2 inlet CO_2 concentration.

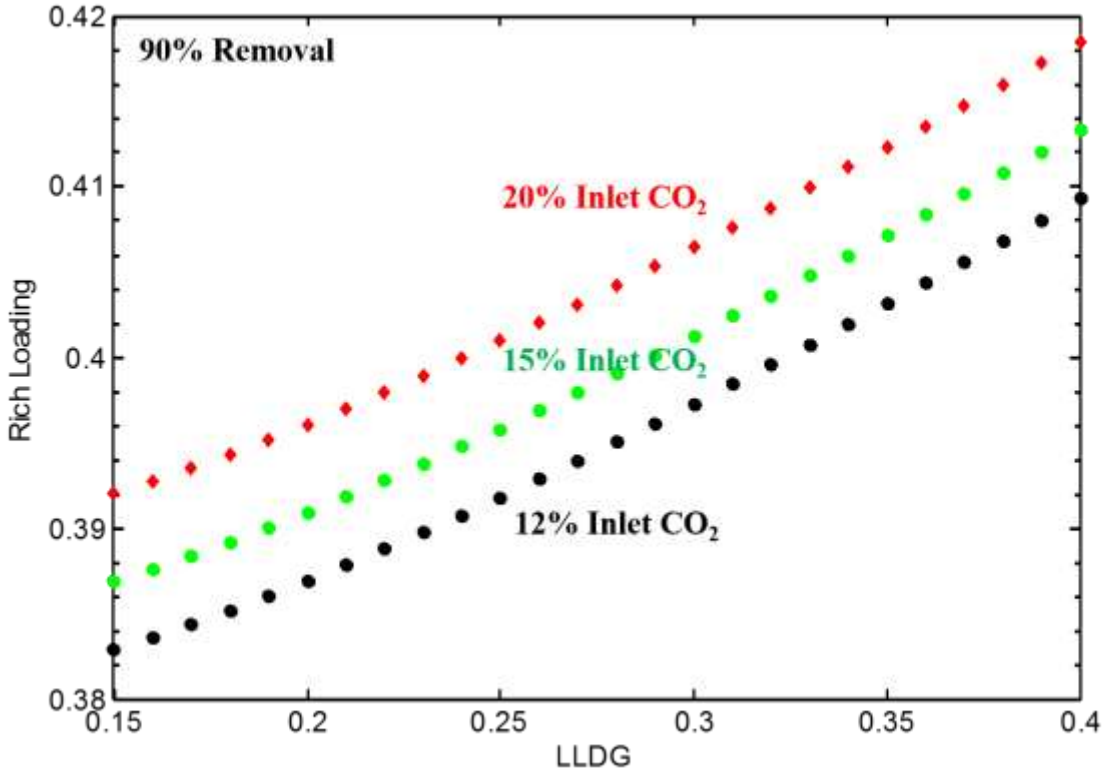

Figure 43: Rich loading correlation plot

For 0.2 lean loading, rich loading is plotted against (1-f) in MATLAB at 0.12, 0.15, and 0.2 inlet CO_2 concentration. Logarithm scale is used for the (1-f) axis.

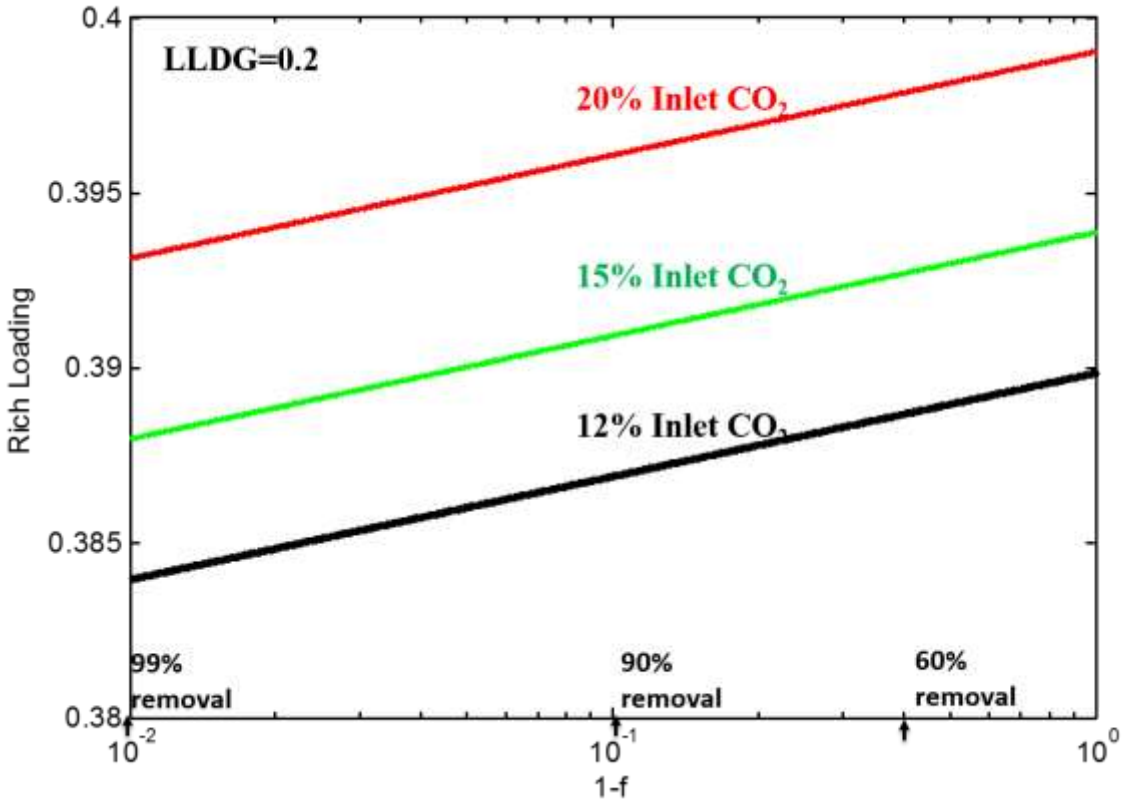

Figure 44: Rich loading correlation plot

As shown in Figure 43, rich loading behaves linearly in high lean loading range and increases with lean loading. Figure 44 shows that rich loading increases slightly with (1-f), suggesting that rich loading decreases with CO_2 removal.

Normalized packing empirical correlation

There are three degrees of freedom: CO_2 Concentration (CO_2 Conc), f, and LLDG. There are twelve terms used for linear regression: the original terms, square terms and cross terms. Terms with p-value greater than 0.05 were canceled, and linear regression was performed again until reasonable p-values were achieved. 25 experiments were performed at different lean loadings.

As a result, there are four variables left: $[\ln(1-f)]^2$, LLDG, $LLDG^2$, and $\ln(CO_2\ Conc)*LLDG$.

Table 11: Normalized packing empirical correlation regression statistics

Variable Names	Coefficients	Standard Error	t Stat	P-value
Intercept	187	52	3.6	1.7E-03
$[\ln(1-f)]^2$	3	1	2.7	1.5E-02
LLDG	-3849	409	-9.4	8.6E-09
$LLDG^2$	7506	730	10.3	2.0E-09
$\ln(CO_2\ Conc)*LLDG$	-982	103	-9.6	6.7E-09

Regression Statistics	
R Square	0.954
Observations	25

Table 10 shows that all the p-values are less than 0.05. This correlation can be trusted and the empirical correlation of normalized packing is:

Normalized packing = 187 + 3*[ln(1-f)]^2 - 3849*LLDG + 7506*LLDG^2 - 982*ln(CO_2 Conc)*LLDG (4)

For 90% removal, normalized packing is plotted against LLDG in MATLAB at 0.12, 0.15, and 0.2 inlet CO_2 concentration.

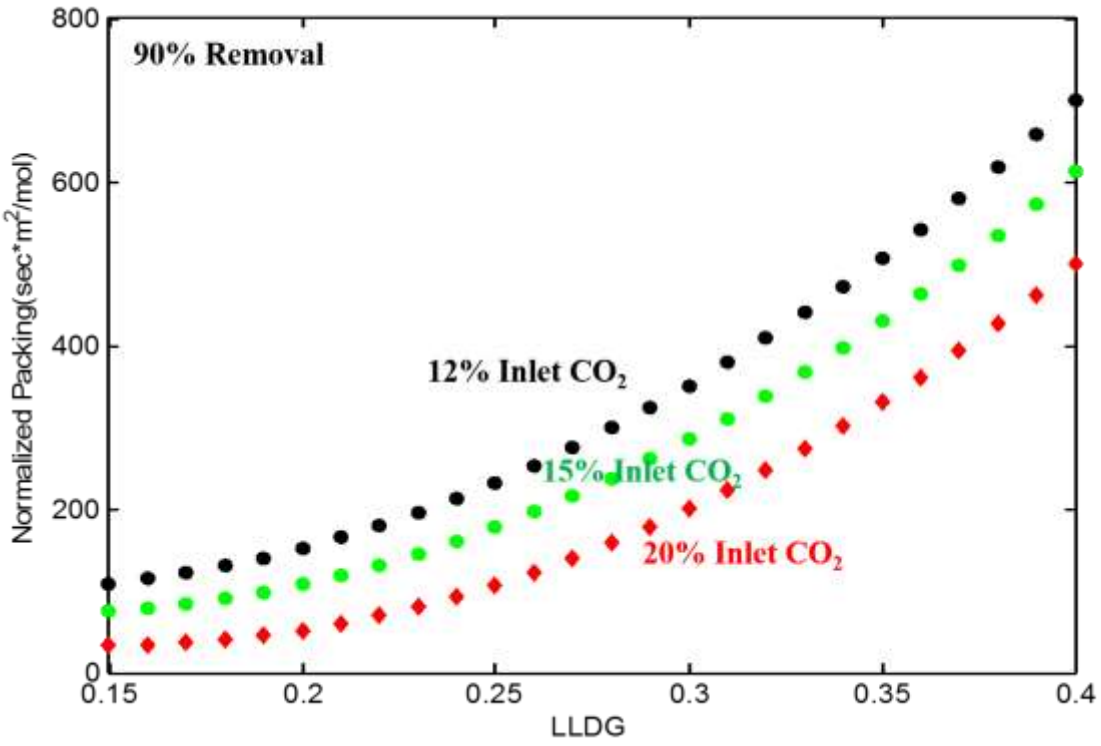

Figure 45: Normalized packing correlation plot

For 0.2 lean loading, normalized packing is plotted against (1-f) in MATLAB at 0.12, 0.15, and 0.2 inlet CO_2 concentration. Logarithm scale is used for the (1-f) axis.

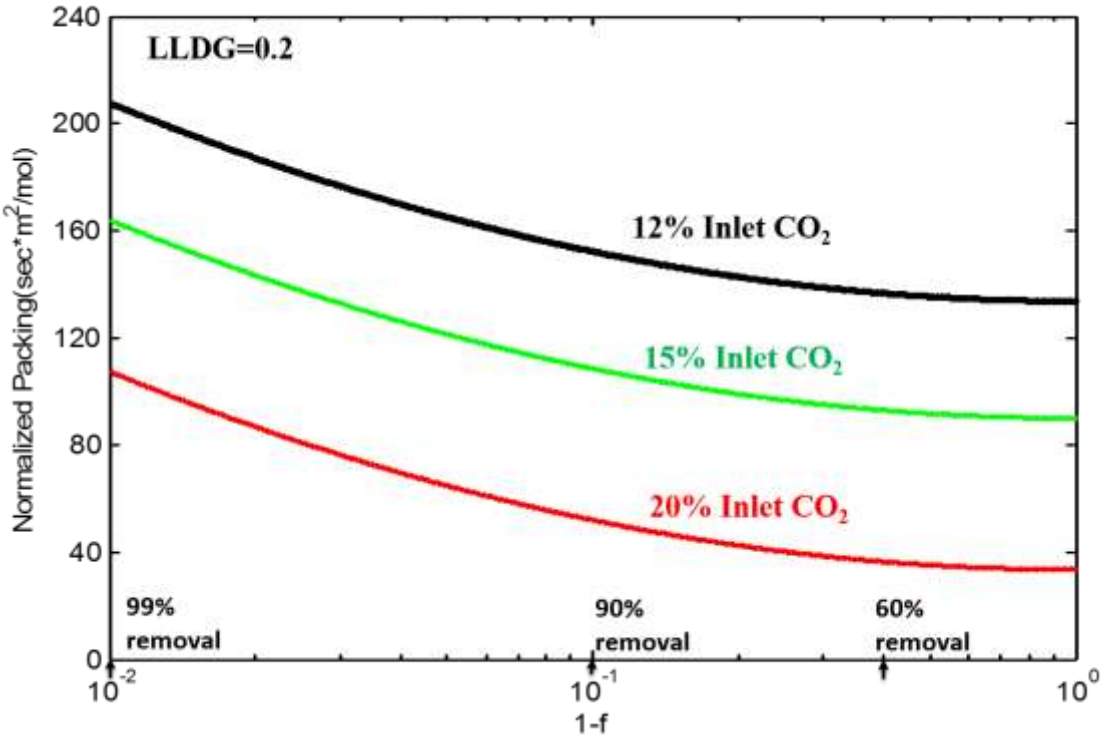

Figure 46: Normalized packing correlation plot

Better absorber performance has lower normalized packing. As shown in Figures 45 & 46, normalized packing increases with lean loading and removal, and decreases with inlet CO_2, suggesting that the absorber has better performance with low lean loading, low removal and high inlet CO_2.

5 m MDEA/5 m PZ

The solvent blend 5 molal (m) MDEA/5 molal (m) PZ offers higher CO_2 capacity and the VLE curve of the solvent blend is flatter at the rich end than that of the PZ solvent. It is expected to result in greater delta loading and lower energy cost. Different intercooling configurations have been tested to get better absorber performance and minimize energy use.

With simple pump-around intercooling

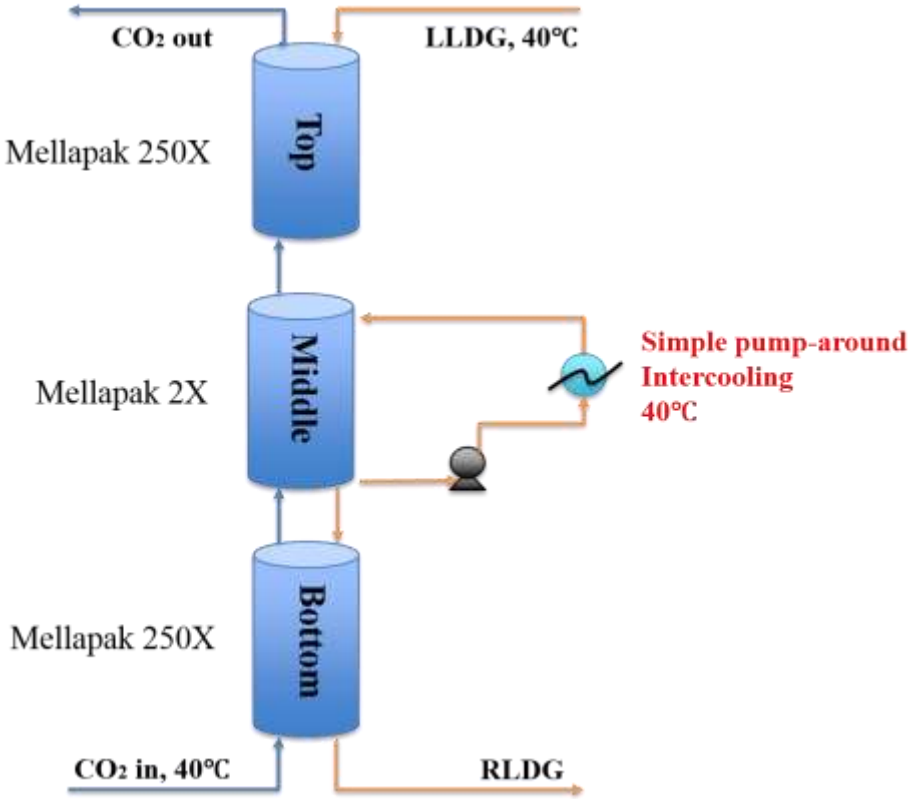

Figure 47: Simple pump-around intercooling

Simple pump-around intercooling around the middle section is first tested. For Case 19, lean loading is chosen as 0.209.

Table 12: Case 19 input information

Case	CO_2 in(%)	Removal (%)	LLDG
19	20	95	0.209

Liquid feed flow rate was first chosen as $1.1*L_{min}$ and the pump-around intercooling L_R/G was chosen as 5 mol/mol. Liquid feed flow rate was increased to $1.2*L_{min}$ and the pump-around intercooling L_R/G was kept at 5 mol/mol, which is Case 19-1. Table 13 shows that total surface area of Case 19-1 decreases, suggesting that the absorber performs better at $1.2*L_{min}$. Then liquid feed flow rate was kept at $1.2*L_{min}$ and the pump-around intercooling L_R/G was increased to 10 mol/mol, which is Case 19-2. Table 13 shows that total surface area of Case 19-2 is lower, suggesting that the absorber performs better at $1.2*L_{min}$ and higher pump-around recycle rate.

Table 13: Case 19 with different L/L_{min} and L_R/G

Case	LLDG	RLDG	L_R/G	L/L_{min}	Total Surface Area($1000*m^2$)	Surface Area Fraction			Normalized Packing($sec*m^2/mol$)
						Top	Mid	Bot	
19	0.209	0.368	5	1.1	1475.7	0.3	0.6	0.1	635
19-1	0.209	0.355	5	1.2	1316.8	0.3	0.6	0.1	566.6
19-2	0.209	0.363	10	1.2	1072.8	0.4	0.5	0.2	461.7

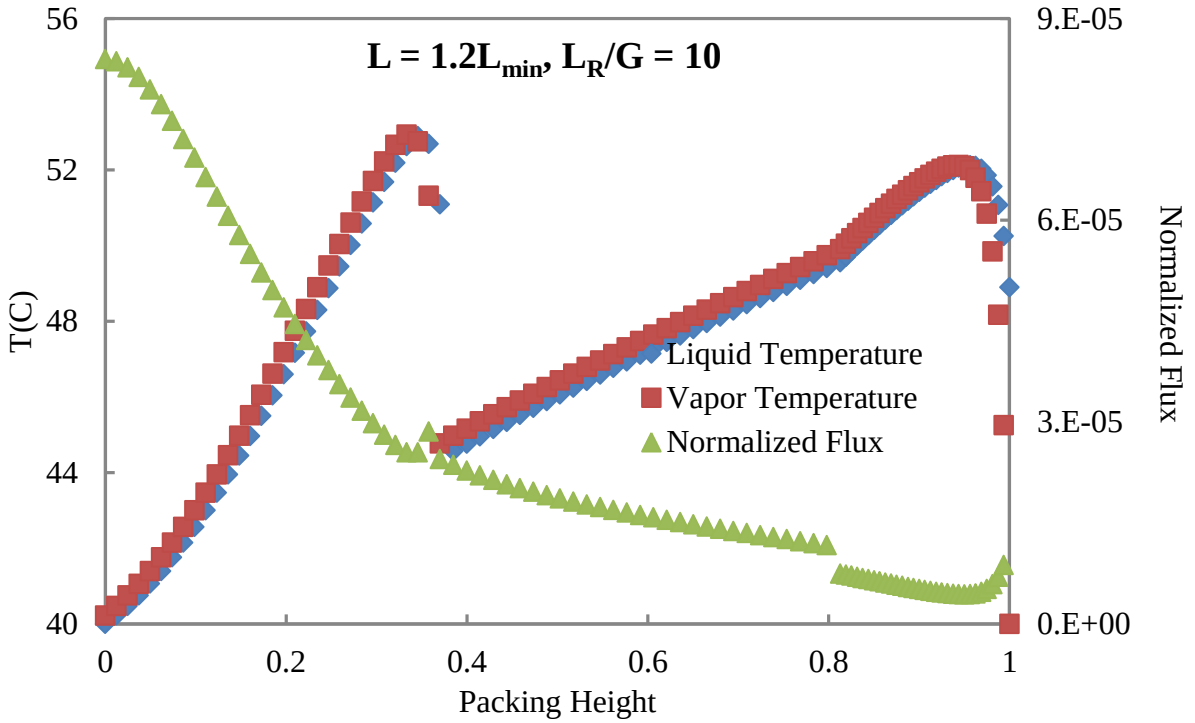

Figure 48: Normalized flux and temperature profile

Figure 48 shows that the simple pump-around intercooling cannot sufficiently cool down the gas, and the temperature bulge in the bottom section limits the mass transfer rate.

With advanced pump-around intercooling

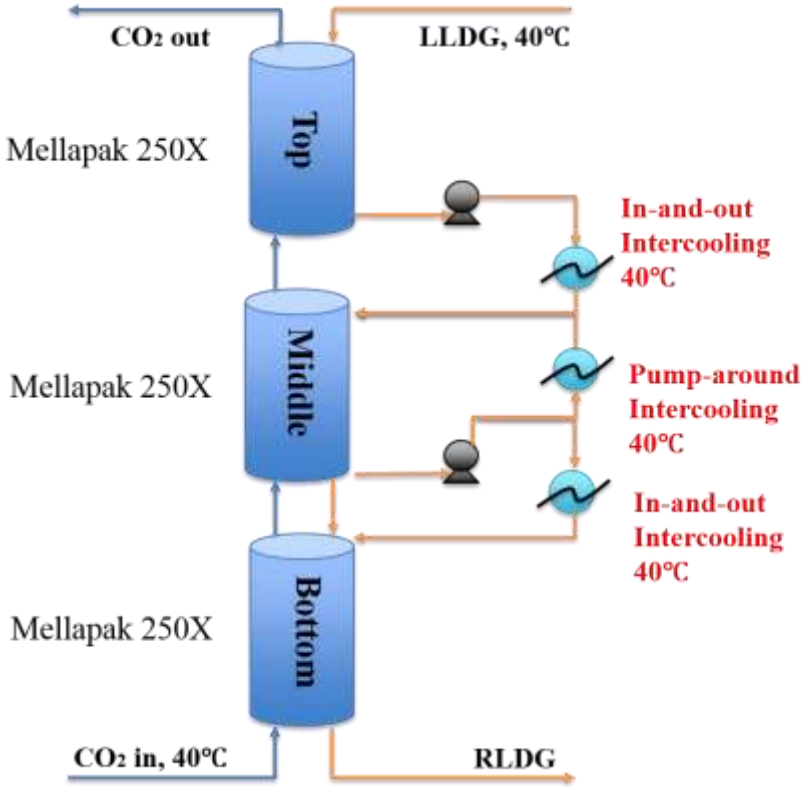

Figure 49: Advanced pump-around intercooling

Two in-and-out intercoolings are added above and below the pump-around intercooling, which is called advanced pump-around intercooling. The liquid feed flow rate was chosen as $1.1*L_{min}$ and the pump-around intercooling L_R/G was chosen as 10 mol/mol. The optimized results of Case 19 are listed in Table 14.

Table 14: Case 19 with advanced pump-around intercooling ($L = 1.1*L_{min}$, $L_R/G = 10$)

Case	LLDG	RLDG	L_R/G	L/L_{min}	Total Surface Area($1000*m^2$)	Surface Area Fraction			Normalized Packing($sec*m^2/mol$)
						Top	Mid	Bot	
19	0.209	0.415	10	1.1	2197.9	0.3	0.5	0.2	945.8

As shown in Table 14, rich loading increases to 0.415, which is good for stripper performance. The absorber performance can be seen from the liquid/gas temperature profile and CO_2 composition profile in Aspen Plus®.

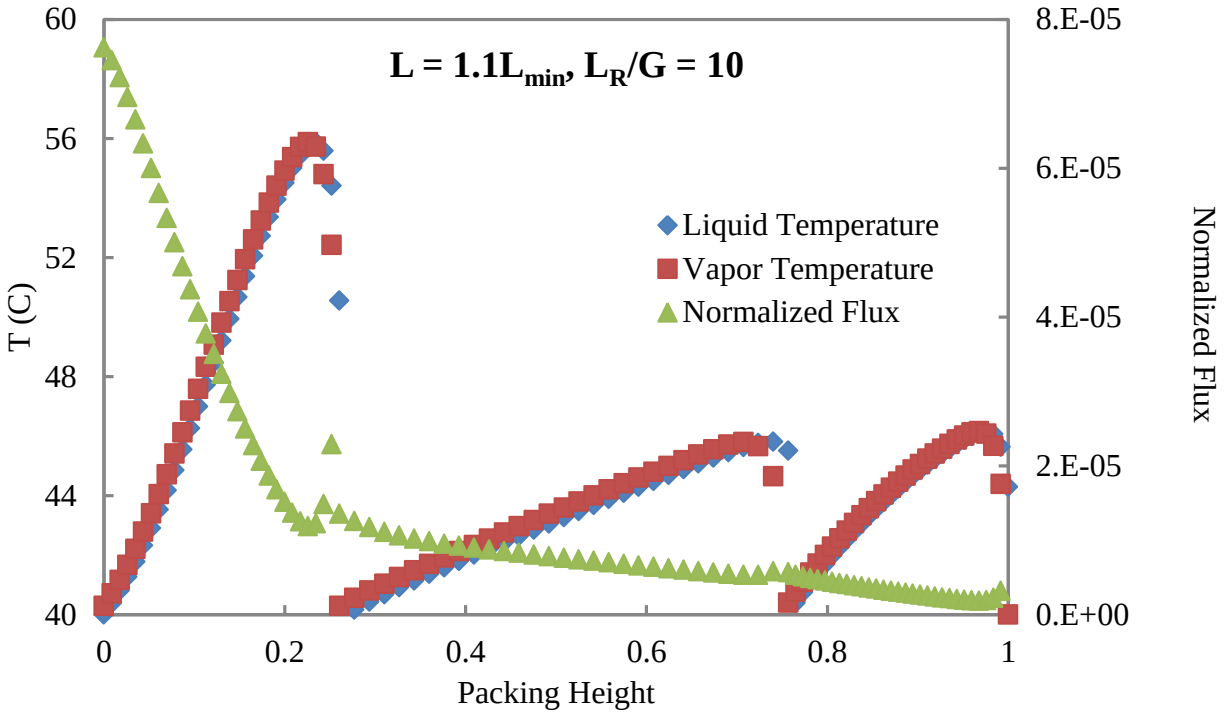

Figure 48: Normalized flux and temperature profile

Figure 48 shows that, with advanced pump-around intercooling, the liquid can sufficiently cool down the gas. The liquid feed flow rate was increased to 1.2*L_{min} and the pump-around intercooling L_R/G was kept at 10 mol/mol. This optimized Case 19-5 is listed in Table 15.

Table 15: Case 19 with advanced pump-around intercooling (L = 1.2*L_{min}, L_R/G = 10)

Case	LLDG	RLDG	L_R/G	L/L_{min}	Total Surface Area(1000*m^2)	Surface Area Fraction			Normalized Packing(sec*m^2/mol)
						Top	Mid	Bot	
19	0.209	0.398	10	1.2	1556.9	0.3	0.4	0.2	669.9

Table 15 shows that the absorber has a smaller total packing area, but rich loading decreases from 0.415 to 0.398. Capital cost can be saved with a smaller packing area while energy performance is worse due to lower rich loading. Further economic analysis will be done to evaluate which choice is better. Considering that a higher pump-around intercooling recycle rate can improve the mass transfer driving force, the pump-around intercooling L_R/G was increased to 15 mol/mol. The optimized results of Case 19 are listed in Table 16.

Table 16: Case 19 with advanced pump-around intercooling (L = 1.2*L_{min}, L_R/G = 15)

Case	LLDG	RLDG	L_R/G	L/L_{min}	Total Surface Area(1000*m^2)	Surface Area Fraction			Normalized Packing(sec*m^2/mol)
						Top	Mid	Bot	
19	0.209	0.400	15	1.2	1632.6	0.3	0.4	0.2	702.5

Table 16 shows that total surface area increases at high solvent recycle rate. A higher pump-around intercooling recycle rate does not always help. Although a larger amount of solvent recycling around the middle section can improve mass transfer driving force, it will make it easier to cause flooding, as a result of which the diameter will be larger and total surface area might increase. It is easier to cause flooding with Mellapak 250X than Mellapak 2X.

Future work

Use Mellapak 2X instead of Mellapak 250X in the middle section.

Further economic analysis will be done to evaluate the trade-off between packing area and rich loading.

Conclusions

1. For every single case, the packing requirement and absorber configuration can be modified by looking at the mass transfer profile and intercooler heat duty in L_{min} cases.

2. The absorber performance can be seen from the normalized packing:

Normalized packing = Total surface area/(Gas flow rate*CO_2 Conc*Removal) (1)

Normalized packing can be given by this correlation:

Normalized packing = 187 + 3*[ln(1-f)]^2 - 3849*LLDG + 7506*LLDG^2 - 982*ln(CO_2 Conc)*LLDG (4)

Because k_g' is not constant, normalized packing is not only a function of (1-f) but also a function of CO_2 concentration and LLDG.

3. For 12% to 20% inlet CO_2, rich loading lies between 0.38 and 0.42. Rich loading can be given by this correlation:

Rich loading = 0.374 + 0.001*ln(1-f) + 0.018*ln(CO_2 Conc) + 0.160*LLDG - 0.014*ln(LLDG) (3)

Rich loading does not vary much with removal. The solvent practically reaches equilibrium with the inlet CO_2.

4. With correlations, rich loading and normalized packing can be predicted from CO_2 concentration (CO_2 Conc), removal (f), and lean loading (LLDG) by interpolating.

5. With high L/G, the in-and-out intercooling is effective. With low L/G, pump-around intercooling is desirable, and the in-and-out intercooling can be removed.

6. A higher pump-around intercooling recycle rate can improve mass transfer driving force, but make it easier to cause flooding. The diameter will be larger and total surface area might increase.

References

Repapetilto. "A graphical depiction of the meaning of p-values." Wikipedia. 2012.

Stripper Performance Using 5 m PZ and MDEA/PZ and Design of Ammonia Purging System

Quarterly Report for April 1 – June 30, 2014

by Junyuan Ding

Supported by the Phillips 66 Fellowship,

Membrane Technology and Research, Inc.,

and the DOE cooperative agreement DE-FE0013188

McKetta Department of Chemical Engineering

The University of Texas at Austin

July 31, 2014

1 Stripper Performance Using 5 m PZ and MDEA/PZ

Abstract

Previous work optimized stripping with 5 m piperazine (PZ) with rich loading from 0.34 to 0.43 mol CO_2/mol N. Equivalent work, CO_2 output pressure, and optimal cold and warm rich bypass were studied to build a correlation with CO_2 rich and lean loading. Four cases given by MTR (Case 13, Case 14, Case 18, and Case 19) were simulated based on absorber performance. The base-case stripping configuration was the advanced flash with warm rich bypass and cold rich exchanger bypass. The Independence model for PZ in Aspen Plus® was used to simulate the stripping performance.

In this quarter, a base case (rich loading of 0.390 mol CO_2/mol N and lean loading of 0.192 mol CO_2/mol N) and Case 17 (rich loading of 0.387 mol CO_2/mol N with lowest lean loading) using 5 m PZ were studied. Equipment costs for Cases 13, 14, 18, and 19 were analyzed by Frailie (2014). Since 5 m MDEA/5 m PZ has a higher CO_2 capacity than 5 m PZ, Case 19-MDEA/PZ (rich loading of 0.398 mol CO_2/mol N and lean loading of 0.209 mol CO_2/mol N) using 5 m MDEA/5 m PZ was studied to reduce the heat duty, compared with Case 19 (rich loading of 0.411 mol CO_2/mol N and lean loading of 0.303 mol CO_2/mol N) using 5 m PZ.

Introduction

A hybrid amine/membrane CO_2 capture model is being developed by combining a CO_2 membrane separator with the absorber/stripper. The membrane separator is being developed by

Membrane Technology and Research, Inc. (MTR). The stripping performance is simulated using the Independence model for PZ in Aspen Plus®.

Figure 1 shows configurations of: a) series Cases 13 (rich loading of 0.406 mol CO_2/mol N and lean loading of 0.290 mol CO_2/mol N) & 14 (rich loading of 0.416 mol CO_2/mol N and lean loading of 0.378 mol CO_2/mol), and b) parallel Cases 18 (rich loading of 0.401 mol CO_2/mol N and lean loading of 0.227 mol CO_2/mol N) & 19 (rich loading of 0.411 mol CO_2/mol N and lean loading of 0.303 mol CO_2/mol).

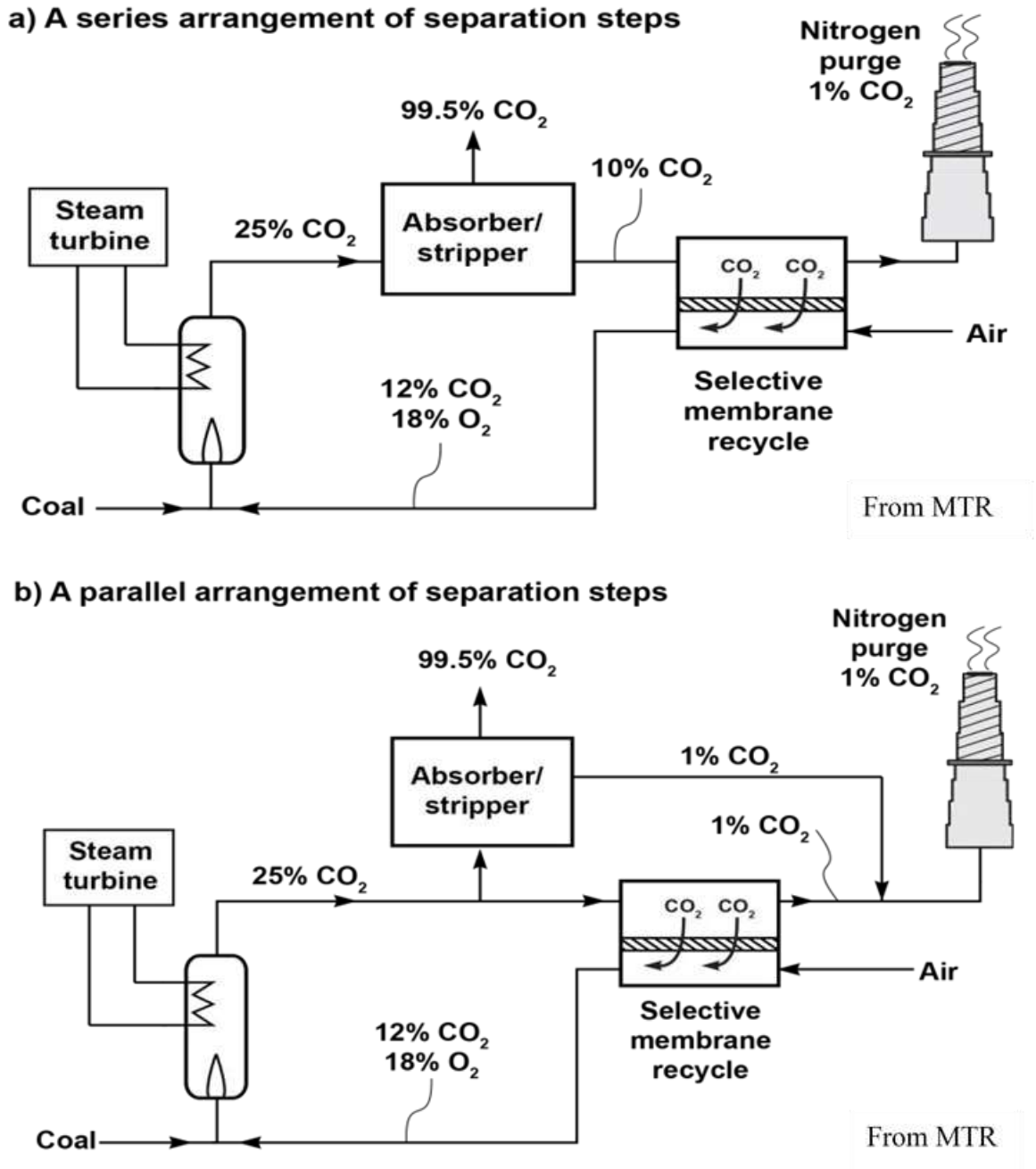

Figure 1: Two configurations of hybrid amine/membrane CO_2 capture model

Methods

Hybrid amine/membrane

The amine regeneration system for the hybrid amine/membrane process was simulated by the Independence model in Aspen Plus®. Figure 2 shows the advanced flash stripper configuration used. It incorporates a cold and warm rich bypass, two split cross-exchangers in series, a convective steam heater, a smaller stripper column, low residence time flash tank, and stripping at high temperature to produce CO_2 at 6 to 18 bar. Solvent flow rate, composition, and temperature of rich and lean solvent were put in the Independence model to match the inlet and outlet states with the absorber.

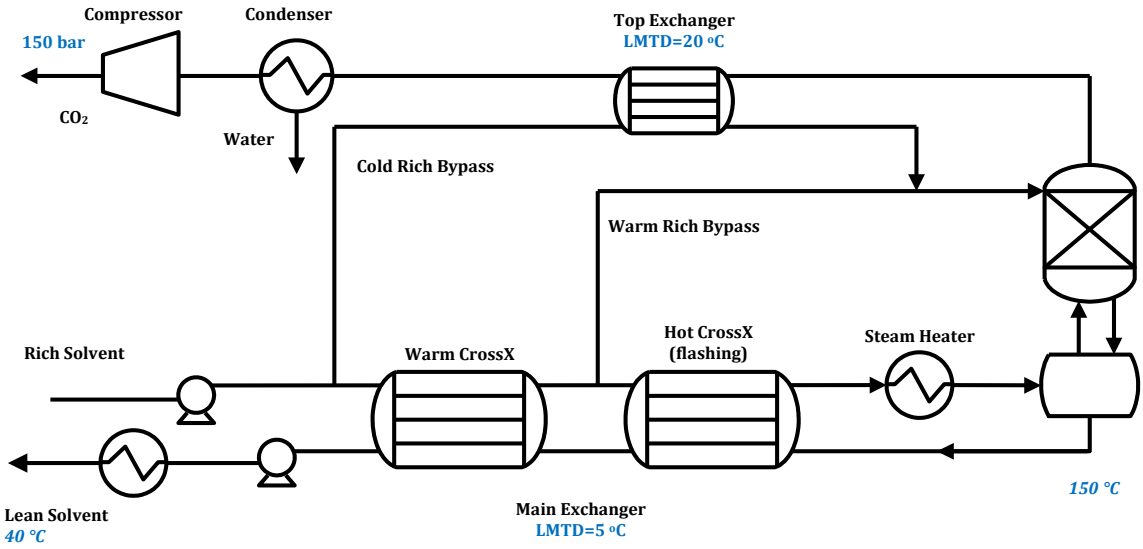

Figure 2: Stripping configuration using 5 m PZ

Equivalent Work Calculation

Equivalent work replaces heat duty as a more general metric of energy use than heat duty alone. It is defined as the sum of pump work, compression work, and heat work, as Equation 1 shows.

$$W_{eq}(\mathrm{kJ/mol\ CO_2}) = W_{heat} + W_{pump} + W_{comp} \quad (1)$$

Heating work can be generated from the heat duty of the reboiler using Equation 2. A typical value of 90% is used for the turbine efficiency (η).

$$W_{heat} = \eta\left(\frac{T_{source}+\Delta T-T_{sink}}{T_{source}+\Delta T}\right)Q_{reb} \quad (2)$$

Compression work can be approximated by Equation 3 from Van Wagener (2011), which is typically assumed to be at a discharge pressure of 150 bar.

$$W_{comp}(\mathrm{kJ/mol\ CO_2}) = \begin{cases} 4.572\ln\left(\frac{150}{P_{in}}\right) - 4.096 & P_{in} \le 4.56\ \mathrm{bar} \\ 4.023\ln\left(\frac{150}{P_{in}}\right) - 2.181 & P_{in} \ge 4.56\ \mathrm{bar} \end{cases} \quad (3)$$

Process Safety

The stripper pressure should never exceed the pressure rating of the vessel. The stripper vessel will be equipped with a relief valve that will discharge the CO_2/amine mixture to a safe, low pressure point, probably the inlet to the absorber.

Results and Discussion

Comparison of Cases 13, 14, 17, 18, 19, and Base Case

Table 1 shows the stripper performance of the six cases. Rich loading and lean loading values are chosen based on absorber performance.

Table 1: Stripper performance using 5 m PZ with stripping at 150 °C, main exchanger LMTD = 5 °C, top exchanger LMTD = 20 °C*.

Case Number	RLDG (mol CO_2/equiv PZ)	LLDG (mol CO_2/equiv PZ)	Stripper P (bar)	CRB (%)	WRB (%)	W_{eq} (kJ/mol CO_2)	heat duty (kJ/mol CO_2)
Add 13	0.404	0.29	8.40	5	9	33.47	93.65
14	0.415	0.378	18.44	1	3	47.95	134.15
18	0.401	0.227	5.90	8	34	34.03	93.60
19	0.411	0.303	8.66	4	10	33.24	93.14
17	0.387	0.172	5.17	13	48	35.85	99.67
base	0.390	0.192	5.44	10	44	34.99	96.67

* RLDG represents rich loading and LLDG represents lean loading. CRB and WRB represent corresponding optimal cold rich bypass ratio and warm rich bypass ratio.

Compared with series Cases 13 & 14, equivalent work of parallel Cases 18 & 19 are closer to their optimal equivalent work value of each rich loading. Case 14 has an especially high total equivalent work because its lean loading is relatively high for its 0.416 CO2 rich loading. The CO_2 capacity is low and much more heat is required.

Economic Analysis with 5 m PZ, advanced flash stripper

Table 2: Equipment prices of four cases

		Hybrid-Series		Hybrid-Parallel	
Description	**PZ-AFS**	**Case 13**	**Case 14**	**Case 18**	**Case 19**
Inlet Gas Blower	2,841,000	2,841,000	2,841,000	2,841,000	2,841,000
Absorber	23,833,000	16,194,000	25,827,000	13,200,000	15,228,000
Absorber Intercooler	1,699,000	2,480,000	2,610,000	2,219,000	2,871,000
Absorber Intercooler Pump	697,000	1,993,000	5,181,000	1,651,000	2,334,000
Rich Amine Pump	820,000	870,000	2,742,000	669,000	1,070,000

Rich Amine Carbon Filter	125,000	182,000	277,000	171,000	182,000
Particulate Filter	136,000	136,000	136,000	136,000	136,000
Rich/Lean Amine Exchanger	19,013,000	22,971,000	73,612,000	16,445,000	28,192,000
Lean Solvent Cooler	914,000	1,175,000	3,393,000	914,000	1,436,000
Stripper	2,169,000	716,000	561,000	1,068,000	736,000
		952,000	1,888,000	811,000	1,077,000
Reboiler	8,298,000	7,925,000	9,893,000	8,550,000	8,407,000
Overhead Condenser	340,000	522,000	392,000	914,000	522,000
Overhead Accumulator	585,000	41,000	21,000	53,000	30,000
Reflux Pump	33,000				
Compressors	10,153,000	9,731,000	9,461,000	10,580,000	10,406,000
Multi-stage Centrifugal Pump	540,000	540,000	540,000	540,000	540,000
Makeup Amine Tank	345,000	345,000	345,000	345,000	345,000
Makeup Amine Pump	9,000	9,000	9,000	9,000	9,000
Water Tank	103,000	103,000	103,000	103,000	103,000
Water Pump	13,000	13,000	13,000	13,000	13,000
Surge Tank	562,000	875,000	1,735,000	745,000	989,000
Lean PZ Pump	447,000	542,000	1,710,000	417,000	667,000
Reclaimer	4,020,000	4,431,000	13,863,000	3,388,000	5,437,000
Dehydration Unit	1,966,000	1,966,000	1,966,000	1,966,000	1,966,000
Total	79,661,000	77,553,000	159,119,000	67,746,000	85,539,000
Capture	67,002,000	65,316,000	147,152,000	54,659,000	72,626,000
Compression	12,659,000	12,237,000	11,967,000	13,086,000	12,912,000

Table 2 shows the purchased equipment costs of the four cases of 593 MWe based on Frailie spreadsheet (2014). For the stripper, the cost centers are the reboiler, compressors, and reclaimer. As Case 14 is a special case, the relative high lean loading leads to high reboiler duty and high reclaimer capital cost. For normal cases, reclaimer costs are almost the same. Combining the energy performance and capital cost of the amine scrubbing system, parallel cases (Cases 13 & 14) are more worthwhile to be considered than serial cases (Cases 18 & 19).

Stripper Performance Using 5 m MDEA/5 m PZ (Case 19-MDEA/PZ)

Considering the higher CO_2 capacity of 5 m MDEA/5 m PZ, this blended amine is chosen as a substitute for 5 m PZ to reduce the energy cost.

Table 3: Comparison of stripper performance using 5 m PZ and MDEA/PZ

Case	Pressure (bar)	RLDG (mol CO_2/mol)	LLDG (mol CO_2/mol)	CRB (%)	WRB (%)	W_{eq} (kJ/mol CO_2)	Heat Duty (kJ/mol CO_2)
5 m PZ	8.66	0.411	0.303	4	10	33.24	93.14
MDEA/PZ	8.93	0.398	0.209	6	15	31.40	88.72

Due to the higher CO_2 capacity, the reboiler duty of MDEA/PZ is lower than that of 5 m PZ. Table 3 shows that the total work is reduced using MDEA/PZ, but the viscosity of MDEA/PZ is higher than 5 m PZ. Bigger heat exchangers are required using MDEA/PZ, which leads to higher capital cost.

Optimization of Stripper Using MDEA/PZ at CO_2 Rich Loading 0.4 mol CO_2/mol alkalinity

For comparison with stripper performance using 5 m PZ, stripper performance using MDEA/PZ was studied over a wide range of lean loading at CO_2 rich loading 0.4 mol CO_2/mol alkalinity.

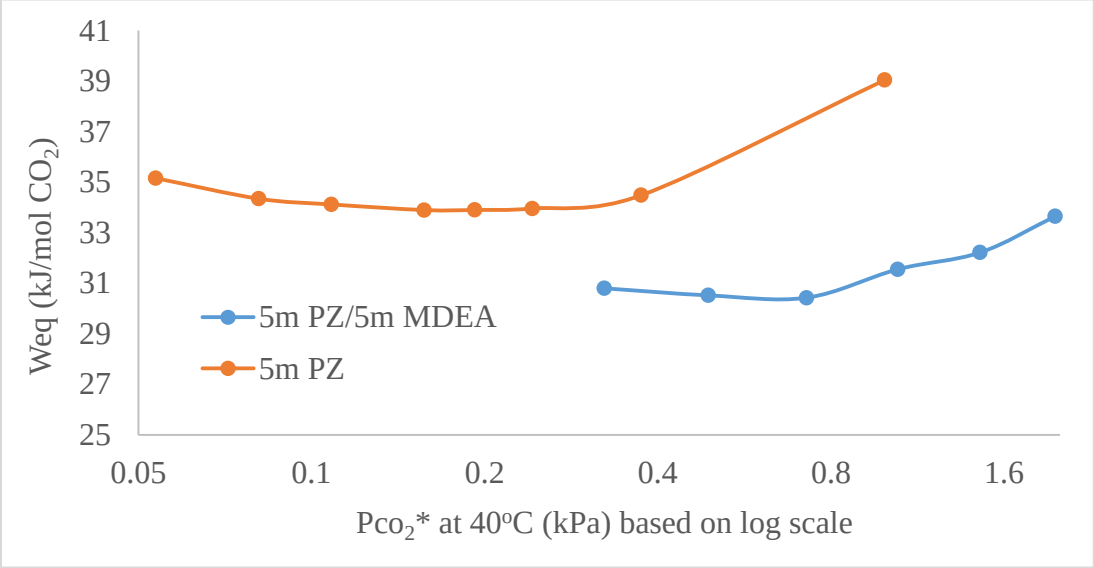

Figure 3: Comparison of stripper performance using MDEA/PZ and 5 m PZ at CO_2 rich loading 0.4 mol CO_2/mol alkalinity

Figure 3 shows that the optimal partial pressure of CO_2 using PZ/MDEA is higher than using 5 m PZ. The total work of stripping PZ/MDEA is much lower than 5 m PZ.

Conclusions

1. Parallel cases are more applicable than serial cases. The total work of parallel Cases 18 and 19 (34.03 kJ/mol CO_2 and 33.24 kJ/mol CO_2) is less than those of series Cases 13 and 14 (33.47 kJ/mol CO_2 and 47.95 kJ/mol CO_2). The capital cost of parallel Cases 18 and 19 ($67,746,000 and $85,539,000) is also less than those of series Cases 13 and 14 ($77,553,000 and $159,119,000).

2. The energy cost of using MDEA/PZ is lower than using 5 m PZ. For Case 19, equivalent work using 5 m PZ (33.24 kJ/mol CO_2) is less than using PZ/MDEA (31.40 kJ/mol CO_2).

2. Model design of Ammonia Purging System

Abstract

Ammonia purging design is required for amine scrubbing. Amine scrubbing may create an air quality problem by releasing ammonia. Some amine is converted to ammonia through oxidative or thermal degradation in the absorber and reboiler. Ammonia is released into air with the treated flue gas from the absorber, serving as a significant precursor of $PM_{2.5}$.

In this work, a top stripper and a reflux flow of the condensate over the stripper is used to concentrate ammonia and the rest is purged, as Figure 4 shows. Different reflux ratios are chosen to see the ammonia concentration and flowrate of the purge. 1 kg/1000 kg mass ratio of NH_3/H_2O is set for the ammonia amount. The base-case stripping configuration was the advanced flash with warm rich bypass and cold rich exchanger bypass. The Independence model for PZ in Aspen Plus® was used to simulate the stripping performance.

Introduction

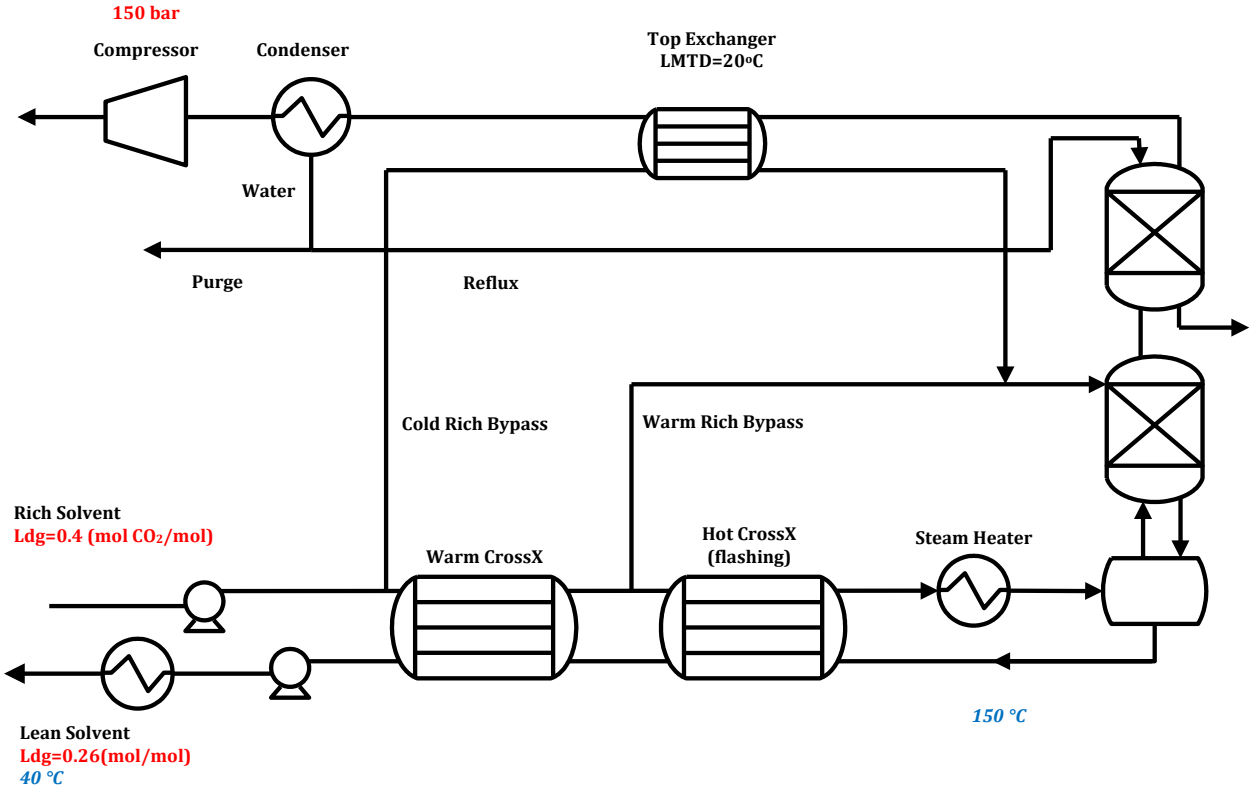

Figure 4: Configuration of the ammonia purging system

Figure 4 shows the configuration of the ammonia purging system. A top stripper is added above the flash stripper. The vapor coming out from the flash stripper goes up across the top stripper, top heat exchanger, and condenser. The vapor from the condenser is compressed to 150 bar. The condensate coming down from the condenser is separated into two parts. One part is sent

back to the top of the top stripper, serving as feeding liquid. The other part is purged. The reflux ratio is defined as the flowrate ratio of the reflux over the whole condensate. The liquid coming out from the bottom of the top stripper at high temperature is also sent away. An applicable way to save the energy it carries and the large amount of water in it is to send it to a cross heat exchanger and then to the water wash, or send it directly down to the flash stripper, serving as a feed flow. As the reflux ratio goes up, ammonia concentration in the reflux loop increases. On the other hand, as more condensate is used for reflux, the amount of the purged flow sent out of the system is reduced. An optimal reflux ratio can be found to have the best value of mol NH_3/mol CO_2 removed.

Methods

Adding ammonia component

Two reactions with ammonia occur in the amine scrubbing system.

$$NH_3 + HCO_3^- \leftrightarrow NH_2COO^- + H_2O \quad (1)$$

$$NH_3 + PZH^+ \leftrightarrow NH_4^+ + PZ \quad (2)$$

Properties of NH_3 and NH_4^+ are in the data bank of Aspen Plus®. The equilibrium coefficient of Equation 1 is set by:

$$\ln (K_{eq}) = -4.5834 + 2900/T \quad (3)$$

New components were added into Aspen Plus® using the methods of Sherman (2013).

Process Safety

The stripper pressure should never exceed the pressure rating of the vessel. The stripper vessel will be equipped with a relief valve that will discharge the CO_2/amine mixture to a safe, low pressure point, probably the inlet to the absorber.

Results and Discussion

Figure 5 shows the total NH_3 mole fraction and flowrate of H_2O and total NH_3 of the purge. The mole amount of water and ammonia in the purge are almost the same. Mole fraction of ammonia is at its top at reflux ratio 0.83.

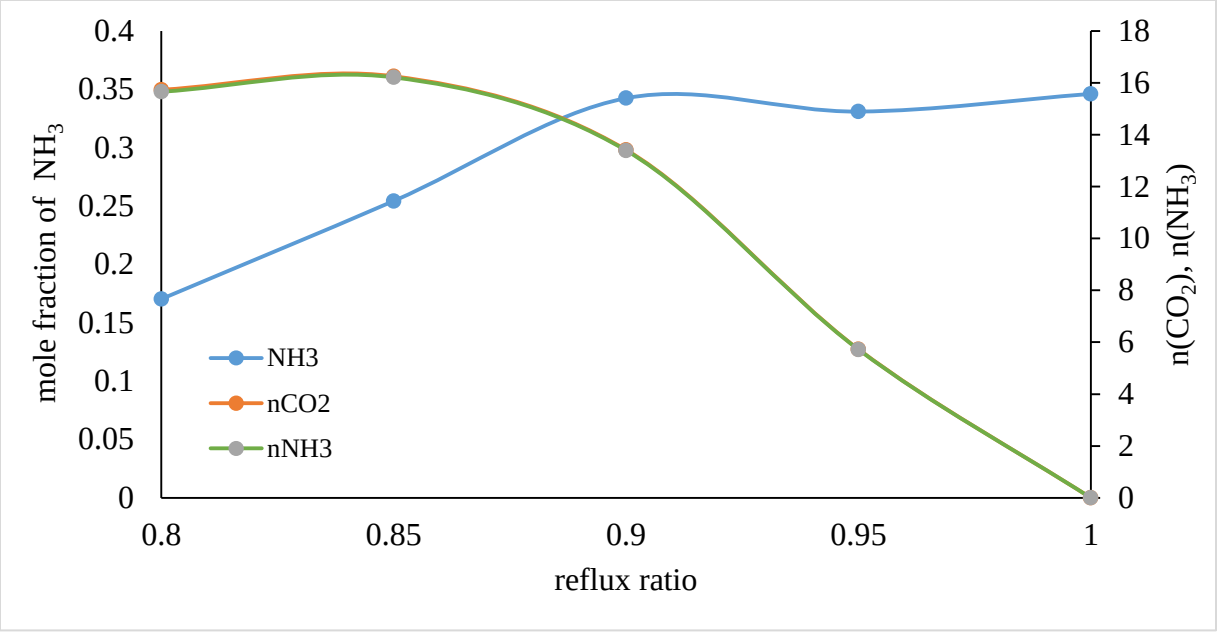

Figure 5: mole fraction of NH_3 and mole flowrate of NH_3 and H_2O of the purge

Figure 6 shows mole fraction of total ammonia and mole NH_3/mol CO_2 removed over kg purge/ton CO_2 removed. Amount of CO_2 removed is based on the CO_2 vapor going to the compressor. As kg purge/ton CO_2 removed increases, the increasing rate of mole fraction of ammonia in the purge slows down. There is a peak value of mole NH_3/mole CO_2 removed around 32 kg purge/ton CO_2 removed. Meanwhile the decreasing rate of mole NH_3/mole CO_2 removed increases.

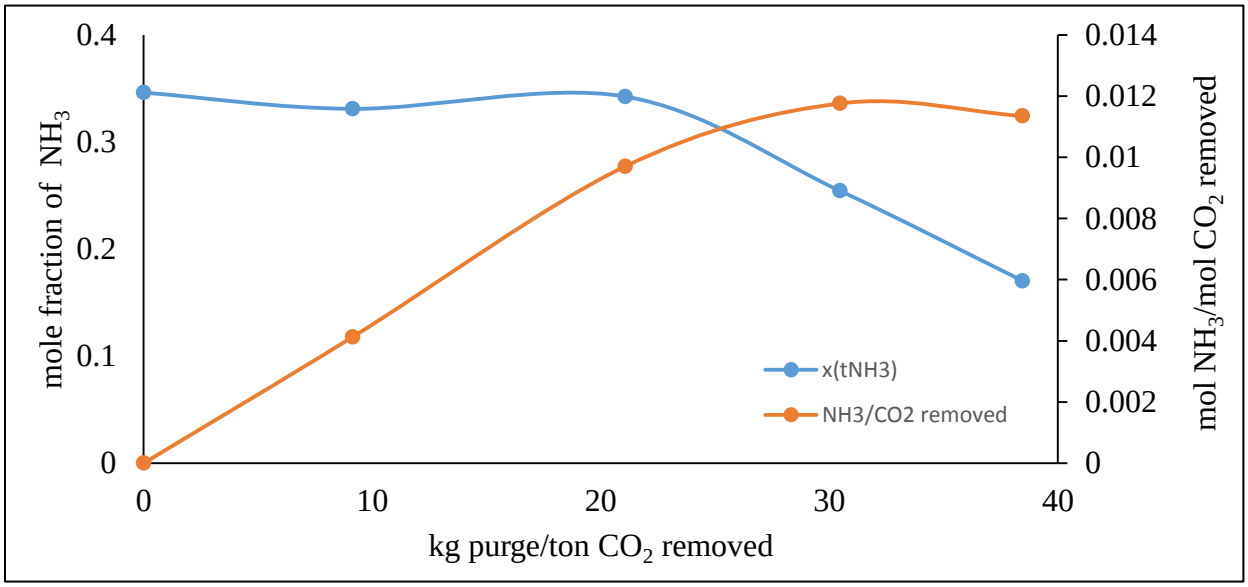

Figure 6: Mole fraction of NH_3 and mole NH_3/mol CO_2 removed over kg purge/ton CO_2 removed

Conclusions

Adding reflux loop concentrate the ammonia in the amine scrubbing system, which is the product of oxidative and thermal degradation. A purge from this loop can reduce the amount of ammonia in the system efficiently.

Future Work

Try more configurations to reduce ammonia in the amine scrubbing system. Design the way of treating the purged flow based on amine degradation rate and ammonia emission standard.

References

Van Wagener DH. *Stripper Modeling for CO_2 Removal Using Monoethanolamine and Piperazine Solvents.* The University of Texas at Austin. Ph.D. Dissertation. 2011.

Sherman BJ. *Importing Non-Databank Components into an Existing Aspen Plus® Simulation.* The University of Texas at Austin. 2013.

Frailie PT. *Modeling of Carbon Dioxide Absorption/Stripping by Aqueous Methyldiethanolamine/Piperazine.* The University of Texas at Austin. Ph.D. Dissertation. 2014.

Mass Transfer Measurements and Models Literature Review

Quarterly Report for April 1 – June 30, 2014

by

Chao Wang

Supported by the Texas Carbon Management Project,

Process Science and Technology Center

and

Frank Seibert

Separations Research Program

The University of Texas at Austin

July 31, 2014

Abstract

In this quarter, a thorough study of previous literature regarding packing mass transfer measurements and models was performed. The review serves as Chapter 2 in the Ph.D. dissertation. Previous methods of measuring the effective area (a_e), gas film mass transfer coefficient (k_G), and liquid film mass transfer coefficient (k_L) were reviewed. In general, these methods used a system that could measure the combination of effective area and mass transfer coefficient (Ka). However, to separate K and a, either a theoretical assumption of area or proposed K models from other work were used. In other words, none of the mass transfer values (k_G, k_L, a_e) were independently validated. In distillation systems, most cases only required the combination (Ka) values, where these models were acceptable. However, the design and optimization of different parts of the amine scrubbing CO_2 capture system needs validated separate values of k_G, k_L, and a_e. Therefore, a consistent measurement of k_G, k_L, a_e in the same condition is performed in this study.

Absorption of CO_2 with NaOH solution was widely used to measure the effective area. The system is a reaction controlled system so most of the mass transfer resistance is in the reaction film. Thus, the overall volumetric mass transfer coefficient ($K_{OG}a$) can be assumed as the liquid film volumetric mass transfer coefficient with reactions (k_g'a). The reaction film mass transfer coefficient k_g' can be calculated and then Ka can be separated. This method is adopted in this study while 0.1 gmol/L NaOH is used to minimize gas film mass transfer resistance.

Gas film controlled systems were used to measure the gas film mass transfer coefficient (k_G). The most commonly used systems were absorption of SO_2/chlorine with NaOH or ammonia/triethylamine with H_2SO_4. Considering the similarity between CO_2 and SO_2, absorption of SO_2 with NaOH is adopted in this study. Since the effective area (a_e) has already been measured in the same column under the same condition, the measured k_Ga value can then be separated to get the k_G value.

Liquid film controlled systems were used to measure the liquid film mass transfer coefficient (k_L). Physical methods (absorption or desorption without chemical reactions) were preferred because it was much easier to control most mass transfer resistance in the diffusion film if there were no chemical reactions. One commonly used system was desorption of oxygen from water by nitrogen. However, this system was preferred in small scale columns. For the pilot scale column in SRP, the expected outlet oxygen concentration would be lower than the range of any oxygen detector. Another system was air stripping of VOCs (volatile organic compounds) from water. Among the organic compounds, toluene is chosen for its relatively large Henry's constant and low toxicity. Toluene stripping from air was used in this study.

Previous mass transfer models were also reviewed in this chapter. Tables 2.1–2.3 in the attached chapter summarize the effective area models and mass transfer coefficient models. A major weakness of these models is the validation of a_e and k_G, k_L at the same time. Thus, mechanistic mass transfer models developed from consistent measurements of a_e, k_L and k_G are needed which is the objective of this work.

A dissertation chapter (Chapter 2, attached) has been written including all the results.

Future Work

Next quarter, work on the dissertation will continue.

Lab Safety issues

1. Steel reinforced gloves are required to prevent being cut when handling sheet metal structured packings.
2. Chemical resistant lab gloves are required when handling a strong base such as NaOH used in effective area measurement, and toxic chemicals such as toluene in k_L measurement. After runs, NaOH should be neutralized before draining.
3. A gas mask with respirator is required when changing SO_2 bottles.

Attached Chapter

Chapter 2: Literature Review

2.1 Effective Area Measurements and Models

2.1.1 Methods of measuring Effective Area

There are several methods of measuring the effective area of packing. Danckwerts (1967, 1970) provides the most widely used method for CO_2-amine systems. This method is based on systems where mass transfer is controlled by a fast chemical reaction in the liquid phase. Thus, the overall mass transfer coefficient is independent of the gas and liquid phase hydrodynamics, and it is determined by the chemical reaction. It can be calculated using the equation:

$$k_r = (r_I D)^{0.5} \qquad (2\text{-}1)$$

where k_r is the mass transfer coefficient in case of absorption, controlled by a first or pseudo-first order fast chemical reaction (m/s);
r_I, the rate constant of the reaction (1/s);
D, the diffusivity of the absorbed component (CO_2) in the liquid phase (m^2/s).

The conditions that determine if the rate of absorption is independent of the hydrodynamics of the gas and liquid phases are given by the equations:

$$k_r >> k_L \qquad (2\text{-}2)$$

and

$$k_r << mk_G \qquad (2\text{-}3)$$

where:
k_L = the liquid side controlled mass transfer coefficient (1/s);
k_G = gas side controlled mass transfer coefficient (1/s);
m = the slope of the equilibrium line.

CO_2 absorption by amines is a fast reaction in the liquid phase. The system fulfills conditions (2-2) and (2-3) so the Danckwerts method can be used to measure the effective area. Variants of the Danckwerts method use different types of chemical reactions such as the absorption of CO_2 from air into NaOH solution, a commonly studied test system. It has the advantage of low costs and ease of operation, low toxicity and volatility compared with amine systems. An additional advantage is that this method has been used to compare areas of different packings (Perry, 1999). Because of these advantages and ease of operation by this method, previous SRP researchers Wilson (2004), and Tsai (2008) applied this method to measure gas-liquid contact area. In this work, absorption of atmospheric CO_2 with 0.1 gmol/L NaOH solution was used to measure effective area of packings.

2.1.2 Previous Effective Area Models

2.1.2.1 Onda et al.

The correlation of Onda and co-workers (Onda et al., 1968) is recognized as the first powerful, most-accepted predictive equation for the effective interfacial area of random packing. The system used was absorption of CO_2 with aqueous NaOH, which is a pseudo first-order reaction. The effective area was calculated:

$$a = \frac{k_L^o a}{\sqrt{k_r C_B D_L}} \qquad (2\text{-}4)$$

where:
k_L^0 is the liquid-phase coefficient for chemical absorption, m/hr;
k_r is the reaction rate constant for second-order reaction, m^3/kg-mole*hr;
C_B is the average concentration of the reactant, kg-moles/m^3.

The model accounts for the effects of hydrodynamics and liquid physical properties on the wetted surface area of random packing. An empirical relation was developed from the results:

$$\frac{a_e}{a_P} = 1 - \exp[-1.45(\frac{\sigma_C}{\sigma_L})^{0.75} \mathrm{Re}_L^{0.1} Fr_L^{-0.05} We_L^{0.2}] \qquad (2\text{-}5)$$

where:
Re_L, Fr_L, and We_L are the liquid phase Reynolds number, Froude number, and Weber number;
σ_C is the critical surface tension (N/m);
σ_L is the liquid phase surface tension (N/m).

However, this correlation was developed mainly based on random packing with nominal size of 12.5 and 15 mm, which had a relatively large surface area. For packing with smaller surface area, this correlation would under predict the effective area. It should also be noted that, based on the data of Raschig Rings, Berl Saddle, spheres and rod packing, and ceramic Pall Rings, this model is not applicable to new-type random packings.

2.1.2.2 Billet and Schultes

Billet and Schultes (1993) analyzed the mass transfer results from a large data bank including 31 different systems and 67 different types and sizes of packings. A dimensionless analysis of the influencing parameters on effective area was performed. The fractional effective area correlation was given by Equation (2-6a) and (2-6b):

$$\frac{a_e}{a_P} = 1.5(a_P d_h)^{-0.5}\left(\frac{u_L d_h}{\nu_L}\right)^{-0.2}\left(\frac{u_L^2 \rho_L d_h}{\sigma}\right)^{0.75}\left(\frac{u_L^2}{g d_h}\right)^{-0.45} \qquad (2\text{-}6a)$$

$$\frac{a_e}{a_P} = 1.5(a_P d_h)^{-0.5}\,\mathrm{Re}_L^{-0.2}\,We_L^{0.75}\,Fr_L^{-0.45} \qquad (2\text{-}6b)$$

where d_h is the hydraulic diameter and can be expressed by Equation (2-7):

$$d_h = 4\frac{\varepsilon}{a_P} \qquad (2\text{-}7)$$

This correlation, the general form originating from a dimensional analysis of the influencing parameters, reflected well the results of the experiments if the surface tension increases from top to bottom. When applied to negative systems, the Marangoni effect, a phenomenon involving the flow of liquid away from regions of low surface tension, would need to be considered. The authors then multiplied a correction factor to account for this effect:

$$\left(\frac{a_e}{a_P}\right)_{negative} = \left(\frac{a_e}{a_P}\right)_{Eq(2-5)}\left(1 - 2.4\times10^{-4}\left|Ma_L\right|^{0.5}\right) \qquad (2\text{-}8)$$

where Ma_L is the Marangoni number and can be expressed by:

$$Ma_L = \frac{d\sigma_L}{dx}\frac{\Delta x}{D_L \mu_L a_P} \qquad (2\text{-}9)$$

where x is the mole fraction of the more volatile component in the liquid phase.

2.1.2.3 Rocha-Bravo-Fair model

The first overall investigation for structured packing was conducted by Bravo et al (1982) based on data from a commercial-scale packed distillation column. The effective interfacial area correlation was obtained by correlating the extensive experimental data bank included in paper by Bolles and Fair (Bolles et al., 1979) which involved a wide range of packings, column size, and systems. This model was called the Bravo-Rocha-Fair (BRF) model. In this model, gas phase mass transfer coefficient (k_G) was based on earlier investigation of wetted wall column results, where Sherwood (1975) concluded that the relationship of Johnstone and Pigford (1942) should be used for the gas side coefficient:

$$\frac{k_G d_{eq}}{D_G} = 0.0328[\frac{d_{eq}\rho_G(u_{G,eff}+u_{L,eff})}{\mu_G}]^{0.77}(\frac{\mu_G}{\rho_G D_G})^{0.33} \qquad (2\text{-}10)$$

The liquid phase mass transfer coefficient (k_L) was based on penetration theory, as first expounded by Higbie (1935):

$$k_L = 2\sqrt{\frac{D_L u_{L,eff}}{\pi S}} \qquad (2\text{-}11)$$

Therefore, the effective area can then be separated from ka values:

$$\frac{a_e}{a_P} = 0.498(\frac{\sigma^{0.5}}{Z^{0.4}})(Ca_L\ \mathrm{Re}_G)^{0.392} \qquad (2\text{-}12)$$

where

Z is the height of the packed bed;

σ is surface tension (dyn/cm);

Ca_L and Re_G are dimensionless liquid capillary number and gas Reynolds number.

Compared with previous correlations, the BRF model introduced the concept "effective" gas and liquid velocities to account for the interaction between the two phases.

Rocha et al. (1993, 1996) updated the BRF model with some new results. In the k_G model, the experimental constant and the exponent were slightly changed. In the k_L model, a correction factor (C_E) was introduced to account for regions in packed bed not conducive to rapid surface renewal. The updated correlations were recognized as the Rocha-Bravo-Fair (RBF) model:

$$\frac{k_G S}{D_G} = 0.054[\frac{\rho_G S(u_{Ge}+u_{Le})}{\mu_G}]^{0.8}(\frac{\mu_G}{D_G\rho_G})^{0.33} \qquad (2\text{-}13)$$

$$k_L = 2\sqrt{\frac{D_L C_E u_{Le}}{\pi S}} \qquad (2\text{-}14)$$

The effective area correlation for the RBF model was based on area model of Shi and Mersmann (1985) by introducing a factor F_{SE} to account for packing variations in surface texture:

$$\frac{a_e}{a_P} = F_{SE}\frac{29.12u_L^{0.4}\nu_L^{0.2}S^{0.359}}{(1-0.93\cos\gamma)(\sin\alpha)^{0.3}\varepsilon^{0.6}}(\frac{\rho_L}{\sigma g})^{0.15} \qquad (2\text{-}15)$$

where $\cos\gamma$ was the contact angle and can be calculated by (2-16a) and (2-16b):

$$\cos\gamma = 5.211\times10^{-16.835\sigma}, \quad \sigma > 55mN/m \qquad (2\text{-}16a)$$

$$\cos\gamma = 0.9, \quad \sigma < 55mN/m \qquad (2\text{-}16b)$$

Both models utilized correlations or assumptions from others work either for the area model or for the $k_{G/L}$ model. Therefore, the area model and k model should be used together to get the ka values instead of using them separately.

2.1.2.4 Tsai model

Tsai et al. (2010) measured the mass transfer contact areas of nine structured packings using the absorption of CO_2 from air into 0.1 gmol/L NaOH. The mass transfer was controlled by the chemical reaction in the liquid phase. The overall mass transfer coefficient K_{OG} can be assumed as the liquid phase mass transfer coefficient with chemical reactions (k_g'). It can be calculated by (2-16):

$$k_g^{'} = \frac{\sqrt{k_{OH^-}[OH^-]D_{CO2,L}}}{H_{CO2}} \qquad (2\text{-}17)$$

Therefore, Tsai was able to separate k and a to obtain the effective area.

A global mass transfer contact area model (2-18) was developed as a function of the liquid Weber and Froude numbers. According to Tsai, the contact area is a function of liquid flow rate, surface tension, liquid density, structured packing geometry and is not a function of gas flow rate and liquid viscosity. The model satisfactorily represented the entire database ($\pm$13%):

$$\frac{a_e}{a_P} = 1.34[(\frac{\rho_L}{\sigma})g^{1/3}(\frac{Q}{L_P})^{4/3}]^{0.116} \qquad (2\text{-}18)$$

where L_P is the wetted parameter specified in terms of packing geometry:

$$L_P = \frac{4S}{Bh}A \qquad (2\text{-}19)$$

2.1.2.5 Delft

Another important correlation to predict packing effective area was proposed by Olujic (1999) called the Delft model (2-20). In this model, the effective area was correlated as a function of liquid velocity and packing perforation factor (Ω), which represents the ratio of packing surface area occupied by the holes to the total surface area:

$$\frac{a_e}{a_P} = \frac{1-\Omega}{1+A/u_{Ls}^B} \qquad (2\text{-}20)$$

where A and B are the packing type and size dependent constants.

2.2 Gas Film Mass Transfer Coefficient Measurements and Models

2.2.1 Methods of measuring gas film mass transfer coefficient

Mehta and Sharma (1966) measured the volumetric gas side coefficient k_Ga and the contact area a_e separately. They determined the true gas-side film coefficient k_G from the overall coefficient k_Ga and area. The systems chosen were such that the liquid side resistance was absent and that the gas-side resistance controlled the mass transfer rate. The systems were sulfur dioxide or chlorine Freon-22 (monochlorodifluorominethane) or Freon-114 (dichlorotetrafluoroethane)) absorbed by aqueous sodium hydroxide solutions (2 gmol/L NaOH). Another potential system was ammonia or triethylamine in different carrier gases absorbed by dilute sulfuric acid (1 to 2 gmol/L H_2SO_4).

The k_Ga was calculated by the equation:

$$k_G a = \frac{u_G \ln(\frac{y_{in}}{y_{out}})}{ZRT} \qquad (2\text{-}21)$$

where:
u_G = gas superficial velocity (m/s);
y_{in}, y_{out} = inlet and outlet gas mole fraction of the transferring solute;
R= gas constant, 8.314 J/(K*mole);
T = absolute temperature, K;
Z = packed height, m;

Yaici and Laurent (1988) used the method of absorption of dilute SO_2 into NaOH and into an organic medium (N,N-dimethylaniline) to determine the value of $k_G a$. For an irreversible, instantaneous chemical reaction at a surface the rate which is controlled by the gas phase resistance, the absorptive flux per unit reactor volume can be written as follows:

$$\phi = k_G a * P \qquad (2\text{-}22)$$

Then the volumetric gas film mass transfer coefficient can be calculated:

$$k_G a = \frac{G_m}{PZ} \ln \frac{P_{in}}{P_{out}} \qquad (2\text{-}23)$$

where:
G_m is the gas flow rate ,kg/s;
P_{in} and P_{out} are the partial pressures of the gaseous solute at the inlet and the outlet Pa;
Z is the reactor of a packed height, m.

Moucha and Linek (2005) measured the $k_G a$ for new types of Intalox metal saddles (IMTP) 25, 40 and 50. The volumetric gas phase mass transfer coefficient, $k_G a$, was determined by absorption of dilute SO_2 (0.02 vol% in air) into 1 M NaOH aqueous solution. The height of the measuring section was 0.5 m. Experiments were performed at liquid flow rates from 3 to 100 $m^3/(m^2 h)$. The temperature of the liquid and gas phases was kept at 20 ± 1C in all experiments.

Considering all the methods and systems used for measuring gas phase mass transfer coefficient, sulfur dioxide absorbed in aqueous sodium hydroxide solutions was chosen as our test system. The advantage of this system is that the reaction between SO_2 and NaOH is an instantaneous reaction so the liquid side mass transfer resistance can be neglected. The gas side mass transfer coefficient $k_G a$, which equals the overall mass transfer $K_{OG} a$ coefficient at this condition, can be measured directly. Since the effective area a_e was already measured from the previous experiment, k_G can be obtained by dividing $k_G a$ by a_e. In this method, both the $k_G a$ and a_e were measured directly, so the k_G obtained was validated. Another advantage of this system is that the properties of SO_2 are similar to CO_2 which is used for area measurement, which will keep the measurement consistent.

2.2.2 Previous Gas Film Mass Transfer Coefficient Models

2.2.2.1 Onda et al.

Onda (1967) developed k_G model based on his effective area model (Equation 2-5). The packings measured in this work were all random packings (Raschig rings, Berl saddles, Spheres). The correlation is:

$$Sh_G = 5.23\,\mathrm{Re}_G^{0.7}\,Sc_G^{1/3}(a_P + D_P)^{-2.0} \qquad \text{(2-24a)}$$

where D_P is the nominal size of packing, m.

For Raschig rings and Berl saddles smaller than 15 mm, the constant in Equation (2-23a) was changed from 5.23 to 2.00 to better fit the data (Equation 2-23b).

$$Sh_G = 2.00\,\mathrm{Re}_G^{0.7}\,Sc_G^{1/3}(a_P + D_P)^{-2.0} \qquad \text{(2-24b)}$$

Onda also measured the rate of vaporization for air-water system under adiabatic conditions to validate the k_G model. Equations (2-24a) and (2-24b) can correlate most of the vaporization data as well. However, Onda's k_G model was mostly based on 1st and 2nd generation random packings. There will be deviations when apply to structured packings and recently developed high performance random packings.

2.2.2.2 Mehta and Sharma

Mehta and Sharma (1966) performed a study of diffusivity effect on the gas film mass transfer coefficient in a liquid continuous or bubble column. The carrier gases were hydrogen, nitrogen, Freon-12 and Freon-114. The solute gases were chlorine, SO_2, ammonia, n-butylamine, di-n-propylamine, triethylamine, methyl ethyl ketone, n-butyl formate and ethyl propionate. By matching different solute gases and different carrier gases, 17 absorption systems and 18 vaporization systems with different diffusivities were tested. The log-log plot of k_Ga against diffusivities of solutes in various carrier gases showed that k_Ga varies as the 0.5 power of the diffusivity. This conclusion is also used in this study when convert k_Ga values measured in SO_2/NaOH system to the targeted CO_2/NaOH system.

Mehta and Sharma also studied the gas flow rate effect and the submergence effect on gas film mass transfer coefficient. It is found that k_Ga varies as 0.75 power of the gas flow rate and 0.33 power of the submergence. The correlation is:

$$k_G a = C * D_G^{0.5} u_G^{0.75} S^{0.33} \qquad \text{(2-25)}$$

where:
C is the experimental constant;
S is the submergence height.

It is recognized this is not a gas continuous packed column, however, it does show the effect of gas diffusivity on the gas film mass transfer coefficients.

2.2.2.3 Billet and Schultes

Billet and Schultes (1993) developed gas film mass transfer coefficient model based on surface renewal theory. The theoretical time interval required for the renewal of the contact area was defined by Equation (2-26):

$$\tau_G = (\varepsilon - h_L) l_\tau \frac{1}{u_G} \qquad \text{(2-26)}$$

where:
ε is the void fraction;
h_L is the liquid fractional hold-up;
u_G is the gas superficial velocity;
l_τ is the length of flow path by Equation (2-27).

$$l_\pi = d_h = 4\frac{\varepsilon}{a_P} \qquad (2\text{-}27)$$

The theoretical proposed correlations for k_G and k_L:

$$k_G = \frac{2}{\sqrt{\pi}}\sqrt{D_G \frac{u_G}{(\varepsilon - h_L)l_\pi}} \qquad (2\text{-}28)$$

$$k_L = \frac{2}{\sqrt{\pi}}\sqrt{D_L \frac{u_L}{h_L l_\pi}} \qquad (2\text{-}29)$$

2.2.2.4 Delft model

The Delft model developed by Olujic (1999) was mainly based on distillation systems. The gas film mass transfer coefficient can be represented as the combination of laminar flow and turbulent flow contributions:

$$k_G = \sqrt{k_{G,lam}^2 + k_{G,turb}^2} \qquad (2\text{-}30)$$

with

$$k_{G,lam} = \frac{Sh_{G,lam} D_G}{d_{hG}} \qquad (2\text{-}31a)$$

$$k_{G,turb} = \frac{Sh_{G,turb} D_G}{d_{hG}} \qquad (2\text{-}31b)$$

The Sherwood number for laminar and turbulent flow can be expressed by:

$$Sh_{G,lam} = 0.664 Sc_G^{1/3}\sqrt{\mathrm{Re}_{Grv}\frac{d_{hG}}{l_{G,pe}}} \qquad (2\text{-}32)$$

$$Sh_{G,turb} = \frac{\mathrm{Re}_{Grv}\, Sc_G \frac{\zeta_{GL}\varphi}{8}}{1 + 12.7\sqrt{\frac{\zeta_{GL}\varphi}{8}}(Sc_G^{2/3} - 1)}\left[1 + \left(\frac{d_{hG}}{l_{G,pe}}\right)^{2/3}\right] \qquad (2\text{-}33)$$

where:
($d_{hG}/l_{G,pe}$) is the ratio of hydraulic diameter and the length of gas flow channel within a packing element;
Re_{Grv} represents the gas phase Reynolds number based on relative velocity:

$$\mathrm{Re}_{Grv} = \frac{\rho_G (u_{Ge} + u_{Le}) d_{hG}}{\mu_G} \qquad (2\text{-}34)$$

ξ_{GL} is the friction factor between liquid and gas:

$$\xi_{GL} = \{-2\log[\frac{(\delta / d_{hG})}{3.7} - \frac{5.02}{\mathrm{Re}_{Grv}}\log(\frac{(\delta / d_{hG})}{3.7} + \frac{14.5}{\mathrm{Re}_{Grv}})]\}^{-2} \qquad (2\text{-}35)$$

2.2.2.5 Rocha-Bravo-Fair model

Rocha et al (1993, 1996) also developed models for gas film mass transfer coefficient based on the distillation and absorption data measured by the Separations Research Program (SRP). The correlation was given by Equation (2-13) and has been explained in Section 2.1.2.3.

2.3 Liquid Film Mass Transfer Coefficient Measurements and Models

2.3.1 Methods of measuring liquid film mass transfer coefficient

Sharma and Danckwerts (Sharma, 1970) explored the chemical methods of measuring liquid side mass transfer coefficient. For a first order reaction (2-36), under certain conditions the reaction is fast enough to keep the concentration of A in the bulk of the B phase equal to zero, while it is not fast enough for any appreciable amount of A to react in the diffusion film at the surface of the B phase.

$$A + zB \rightarrow products \qquad (2\text{-}36)$$

Under these conditions, the rate of transfer is that for physical mass transfer:

$$R = k_L C_A^* \qquad (2\text{-}37)$$

The condition to be satisfied if $[A]_B$ is to be zero is:

$$k_L a << V_B k_2 [B]^0 \qquad (2\text{-}38)$$

where:
$[A]_B$ is the bulk concentration of A in the B phase;
C_A^* is the concentration of A at surface;
$[B]^0$ is the concentration of B in the bulk phase;
V_B is the volume of B phase per unit volume of the system.

The condition to be satisfied if no A is to react in the diffusion film is:

$$D_{AB} k_2 [B]^0 / k_L^2 << 1 \qquad (2\text{-}39)$$

where D_{AB} is the diffusivity of A in the B phase.

Sharma and Danckwerts also suggest possible experimental test systems to validate this theory. The gas-liquid system could be the absorption of CO_2 into a carbonate-bicarbonate buffer solution. The reaction is second order. Another system could be oxygen absorbed from air into dilute acid solutions of CuCl, which is oxidized to $CuCl^{2-}$. Oxygen may be also absorbed from air into sodium sulphite solution, using $CoSO_4$ or $CuSO_4$ as a catalyst. The reaction appears to be second order in O_2 and zero order in SO_3^{2-} under usual conditions. In all the above cases it is necessary to ensure that conditions (2-38) and (2-39) apply.

Although the chemical method of measuring the liquid film mass transfer coefficient is valid and has some advantages, it is more suitable for small scale experiments. For larger scale device, it is hard to keep conditions (2-38) and (2-39) valid at all the time.

Onda (1959) investigated the physical absorption of gas by water in a tower packed with Raschig ring. The liquid film mass transfer coefficient was separated by dividing the capacity coefficient by the wetted surface area. Fundamental equations to calculated k_L using dimensionless numbers were discussed from the standpoints of two-film theory and penetration theory. The purity of the gas used (CO_2 or H_2) was more than 99%. Tap water was introduced from the head

tank into the tower through the thermostat. The liquid film mass transfer coefficient can be computed from:

$$k_L a = \{L/(\rho Z)\}\{\ln(C_S - C_1)/(C_S - C_2)\} \qquad (2\text{-}40)$$

where:
L is the mass flow rate of liquid, kg/(m^2*hr);
ρ is the density of liquid, kg/m3;
Z is the height of packing, m;
C_1, C_2, and C_S are the concentration of liquid at the entrance, at the exit of the tower, and at the saturation, respectively, kg/m^3.

To derive k_L from $k_L a$, Onda assumed that the effective area a_e equals the wetted area a_w and used a formula developed by Fujita (1954).

Akita (1973) measured the volumetric liquid phase mass transfer coefficient $k_L a$ in gas bubble columns with various systems using the physical method. The systems used for $k_L a$ were water-oxygen, glycerol solution-oxygen, glycol solution-oxygen, methanol-oxygen and 0.15 M Na_2SO_3 solution-air. The column was operated continuously with respect to the gas flow. Values of the volumetric coefficient for liquid phase mass transfer $k_L a$ with respect to the unit volume of aerated liquid were obtained from experiments of oxygen absorption into various liquids. Oxygen from a cylinder was supplied to the gas chamber at the column bottom through a surge tank. Before an absorption experiment, oxygen was stripped from the liquid in the column by sparging nitrogen for 5-10 min at a superficial gas velocity of about 100 meters per hour. The concentration of dissolved oxygen in the liquid sample was analyzed chemically by the Winkler method. Since the gas phase resistance for mass transfer was negligible, the values of $k_L a$ for the batch experiments on the physical absorption of oxygen were obtained by the following relationship:

$$k_L a = \frac{1-\varepsilon_G}{t} \ln \frac{C^* - C_i}{C^* - C_f} \qquad (2\text{-}41)$$

where:
t is the absorption time;
C^* is the dissolved oxygen concentration at saturation, ml-^{3};
C_i, C_f is the initial and final concentrations of dissolved oxygen in liquid, respectively, ml^{-3}.

In the experiment, C^* was determined by sparging pure oxygen through the liquid in the column for a sufficient length of time, in case published data were not available.

Linek (1984) measured the liquid side volumetric mass transfer coefficient $k_L a$ for Pall rings of nominal sizes 15, 25, 35 and 50 mm made of polypropylene and polyvinylidenflouride. The $k_L a$ values were obtained by physical desorption of oxygen from water into pure nitrogen stream. The column was packed to the height of one m. The set-up permitted the measurement of either the absorption of atmospheric oxygen into oxygen-free water or the desorption of oxygen dissolved in water into a pure nitrogen stream. The majority of their experiments were performed in the counter-current desorption mode. Nitrogen was led into the column at constant superficial velocity of 0.0253 m/s. At 20 °C liquid superficial velocities from 2.02×10^{-3} up to 0.0252 m/s were used. A polarographic oxygen probe was used to monitor the oxygen concentration in the outlet gas and in the inlet and outlet liquid streams. The $k_L a$ values were

calculated from the steady state oxygen concentrations in the column inlet, C_{LA1}, and outlet, C_{LA2}, liquid streams using the relationships for stripping efficiency analysis.

$$k_L a = \frac{v_L}{H} \ln(c_{LA1} / c_{LA2}) \qquad (2\text{-}42)$$

For absorption experiments the equation was:

$$k_L a = \frac{v_L}{H} \ln[(c_{LA}^{+} - c_{LA1}) / (c_{LA}^{+} - c_{LA2})] \qquad (2\text{-}43)$$

Here C_{LA+} was the oxygen concentration in air-saturated water under the given experimental conditions. In deriving these two equations it was assumed (i) that the oxygen concentration in the gas phase was constant along the column and equaled its concentration in the incoming gas stream and (ii) that the liquid phase conformed to plug flow. The first assumption was met safely inasmuch as the oxygen concentration changes in the gas phase never exceeded 0.2 vol% in the experiments, due to low oxygen solubility in water. Such negligible concentration changes also were a guarantee of negligible influence of axial dispersion in the gas phase. The liquid phase axial dispersion had some effect on the k_La data and this should be taken into consideration. However, reliable data on liquid phase axial mixing is scarce and not available for this case. The results of this article fitted well with the data by Billet and Mackowiak (Billet, 1980) for 25mm Pall rings, Sahay and Sharma (Sahay, 1973) for 25.4 mm Pall rings.

Physical methods are preferred towards chemical methods for measuring liquid phase mass transfer coefficient, because it is difficult to satisfy conditions (2-38) and (2-39) simultaneously at all the time, especially for lager equipment being used in SRP. Desorption of oxygen from water by nitrogen is eliminated because the column height for our system is 3 times the column height used by Linek. The expected outlet oxygen concentration is lower than the range of any oxygen detector. While absorption of oxygen with water from nitrogen is possible, the ability of absorbing oxygen is limited so the inlet oxygen concentration has to be high enough so the outlet oxygen concentration in water accurately detectable.

Another physical method is the stripping of organic chemicals from water. Air striping of VOCs (volatile organic compounds) from water is a standard method and widely applied in industry (JPI, 1996; Kunesh, 1996; El-Behlil, 2012). Among the organic compounds, toluene is chosen for its relatively large Henry's constant and low toxicity. The toluene stripping from air method will be used for measurements of liquid film mass transfer coefficient. Low concentrations of toluene in the ppm level can be accurately measured using a concentration step and a FID gas chromatograph.

2.3.2 Previous Liquid Film Mass Transfer Coefficient Models

2.3.2.1 Onda et al.

Onda and co-authors (1968) developed liquid film mass transfer coefficient models based on literature and experimental data of gas absorption into water and desorption from water. The packings investigated were mostly random packings: Raschig Rings, Berl Saddles, Pall Rings, Spheres, and Rods. Their correlation is given in Equation (2-44):

$$k_L(\rho_L / \mu_L g)^{1/3} = 0.0051(L / a_w \mu_L)^{2/3}(\mu_L / \rho_L D_L)^{-1/2} \times (a_P D_P)^{0.4} \qquad (2\text{-}44)$$

where:

a_w is the wetted area (effective area) given by Equation (2-5);

D_P is the packing nominal size, m.

Onda also studied the gas absorption of pure CO_2 into methanol and carbon tetrachloride. The columns used were 6 and 12 cm I.D. and packed with 10-25 mm Raschig Rings, Berl saddles, spheres and rods for 20-30 cm height. The results were used to verify the k_L model by (2-44) and the agreement was satisfactory. The overall error of Equation (2-44) was within $\pm$20% for gas absorption and desorption into water as well as organic solvents.

2.3.2.2 Linek et al.

Linek et al. (2001) proposed an empirical model for predicting k_L based on their experimental results. The experiments were performed in a 0.29 m I.D. column with a packed height of 1.04 m. The random packings includedRMSR 25, 40, and 50. The results were represented by:

$$k_L = \frac{d_1}{b_1} B^{d_2 - b_2 + b_3 \log B} \qquad (2\text{-}45)$$

where:
B is the liquid load, m/h;
b_1, b_2, b_3 and d_1 are experimental parameters differ between packings.

2.3.2.3 Mangers and Ponter

Mangers and Ponter (1980) investigated the effect of diffusivity and viscosity on the liquid film mass transfer coefficient. The system was absorption of carbon dioxide into pure water and aqueous glycerol mixtures at 25 C covering a viscosity range of 0.9 to 26 cP. The apparatus was a 10 cm I.D. glass column packed with 1 cm glass Raschig Rings. Their correlation is:

$$\frac{k_L a}{D} = 3.90 \times 10^{-3} \left(\frac{L}{\mu}\right)^{\alpha} \left(\frac{\mu}{\rho D}\right)^{0.50} \left(\frac{\rho^2 g d^3}{\mu^2}\right)^{0.27} \left(\frac{\rho \sigma^3}{\mu^4 g}\right)^{0.33} \times \left(\frac{1}{M.W.R.}\right)^{1.67} \qquad (2\text{-}46)$$

where:
L is the liquid flow rate, $MT^{-1}L^{-2}$;
D is the diffusion coefficient, L^2T^{-1};
μ is the viscosity, $ML^{-1}T^{-1}$;
α is the slope for water system and for glycerol-water mixtures, can be calculated by:

$$\alpha = 0.49[(1 - \cos\theta)^{0.6} \left(\frac{\rho \sigma^3}{\mu^4 g}\right)^{0.2}]^{0.108} \qquad (2\text{-}47)$$

M.W.R. refers to the minimum wetting rate, can be calculated by:

$$M.W.R. = 1.12[(1 - \cos\theta)^{0.6} \left(\frac{\rho \sigma^3}{\mu^4 g}\right)^{0.2}] \qquad (2\text{-}48)$$

The relations between the liquid film mass transfer coefficient and diffusivity as well as viscosity from Mangers and Ponter's work will be adopted in this paper when converting k_L measured in the toluene/water system to the CO_2/piperazine system.

2.3.2.4 Brunazzi and Paglianti

Brunazzi and Paglianti (1997) studied the mixing in the junctions between packing elements. A parameter, H, representing the flow distance was defined. In the case of complete mixing, H is a function of the channel dimension, whereas in the case of partial mixing, H needs to be

computed as the distance covered by the liquid phase flowing into the column. The author proposed a correlation to calculate H:

$$H = \frac{Z}{\sin\alpha} \tag{2-49}$$

where:
Z is the packing height, m;
α is the slope of the steepest descent line with respect to the horizontal axis, deg.

Finally, a k_L correlation including the influence of mixing in the junctions was proposed:

$$Sh_L = A\frac{Gz^B}{Ka^C} \tag{2-50}$$

where:

$$Sh_L = \frac{k_L d}{D_L} \tag{2-51}$$

$$Ka = \frac{\sigma^3 \rho_L}{\mu_L^4 g} \tag{2-52}$$

$$Gz = \mathrm{Re}_L\, Sc_L \frac{\delta}{H} \tag{2-53}$$

2.3.2.5 Delft model

The Delft model proposed by Olujic (1999) has been discussed in the area model section (2.1.2.5) and the k_G model section (2.2.2.4) before. As for the k_L model, the Delft model used the same expression as proposed by Bravo et al. (1992). However, instead of the corrugation side, s, the Delft model used the hydraulic diameter of the triangular flow channel as the characteristic length of liquid flow. The hydraulic diameter was defined by:

$$d_{hG} = \frac{\frac{(bh-2\delta s)^2}{bh}}{[(\frac{bh-2\delta s}{2h})^2 + (\frac{bh-2\delta s}{b})^2]^{0.5} + \frac{bh-2\delta s}{2h}} \tag{2-54}$$

where:
b is the corrugation base length, m;
h is the corrugation height, m;
s is the corrugation side length, m;
δ is the liquid film thickness, m.

The k_L correlation can then be calculated:

$$k_L = 2\sqrt{\frac{D_L u_{Le}}{\pi 0.9 d_{hG}}} \tag{2-55}$$

2.4 Conclusions

2.4.1 Methods of measuring effective area, gas and liquid film mass transfer coefficient

After reviewing various methods of measuring contact area a_e, the Danckwerts method (1970), absorption of CO_2 from air into 0.1 gmol/L NaOH, is adopted for measuring a_e. The Sharma (1966) and Moucha (2005) method of absorbing SO_2 from air into 0.1 gmol/L NaOH is the most suitable method for determining the gas film mass transfer coefficient. Desorption of toluene from saturated water by air is used for determining the liquid film mass transfer coefficient.

2.4.2 Models of predicting effective area, gas and liquid film mass transfer coefficient

A large number of previous correlations for a_e, k_G and k_L have been discussed in this chapter. Table 2.1-2.3 summarizes the effective area models and mass transfer coefficient models. A major weakness of these models is the validation of a_e and k_G, k_L at the same time. Either a theoretical assumption of area or proposed theoretical film coefficient models were used to separate the "k" and "a" values. Thus, mechanistic mass transfer models developed from consistent measurements of a_e, k_L and k_G are needed which is the objective of this work.

Table 2.1. Summary of models for effective area

Author	Correlations
Onda (1968)	$\frac{a_e}{a_P} = 1 - \exp[-1.45(\frac{\sigma_C}{\sigma_L})^{0.75} \mathrm{Re}_L^{0.1} Fr_L^{-0.05} We_L^{0.2}]$
Billet and Schultes (1993)	$\frac{a_e}{a_P} = 1.5(a_P d_h)^{-0.5} \mathrm{Re}_L^{-0.2} We_L^{0.75} Fr_L^{-0.45}$
Rocha-Bravo-Fair (1996)	$\frac{a_e}{a_P} = F_{SE} \frac{29.12 u_L^{0.4} \nu_L^{0.2} S^{0.359}}{(1-0.93\cos\gamma)(\sin\alpha)^{0.3} \varepsilon^{0.6}} (\frac{\rho_L}{\sigma g})^{0.15}$
Tsai (2010)	$\frac{a_e}{a_P} = 1.34[(\frac{\rho_L}{\sigma}) g^{1/3} (\frac{Q}{L_P})^{4/3}]^{0.116}$
Olujic (1999)	$\frac{a_e}{a_P} = \frac{1-\Omega}{1 + A/u_{Ls}^B}$

Table 2.2. Summary of models for gas film mass transfer coefficient

Author	Correlations
Onda (1968)	$Sh_G = 5.23 \mathrm{Re}_G^{0.7} Sc_G^{1/3} (a_P + D_P)^{-2.0}, D_P > 15\,mm$ $Sh_G = 2.00 \mathrm{Re}_G^{0.7} Sc_G^{1/3} (a_P + D_P)^{-2.0}, D_P \le 15\,mm$
Mehta and Sharma (1966)	$k_G a = C * D_G^{0.5} u_G^{0.75} S^{0.33}$
Billet and Schultes (1993)	$k_G = \frac{2}{\sqrt{\pi}} \sqrt{D_G \frac{u_G}{(\varepsilon - h_L) l_\pi}}$

Olujic (1999)	$k_G = \sqrt{(\frac{Sh_{G,lam} D_G}{d_{hG}})^2 + (\frac{Sh_{G,turb} D_G}{d_{hG}})^2}$ $Sh_{G,lam} = 0.664 Sc_G^{1/3} \sqrt{\mathrm{Re}_{Grv} \frac{d_{hG}}{l_{G,pe}}}$ $Sh_{G,turb} = \frac{\mathrm{Re}_{Grv} Sc_G \frac{\zeta_{GL}\varphi}{8}}{1+12.7\sqrt{\frac{\zeta_{GL}\varphi}{8}}(Sc_G^{2/3}-1)} [1+(\frac{d_{hG}}{l_{G,pe}})^{2/3}]$
Rocha-Bravo-Fair (1996)	$\frac{k_G S}{D_G} = 0.054[\frac{\rho_G S(u_{Ge}+u_{Le})}{\mu_G}]^{0.8} (\frac{\mu_G}{D_G \rho_G})^{0.33}$

Table 2.3. Summary of models for liquid film mass transfer coefficient

Author	Correlations
Onda (1968)	$k_L(\rho_L/\mu_L g)^{1/3} = 0.0051(L/a_w\mu_L)^{2/3}(\mu_L/\rho_L D_L)^{-1/2} \times (a_P D_P)^{0.4}$
Linek (2001)	$k_L = \frac{d_1}{b_1} B^{d_2 - b_2 + b_3 \log B}$
Mangers and Ponter (1980)	$\frac{k_L a}{D} = 3.90\times10^{-3} (\frac{L}{\mu})^{\alpha} (\frac{\mu}{\rho D})^{0.50} (\frac{\rho^2 g d^3}{\mu^2})^{0.27} (\frac{\rho\sigma^3}{\mu^4 g})^{0.33} \times (\frac{1}{M.W.R.})^{1.67}$
Brunazzi (1997)	$Sh_L = A\frac{Gz^B}{Ka^C}$, $Ka = \frac{\sigma^3\rho_L}{\mu_L^4 g}$, $Gz = \mathrm{Re}_L Sc_L \frac{\delta}{H}$
Olujic (1999)	$k_L = 2\sqrt{\frac{D_L u_{Le}}{\pi 0.9 d_{hG}}}$
Billet and Schultes (1993)	$k_L = \frac{2}{\sqrt{\pi}} \sqrt{D_L \frac{u_L}{h_L l_\pi}}$
Rocha-Bravo-Fair (1996)	$k_L = 2\sqrt{\frac{D_L C_E u_{Le}}{\pi S}}$

References

Akita K, Yoshida F. "Gas holdup and volumetric mass transfer coefficient in bubble columns: effects of liquid properties." *Industrial & Engineering Chemistry Process Design and Development.* 1973;12(1):76–80.

Bravo JL, et al. "Mass Transfer in Gauze Packings." *Hydrocarbon Processing.* 1985;91–95.

Bravo JL, Rocha JA, Fair JR. "A comprehensive model for the performance of columns containing structured packings." *ICHEME Symp. Ser.* 1992;128:489–507.

Billet R, Mackowiak J. "Recent progress in distillation design." *5th International Congress in Scandinavia on Chemical Engineering.* Copenhagen, Denmark. 1980.

Billet R, Schultes M. "Predicting mass transfer in packed column." *Chem. Eng. Technol.* 1996;16:1–9.

El-Behlil MA, El-Gezawi SM, Adma SA. "Volatile Organic Chemicals Removal from Contaminated Water using Air Stripping Low Profile Sieve Tray Towers." *Sixteenth International Water Technology Conference*, Istanbul, Turkey, 2012.

Fujita S, Sakuma S. "Wetted area of Raschig rings in packed columns." *Chem. Eng. (Japan).* 1954;18:64–67.

Higbie, R. "The rate of absorption of a pure gas into a still liquid during short periods of exposure." *Trans. Am. Inst. Chem. Engrs.* 1935;31:365–383.

Johnstone HF, and Pigford RL. "Distillation in wetted-wall column." *Trans. Am. Inst. Chem. Engrs.* 1942;38:25–50.

JPI. *Air Stripping of VOCs from Water.* Houston, Texas, Jaeger Products Inc (JPI). 1996.

Kunesh JG, et al. "Sieve Tray Performances for Steam Stripping Toluene from Water in a 4-ft Diameter Column." *Ind. Eng. Chem. Res.* 1996;35:2660–2671.

Linek V, Moucha T, Rejl FJ. "Hydraulic and mass transfer characteristics of packings for absorption and distillation columns. Rauschert-Metall-Sattel-Rings." *Trans IChemE.* 2001;79:725–732.

Linek V, Petericek P. "Effective interfacial area and liquid side mass transfer coefficients in aborption columns packed with hydrophilised and untreated plastic packings." *Chem Eng Res Des.* 1984;62:13–21.

Mangers RJ, Ponter AB. "Effect of viscosity on liquid film resistance to mass transfer in a packed column." *Ind. Eng. Chem. Process Des. Dev.* 1980;19:530–537.

Mehta VD, Sharma MM. "Effect of diffusivity on gas-side mass transfer coefficient." *Chemical Engineering Science.* 1966;21:361–365.

Mouch T, Linek V, Prokopová E. "Effect of packing geometrical details influence of free tips on volumetric mass transfer coefficients of Intalox saddles." *Chem. Eng. Res. Des.* 2005;83:88–92.

Olujic Z, Kamerbeek AB, de Graauw J. "A Corrugation Geometry Based Model for Efficiency of Structured Distillation Packing." *Chem. Eng. Process.* 1999;38:683–695.

Onda K, Sada E. "Liquid-side mass transfer coefficient packed towers." *AIChE Journal.* 1959;5:235–239.

Onda K, Takeuchi H, Okumoto Y. "Mass transfer coefficients between gas and liquid phases in packed columns." *Journal of Chemical Engineering of Japan.* 1968;1(1):56–62.

Rocha JA, Bravo JL, Fair JR. "Distillation Columns Containing Structured Packings: A Comprehensive Model for Their Performance. 1. Hydraulic Models." *Ind. Eng.Chem. Res.* 1993;32(4):641–651.

Rocha, JA, Bravo JL, Fair JR. "Distillation Columns Containing Structured Packings: A Comprehensive Model for Their Performance. 2. Mass-Transfer Models." *Ind. Eng. Chem. Res.* 1996;35:1660.

Sahay BN, Sharma MM. "Effective interfacial area and liquid and gas side mass transfer coefficients in a packed column." *Chemical Engineering Science.* 1973;28:41–47.

Sharma MM, Danckwerts PV. "Chemical methods of measuring interfacial area and mass transfer coefficients in two-fluid systems." *British Chemical Engineering.* 1970;15(4):522–528.

Sherwood, TK. et al., *Mass transfer*. McGraw-Hill, New York, 1975.

Shi MG, Mersmann A. "Effective Interfacial Area in Packed Columns." *Ger. Chem. Eng.*1985;8:87–96.

Effect of liquid viscosity on the liquid film mass transfer coefficient in packed columns

Quarterly Report for April 1 – June 30, 2014

by Di Song

Supported by the Texas Carbon Management Program

and the

Process Science and Technology Center

The University of Texas at Austin

July 31, 2014

Abstract

In this quarter, the reaction kinetics (k_g') of CO_2/NaOH/H_2O/glycerol was measured in the wetted wall column (WWC) for reproducibility. Different amounts of glycerol (0–89 wt %) were added to achieve a liquid viscosity (μ_L) from 0.89 cP to about 65 cP at 20, 30, and 40 °C. k_g' was found first to increase then decrease with increasing glycerol concentration. Empirical correlations were updated to predict k_g' as a function of temperature and μ_L.

Modified models were built to estimate diffusion coefficient (D), Henry's constant (H), and activity coefficient (α) of CO_2/NaOH/H_2O/glycerol.

In a worst case scenario, surface depletion of alkalinity accounts for 8.2% of total alkalinity for WWC experiments #1–8, and 16.8% for #1R–10R.

Sterilization experiments were carried out to inspect bacteria growth in NaOH/H_2O/glycerol. The only significant change of the system as a function of time is the water vaporization. No significant property change (μ_L, ρ, pH) was found between blank solutions and solutions with 0.02 w/v % NaN_3. No biocide is needed for NaOH/H_2O/glycerol.

Introduction

Packed columns are important for separation processes including post-combustion CO_2 capture. Since the amine solvent used for CO_2 scrubbing may have a viscosity significantly greater than water, it is important to know how μ_L affects k_L in the column. Few of the existing k_L (k_La) correlations provide satisfactory predictions for the influence of μ_L (Rochelle et al., 2013). This project aims to build a reliable k_L correlation to predict the effect of μ_L on k_L. The overall plan for the project is summarized in Table 1.

Table 1: Project plan

Stage	1	2	3	4
Target data	k_g'	a_e	k_L	$D_{Toluene}$
System	CO_2 + NaOH/water/glycerol	Same as left	Toluene + water/glycerol	Same as left
Equipment	WWC (Chen et al., 2011)	Pilot PVC column (Tsai et al., 2008)		TBD
Packing	N/A	MP 250X/Y	Various random and structured packings	N/A
Approx. range of μ_L	0.89–60 cP	0.89–100 cP		TBD
Wt % of glycerol	0–89	0–89		TBD
Expected finish time	Apr. 2014	Sept. 2014	TBD	TBD

Experimental Methods

WWC Experimental Methods

The WWC was used to measure the k_g' of CO_2/NaOH/H_2O/glycerol. The bench-scale gas-liquid contactor has a known interfacial area. The apparatus has been previously used and described by Cullinane (2005), Tsai (2010), and Chen (2011).

Information about solution preparation for experiments #1R-10R was summarized in the last report (Rochelle et al., 2014). Updated information about the experiment setup is summarized in Table 2. The goal of experiments #1R–10R was to check the reproducibility of the k_g' data acquired in experiments #1–8.

Sterilization Experimental Methods

Sterilization experimental methods were summarized in the last report (Rochelle et al., 2014). In this quarter, experiment time was lengthened to 45 days.

Supporting Methods and Equipment

Summarized in last report (Rochelle et al., 2014).

Table 2: WWC experiments #1R–10R setup

Soln. #	T (°C)	G (stdL/min)	Rotameter reading	L[a] (cc/s)	P (psig)	$P_{CO2,\ Inlet}$ (Pa)				
						1	2	3	4	5
1R–3R	20, 30, 40	4	8.3–10	3.47–4.16	40	150	300	450	600	750
4R	20	4	10	4.01	40	200	400	600	800	1000
	30	4	10	4.01						
			7	2.73						
	40	4	8.5	3.37						
5R, 6R	20, 30, 40	4	10	3.94–4.70	40	200	400	600	800	1000
7R, 8R		3		~4.7						
9R	30, 40	3		4.58						
10R	403	3		4.55						

[a] The liquid flow rate is calculated from rotameter reading by calibrating correlation (Cullinane, 2005).

Results

The k_g' obtained from WWC experiments #1–8 and #1R–10R is shown in Figure 1. The relative error between two experiments is only 5.3% when glycerol concentration is lower than 65 wt %. However, the relative error increases to 73.9% when glycerol concentration is higher than 75 wt %. The large relative error might result from the lower gas flow rate for experiments #7R–10R. More experiments are needed to check the reproducibility of k_g' data.

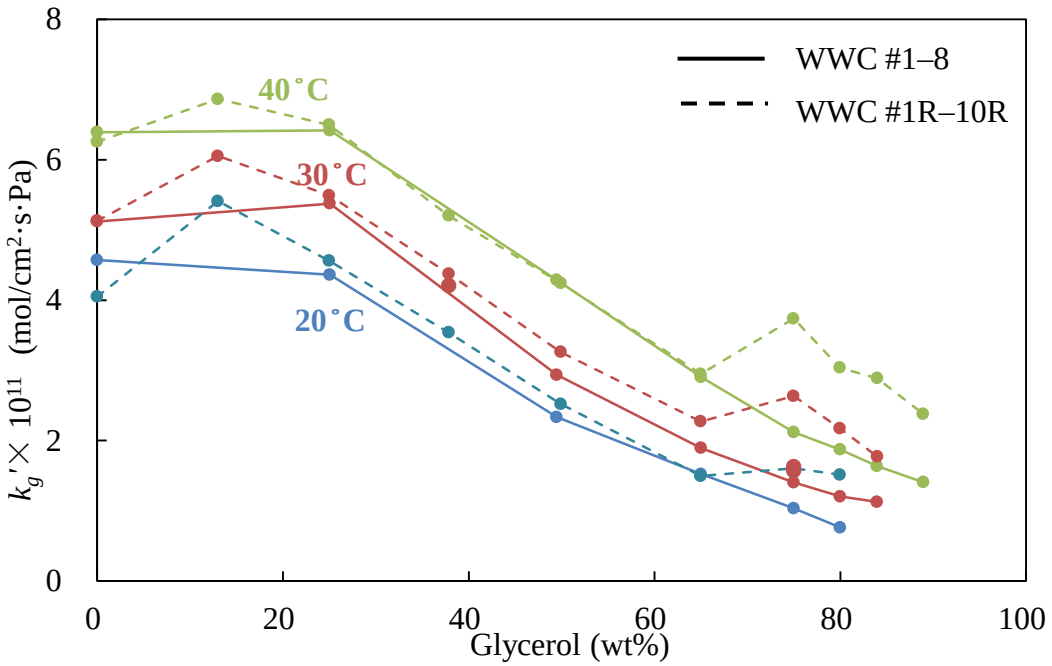

Figure 1: k_g' of CO_2/NaOH/H_2O/glycerol obtained from WWC experiments, nominally 0.1 M NaOH

Modified models of physical properties (*α, D, H*) of CO_2/NaOH/H_2O/glycerol were built. More literature data were found for better prediction.

Parameters of NRTL (Equations 1–4) and UNIQUAC (Equations 5–9) models for H_2O/glycerol were correlated based on literature data for α (Zaoui-Djelloul-Daouadji et al., 2014) (see Table 3). Predicted values of α are shown in Figure 2.

$$\ln \gamma_i = x_j^2 \left[\tau_{ji} \left(\frac{G_{ji}}{x_i + x_j G_{ji}} \right)^2 + \frac{\tau_{ij} G_{ij}}{(x_j + x_i G_{ij})^2} \right] \quad (1)$$

$$\ln G_{ij} = -\alpha_{ij} \tau_{ij} \quad (2)$$

$$\alpha_{ij} = \alpha_{ji} \quad (3)$$

$$\tau_{ij} = A_{ij} + \frac{B_{ij}}{T} \quad (4)$$

$$\ln \gamma_i = \ln \frac{\Phi_i}{x_i} + \left(\frac{Z}{2}\right) q_i \ln \frac{\theta_i}{\Phi_i} + \Phi_j \left(l_i - \frac{r_i}{r_j} l_j \right) - q_i \ln\left(\theta_i + \theta_j \tau_{ji}\right) + \theta_j q_i \left(\frac{\tau_{ji}}{\theta_i + \theta_j \tau_{ji}} - \frac{\tau_{ij}}{\theta_j + \theta_i \tau_{ij}} \right) \quad (5)$$

$$\Phi_i = \frac{r_i x_i}{r_i x_i + r_j x_j} \quad (6)$$

$$\theta_i = \frac{q_i x_i}{q_i x_i + q_j x_j} \quad (7)$$

$$\ln \tau_{ij} = A_{ij} + \frac{B_{ij}}{T} \quad (8)$$

$$l_i = \left(\frac{Z}{2}\right)(r_i - q_i) - (r_i - 1) \quad (9)$$

where:

γ = activity coefficient;
x = mole fraction;
τ = dimensionless interaction parameter;
G = parameter defined in Equation 2;
α = non-randomness parameter;
T = temperature, K;
A, B = parameters for τ calculation;
Φ = segment fraction;
r = pure-component Van der Waals volume parameter;
q = pure-component Van der Waals surface area parameter;
ϑ = area fraction;
Z = coordination number.

Table 3: NRTL and UNIQUAC[a] parameters for H_2O/glycerol

Model[b]	A_{12}	A_{21}	B_{12}	B_{21}	α_{12}	Z	σ^{2} [c]	AAD[d]
NRTL	0.0933	-0.8763	752.1	-193.3	0.4757	-	0.00103	2.93%
UNIQUAC	-0.0101	1.9212	537.9	-284.4	-	10	0.7181	1.39%

[a] Van der Waals parameters were obtained from Aspen Plus®: $q_1 = 1.4$, $q_2 = 3.06$, $r_1 = 0.92$, $r_2 = 3.385$; [b] subscript 1 = water, 2 = glycerol; [c] $\sigma^2 = \sum(\gamma_{calc} - \gamma_{expt})^2 / (\text{no. of data points} - \text{no. of parameters})$; [d] $AAD = (100\%/(\text{no. of data points})) \sum(|\gamma_{calc} - \gamma_{expt}|/\gamma_{expt})$

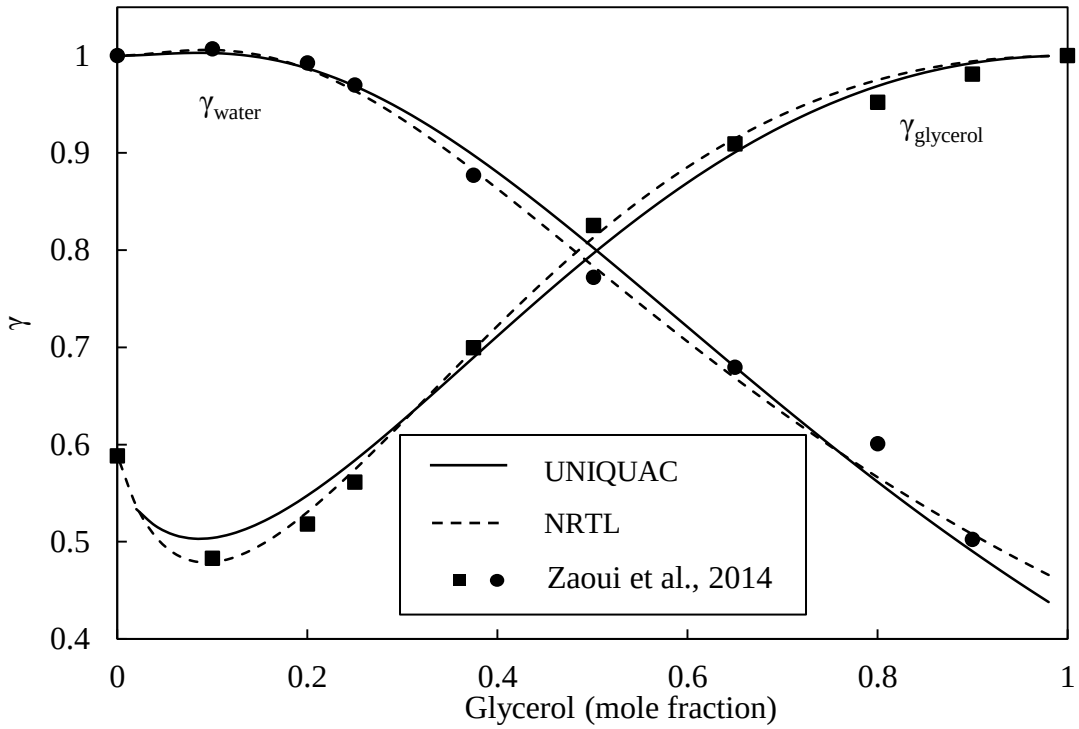

Figure 2: Activity coefficient of H_2O/glycerol at 20 °C

Correlation of H_{CO2} for CO_2/NaOH/H_2O/glycerol takes the form of Equations 10 & 11:

$$\log\frac{H_{CO_2,g-w}}{H_{CO_2,w}} = (Aw + B\ln(w+1) + C ln^2(w+1)) \times \left(\frac{D}{T} + E + FT + G\ln T\right) \quad (10)$$

$$\log H_{CO_2,w} = -7.8857 \times 10^{-5} T(K)^2 + 5.9044 \times 10^{-2} T(K) - 9.1229 \quad (11)$$

where:

H_{CO2} = Henry's constant of CO_2 (bar·L/mol);
w = weight fraction of glycerol;
T = temperature ($°C$ or K);
A, B, C, D, E, F, G = correlation parameters;
subscript g = glycerol, w = water.

Parameters in Equation 10 (see Table 4) were obtained from least square regression of literature data (Buzek & Jaroszynski, 1973; Laddha et al., 1981; Rischbieter et al., 1996; Vazquez Una et al., 1994). Equation 11 is obtained from Barrett (1966). Predicted and literature values of H_{CO2} are shown in Figure 3. The model shows good agreement with literature data from 15 to 40 °C, and 0 to 90 wt % glycerol. This is the temperature and concentration range proposed for future experiments. The model overpredicts H_{CO2} for pure glycerol, which might result from the inaccuracy of H_{CO2} data for pure glycerol (Ostonen et al., 2014).

The effect of NaOH on H_{CO2} is neglected because it is hard to know the exact concentration of each ion species, and thus hard to calculate the exact influence of ions on H_{CO2}. In the worst case scenario, the influence of ions is less than 5% using methods of Pohorecki & Moniuk (1988), so the assumption is safe.

Table 4: Parameters in Equation 10

Parameter	A	B	C	D	E	F	G
Value	3.280	-3.430	-2.264	14.63	-7.086	-0.004156	1.511

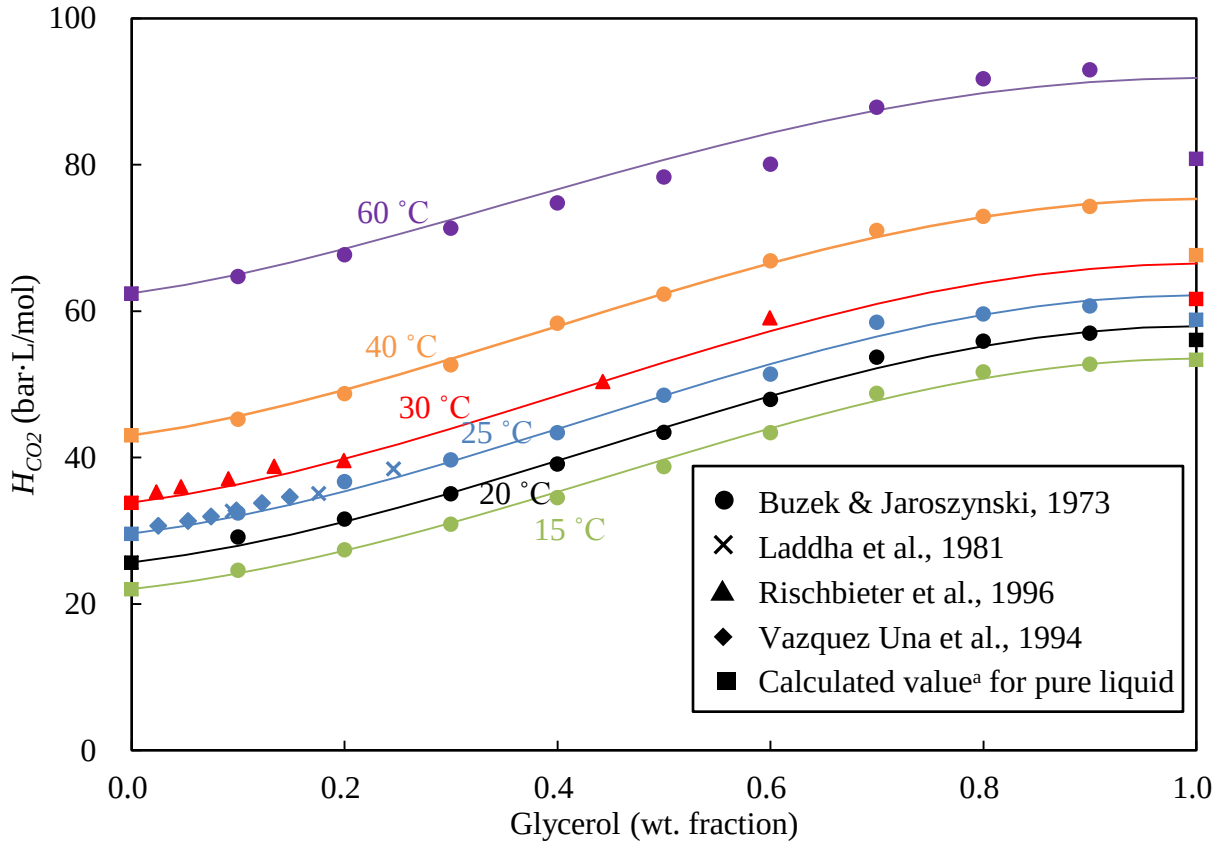

Figure 3: H_{CO2} of CO_2/NaOH/H_2O/glycerol

([a] H_{CO2} of water is calculated from Equation 11, H_{CO2} of glycerol is calculated from Ostonen et al. (2014))

Correlation of mutual diffusion coefficient of H_2O/glycerol $D_{g\text{-}w}$ is shown in Equation 12:

$$D_{g-w} = 0.3403T^{0.3134}\mu^{-0.5557} \quad (12)$$

where:

$D_{w\text{-}g}$ = mutual diffusion coefficient of H_2O/glycerol ($10^{-9}m^2/s$);
T = temperature (°C);
μ = liquid viscosity (cP).

Parameters in Equation 12 were regressed from different data sources (D'Errico et al., 2004; Garner & Marchant, 1961; Grossmann & Winkelmann, 2005; Nishijima & Oster, 1960; Riede & Schlunder, 1991; Rutten, 1992; Ternström et al., 1996). Calculated and literature data are shown in Figure 4.

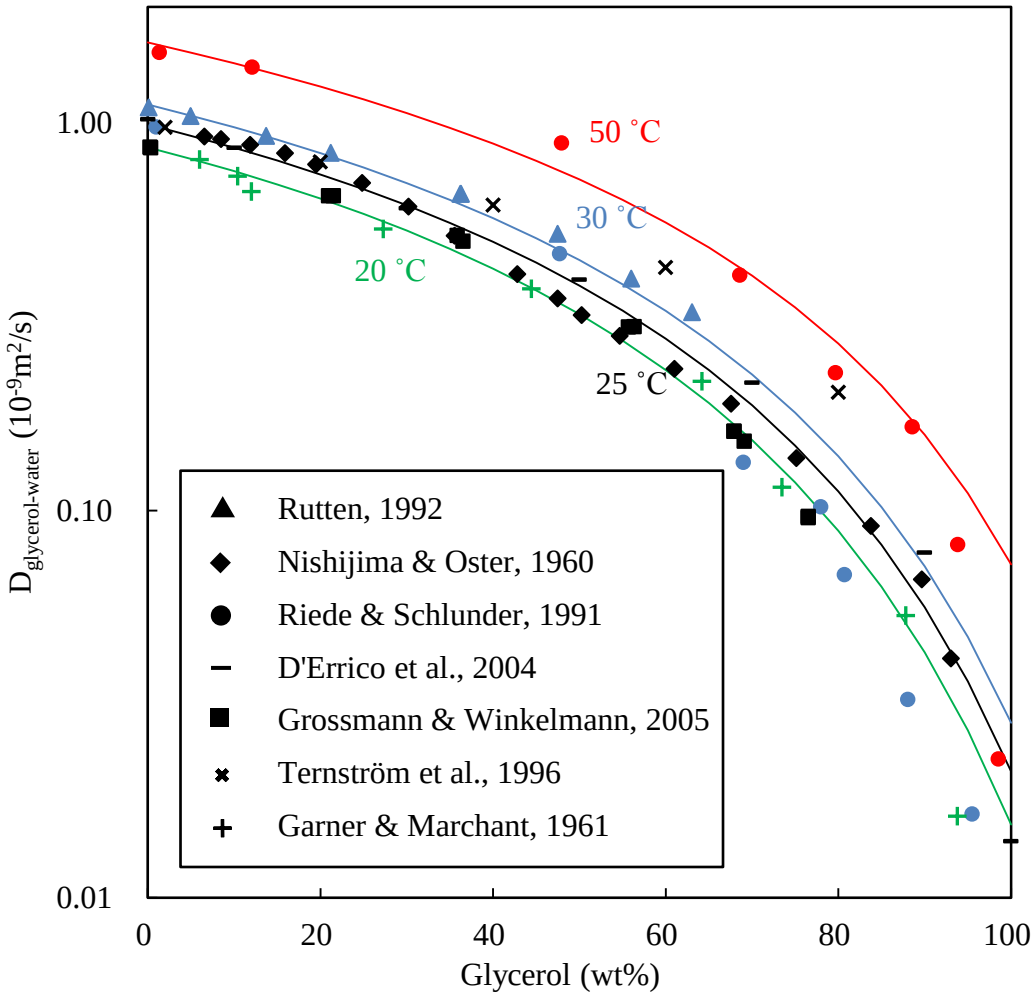

Figure 4: Mutual diffusion coefficient of H_2O/glycerol

Correlation of diffusion coefficient of CO_2 in H_2O/glycerol $D_{CO2,g\text{-}w}$ is shown in Equation 13:

$$D_{CO_2,g-w} = 0.3169T^{0.5206}\mu^{-0.7407} \quad (13)$$

where:

$D_{CO2,w\text{-}g}$ = diffusion coefficient of CO_2 in H_2O/glycerol ($10^{-9}m^2/s$);
T = temperature (°C);
μ = liquid viscosity (cP).

Parameters in Equation 13 were regressed from different data sources (Brignole & Echarte, 1981; Calderbank, 1959; Diaz et al., 1988; Kreulen, 1993; Onda et al., 1960; Thomas & Adams, 1965). Calculated and literature data are shown in Figure 5.

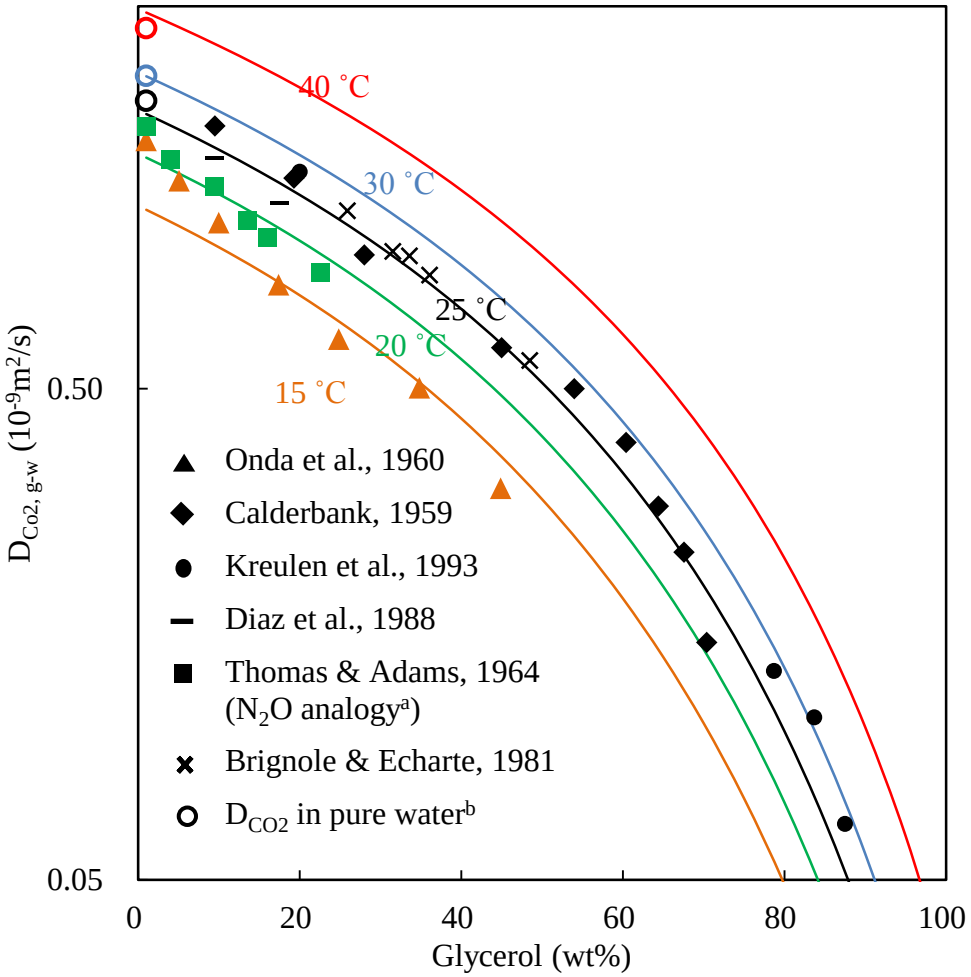

Figure 5: Diffusion coefficient of CO_2 in H_2O/glycerol
([a] $D_{N2O,w}/D_{CO2,w} = D_{N2O,w\text{-}g}/D_{CO2,w\text{-}g}$; [b] $D_{CO2,w}$ is calculated from Versteeg & van Swaalj, (1988))

Surface depletion of alkalinity has been calculated for each WWC experiment. The pseudo-first-order assumption central to this work is only valid when there is no appreciable depletion of alkalinity at the liquid surface. From the reaction stoichiometry, there is Equation 14:

$$\boldsymbol{N_{Alkalinity} = 2N_{CO_2}} \tag{14}$$

where:

N = molar flux (mol/m^2·s).

The flux of alkalinity can be calculated by Equation 15:

$$N_{Alkalinity} = k_L^0 \left([Alk]^b - [Alk]^i\right) \tag{15}$$

where:

k_L^0 = physical liquid-film mass transfer coefficient (m/s);
[Alk] = concentration of alkalinity (mol/m^3);
Superscript b = bulk liquid, i = liquid interface.

The worst case scenario was calculated for surface alkalinity depletion, so N_{CO2} at the highest partial pressure of CO_2 was used for each WWC experiment. k_L^0 was calculated from the theory of Pigford (Equations 16–21) (Bird et al., 2002; Pigford, 1942). Since D_{OH^-} is larger than $D_{glycerol^-}$, and $D_{glycerol^-}$ is approximately equal to $D_{glycerol}$, the mutual diffusion coefficient of H_2O/glycerol (Equation 12) was used for the k_L^0 calculation. The average ratios of surface depletion are 6.03% and 9.14% for WWC #1–8 and #1R–10R, respectively. The worst case ratios are 8.25% and 16.79% for WWC #1–8 and #1R–10R, respectively.

$$\begin{cases} \Theta = 0.7857\exp(-5.121\eta) + 0.1001\exp(-39.21\eta) \\ \qquad +0.036\exp(-105.6\eta) + 0.0181\exp(-204.7\eta), \ \text{for } \eta > 0.01 \\ \Theta = 1 - 3\sqrt{\frac{\eta}{\pi}} \qquad\qquad\qquad\qquad\qquad\qquad \text{for } \eta < 0.01 \end{cases} \tag{16}$$

$$\eta = \frac{D_{Alk}\tau}{\delta^2} \tag{17}$$

$$\tau = \frac{h}{u_{surf}} \tag{18}$$

$$\delta = \sqrt[3]{\frac{3\mu_L Q_L}{\rho_L g P}} \tag{19}$$

$$u_{surf} = \frac{\rho_L g \delta^2}{2\mu_L} \tag{20}$$

$$k_L^0 = \left(\frac{Q_L}{a}\right)(1 - \Theta) \tag{21}$$

where:

Θ = dimensionless concentration change, defined in Equation 16;
η = parameter in Pigford mass transfer model;
τ = exposure time of liquid surface (s);
h = length of the wetted wall column tube (m);
u_{surf} = velocity at liquid surface (m/s);
δ = thickness of liquid film (m);
μ = liquid viscosity (cP);
Q_L = liquid flow rate (m^3/s);
ρ = liquid density (kg/m^3);
P = wetted perimeter of the wetted wall column (m).

The time for the sterilization experiment has been lengthened to 45 days, during which time no visible bacteria growth was observed in any sample. Figure 6 shows the change of total sample weight and glycerol weight concentration as a function of time. The glycerol weight concentration was back calculated based on the assumption that the only significant change to the sample is water vaporization. To validate the assumption, physical properties (ρ, μ) of the samples at different times were measured and compared to the literature value for H_2O/glycerol at each corresponding concentration (see Figure 7). The pH of sterilization samples was also measured as a function of time and glycerol concentration. From Figure 8 it can be seen that the samples with NaOH lose their alkalinity rapidly (e.g., from 13 to 10 within 14 days). Therefore, a_e measurement in the future should be finished in a relatively short time and the pH of the liquid should be checked frequently despite the fact that alkalinity may decline more slowly for pilot-scale experiment because of the higher volume-surface area ratio of the liquid reservoir.

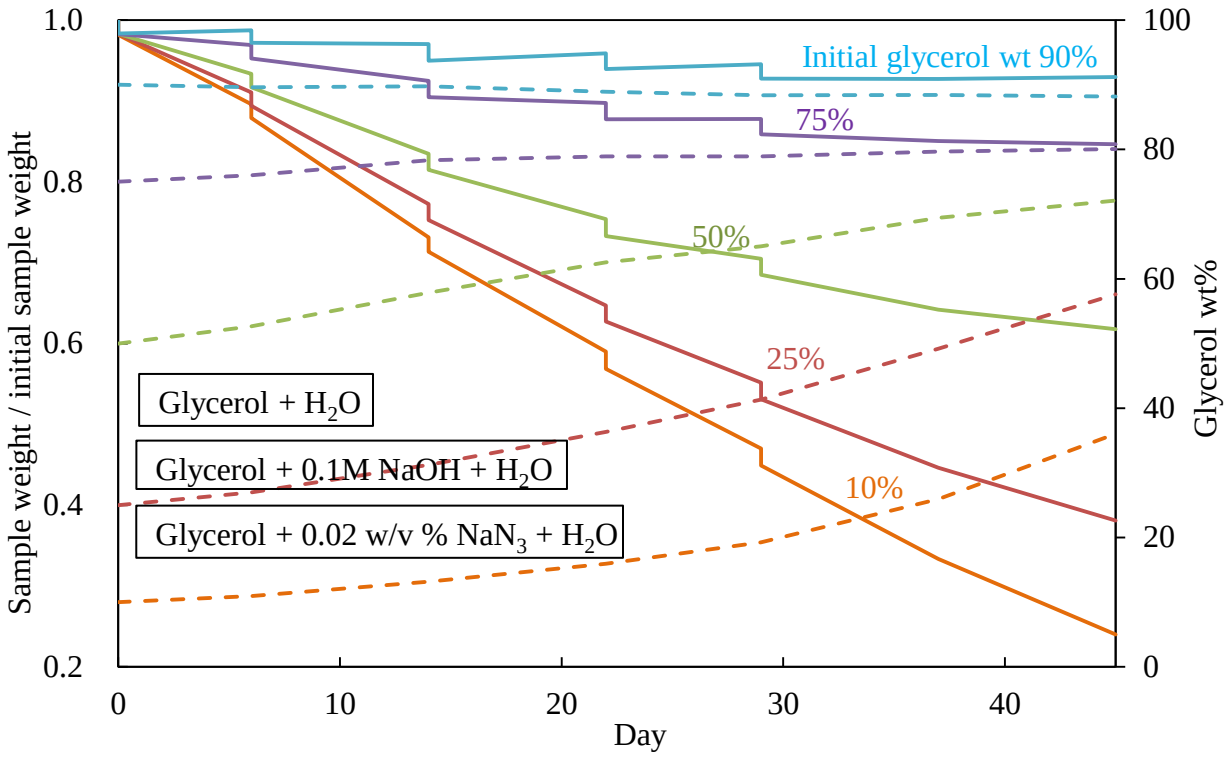

Figure 6: Total sample weight and glycerol concentration of sterilization experiment as a function of time

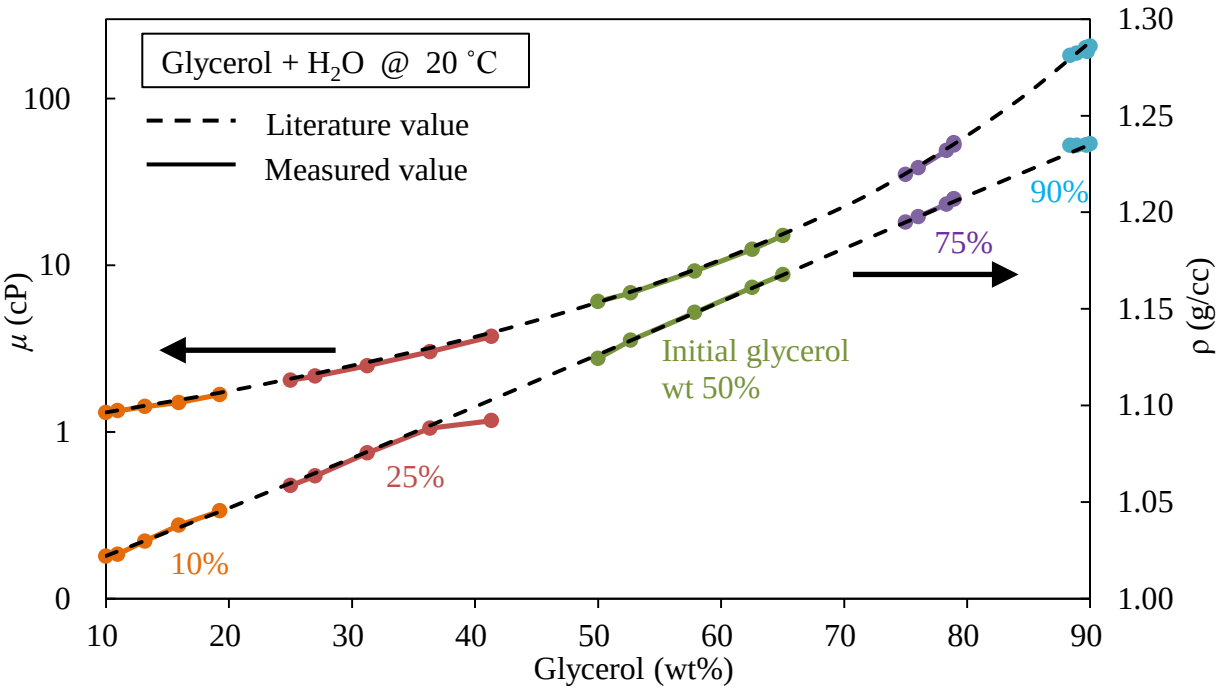

Figure 7: Measured and literature data for μ and ρ of sterilization samples

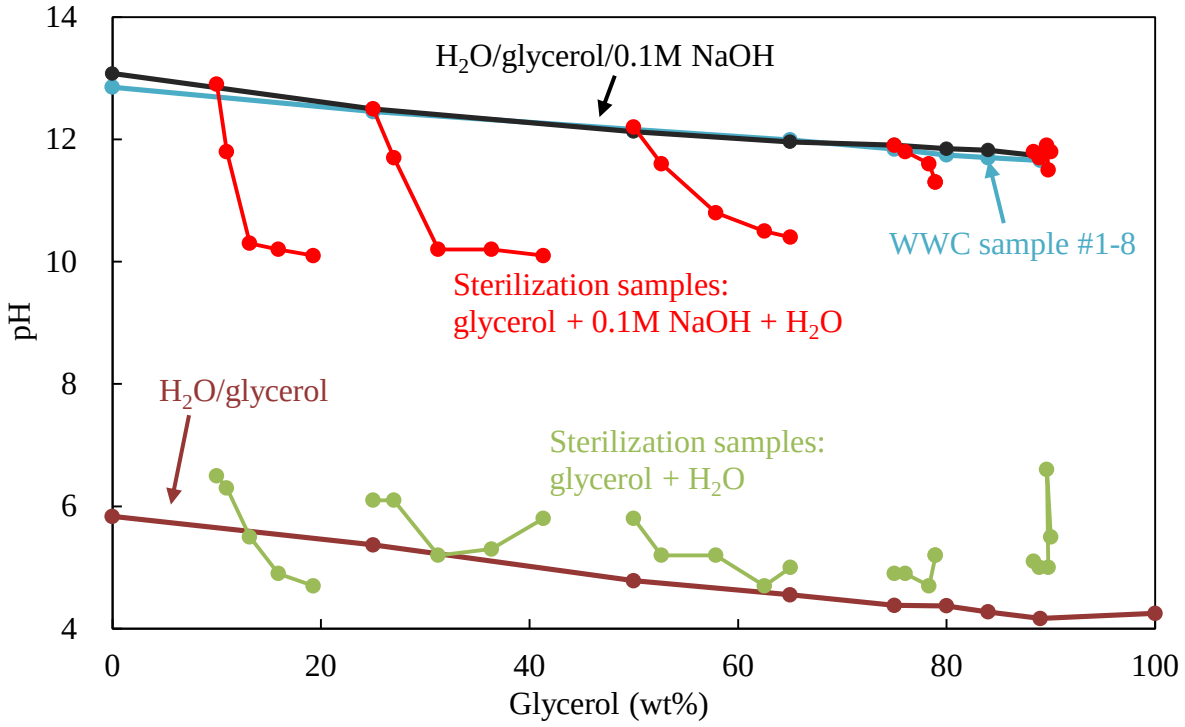

Figure 8: pH of WWC & sterilization samples

Discussion

The large relative error between WWC #1–8 and #1R–10R when glycerol concentration is greater than 75 wt % might result from the lower gas flow rate (3 stdL/min) used in WWC # 7R–10R. More experiments are needed at this glycerol concentration and higher gas flow rate (4 stdL/min) to check reproducibility.

The model of α for H_2O/glycerol, model of H_{CO2} for CO_2/NaOH/H_2O/glycerol, and model of $D_{g\text{-}w}$ fit well with literature data. The reliability of the model of D_{CO2} for CO_2/NaOH/H_2O/glycerol is not as good as the previously mentioned ones because of a lack of literature data. The model neglects the effect of ions which may result in inaccuracy.

Safety Issues

1. Hard hats are required for experiments outside the control room.
2. Alkaline solvents (NaOH) should be neutralized to pH 6–10 before disposal.
3. A gas mask with respirator is required when handling volatile and toxic chemicals.
4. Steel reinforced gloves are required when handling sheet metal structured packing.
5. During WWC experiments, special caution should be taken to keep the reaction chamber pressure constant by adjusting the gas flow rate and needle valve. A too high pressure may cause leakage or failure of glass tubes.

Conclusions

The relative error between k_g' data obtained from two WWC experiments are 5.3% when glycerol concentration is less than 75 wt % and 73.9% when glycerol concentration is greater than 75 wt %.

Modified models were built to estimate D, H, and α of CO_2/NaOH/H_2O/glycerol.

Activity coefficients for both H_2O and glycerol increases with increasing concentration in H_2O/glycerol, from 0.5 to 1 for H_2O, and 0.6 to 1 for glycerol.

H_{CO2} of CO_2/NaOH/H_2O/glycerol increases with increasing glycerol concentration and temperature, ranging from 25 to 74 bar·L/mol from 20 °C to 40 °C.

$D_{g\text{-}w}$ and $D_{CO2,\text{g-w}}$ decreases with increasing μ and decreasing T. The dependence on μ are -0.5557 and -0.7407, and the dependence on T are 0.3134 and 0.5206 for $D_{g\text{-}w}$ and $D_{CO2,\text{g-w}}$, respectively.

For sterilization samples, no bacteria growth or physical property change was observed apart from the water vaporization. No biocide is needed for future pilot-scale experiment.

Future Work

1. Conduct WWC experiments with higher NaOH concentration (1M), variable pre-saturation P_{water}, and random measurement order.
2. Model the k_{Alk} as a function of temperature, K_W, $K_{glycerol}$, $k_{OH\text{-}}$, and $k_{glycerol\text{-}}$.

References

Barrett PVL. *Gas Absorption on a Sieve Plate*. University of Cambridge. Ph.D. Dissertation. 1966.

Bird RB, Stewart WE, Lightfoot EN. *Transport Phenomena*. New York, John Wiley & Sons. 2002.

Brignole EA, Echarte R. "Mass transfer in laminar liquid jets. Measurement of diffusion coefficients." *Chem Eng Sci*. 1981;36(4):695–703.

Buzek J, Jaroszynski M. "Determination of Henry's constant for the ternary system: carbon dioxide-glycerol-water." *Inzynieria Chemiczna*. 1973;3(3):449–460.

Calderbank PH. "Physical rate processes in industrial fermentation -- 2. Mass transfer coefficients in gas-liquid contacting with and without mechanical agitation." *Trans Inst Chem Eng*. 1959;37(3):173–185.

Chen X. *Carbon Dioxide Thermodynamics, Kinetics, and Mass Transfer in Aqueous Piperazine Derivatives and Other Amines*. The University of Texas at Austin. Ph.D. Dissertation. 2011.

Chen X, Closmann F, Rochelle GT. "Accurate screening of amines by the Wetted Wall Column." *Energy Proc*. 2011;4(0):101–108.

Cullinane JT. *Thermodynamics and Kinetics of Aqueous Piperazine with Potassium Carbonate for Carbon Dioxide Absorption*. The University of Texas at Austin. Ph.D. Dissertation. 2005.

D'Errico G, Ortona O, Capuano F, Vitagliano V. "Diffusion Coefficients for the Binary System Glycerol + Water at 25 °C. A Velocity Correlation Study." *J Chem Eng Data*. 2004;49(6):1665–1670.

Diaz JM, Vega A, Coca J. "Diffusivities of carbon dioxide and nitrous oxide in aqueous alcohol solutions." *J Chem Eng Data*. 1988;33(1):10–12.

Garner FH, Marchant PJM. "Diffusivities of associated compounds in water." *Trans Inst Chem Eng*. 1961;39:397–408.

Grossmann T, Winkelmann J. "Ternary Diffusion Coefficients of Glycerol + Acetone + Water by Taylor Dispersion Measurements at 298.15 K." *J Chem Eng Data*. 2005;50(4):1396–1403.

Kreulen H. "Microporous hollow fibre membrane modules as gas-liquid contactors. Part 1. Physical mass transfer processes." *J Membr Sci*. 1993;78(3):197–216.

Laddha SS, Diaz JM, Danckwerts PV. "The nitrous oxide analogy: the solubilities of carbon dioxide and nitrous oxide in aqueous solutions of organic compounds." *Chem Eng Sci*. 1981;36(1):228–229.

Nishijima Y, Oster G. "Diffusion in Glycerol-Water Mixture." *Bull Chem Soc Jpn*. 1960;33(12):1649–1651.

Onda K, Okamoto T, Yamaji Y. "Measurement of the diffusivities of CO_2 in liquids by liquid jets." *Chem Eng (NY)*. 1960;24(12):918–925.

Ostonen A, Sapei E, Uusi-Kyyny P, Klemelä A, Alopaeus V. "Measurements and modeling of CO_2 solubility in 1,8-diazabicyclo-[5.4.0]-undec-7-ene—Glycerol solutions." *Fluid Phase Equilib*. 2014;374(0):25–36.

Pigford RL. *Counter-diffusion in a wetted wall column*. The University of Illinois at Urbana Champaign. Ph.D. Dissertation. 1942.

Pohorecki R, Moniuk W. "Kinetics of reaction between carbon dioxide and hydroxyl ions in aqueous electrolyte solutions." *Chem Eng Sci*. 1988;43(7):1677–1684.

Riede T, Schlunder EU. "Diffusivities of the ternary liquid mixture 2-propanol-water-glycerol and three-component mass transfer in liquids." *Chem Eng Sci*. 1991;46(2):609–617.

Rischbieter E, Schumpe A, Wunder V. "Gas Solubilities in Aqueous Solutions of Organic Substances." *J Chem Eng Data*. 1996;41(4):809–812.

Rochelle GT et al. "CO_2 Capture by Aqueous Absorption, Third Quarterly Progress Report 2013." Texas Carbon Management Program. The University of Texas at Austin. 2013.

Rochelle GT et al. "CO_2 Capture by Aqueous Absorption, First Quarterly Progress Report 2014." Texas Carbon Management Program. The University of Texas at Austin. 2014.

Rutten PWM. *Diffusion in liquids*. Technische Universiteit Delft (The Netherlands). C298751 Dissertation. 1992.

Ternström G, Sjöstrand A, Aly G, Jernqvist Å. "Mutual Diffusion Coefficients of Water + Ethylene Glycol and Water + Glycerol Mixtures." *J Chem Eng Data*. 1996;41(4):876–879.

Thomas WJ, Adams MJ. "Measurement of the diffusion coefficients of carbon dioxide and nitrous oxide in water and aqueous solutions of glycerol." *Trans Faraday Soc*. 1965;61(0):668–673.

Tsai RE. *Mass Transfer Area of Structured Packing*. The University of Texas at Austin. Ph.D. Dissertation. 2010.

Tsai RE, Schultheiss P, Kettner A, Lewis JC, Seibert AF, Eldridge RB, Rochelle GT. "Influence of surface tension on effective packing area." *Ind Eng Chem Res*. 2008;47(4):1253–1260.

Vazquez Una G, Chenlo Romero F, Pereira Goncalves G, Peaguda Lorenzo J. "Solubility of CO_2 in Aqueous solutions of Saccharose, Glucose, Fructose, and Glycerin." *J Chem Eng Data*. 1994;39(4):639–642.

Versteeg GF, Van Swaalj W. "Solubility and diffusivity of acid gases (carbon dioxide, nitrous oxide) in aqueous alkanolamine solutions." *J Chem Eng Data*. 1988;33(1):29–34.

Zaoui-Djelloul-Daouadji M, Negadi A, Mokbel I, Negadi L. "(Vapor-liquid) equilibria and excess Gibbs free energy functions of (ethanol+glycerol), or (water+glycerol) binary mixtures at several temperatures." *J Chem Thermodyn*. 2014;69(0):165–171.

Kinetic Modeling of 4.8 m AMP and 4 m 2MPZ/4 m PZ

Quarterly Report for April 1 – June 30, 2014

by Brent Sherman

Supported by the Texas Carbon Management Program

and the Carbon Capture Simulation Initiative

McKetta Department of Chemical Engineering

The University of Texas at Austin

July 31, 2014

Abstract

Two different process models were advanced: 4 m 2MPZ/4 m PZ and AMP/PZ. For the former, the density and viscosity were regressed, and the model was found to fit the data and to extrapolate well. The reaction set for 4 m 2MPZ/4 m PZ is difficult due to equal molality and similar chemistry. This resulted in a large reaction set for regression. For the AMP/PZ system, 4.8 m AMP wetted wall column data were used to regress the AMP reaction rates. The reaction set treated the carbamate reaction as instantaneous. Due to the low carbamate stability constant, this reaction was only significant at 40 °C. The model overpredicts at this temperature, and then linearly moves from underpredicting at 60 °C to overpredicting at 100 °C. There is a less pronounced linear trend of increasing flux with increasing loading. Overall, 80% of the data were fit within 20% of the experimental value.

Introduction

This work has four goals: rigorous thermodynamic and kinetic models, a generic amine modeling method, viscosity process effects, and economic evaluation. Developing more rigorous models offers the necessary insight into model development to create a generic amine modeling method. The aim of the method is to streamline model development, thus allowing more rapid screening

of solvents. Then, using the rigorous and generic models, process performance can be evaluated from an economic standpoint with special interest paid to viscosity effects.

The past quarter focused on developing two process models: 2-methylpiperazine (2MPZ)/piperazine (PZ) and 2-amino-2-methyl-1-propanol (AMP)/PZ. As the thermodynamic model for each one is done, the next step is the kinetic model. As a necessary precursor to the AMP/PZ model, kinetics for the AMP system were finished. For the 2MPZ/PZ system, the density and viscosity were fit as well as picking a reaction set.

A discretized heat plate-and-frame heat exchanger was constructed in MATLAB as a two-week project for a class. This will be used as a starting point to study amine viscosity effects on the economics of the cross exchanger. The class report is included in the appendix.

CCSI Involvement

The ongoing collaboration with the Carbon Capture Simulation Initiative (CCSI) is now focused on correlating 2MPZ model parameters using a Bayesian Smoothing Spline (BSS) ANOVA framework. At the CCSI All Hands meeting at the end of April this collaboration as well as the overall program direction were discussed. At the request of the industrial advisory board, CCSI is focusing more on solvents with an effort to validate the Phoenix monoethanolamine (MEA) model (Plaza, 2011). The 2MPZ model will be used to determine the best way to quantify the uncertainty in an Aspen Plus® model.

Modeling Methods

2MPZ/PZ Viscosity and Density

Prior to regressing kinetics, the viscosity and density are regressed. These two properties are not regressed using the Aspen Plus® data regression system (DRS), but rather using a least squares minimization in Excel. Subroutines calculate each property by Equations 1 and 2.

$$\frac{\mu_{2MPZ+PZ}}{\mu_{H2O}} = exp\left\{[(ax_{2MPZ} + bx_{PZ} + c)T + dx_{2MPZ} + ex_{PZ} + f] * [(gx_{2MPZ} + hx_{PZ} + iT + j)\alpha + 1] * \frac{x_{2MPZ+PZ}}{T^2}\right\} \quad (1)$$

$$\rho_{2MPZ+PZ} = x_{H_2O}\rho_{\boldsymbol{H_2O}} + x_{2MPZ}\left(a\hat{T} + b\right) + x_{PZ}\left(c\hat{T} + d\right) + x_{CO_2}\left(e\hat{T} + f\right) + x_{CO_2}(x_{2MPZ} + x_{PZ})\left(g\hat{T} + h\right) \quad (2)$$

where all *a–j* are regressed parameters and $\hat{T} = T - 313.15$ K.

In the process of regressing viscosity, the data reported by Chen (2011) were found to be inconsistent with new data (Salta, 2014) because the two moles of alkalinity were not used in the loading calculation. To correct this, the reported loading should be multiplied by two. Rather than use a data set that could have other issues, such as only using gravimetric loading, the data of Salta (2014) were employed.

Subroutines are problematic and hinder using models in other software, namely gPROMS and MATLAB. The original reason for using these subroutines was to use an apparent-speciation basis. However, the density subroutine cannot be on an apparent-speciation basis, as it actually calculates specific molar volume V_m:

$$\rho = \frac{M}{V_m} \quad (3)$$

where ρ is density and M is the true-speciation molar mass. To find density, the true-speciation M is used. Plaza recognized this problem and used the built-in Aspen Plus® model (Rochelle et al., 2009). This was attempted here, but the fit was not satisfactory. In the end, the subroutine was still used as it needed fewer parameters and yielded a better result.

4 m 2MPZ/4 m PZ Kinetics

With the thermodynamic model regressed, and the density and viscosity set, the only outstanding component for a process model is a kinetic model. The first step is determining the relevant reactions. Typical diamine solvents involve one amine forming carbamate with the other amine serving as the base, e.g., PZ/methyldiethanolamine (MDEA) or PZ/AMP. However, in this system both amines form carbamate. Further compounding the issue is that 2MPZ and PZ are present in equal quantities. For this reason, the important reactions are not apparent, and so few reactions can be neglected. The kinetic reactions are presented in Table 1, while the equilibrium reactions are in Table 2.

Table 1: Kinetic reactions for 4 m 2MPZ/4 m PZ

Amine	***Reaction***
PZ	$PZ + H_2O + CO_2 \leftrightarrow PZH^+ + HCO_3^-$
PZ	$2\ PZ + CO_2 \leftrightarrow PZH^+ + PZCOO^-$
PZ	$2\ PZCOO^- + CO_2 \leftrightarrow {}^+HPZCOO^- + PZ(COO)_2^{2-}$
2MPZ	$2\ 2MPZ + CO_2 \leftrightarrow 2MPZH^+ + 2MPZCOO^-$
2MPZ	$2MPZCOO^- + H_2O + CO_2 \leftrightarrow {}^+H2MPZCOO^- + HCO_3^-$
mixed	$PZ + 2MPZ + CO_2 \leftrightarrow 2MPZH^+ + PZCOO^-$
mixed	$PZ + 2MPZ + CO_2 \leftrightarrow PZH^+ + 2MPZCOO^-$
mixed	$PZCOO^- + 2MPZ + CO_2 \leftrightarrow PZ(COO)_2^{2-} + 2MPZH^+$

Table 2: Equilibrium reactions for 4 m 2MPZ/4 m PZ

Amine	***Reaction***
PZ	$PZCOO^- + PZH^+ \leftrightarrow {}^+HPZCOO^- + PZ$
2MPZ	$2MPZCOO^- + 2MPZH^+ \leftrightarrow {}^+H2MPZCOO^- + 2MPZ$
mixed	$PZH^+ + 2MPZCOO^- \leftrightarrow PZ + {}^+H2MPZCOO^-$
mixed	$2MPZH^+ + PZCOO^- \leftrightarrow 2MPZ + {}^+HPZCOO^-$
mixed	$2MPZ + PZH^+ \leftrightarrow 2MPZH^+ + PZ$

The starting kinetic values for reactions coming from the PZ/MDEA model or the 2MPZ model are set to those from the constituent model. These are the reactions in Table 1 not marked "mixed". The kinetic model framework is identical to that of the AMP system discussed in the next section.

4.8 m AMP Kinetics

As a precursor to the AMP/PZ kinetic model, the AMP kinetics were finished. The kinetics were regressed using the Aspen Plus® wetted wall column (WWC) model to match experimental flux values (Chen, 2011). The reaction set used is shown in Equations 4–6.

$$AMP + H_2O + CO_2 \rightarrow AMP + HCO_3^- \tag{4}$$

$$AMP + HCO_3^- \rightarrow AMP + H_2O + CO_2 \tag{5}$$

$$2\,AMP + CO_2 \leftrightarrow AMP^+ + AMPCOO^- \tag{6}$$

The kinetics were represented using activity-based Arrhenius power law equations for the two kinetic reactions, as shown in Equation 7. The two kinetic reactions represent one equilibrium reaction, wherein the forward reaction is regressed (4) and the reverse reaction (5) parameters are set from the equilibrium constant calculated from the thermodynamic model. As the last reaction (6) is an equilibrium reaction, it is calculated by the thermodynamic model. It was modeled as an equilibrium reaction for two reasons: 1) the reaction is far faster than the bicarbonate reaction, and 2) little carbamate is made, so the reaction will quickly reach equilibrium.

$$k = k_0 \exp\left[\frac{-E_A}{R}\left(\frac{1}{T} - \frac{1}{T_{ref}}\right)\right] \tag{7}$$

The diffusion of reactants and products is represented using Equation 8.

$$D_{Am-Prod} = D_0 \left(\frac{T}{T_{ref}}\right)^{\alpha} \left(\frac{\mu}{\mu_{ref}}\right)^{\beta} \tag{8}$$

Equations 7 and 8 show that the available parameters are k_0, E_A, D_0, α, and β. The diffusivity parameters were defaulted to the PZ model values. The reaction parameters are found by first adjusting the loading of two mid-loading (0.434 and 0.454 mol CO_2/mol alk) desorption flux values at 40 and 60 °C. The loading is adjusted to within 1% of parity between the absorption and desorption predictions. The experimental flux at those two points is matched by adjusting the rate of the forward reaction. Then reverse values are backcalculated from K_{eq}. The reaction and diffusivity parameters are fixed, and a loading adjustment is performed on all data. The loading of each point is adjusted up to 10% of the operational loading range (here, 0.029 mol CO_2/mol alk). Based on the results, the reaction rate and diffusivity are adjusted, and another iteration is done.

The above parameters control the kinetic reactions and diffusivity of amine products with no effect on the equilibrium reaction. The two parameters controlling the K_{eq} of reaction 6 are $\Delta G_{f,aq}$ (DGAQFM) and $\Delta H_{f,aq}$ (DHAQFM) for the carbamate species. The $\Delta G_{f,aq}$ (DGAQFM) controls how much carbamate is present at the thermodynamic reference temperature of 25 °C. Thus DGAQFM was set to match the data of Ciftja et al. (2011).

As there are no other temperature NMR data available, DHAQFM could not be regressed. It was adjusted to match the 40 °C WWC data (Chen, 2011). At higher temperature, the carbamate reaction contribution to flux is negligible. This can be attributed to the very low carbamate stability constant. The higher temperature data were fit with the bicarbonate reaction and diffusivity of amine-product parameters.

Results and Discussion

2MPZ/PZ Viscosity and Density

The least squares regression of the Salta data (2014) for viscosity yielded the following correlation:

$$\frac{\mu_{2MPZ+PZ}}{\mu_{H2O}} = exp\left\{\begin{matrix}\begin{bmatrix}(6.43x_{2MPZ} + 5.43x_{PZ} + 46.01)T\\ -10.10x_{2MPZ} + 340.20x_{PZ} + 0.08\end{bmatrix}\\ * [(10.01x_{2MPZ} - 29.87x_{PZ} + 0.01T + 2.72)\alpha + 1]\\ * \frac{x_{2MPZ+PZ}}{T^2}\end{matrix}\right\} \quad (9)$$

The model results in Figure 1 show that the data are fit and the extrapolations are reasonable.

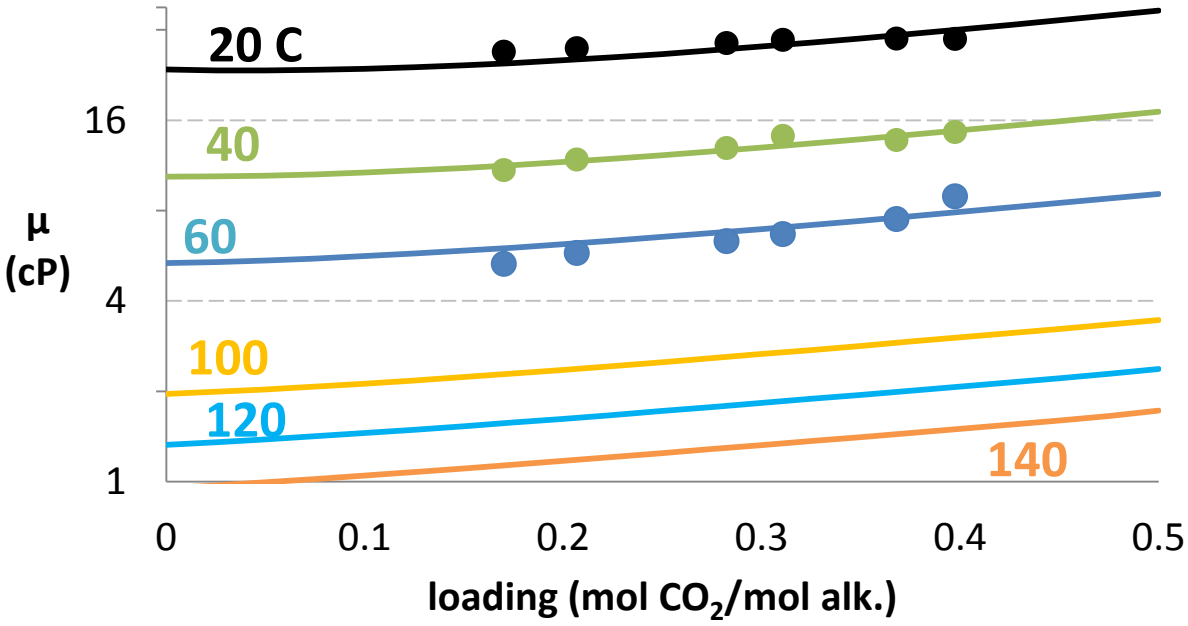

Figure 1: 4 m 2MPZ/4 m PZ viscosity predictions (lines) and data (points) (Salta, 2014)

Least squares regression for density yielded the following correlation:

$$\begin{aligned}\rho_{2MPZ+PZ} = {} & x_{H_2O}\rho_{H_2O} + x_{2MPZ}\left(-2.90\hat{T} + 1190\right) + x_{PZ}\left(-2.90\hat{T} + 1190\right)\\ & + x_{CO_2}\left(2.06\hat{T} + 3290\right) + x_{CO_2}(x_{2MPZ} + x_{PZ})\left(-6.47\hat{T}\right.\\ & \left. - 7580\right)\end{aligned} \quad (10)$$

The model results in Figure 2 show that the data are fit, and the extrapolations are reasonable.

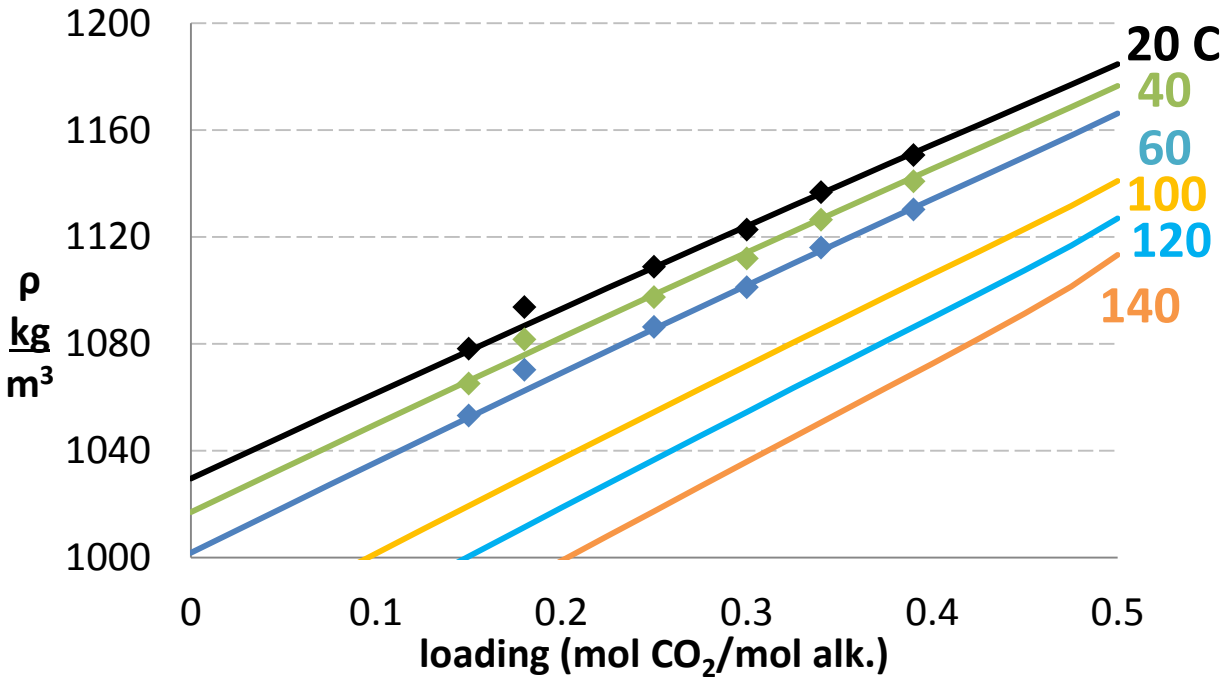

Figure 2: 4 m 2MPZ/4 m PZ density predictions (lines) compared to data (points) (Freeman, 2011)

AMP Kinetics

The 4.8 m AMP kinetics were fit using flux data from Chen (2011). The kinetic reaction parameters are shown in Table 3, the diffusion parameters in Equation 11, and the parameters governing the carbamate equilibrium in Table 4.

Table 3: 4.8 m AMP kinetic reaction parameters

Reaction	k_o (kmol/s-m^3)	E_A (J/mol)
1	9.86×10^{7}	2.76×10^{2}
2	1.51×10^{5}	6.60×10^{4}

$$D_{Am-Prod} = 7.00x10^{-11}\left(\frac{T}{313.15\ K}\right)^{-2.58}\left(\frac{\mu}{3.59\ cP}\right)^{-3.00} \quad (11)$$

Table 4: Equilibrium reaction parameters

$AMPCOO^-$ parameter	Value ($x10^8$ J/kmol)
$\Delta G_{aq,f}$	-4.53
$\Delta H_{aq,f}$	-10.4

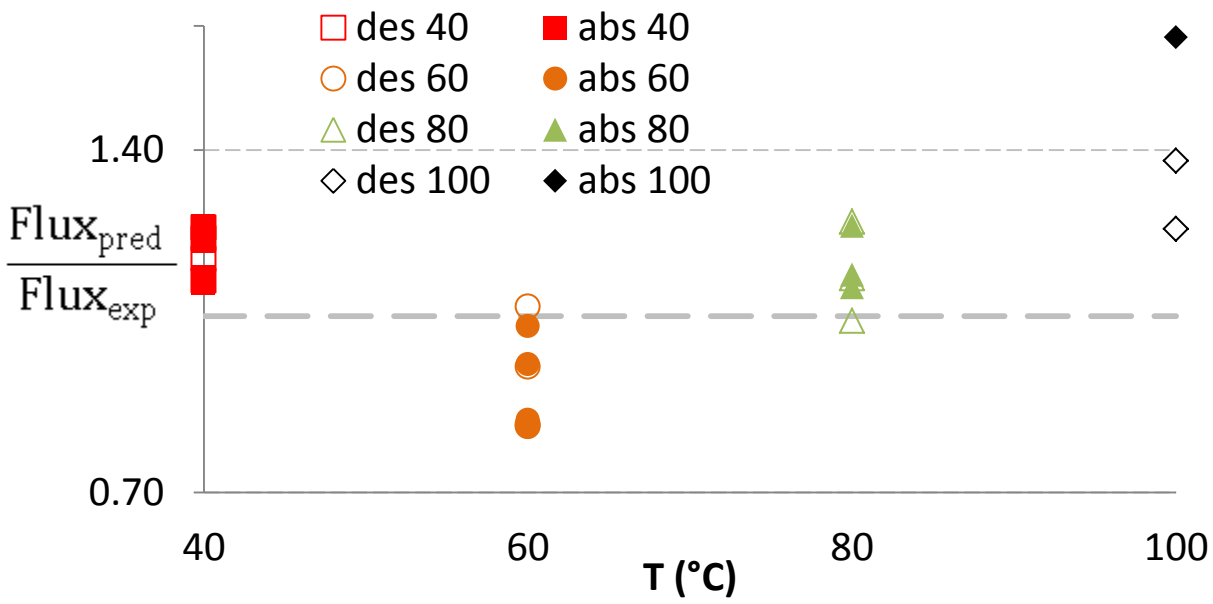

Figure 3: 4.8 m AMP kinetics (Chen, 2011)

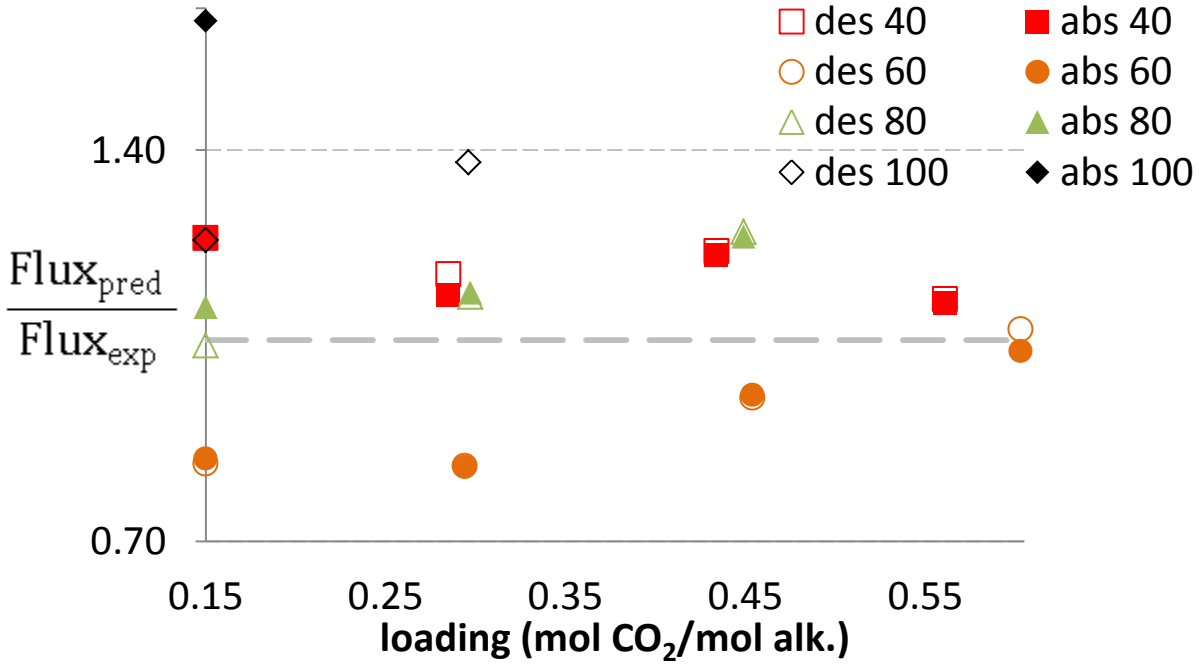

Figure 4: 4.8 m AMP kinetics (Chen (2011).

Looking at Figure 3, the data are overpredicted at 40 °C, then there is a linear trend with the other temperatures. This trend is a result of having only one reaction to fit the temperature range. As the temperature increases, both the reaction rate and the diffusivity of amine-products increase. As there are no other parameters with temperature dependence, there is no way to correct for this trend. This bias is not seen in other systems because additional reactions are available for regression.

Figure 4 shows that there is no bias with loading at 40 °C, yet there is a linear bias at the other temperatures. (Only one absorption data point was available at 100 °C as the other point was collected too near equilibrium.) Nevertheless, 80% of the data are fit within 20%.

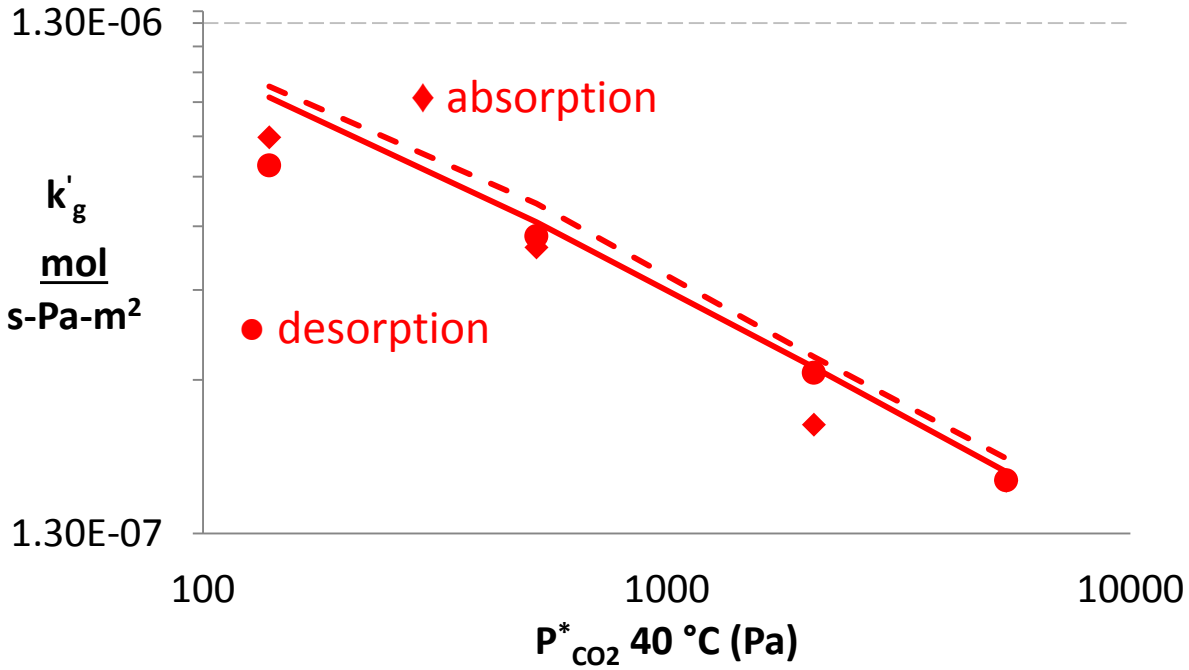

Figure 5: 4.8 m AMP k'_g. Points are data from Chen (2011). The two curves are model predictions with dashed being absorption and solid desorption.

As expected from the predicted flux at 40 °C, Figure 5 shows that k'_g is overpredicted regardless of simulating the WWC in absorption or desorption mode.

Taken as a whole, the fit is adequate to move on to regressing AMP/PZ kinetics. The reaction parameters determined from fitting 4.8 m AMP will be used as a starting point. While the fit could be improved, the resulting parameters give a better fit than was achieved for the MEA (Phoenix) model (Plaza, 2011). Similarly, MEA has one dominant reaction, and this paucity of parameters led to physically meaningless values in an attempt to fit data, such as

$$D_{MEA-soln} = D^{o}_{MEA}\left(\frac{T}{313.15\ K}\right)^{n}\left(\frac{\mu_{water}}{\mu_{soln}}\right)^{-0.8} \tag{12}$$

where $D°_{MEA}$ is the diffusion coefficient of MEA at 40 °C and 0.30 mol/mol alk. It was found to be $9.85\text{x}10^{-10}$ for 7 m MEA and $8.27\text{x}10^{-10}$ for 9 m MEA. *n* was used to fit the WWC data at 100 °C and was found to be 22.6 for 7 m and 17.55 for 9 m. While $D°_{MEA}$ is reasonable, *n* is not.

This attempt was partially successful, but breaks down in the operational loading range of 0.4 to 0.5 mol CO_2/mol alk, as shown in Figure 6.

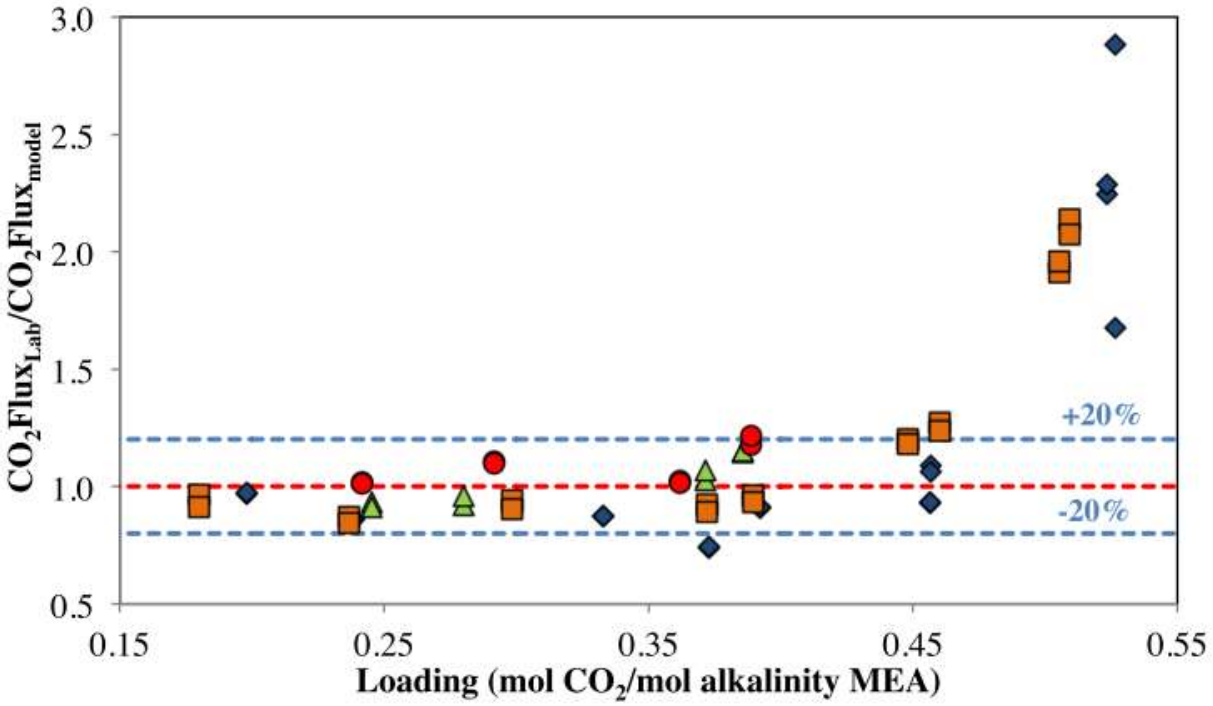

Figure 3.25: WWC Carbon dioxide flux comparison for 7m and 9m MEA. (♦) 40°C, (■) 60°C, (▲) 80°C (●) 100°C.

Figure 6 : Reproduction from Plaza (2011).

Conclusions

1. 4 m 2MPZ/4 m PZ density and viscosity have been regressed.
2. 4 m 2MPZ/4 m PZ kinetic reactions have been chosen.
3. 80% of 4.8 m AMP WWC fluxes are fit within 20%.
4. The AMP carbamate reaction can be treated as an equilibrium reaction.
5. The AMP carbamate equilibrium reaction is only significant at 40 °C and below.
6. As a hindered amine, the carbamate reaction of AMP is what differentiates it kinetically from tertiary amines that are incapable of forming carbamates (e.g., MDEA).

Future Work

The kinetic model for 4 m 2MPZ/4 m PZ will be finished next quarter, as will the kinetic model for AMP/PZ.

Safety

Solvents that can precipitate, such as 2MPZ/PZ, pose a safety hazard. A thorough HAZOP analysis should be completed prior to their use to ensure that plugs of solid cannot create an unsafe environment. One way this could occur, is a plug in the cross exchanger. This could over-pressure the gasket leading to a leak of amine. As amine degradation productions include carcinogens, such a leak is highly hazardous.

References

Chen X. *Carbon Dioxide Thermodynamics, Kinetics, and Mass Transfer in Aqueous Piperazine Derivatives and Other Amines*. The University of Texas at Austin. Ph.D. Dissertation. 2011.

Ciftja AF, Hartono A, da Silva EF, Svendsen HF. "Study on carbamate stability in the AMP/CO_2/H_2O system from ^{13}C-NMR spectroscopy." *Energy Proc*. 2011;4:614–620.

Freeman SA. *Thermal Degradation and Oxidation of Aqueous Piperazine for Carbon Dioxide Capture*. The University of Texas at Austin. Ph.D. Dissertation. 2011.

Plaza JM. *Modeling of Carbon Dioxide Absorption using Aqueous Monoethanolamine, Piperazine and Promoted Potassium Carbonate*. The University of Texas at Austin. Ph.D. Dissertation. 2011.

Rochelle GT et al. "CO_2 Capture by Aqueous Absorption, Third Quarterly Progress Report 2009." Luminant Carbon Management Program. The University of Texas at Austin. 2009.

Salta N. Personal communication. 2014.

Appendix

Discretized Plate-and-Frame Heat Exchanger for Amine Scrubbing

Brent Sherman

ChE 384

May 9th, 2014

Introduction

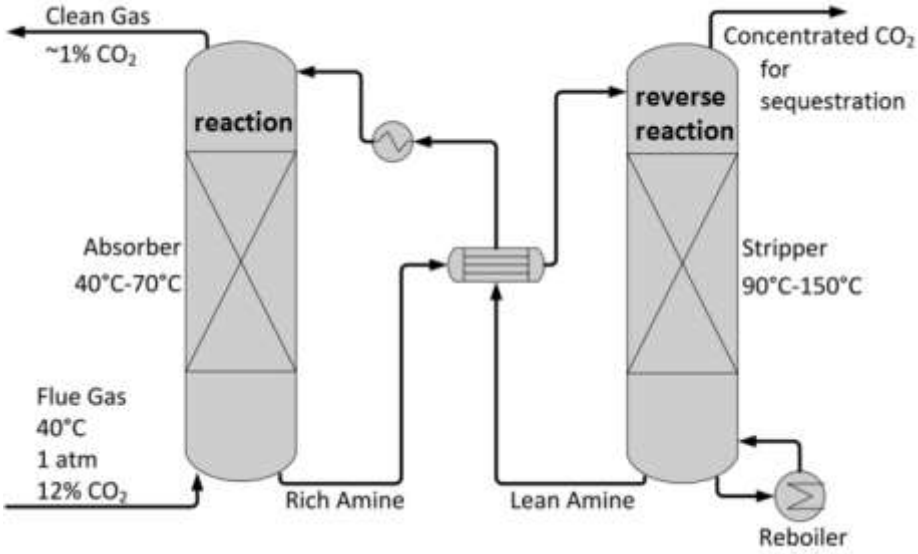

Figure 1. Amine scrubbing process flow diagram.

Amine scrubbing is a method to capture carbon dioxide from the flue gas of coal or natural gas power plants. In **Figure** , the flue gas from the power plant enters the bottom of the absorber, where it counter-currently contacts the amine solvent. As the gas flows upwards, CO_2 transfers from the gas into the liquid solvent by reacting with the amine. The solvent loading, measured in mol CO_2/mol alkalinity, increases from lean loading at the inlet to rich loading at the outlet. The rich amine solvent enters the cross exchanger, where it is heated by lean amine solvent leaving the stripper. The now hot rich solvent enters the top of the stripper, where it counter-currently contacts rising steam. This reverses the reaction, and CO_2 leaves the top of the stripper for sequestration. The lean solvent can be passed back through the cross exchanger, a trim cooler, and then back into the absorber.

Heat integration is critical to process performance. Recent improvements to the stripper efficiency have been through increasing heat integration by adding additional heat exchangers (Frailie, 2014; Madan, 2013; Wagener, 2011). This reduces the operating expense of the stripper by increasing the capital cost of the heat integration. This project will consider the advanced flash stripper (AFS) configuration using 8 molal (m) piperazine (PZ), as shown in **Figure** . The three plate-and-frame heat exchangers labeled X2, X3, and X4 will be simulated.

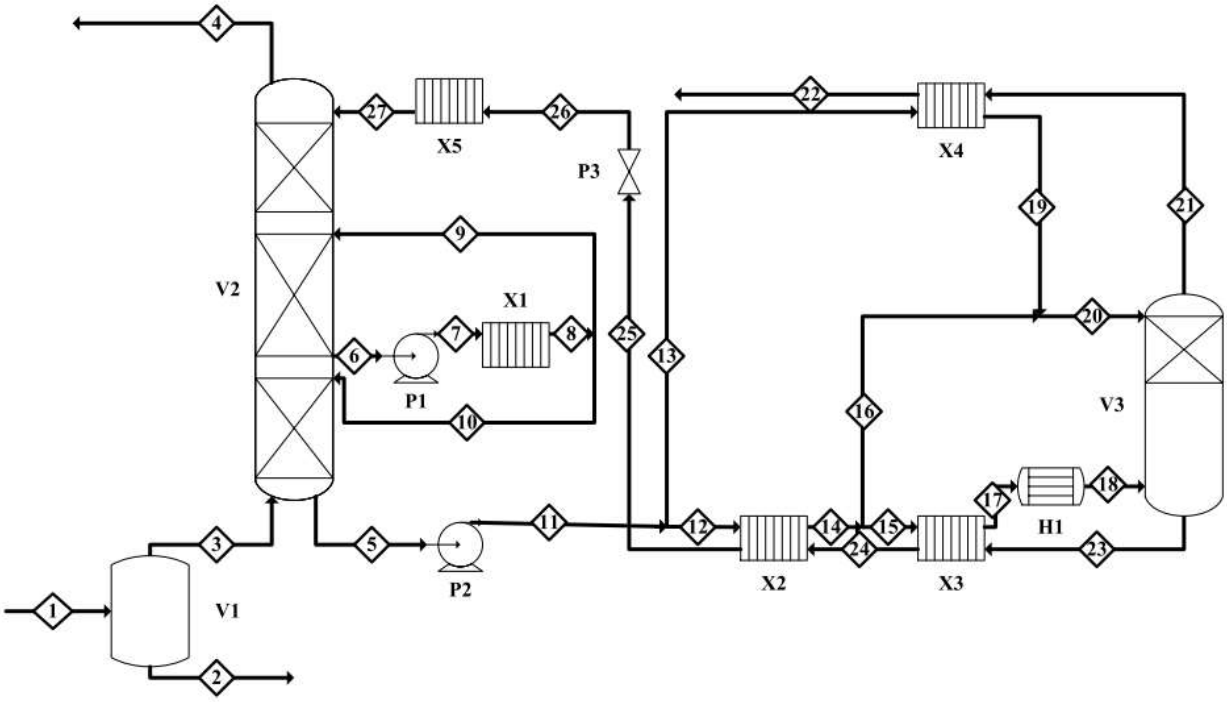

Figure 2. 8 m piperazine advanced flash stripper process flow diagram.

Frailie simulated this AFS design for a 593 MWe coal-fired power plant using the Aspen Plus® Independence model (Frailie, 2014). After sizing and calculating the purchased equipment cost (PEC), the three stripper-side heat exchangers accounted for 27% of the overall PEC of ~70 million ($USD 2014), as shown in **Figure** . This is almost equal to the PEC of the absorber or the combined PEC of the compressor and stripper. The motivation for this project is to improve the modeling of the heat exchangers over simply matching the heat duty of the hot and cold streams as is done in the Aspen Plus® simulations.

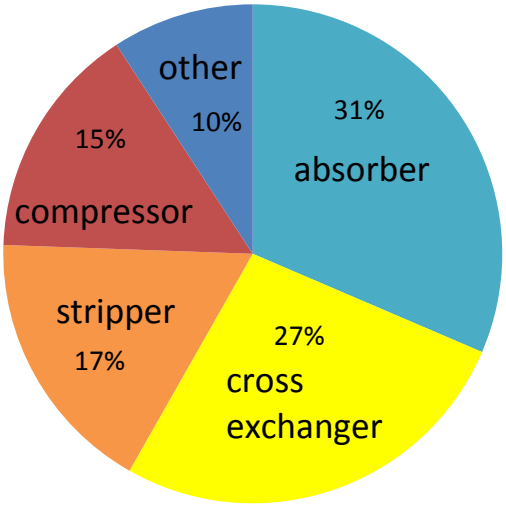

Figure 3. PEC cost for advanced flash stripper case in Frailie (2014). Total PEC is ~70 million ($USD 2014).

Methods

Shooting Algorithm

A discretized single-pass plate-and-frame heat exchanger model was constructed in MATLAB to simulate X2, X3, and X4 of **Figure** . For each exchanger, the two inlet streams and the hot-side temperature approach were taken from the simulated 8 m PZ AFS case. Each exchanger divided into nine segments and solved from the hot side using a shooting method. It is important to note that each exchanger was modeled without flashing. This simplification has serious implications, as discussed in the results section.

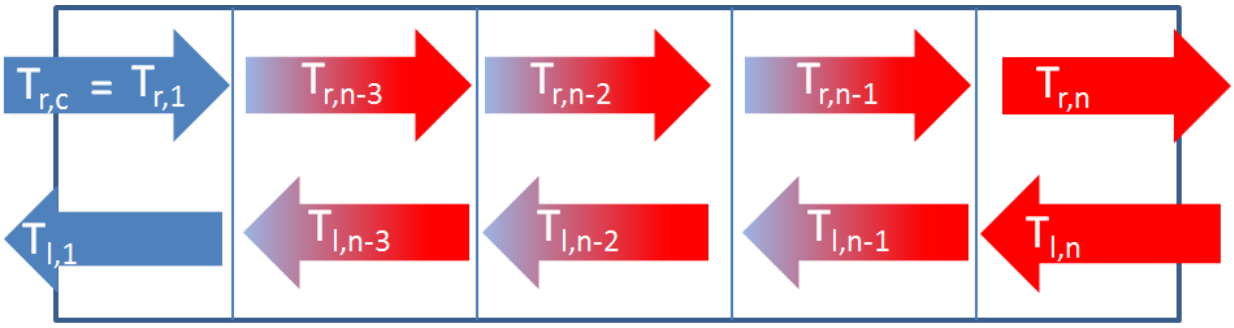

Figure 4. Shooting method schematic. Each line represents a node.

The discretization scheme is described in **Figure 4**. The algorithm proceeds as follows:

1. Given $T_{l,n}$ and $T_{r,n}$, guess $T_{l,n-1}$

2. Solve $\mathrm{Q_{n-1}} = \dot{m}_l C_{l,n}\left(T_{l,n} - T_{l,n-1}\right)$
3. Solve $T_{r,n-1} = T_{r,n} - \frac{\mathrm{Q_{n-1}}}{\dot{m}_r C_{r,n}}$
4. Guess $\mathrm{T_{l,n-2}}$
5. Solve $\mathrm{Q_{n-2}} = \dot{m}_l C_{l,n-1}\left(T_{l,n-1} - T_{l,n-2}\right)$
6. Solve $T_{r,n-2} = T_{r,n-1} - \frac{\mathrm{Q_{n-2}}}{\dot{m}_r C_{r,n-1}}$

Steps 4 through 6 are repeated for each interior segment, until the final cold-side segment is reached. Then, the same steps are used to find $\mathrm{T_{r,1}}$, viz.:

7. Guess $\mathrm{T_{l,1}}$
8. Solve $\mathrm{Q_1} = \dot{m}_l C_{l,2}\left(T_{l,2} - T_{l,1}\right)$
9. Solve $T_{r,1} = T_{r,2} - \frac{\mathrm{Q_1}}{\dot{m}_r C_{r,2}}$

At this point, the shooting method is checked against the temperature of cold, rich stream given by the Aspen Plus® simulation.

10. Check if $T_{r,1} = T_{r,c}$, and update guess

The shooting procedure iterates until $T_{r,1} = T_{r,c} \pm 0.001\ K$, and then the area ($\mathrm{m^2}$) of each segment is calculated using Equation 1.

$$A = \frac{Q_{i-1}}{\left\{\frac{U_i\left(T_{l,i-1} - T_{r,i-1}\right) - U_{i-1}\left(T_{l,i} - T_{r,i}\right)}{\ln\left[U_i\left(T_{l,i-1} - T_{r,i-1}\right)/U_{i-1}\left(T_{l,i} - T_{r,i}\right)\right]}\right\}} \tag{1}$$

where $\mathrm{U_i}$ is the overall heat transfer coefficient of each segment ($\mathrm{W/m^2}$-K) and $\mathrm{Q_{i-1}}$ is the heat duty of each segment in Watts.

Variable Properties

It is necessary to take into account the change in solvent properties as a function of temperature and loading. The streams span temperature from 40 °C to 150 °C and loading from 0.3 to 0.4 mol $\mathrm{CO_2}$/mol alkalinity. To avoid the need to call Aspen Plus® for each property evaluation, the values of 8 m PZ were tabulated for the necessary range of loading and temperature, using 0.025 mol/mol alk. and 20 °C increments. The property values for *C* heat capacity (J/kg–K), ρ density ($\mathrm{kg/m^3}$), *k* thermal conductivity (W/m–K), μ viscosity (Pa-s) are linearly interpolated as needed. The overall heat transfer coefficient for each segment is calculated using Equation 2, where h_h ($\mathrm{W/m^2}$–K) is heat transfer coefficient of the hot stream, h_c is for the cold stream, *t* is the plate thickness (m), and k_p is the thermal conductivity for the plate assuming 316 stainless steel, as calculated by Equation 3. Assuming turbulent flow, *h* for a stream is calculated using Equation 4 from Hewitt et al. (1994).

$$\frac{1}{U} = \frac{1}{h_h} + \frac{1}{h_c} + \frac{t}{k_p} \quad (2)$$

$$k_p = 14.6 + 0.0127T \quad (3)$$

$$h_i = \frac{0.4k}{D_l}(\mathrm{Pr})^{0.4}(\mathrm{Re})^{0.64} \quad (4)$$

In Equation 4, D_l is twice the plate spacing, *Pr* is the Prandtl number, and *Re* is the Reynolds number. *Pr* is entirely a function of solvent properties, however $Re = \rho v D_l/\mu$ includes velocity and plate spacing, which are functions of the exchanger geometry, as $v = \dot{m}/(\rho * XA)$, where XA is the cross-sectional area (m^2).

Exchanger Specifics

The three exchangers shown in **Figure** have the same rich and lean loadings (0.396 and 0.029 mol CO_2/mol alk.) and number of plates (60,000 plates). The other inputs are listed in **Table 5**.

Table 5. Input specifications

Exchanger	$\dot{m}_l$ (kg/s)	$\dot{m}_r$ (kg/s)	$T_{l,n}$ (K)	ΔT_h (K)	$T_{r,1}$ (K)	D_l (m)	XA (m^2)
X2	2964.33	2955.51	397.97	3.83	314.52	0.004	0.001
X3	2964.33	2630.40	422.80	10.80	394.14	0.002	4.78
X4	4.497	130.44	383.51	8.52	338.66	0.002	100

Results and Discussion

Temperature profiles for each exchanger are plotted against the heat duty in each segment in Figures 5–7. (As there are ten temperature nodes but only nine segments, the hot-side temperatures are not plotted.) The unequal thermal masses for X3 and X4 lead to the non-parallel curves.

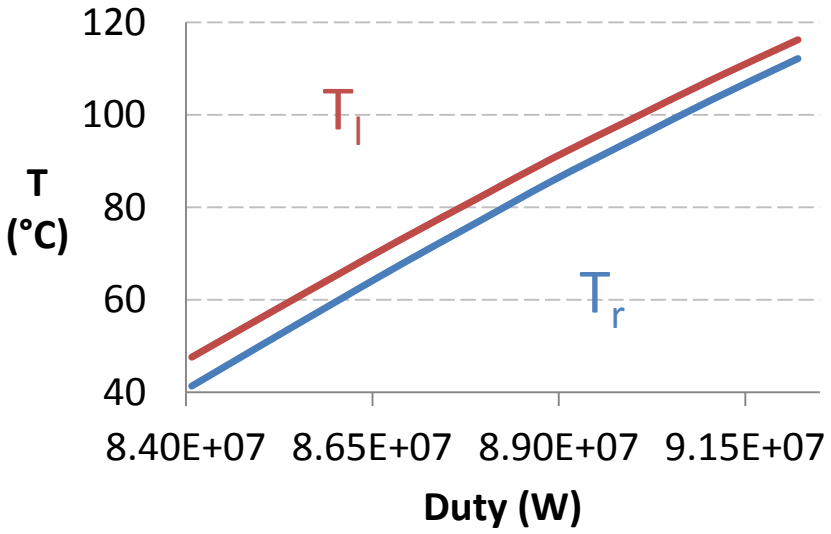

Figure 5. Temperature profile for X2.

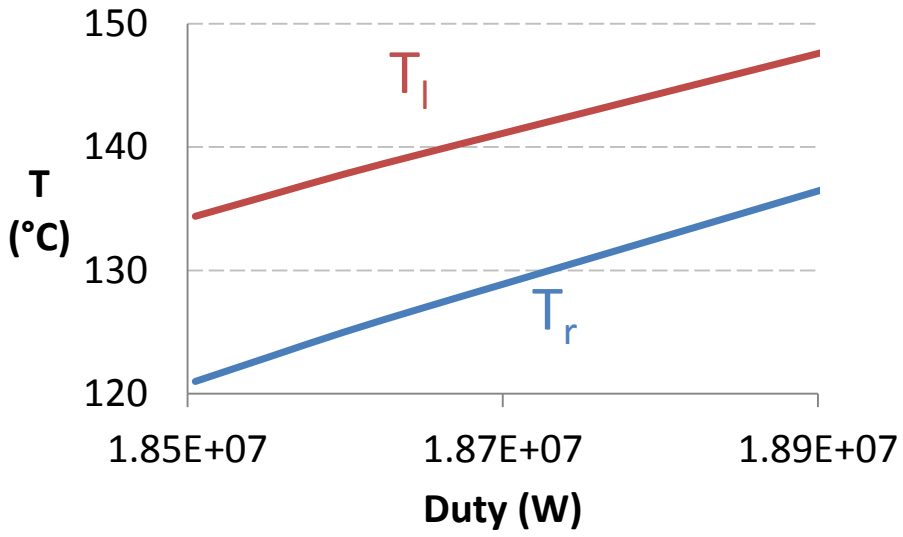

Figure 6. Temperature profile for X3.

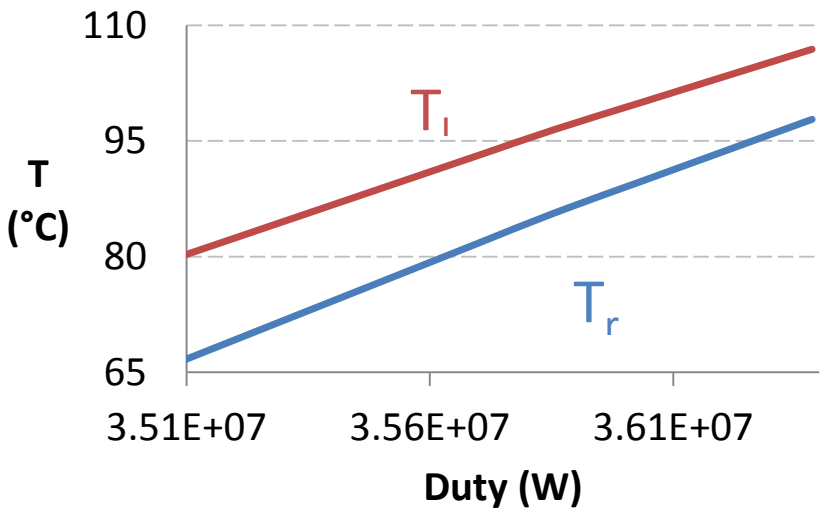

Figure 7. Temperature profile for X4.

In Figures 8–10, the heat duty was ratioed to area and plotted against normalized distance through the exchanger along with the temperature driving force. At the hot side, the Q/A ratio is poorer due to the decreased driving force.

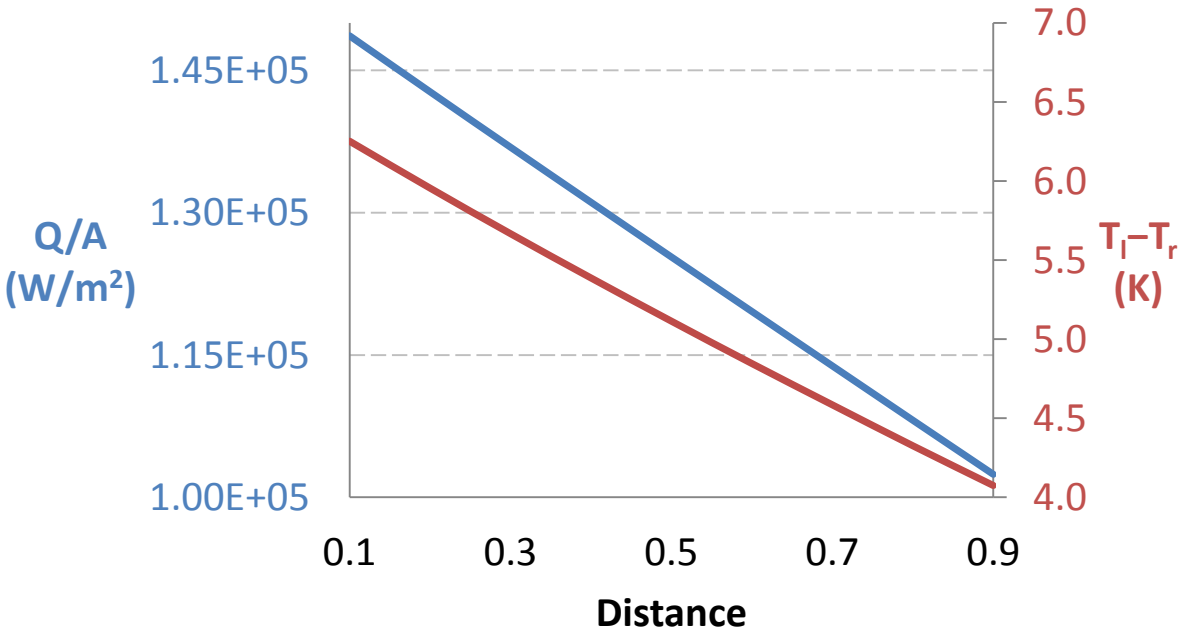

Figure 8. X2 heat duty, area, and driving force.

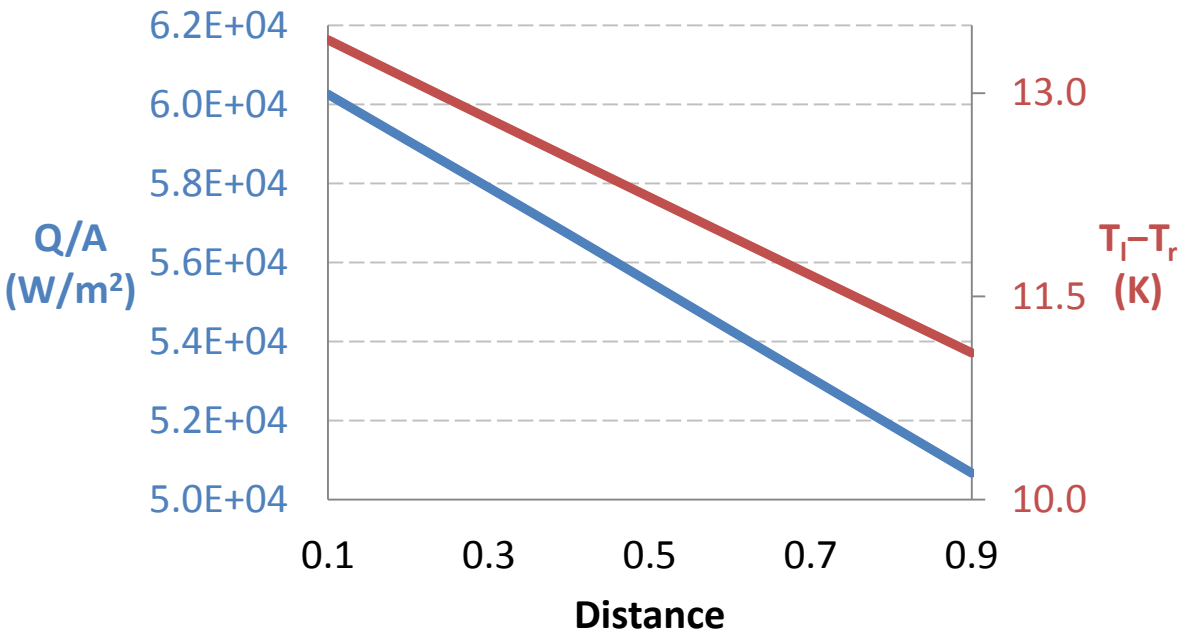

Figure 9. X3 heat duty, area, and driving force.

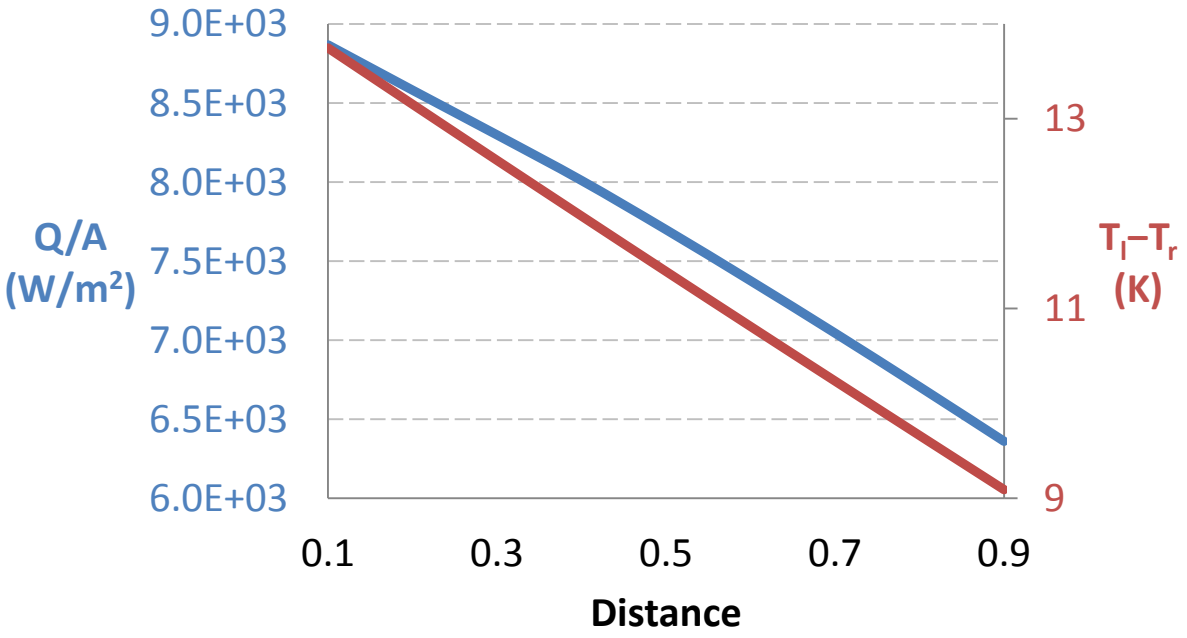

Figure 10. X4 heat duty, area, and driving force.

The results from the discretized model are compared to the Aspen Plus® results in **Table 6**. The large discrepancies in X3 and X4 are due to not modeling the two-phase flow, which would result in greater heat transfer. While X2 is modeled as a non-flashing exchanger in the Aspen

Plus® simulation, there is a discrepancy . due to the changing thermophysical properties. Across X2, U changes by 7%, and C by 14%. It is unclear how Aspen Plus® handles these changing properties, but it probably uses a log-mean approach for just the inlet and outlet streams to calculate the overall heat duty.

Table 6. Results comparison. S is the shooting method, A is Aspen Plus®, D is the percent relative difference.

Exchanger	ΔT_c (K)			Heat Rate (10^8 W)		
	S	A	D %	S	A	D %
X2	6.25	5.36	17	7.92	8.31	-5
X3	13.39	3.83	250	1.69	2.78	-39
X4	13.75	24.14	-43	3.21	0.338	852

Conclusions

As the purchased equipment cost for heat integration is comparable to the absorber or the stripper added to the compressor equipment PEC, a better model of the heat exchanger is desired than a log-mean approach. For this reason, a discretized plate-and-frame heat exchanger model was developed in MATLAB using a shooting method to calculate a temperature, heat duty, and area through the exchanger. It was used to model three exchangers in an 8 m PZ AFS case for a 593 MWe coal-fired power plant that had been previously simulated in Aspen Plus® by Frailie (2014). The MATLAB model did not account for flashing, and this led to large discrepancies with the prior results. The tightest agreement was with for X2, which was non-flashing. The discrepancy for X2 is due to the changing thermophysical properties throughout the exchanger.

Future Work

The biggest improvement to the model would be to account for flashing in the exchangers. This would necessitate different equations for calculating heat transfer coefficients and new

equations to determine the amount of flashing. The shooting method would change to guessing heat duty as during a phase change T will not change.

With the current non-flashing model additional work could be done on the non-flashing exchanger to study the sensitivity to the hot-side temperature approach and exchanger geometry (number of plates and spacing). An important study would be to set the total desired pressure drop, and then vary the number of plates and plate spacing needed to maintain the overall heat duty. This can lead to significantly different costs for the exchanger. Additional solvent concentrations should be examined as the concentration affects Pr, as viscosity is a strong function of solvent concentration. Lastly, pilot plant heat exchanger data could also be simulated to confirm the model validity.

References

Chen, X. *Carbon Dioxide Thermodynamics, Kinetics, and Mass Transfer in Aqueous Piperazine Derivatives and Other Amines*. The University of Texas at Austin. Ph.D. Dissertation. 2011.

Frailie, P. T. *Modeling of Carbon Dioxide Absorption/Stripping by Aqueous Methyldiethanolamine/Piperazine*. Ph.D. Dissertation. 2014.

Freeman, S. A. *Thermal Degradation and Oxidation of Aqueous Piperazine for Carbon Dioxide Capture*. The University of Texas at Austin. Ph.D. Dissertation. 2011.

Madan, T. *Modeling of Stripper Configurations for CO_2 Capture using Aqueous Piperazine*. The University of Texas at Austin. M.S. Thesis. 2013.

Plaza, J. M. *Modeling of Carbon Dioxide Absorption using Aqueous Monoethanolamine, Piperazine and Promoted Potassium Carbonate*. The University of Texas at Austin. Ph.D. Dissertation. 2011.

Rochelle G. T. et al. "CO_2 Capture by Aqueous Absorption, Third Quarterly Progress Report 2009." Luminant Carbon Management Program. The University of Texas at Austin. 2009.

Van Wagener, D. H. *Stripper Modeling for CO_2 Removal Using Monoethanolamine and Piperazine Solvents*. The University of Texas at Austin. Ph.D. Dissertation. 2011.

Supplemental Materials

The three MATLAB files necessary to run the model are below.

---

callheatx.m

```
% Brent Sherman
% ChE 384
% 2014-04-19
% Project
% Purpose: This is a script file that calls the heat exchanger function.

% Specify the temperature of the rich inlet and lean inlet streams.

% Variable list

clear all;clc;close all;
% n=3; % for use with V3_3 and prior
n=10; % for V3_4

ldgr=0.39643203; % mol CO2/mol alk.
ldgl=0.29047815; % mol CO2/mol alk.
% Case 1 specifics
XA=0.001; % for case 1 % cross-sectional area m^2
D=0.004; % case 1 m plate spacing
mdotr=2955.50533; % kg/s
mdotl=2964.33105; % kg/s
Tcr=314.521237; % K cold rich inlet
DThot=3.825562; % K hot side approach
Thl=397.967615; % K hot lean inlet
% A=7241.17533; % m2 area
[Tr,Tl,Q,A]=heatxV3_4(Tcr,Thl,n,mdotr,mdotl,ldgr,ldgl,XA,D,DThot);
%
% figure
% seg=[0:1/(n-1):1];
% plot(seg,Tr-273.15,seg,Tl-273.15)
% title('Temperature Profile')
% xlabel('Distance')
% ylabel('T (C)')
% legend('Rich','Lean','Location','NorthWest');
% I should be using structures to pass all this information back and forth.
% case HX1
%
[Tr,Tl,Q]=heatxV3_1(314.521237,397.967615,7241.17533,n,mdotr,mdotl,ldgr,ldgl)
;
% case HX2
% Tcr=394.142053;
% Thl=422.799762;
% DThot=10.797878;
% % A=12305.53765;
% mdotr=2630.39982; % kg/s
% mdotl=2964.33105; % kg/s
% ldgr=0.39643203; % mol CO2/mol alk.
% ldgl=0.29047815; % mol CO2/mol alk.
```

```
% XA=4.755025325; % for case 2 % cross-sectional area m^2
% D=0.002; % case 2 m plate spacing
% [Tr,Tl,Q,A]=heatxV3_4(Tcr,Thl,n,mdotr,mdotl,ldgr,ldgl,XA,D,DThot);
%
% figure
% seg=[0:1/(n-1):1];
% plot(seg,Tr-273.15,seg,Tl-273.15)
% title('Temperature Profile')
% xlabel('Distance')
% ylabel('T (C)')
% legend('Rich','Lean','Location','NorthWest');

% case HX3
% Tcr=338.662047;
% Thl=383.507936;
% DThot=8.523086;
% % A=234365.6007; % m^2
% mdotr=130.43909; % kg/s
% mdotl=4.49679639; % kg/s
% ldgr=0.39643203; % mol CO2/mol alk.
% ldgl=0.29047815; % mol CO2/mol alk.
% XA=100; % cross-sectional area m^2
% D=0.002; % case 2 m plate spacing
% [Tr,Tl,Q,A]=heatxV3_4(Tcr,Thl,n,mdotr,mdotl,ldgr,ldgl,XA,D,DThot);

figure
seg=[0:1/(n-1):1];
plot(seg,Tr-273.15,seg,Tl-273.15)
title('Temperature Profile')
xlabel('Distance')
ylabel('T (C)')
legend('Rich','Lean','Location','NorthWest');
```

heatxV3_4.m

```
function [Tr,Tl,Q,A] = heatxV3_4(Tcr,Thl,n,mdotr,mdotl,ldgr,ldgl,XA,D,DThot)
% [Tcr,Tcl] = heatx(Tcr,Thl,A,mdotr,mdotl)
% test with (315,398,7241)
% V0 - two segements
%      constant properties
%      works for HX1 Excel case 2014-04-22
% V1 - trying to get the Qcheck to work out
%      given up on that and working center node
% V2 - using variable heat capacity for the 3 nodes
% V3 - using variable U for one section
% V3_1 - using variable props for all nodes
% V3_2 - change to shooting method
% V3_3 - specify a hot side approach
% V3_4 - increase the number of segments to 10

% Variable Units     Description
% A                 total area initially; then A of segments
% Cpl      J/kg-K   heat capacity of the lean fluid
% Cpr      J/kg-K   heat capacity of the rich fluid  (J/kg-K)
% Q        J        heat duty of each segment (J)
% Qcheck   J        heat duty of first segment used for iteration test
```

```
% Tcl      K        T of cold, lean outlet
% Tcr      K        T of cold, rich inlet
% Tfun
% Thl      K        T of hot, lean inlet
% Thr      K        T of hot, rich outlet
% Tl       K        T of cold, lean inlet
% Tr       K        T for function; stand-in
% Trg      K        T of cold, lean inlet
% Uc                overall heat tx.  coeff.  for cold side
% Uh                overall heat tx.  coeff.  for hot  side
% mdotl    kg/s     mass flow rate of lean fluid
% mdotr    kg/s     mass flow rate of rich fluid
% n                 number of nodes; # of segments=n-1


% define properties
% for now they are constant, so use a function call that simply returns a
% constant

% [props]=propcall[Thr,ldg,CAm];

% let's set it up with two sections for now
% try to make it general
i=0; % while loop counter
% store the rich and lean temperatures in two vectors
Tl=zeros(n,1);
Tr=zeros(n,1);
% store BC's
Tl(n)=Thl;
Tr(n)=Thl-DThot;
propl(n)=propcall(Tl(n),ldgl,mdotl,XA,D);
propr(n)=propcall(Tr(n),ldgr,mdotr,XA,D);
% Tr(1)=Tcr;
Toff=10; % initialize while loop
% start solving from hot side back

guess=75/n; % was 112.87/n for case 2
while abs(Toff)>0.001

    for j=1:n-1
        % 1.  guess Tl(n-1)
        % convergence depends on this guess
        % Tl(n-1)=Tl(n)-120/n; % case 1 guess

        Tl(n-j)=Tl(n-j+1)-guess; % case 2 guess
        propl(n-j)=propcall(Tl(n-j),ldgl,mdotl,XA,D); %using the guessed
value
        %%
        % 2.  solve for Q(n-1)
        % property calls
        % Since the Cp changes over the course of the segment, using the hot
side
        % Cp is an approximation.  This improves as the number of segments
        % increases.
```

```
        Q(n-j)=mdotl*propl(n-j+1).Cp*(Tl(n-j+1)-Tl(n-j));
        % Qr(n-j)=mdotr*propr(n-j+1).Cp*(Tr(n-j+1)-Tr(n-j));
        %%
        % 3.  solve for Tr(n-1)
        Tr(n-j)=Tr(n-j+1)-Q(n-j)/(mdotr*propr(n-j+1).Cp);
        propr(n-j)=propcall(Tr(n-j),ldgr,mdotr,XA,D);
        % at this point the T of the last segment aredefined
        %%
        % 4.  Calculate the segment area.

        % solve for individual U values
        % now find the plate resistance
        kph=(propr(n-j+1).kp+propl(n-j+1).kp)/2; % average the two
        kpc=(propr(n-j).kp+propl(n-j).kp)/2;
        % calculate the U's in the last segment
        t=0.0006; % m plate thickness
        U(n-j+1)=(1/propl(n-j+1).h+1/propr(n-j+1).h+(t/kph))^-1;
        U(n-j)=(1/propl(n-j).h+1/propr(n-j).h+(t/kpc))^-1;



        % move to the next segment
    end

    %%
    % 6.  check Tcr and iterate if needed
    Toff=Tr(1)-Tcr
    guess=guess+.1*Toff; % adjust to meet error criterion
    if i>100% break to avoid computational trap
        disp('Max iterations reached')
        break
    end
    i=i+1;

end
for j=1:n-1
    A(n-j)=Q(n-j)/(((U(n-j+1)*(Tl(n-j)-Tr(n-j)))-U(n-j)*(Tl(n-j+1)-Tr(n-
j+1)))...
        /log(((U(n-j+1)*(Tl(n-j)-Tr(n-j))))/(U(n-j)*(Tl(n-j+1)-Tr(n-j+1)))));
end
DThot=Tl(end)-Tr(end)
DTcold=Tl(1)-Tr(1)
Tcr=Tr(1);
Tcl=Tl(1);
Thr=Tr(n);

% code the tolerance and loop in later
```

propcall.m

```
function [props] = propcall(T,ldg,mdot,XA,D)
% [props] = propcall(T,ldg)
% These are all for 8 m PZ from the Independence model (Indep cutdown
% V0.bkp).
```

```
% Variable List
% Name     I/O     Description
% T         I      The temperature at which the properties are calculated in
K.
% props     O      A vector containing all the properties needed.
% ldg       I      The solvent loading in (mol CO2/mol alk.)
% CAm       I      The concentration of the amine in molal (mol/kg
%                  solvent).
% Cp        O      Heat capacity in J/kg-K.
% mu        O      Viscosity in Pa-s.
% k         O      Thermal conductivity in W/m-K
% rho       O      Density in kg/m^3.

% dump identifying characteristics into structure first
% may not need the (1) after props, as I'll calculate it at each point.  .  .
props(1).T=T;
props(1).ldg=ldg;

% set up for interp2
% have everything use the same grid
ldgMesh=0:0.025:0.5;
TMesh=293.15:20:433.15;
[X,Y]=meshgrid(ldgMesh,TMesh');

% store the properties in tables where the loading is increasing from left
% to right and T is increasing from top down

% VISCOSITY cP
visc=[24.3181   9.1884  10.072  10.9753 11.8925 12.8179 13.7455 14.6698
15.5853 16.4865 17.3687 18.227  19.0572 19.8556 20.6185 21.3431 22.0266
22.66682    23.26201    23.80626    24.29381
12.02589    5.176598    5.616924    6.061505    6.507525    6.952209
7.392866    7.826919    8.251937    8.665656    9.066   9.451091    9.81926
10.16905    10.49923    10.80875    11.09677    11.36269    11.60633
11.82838    12.03021
6.734695    3.25136 3.496435    3.741068    3.983753    4.223045    4.457578
4.686079    4.907382    5.120428    5.324279    5.518114    5.701235
5.873064    6.033141    6.181116    6.316754    6.439979    6.551159
6.652615    6.74915
4.123319    2.203795    2.351141    2.49665 2.639469    2.778806    2.913929
3.044177    3.168957    3.287755    3.40013 3.505712    3.604216    3.695419
3.779164    3.855369    3.924029    3.985285    4.039778    4.090082
4.14184
2.703728    1.582445    1.676307    1.768048    1.857169    1.943221
2.025798    2.104547    2.179162    2.249389    2.31502 2.375915    2.431955
2.483072    2.529247    2.570511    2.606967    2.638891    2.667102
2.694008    2.724952
1.872913    1.189356    1.251895    1.312407    1.370596    1.426202
1.478997    1.528792    1.575431    1.618796    1.658819    1.695434
1.728618    1.758382    1.784771    1.807878    1.827882    1.845167
1.86065 1.876423    1.897597
1.356893    0.9275521   0.9707183   1.012068    1.051425    1.088636
1.123577    1.156149    1.186294    1.213973    1.239152    1.261833
1.282043    1.299836    1.315297    1.328569    1.339895    1.349738
1.359009    1.36956 1.387613
```

```
1.020091    0.745547    0.7761754   0.8052163   0.8325646   0.8581349
0.8818618   0.9037404   0.9237236   0.9418048   0.9580016   0.9723517
0.984914    0.9957731   1.00505 1.012927    1.019696    1.025849    1.032284
1.041128    1.067785];
props(1).mu=interp2(X,Y,visc,ldg,T)/1000; %Pa-s

% DENSITY kg/m^3
rho=[1185.126   1045.968    1053.9  1061.76 1069.548    1077.266    1084.914
1092.494    1100.005    1107.45 1114.827    1122.14 1129.387    1136.571
1143.691    1150.747    1157.741    1164.673    1171.569    1178.598
1185.907
1177.892    1035.089    1043.218    1051.274    1059.259    1067.172
1075.016    1082.79 1090.495    1098.133    1105.704    1113.208    1120.647
1128.021    1135.331    1142.577    1149.76 1156.884    1163.979    1171.25
1179.002
1168.338    1021.615    1029.957    1038.226    1046.423    1054.548
1062.602    1070.585    1078.5  1086.346    1094.124    1101.835    1109.479
1117.058    1124.572    1132.023    1139.411    1146.745    1154.067
1161.615    1169.85
1156.948    1006.085    1014.654    1023.148    1031.569    1039.918
1048.194    1056.4  1064.536    1072.602    1080.599    1088.528    1096.39
1104.187    1111.918    1119.587    1127.197    1134.764    1142.353
1150.239    1159.009
1143.979    988.7897    997.5954    1006.326    1014.983    1023.565
1032.076    1040.514    1048.881    1057.178    1065.405    1073.564
1081.657    1089.683    1097.647    1105.552    1113.409    1121.248
1129.17 1137.488    1146.89
1129.582    969.8962    978.9494    987.9265    996.8283    1005.656
1014.409    1023.09 1031.7  1040.238    1048.708    1057.111    1065.448
1073.724    1081.943    1090.116    1098.264    1106.444    1114.8  1123.679
1133.928
1113.834    949.4914    958.8022    968.036 977.1937    986.2761    995.2843
1004.22 1013.083    1021.878    1030.606    1039.271    1047.878    1056.434
1064.95 1073.447    1081.967    1090.601    1099.535    1109.164    1120.831
1096.751    927.5946    937.1744    946.6768    956.1026    965.4529
974.7293    983.934 993.0698    1002.141    1011.153    1020.113    1029.032
1037.924    1046.811    1055.733    1064.758    1074.01 1083.73 1094.505
1110.645];
props(1).rho=interp2(X,Y,rho,ldg,T);

% HEAT CAPACITY kJ/kg-K
Cp=[3.322724    3.304038    3.287131    3.271298    3.256362    3.242235
3.228917    3.216276    3.204207    3.19242 3.180319    3.167127    3.152171
3.135211    3.116423    3.095183    3.07216 3.043699    3.007026    2.976281
2.967719
3.380491    3.364501    3.350314    3.337158    3.324834    3.313172
3.302176    3.291616    3.281255    3.270783    3.259569    3.246961
3.232701    3.216681    3.197702    3.179585    3.157743    3.131124
3.095173    3.058767    3.043238
3.444038    3.430702    3.41918 3.408673    3.39893 3.389728    3.38093
3.372286    3.363522    3.354106    3.343583    3.3315  3.317758    3.302053
3.285206    3.266651    3.245554    3.219845    3.185503    3.147845
3.127213
3.510979    3.500238    3.491329    3.483412    3.476116    3.469293
3.462634    3.455805    3.448424    3.440004    3.430041    3.418373
```

```
3.404279    3.389314    3.372792    3.354583    3.333844    3.308712
3.276657    3.241782    3.219126
3.582073    3.573968    3.567695    3.562293    3.557524    3.55302 3.548537
3.543595    3.537691    3.53038 3.521253    3.508938    3.4958  3.480919
3.464535    3.446337    3.425794    3.401595    3.372585    3.342651
3.320454
3.658484    3.653086    3.649512    3.646815    3.644631    3.642695
3.640544    3.637724    3.633682    3.593697    3.618163    3.607847
3.595323    3.580729    3.564487    3.546475    3.526282    3.503531
3.478225    3.453412    3.432069
3.740925    3.738407    3.737782    3.737977    3.738714    3.739595
3.740157    3.739912    3.735733    3.73213 3.725928    3.717063    3.705503
3.691748    3.676029    3.658545    3.639404    3.618671    3.59687 3.575542
3.552126
3.830128    3.830752    3.833376    3.836931    3.841041    3.845252
3.849142    3.848865    3.850433    3.84962 3.845818    3.838999    3.829077
3.816635    3.80185 3.785418    3.767481    3.748419    3.728561    3.706695
3.666179];
props(1).Cp=interp2(X,Y,Cp,ldg,T)*1000; % J/kg-K

% THERMAL CONDUCTIVITY W/m-K
K=[0.2154467    0.2208266   0.2267563   0.2337158   0.2419738   0.2517315
0.2630676   0.2757102   0.2883534   0.2975582   0.2973719   0.2838554
0.2613841   0.2379881   0.2178136   0.2013862   0.187907    0.1763358
0.1660314   0.1582338   0.1534949
0.209044    0.2140264   0.2192965   0.2254304   0.2326649   0.2410967
0.250603    0.2605316   0.2691455   0.273063    0.2683272   0.2543492
0.2355766   0.2170126   0.2009436   0.1876149   0.1764832   0.1667697
0.1576777   0.1497291   0.1442413
0.2023068   0.2067663   0.2111988   0.2162749   0.2221852   0.228919
0.2361944   0.2431831   0.2481825   0.2485916   0.2422238   0.2296646
0.2141957   0.1990768   0.1858012   0.1745673   0.1650332   0.1566326
0.1487127   0.1414395   0.1361454
0.1953266   0.1991625   0.2026396   0.2065276   0.2109778   0.2159105
0.2209435   0.2252746   0.2275109   0.2258843   0.2193032   0.2084857
0.1956746   0.1830687   0.1717761   0.1620371   0.1536475   0.1462129
0.1392892   0.1329596   0.1281578
0.1881659   0.1912986   0.1937525   0.1964098   0.1993972   0.2025898
0.2056095   0.2077596   0.2080104   0.2052356   0.1988975   0.1896236
0.178895    0.1681965   0.1584272   0.1498428   0.1423557   0.1357197
0.1296901   0.1243732   0.1202677
0.1808684   0.1832283   0.1846184   0.1860455   0.1876299   0.189242
0.1905394   0.1909623   0.1897831   0.1863123   0.1802847   0.1722059
0.1630781   0.1539136   0.1454077   0.1378222   0.1311563   0.1252917
0.1201377   0.1157893   0.1124152
0.1734654   0.1749733   0.1752546   0.1754557   0.1757103   0.1758997
0.1757332   0.1747775   0.1725282   0.1685721   0.1628111   0.1556369
0.1477349   0.13985 0.1324629   0.1258353   0.1200154   0.1149751   0.1106965
0.1072028   0.1044687
0.1659798   0.1665097   0.1655848   0.1645273   0.1634882   0.1623673
0.160924    0.1588272   0.1557339   0.151408    0.1458531   0.1393701
0.1324863   0.1257111   0.1193896   0.1137416   0.1088307   0.104659
0.1012021   0.0984089   0.0961522];
props(1).k=interp2(X,Y,K,ldg,T);

% find the Prandtl #
```

```
props(1).Pr=(props(1).Cp*props(1).mu)/props(1).k;

% find the Reynolds #
props(1).v=mdot/(props(1).rho*XA); % velocity in m/s
props(1).Re=(props(1).rho*props(1).v*D)/props(1).mu;

% the coeff.  and powers differ from Peter's XL sheet
% however, these are from Hewitt for turbulent flow in a plate and frame
% cf example 8.1 where Nu=0.4*Pr^0.4*Re^0.64
props(1).h=(0.4*props(1).k/D)*(props(1).Pr^0.4)*(props(1).Re^0.64);
% h = W/m^2-K
% assume 316 SS for the wall
props(1).kp=14.6+0.0127*(props(1).T-273.15); % W/m-K
```

Reduced Order Modeling and Time Scale Analysis of Amine Scrubbing

Quarterly Report for April 1 – June 30, 2014

by Matthew S. Walters

Supported by the Texas Carbon Management Program

McKetta Department of Chemical Engineering

The University of Texas at Austin

July 31, 2014

Abstract

Amine scrubbing is a highly integrated process that uses extensive material and energy recycling to reduce costs and increase efficiency. As a result, there are two distinct time scales that exist in the process dynamics: a fast time scale at the unit level associated with the large recycle flows and a slow time scale at the process level associated with the small feed and product flows. A reduced order model was developed to identify the time scale of each state variable. Many variables have both fast and slow components; a variable transformation will be required in future work to explicitly separate the variables for use in a model-based controller. Previous works in the literature have attempted to use the large internal recycle flowrate to control the removal rate of CO_2 in the absorber. The time scale decomposition shows that the liquid CO_2 composition in the absorber has slow components that must be stabilized by controlling a small product flow. Therefore, controlling CO_2 removal with a large internal flowrate will likely lead to an ill-conditioned controller and produce oscillations within the system.

Introduction

The general trend in the chemical process industry is the development of increasingly integrated process designs that use extensive material and energy recycling and minimize overall inventory. With enormous capital and operating costs, post-combustion amine scrubbing adheres to this trend. After the amine solvent has absorbed CO_2, it is regenerated at high temperatures and completely recycled back to the absorber. Additionally, most of the sensible heat in the process is recovered either through direct contact packing or in a cross heat exchanger. To reduce capital cost associated with buying solvent, buffer tanks will be designed to hold the minimum amount of inventory for safe operation and will likely not be large enough to effectively dampen disturbances that propagate through the system.

In order to develop an effective control strategy for amine scrubbing, the time scales of the process variables that result from material and energy recycling must be taken into consideration. The goal of this work is to develop a simplified model with adjustable parameters that adequately represents the physical behavior of the true plant. To control the process, variables that have a fast component must be stabilized on the fast time scale and variables with a slow component must be stabilized on the slow time scale. The system should ultimately be

transformed into singularly perturbed form shown in Equations 1–2 to systematically identify fast and slow variables, where **x** represents the slow variables, **z** the fast variables, and ε is some small parameter. In the limit where $\varepsilon \rightarrow 0$ (infinite recycle), the left hand side of Equation 2 becomes zero and the fast variables are approximately at steady state (Kokotović et al., 1986).

$$\frac{dx}{dt} = f(x, z) \tag{1}$$

$$\varepsilon \frac{dz}{dt} = g(x, z) \tag{2}$$

Reduced Order Model Development

In model-based control of a process with time scale multiplicity, the process model needs to be explicitly separated into fast and slow variables (Chen et al., 2012). A reduced order model (ROM) will be used to separate the variables into different time scales for the advanced amine scrubbing process using aqueous piperazine (PZ) described in Figure 1. First, a system of differential and algebraic equations (DAEs) has been developed from first principles. The absorber (AB), which contains structured packing, is modeled using constant rate-based mass and energy transfer coefficients. The CO_2 mass transfer coefficient accounts for the rate enhancement due to chemical reaction. The absorber packing is discretized into ten well-mixed segments for material and energy balances. The number of stages has been somewhat arbitrarily selected; the number of stages required to best represent the system will be considered in future work.

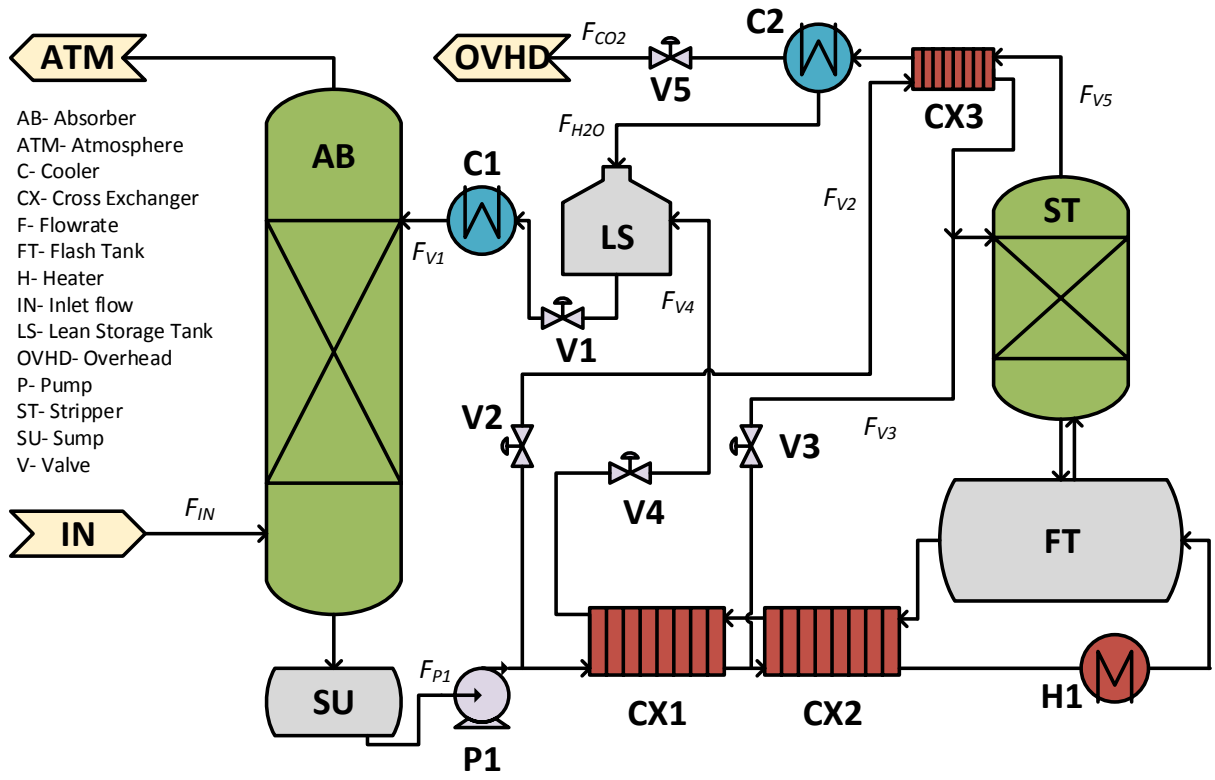

Figure 1: Process flow diagram with advanced flash stripper configuration

Tanks, including the absorber sump (SU), flash tank (FT), and lean storage tank (LS) are treated as well-mixed equilibrium stages within the system. They each have material and energy balances on only the liquid hold-up. The main cross exchangers (CX1 and CX2) are assumed to exchange only sensible heat. This is likely a bad assumption for CX2 since flashing is known to occur in the rich solvent on the cold side of the exchanger; the assumption will be revisited in future work. The stripper (ST) and bypass exchanger (CX3) allow energy to be recovered from steam by heating the bypass streams. The stripper is modeled using rate-based mass transfer, but the bulk convection between the liquid and vapor is ignored. While ignoring bulk convection is a good assumption in the absorber since the gas is mostly inert, it may cause deviation from the true behavior of the plant in the stripper. The steam heater (H1) uses steam from the power plant to provide some sensible heat ($\Delta T \sim 5$ °C) and most of the latent heat requirement of the process. The trim cooler (C1) and overhead condenser (C2) are currently being treated as perfect heat exchangers: the lean solvent fed to the absorber is always at 40 °C and all of the water vapor is condensed out of the overhead gas. C1 and C2 will be modeled explicitly in future work.

Several other assumptions have been made while constructing a model for the system, including:

- Liquid molar hold-up in the packing is constant.
- The amine is nonvolatile.
- N_2 and O_2 are insoluble.
- Heat capacity, heat of desorption, heat of vaporization, molar density, heat transfer coefficients, and mass transfer coefficients are constant.
- Internal energy can be approximated as enthalpy for both the liquid and gas.

The control (input) variables are the molar flows associated with the pump and valves (F_{P1}, F_{V1}, F_{V2}, F_{V3}, F_{V4}, F_{V5}, and F_s). The inlet gas flowrate to the absorber and the steam quality are functions of the upstream power plant and are treated as disturbances. The process control objectives are to maintain an optimum removal rate of CO_2 (or alternatively to maintain a removal rate required by environmental regulation), stabilize the level of the sump and flash tank, maintain the temperature of the flash tank at the maximum solvent degradation temperature, and maintain the temperature of the hot side fluid exiting CX1 and CX3 at their optimum values. The temperature control objectives are related to the energy performance of the process and solvent management.

A DAE system is set up by performing material and energy balances at each node in the process. The differential conservation equations have a related set of algebraic equations that govern thermodynamics, mass transfer, and heat transfer, respectively:

$$H,\ y_i^* = f(T, P, M_i) \tag{3}$$

$$N_i = KA(y_i - y_i^*) \tag{4}$$

$$N_H = UA\Delta T_{LM} \tag{5}$$

The thermodynamics were based on a semi-empirical model by Xu (2011). The convective mass and heat transfer coefficients in the packing were treated as adjustable parameters to minimize the error between the ROM and a rigorous Aspen Plus® model for a given set of conditions. Overall heat transfer coefficients in the plate-and-frame cross exchangers are taken from heat exchanger heuristics. The full DAE system can be found in Appendix A.

For the purpose of analysis, the DAE system was transformed into ordinary differential equation (ODE) form (or nonlinear state space form). This required extensive manipulation of the algebraic equations given in Appendix A. The ODE representation of the system can be found in Appendix B.

Time Scale Analysis

A time scale analysis was performed on the ODE model of the process based on the work of Baldea and Daoutidis (2012). First we will consider the material time scales. Figure 2 shows a rate-based absorber where CO_2 is transferring into the solvent from the flue gas at all k segments. The recycle flowrate, F_{V1}, is much greater than the amount of CO_2 fluxing into the system. Furthermore, the flowrate of CO_2 in the amine into the absorber is larger than the flowrate of CO_2 in the flue gas. We can therefore define a material recycle number, Rc, that is a ratio of the large recycle flowrate to the small feed flowrate:

$$Rc = \frac{1}{\varepsilon_m} = \frac{{F_{V1}}^s}{{N_{CO2,k=Ns}}^s} \tag{6}$$

The CO_2 flux is generally expected to be greatest at the bottom of the column, so the flux at the bottom segment is selected for the recycle number definition. An important implication of this selection is that the transfer rates at other segments of the column are of the same order of magnitude or less.

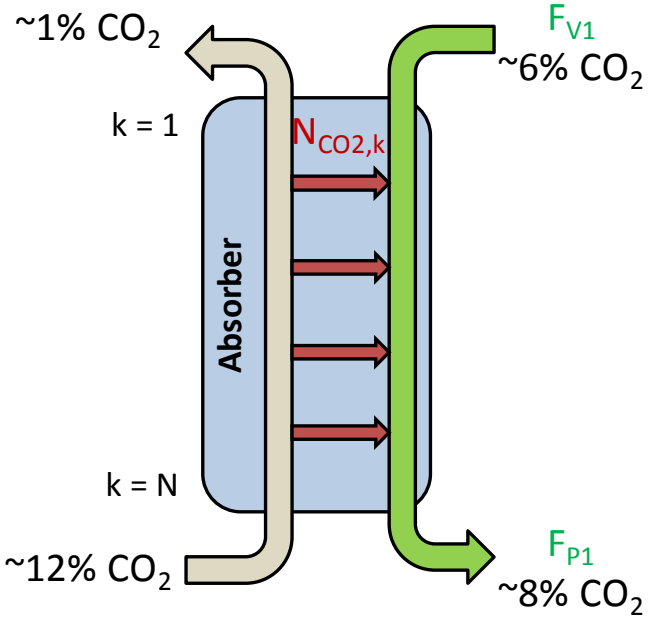

Figure 2: CO_2 transfers from the flue gas (grey) to the liquid (green) at each k segment of the column, but this flow is relatively small compared to the total liquid flow into the column.

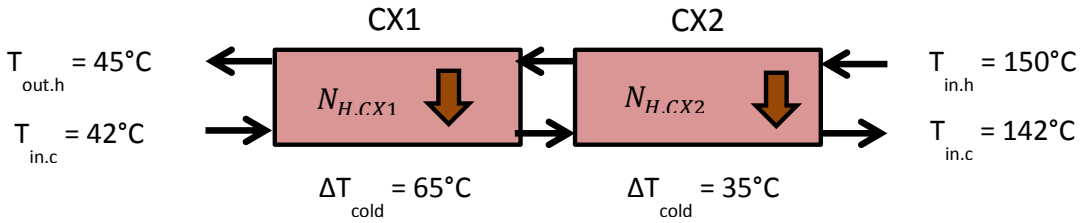

Figure 3: A small flow of sensible heat enters the cold side of the cross exchanger and a large flux of energy is transferred to the cold side from the hot side.

Next, the large energy recycle is considered. There is significant energy recovery in the main cross exchangers (CX1 and CX2), mostly in the form of sensible heat. The solvent from the absorber, which nominally operates at 40 °C, must be heated for high temperature stripping. Figure 3 demonstrates the energy recovery process. Assuming a reference temperature of 40 °C, the inlet solvent from the absorber carries very little sensible heat. The amount of energy fluxing from the hot side of the cross exchanger to the cold side is considerably larger than the entering stream based on the temperature differences. We can therefore define an energy recovery number, Erc, that is the ratio of the large energy flux to the small inlet energy flowrate:

$$Erc = \frac{1}{\varepsilon_E} = \frac{{N_{H,CX1}}^S}{[F_{P1}Cp(T_{in,c}-T_{ref})]^S} = \frac{\varepsilon_M {N_{H,CX1}}^S}{{N_{CO2,k=Ns}}^S \omega_p Cp[(T_{in,c}-T_{ref})]^S} \quad (7)$$

The recycle and energy recovery numbers will be substituted into the ODE system in the following subsections to rearrange the equations into singularly perturbed form. The form shown here is *nonstandard* singularly perturbed form, given by Equation 8. The dimensionless quantities in Table 1 are used for convenience in constructing the system. In the nonstandard form, variables are not explicitly separated into fast and slow time scales.

$$\dot{\boldsymbol{x}} = \boldsymbol{F}(x) + \boldsymbol{G}_{small}(\boldsymbol{x})\boldsymbol{u}_{small} + \frac{1}{\varepsilon_m}\boldsymbol{G}_{large,m}(\boldsymbol{x})\boldsymbol{u}_{large} + \frac{1}{\varepsilon_e}\boldsymbol{G}_{large,e}(\boldsymbol{x})\boldsymbol{u}_{large} \quad (8)$$

Table 1: Scaled parameters used in singularly perturbed model

Inputs	$\mathcal{O}(1)$ Quantities	Other Parameters
$u_1 = \frac{F_{V1}^L}{{F_{V1}^L}^s}$	$\omega_{AB,i,k} = \frac{{N_{AB,i,k}}^s}{{N_{AB,CO2,k=Ns}}^s}$	$\psi_{CX1,H} = \frac{N_{CX1,H}}{{N_{CX1,H}}^s}$
$u_2 = \frac{F_{V2}^L}{{F_{V2}^L}^s}$	$\omega_{ABT,k} = \frac{{\sum_{k=1}^{k-1} N_{AB,k}}^s}{{N_{AB,CO2,k=1}}^s}$	$\psi_{CX1,c} = \frac{(F_{P1}^L - F_{V2}^L)(T_{CX1,c}^L - T_{ref})}{[(F_{P1}^L - F_{V2}^L)(T_{CX1,c}^L - T_{ref})]^s}$
$u_3 = \frac{F_{V3}^L}{{F_{V3}^L}^s}$	$\omega_{AB,k} = \frac{{N_{AB,k}}^s}{{N_{AB,CO2,k=1}}^s}$	$\psi_{CX2,h} = \frac{F_{V4}^L(T_{CX2,h}^L - T_{ref})}{[F_{V4}^L(T_{CX2,h}^L - T_{ref})]^s}$
$u_4 = \frac{F_{V4}^L}{{F_{V4}^L}^s}$	$\omega_{ABS,k} = \frac{{\sum_{k=1}^{k} N_{AB,k}}^s}{{N_{AB,CO2,k=1}}^s}$	$d_{AB,i,k} = \frac{N_{AB,i,k}}{{N_{AB,i,k}}^s}$
$u_5 = \frac{F_5^V}{F_5^{Vs}}$	$\omega_{CX1,c} = \frac{[(F_{P1}^L - F_{V2}^L)(T_{CX1,c}^L - T_{ref})]^s}{{N_{CX1,H}}^s}$	$d_{AB,k} = \frac{N_{AB,k}}{{N_{AB,k}}^s}$
$u_p = \frac{F_{P1}^L}{{F_{P1}^L}^s}$	$\omega_{CX1,h} = \frac{[F_{V4}^L(T_{CX2,h}^L - T_{ref})]^s}{{N_{CX1,H}}^s}$	$d_{ABT,k} = \frac{\sum_{k=1}^{k-1} N_{AB,k}}{{\sum_{k=1}^{k-1} N_{AB,k}}^s}$
$u_s = \frac{Q_s}{{Q_s}^s}$	$\omega_{STT,k} = \frac{{\sum_{k=1}^{k-1} N_{ST,k}}^s}{{N_{AB,CO2,k=1}}^s}$	$d_{ABS,k} = \frac{\sum_{k=1}^{k} N_{AB,k}}{{\sum_{k=1}^{k} N_{AB,k}}^s}$
	$\omega_p = \frac{{F_{P1}^L}^s}{{F_{V1}^L}^s}$	
	$\omega_{p-V2} = \frac{{F_{P1}^L}^s - {F_{V2}^L}^s}{{F_{V1}^L}^s}$	
	$\omega_4 = \frac{{F_{V4}^L}^s}{{F_{V1}^L}^s}$	

Absorber

Equations 9–10 show the absorber model from Appendix B represented in nonstandard singularly perturbed form. Only the liquid side balances are considered here since the flue gas inlet is considered a disturbance. When i = PZ, the $d_{AB,i,k}$ term becomes zero (not indeterminate) since there is assumed to be no flux of PZ.

$$\dot{x}_{AB,i,k} = \frac{1}{M_{AB}^L}\Big[{N_{AB,CO2,k=Ns}}^s\big(d_{AB,i,k}\omega_{AB,i,k} + x_{AB,i,k-1}d_{ABT,k}\omega_{ABT,k} - x_{AB,i,k}d_{ABS,k}\omega_{ABS,k}\big) + \frac{1}{\varepsilon_m}u_1{N_{AB,CO2,k=Ns}}^s\big(x_{AB,CO2,k-1} - x_{AB,CO2,k}\big)\Big], \forall i, i \neq H_2O, N_2, O_2 \quad (9)$$

$$\dot{T}_{AB,k}^L = \frac{1}{Cp^L M_{AB}^L}\Big[N_{AB,H,k} + {N_{AB,CO2,k=Ns}}^s\big(\widehat{H}_{AB,k-1}^L d_{ABT,k}\omega_{ABT,k} - \widehat{H}_{AB,k}^L d_{ABS,k}\omega_{ABS,k}\big) + \frac{1}{\varepsilon_m}u_1{N_{AB,CO2,k=Ns}}^s\big(\widehat{H}_{AB,k-1}^L - \widehat{H}_{AB,k}^L\big)\Big] + \frac{1}{Cp^L}\big[(\Delta H_{CO2} - \Delta H_{H2O})\dot{x}_{AB,CO2,k} - \Delta H_{H2O}\dot{x}_{AB,PZ,k}\big] \quad (10)$$

Absorber Sump

The absorber sump model (a single-phase, well-mixed tank) is given by Equations 11–13.

$$\dot{l}_{SU}^{L} = \frac{4}{\pi {D_{SU}}^2 C_{SU}^{L}}\left[{N_{AB,CO2,k=Ns}}^{s} d_{ABS,k=Ns}\omega_{ABS,k=Ns} + \frac{1}{\varepsilon_m}{N_{AB,CO2,k=Ns}}^{s}\left(u_1 - \omega_p u_P\right)\right] \tag{11}$$

$$\dot{x}_{SU,i} = \frac{4}{\pi {D_{SU}}^2 C_{SU}^{L} l_{SU}^{L}}\left[{N_{AB,CO2,k=Ns}}^{s} d_{ABS,k=Ns}\omega_{ABS,k=Ns}\left(x_{AB,i,k=N_s} - x_{SU,i}\right) + \frac{1}{\varepsilon_m}{N_{AB,CO2,k=Ns}}^{s} u_1\left(x_{AB,i,k=N_s} - x_{SU,i}\right)\right], \forall i, i \neq H_2O, N_2, O_2 \tag{12}$$

$$\dot{T}_{SU}^{L} = \frac{4}{\pi {D_{SU}}^2 C_{SU}^{L} l_{SU}^{L} Cp^{L}}\left[{N_{AB,CO2,k=Ns}}^{s} d_{ABS,k=Ns}\omega_{ABS,k=Ns}\left(\widehat{H}_{AB,k=N_s}^{L} - \widehat{H}_{SU}^{L}\right) + \frac{1}{\varepsilon_m}{N_{AB,CO2,k=Ns}}^{s} u_1\left(\widehat{H}_{AB,k=N_s}^{L} - \widehat{H}_{SU}^{L}\right)\right] + \frac{1}{Cp^{L}}\left[\left(\Delta H_{CO2} - \Delta H_{H2O}\right)\dot{x}_{SU,CO2} - \Delta H_{H2O}\dot{x}_{SU,PZ}\right] \tag{13}$$

Main Cross Exchangers

The hot and cold side energy balances for the main cross exchanger are given by Equations 14–15. The analysis is shown here only for CX1; the analysis for CX2 directly follows by assuming $\frac{{N_{CX2,H}}^{s}}{{N_{CX1,H}}^{s}} \sim \mathcal{O}(1)$.

$$\dot{T}_{CX1,c}^{L} = \frac{1}{M_{CX1,c}^{L}}\left[-u_2 {F_{V2}^{L}}^{s}\left(T_{SU}^{L} - T_{ref}\right) + \frac{1}{\varepsilon_m}{N_{AB,CO2,k=Ns}}^{s}\omega_p u_P\left(T_{SU}^{L} - T_{ref}\right) + \frac{1}{\varepsilon_e \varepsilon_m}{N_{AB,CO2,k=Ns}}^{s}\omega_{p-V2}\left[\left(T_{SU}^{L} - T_{ref}\right)\right]^{s}\left(-\omega_{CX1,c}\psi_{CX1,c} + \psi_{CX1,H}\right)\right] + \frac{1}{Cp^{L}}\left[\left(\Delta H_{CO2} - \Delta H_{H2O}\right)\dot{x}_{SU,CO2} - \Delta H_{H2O}\dot{x}_{SU,PZ}\right] \tag{14}$$

$$\dot{T}_{CX1,h}^{L} = \frac{1}{M_{CX1,c}^{L}}\left[-\frac{1}{\varepsilon_m}{N_{AB,CO2,k=Ns}}^{s}\omega_4 u_4\left(T_{CX1,h}^{L} - T_{ref}\right) + \frac{1}{\varepsilon_e \varepsilon_m}{N_{AB,CO2,k=Ns}}^{s}\omega_{p-V2}\left[\left(T_{SU}^{L} - T_{ref}\right)\right]^{s}\left(\omega_{CX1,h}\psi_{CX2,h} - \psi_H\right)\right] + \frac{1}{Cp^{L}}\left[\left(\Delta H_{CO2} - \Delta H_{H2O}\right)\dot{x}_{FT,CO2} - \Delta H_{H2O}\dot{x}_{FT,PZ}\right] \tag{15}$$

Flash Tank

Currently, the steam heater is being grouped together with the flash tank. The two-phase heated tank model is given by Equations 16–18.

$$\dot{l}_{FT}^{L} = \frac{4}{\pi {D_{FT}}^2 C_{FT}^{L}}\left[-u_5 {F_{V5}^{V}}^{s} + \frac{1}{\varepsilon_m}{N_{AB,CO2,k=1}}^{s}\left(\omega_p u_p - \omega_4 u_4\right)\right] \tag{16}$$

$$\dot{x}_{FT,i} = \frac{4}{\pi {D_{FT}}^2 C_{FT}^{L} l_{FT}^{L}}\left[\left(x_{ST,i,k=Ns} - x_{SU,i}\right)\left(u_2 {F_{V2}^{L}}^{s} + u_3 {F_{V3}^{L}}^{s}\right) + \left(x_{FT,i} - y_{FT,i}\right)u_5 {F_{V5}^{V}}^{s} + \left(x_{ST,i,k=Ns} - y_{FT,i}\right)\sum_{k=1}^{N_s} N_{ST,k} + \frac{1}{\varepsilon_m}{N_{AB,CO2,k=1}}^{s}\left(x_{SU,i} - x_{FT,i}\right)u_p\omega_p\right], \forall i, i \neq H_2O, N_2, O_2 \tag{17}$$

$$\dot{T}_{FT}^{L} = \frac{4}{\pi {D_{FT}}^2 C_{FT}^{L} l_{FT}^{L} Cp^{L}}\Big[\big(\widehat{H}_{ST,k=Ns}^{L} - \widehat{H}_{CX2,c}^{T}\big)\big(u_2 {F_{V2}^{L}}^{S} + u_3 {F_{V3}^{L}}^{S}\big) + \big(\widehat{H}_{ST,k=Ns}^{L} - \widehat{H}_{FT}^{V}\big)\sum_{k=1}^{N_s} N_{ST,k} + \big(\widehat{H}_{FT}^{L} - \widehat{H}_{FT}^{V}\big)u_5 {F_{V5}^{V}}^{S} + Q_{FT} + \frac{1}{\varepsilon_m} {N_{AB,CO2,k=1}}^{S}\big(\widehat{H}_{CX2,c}^{T} - \widehat{H}_{FT}^{L}\big)u_p \omega_p\Big] + \frac{1}{Cp^{L}}\big[(\Delta H_{CO2} - \Delta H_{H2O})\dot{x}_{FT,CO2} - \Delta H_{H2O}\dot{x}_{FT,PZ}\big] \quad (18)$$

Stripper

The stripper model is shown in Equations 19–22.

$$\dot{x}_{ST,i,k} = \frac{1}{M_{ST}^{L}}\big[\big(x_{ST,i,k-1} - x_{ST,i,k}\big)\big(u_2 {F_{V2}^{L}}^{S} + u_3 {F_{V3}^{L}}^{S} + \sum_{k=1}^{k-1} N_{ST,k}\big) - x_{ST,i,k} N_{ST,k} + N_{ST,i,k}\big] \; \forall i, i \neq H_2O, N_2, O_2 \quad (19)$$

$$\dot{T}_{ST,k}^{L} = \frac{1}{Cp^{L} M_{ST}^{L}}\big[\big(\widehat{H}_{ST,k-1}^{L} - \widehat{H}_{ST,k}^{L}\big)\big(u_2 {F_{V2}^{L}}^{S} + u_3 {F_{V3}^{L}}^{S} + \sum_{k=1}^{k-1} N_{ST,k}\big) - \widehat{H}_{ST,k}^{L} N_{ST,k} + N_{ST,H,k}\big] + \frac{1}{Cp^{L}}\big[(\Delta H_{CO2} - \Delta H_{H2O})\dot{x}_{ST,CO2,k} - \Delta H_{H2O}\dot{x}_{ST,PZ,k}\big] \quad (20)$$

$$\dot{y}_{ST,CO2,k} = \frac{1}{M_{ST,k}^{V}}\big[\big(y_{ST,CO2,k+1} - y_{ST,CO2,k}\big)\big(u_5 {F_{V5}^{V}}^{S} + \sum_{k=1}^{k-1} N_{ST,k}\big) + y_{ST,CO2,k+1} N_{ST,k} - N_{ST,CO2,k}\big] \quad (21)$$

$$\dot{T}_{ST,k}^{V} = \frac{1}{Cp_{IG}^{V} M_{ST,k}^{V}}\big[\big(\widehat{H}_{ST,k+1}^{V} - \widehat{H}_{ST,k}^{V}\big)\big(u_5 {F_{V5}^{V}}^{S} + \sum_{k=1}^{k-1} N_{ST,k}\big) + \widehat{H}_{ST,k+1}^{V} N_{ST,k} - N_{ST,H,k}\big] \quad (22)$$

Lean Storage Tank

The lean storage tank is modeled as a single-phase well-mixed tank and is given in Equations 23–24. No energy balance is shown because of the perfect condenser assumption.

$$\dot{l}_{LS}^{L} = \frac{4}{\pi {D_{LS}}^2 C_{LS}^{L}}\Big[F_{Makeup}^{L} - \frac{1}{\varepsilon_m} {N_{AB,CO2,k=1}}^{S}(\omega_4 u_4 - u_1)\Big] \quad (23)$$

$$\dot{x}_{LS,i} = \frac{4}{\pi {D_{LS}}^2 C_{LS}^{L} l_{LS}^{L}}\Big[\big(1 - x_{LS,i}\big)F_{Makeup,i}^{L} + \frac{1}{\varepsilon_m} {N_{AB,CO2,k=1}}^{S}\omega_4 u_4\big(x_{FT,i} - x_{LS,i}\big)\Big], \forall i, i \neq H_2O, N_2, O_2 \quad (24)$$

Discussion

Since the amine scrubbing system model can be represented in nonstandard singularly perturbed form, there are both fast and slow time scales associated with the state variables. A variable transformation is required to arrange the model into standard form, which will be considered in future work. It is clear from this analysis that CO_2 removal rate (or equivalently the difference between the lean and rich loadings) has a slow component associated with the overall CO_2 inventory in the system. A control strategy that attempts to achieve a desired CO_2 removal set point must account for the slow dynamics of this system output. Failing to account for the slow time scale will likely lead to an ill-conditioned controller (Baldea & Daoutidis, 2012).

There are two notable studies on plantwide control of the amine scrubbing process in the literature. Panahi et al. (2010) developed a self-optimizing control structure for an absorber, reboiled stripper, and lean storage tank, shown in Figure 4. Stripper top pressure and CO_2

removal rate are treated as process constraints that must be satisfied. The temperature control within the stripper is related to optimizing the energy performance of the process. This strategy is attempting to control the small CO_2 flux in the absorber with the large solvent flowrate in order to maintain a desired removal rate of CO_2. As discussed previously, the composition controller will likely be ill-conditioned and lead to oscillations in the process variables.

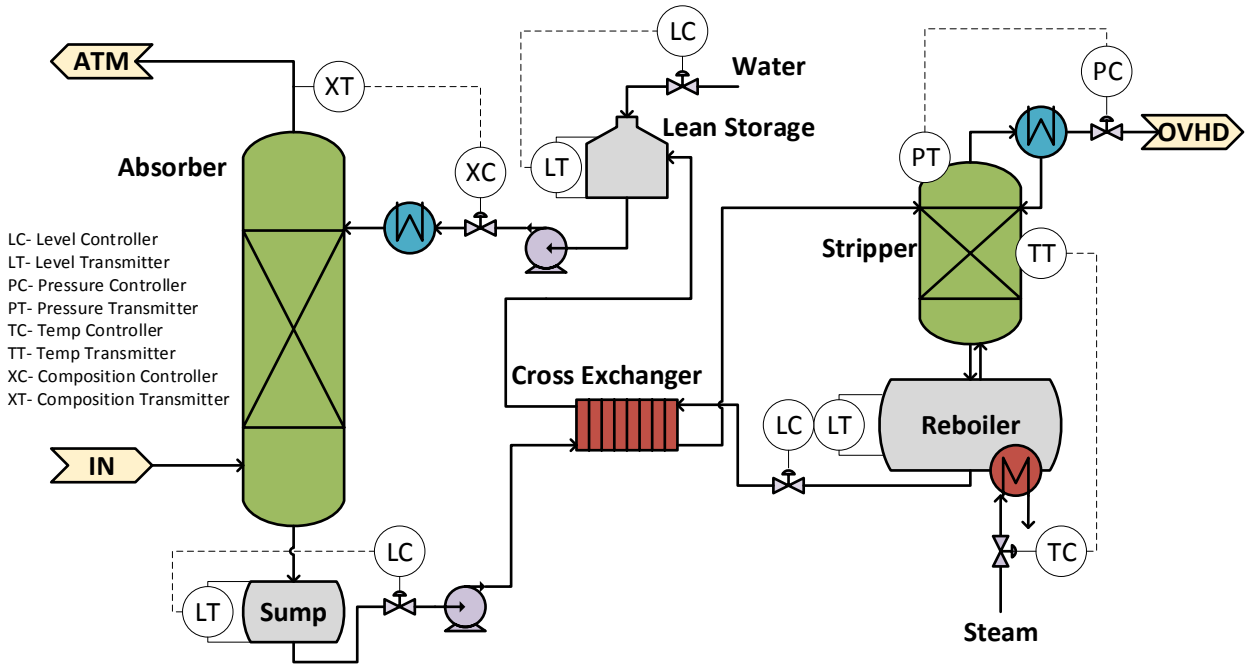

Figure 4: Control strategy proposed by Panahi et al. (2010)

Ziaii (2012) proposed a control strategy where the controlled variable set points are determined by a real time optimization for an absorber, reboiled stripper, lean storage tank, and rich storage tank, shown in Figure 5. There is no control on the removal rate of CO_2 in this strategy. In the case where there is no plant-model mismatch and no disturbances, the plant will be at the desired CO_2 removal rate. However, there is no guarantee that the desired removal rate will be achieved. Ziaii found that controlling removal rate with the recycle flow caused oscillations in the stripper top pressure, further confirming the need to consider the multiple time scale behavior of the system.

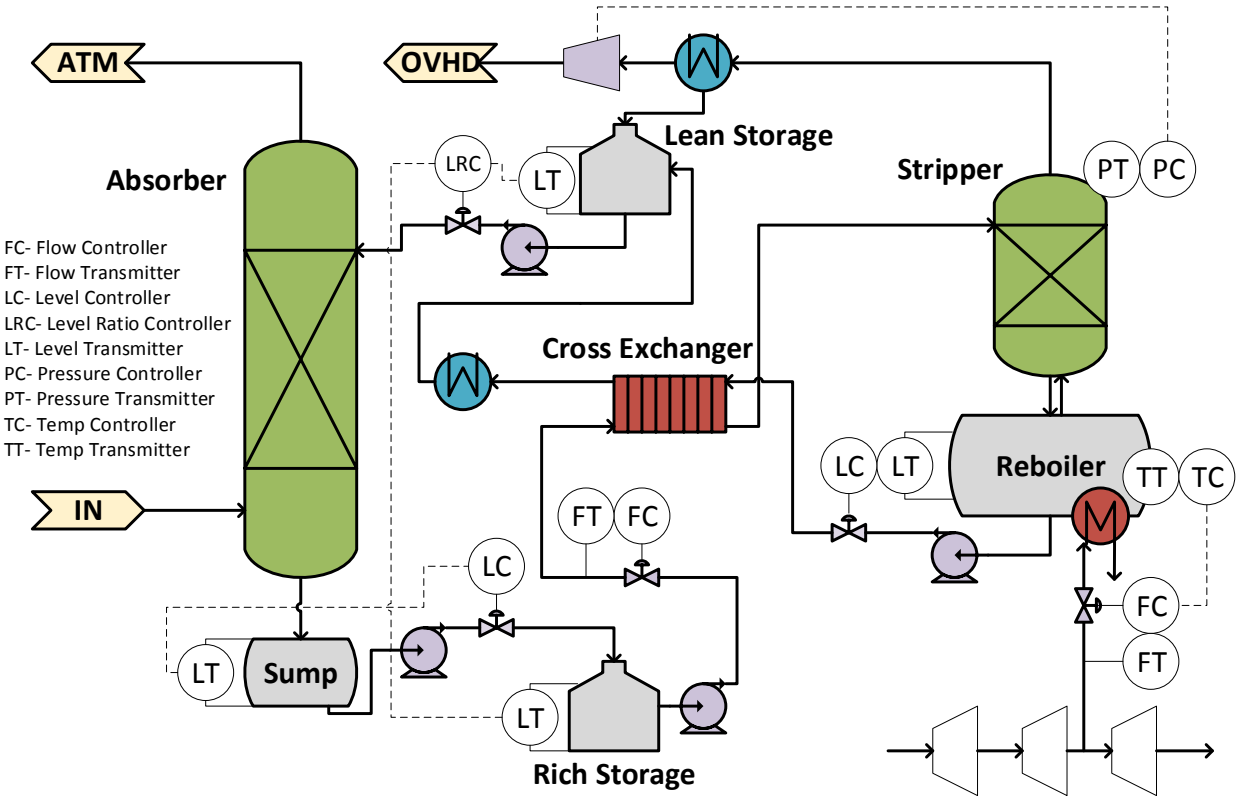

Figure 5: Control strategy proposed by Ziaii (2012)

Conclusions

- The amine scrubbing process has a fast time scale associated with large recycle flowrates and a slow time scale associated with small feed and product flowrates.
- The reduced order model of the system was shown to be in nonstandard singularly perturbed form, meaning that the state variables have both fast and slow components.
- CO_2 removal rate cannot be controlled using only the large internal recycle flow because its slow time scale is not being addressed.
- Control strategies in the literature have either avoided controlling CO_2 removal rate or have proposed a strategy that will likely lead to an ill-conditioned controller.

Future Work

- Include models for the trim cooler and overhead condenser.
- Allow flashing in the cross exchangers and explicitly model the steam heater.
- Simulate the reduced order model in MATLAB® to confirm it is adequately representing the system.
- Find a state space realization of the slow dynamics using a coordinate transformation.
- Propose a hierarchical control strategy, using the slow dynamics state space form in a model-based controller.

Notation

a	Specific area [m^2/m^3]
C	Molar density [mol/m^3]
Cp	Specific heat capacity [J/mol*K]
D	Diameter [m]
Erc	Energy recovery number [-]
F	Mole flowrate [mol/s]
H	Enthalpy [J]
$\widehat{H}$	Specific enthalpy [J/mol]
hA	Convective heat transfer coefficient multiplied by effective area [W/K]
KA	Overall mass transfer coefficient multiplied by effective area [mol/Pa*s]
L	Length [m]
l	Level [m]
M	Molar amount [mol]
N	Rate of transfer [amount/s]
Ns	Number of stages [-]
P	Pressure [Pa]
P^*	Equilibrium pressure [Pa]
Q	Heat duty [J/s]
Rc	Recycle Number [-]
T	Temperature [K]
UA	Overall heat transfer coefficient [W/K]
v	Velocity [m/s]
vf	Vapor fraction [mol/mol or kg/kg]
x	Liquid mole fraction [mol/mol]
y	Vapor mole fraction [mol/mol]
z	Bulk mole fraction [mol/mol]
Greek	
ΔH	Heat of phase change [kJ/mol]
ΔP	Pressure drop [Pa]
ΔT_{LM}	Log mean temperature difference [K]
ε	Liquid hold-up [m^3/m^3]

ε_E	Small energy flow parameter [-]
ε_M	Small mole flow parameter [-]
Subscripts	
AB	Absorber
$C\#$	Cooler or condenser
$CX\#$	Cross exchanger
E	Energy basis
FT	Flash tank
H	Enthalpy
$H\#$	Heater
i	Component
j	Component
k	Segment
l	Stream number
R	Reference
s	Steam
ST	Stripper
SU	Absorber sump
$V\#$	Valve
Superscripts	
L	Liquid phase
T	Total
V	Vapor phase

References

Baldea M, Daoutidis P. *Dynamics and Nonlinear Control of Integrated Process Systems*. New York, Cambridge University Press. 2012.

Chen X, Heidarinejad M, Liu J, Christofides PD. "Composite fast-slow MPC design for nonlinear singularly perturbed systems." *AIChE J*. 2012:58(6);1802–1811.

Kokotović P, Khalil HK, O'Rielly J. *Singular Perturbation Methods in Control: Analysis and Design*. London, Academic Press. 1986.

Panahi M, Karimi M, Skogestad S, Hillestad M, Svendsen HF. "Self-Optimizing and Control Structure Design for a CO_2 Capturing Plant." *2nd Ann Gas Proc Symp*, Qatar. 2010.

Ziaii SF. *Dynamic Modeling, Optimization, and Control of Monoethanolamine Scrubbing for CO_2 Capture*. The University of Texas at Austin. Ph.D. Dissertation. 2012.

Appendix A- ROM Equations

Differential Equations

Absorber

$$\dot{M}^L_{AB,k} = F^L_{AB,k-1} - F^L_{AB,k} + N_{AB,k} = 0 \quad (25)$$

$$\dot{M}^L_{AB,i,k} = x_{AB,i,k-1}F^L_{AB,k-1} - x_{AB,i,k}F^L_{AB,k} + N_{AB,i,k}, \forall i, i \neq H_2O, N_2, O_2 \quad (26)$$

$$\dot{H}^L_{AB,k} = \hat{H}^L_{AB,k-1}F^L_{AB,k-1} - \hat{H}^L_{AB,k}F^L_{AB,k} + N_{AB,H,k} \quad (27)$$

$$\dot{M}^V_{AB,k} = F^V_{AB,k+1} - F^V_{AB,k} - N_{AB,k} = 0 \quad (28)$$

$$\dot{M}^V_{AB,i,k} = y_{AB,i,k+1}F^V_{AB,k+1} - y_{AB,i,k}F^V_{AB,k} - N_{AB,CO2,k}, \forall i, i \neq H_2O, PZ \quad (29)$$

$$\dot{H}^V_{AB,k} = \hat{H}^V_{AB,k+1}F^V_{AB,k+1} - \hat{H}^V_{AB,k}F^V_{AB,k} - N_{AB,H,k} \quad (30)$$

Liquid equations at the top stage of the column (k = 1):

$$\dot{M}^L_{AB,k=1} = F^L_{V1} - F^L_{AB,k=1} + N_{AB,k=1} = 0 \quad (31)$$

$$\dot{M}^L_{AB,i,k=1} = x_{LS,i}F^L_{V1} - x_{AB,i,k=1}F^L_{AB,k=1} + N_{AB,i,k=1}, \forall i, i \neq H_2O, N_2, O_2 \quad (32)$$

$$\dot{H}^L_{AB,k=1} = \hat{H}^L_{TC,V1}F^L_{V1} - \hat{H}^L_{AB,k=1}F^L_{AB,k=1} + N_{AB,H,k=1} \quad (33)$$

Vapor equations at the bottom stage of the column (k = Ns):

$$\dot{M}^V_{AB,k=N_s} = F^V_{IN} - F^V_{AB,k=N_s} - N_{AB,k=N_s} = 0 \quad (34)$$

$$\dot{M}^V_{AB,i,k=N_s} = y_{IN,i}F^V_{IN} - y_{AB,i,k=N_s}F^V_{AB,k=N_s} - N_{AB,i,k=N_s}, \forall i, i \neq H_2O, PZ \quad (35)$$

$$\dot{H}^V_{AB,k=N_s} = \hat{H}^V_{IN}F^V_{IN} - \hat{H}^V_{AB,k=N_s}F^V_{AB,k=N_s} - N_{AB,H,k=N_s} \quad (36)$$

Absorber Sump

$$\dot{M}^L_{SU} = F^L_{AB,k=N_s} - F^L_{P1} \quad (37)$$

$$\dot{M}^L_{SU,i} = x_{AB,i,k=N_s}F^L_{AB,k=N_s} - x_{SU,i}F^L_{P1}, \forall i, i \neq H_2O, N_2, O_2 \quad (38)$$

$$\dot{H}^L_{SU} = \hat{H}^L_{AB,k=N_s}F^L_{AB,k=N_s} - \hat{H}^L_{SU}F^L_{P1} \quad (39)$$

Cross Exchanger #1

$$\dot{H}^L_{CX1,c} = \left(\hat{H}^L_{SU} - \hat{H}^L_{CX1,c}\right)(F^L_{P1} - F^L_{V2}) + N_{CX1,H} \quad (40)$$

$$\dot{H}^L_{CX1,h} = \left(\hat{H}^L_{CX2,h} - \hat{H}^L_{CX1,h}\right)F^L_{V4} - N_{CX1,H} \quad (41)$$

Cross Exchanger #2

$$\dot{H}^L_{CX2,c} = \left(\hat{H}^L_{CX1,c} - \hat{H}^L_{CX2,c}\right)(F^L_{P1} - F^L_{V2} - F^L_{V3}) + N_{CX2,H} \quad (42)$$

$$\dot{H}^L_{CX2,h} = \left(\hat{H}^L_{FT} - \hat{H}^L_{CX2,h}\right)F^L_{V4} - N_{CX2,H} \quad (43)$$

Cross Exchanger #3

$$\dot{H}^L_{CX3,c} = \left(\widehat{H}^L_{SU} - \widehat{H}^L_{CX3,c}\right)F^L_{V2} + N_{CX3,H} \tag{44}$$

$$\dot{H}^L_{CX3,h} = \left(\widehat{H}^V_{ST,k=1} - \left(1 - vf_{CX3,h}\right)\widehat{H}^L_{CX3,h} - vf_{CX3,h}\widehat{H}^V_{CX3,h}\right)F^T_{V5} - N_{CX3,H} \tag{45}$$

Steam Heater

$$\dot{H}^L_{H1} = (\widehat{H}^T_{CX2,c} - (1 - vf_{H1})\widehat{H}^L_{H1} - vf_{H1}\widehat{H}^V_{H1})(F^L_{P1} - F^L_{V2} - F^L_{V3}) + Q_{H1} \tag{46}$$

Flash Tank

$$\dot{M}^L_{FT} = (F^L_{P1} - F^L_{V2} - F^L_{V3}) + F^L_{ST,k=Ns} - F^L_{V4} - \left(F^V_{ST,k=Ns} + N_{ST,k=N_s}\right) \tag{47}$$

$$\dot{M}^L_{FT,i} = x_{SU,i}(F^L_{P1} - F^L_{V2} - F^L_{V3}) + x_{ST,i,k=Ns}F^L_{ST,k=Ns} - x_{FT,i}F^L_{V4} - y_{FT,i}\left(F^V_{ST,k=Ns} + N_{ST,k=N_s}\right), \forall i, i \neq H_2O, N_2, O_2 \tag{48}$$

$$\dot{H}^L_{FT} = \widehat{H}^T_{H1}(F^L_{P1} - F^L_{V2} - F^L_{V3}) + \widehat{H}^L_{ST,k=Ns}F^L_{ST,k=Ns} - \widehat{H}^L_{FT}F^L_{V4} - \widehat{H}^V_{FT}\left(F^V_{ST,k=Ns} + N_{ST,k=N_s}\right) \tag{49}$$

Stripper

$$\dot{M}^L_{ST,k} = F^L_{ST,k-1} - F^L_{ST,k} + N_{ST,k} = 0 \tag{50}$$

$$\dot{M}^L_{ST,i,k} = x_{ST,i,k-1}F^L_{ST,k-1} - x_{ST,i,k}F^L_{ST,k} + N_{ST,i,k}, \forall i, i \neq H_2O, N_2, O_2 \tag{51}$$

$$\dot{H}^L_{ST,k} = \widehat{H}^L_{ST,k-1}F^L_{ST,k-1} - \widehat{H}^L_{ST,k}F^L_{ST,k} + N_{ST,H,k} \tag{52}$$

$$\dot{M}^V_{ST,k} = F^V_{ST,k+1} - F^V_{ST,k} - N_{ST,k} = 0 \tag{53}$$

$$\dot{M}^V_{ST,CO2,k} = y_{ST,CO2,k+1}F^V_{ST,k+1} - y_{ST,CO2,k}F^V_{ST,k} - N_{ST,CO2,k} \tag{54}$$

$$\dot{H}^V_{ST,k} = \widehat{H}^V_{ST,k+1}F^V_{ST,k+1} - \widehat{H}^V_{ST,k}F^V_{ST,k} - N_{ST,H,k} \tag{55}$$

Equations at the top stage of the column (k = 1):

$$\dot{M}^L_{ST,k=1} = F^L_{V2} + F^L_{V3} - F^L_{ST,k=1} + N_{ST,k=1} = 0 \tag{56}$$

$$\dot{M}^L_{ST,i,k=1} = x_{SU,i}(F^L_{V2} + F^L_{V3}) - x_{ST,i,k=1}F^L_{ST,k=1} + N_{ST,i,k=1}, \forall i, i \neq H_2O, N_2, O_2 \tag{57}$$

$$\dot{H}^L_{ST,k=1} = \widehat{H}^L_{CX3,c}F^L_{V2} + \widehat{H}^L_{CX1,c}F^L_{V3} + N_{ST,H,k=1} - \widehat{H}^L_{ST,k=1}F^L_{ST,k=1} \tag{58}$$

$$\dot{M}^V_{ST,k=1} = F^V_{ST,k=2} - F^V_{V4} - N_{ST,k=1} = 0 \tag{59}$$

$$\dot{M}^V_{ST,CO2,k=1} = y_{ST,CO2,k=2}F^V_{ST,k=2} - y_{ST,CO2,k=1}F^V_{V4} - N_{ST,CO2,k=1} \tag{60}$$

$$\dot{H}^V_{ST,k=1} = \widehat{H}^V_{ST,k=2}F^V_{ST,k=2} - \widehat{H}^V_{ST,k=1}F^V_{V4} - N_{ST,H,k=1} \tag{61}$$

Equations at the bottom stage of the column (k = Ns):

$$\dot{M}^V_{ST,k=N_s} = F^V_{ST,k=N_s} - F^V_{ST,k} - N_{ST,k=N_s} = 0 \tag{62}$$

$$\dot{M}^V_{ST,CO2,k=N_s} = \left(y_{FT,CO2} - y_{ST,CO2,k=N_s}\right)F^V_{ST,k=N_s} + y_{FT,CO2}N_{ST,k=N_s} - N_{ST,CO2,k=N_s} \tag{63}$$

$$\dot{H}^V_{ST,k=N_s} = \left(\widehat{H}^V_{FT} - \widehat{H}^V_{AB,k=N_s}\right)F^V_{AB,k=N_s} + \widehat{H}^V_{FT}N_{ST,k=N_s} - N_{ST,H,k=N_s} \quad (64)$$

Lean Storage Tank

$$\dot{M}^L_{LS} = F^L_{V4} + F^L_{Makeup} - F^L_{V1} \quad (65)$$

$$\dot{M}^L_{LS,i} = x_{FT,i}F^L_{V4} + F^L_{Makeup,i} - x_{LS,i}F^L_{V1}, \forall i, i \neq H_2O, N_2, O_2 \quad (66)$$

Algebraic Relations

$$M^L_i = x_i M^L \quad (67)$$

$$M^V_i = y_i M^V \quad (68)$$

$$H^L = \widehat{H}^L M^L \quad (69)$$

$$H^V = \widehat{H}^V M^V \quad (70)$$

$$P^*_{CO2} = \exp\left[35.3 + \frac{-11054}{\mathrm{T}^L} - 18.9\left(\frac{x_{CO_2}}{2x_{PZ}}\right)^2 + \frac{4958}{\mathrm{T}^L}\left(\frac{x_{CO_2}}{2x_{PZ}}\right) + \frac{10163}{\mathrm{T}^L}\left(\frac{x_{CO_2}}{2x_{PZ}}\right)^2\right] \quad (71)$$

$$P^*_{H2O} = \left(\frac{1-x_{CO_2}-x_{PZ}}{1-x_{CO_2}}\right)\exp\left[73.649 - \frac{7258.2}{\mathrm{T}^L} - 7.3037ln(\mathrm{T}^L) + \left(4.1653\mathrm{E}{-}6\right)(\mathrm{T}^L)^2\right] \quad (72)$$

$$P^*_i = 0, \forall i, i \neq CO_2, H_2O \quad (73)$$

$$P_i = y_i P \quad (74)$$

$$N_i = \frac{\pi D^2 L}{4}K_i A(P_i - P^*_i), i = CO_2, H_2O \quad (75)$$

$$N_i = 0, \forall i, i \neq CO_2, H_2O$$

$$N = N_{CO2} + N_{H2O} \quad (76)$$

$$\widehat{H}^L = -x_{CO2}\Delta H_{CO2} - (1 - x_{CO2} - x_{PZ})\Delta H_{H2O} + Cp^L\left(\mathrm{T}^L - T_{ref}\right) \quad (77)$$

$$\widehat{H}^V = Cp^V\left(\mathrm{T}^V - T_{ref}\right) \quad (78)$$

$$N_{AB\ or\ ST,H} = \widehat{H}^V N + \frac{\pi D^2 L}{4}hA\left(T^V_{AB,k} - T^L_{AB,k}\right) \quad (79)$$

$$N_{CX,H} = UA\Delta T_{LM}$$

$$M^L = \frac{\pi D^2 C^L}{4}l \quad (80)$$

$$P_{FT} = P^*_{FT,CO2} + P^*_{FT,H2O} \quad (81)$$

$$y_{FT,CO2} = \frac{P^*_{FT,CO_2}}{P_{FT}} \quad (82)$$

$$\widehat{H}^L_{FT} = -x_{FT,CO2}\Delta H_{CO2} - \left(1 - x_{FT,CO2} - x_{FT,PZ}\right)\Delta H_{H2O} + Cp^L\left(T_{FT} - T_{ref}\right) \quad (83)$$

$$\widehat{H}^V_{FT} = y_{FT,CO2}Cp^V_{CO2}\left(T_{FT} - T_{ref}\right) + (1 - y_{FT,CO2})Cp^V_{H2O}\left(T_{FT} - T_{ref}\right) \quad (84)$$

Appendix B- ROM in Nonlinear State Space Form

Some algebraic variables have not been substituted for conciseness, but all algebraic variables that remain are explicit functions of the states.

Absorber

$$\dot{x}_{AB,i,k} = \frac{1}{M^L_{AB}}\left[x_{AB,i,k-1}\left(F^L_{V1} + \sum_{k=1}^{k-1} N_{AB,k}\right) - x_{AB,i,k}\left(F^L_{V1} + \sum_{k=1}^{k} N_{AB,k}\right) + N_{AB,i,k}\right], \forall i, i \neq H_2O, N_2, O_2 \quad (85)$$

$$\dot{T}^L_{AB,k} = \frac{1}{Cp^L M^L_{AB}}\left[\widehat{H}^L_{AB,k-1}\left(F^L_{V1} + \sum_{k=1}^{k-1} N_{AB,k}\right) - \widehat{H}^L_{AB,k}\left(F^L_{V1} + \sum_{k=1}^{k} N_{AB,k}\right) + N_{AB,H,k}\right] + \frac{1}{Cp^L}\left[(\Delta H_{CO2} - \Delta H_{H2O})\dot{x}_{AB,CO2,k} - \Delta H_{H2O}\dot{x}_{AB,PZ,k}\right] \quad (86)$$

$$\dot{y}_{AB,i,k} = \frac{1}{M^V_{AB,k}}\left[y_{AB,i,k+1}\left(F^V_{IN} - \sum_{k=k+1}^{N_s} N_{AB,k}\right) - y_{AB,i,k}\left(F^V_{IN} - \sum_{k=k}^{N_s} N_{AB,k}\right) - N_{AB,i,k}\right], \forall i, i \neq H_2O, PZ \quad (87)$$

$$\dot{T}^V_{AB,k} = \frac{1}{Cp^V_{IG} M^V_{AB,k}}\left[\widehat{H}^V_{AB,k+1}\left(F^V_{IN} - \sum_{k=k+1}^{N_s} N_{AB,k}\right) - N_{AB,H,k} - \widehat{H}^V_{AB,k}\left(F^V_{IN} - \sum_{k=k}^{N_s} N_{AB,k}\right)\right] \quad (88)$$

Liquid equations at the top stage of the column (k = 1):

$$\dot{x}_{AB,i,k=1} = \frac{1}{M^L_{AB}}\left[x_{LS,i}F^L_{V1} - x_{AB,i,k=1}\left(F^L_{V1} + N_{AB,k=1}\right) + N_{AB,i,k=1}\right], \forall i, i \neq H_2O, N_2, O_2 \quad (89)$$

$$\dot{T}^L_{AB,k=1} = \frac{1}{Cp^L M^L_{AB}}\left[\widehat{H}^L_{TC,V1}F^L_{V1} - \widehat{H}^L_{AB,k=1}\left(F^L_{V1} + N_{AB,k=1}\right) + N_{AB,H,k=1}\right] + \frac{1}{Cp^L}\left[(\Delta H_{CO2} - \Delta H_{H2O})\dot{x}_{AB,CO2,k=1} - \Delta H_{H2O}\dot{x}_{AB,PZ,k=1}\right] \quad (90)$$

Vapor equations at the bottom stage of the column (k = Ns):

$$\dot{y}_{AB,i,k=N_s} = \frac{1}{M^V_{AB,k=N_s}}\left[y_{IN,i}F^V_{IN} - y_{AB,i,k=N_s}\left(F^V_{IN} - N_{AB,k=N_s}\right) - N_{AB,CO2,k=N_s}\right], \forall i, i \neq H_2O, PZ \quad (91)$$

$$\dot{T}^V_{AB,k=N_s} = \frac{1}{Cp^V_{IG} M^V_{AB,k=N_s}}\left[\widehat{H}^V_{IN}F^V_{IN} - N_{AB,H,k=N_s} - \widehat{H}^V_{AB,k=N_s}\left(F^V_{IN} - N_{AB,k=N_s}\right)\right] \quad (92)$$

Absorber Sump

$$l^L_{SU} = \frac{4}{\pi {D_{SU}}^2 C^L_{SU}}\left[\left(F^L_{V1} + \sum_{k=1}^{N_s} N_{AB,k}\right) - F^L_{P1}\right] \quad (93)$$

$$\dot{x}_{SU,i} = \frac{4}{\pi {D_{SU}}^2 C^L_{SU} l^L_{SU}}\left[\left(x_{AB,i,k=N_s} - x_{SU,i}\right)\left(F^L_{V1} + \sum_{k=1}^{N_s} N_{AB,k}\right)\right], \forall i, i \neq H_2O, N_2, O_2 \quad (94)$$

$$\dot{T}^L_{SU} = \frac{4}{\pi {D_{SU}}^2 C^L_{SU} l^L_{SU} Cp^L}\left[\left(\widehat{H}^L_{AB,k=N_s} - \widehat{H}^L_{SU}\right)\left(F^L_{V1} + \sum_{k=1}^{N_s} N_{AB,k}\right)\right] + \frac{1}{Cp^L}\left[(\Delta H_{CO2} - \Delta H_{H2O})\dot{x}_{SU,CO2} - \Delta H_{H2O}\dot{x}_{SU,PZ}\right] \quad (95)$$

Cross Exchanger #1

$$\dot{T}^L_{CX1,c} = \frac{1}{Cp^L M^L_{CX1,c}}\left[\left(\widehat{H}^L_{SU} - \widehat{H}^L_{CX1,c}\right)\left(F^L_{P1} - F^L_{V2}\right) + N_{CX1,H}\right] + \frac{1}{Cp^L}\left[\left(\Delta H_{CO2} - \Delta H_{H2O}\right)\dot{x}_{SU,CO2} - \Delta H_{H2O}\dot{x}_{SU,PZ}\right] \quad (96)$$

$$\dot{T}^L_{CX1,h} = \frac{1}{Cp^L M^L_{CX1,h}}\left[\left(\widehat{H}^L_{CX2,h} - \widehat{H}^L_{CX1,h}\right)F^L_{V4} - N_{CX1,H}\right] + \frac{1}{Cp^L}\left[\left(\Delta H_{CO2} - \Delta H_{H2O}\right)\dot{x}_{FT,CO2} - \Delta H_{H2O}\dot{x}_{FT,PZ}\right] \quad (97)$$

Cross Exchanger #2

$$\dot{T}^L_{CX2,c} = \frac{1}{Cp^L M^L_{CX2,c}}\left[\left(\widehat{H}^L_{CX1,c} - \widehat{H}^L_{CX2,c}\right)\left(F^L_{P1} - F^L_{V2} - F^L_{V3}\right) + N_{CX2,H}\right] + \frac{1}{Cp^L}\left[\left(\Delta H_{CO2} - \Delta H_{H2O}\right)\dot{x}_{SU,CO2} - \Delta H_{H2O}\dot{x}_{SU,PZ}\right] \quad (98)$$

$$\dot{T}^L_{CX2,h} = \frac{1}{Cp^L M^L_{CX2,h}}\left[\left(\widehat{H}^L_{FT} - \widehat{H}^L_{CX2,h}\right)F^L_{V4} - N_{CX2,H}\right] + \frac{1}{Cp^L}\left[\left(\Delta H_{CO2} - \Delta H_{H2O}\right)\dot{x}_{FT,CO2} - \Delta H_{H2O}\dot{x}_{FT,PZ}\right] \quad (99)$$

Cross Exchanger #3

$$\dot{T}^L_{CX3,c} = \frac{1}{Cp^L M^L_{CX3,c}}\left[\left(\widehat{H}^L_{SU} - \widehat{H}^L_{CX3,c}\right)F^L_{V2} + N_{CX3,H}\right] + \frac{1}{Cp^L}\left[\left(\Delta H_{CO2} - \Delta H_{H2O}\right)\dot{x}_{SU,CO2} - \Delta H_{H2O}\dot{x}_{SU,PZ}\right] \quad (100)$$

$$\dot{T}^T_{CX3,h} = \frac{1}{Cp^L M^L_{CX3,h}}\left[\widehat{H}^V_{ST,k=1}F^T_{V5} - \widehat{H}^L_{CX3,h}\left(1 - vf_{CX3,h}\right)F^T_{V5} - \widehat{H}^V_{CX3,h}vf_{CX3,h}F^T_{V5} - N_{CX3,H}\right] + \frac{1}{Cp^L}\left[\left(\Delta H_{CO2} - \Delta H_{H2O}\right)\dot{x}_{ST,CO2,k=1} - \Delta H_{H2O}\dot{x}_{ST,PZ,k=1}\right] \quad (101)$$

Steam Heater

$$\dot{T}^T_{H1} = \frac{1}{Cp^L M^L_{H1}}\left[\left(\widehat{H}^T_{CX2,c} - (1 - vf_{H1})\widehat{H}^L_{H1} - vf_{H1}\widehat{H}^V_{H1}\right)\left(F^L_{P1} - F^L_{V2} - F^L_{V3}\right) + Q_{H1}\right] + \frac{1}{Cp^L}\left[\left(\Delta H_{CO2} - \Delta H_{H2O}\right)\dot{x}_{SU,k=1} - \Delta H_{H2O}\dot{x}_{SU,k=1}\right] \quad (102)$$

Flash Tank

$$\dot{l}^L_{FT} = \frac{4}{\pi {D_{FT}}^2 C^L_{FT}}\left[F^L_{P1} - F^L_{V4} - F^V_{V5}\right] \quad (103)$$

$$\dot{x}_{FT,i} = \frac{4}{\pi {D_{FT}}^2 C^L_{FT} l^L_{FT}}\left[\left(x_{SU,i} - x_{FT,i}\right)F^L_{P1} + \left(x_{ST,CO2,k=Ns} - x_{SU,CO2}\right)\left(F^L_{V2} + F^L_{V3}\right) + \left(x_{ST,CO2,k=Ns} - y_{FT,CO2}\right)\sum_{k=1}^{N_s} N_{ST,k} + \left(x_{FT,CO2} - y_{FT,CO2}\right)F^V_{V5}\right], \forall i, i \neq H_2O, N_2, O_2 \quad (104)$$

$$\dot{T}^L_{FT} = \frac{4}{\pi {D_{FT}}^2 C^L_{FT} l^L_{FT} Cp^L}\left[\left(\widehat{H}^T_{CX2,c} - \widehat{H}^L_{FT}\right)F^L_{P1} + \left(\widehat{H}^L_{ST,k=Ns} - \widehat{H}^T_{H1}\right)\left(F^L_{V2} + F^L_{V3}\right) + \left(\widehat{H}^L_{ST,k=Ns} - \widehat{H}^V_{FT}\right)\sum_{k=1}^{N_s} N_{ST,k} + \left(\widehat{H}^L_{FT} - \widehat{H}^V_{FT}\right)F^V_{V5}\right] + \frac{1}{Cp^L}\left[\left(\Delta H_{CO2} - \Delta H_{H2O}\right)\dot{x}_{FT,CO2} - \Delta H_{H2O}\dot{x}_{FT,PZ}\right] \quad (105)$$

Stripper

$$\dot{x}_{ST,i,k} = \frac{1}{M^L_{ST}}\left[x_{ST,i,k-1}\left(F^L_{V2} + F^L_{V3} + \sum_{k=1}^{k-1} N_{ST,k}\right) - x_{ST,i,k}\left(F^L_{V2} + F^L_{V3} + \sum_{k=1}^{k} N_{ST,k}\right) + N_{ST,i,k}\right], \forall i, i \neq H_2O, N_2, O_2 \quad (106)$$

$$\dot{T}^L_{ST,k} = \frac{1}{Cp^L M^L_{ST}}\left[\widehat{H}^L_{ST,k-1}\left(F^L_{V2} + F^L_{V3} + \sum_{k=1}^{k-1} N_{ST,k}\right) + N_{ST,H,k} - \widehat{H}^L_{ST,k}\left(F^L_{V2} + F^L_{V3} + \sum_{k=1}^{k} N_{ST,k}\right)\right] + \frac{1}{Cp^L}\left[(\Delta H_{CO2} - \Delta H_{H2O})\dot{x}_{ST,CO2,k} - \Delta H_{H2O}\dot{x}_{ST,PZ,k}\right] \quad (107)$$

$$\dot{y}_{ST,CO2,k} = \frac{1}{M^V_{ST,k}}\left[y_{ST,CO2,k+1}\left(F^V_{V5} + \sum_{k=1}^{k} N_{ST,k}\right) - y_{ST,CO2,k}\left(F^V_{V5} + \sum_{k=1}^{k-1} N_{ST,k}\right) - N_{ST,CO2,k}\right] \quad (108)$$

$$\dot{T}^V_{ST,k} = \frac{1}{Cp^V_{IG} M^V_{ST,k}}\left[\widehat{H}^V_{ST,k+1}\left(F^V_{V5} + \sum_{k=1}^{k} N_{ST,k}\right) - N_{ST,H,k} - \widehat{H}^V_{ST,k}\left(F^V_{V5} + \sum_{k=1}^{k-1} N_{ST,k}\right)\right] \quad (109)$$

Equations at the top stage of the column (k = 1):

$$\dot{x}_{ST,i,k=1} = \frac{1}{M^L_{ST}}\left[x_{SU,i}(F^L_{V2} + F^L_{V3}) - x_{ST,i,k=1}\left(F^L_{V2} + F^L_{V3} + N_{ST,k=1}\right) + N_{ST,i,k=1}\right], \forall i, i \neq H_2O, N_2, O_2 \quad (110)$$

$$\dot{T}^L_{ST,k=1} = \frac{1}{Cp^L M^L_{ST}}\left[\widehat{H}^L_{CX3,c} F^L_{V2} + \widehat{H}^L_{CX1,c} F^L_{V3} + N_{ST,H,k=1} - \widehat{H}^L_{ST,k=1}\left(F^L_{V2} + F^L_{V3} + N_{ST,k=1}\right)\right] + \frac{1}{Cp^L}\left[(\Delta H_{CO2} - \Delta H_{H2O})\dot{x}_{ST,CO2,k=1} - \Delta H_{H2O}\dot{x}_{ST,PZ,k=1}\right] \quad (111)$$

$$\dot{y}_{ST,CO2,k=1} = \frac{1}{M^V_{ST,k=1}}\left[y_{ST,CO2,k=2}\left(F^V_{V5} + N_{ST,k=1}\right) - y_{ST,CO2,k=1} F^V_{V5} - N_{ST,CO2,k=1}\right] \quad (112)$$

$$\dot{T}^V_{ST,k=1} = \frac{1}{Cp^V_{IG} M^V_{ST,k=1}}\left[\widehat{H}^V_{ST,k=2}\left(F^V_{V5} + N_{ST,k=1}\right) - N_{ST,H,k=1} - \widehat{H}^V_{ST,k=1} F^V_{V5}\right] \quad (113)$$

Equations at the bottom stage of the column (k = Ns):

$$\dot{y}_{ST,CO2,k=N_s} = \frac{1}{M^V_{ST,k=N_s}}\left[\left(y_{FT,CO2} - y_{ST,CO2,k=N_s}\right)\left(F^V_{V5} + \sum_{k=1}^{N_s-1} N_{ST,k}\right) + y_{FT,CO2} N_{ST,k=N_s} - N_{ST,CO2,k=N_s}\right] \quad (114)$$

$$\dot{T}^V_{ST,k=N_s} = \frac{1}{Cp^V_{IG} M^V_{ST,k=N_s}}\left[\left(\widehat{H}^V_{FT} - \widehat{H}^V_{AB,k=N_s}\right)\left(F^V_{V4} + \sum_{k=1}^{N_s-1} N_{ST,k}\right) + \widehat{H}^V_{FT} N_{ST,k=N_s} - N_{ST,H,k=N_s}\right] \quad (115)$$

Lean Storage Tank

$$\dot{l}^L_{LS} = \frac{4}{\pi {D_{LS}}^2 C^L_{LS}}\left[F^L_{V4} + F^L_{Makeup} - F^L_{V1}\right] \quad (116)$$

$$\dot{x}_{LS,i} = \frac{4}{\pi {D_{LS}}^2 C^L_{LS} l^L_{LS}}\left[\left(x_{FT,i} - x_{LS,i}\right)F^L_{V4} + (1 - x_{LS,i})F^L_{Makeup,i}\right], \forall i, i \neq H_2O, N_2, O_2 \quad (117)$$

Thermal Degradation of PZ-Activated Tertiary Morpholine Solvents for Carbon Capture from Coal Combustion and Gas Treating

Quarterly Report for April 1 – June 30, 2014

by Omkar Namjoshi

Supported by the Texas Carbon Management Program

McKetta Department of Chemical Engineering

The University of Texas at Austin

July 31, 2014

Abstract

The thermal degradation of piperazine (PZ)-activated tertiary morpholine blends in the presence of CO_2 as well as H^+ at 150 °C was studied this quarter. In addition the thermal degradation of unpromoted tertiary morpholine solvents in the presence of H^+ at 150 °C was studied. The initial composition of the solvent under CO_2-loaded conditions was 5 m PZ/5 m tertiary morpholine at a loading of 0.22 mol CO_2/mol alkalinity. The initial composition of the solvent under H^+-loaded conditions was 2.5 m PZ/2.5 m tertiary morpholine at a loading of 0.137 mol H^+/mol alkalinity. The composition of the unpromoted tertiary morpholine solvents was initially 5 m tertiary morpholine with an initial acid loading of 0.198 mol H^+/mol alkalinity. The tertiary morpholines that were tested included hydroxyethylmorpholine (HEM), hydroxypropylmorpholine (HPM), and hydroxyisopropylmorpholine (HIPM).

The thermal degradation rate for the PZ-activated tertiary morpholine solvents in the presence of CO_2 is as follows: HEM ($11*10^{-9}$ sec^{-1} for the tertiary morpholine, and $17*10^{-9}$ sec^{-1} for PZ), HIPM ($11*10^{-9}$ sec^{-1}/$14*10^{-9}$ sec^{-1}), and HPM ($5*10^{-9}$ sec^{-1}/$10*10^{-9}$ sec^{-1}). If an activation energy of 180 kJ/mol is assumed, the maximum stripper temperature for the tertiary amine blends is 154 °C for HEM/PZ, 155 °C for HIPM/PZ, and 158 °C for HPM/PZ.

The thermal degradation rate for the PZ-activated tertiary solvents in the presence of H^+ is as follows: HEM (0.01 mmol/kg/h for the tertiary morpholine, 0.01 mmol/kg/h for PZ), HIPM (0.04 mmol/kg/h/0.05 mmol/kg/h), and HPM (0.01 mmol/kg/h/0.01 mmol/kg/h). The tertiary morpholines did not degrade in the presence of H^+ and without the presence of PZ after 650 hours of exposure to 150 °C conditions.

Experimental Methods

Samples were prepared gravimetrically. The solutions were then placed inside 3/8" Swagelok® stainless steel cylinders with a 4.5 ml capacity; the cylinders were fully loaded with amine solution for acid-loaded experiments and filled to 90% of capacity for CO_2-loaded experiments. The Swagelok® cylinders were sealed and placed in forced convection ovens at set temperatures

and removed periodically for analysis. Cation chromatography (Dionex ICS-2100) was used to analyze for parent amine concentrations and degradation by-product concentrations; samples were diluted by a factor of 5000 to 10000, and the separation was carried out using a Dionex CS17 column. These methods are described in previous quarterly reports and dissertations (Rochelle, 2013) and will not be described in detail here.

Each CO_2-loaded PZ-activated tertiary morpholine was prepared with 5 m tertiary amine/5 m PZ with an initial loading of 0.22 mol CO_2/mol alkalinity. This loading corresponds to the operational lean loading of 5 m PZ/5 m MDEA when used to capture CO_2 from coal-derived flue gas. Each acid-loaded PZ-activated tertiary morpholine solvent was prepared with 2.5 m tertiary amine/2.5 m PZ with an initial loading of 0.137 mol H^+/mol alkalinity. Each unpromoted tertiary morpholine system was prepared with 5 m tertiary amine with an initial loading of 0.198 mol H^+/mol alkalinity.

The tertiary morpholines that were tested included hydroxyethylmorpholine (HEM), hydroxypropylmorpholine (HPM), and hydroxyisopropylmorpholine (HIPM). Structures of these amines are presented in Table 1.

Table 1: List of amines (names, abbreviated names, structure) tested this quarter

Amine Name Abbreviation	Molecular Weight	Structure
Hydroxyethylmorpholine HEM	131.2	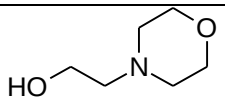
Hydroxyisopropylmorpholine HIPM	145.2	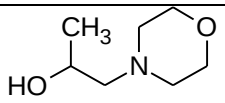
Hydroxypropylmorpholine HPM	145.2	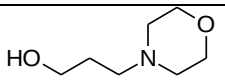
Piperazine PZ	86.1	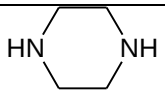

Safety

The SOP for the thermal cylinder experiments has been updated to cover amine solvents prepared with materials known to contain halogens, such as chlorides. The halogens can cause stress corrosion cracking of the metal used in the cylinder. The updated SOP is included in the quarterly report as an attachment.

Results & Discussion

Table 2 shows the pseudo-first-order degradation constant for the PZ-activated tertiary morpholines in addition to PZ-activated methyldiethanolamine (MDEA), diethylaminoethanol (DEAE), and triethanolamine (TEA) at 5 m PZ/5 m tertiary amine and loading of about 0.23 mol

CO_2/mol alkalinity at 150 °C. For reference, the pseudo-first-order degradation rate of 8 m PZ at 150 °C and an initial loading of 0.3 mol CO_2/mol alkalinity is $6.1*10^{-9}$ sec^{-1}. The maximum stripper temperature, which corresponds to the stripper temperature for a 2% amine loss per week, is also presented in Table 2. The activation energy of thermal degradation used to estimate the maximum stripper temperature was assumed to be 180 kJ/mol for the tertiary morpholine/PZ blends; this value is consistent with the activation energy of thermal degradation of concentrated PZ solutions.

Table 2: Pseudo-First-Order Degradation Rate Constants and Maximum Stripper Temperatures of PZ/Tertiary Amine Blends. Conditions: 5 m PZ/5 m Tertiary Amine, 0.23 mol CO_2/mol alkalinity, 150 °C.

Tertiary Amine in Blend	k_1, PZ, $1/s*10^9$	k_1, Tertiary Amine, $1/s*10^9$	Maximum Stripper Temperature	Activation Energy, kJ/mol PZ/Tert Amine
HEM	17	11	154 °C	180/180
HIPM	14	11	155 °C	180/180
HPM	5	6	158 °C	180/180
MDEA	780	330	117 °C	140/139
DEAE	260	170	132 °C	175/168
TEA	280	160	130 °C	169/190

The results show that the PZ-activated tertiary morpholine solvents have a similar rate of thermal degradation to concentrated PZ and are at least one to two orders of magnitude more stable than PZ-activated MDEA, DEAE, and TEA. Unlike the tertiary morpholines, MDEA, DEAE, and TEA are all aliphatic tertiary amine solvents and do not have the nitrogen bound within a heterocycle. The degradation data for PZ/HEM and PZ/MDEA are plotted in Figure 1.

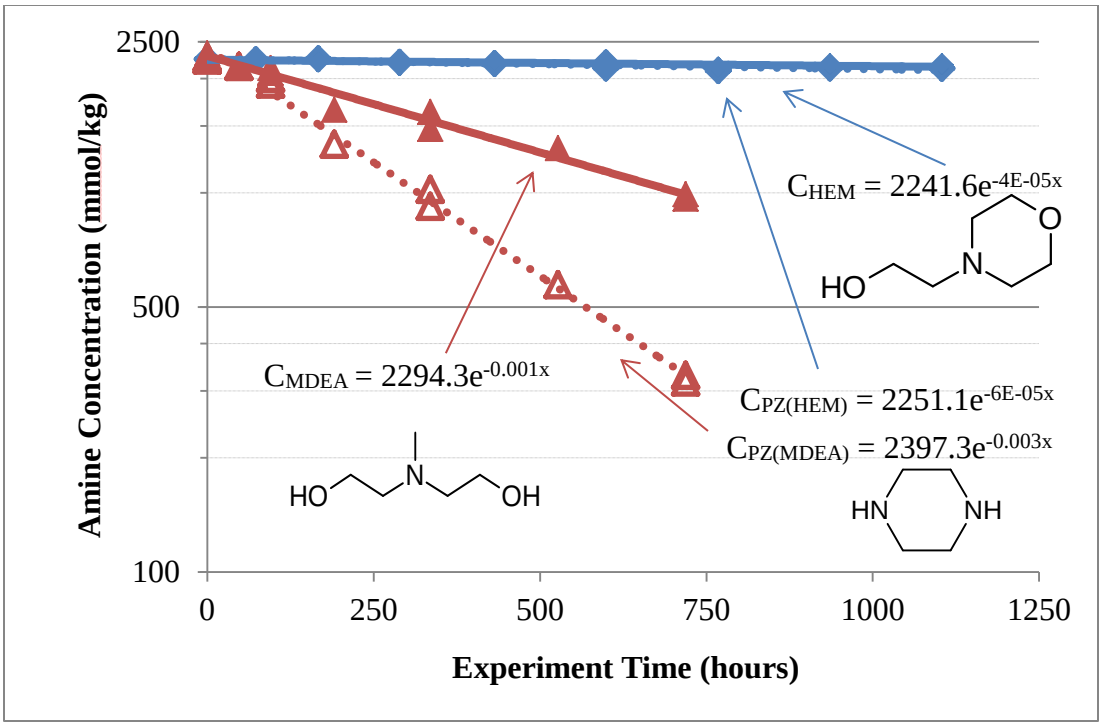

Figure 1: Degradation of PZ/HEM and PZ/MDEA at 150 °C at an initial concentration of 5 m PZ/5 m Tertiary Amine and loading of 0.23 mol CO_2/mol alkalinity. The PZ/HEM blend is resistant to thermal degradation, whereas the PZ/MDEA blend is not thermally stable.

The degradation mechanism of PZ-activated tertiary morpholines is thought to be initiated by a free PZ molecule attacking a carbon alpha to a protonated amino group on the tertiary morpholine ring, opening the ring and creating a triamine byproduct. This is shown in Figure 2.

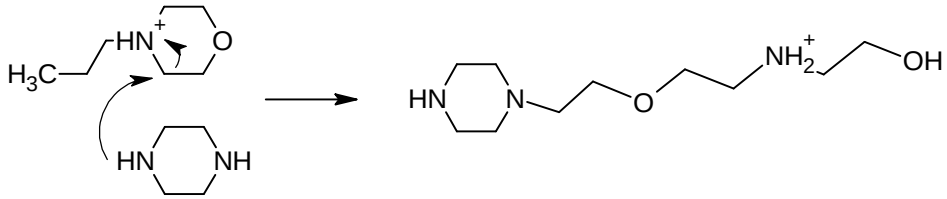

Figure 2: Initial Triamine Degradation Product Pathway between PZ and the Tertiary Morpholine (hydroxyethyl morpholine shown)

The triamine byproduct can undergo several different reactions. It can ring close to regenerate a PZ molecule and a tertiary morpholine, shown in Figure 3. This reaction is essentially the reverse of the reaction shown in Figure 2. The triamine can also form an oxazolidinone and react with free PZ via the carbamate polymerization pathway. These reactions are shown in Figure 4, and the overall degradation rate of PZ and tertiary morpholine suggest that the rate of reaction in Figure 3 is much faster than the rate of reaction in Figure 4. In particular, the reaction between the PZ and the oxazolidinone is a reason why the rate of PZ degradation is greater than the rate of tertiary amine degradation in the presence of CO_2.

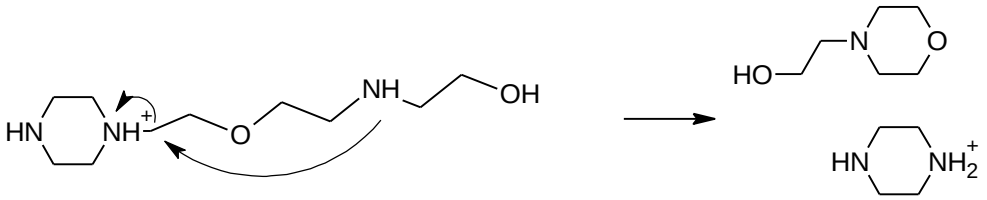

Figure 3: Ring Closing of Triamine to Generate PZ and the Tertiary Morpholine (hydroxyethyl morpholine shown)

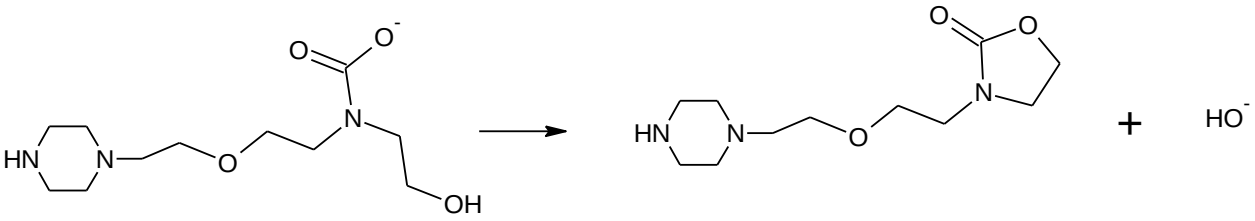

Figure 4: Irreversible Carbamate Polymerization Degradation Pathway between the Triamine Carbamate and PZ

The net rate of the reaction shown in Figure 2 is much slower than S_N2 attack of alkyl substituent groups attached to protonated tertiary amines, which is the primary degradation pathway seen in activated MDEA and DEAE solvents. This could be due to either the stability of the carbons alpha to the amino function within the ring or to the instability of the triamine to regenerate both parent amines.

Morpholine was present in degraded solutions of PZ-activated tertiary morpholines. However, the quantity of morpholine in degraded samples is too small to be quantified, and suggests that alpha carbon attack on the substituent group likely is not significant.

Table 3 shows the pseudo-zeroth-order degradation rate for the PZ-activated tertiary morpholines in addition to PZ-activated methyldiethanolamine (MDEA), diethylaminoethanol (DEAE), and triethanolamine (TEA) at an initial concentration of 5 m PZ/5 m tertiary amine and loading of about 0.14 mol H^+/mol alkalinity at 150 °C.

Table 3: Pseudo-First-Order Degradation Rate Constants and Maximum Stripper Temperatures of PZ/Tertiary Amine Blends. Conditions: 2.5 m PZ/2.5 m Tertiary Amine, 0.14 mol H^+/mol alkalinity, 150 °C.

Tertiary Amine in Blend	k_0, Tertiary Amine, mmol/kg/h	$k_{0,PZ} / k_{0,TA}$
HEM	0.01	1.0
HIPM	0.04	1.2
HPM	0.01	1.0
MDEA	0.47	1.0
DEAE	0.15	1.0
TEA	0.13	1.0

The results show that the PZ-activated tertiary morpholine solvents are at least an order of magnitude more stable than the PZ-activated aliphatic tertiary amine solvents in the presence of H^+. The rate of PZ loss in these systems is almost identical to the rate of tertiary amine loss, suggesting that thermal degradation is initiated by the presence of a protonated amine.

The tertiary morpholines, at an initial loading of 0.198 mol H^+/mol alkalinity and an initial concentration of 5 m tertiary amine, did not show appreciable degradation at 150 °C. These data are shown in Figure 5.

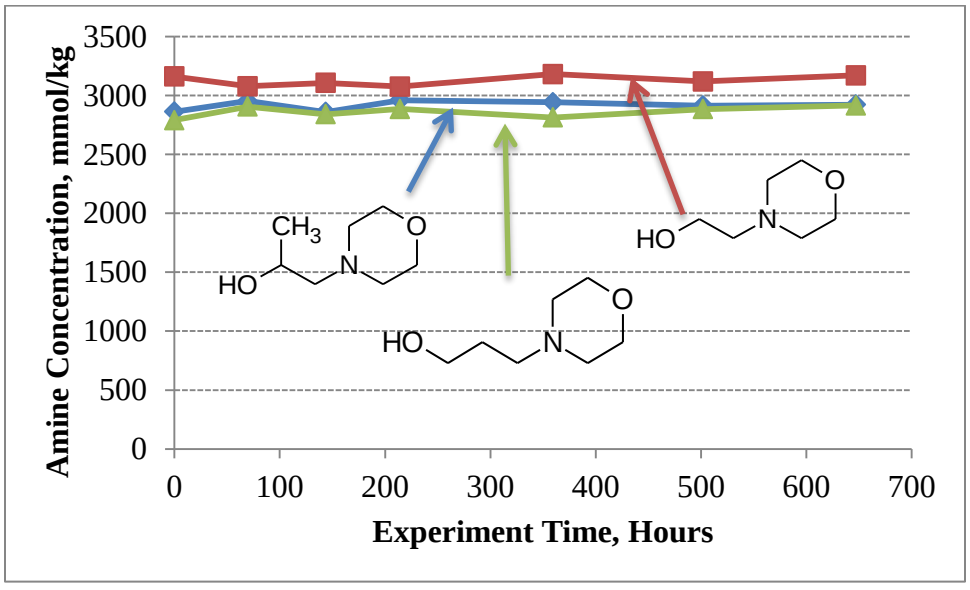

Figure 5: Degradation of 5 m Tertiary Morpholine at 150 °C and an acid loading of 0.198 mol H^+/mol alkalinity. None of the tertiary morpholine solvents tested show quantifiable degradation at the experiment conditions.

Conclusions

1. The thermal degradation rate for the PZ-activated tertiary morpholine solvents in the presence of CO_2 is as follows: HEM ($11*10^{-9}$ sec^{-1} for the tertiary morpholine, and $17*10^{-9}$ sec^{-1} for PZ), HIPM ($11*10^{-9}$ sec^{-1} for the tertiary morpholine, and 14*10-9 sec-1 for PZ), and HPM ($5*10^{-9}$ sec^{-1} for the tertiary morpholine, and $10*10^{-9}$ sec^{-1} for PZ). If an activation energy of 180 kJ/mol is assumed, the maximum stripper temperature for the tertiary amine blends is 154 °C for HEM/PZ, 155 °C for HIPM/PZ, and 158 °C for HPM/PZ. The solvents were tested at 150 °C with an initial concentration of 5 m PZ/5 m tertiary morpholine at a loading of 0.23 mol CO_2/mol alkalinity.
2. The thermal degradation rate for the PZ-activated tertiary solvents in the presence of H^+ is as follows: HEM (0.01 mmol/kg/h for the tertiary morpholine, 0.01 mmol/kg/h for PZ), HIPM (0.04 mmol/kg/h for the tertiary morpholine, 0.05 mmol/kg/h for PZ), and HPM (0.01 mmol/kg/h for the tertiary morpholine, 0.01 mmol/kg/h for PZ) at an initial concentration of 2.5 m PZ/2.5 m tertiary morpholine and a loading of 0.14 mol H+/mol alkalinity and at 150 °C.
3. The tertiary morpholines did not degrade in the presence of H+ and without the presence of PZ after 650 hours of exposure at 150 °C at an initial concentration of 5 m tertiary morpholine at a loading of 0.198 mol H+/mol alkalinity.

Future Work

Future work will focus on rigorous kinetic modeling of MDEA and PZ/MDEA degradation in the presence of H^+.

References

Rochelle GT et al. "CO_2 Capture by Aqueous Absorption, Fourth Quarterly Progress Report 2012." Luminant Carbon Management Program. The University of Texas at Austin. 2013.

Rochelle Group

Standard Operating Practices: Handling Swagelok® Cylinders for Thermal Degradation Experiments; Revision 4 last modified 10 July 2014

by Omkar Namjoshi

Never work by yourself while preparing, tightening, or untightening cylinders. Always make sure someone else is in one of the labs.

Proper PPE must be worn while handling cylinders. This includes a lab coat, safety glasses or goggles, and nitrile gloves. Latex gloves should not be worn as latex is a poor barrier for amine solutions. Heat resistant leather gloves must be worn on top of the nitrile gloves when placing cylinders in and out of the oven.

Cylinders must be capable of handling corrosive liquids at temperatures greater than 175 °C and pressures greater than 130 barg. The 4.5 ml Swagelok® cylinders are all capable of handling this rating. These cylinders are constructed from stainless steel, are about 4" long, and have end caps and nuts that are sealed at each end of the cylinder. Catastrophic failure can occur if the cylinder is not rated for this service.

Halogens can cause stress corrosion cracking in the stainless steel tubing and fittings used in the cylinder. For this reason, cylinders used to degrade solutions with known quantities of halogens must be segregated from cylinders used to degrade solutions with other solvents. The cylinders used to degrade solutions known to contain halogens must be marked as such and discarded after one year of use.

1. Loading samples in the cylinder.
    a. Use a 10 ml pipette and place about 4 ml of solution in the cylinder (for 4.5 ml volume cylinders) if using solutions loaded with CO_2.
    b. Load cylinders in a ventilated hood for particularly volatile, toxic, or foul-smelling solutions.
2. Torquing and tightening the cylinders.
    a. There is no set value that the cylinder needs to be torqued to – Swagelok® (manufacturer of the cylinders) recommends that the cylinder be tightened between a quarter turn to half turn past hand-tight. Some cylinders cannot be tightened appreciably by hand.
    b. Once the sample is loaded in the cylinder, tighten by hand as much as possible. Weigh the cylinder mass and record. Also make a note of any markings, etc., on the cap of the cylinder that was opened – this makes it easier to open the side of the cylinder that was loosened to load solvent.
    c. Put the cylinder in the vise and clamp the vise on the nut of the cylinder as tightly as possible. If the cylinder cap does not smoothly thread into the nut by hand, use the small ratchet and, without using too much force, tighten the cylinder as tightly as you can using only the palm of your hand. The cap should thread into the nut quickly and smoothly, even for old cylinders. There will be a

point at which you have to use force to tighten the cylinder further – this is the Swagelok® definition of "hand-tight."

   d. To fully tighten and seal the cylinder, use the ratchet or a large wrench to turn the cylinder nut a quarter turn past hand-tight. Use the cylinder markings as a guide.
   e. Mark the cylinder (e.g., on the tube) each time it is used. Retire cylinders that have been used more than 5 times on each side.

3. Placing the cylinder in the oven.
   a. Make sure that the ventilation is drawing air from the convection oven prior to placing cylinders inside by ensuring that there is a net negative pressure at the inlet of the ventilation duct on the top of the oven.
   b. Open the oven. Slowly crack the open door away from the line of fire and check to see if any gases are escaping from the door. **Caution**: If there are any gases coming out, leave the door cracked slightly to allow the ventilation system to suck the ambient air through the oven so any contaminants can be vented outside. Using a leather glove, place the cylinders on one of the oven racks. Close the oven door.
   c. Keep a clear record of experiments that are being run (e.g., in a lab notebook) in a particular oven that is accessible to lab personnel as needed.
4. Removing cylinders.
   a. Using a leather glove, remove the cylinder and place it on the lab bench to cool. (For experiments with short time scales, generally less than 48 hours, cool the cylinder by quenching it in a water bath.) Record which cylinder is removed and weigh it. Use the same precautions as described in the above section when opening the oven door.
5. Opening cylinders.
   a. **Caution:** Before opening the cylinder, ensure that the cylinder has cooled to room temperature (25 °C) or below. If the cylinder has not cooled, its contents will be under pressure, and could result in loss of containment, spraying amine through
   b. Place the cylinder inside a vise (see Figure 1) and tighten the vise jaws to hold the cylinder securely. Slowly open the cylinder with a large wrench or the ratchet. Opening it slowly will relieve any residual pressure in the cylinder; opening it too quickly can also result in a containment loss. Cylinders that are pressured will generally make fizzing sounds and small amounts of liquid might leak from the seal; if this is the case, open the cylinder very slowly (e.g., speeds of 1 rpm and below) and away from the line of fire if the cylinder is pressurized.

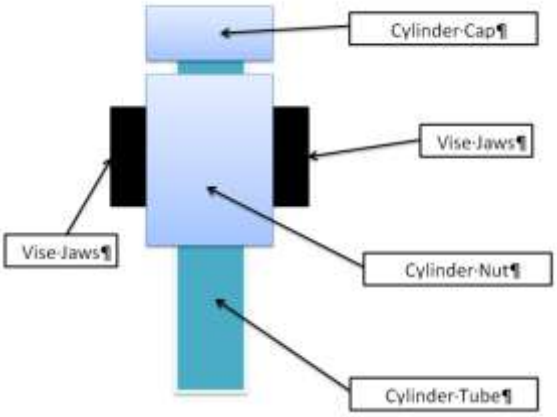

Figure 1: Schematic of Cylinder Placement in Vise

c. Once the cap becomes loose, use the ratchet to untighten the cylinder. After the seal has broken, the cylinder pressure will be equal to the atmospheric pressure.
d. If the cap does not come off (still swaged inside), use the ratchet to pry the cap off. Sometimes the seals can become stuck. The cylinder will likely not be under much pressure at this time. Consider wearing a face shield while performing this task.
e. Put the cylinder contents in a vial and label it. This should be completed in the fume hood for cylinders whose contents are toxic and/or volatile.

6. Cleaning cylinders
   a. Ensure that the cylinder is completely free of any free liquid (i.e., has been drained).
   b. Rinse the cylinder with DI water.
   c. Put a small quantity of hand soap in a Nalgene PP tub and fill with DI water. Place the rinsed (and open) cylinder in the tub.
   d. Allow the cylinder to soak in the soap solution for several days. This removes any residual water-soluble contamination from the cylinder.
   e. After soaking, remove the cylinder and rinse with DI water a couple of times. Scrape the cylinder with a brush to remove any residue left inside and follow with at least three final DDI washes.
   f. Dry the cylinder in an oven that is designated for cleaning equipment. Set temperature to 60 °C and place the cylinders on the rack or in the Nalgene PP tub. At these conditions, the cylinders will generally take about three days to dry out completely.
   g. For rapid drying, set the oven temperature to 110 °C and allow the cylinders to dry for at least 24 hours. Ensure that the oven will not be used to dry plastics and other materials that cannot tolerate high temperature during this time.
   h. Decant the liquid in the sink.

Standard Operating Practices: Making Swagelok® Cylinders for Thermal Degradation Experiments

by Omkar Namjoshi

Never work by yourself while preparing, tightening, or untightening cylinders. Always make sure someone else is in one of the labs.

Proper PPE must be worn while handling cylinders. This includes a lab coat, safety glasses or goggles, and nitrile gloves. Latex gloves should not be worn as latex is a poor barrier for amine solutions.

Cylinders must be capable of handling corrosive liquids at temperatures greater than 175 °C and pressures greater than 130 barg. The 4.5 ml Swagelok® cylinders are all capable of handling this rating. Catastrophic failure can occur if the cylinder is not rated for this service. The cylinders have an OD of 3/8" and a length of 4" and are constructed from stainless steel. ONLY USE GENUINE SWAGELOK® PARTS FOR MAKING CYLINDERS. Part numbers for 3/8" stainless steel cylinders are as follows:

- **For cap, ferrule, and nut assembly: SS-600-C**
- **For tubing: SS-T6-S-035-20 (CHE shop can cut these in 4" increments)**

1. Preparation of materials
    a. The Swagelok® caps come pre-assembled (the cap is already hand-tight in the nut, and the ferrule is also in the nut). Take out the assembly and hand tighten the cap to the nut as tightly as possible (in most cases, only minor adjustments need to be made, if any) and make a marking on the 12:00 side of the nut and the 9:00 side of the cap using a Sharpie marker.
    b. Turn the cap assembly upside down so the open hole (female side) of the assembly is facing upwards. Insert the tube into the female side of the assembly.
    c. Turn the cap assembly with the tube inserted right side up while holding one hand on the tube. Otherwise, the tube will fall off the assembly.
2. Performing the initial swage
    a. With the tube/cap assembly held right side up, place the assembly in the vise, ensuring that the nut (and not the tube) is gripped by the vise jaws. Keep your hand on the tube at all times.
    b. Using a ratchet and one hand, tighten the cylinder assembly 1.25 turns past hand-tight and take care not to allow the tube to fall to the ground.
    c. The ferrule will be swaged to the tube and a seal will be created after you have turned the assembly 1.25 turns past hand-tight. The two markings made on the cap and on the nut should be parallel to one another.
    d. To fully ensure that the cylinder is swaged properly, use the Swagelok® Gauging Guide and make sure that it does not slip inside the threaded gap between the cap and the nut. If it does, tighten the cylinder enough so that the Gauging Guide does not slip inside the threaded gap.
3. Repeat steps 1 and 2 to install the nut and cap on the opposite end of the cylinder.

Oxidative Degradation of Amine Solvents for CO_2 Capture

Quarterly Report for April 1 – June 30, 2014

by Hanbi Liu

Supported by the Texas Carbon Management Program

McKetta Department of Chemical Engineering

The University of Texas at Austin

July 31, 2014

Abstract

The oxidative degradation of diamines was measured in a stirred reactor at 70 ℃, 98kPa O_2, and 2kPa CO_2. Amines studied this quarter include hexamethylenediamine (HMDA), propanolamine (MPA), Diglycolamine® (DGA®), and bisaminoethyl ether. Amine solutions with an initial concentration of 10 m alkalinity, an initial loading of 0.4 mol CO_2/mol alkalinity, and an initial metals concentration of 0.4 mM Fe, 0.2 mM Mn, 0.1 mM Ni, and 0.05 mM Cr were oxidatively degraded.

The degradation of HMDA follows first order kinetics with rate constant k = 0.01/hour. About 80% of HMDA was lost after 200 hours. The degradation of bisaminoethyl ether follows first order kinetics with rate constant k = 0.023/hour, and 90% of Jeffamine® was lost after 300 hours. DGA® degradation also follows first-order kinetics with rate constant k = 0.008/hr, and 80% of DGA® was lost after 200 hours. HMDA, Jeffamine®, and DGA® degradation are all kinetically controlled. MPA showed negligible degradation after 260 hours of run time. There was no significant degradation observed for PDA with normal and high metals concentration in previous experiments. PDA was tested with antifoam and it did not show measurable degradation.

Experimental Methods

Solutions were prepared gravimetrically. The target amine concentration was 10 m alkalinity and the target CO_2 loading was 0.4 mol CO_2/mol alkalinity.

A schematic of the low gas flow apparatus is shown below. The apparatus is identical to the LGF reactor used by Voice (2013). Carbon dioxide and oxygen from their respective gas cylinders were passed through two calibrated mass flow controls to maintain a reactor pressure of 98 kPa O_2 and 2 kPa CO_2, and the jacketed glass reactor was charged with approximately 350 ml of amine solution. The reactor head was sealed with a Teflon® cap. The O_2/CO_2 mixture was saturated with water before being fed to the reactor through the Teflon® cap. The reactor was agitated at 1400 rpm and maintained at 70 ^oC.

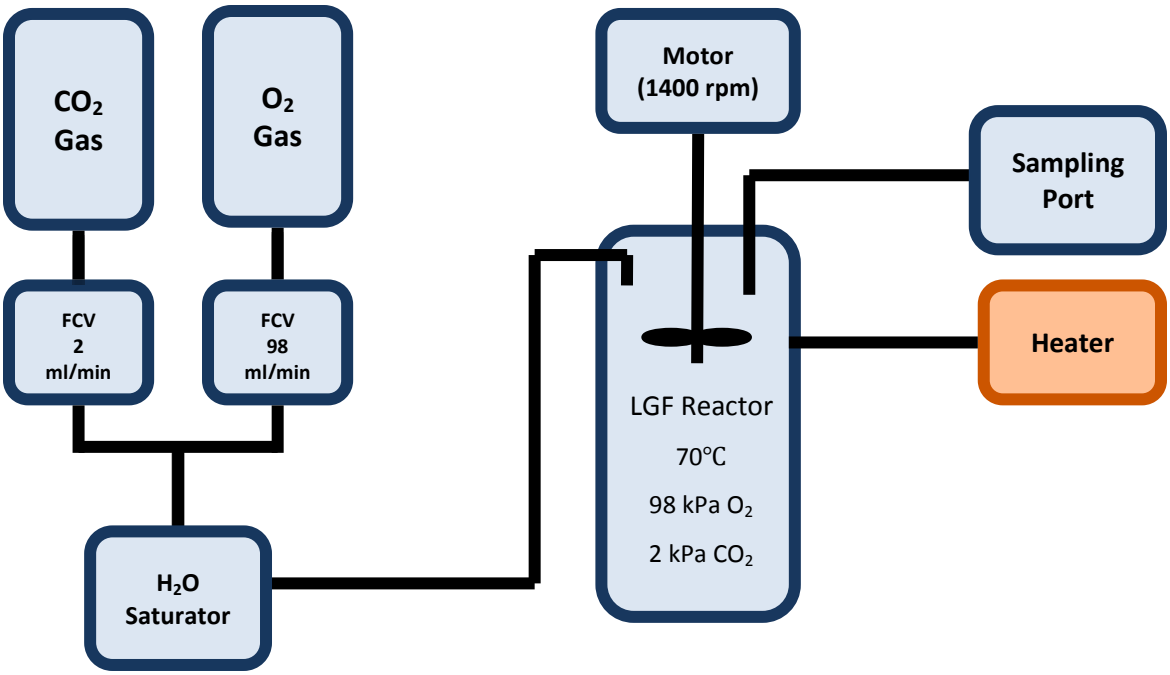

Figure 1: Low gas flow oxidation apparatus used in the experiment

The water balance was maintained each time a sample was removed to make up for water loss through evaporation. Table 1 lists a sampling schedule that was generally followed for each experiment. The amines tested in this study included ethylenediamine (EDA), 1,3-diaminopropane (PDA), putrescine, hexamethylenediamine (HMDA), propanolamine (MPA), Diglycolamine® (DGA®), and bisaminoethyl ether (Jeffamine®). The structures of these amines are listed in Table 2.

Table 1: General sampling schedule of oxidation experiments

Sample number	**Time since start of experiment**
1	At starting time
2	1 day
3	2 day
4	3 days
5	4~5 days
6	6~7 days
7	9~10 days
8	13~14 days

Table 2: Diamines tested in the LGF

Amine Name	Abbreviation	Structure
Ethylenediamine	EDA	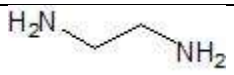
1,3-diaminopropane	PDA	
1,4-diaminobutane	Putrescine	
Hexamethylenediamine	HMDA	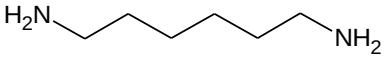
Propanolamine	MPA	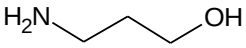
Diglycolamine®	DGA®	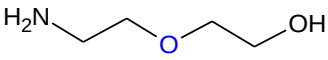
Bisaminoethyl ether	Jeffamine®	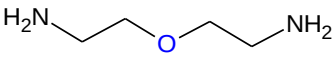

Cation chromatography was used to analyze for parent amine concentrations and degradation by-product concentrations; samples were diluted by a factor of 10000, and the separation was carried out using a Dionex CS17 column. Anion chromatography was used to qualitatively analyze for formate salts and nitrite. Samples were first hydrolyzed using concentrated sodium hydroxide and then diluted by a factor of 100. The separation was carried out using a Dionex AS15 column. The analytical methods are identical to those of Voice (2013).

Safety

Amine solutions were prepared in the fume hood as several of the amines were volatile, and the oxidation experiment was also conducted in the fume hood to vent any volatile degradation products away from the lab.

Hydrolyzing amine samples for anion chromatography involves working with concentrated NaOH. Goggles must be worn while working with concentrated acids or bases.

Results

Figure 2 shows the degradation of putrescine. Putrescine seems to undergo a short induction stage where degradation is very slow at first but then rapidly accelerates. The degradation of putrescine is kinetically controlled and follows first order kinetics with rate constant k = 0.01/hr. About 96% of the initial amount of amine was lost to degradation.

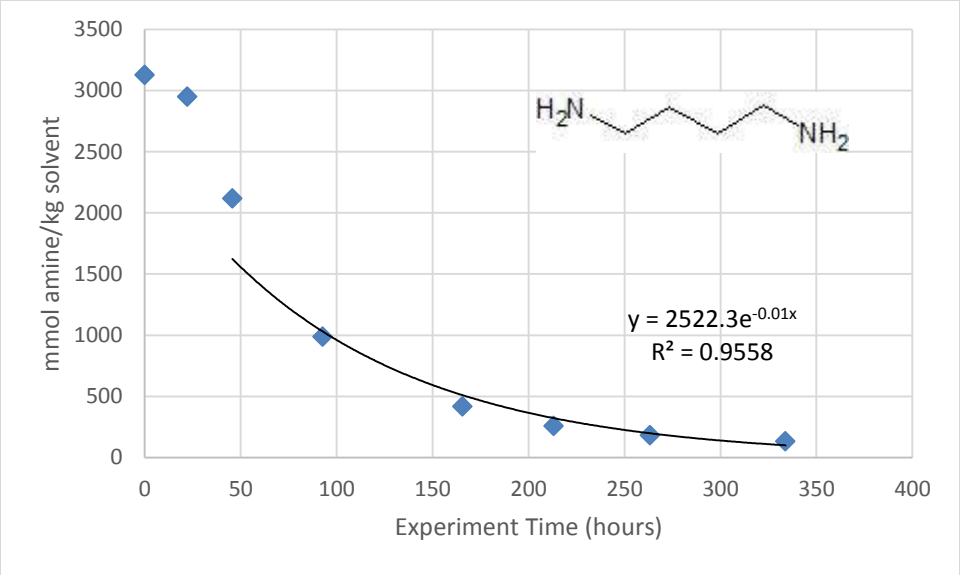

Figure 2: Oxidation of 5 m putrescine. Conditions: 70 °C, 98 kPa O_2, 2 kPa CO_2, 100 ml/min gas flow, 1400 rpm.

Anion chromatography data of heat stable salt products formed from putrescine oxidation is shown in Figure 3. The ratio of formate heat stable salts to oxalate heat stable salts is about 3:1.

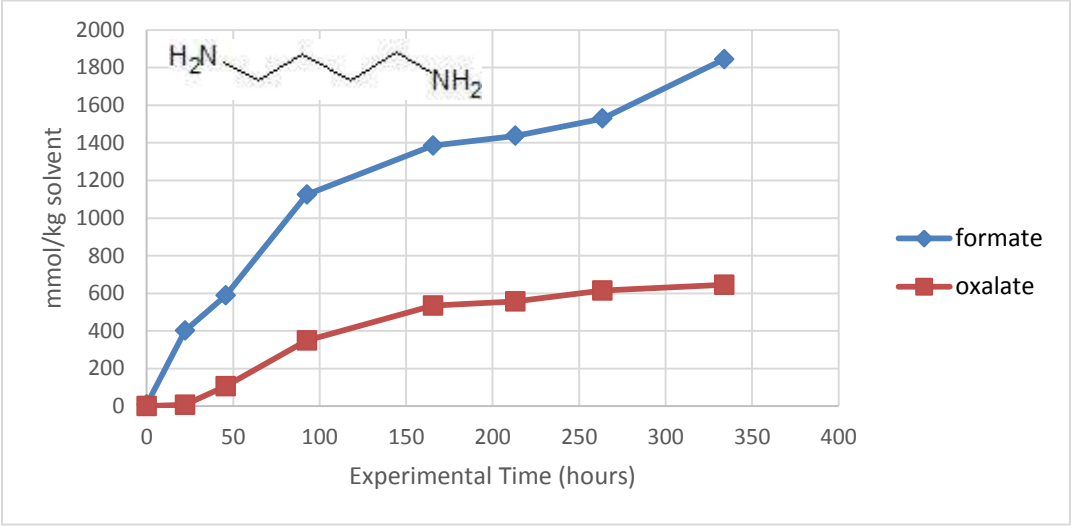

Figure 3: Total formate and total oxalate of putrescine. Conditions: 70 °C, 98 kPa O_2, 2 kPa CO_2, 100 ml/min gas flow, 1400 rpm.

Figure 4 shows the degradation of HMDA. The presence of an induction period similar to that in putrescine is observed, so only the last four data points were used to calculate the rate of degradation. HMDA shows degradation that is kinetically controlled following first-order reaction kinetics with rate constant k = 0.01/hr. About 80% of the initial amount of amine was lost to degradation.

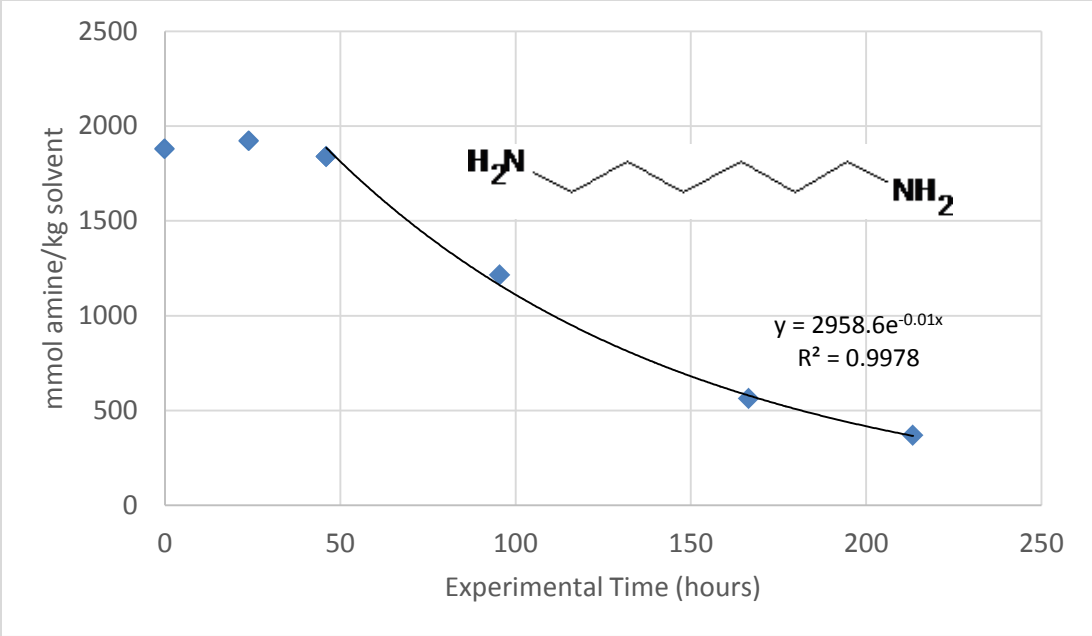

Figure 4: Oxidation of HMDA. Conditions: 70 °C, 98 kPa O_2, 2 kPa CO_2, 100 ml/min gas flow, 1400 rpm.

Figure 5 shows the heat stable salts produced from oxidation of HMDA. Formate forms at slightly greater rate compared to oxalate, and the amount of heat stable salts formed is much less than that for putrescine. The general trend for heat stable salt formation agrees with the rate of amine loss in Figure 4.

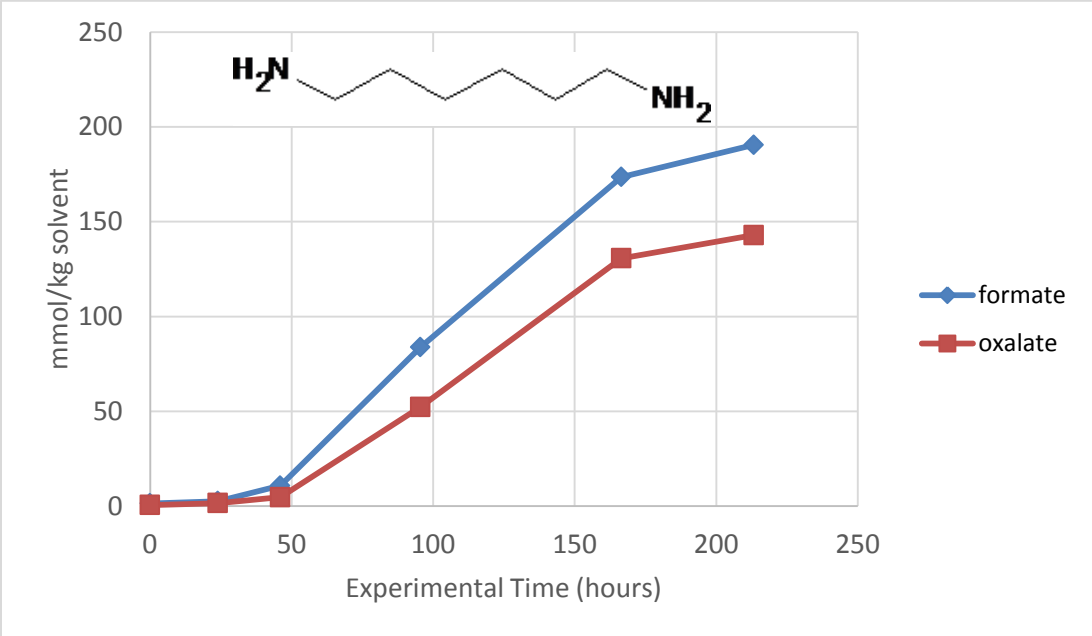

Figure 5: Total formate and total oxalate of HMDA. Conditions: 70 °C, 98 kPa O_2, 2 kPa CO_2, 100 ml/min gas flow, 1400 rpm.

Figures 6 shows the degradation of Jeffamine®. There is no observable induction stage for this amine, but the degradation is still kinetically controlled following first-order reaction kinetics with rate constant k = 0.023/hr. The rate constant is much higher than that of the other amines tested. About 90% of the initial amount of amine was lost to degradation.

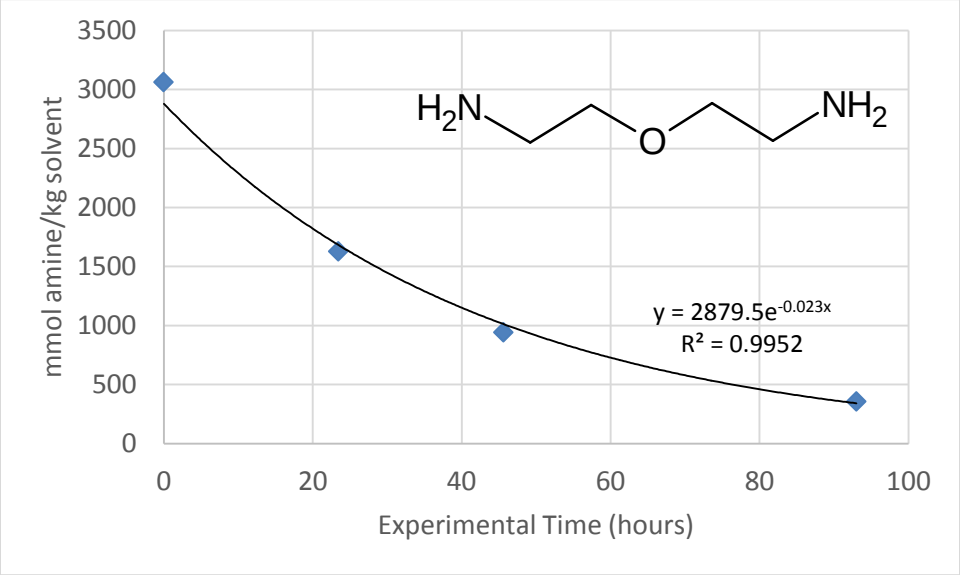

Figure 6: Oxidation of Jeffamine®. Conditions: 70 °C, 98 kPa O_2, 2 kPa CO_2, 100 ml/min gas flow, 1400 rpm.

Figure 7 shows the formate from oxidation of Jeffamine®. Oxalate was detected but could not be quantified.

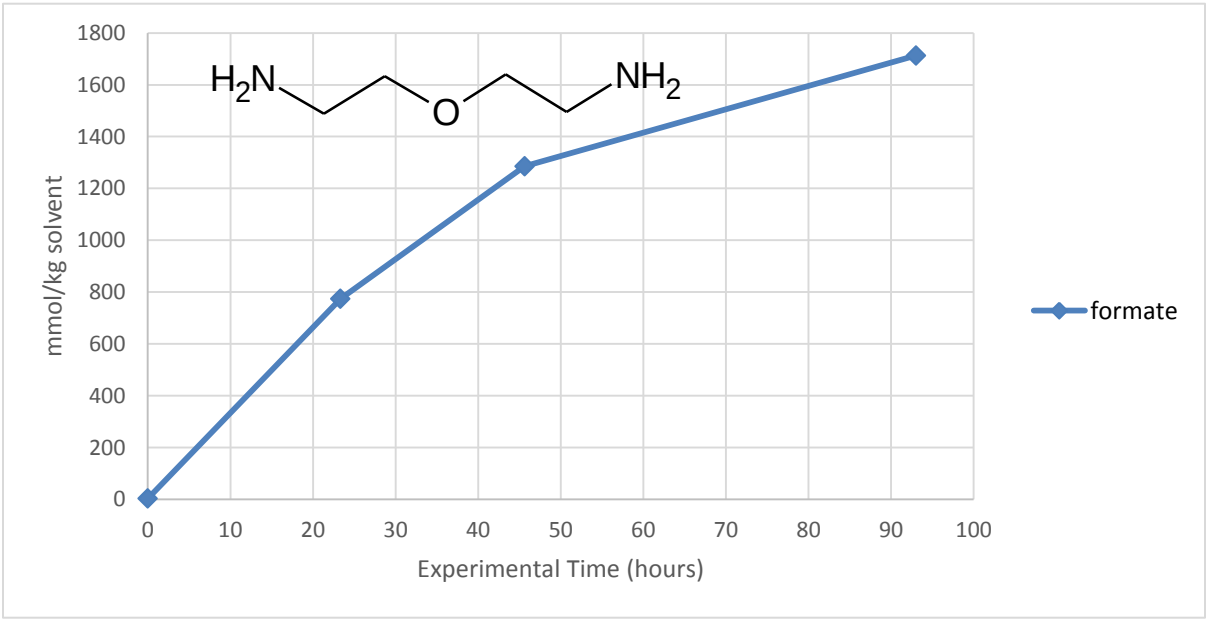

Figure 7: Total formate of Jeffamine®. Conditions: 70 °C, 98 kPa O_2, 2 kPa CO_2, 100 ml/min gas flow, 1400 rpm.

Figures 8 shows the degradation of DGA®. There is no observable induction stage for this amine, but the degradation is still kinetically controlled following first-order reaction kinetics with rate constant k = 0.008/hr. About 80% of the initial amount of amine was lost to degradation.

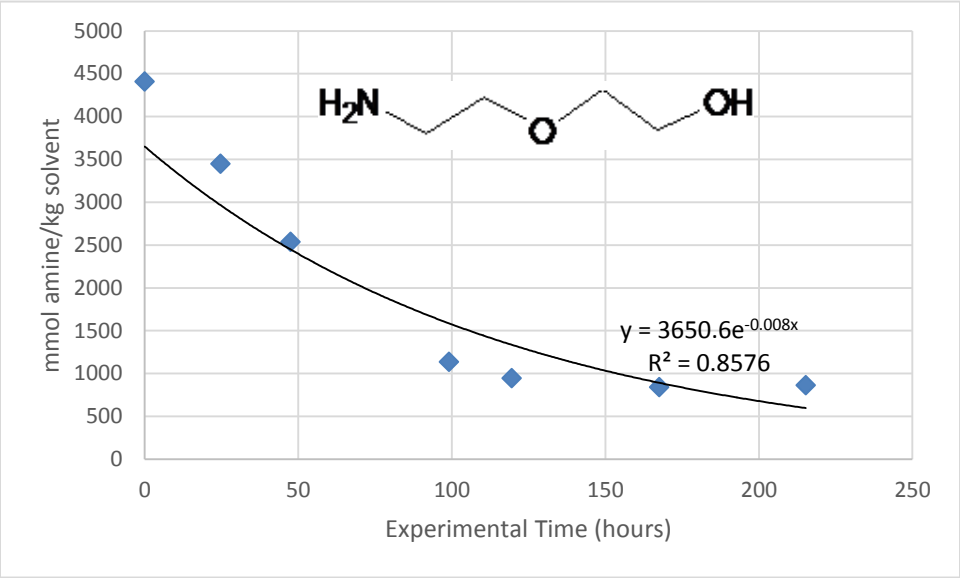

Figure 8: Oxidation of DGA®. Conditions: 70 °C, 98 kPa O_2, 2 kPa CO_2, 100 ml/min gas flow, 1400 rpm.

Figure 9 shows the degradation of MPA. This amine showed negligible degradation with a 10% amine loss over 260 hours.

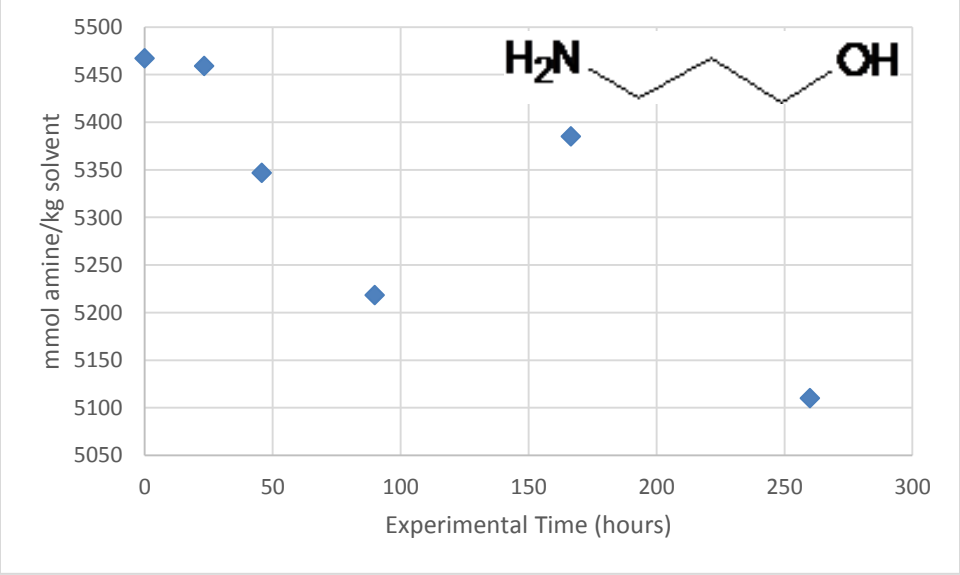

Figure 9: Oxidation of MPA. Conditions: 70 °C, 98 kPa O_2, 2 kPa CO_2, 100 ml/min gas flow, 1400 rpm.

Figure 10 shows the degradation of PDA. As described the Q3 2013 report (Rochelle et al., 2013), PDA had negligible degradation. PDA-1 was performed with high metals concentration at 4 mM Fe, 2 mM Mn, 1 mM Ni, 0.5 mM Cr. PDA-3 was performed with metals concentration at 0.4 mM Fe, 0.2 mM Mn, 0.1 mM Ni, 0.05 mM Cr. A considerable amount of foam formed at the gas-liquid interface during the experiments PDA-1 and PDA-3. As a result, PDA-5 was performed to test whether foaming on the solution surface is hindering oxygen diffusion into the bulk solution and hindering oxidation. Approximately 1 ml of antifoam was added to the PDA solution together with the metals at the start of the experiment, and as data in Figure 10 shows, antifoam did not alter the degradation behavior of PDA-5 which, like PDA-1 and PDA-3, shows almost no degradation.

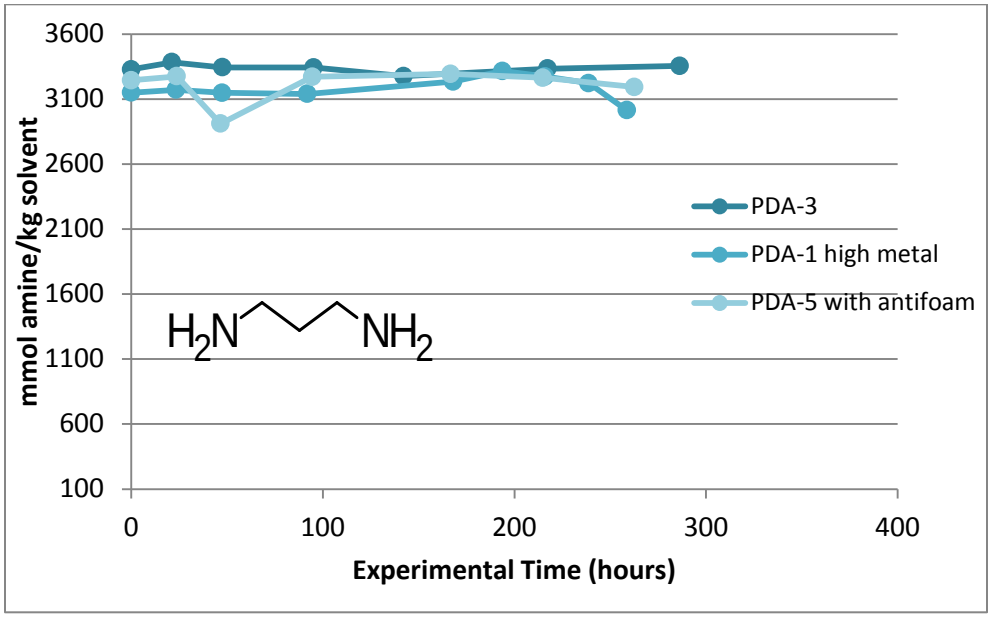

Figure 10: Oxidation of PDA. Conditions: 70 ^{o}C, 98 kPa O_2, 2 kPa CO_2, 100 ml/min gas flow, 1400 rpm.

The concentration of heat stable salts for PDA-5 is shown in Figure 11. The concentration of heat stable salts is almost zero, indicating that almost no oxidative degradation took place.

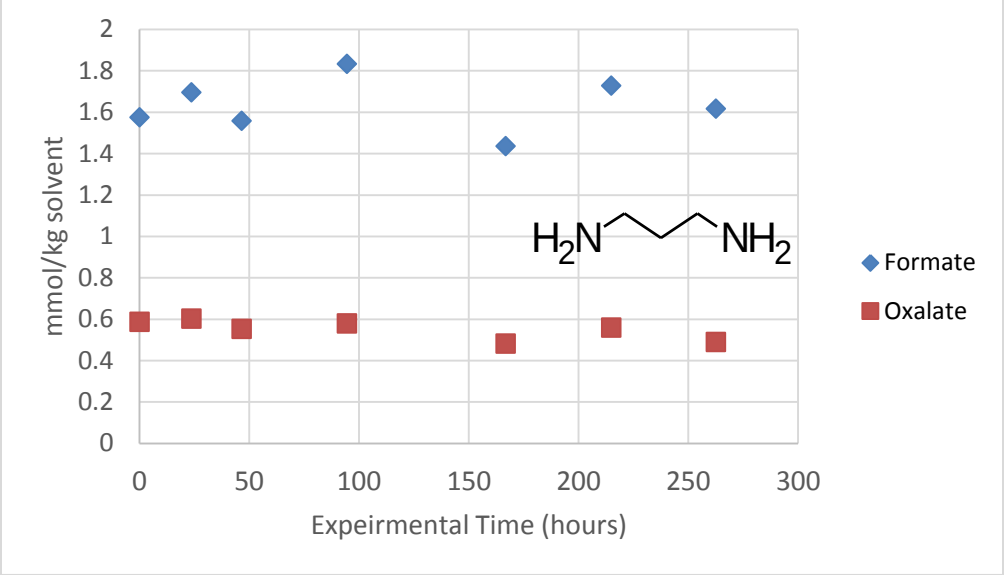

Figure 11: Total formate and total oxalate of PDA-5. Conditions: 70 ^{o}C, 98 kPa O_2, 2 kPa CO_2, 100 ml/min gas flow, 1400 rpm.

The amines that showed significant degradation all have even numbers of carbon atoms in their chains. MPA and PDA both contain three carbons in their alkyl chain and both showed negligible degradation. Catalysts form a homogenous solution with the amine samples that degraded significantly, but settled out of solution in the case of MPA and PDA. Data from thermal degradation of PDA showed that PDA and its thermal degradation products are not corrosive, further suggesting that metals likely did not catalyze oxidative degradation due to their insolubility in MPA and PDA (current research).

An induction stage was observed in many amines that showed significant degradation. The initial degradation products may have dissolved the added metals, which subsequently catalyzed degradation and caused rapid amine loss. The same behavior was observed for amines tested in Q3 2013.

Conclusions

1. PDA does not show appreciable oxidation at 70 ^{o}C, 98 kPa O_2, 2 kPa CO_2, and a metals concentration of 0.4 mM Fe, 0.2 mM Mn, 0.1 mM Ni, and 0.05 mM Cr with antifoam. This shows that foaming is not the reason for PDA resistance to oxidative degradation and experimental observations suggest that metal insolubility is the cause.
2. MPA does not show appreciate oxidation at 70 ^{o}C, 98 kPa O_2, 2 kPa CO_2, and a metals concentration of 0.4 mM Fe, 0.2 mM Mn, 0.1 mM Ni, and 0.05 mM Cr. Experimental observations suggest that metal insolubility may cause MPA to be resistant to oxidative degradation.
3. Putrescine oxidizes at 0.01/hr at 70 ^{o}C, 98 kPa O_2, 2 kPa CO_2 with 0.4 mM Fe, 0.2 mM Mn, 0.1 mM Ni, and 0.05 mM Cr. Putrescine degradation follows first order kinetics and

is strongly catalyzed by the presence of metals. Degradation of putrescine produces formate and oxalate at a concentration ratio of approximately 3:1.

4. HMDA oxidizes at 0.01/hr at 70 ^{o}C, 98 kPa O_2, 2 kPa CO_2 with 0.4 mM Fe, 0.2 mM Mn, 0.1 mM Ni, and 0.05 mM Cr. HMDA degradation follows first order kinetics and appears to be kinetically controlled. Degradation produces about the same amount of formate and oxalate.
5. Bisaminoethyl ether oxidizes at 0.023/hr at 70 ^{o}C, 98 kPa O_2, 2 kPa CO_2 with 0.4 mM Fe, 0.2 mM Mn, 0.1 mM Ni, and 0.05 mM Cr. Jeffamine® degradation follows first order kinetics and appears to be kinetically controlled.
6. DGA® oxidizes at 0.008/hr at 70 ^{o}C, 98 kPa O_2, 2 kPa CO_2 with 0.4 mM Fe, 0.2 mM Mn, 0.1 mM Ni, and 0.05 mM Cr. DGA® degradation follows first order kinetics and appears to be kinetically controlled.

Future Work

MEA will be studied under the same conditions to serve as a benchmark for comparison against the other amines. A blend of PDA and MEA will be studied to investigate whether degradation products of MEA that solubilize the metals will lead to an increase in PDA degradation. The EDA oxidation experiment will be repeated to understand and quantify repeatability of the experimental apparatus.

Metals concentration analysis degraded amine samples will be analyzed for bulk solution amine concentration to quantify the difference in metal concentration between amines that showed significant degradation and those that did not.

References

Goff GS. *Oxidative Degradation of Aqueous Monoethanolamine in CO_2 Capture Processes: Iron and Copper Catalysis, Inhibition, and O_2 Mass Transfer*. The University of Texas at Austin. Ph.D. Dissertation. 2005.

Sexton AJ. *Amine Oxidation in CO_2 Capture Processes*. The University of Texas at Austin. Ph.D. Dissertation. 2008.

Rochelle GT et al. "CO_2 Capture by Aqueous Absorption, Third Quarterly Progress Report 2013." Texas Carbon Management Program. The University of Texas at Austin. 2013.

Voice AK, *Amine Oxidation in Carbon Dioxide Capture by Aqueous Scrubbing*. The University of Texas at Austin Ph.D. Dissertation. 2013.

Thermal Degradation of Linear Amines

Quarterly Report for April 1 – June 30, 2014

by Daniel Hatchell

Supported by the Texas Carbon Management Program

McKetta Department of Chemical Engineering

The University of Texas at Austin

July 31, 2014

Abstract

This report investigates the thermal degradation of eight linear amines loaded with CO_2 and H^+ at 135 °C, 150 °C, and 165 °C. The rate data for the degradation of 1,2-diaminoethane (EDA), propane-1,3-diamine (PDA), butane-1,4-diamine (DAB), 2-(2-aminoethoxy)ethanamine (BAE), hexane-1,6-diamine (HMDA), 2-aminoethanol (MEA), 2-aminopropanol (MPA), and 2-(2-aminoethoxy)ethanol (DGA®) are presented. CO_2-loaded EDA and PDA degradation has been measured at 135 °C; the degradation of CO_2-loaded EDA, PDA, DAB, BAE, and HMDA has been measured at 150 °C; the degradation of all eight amines loaded with CO_2 has been measured at 165 °C. The degradation rate of H^+-loaded EDA, PDA, DAB, and BAE at 165 °C has been measured. CO_2-loaded solvents were prepared with an initial concentration of 10 m alkalinity and an initial CO_2 loading of 0.4 mol CO_2/mol alkalinity; HMDA was prepared at an initial concentration of 5 m alkalinity due to solid solubility issues. Acid-loaded solvents were prepared with an initial loading of 5 m alkalinity and an initial H^+ loading of 0.2 mol H^+/mol alkalinity.

The degradation rate of structurally analogous molecules tends to decrease with chain length. HMDA, the diamine with the longest chain, was found to be the most thermally resistant of the eight amines under CO_2 loading. DAB was the only amine studied under acid loading that did not exhibit a major decrease in reaction rate, suggesting that the reaction mechanism is initiated by H^+. EDA, BAE, HMDA, and DGA® reach a thermodynamic equilibrium with their degradation products.

This report also presents concentration data for metals and formate in the solvents of the 150 °C temperature series. It was observed that the accumulation of formate and dissolved metals in degrading amines is correlated. EDA is particularly corrosive and produces substantial amounts of formate and metals after four weeks of degradation.

Experimental Methods

The CO_2-loaded amine solutions were prepared with an initial amine concentration of 10 m alkalinity and loaded with 0.4 mol CO_2/mol alkalinity. CO_2-loaded HMDA, and all acid-loaded experiments, were prepared with an initial amine concentration of 5 m alkalinity. The acid-loaded experiments had an initial loading of 0.2 mol H^+/mol alkalinity. 4 ml of each CO_2-loaded solution and 4.5 ml of each acid-loaded solution was placed inside 3/8" Swagelok® stainless steel

cylinders with volumes of 4.5 ml. These cylinders were sealed and heated to the given temperature (135 °C, 150 °C, or 165 °C) in a convection oven. Cylinders were periodically removed at predetermined intervals and promptly cooled in a refrigerator to halt any further thermal degradation.

After all Swagelok® cylinders had been removed from the oven and refrigerated, they were opened and the contents diluted by a factor of 10000 for analysis by cation chromatography (Dionex ICS-2100). Each series of amine was removed after 700 to 800 hours of heating. The dissolved products in these diluted samples were separated in a Dionex CS17 column and the relative quantities of each were plotted in a chromatograph. The concentrations of dissolved compounds in the analyzed solutions could be calculated by comparison to a known standard. The analytical and experimental techniques are similar to Freeman (2011) and are described in detail in previous quarterly reports. Degraded samples of PDA and BAE were heated to around 60 ^{o}C before diluting to melt any remaining solids.

Formate and metals concentration data were obtained for samples of EDA, PDA, DAB, and BAE degraded in the 150 ^{o}C temperature experiment series. Formate concentrations were taken of the first, fourth, and twelfth (last) samples to cover the entire range of degradation. These samples were hydrolyzed and subsequently analyzed by anion chromatography to obtain concentration data. Metals concentrations were measured for the twelfth, most degraded sample of the series to compare the amines in the cylinders in their most corroded state.

This report examines the following linear amines: 1,2-diaminoethane (EDA), propane-1,3-diamine (PDA), and butane-1,4-diamine (DAB), 2-(2-aminoethoxy)ethanamine (BAE), hexane-1,6-diamine (HMDA), 2-aminoethanol (MEA), 2-aminopropanol (MPA), and 2-(2-aminoethoxy)ethanol (DGA®). These compounds and their structures are listed in Table 1.

Table 1: Linear Diamines Tested

Amine Name	Abbreviation	Amine Structure
1,2-diaminoethane	EDA	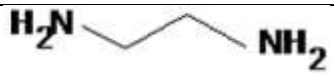
propane-1,3-diamine	PDA	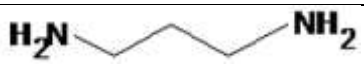
butane-1,4-diamine	DAB	
2-(2-aminoethoxy)ethanamine	BAE	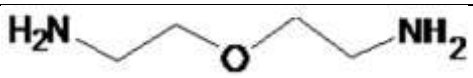
hexane-1,6-diamine	HMDA	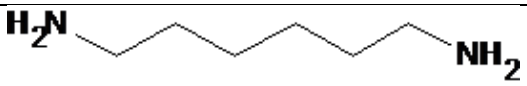
2-aminoethanol	MEA	
3-aminopropanol	MPA	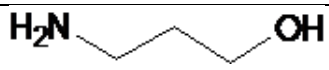
2-(2-aminoethoxy)ethanol	DGA®	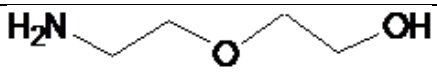

Results and Discussion

All eight of the listed amines were degraded at 165 °C with a CO_2 loading of 0.4. Figures 1 and 2 plot the absolute concentrations of these amines over time as they degrade.

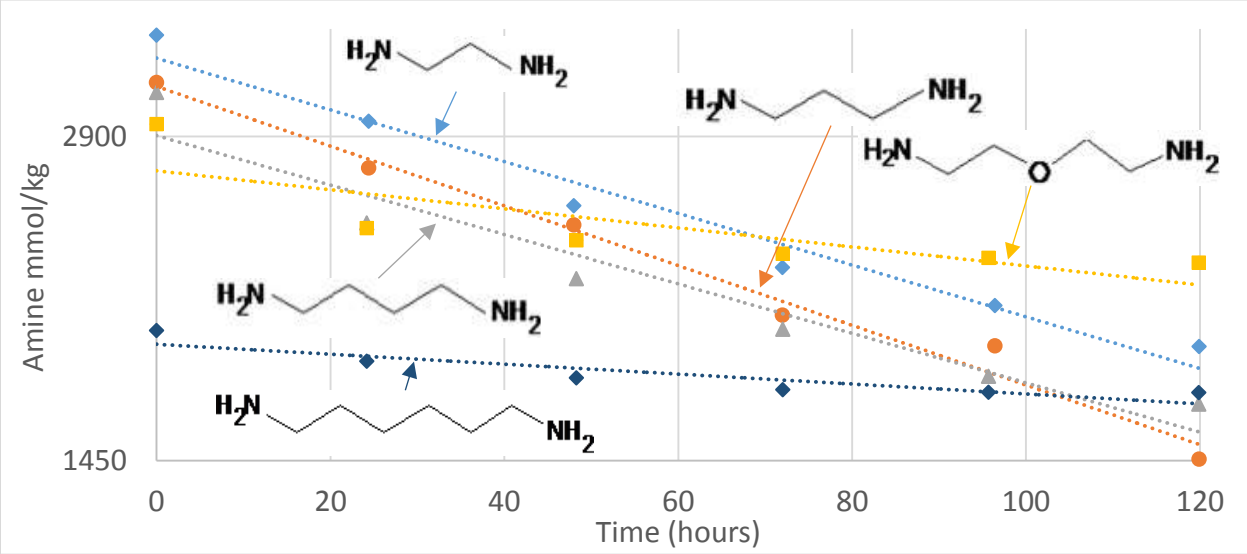

Figure 1: 5 m EDA, 5 m PDA, 5 m DAB, 5 m BAE, and 2.5 m HMDA degraded at 165 °C at 0.4 CO_2 loading. BAE appears to reach equilibrium with the degradation products.

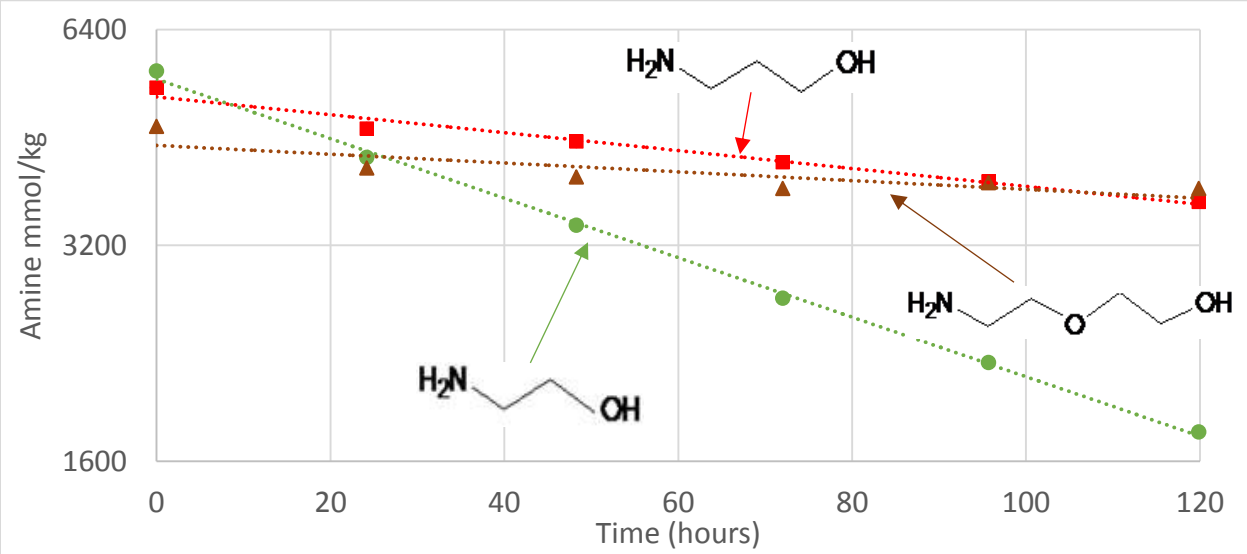

Figure 2: 10 m MEA, 10 m MPA, and 5 m DGA® degraded at 165 °C at 0.4 CO_2 loading. DGA® appears to reach equilibrium with the degradation products.

EDA, MEA, and MPA follow close exponential fits suggesting a first-order degradation mechanism. PDA and HMDA also appear to follow first-order fits, although to less certainty.

DAB, BAE, and DGA® do not show a strong first-order reaction rate but are fitted to an exponential trend line for the purpose of comparison. BAE and DGA® appear to be reaching equilibrium by the second data point at 24 hours, so the initial rate constants estimated for these amines are likely inaccurate. Table 1 lists the first-order rate constants in units of hr^{-1} of each amine for this 165 °C experiment and for each successive temperature.

Table 2: First-order rate constants (hr^{-1}) for degradation reactions and associated activation energies (kJ/mol). The 'eq' header indicates that the amine reached equilibrium with its degradation products. Amines are ordered by degradation rate at 165 °C.

Amine	165 °C (CO_2 = 0.4)	165 °C (Acid = 0.2)	150 °C (CO_2 = 0.4)	135 °C (CO_2 = 0.4)	Activation Energy (kJ/mol)
10 m MEA	0.00956	n/a	n/a	n/a	n/a
5 m EDA	0.00698^{eq}	0.00142	0.00287^{eq}	0.00056^{eq}	130
5 m PDA	0.00639	0.00069	0.00147	0.00036	140
5 m DAB	0.00529	0.00457	0.00097	n/a	170
5 m BAE	0.00515^{eq}	0.00016	0.00105^{eq}	n/a	160
10 m MPA	0.00288	n/a	n/a	n/a	n/a
5 m DGA®	0.00262^{eq}	n/a	n/a	n/a	n/a
2.5 m HMDA	0.00173^{eq}	n/a	0.00069^{eq}	n/a	90

Structurally analogous amines tend to degrade more slowly as chain length increases, based on the 165 °C data. This is consistent across the diamines (EDA degrading the most quickly, HMDA degrading the most slowly) and the alkanolamines (MEA degrades the fastest, followed by MPA and then DGA®).

Figure 3 shows the degradation of EDA, PDA, DAB, and BAE at an initial concentration of 0.2 mol H^+/mol alkalinity.

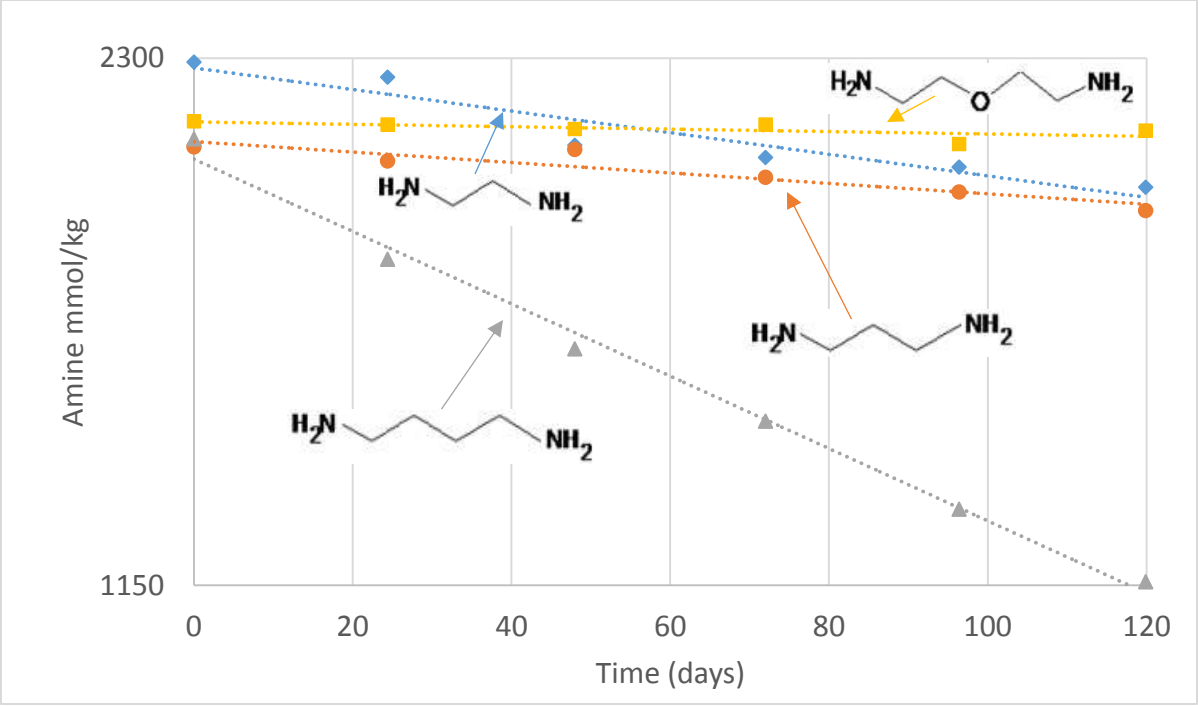

Figure 3: 5 m EDA, 5 m PDA, 5 m DAB, and 5 m BAE degraded at 165 °C at 0.2 H^+ loading. DAB maintains a similar degradation rate in acid conditions but the other three do not show appreciable degradation.

EDA, PDA**,** and BAE all degrade much more slowly under acidified conditions. The rate constants are tabulated in Table 2. The rate constant for EDA drops from 0.00553 hr^{-1} to 0.00142 hr^{-1}, for PDA from 0.00639 hr^{-1} to 0.00069 hr^{-1}, and for BAE from 0.00515 hr^{-1} to 0.00016 hr^{-1}. The degradation rate constant of DAB drops much less, from 0.00529 hr^{-1} to 0.00457 hr^{-1}. This small change compared to the other three amines suggests that DAB degrades by some mechanism that does not incorporate CO_2 into the final degradation product. This would be consistent with the following proposed reaction (Lepaumier, 2010):

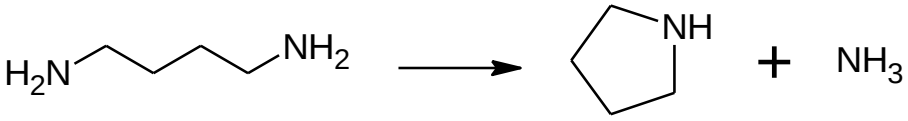

Figure 4: Proposed degradation pathway of acidified DAB to form pyrrolidine. CO_2 serves as an acidifying catalyst and not a reactant.

This mechanism involves the protonation of an amino group and subsequent attack on the alpha carbon by the other, non-protonated amino group of the DAB molecule. The molecule ring-closes to form pyrrolidine and eliminates an ammonia molecule. EDA and PDA do not appear to degrade as significantly under acid loading, and more likely follow reactions that combine with CO_2 to form a cyclic urea (Zhao et al., 2010):

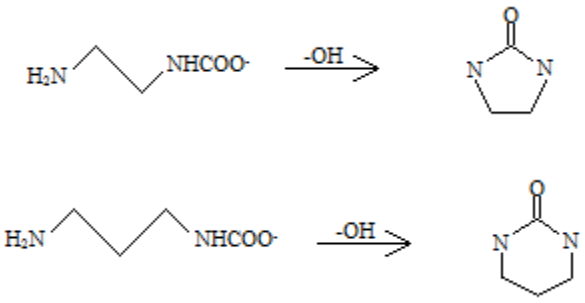

Figure 5: EDA and PDA ring-close to form cyclic ureas.

BAE hardly degrades at all under acid loading but has too long a chain to form a cyclic urea by the above mechanism.

Figure 6 plots the degradation of EDA, PDA, DAB, BAE, and HMDA at 150 °C with 0.4 loading of CO_2.

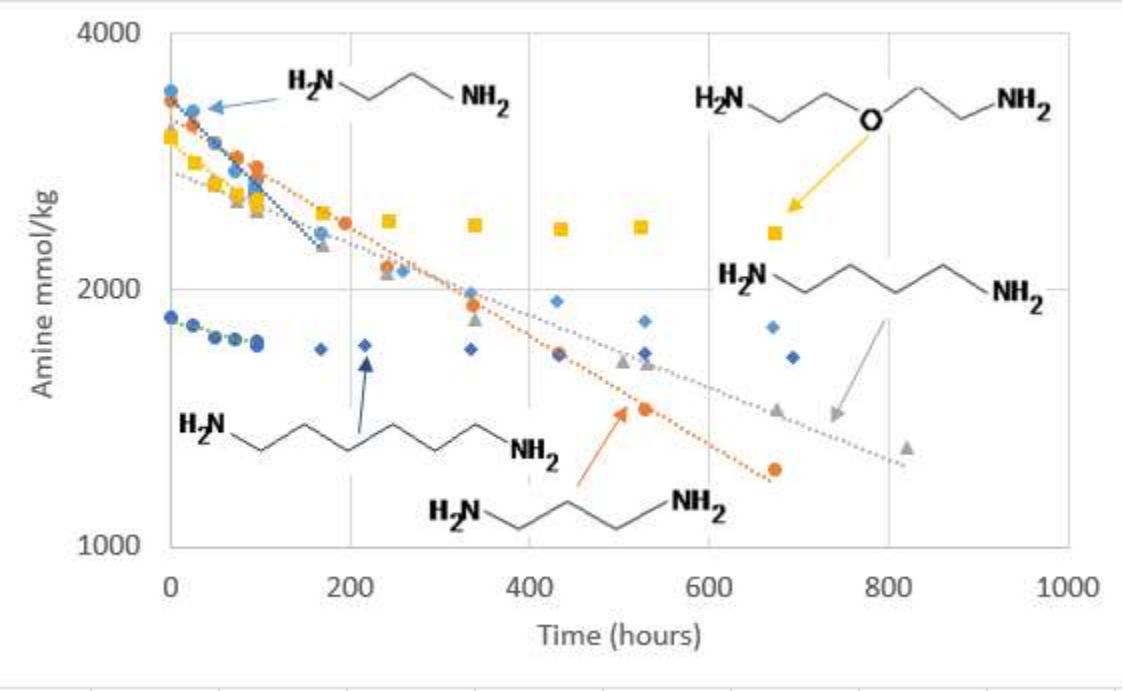

Figure 6: 5 m EDA, 5 m PDA, 5 m DAB, 5 m BAE, and 2.5 m HMDA degraded at 150 °C at 0.4 CO_2 loading.

BAE and HMDA reach equilibrium at around 100 hours at 150 °C, encompassing more concentration measurements and consequently revealing the initial degradation rate behavior in more detail. EDA and PDA appear to follow first-order behavior. The rate behavior of HMDA and BAE is not as clear, and DAB seems to react by some mechanism greater than first-order. The rate constants or initial rate constants are listed in Table 2.

Figure 7 plots the degradation of EDA and PDA at 135 °C at a CO_2 loading of 0.4.

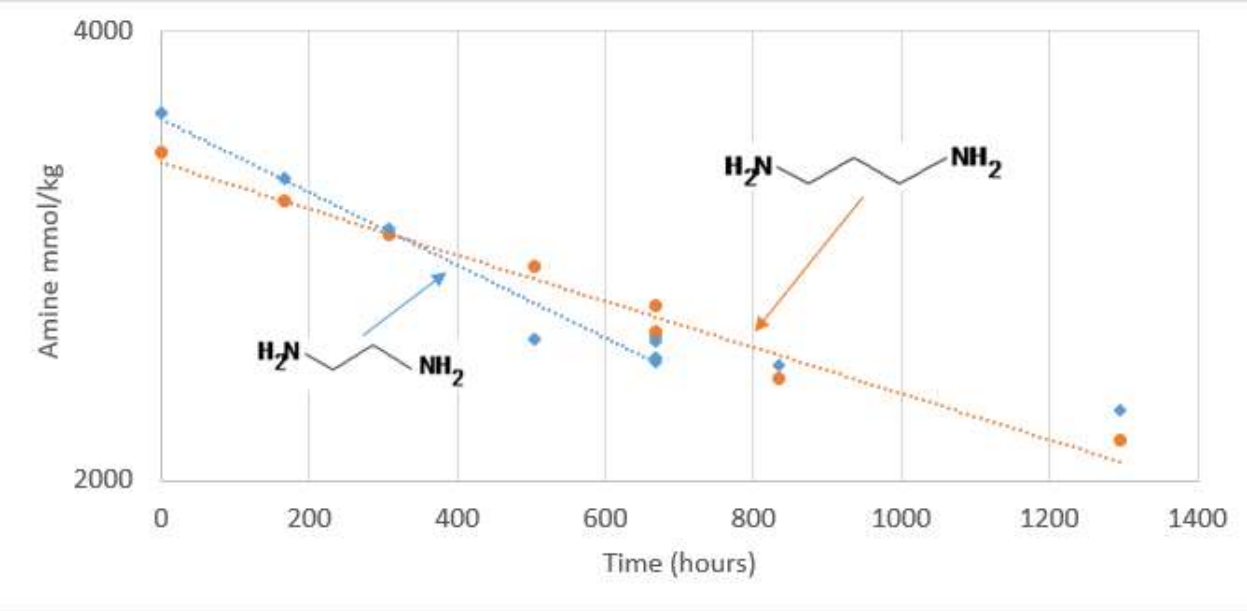

Figure 7: 5 m EDA ad 5 m PDA degraded at 135 °C at 0.4 CO_2 loading. EDA degradation slows after 700 hours.

EDA appears to reach equilibrium in 700 hours at 135 °C. Both PDA and EDA demonstrate first-order rate behavior in the first 700 hours of degradation, the rate constants of which are listed in Table 2.

Extensive data is required to determine activation energy accurately, and because DAB, BAE, and HMDA were only degraded at two different temperatures there is no way to tell how accurate the activation energy calculation by fitting to an Arrhenius equation is. Estimates of activation energy for the five diamines are listed above in Table 2. This analysis gives activation energies of 130 kJ/mol for EDA, 140 kJ/mol for PDA, 170 kJ/mol for DAB, 160 kJ/mol for BAE, and 90 kJ/mol for HMDA.

Figure 8 compares the rate constant data of EDA and DAB with existing data by Zhou (EDA) and Namjoshi (DAB).

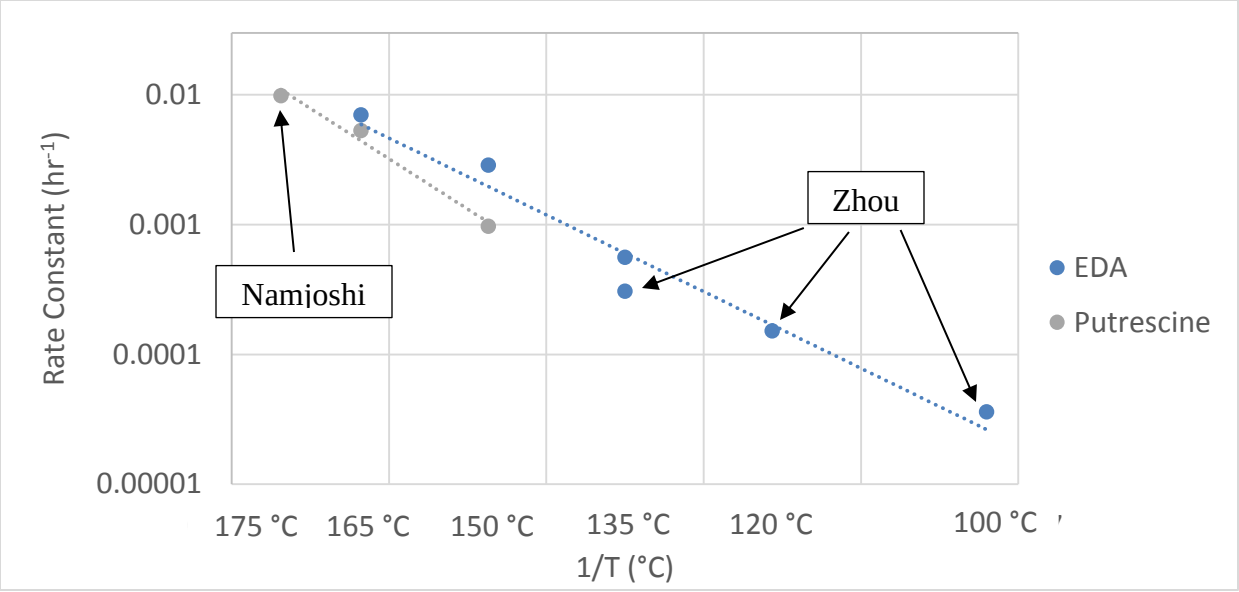

Figure 8: Degradation rate constants of EDA and DAB at 0.4 CO_2 loading in six temperatures across three studies. Zhou uses 8 m EDA; Namjoshi uses 8 m DAB; this work uses 5 m EDA and 5 m DAB.

The work by Zhou studied the degradation of 8 m EDA at 135 °C, 120 °C, and 100 °C with a CO_2 loading of 0.4. The data point from Namjoshi comes from the degradation of 8 m DAB at 175 °C with a 0.4 CO_2 loading. These experiments used different initial concentrations for the amines than used in this report; however, the calculated first-order rate constant is concentration independent so the initial concentration does not matter. The recalculated EDA activation energy is 110 kJ/mol compared with 130 kJ/mol; the recalculated DAB activation energy is 150 kJ/mol compared with 160 kJ/mol. Assuming that the effect on degradation by molality is minimal, this comparison shows relatively consistent data across the three studies.

It was found that the concentration of formate and dissolved metals increased over time as some amines degraded in the metal cylinders. Figure 9 plots the concentration of formate in the samples of EDA, PDA, DAB, and BAE as they degrade at 150 °C at 0.4 CO_2 loading.

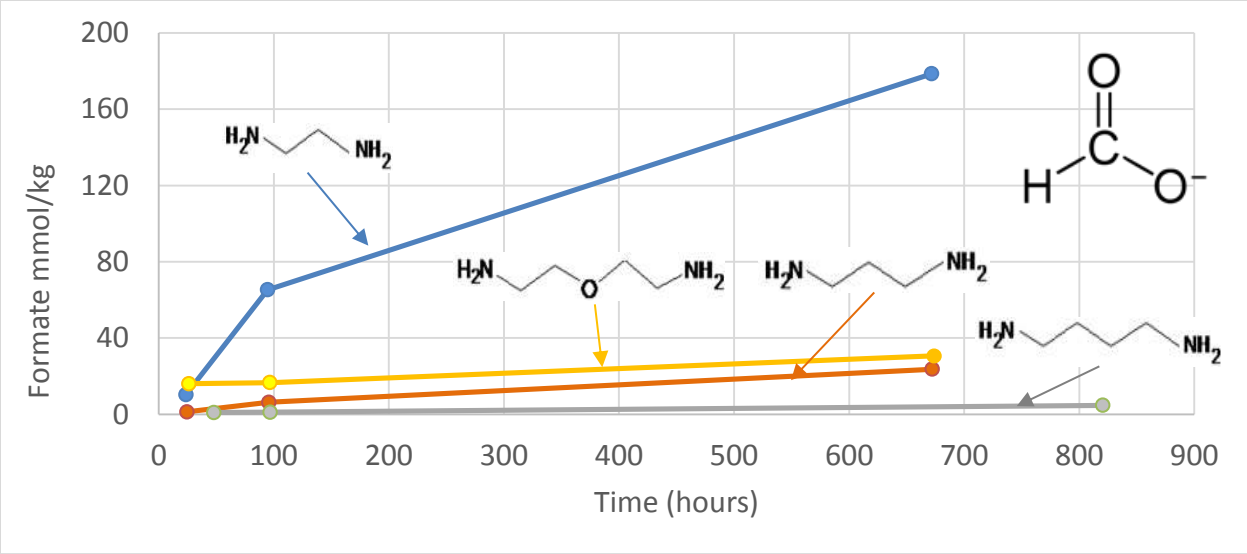

Figure 9: Total formate generation in degraded 5 m EDA, 5 m PDA, 5 m DAB, and 5 m BAE. Samples degraded at 150 °C with a CO_2 loading of 0.4.

Figure 10 displays the concentrations of chromium, nickel, manganese, and iron in the last of the degraded samples from the 150 °C series (this corresponds to 670 hours of degradation for EDA, PDA, and DAB, and 810 hours of degradation for BAE).

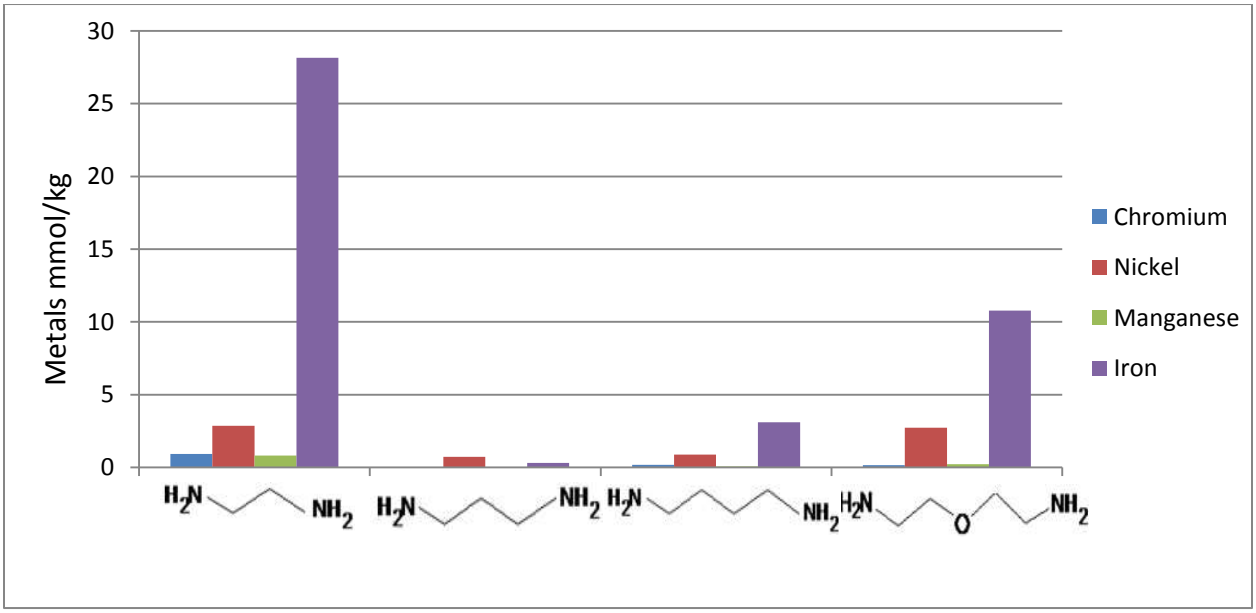

Figure 10: Concentration of metals in twelfth (last) amine sample of 150 °C, 0.4 CO_2 loading degradation series. Metals and formate are most prominent in EDA.

These two plots reveal a correlation in the concentration of heat-stable salts in solution and the concentration of corroded metals. EDA is especially corrosive and generates a large amount of

formate while degrading, while DAB and PDA contain significantly less formate and metals in the degraded solution. These results have implications in oxidative degradation. Metals are known to catalyze the oxidative degradation of certain amines (Liu, 2014). It is unknown whether the generation of heat-stable salts drives corrosion or if dissolved metals catalyze heat-stable salt formation. Describing this relationship may lead to a better understanding of how to identify compounds resistant to corrosion and oxidation.

Conclusions

1. The following degradation rate constants were observed for the tested amines with 0.4 CO_2 loading at 165 °C: 10 m MEA = 0.00956 hr^{-1}, 5 m EDA = 0.00698 hr^{-1}, 5 m PDA = 0.00639 hr^{-1}, 5 m DAB = 0.00529 hr^{-1}, 5 m BAE = 0.00515 hr^{-1}, 10 m MPA = 0.00288 hr^{-1}, 5 m DGA® = 0.00262 hr^{-1}, 2.5 m HMDA = 0.00173 hr^{-1}; at 150 °C: 5 m EDA = 0.00287 hr^{-1}, 5 m PDA = 0.00147 hr^{-1}, 5 m DAB = 0.00097 hr^{-1}, 5 m BAE = 0.00105 hr^{-1}, 2.5 HMDA = 0.00069 hr^{-1}; at 135 °C: 5 m EDA = 0.00056 hr^{-1}, 5 m PDA = 0.00036 hr^{-1}.
2. The following degradation activation energies were calculated for 0.4 CO_2 loading: 5 m EDA = 130 kJ/mol, 5 m PDA = 140 kJ/mol, 5 m DAB = 170 kJ/mol, 5 m BAE = 160 kJ/mol, 2.5 m HMDA = 90 kJ/mol.
3. DAB degrades with rate constant 0.00457 hr^{-1} when loaded with 0.2 acid loading. Rates of EDA, PDA and BAE degrade under 0.2 acid loading with rate constants of 0.00142 hr^{-1}, 0.00069 hr^{-1}, and 0.00016 hr^{-1}, respectively.
4. BAE and DGA® consistently reach equilibrium with the degradation products. EDA reaches equilibrium with its urea at lower temperatures. At 165 °C, BAE and DGA® concentrations equilibrate after 24. At 150 °C, BAE and HMDA both equilibrate after 100 hours and EDA degradation begins to slow after 200 hours. EDA degradation also significantly slows after 700 hours at 135 °C.
5. 5 m EDA is the most corrosive amine tested and generates the most formate at 150 °C (178.6 mmol/kg).

Future Work

Further examination of the samples by Total Inorganic Carbon analysis and by titration will help determine the identity of the degradation mechanisms and products and discover whether the loss of amine is accompanied by a loss in alkalinity. Degradation data for MEA, MPA, and DGA® at 150 °C will also be collected to complete the temperature series. More data regarding the degradation of BAE and HMDA at 165 °C may be required to calculate accurate rate constant data because the two amines reached equilibrium somewhere in between the first two data points. Further work will study the thermal degradation of piperazine blends with hindered amines.

References

Freeman SA. *Thermal Degradation and Oxidation of Aqueous Piperazine for Carbon Dioxide Capture.* The University of Texas at Austin. Ph.D. Dissertation. 2011.

Lepaumier H, Martin S, Picq D, Delfort B, Carrette P-L. "New Amines for CO_2 Capture. III. Effect of Alkyl Chain Length between Amine Functions on Polyamines Degradation." *Ind. Eng. Chem. Res.* 2010;49:4553–4560.

Liu Hi. Personal interview. April 29, 2014.

Namjoshi O, Li L, Du Y, Rochelle GT. "Thermal Degradation of Piperazine Blends withDiamines." *Energy Proc.* 2013;37:1904–1911.

Zhou S, Chen X, Nguyen T, Voice AK, Rochelle GT. "Aqueous Ethylenediamine for CO_2 Capture." *ChemSusChem*. 2010;3(8):913–918.

Aerosol Mitigation in CO_2 Capture

Quarterly Report for April 1 – June 30, 2014

by Steven Fulk

Supported by the Texas Carbon Management Program

and DOE/URS contract DE-FE0005654

McKetta Department of Chemical Engineering

The University of Texas at Austin

July 31, 2014

Acknowledgement: This material is based on work supported in part by the Department of Energy under Award Number DE-FE0005654.

Abstract

Work in this quarter focused on experimental measurements using the Aerosol Growth Column (AGC) with aerosol injection from the Liquid Vaporizer and Injector (LVI). Improvements to the AGC included the addition of a liquid sample port upstream of the solvent pump, a temperature measurement in the presaturator head-space logged with LabVIEW™, and a condenser to manage condensate removal from the vent gas. Additionally, all wettable surfaces in the LVI were replaced with Dursan® coated stainless steel and the gas ducts were increased from 1/2" to 5/8" ID to reduce gas-liquid entrainment following condensation.

Two types of experiments were run: (1) LVI tests with piperazine (PZ) to demonstrate LVI pump operation stability, and (2) tests to demonstrate CO_2 removal and control via the LabVIEW™ application. Parallel objectives included condensate control and removal as well as liquid sampling during operation.

Operation of the LVI was verified by injecting a 0.5 m PZ solution which could be traced using hot-gas Fourier-Transform Infrared Spectroscopy (FTIR). 90 and 120 ppmv PZ were measured at the absorber outlet for LVI flowrates of 1.0 and 1.5 mL/min, respectively. Assuming an eductor flowrate of 0.9 SCFM, LVI flowrates of 1.0 and 1.5 mL/min produce 220 and 330 ppmv PZ, respectively. Testing showed that the LVI pump produces repeatable, but not stable operation, especially at the higher flow rate of 1.5 mL/min. It is hypothesized that the pump sleeve, which serves as both the inlet and outlet check valves, no longer seals properly when

under eductor suction. The old pump head was removed and replaced with a new pump head (Fluid Metering, Inc. H00CKCLF). Testing with the new pump head will commence in the next quarter.

Following the LVI tests, PZ was added to the solvent (H_2O) to make 0.3 m PZ. The CO_2 concentration in the inlet gas was varied from 0–10 vol % while the solvent rate was varied from 0.1–0.3 GPM (L/G of 10–30 mol/mol) at 25–40 ºC. The maximum CO_2 capture rate achieved was 65%. Due to the low solvent concentration, the solution reached CO_2 saturation in less than 4 hours of operation. After the capture tests, the inlet gas was turned off and the solvent temperature was varied from 40–60 ºC to demonstrate stripping. The slow increase and decrease in CO_2 saturation during absorption and stripping was observable on the FTIR.

Other observations from the tests included the onset of foaming at high liquid rates. Foaming was caused by intense liquid mixing in the gravity drain line leading from the absorber to the solvent tank. When liquid filled the drain line, the head space on the solvent tank was blocked so that it could not adjust to the varying liquid level. Large bubbles of gas would eventually form and burst in the drain line causing the liquid to be pushed back, circulate, and ultimately become aerated. The drain line diameter will be increased in the upcoming quarter. Additionally, liquid sampling using a syringe and septum was successfully performed throughout all CO_2 capture experiments. Liquid samples will be analyzed in the next quarter. Condensate control was greatly improved using a pipe-and-tube counter-current exchanger. Tap water was used as the cold-side fluid.

Finally, liquid channeling may be occurring in the column. The removal rates of CO_2 were less than expected. Mesh redistribution cones will be added at the top, bottom, and middle of the column prior to repeating the CO_2 capture testing.

Introduction

Volatile emissions are a primary concern for CO_2 capture plants using amine scrubbers. Emissions constitute increased economic expense through solvent loss as well as being a source of potentially hazardous environmental pollutants. Compounds found in treated flue gas include contaminants from thermal degradation and oxidation as well as combustion byproducts. Degradation and reaction products have a wide range of toxicity and biodegradation characteristics, which potentially represent unacceptable emissions; as a result, recent work has focused on estimating volatile losses and assessing their toxicological impact.

Volatile emissions can be reduced through the use of an absorber column using recycled water as a solvent, called a water wash. Design considerations for water wash systems include liquid distribution methods to adequately wet packing with small liquid rates, and balancing water in the absorber/stripper system by adjusting the total volatile concentration in the wash water. Water wash columns have relatively flat efficiency profiles, meaning the removal efficiency is not a strong function of either the gas or liquid flowrates or the operating temperature.

Emissions with Aerosols

Recent pilot plant measurements have shown that normal water wash columns are ineffective at controlling volatile loss of amine and other pollutants due to the presence of aerosols. In 2011, MHI presented pilot test results for both KS-1™ and MEA which showed that emissions were proportional to inlet SO_3 concentration (MHI, 2012). Amine levels out of the wash section were

0.4–23.2 ppmv and 0.8–67.5 ppmv for KS-1™ and MEA, respectively, for 0–3 ppmv inlet SO_3. Aerosols were visibly present at the direct-contact cooler (DCC) and wash outlets. At the Maasvlakte pilot plant, TNO and SINTEF jointly tested a 30 wt % MEA CO_2 capture unit with a downstream water wash complete with online gas and aerosol phase sampling (TNO, 2012; SINTEF, 2012). Excessive emissions were observed; aerosols, not physical entrainment, were responsible for the increase. Lithium and rubidium carbonate (Li_2CO_3, Rb_2CO_3) tracers in the solvent and wash loops verified negligible entrainment. A Brownian demister unit (BDU) was installed downstream from the wash section which reduced emissions to previously simulated levels, indicating the bulk of emissions were contained in the droplet phase. Mean droplet diameters (d_{Drop}) were measured using light extinction coefficients and ranged from 0.76–7.88 μm at the BDU inlet and 0.2–1.74 μm at the outlet. The quality of the inlet flue gas and the absolute temperature of the absorber influenced the emission rate. More recently, a baseline study using MEA at NCCC in Wilsonville, Alabama saw higher amine emissions than expected (NCCC, 2012). The number of absorber beds (2–3), intercoolers (0–2), and inlet SO_3 concentration (1.8 and 3.2 ppmv) were varied as part of a parametric test on emission rate. The work concluded that carryover was proportional to inlet SO_3 and also to the concentration of MEA in the wash water. Emissions were inversely related to absorber temperature. In all studies, aerosols increased emissions roughly 1–2 orders of magnitude.

It is clear from pilot plant observations and emission studies that removing aerosols is a key part of reducing possible releases from amine-based CO_2 capture plants. The failure of conventional wash columns and the potential financial impact of particle collectors necessitate fundamental research to identify more practical means of controlling emissions for large-scale processes. Understanding interconnectivities of the bulk CO_2 removal process operating conditions and aerosol dynamics can provide the necessary insight required to either design or operate a system with the intention of suppressing droplet growth; or conversely, to condition aerosols for easier removal.

Safety

The FTIR and peripheral equipment are maintained at 180 °C to prevent condensation inside the analyzer. The surface temperature of fittings and any metal tubing used for connections present potential burn hazards when in operation. Any heated transition or connection should be insulated to prevent contact burns. Insulation also serves the purpose of preventing cold spots which can lead to condensation. Leather work gloves should always be worn when working with FTIR lines and fittings to prevent burns.

All lines that directly connect to heated fittings must be Teflon® to prevent melting and gas loss from the process. Melted tubing can lead to hazardous gas release. Tubing should be confirmed to be of Teflon® grade or higher prior to use with the FTIR.

Aerosol Growth Column (AGC)

An updated P&ID of the AGC is shown in Figure 1–Figure 3 below. The P&ID is broken up into three sections: (Figure 1) gas distribution and mixing, including the LVI, (Figure 2) pre- and post-gas preparation including presaturation and condensation, and (Figure 3) the absorber section with local analysis.

N_2

N_2 is a distributed utility taken from a large, outdoor dewar. The supply is split following an isolation valve into three streams used for the absorber gas supply, the LVI gas supply, and FTIR maintenance and calibration.

The flowrate to the absorber is controlled by an analog 100 SLPM Brooks 5851 I-Series mass-flow controller connected to an NI 9265 4-ch, 20 mA current output module and an NI 9203 8-ch, 20 mA current input module. Connection is made with a 15 pin D-Sub cable at the controller side and crimp pin connections at the NI module side. The NI modules are connected to a cDAQ-9174 USB chassis which is controlled by LabVIEW™ via a laptop and USB2.0 connection.

The flowrate to the LVI is controlled by a pressure regulator.

The flowrate to the FTIR optical purge line is controlled by a pressure regulator with a Bird Precision critical orifice (0.004" ID). The regulator sets the pressure upstream of the orifice which allows very precise control of the small flowrate.

CO_2

Bone dry, Gr. 3.0 CO_2 (Airgas® CDBD200) is stored in an adjacent lab and is sent through an overhead line into the AGC vent hood. The delivery pressure is regulated using a Y11-N245D320, CGA320 regulator attached to the tank. The flowrate of CO_2 is controlled by a 15 SLPM Brooks 5850 I-Series mass-flow controller using the same NI modules and chassis as described for N_2.

At the end of experiments, the CO_2 line is isolated at the AGC wall isolation valve and the remaining CO_2 is bled to a vent hood to prevent leakage from the cylinder.

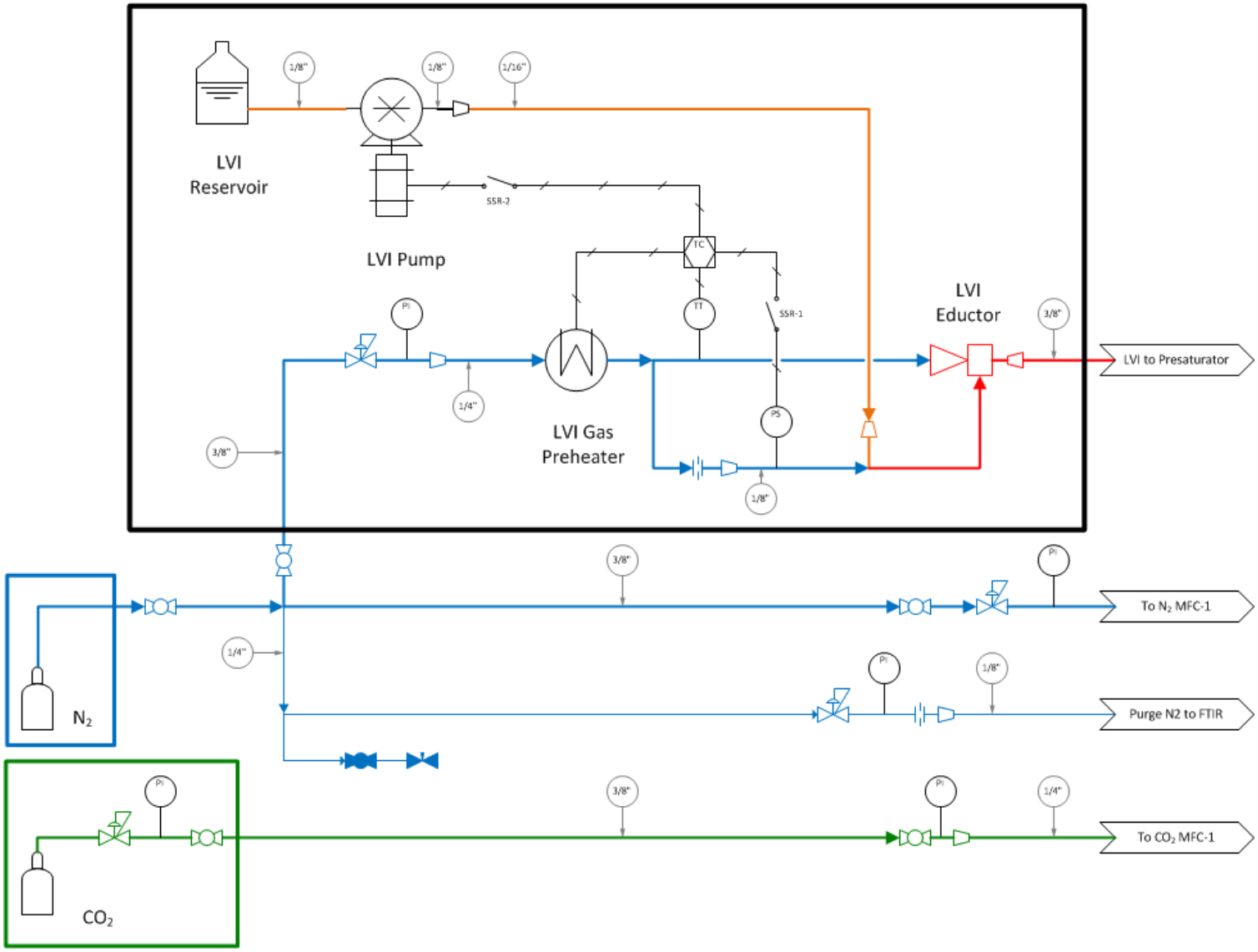

Figure 1: Aerosol Growth Column P&ID Sheet #1

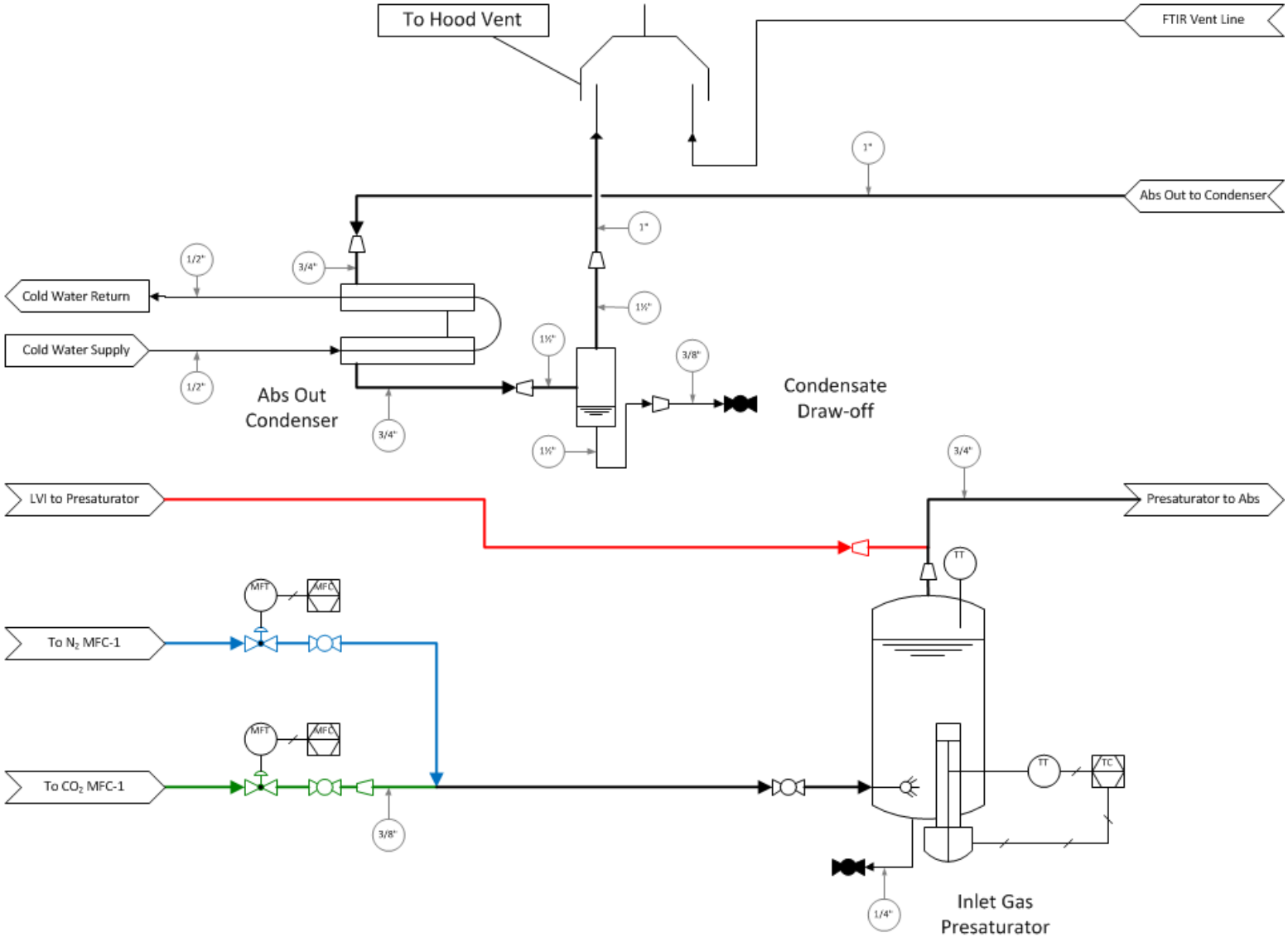

Figure 2: Aerosol Growth Column P&ID Sheet #2

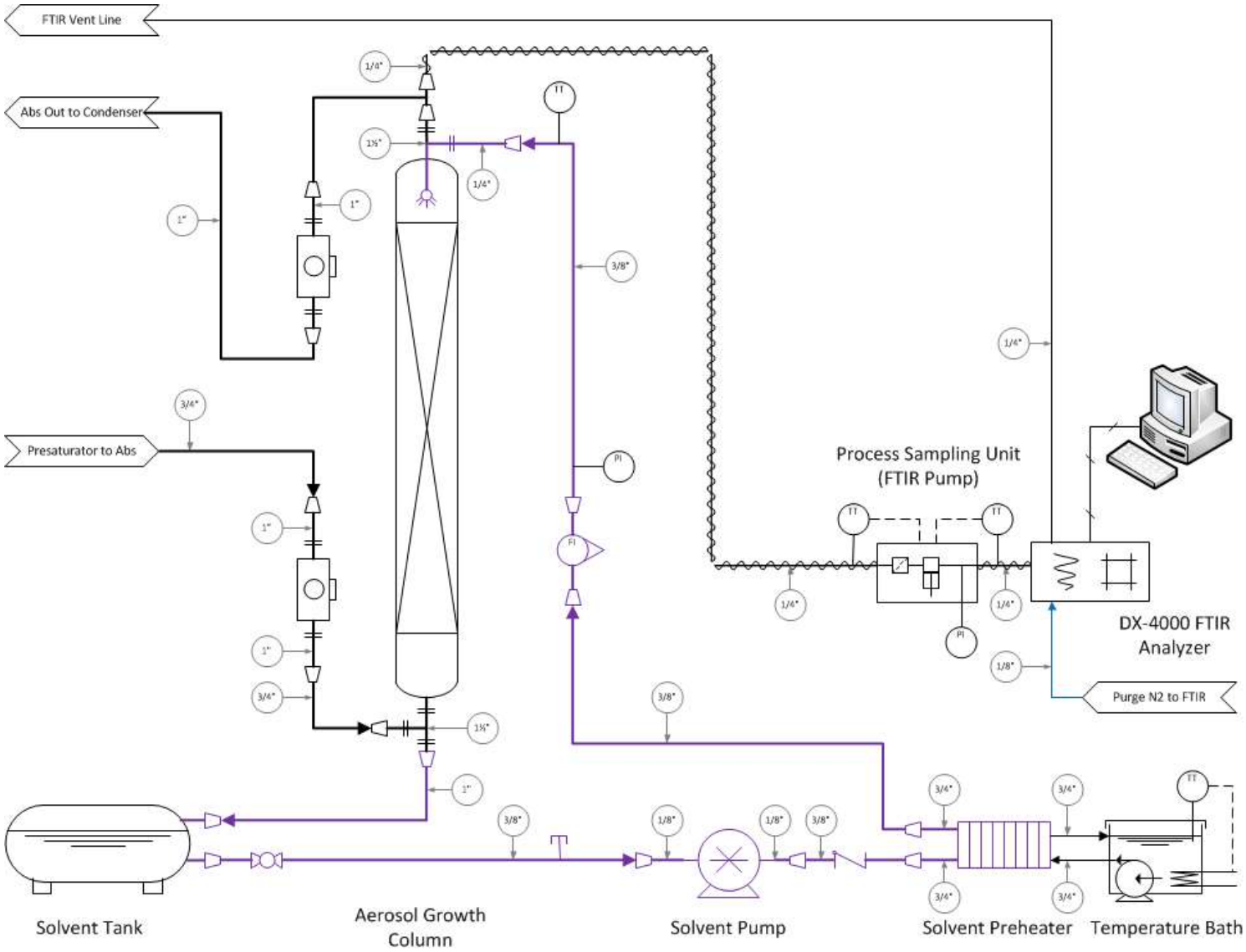

Figure 3: Aerosol Growth Column P&ID Sheet #3

LVI

The LVI is designed to produce H_2SO_4 aerosol up to 5 ppmv in a 350 ACFM gas stream. The LVI blends hot gas (310 ºC) with a metered stream (FMI RH00 pump and FMI VS200 controller) of liquid in an eductor (Air-VAC HAVR062HSS) body. The vaporized material is then introduced into the cold, main process gas stream where condensation occurs. Provided a high enough supersaturation, the vaporized liquid should form small, homogeneous aerosol nuclei. The vaporization/condensation nucleation mechanism will work for any compound with sufficient supersaturation.

Several safety interlocks are present in the LVI circuitry. Power to the temperature controller, air preheater, and liquid pump are relayed to a pressure switch, or Solid-state relay #1 (SSR-1) shown in **Error! Reference source not found.** If sufficient flowrate is not being sent to the eductor, the vacuum level will decrease and disconnect power to the remaining devices. The temperature controller has an alarm channel connected to SSR-2 which is relayed to the pump motor power supply. If the temperature alarm condition is not met, the pump cannot operate. SSR-3, as described in the LVI manual, provides a relay signal between the temperature controller and the air preheater.

The LVI controls and liquid reservoir (500 mL G45 amber bottle) are contained in a Hoffman 19" x 16" x 14" enclosure. The eductor, air preheater, and tubing are housed in a Wigman 10" x 8" x 4" steel enclosure with a 3/8" 316SS bulkhead fitting. The Wigman enclosure is stuffed with several layers of internal closed-cell silicone foam insulation. The power, control, and liquid lines between the two enclosures are wrapped in a 15' woven umbilical line.

Presaturator

The N_2/CO_2 gas streams are bubbled though a presaturator to approximately maintain H_2O balance within the absorber column. The presaturator (Figure 2) for the AGC is constructed of 6" 304SS Sch. 10 pipe with #150 flanges. Temperature is controlled with a screw-plug immersion heater with a relayed temperature controller. The head-space temperature is logged with a separate K-type thermocouple connected to a 4-ch ± 80 mV NI-9211 module.

The inlet gas is sparged into the presaturator by a 3/8" straight tube with small drilled holes. The total liquid height in the saturator is maintained at over 20".

The hot gas mixture from the LVI is mixed with the saturated process gas at the outlet of the presaturator in a 3/4" stainless steel tee fitting.

Absorber

The absorption section of the AGC (Figure 3) is constructed out of a 1½" 304SS Sch. 10 pipe with flanged ends. The packing is supported using removable lugs and a mesh screen support. The column can support 6' of packing. The packing used in this work was RSR-0.3 random packing.

Gas is introduced into a flanged tee at the bottom of the column. The inlet to the column has an FTIR sample point constructed from a 3/4" threaded pipe tee reduced to a 1/4" tubing connection using a reducer bushing and a Swagelok® adapter. The sample point was plugged during this quarter.

Solvent is drawn from a 16 gal SS tight-head drum (The Cary Company 26B6SS) by a Micropump® A-mount suction shoe pump head controlled by a Cole Parmer Console Drive. The flowrate is measured by a rotameter (Omega FL46302). The solvent temperature is controlled by cross exchanging it with recirculated H_2O provided by a Lauda ECO E4G temperature bath. The cross exchanger is a Thermal Transfer Systems AN14-20H plate-and-frame heat exchanger. The solvent is delivered into the top of the column using hollow-cone spray nozzles (Kyser and Associates 1/4A-316SS2 & 1/4A-316SS-5) connected to a blind flange. The solvent temperature is measured at the flange using a K-type thermocouple. The CO_2-rich liquid drains through a 1" ID gravity line back into the solvent tank.

Condenser

A condenser (Figure 2) was designed and built this quarter to control condensation of the saturated gas exiting the absorber column. Condensation in the exit line eventually leads to liquid-filled lines since the duct velocity prevents drainage to low points for liquid collection. The condenser is a counter-current, pipe-and-tube exchanger with the gas on the shell-side and cooling H_2O on the tube-side. Graphite ferrules were used on the tubes so they can be removed so that all the shell and tube surfaces can be cleaned periodically.

The condenser area was designed using a heat transfer coefficient of 400 $W/m^2 \cdot K$ and assuming a cooling water temperature of 10 ºC. However, chilled H_2O lines were not available in the AGC laboratory, so tap H_2O was used instead.

The cooled gas exiting the exchanger is sent to a 2" pipe tee to reduce the velocity such that condensate will drop out and drain to the condensate collection point located at the bottom of the column. The amount of condensate is observable in a clear tubing line with an isolation valve. The condensate is collected in a 5 gal plastic carboy and is mixed back into the solvent. Gas exits the knock-out tee at the top of the vent hood.

Analysis

FTIR

The total concentrations of species present in the gaseous and aerosol phases are measured using hot-gas FTIR. The AGC has two FTIR sampling ports: a parallel sampling port at the absorber exit, and a perpendicular sampling port at the absorber entrance. This report includes FTIR results at the outlet sampling point only. All connections of the FTIR are insulated and heat-traced using glass wool and heat tape controlled by AC Variable Autotransformers (variac). Variacs are typically set to 35% of full voltage (120V).

Low resolution FTIR is a powerful quantification tool used to measure species concentrations in the gas or vapor phase. Individual constituents are distinguished by their absorption of light at particular wavenumbers in the mid-infrared region (500–4000 cm^{-1}). Absorption in the mid-infrared region causes molecular vibrations and rotations. The differences in molecular structure and bond strengths result in unique absorption spectra for individual molecules. These spectral features can be used in combination with the Beer-Lambert law to quantify individual species present in a multicomponent matrix. Absorption is assumed to be proportional to concentration; reference (calibration) spectra for each individual component are multiplied by a scalar and summed across the measured range of wavelengths to reproduce the gross spectra measured by the FTIR.

The specific hardware used in this work is the Gasmet™ DX–4000 portable FTIR spectrometer. The path length is 5 m and the wavenumber resolution is 8 cm^{-1}. Peripheral equipment including heated sample lines and sample pump is maintained at 180 °C to prevent condensation during transport and analysis. Calcmet™ software is used for chemometric analysis.

Sample flow is kept at 2–12 SLPM by a diaphragm pump connected to the inlet of the FTIR cell.

Liquid Sampling

A liquid sampling port was added on the suction side of the solvent pump. The sample port consists of a 3/8" Swagelok® tee with a 12.7 mm OD RESTEK® BTO Septa. Liquid samples are drawn using a 2 mL syringe and are transferred to 4 mL (1 dr.) amber vials for subsequent analysis.

Initially, the sample location was downstream of the solvent pump; however, as the pressure in the line increased, the septum would swell and the syringe plunger would be forced outward. Relocating the sample port upstream of the pump reduced swelling and possible leakage of the septum making sampling safer and easier.

Results

LVI Stability Tests

The first set of experiments in this report encompasses measuring the performance of the LVI by introducing a tracer into the vaporized material which is observable by FTIR. A solution of 0.5 m PZ was gravimetrically mixed to create as the LVI trace solution. The LVI flowrate was then varied and the outlet PZ was measured. The solvent in the AGC was tap H_2O during these experiments. LabVIEW™ controls and temperature measurements were tested in tandem.

Figure 4 shows the H_2O measurement as the solvent temperature was varied for the first experiment. The black curve shows the value that would be observed if Raoult's Law is calculated using the measured solvent temperature. The smoothness of the curves shows that entrainment or condensation in the FTIR lines and connections is not present. The colored squares indicate when the LVI is injecting into the process gas. The injection rates were 1.5 and 1.0 mL/min as color-coded. The H_2O curves clearly show the addition of H_2O into the gas as well as their proportional relationship with the LVI flowrate.

Figure 5 shows the PZ measurement during the second LVI injection timeframe. Assuming an eductor flowrate of 0.9 SCFM and 0.5 m PZ in the injection liquid, the concentration of PZ should be 220 and 330 ppmv PZ for injection rates of 1.0 and 1.5 mL/min. Since the absorption solvent was H_2O, the column was operating as a water wash. The levels measured by the FTIR correspond to 36–40% removal of PZ in the wash solution.

The LVI showed relatively stable operation during the 1.0 mL/min injection periods; however, the measured PZ was considerably less stable during an injection rate of 1.5 mL/min. It was discovered that while the pump was off, liquid was sucked through the lines, indicating that the pump sleeve was not sealing properly. At higher liquid flowrates, the air preheater was receiving too much liquid to vaporize, leading to intermittent condensation.

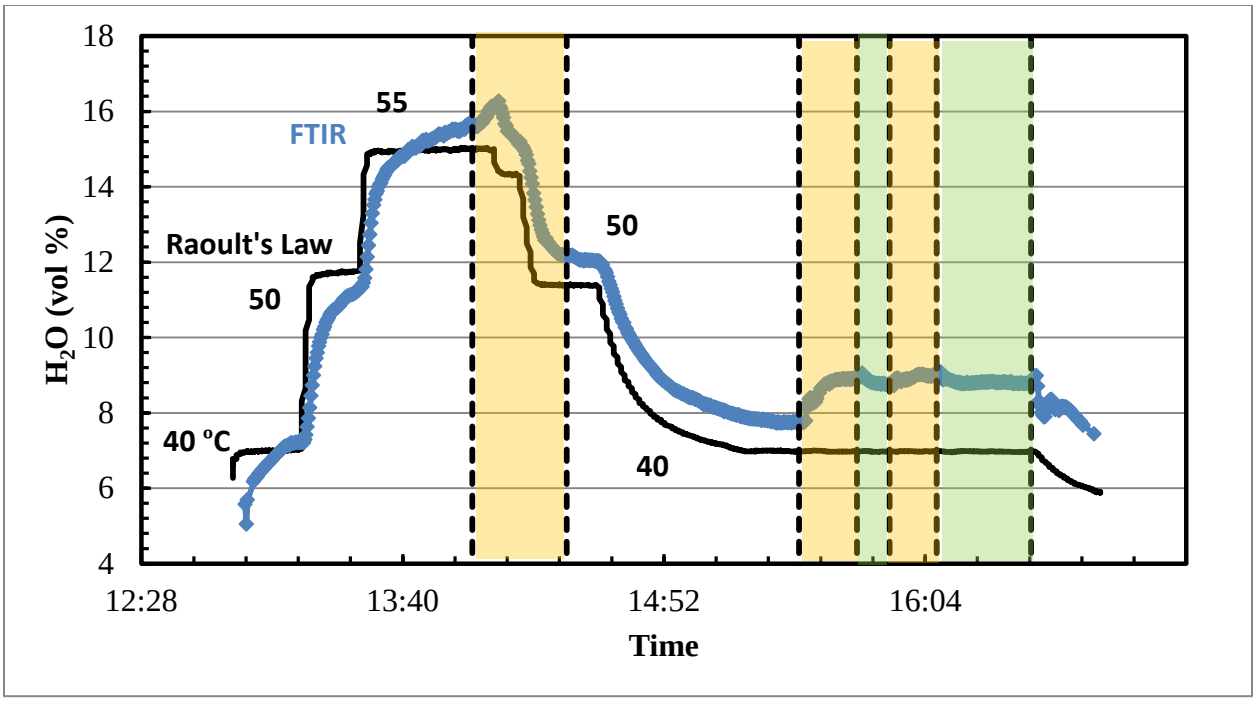

Figure 4: FTIR measurements of H_2O with varying solvent T and LVI flowrates. LVI Flowrates: 1.5 mL/min, 1.0 mL/min.

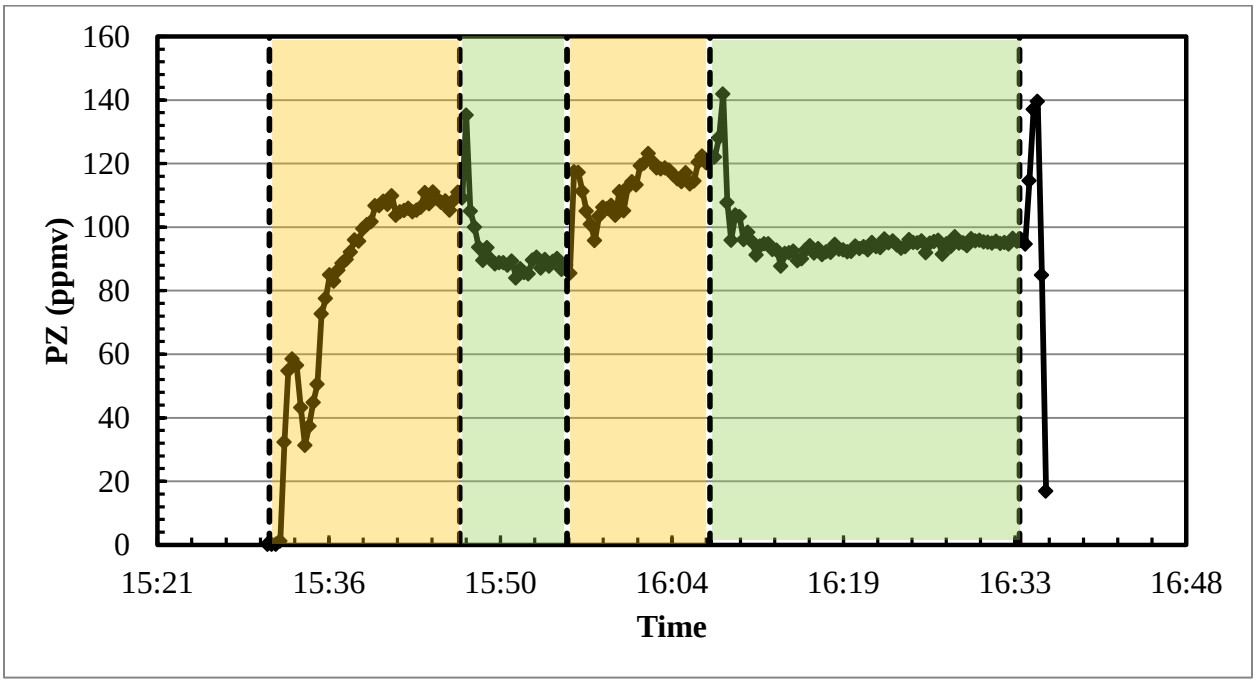

Figure 5: FTIR measurements of PZ with varying solvent T and LVI flowrates. LVI Flowrates: 1.5 mL/min, 1.0 mL/min.

Figure 6 shows a repeat experiment including the addition of CO_2 in the absorber inlet gas. The LVI flowrate was kept at a constant 1.0 mL/min. The LVI instability is prevalent throughout.

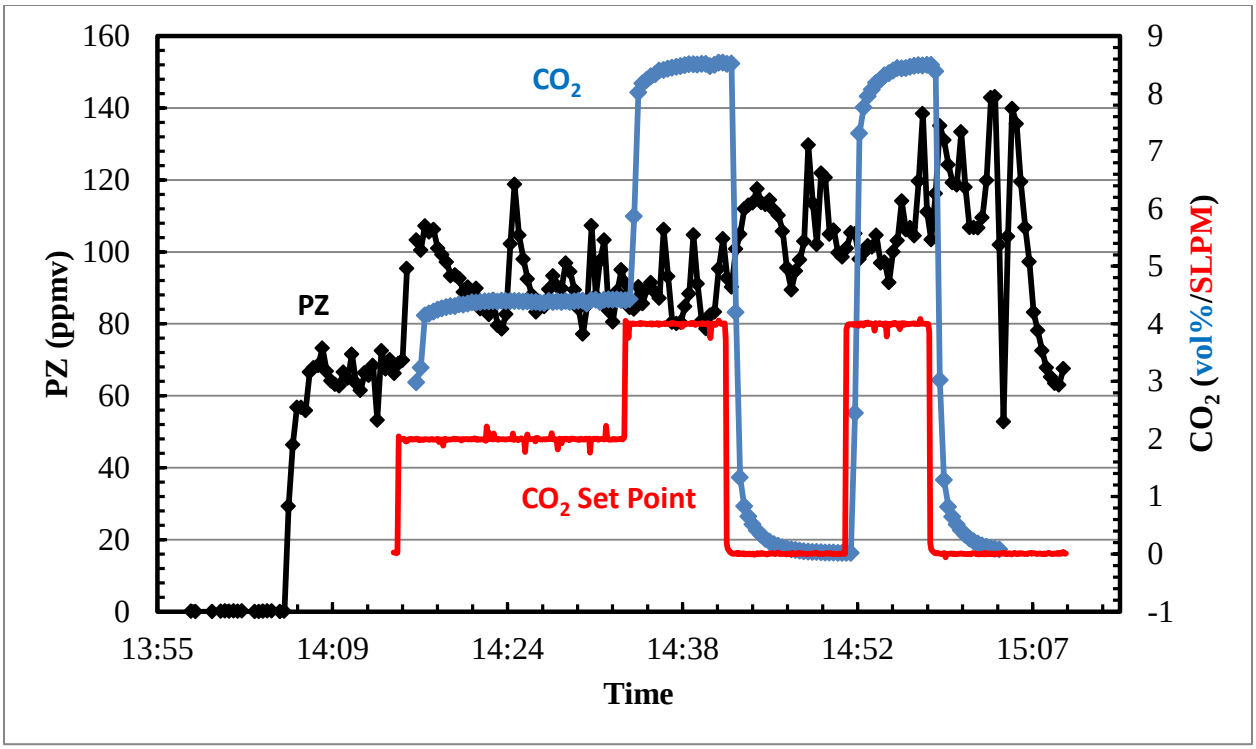

Figure 6: FTIR measurement of PZ with varying inlet CO_2 concentration. LVI: 0.5 m PZ at 1.0 mL/min. Absorber Solvent: H_2O at 40 °C.

CO_2 Capture Tests

After the LVI tests, the H_2O solvent was drained out of the solvent tank and 9 gallons of 0.3 m PZ was gravimetrically made using a freight scale and pumped into the solvent tank. The unloaded PZ solvent was used to measure CO_2 removal during variable operating conditions.

Figure 7 shows the CO_2 measurement at the outlet and the inlet CO_2 concentration assuming complete saturation at the measured presaturator head-space temperature.

Table 1 shows the operating conditions during the corresponding bracketed operating times.

The CO_2 capture rate varied from 32–65% and trended as expected; higher solvent flowrates and lower solvent temperatures produced higher removal rates. Since the solvent capacity was very low, the loading increased rapidly during the experiment. The decreasing removal rates indicate the loading of the solution. No redistributors were used; therefore, liquid maldistribution may lead to less effective area than expected, and consequently the lower observed capture rates. This is further exacerbated by the hollow-cone spray geometry which would introduce the liquid at the walls or edge of the packing.

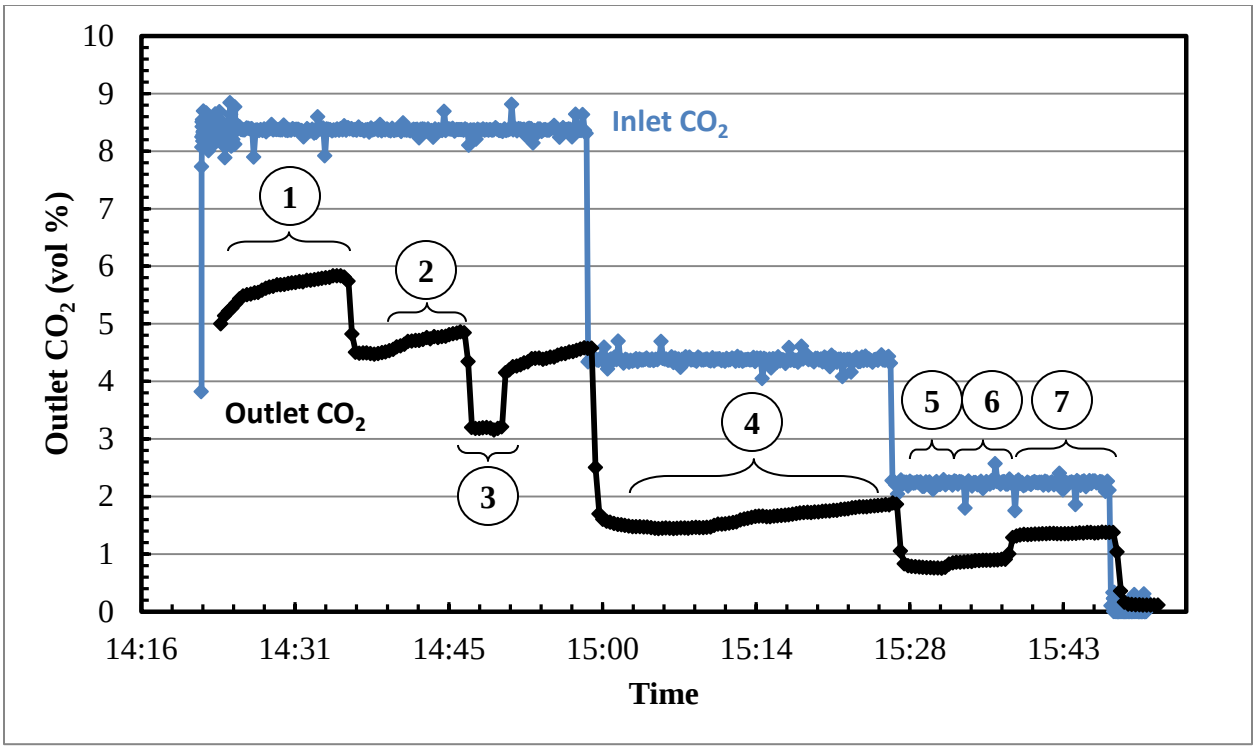

Figure 7: 06/24/14 CO_2 Capture test. Inlet and outlet CO_2 concentrations. Solvent: 0.3 m PZ.

Table 1: 06/24/14 AGC operation data

Meas. Range	Gas Rate (SLPM)	Solvent Rate (GPM)	Solv. Inlet T (ºC)	CO_2 In (vol %)	CO_2 Out (vol %)	CO_2 Cap. (%)
1	44.19	0.1	40.01	8.35	5.62	32.69
2	44.20	0.2	40.35	8.35	4.66	44.19
3	44.27	0.3	40.39	8.35	3.20	61.68
4	42.23	0.3	37.00	4.38	1.65	62.33
5	41.31	0.3	34.68	2.24	0.79	64.73
6	41.26	0.2	34.44	2.24	0.86	61.61
7	41.19	0.1	33.89	2.24	1.35	39.73

Figure 8 shows outlet measurements of CO_2 and PZ during the 06/24/14 test. As the solvent and presaturator warm up, PZ increases closely with temperature to about 2 ppmv. When CO_2 is introduced into the gas stream, PZ drops to the quantification limit of about 0.5 ppmv. The measured PZ volatility shows an inverse relationship with outlet CO_2 concentration.

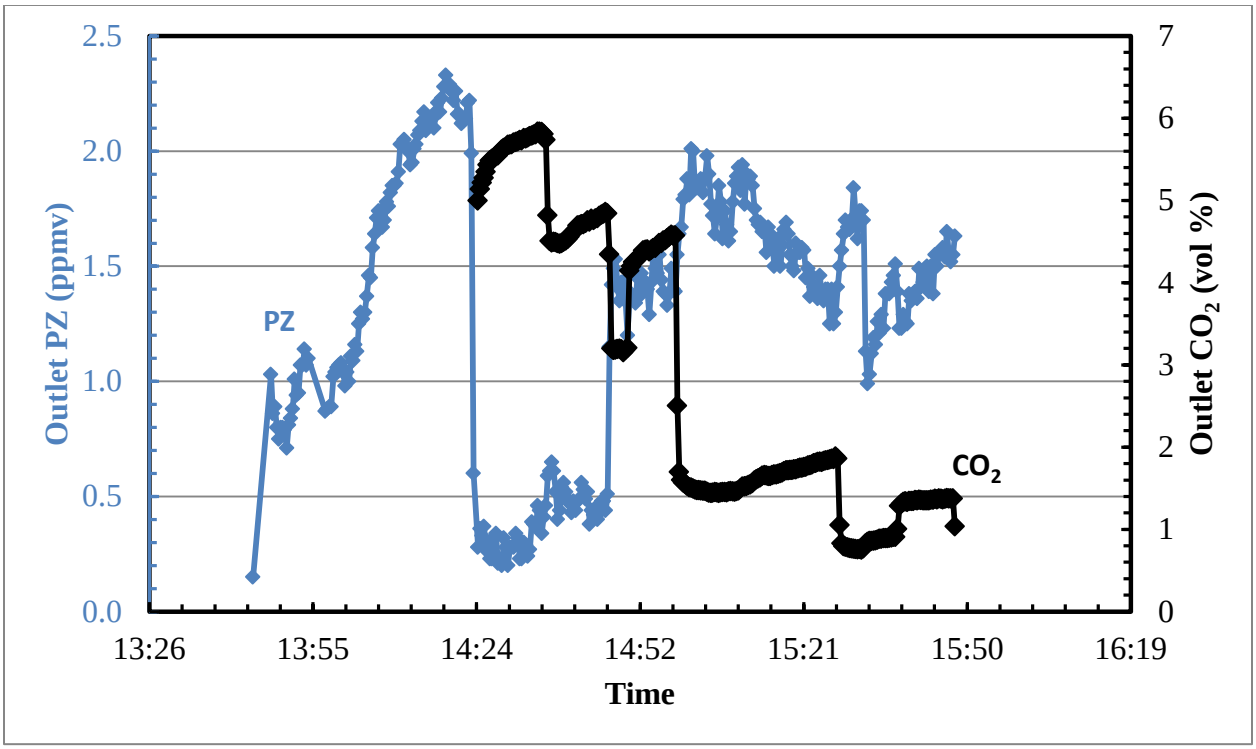

Figure 8: 06/24/14 CO_2 Capture test. Absorber outlet measurements of PZ and CO_2 by FTIR.

Figure 9 shows a CO_2 capture test the following day using the same solvent inventory however the orifice on the spray nozzle was removed to introduce the solvent by a single drip point to investigate liquid distribution effects on the CO_2 capture rate. The corresponding operating conditions can be found in

Table 2.

Though the capture rates appear much lower than those observed on 06/24/14, it was clear that the solvent was approaching CO_2 saturation during the experiment and therefore no conclusions on the effect of the spray nozzle on capture rate can be drawn from these results.

Following the 06/25/14 CO_2 capture experiment, the inlet CO_2 turned off and the solvent temperature was increased to mimic stripping operation. The results from this test are shown in Figure 10 with the corresponding operation parameters found in

Table 3. It is clear from the developed CO_2 partial pressures that the solvent was nearly saturated with CO_2.

Figure 9

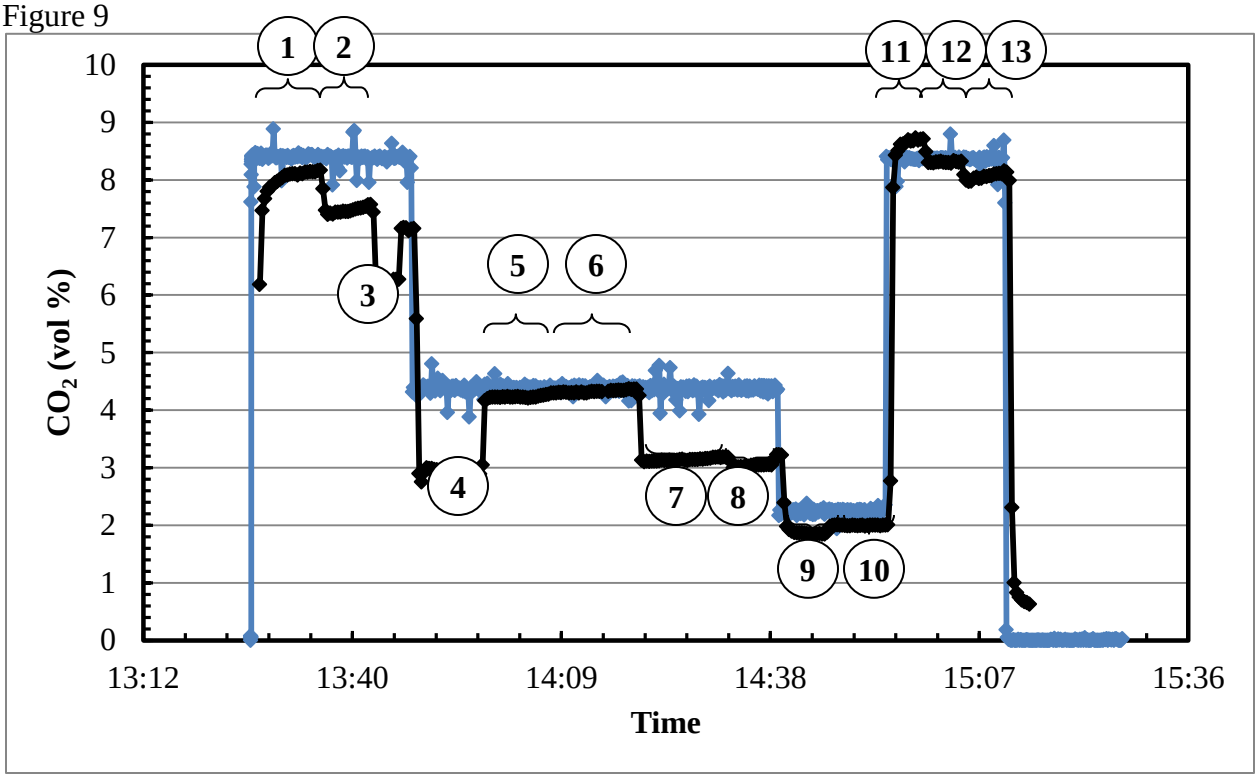

Figure 9: 06/25/14 CO_2 Capture test. Inlet and outlet CO_2 concentrations. Solvent: 0.3 m PZ.

Table 2: 06/25/14 AGC operation data

Meas. Range	Gas Rate (SLPM)	Solvent Rate (GPM)	Solv. In T (ºC)	CO_2 In (vol %)	CO_2 Out (vol %)	CO_2 Cap. (%)
1	44.21	0.1	25.69	8.38	8.07	3.70
2	44.26	0.2	25.75	8.39	7.45	11.20
3	44.21	0.3	25.78	8.38	6.22	25.76
4	42.17	0.2	25.86	4.35	2.87	34.02
5	42.21	0.1	26.92	4.40	4.21	4.32
6	42.17	0.1	40.04	4.38	4.32	1.37
7	42.21	0.2	40.42	4.37	3.14	28.15
8	42.21	0.3	40.46	4.38	3.08	29.68
9	41.26	0.2	40.46	2.25	1.88	16.44
10	41.28	0.1	40.16	2.23	2.39	**-7.17**
11	44.23	0.1	40.18	8.37	8.60	**-2.75**
12	44.22	0.2	40.51	8.39	8.30	1.07

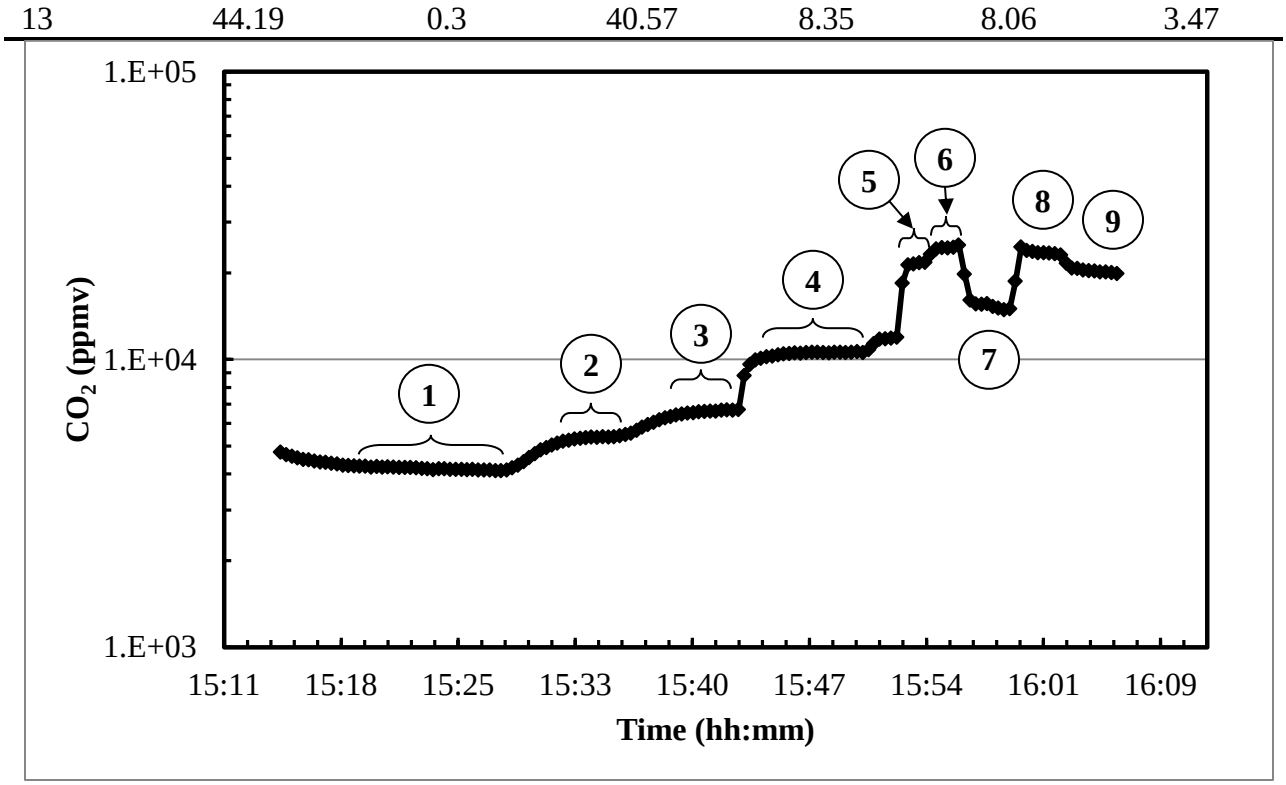

Figure 10: 06/25/2014 CO_2 stripping operation outlet CO_2 FTIR measurements

Table 3: 06/25/2014 CO_2 Stripping operation data

Meas. Range	N_2 Flow (SLPM)	Liquid Rate (GPM)	Solvent T (°C)
1	40.23	0.1	40.35
2	40.20	0.1	48.73
3	40.22	0.1	58.56
4	40.24	0.2	59.85
5	10.02	0.3	59.99
6	5.13	0.3	60.01
7	1.15	0.3	60.03
8	5.21	0.3	60.03
9	10.14	0.3	60.06

Conclusions

Experimental achievements are summarized below:

- 0.5 m PZ solution used as tracer to quantify LVI operation.
- LVI liquid flowrates of 1.0 and 1.5 mL/min of 0.5 m PZ produced 90 and 120 ppmv of PZ at the AGC outlet as measured by FTIR. This is indicative of aerosol formation.
- AGC achieved 65% CO_2 capture with a 0.3 m PZ solvent at 40 ºC.
- FTIR successfully measured AGC outlet gas without condensation or entrainment problems.

Future Work

The AGC solvent PZ concentration will be increased incrementally from 0.3 m to 1.2 m and further CO_2 capture/LVI tests will be performed. Liquid redistributors will be added to reduce the likelihood of liquid channeling. The new LVI pump head will be tested with both PZ and H_2SO_4 to verify stable operation. Liquid samples will be analyzed to track loading and H_2O balance.

The solvent produced during AGC testing will be stripped by increasing the solvent inlet temperature to 80 ºC.

References

Fulk SM. "Modeling Aerosols in Amine-Based CO_2 Capture." *Energy Proc. 2013;37:1706-1719.*

Mitsubishi Heavy Industries (MHI). "Amine Emission Control Technology of KM CDR Process™." Presented at the Amine Workshop in Palo Alto, California. August 16, 2011.

National Carbon Capture Center (NCCC). "National Carbon Capture Center: Post Combustion." Presented at the 2012 NETL CO_2 Capture Technology Meeting. July 10, 2012.

Netherlands Organization for Applied Scientific Research (TNO). "Emission Reducing Technologies Aerosols." Presented at UTCCS-1 in Austin, Texas. January 25, 2012.

Rochelle GT et al. "CO_2 Capture by Aqueous Absorption, Fourth Quarterly Progress Report 2013." Texas Carbon Management Program. The University of Texas at Austin. 2014.

SINTEF. "Emission Studies at the Maasvlakte CO_2 Capture Pilot Plant." Presented at UTCCS-1 in Austin, Texas. January 25, 2012.

Xu Q. *Thermodynamics of CO_2 Loaded Aqueous Amines.* The University of Texas at Austin. Ph.D. Dissertation. 2011.

Aerosol Observation and Separation in Amine-Based CO_2 Capture

Quarterly Report for April 1 – June 30, 2014

by Matt Beaudry

Supported by the Texas Carbon Management Program

McKetta Department of Chemical Engineering

The University of Texas at Austin

July 31, 2014

Abstract

Amine emission in aerosol form has recently been observed as a significant problem for amine-based CO_2 capture plants. Soot and hydrolyzed SO_3 condense in the absorber while collecting amine. Conventional water wash columns are ineffective at recouping the amine once it is captured in the aerosols. While Brownian diffusion units have proven to be fairly effective at reducing amine emissions, cyclonic separators offer the potential for improved capture performance with a simpler system at a lower cost. A preliminary design is presented for use with both the Aerosol Growth Column and the PRC Pilot Plant. The design is capable of achieving separation at various aerosol particle diameters, depending on the needs of the given experiment. In situ observation of the aerosol properties with both a PDI and an FTIR is possible with this design, either before or after the cyclonic separator.

Introduction

Aerosols and Emissions

The emission of volatile compounds is a major concern at CO_2 capture facilities utilizing amine scrubbing. Amine solvent lost through the overhead of absorber columns represents not only an environmental and safety hazard, but also has undesirable economic implications. Amine losses can occur via three different processes: through the gas phase as a function of vapor pressure in the absorber column, liquid entrainment as the gas velocity increases, and as a mist composed of aerosols. Losses through the gas phase can be mitigated with the use of water washes. These operate by passing the gas countercurrently through a packed column with recycled process water. Liquid entrainment can be reduced by designing the column to use a gas velocity that prevents the entrainment of liquid droplets.

Amine losses through aerosols are a relatively recently observed phenomenon. In 2011, MHI presented pilot plant results that indicated amine emissions were proportional to SO_3 concentration in the inlet flue gas (MHI, 2011). A demister unit, which operates by utilizing Brownian diffusion to remove aerosols of certain radii, was placed downstream from the water wash column. This was found to greatly reduce the amine emissions while having no effect on the release of gas-phase ammonia, indicating that the amine losses were through mist. Aerosol

emissions were found to be influenced by the temperature gradient and relative humidity within the column as well.

Research conducted by Khakharia et al. observed the effect of both SO_3 and soot particle addition to flue gas entering an absorber column (TNO, 2013). The emission of MEA increased with the increasing concentration of SO_3, endorsing the findings by MHI. Amine emissions were even more heavily influenced by soot concentrations, which provide another nucleus for aerosols to form. Khakharia et al. also found that the CO_2 concentration plays a greater role in aerosol formation than the presence of a temperature bulge in the absorber column.

Aerosol Collection

Research conducted by MHI utilized demister units that operate under Brownian diffusion principles. Brownian diffusion is the seemingly random motion of particles in a fluid field that is a result of their impact with the high velocity atoms that the field is composed of. Demister units in amine-based CO_2 capture plants pass the gas discharge from the water wash through a system of mesh screens. These screens, which are similar in coarseness and density to steel wool, collect aerosol particles along their random Brownian diffusion pathways, thus preventing their emission to atmosphere. MHI's Brownian demister unit was found to be effective at reducing amine losses.

Demister units provide one possible means for aerosol removal. Another possible option is the use of cyclonic separators, which operate by using centrifugal forces to separate particles from a fluid stream. Figure 1 provides a simple schematic of the fluid flow through a cyclonic separator. These devices are frequently used in agricultural and coal processing industries, and are relatively easy to implement, thanks to their simple design and absence of moving parts. Design specifications and methodologies are well outlined in the publications by Hoffmann and Stein, (Hoffman, 2002), while further clarification is provided by Funk and Baker's literature review on dust cyclone technology (Funk, 2013). Funk and Baker's comparison of varying cyclone body types contributed significantly to the design outlined in the next section.

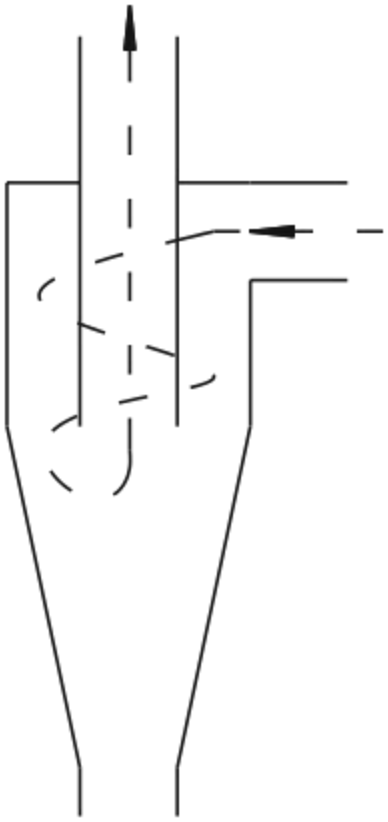

Figure 1: Schematic of cyclonic separator

Two important parameters in designing cyclonic separators are the cut size and the steepness of the cut curve. The cut size refers to the cutoff collection size for the separator. If a cyclonic separator has a cutoff size of 1 µm, this means that particles 1 µm and larger will be collected, while smaller particles will pass through the system. The steepness of the cut curve determines the effectiveness of the separator. A sharp cut curve indicates that the separator collects almost all particles above the designed cut size, while a soft cut curve shows that the separator is more lenient on the collection of larger particles. For the purposes of these experiments, a sharper cut curve is preferred.

Kenny and Gussman utilized cyclonic separators with modular parts to evaluate the effectiveness of varying structural parameters on the cut size and curve sharpness (Kenny, 2000). While it has been noted previously that higher fluid flow rates through cyclonic separators result in the capture of smaller particles, it was determined that higher flow rates result in a sharper cut curve. An order of importance of various sections of the separators was also established, with the inlet configuration being more important than the cone, top, and base, respectively. Wang et al. observed that inserting a reducing pressure drop stick in cyclonic separators reduced pressure drop through the separator while still allowing desirable particle recovery, due to the introduction of increased turbulence in the cyclone (Wang, 2001). This feature may be incorporated into future experimental designs.

Safety

While performing bench and pilot-scale experimental apparatus design, it is important to predict possible hazards that may occur in the process. The cyclonic separators are exposed to aerosols containing sulphuric acid and amines, and must be designed and built with materials that will not corrode under extended use. Operating procedures must be established for both the Aerosol Growth Column and the cyclonic separator apparatus for the dual purposes of aiding training of new experimentalists and to reduce the potential of undesired acid and amine releases.

Experimental Methods

Aerosol Collection

An aerosol collection system is desired for use with both the Aerosol Growth Column and the PRC Pilot Plant. Therefore, flexibility of the design is of upmost importance. Instead of using a conventional cyclonic separator, a swirl tube design will be implemented. Swirl tubes, as represented in Figure 2, utilize angled vanes tangential inlets to generate the cyclonic motion. The swirl tube is designed to be approximately 6.35 cm at the outermost diameter and have a total length of 130 cm. The long length is to allow for flow stabilization before entering the vaned section of the swirl tube, and for the variation of cyclone length. The vanes will have an entry angle in line with the flow and the tube body, and an exit angle of 20°.

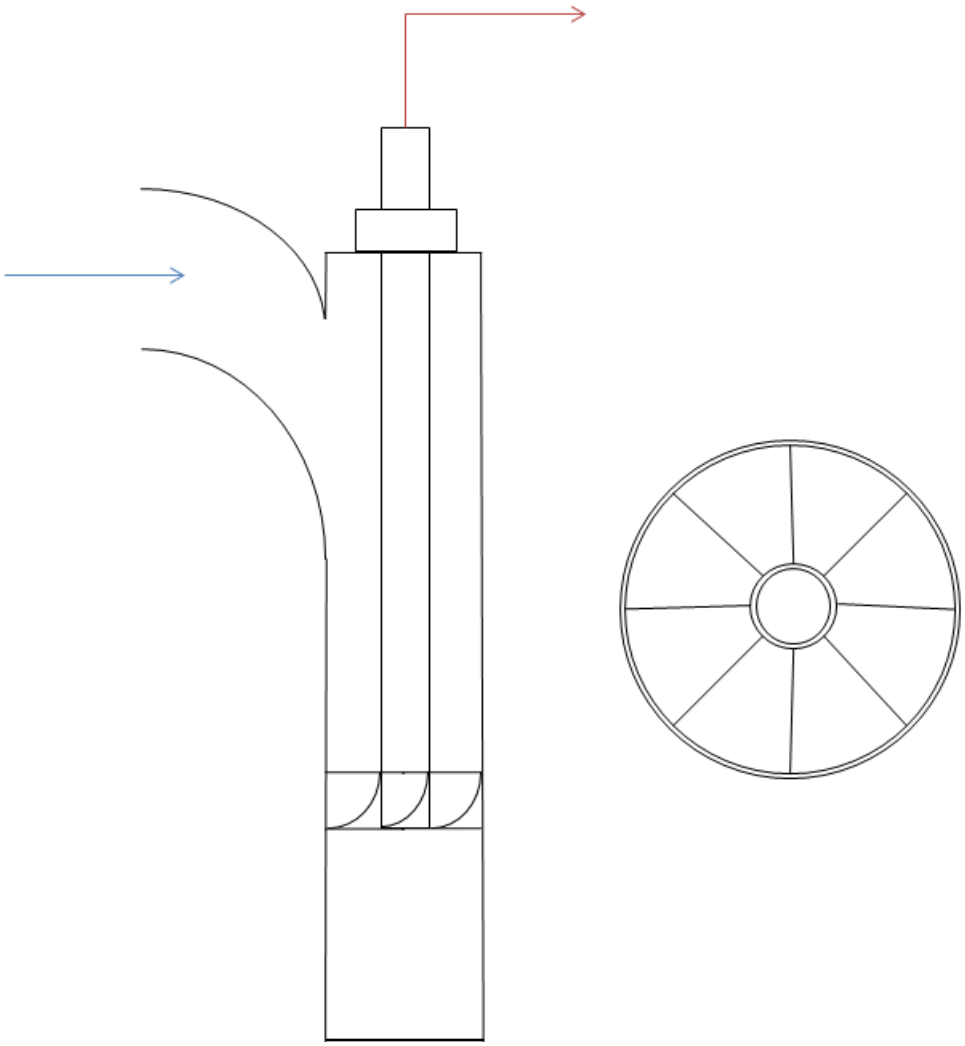

Figure 2: Side view of swirl tube apparatus, and cross sectional view of vane section.

As mentioned previously, flexibility of operation is vitally important. The system should be capable of collecting aerosols of varying cut sizes. One of the key parameters for determining cut size in this design is the diameter of the vortex finder, or the gas outlet. This system is designed to use ¼", ½", and ¾" tubing. Combined with varying the total gas flow rate, this will allow for the collection of particles at any cut size between 1 and 5 µm. This is presented in Table 1. Pressure drop was calculated by Barth's semi-empirically determined equations, (Hoffman 2002).

Table 1: Vortex finder diameter, gas flow rate, and estimated pressure drop for various particle diameter cut sizes

Maximum Particle Diameter Collected	Vortex Finder Diameter	Vortex Finder Diameter	Total Gas Flow	Inlet Velocity	Estimated Pressure Drop
µm	cm	in	L min^{-1}	cm s^{-1}	in H_2O
1.0	0.64	0.25	79.4	69.6	0.05
2.0	1.27	0.50	83.8	91.9	0.03
3.0	1.91	0.75	79.4	149.2	0.01
4.0	1.91	0.75	45.7	85.9	0.03
5.0	1.91	0.75	29.1	54.7	0.07

Aerosol Observation

The effectiveness of the swirl tubes will be evaluated with a Fourier Transform Infrared Spectrometer (FTIR) and a Phase Doppler Interferometer (PDI). The FTIR will be used to quantify the amount of amine that is captured in the aerosols at varying points in the system. Obtaining FTIR samples before and after the swirl tube will determine how successful the swirl tube is at capturing the amine-laden aerosols.

FTIR sampling will not provide data on how successful the swirl tube is in achieving its desired cut size. The PDI will be used to determine the effectiveness of the swirl tube. The PDI allows for in situ observation of aerosols. This is important because removing the aerosols from the system for sampling purposes can result in an undesired variation of their properties through transmission losses, evaporation, condensation, and agglomeration.

The PDI operates by intersecting two lasers at an angle through a small, well-defined volume. A particle that passes through this volume scatters light that is collected by an optical receiver, which uses a phase-doppler type analysis to determine the particle sizes and concentration. Figure 3 presents the proposed configuration of the swirl tube and PDI. Since these components are designed to be immobile during operation, swapping the order of these two units will be accomplished by safely bypassing the system and reconfiguring the system tubing. In Figure 3, the green stream represents the bypass line, the blue stream represents the PDI sampling before the swirl tube, and the red represents the PDI sampling after the aerosol and gas pass through the swirl tube. FTIR sampling ports can be added before the inlet and after the outlet of the swirl tube without affecting the configuration in use.

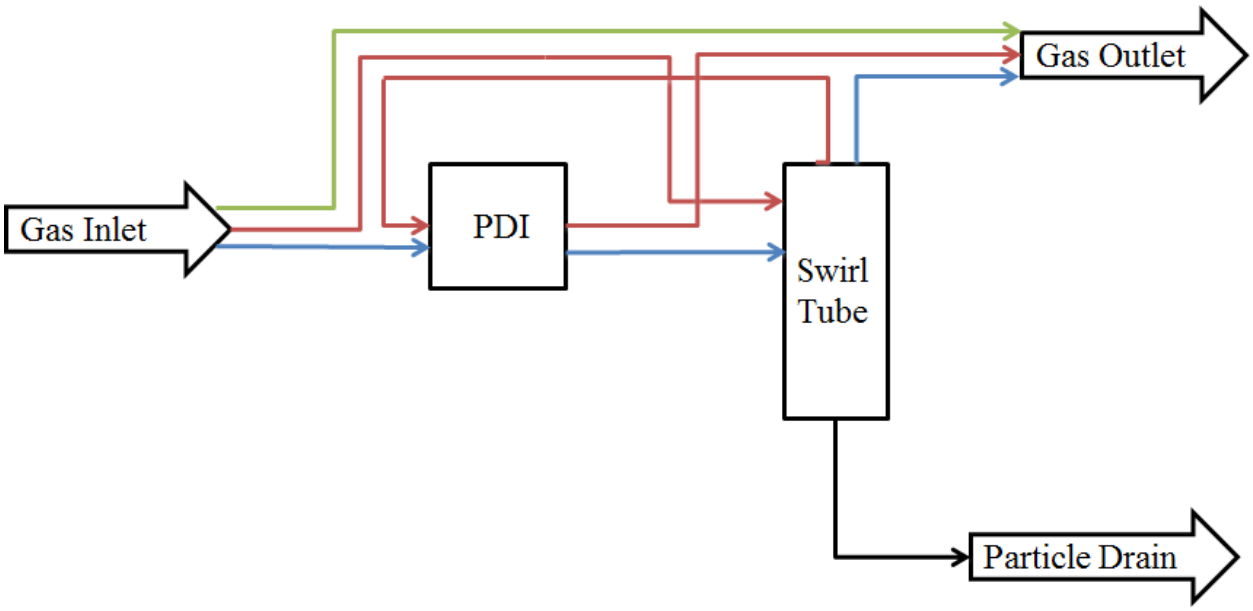

Figure 3: Proposed configuration of swirl tube-PDI system

Effective aerosol collection from absorber outlet streams should be possible with the use of swirl tubes. Minimal pressure drop is expected across these cyclonic separators, as shown in Table 1. The magnitude of the pressure drop is dependent on the aerosol concentration, and varying the amount of aerosol produced in the Aerosol Growth Column or the pilot plant may result in an increased pressure drop across the swirl tube. Current calculations indicate that pressure drop should not be severe enough to negatively affect performance of the Aerosol Growth Column or the PRC Pilot Plant. At this time, it is believed that combining this technique with FTIR analysis will be a cost effective method for capturing and characterizing aerosols.

Cyclonic separators are most efficient when high gas velocities are utilized. This maximizes the centrifugal forces in the cyclone and results in greater collection efficiency of particles of the desired diameter, (Kenny, 2000). Table 1 presents the inlet gas velocities for each collection size specified. The cut sizes that require higher velocities will be more effective at capturing aerosols of the desired diameters. This is an important caveat when analyzing the results from experiments using swirl tubes. Increasing collection efficiency has been and will continue to be a point of emphasis when designing swirl tube systems.

Future Work

The goal of this proposed experimental project is to determine the effectiveness of swirl tubes or other cyclonic separators at removing aerosols from the outlet stream of an amine-based CO_2 capture plant. Next quarter, the swirl tube design will be finalized and construction of the swirl tube itself will be completed. If the PDI is received from Artium Technologies this quarter, testing will begin on determining the effectiveness of the swirl tube design at removing aerosol particles at the desired cut sizes from the Aerosol Growth Column. If not, preliminary work troubleshooting potential pitfalls will be accomplished by using the FTIR.

Additional work will focus on preparing for the upcoming PRC Pilot Plant campaign in November, and on improving the performance of the Aerosol Growth Column under the direction of Steven Fulk.

References

Funk PA, Baker KD. "Dust Cyclone Technology- A Literature Review." *J. Cotton Sci*. 2013;17:40–51.

Hoffmann AC, Stein LE. "Gas Cyclones and Swirl Tubes". Berlin, Germany, Springer-Verlag Berlin Heidelberg New York, 2002.

Kenny LC, Gussman RA, "A Direct Approach to the Design of Cyclones for Aerosol-Monitoring Applications." *J. Aerosol Sci*. 2000;31(12):1407–1420.

Khakharia P et al. "Investigation of aerosol based emission of MEA due to sulphuric acid aerosol and soot in a Post Combustion CO_2 Capture process." *Int. J. of Greenhouse Gas Control*. 2013;19:138–144.

Mitsubishi Heavy Industries (MHI). "Amine Emission Control Technology of KM CDR Process™." Presented at the Amine Workshop in Palo Alto, California. August 16, 2011.

Rochelle GT et al. "CO_2 Capture by Aqueous Absorption, First Quarterly Progress Report 2013." Texas Carbon Management Program. The University of Texas at Austin. 2013.

Rochelle GT et al. "CO_2 Capture by Aqueous Absorption, First Quarterly Progress Report 2014." Texas Carbon Management Program. The University of Texas at Austin. 2014.

Wang L et al. "Effect of a Stick on the Flow Field in a Cyclone and the Pressure Drop Reduction Mechanism" *Aerosol Sci. and Tech.* 2001;35:909–913.

Amine Degradation in Pilot Plants

Quarterly Report for April 1 – June 30, 2014

by Paul Nielsen

Supported by the Texas Carbon Management Program

McKetta Department of Chemical Engineering

The University of Texas at Austin

July 31, 2014

Abstract

The MEA degradation product N-hydroxyethyl-glycine (HEGly) is very important due to its ability to form a stable carcinogenic nitrosamine. HEGly reacts in equilibrium with MEA to form a reversible amide. In degraded pilot plant and bench-scale oxidized MEA samples, the equilibrium ratio of free HEGly to total HEGly was typically 60% ± 10%. 212 mmol/kg of total HEGly accumulated in a cyclic oxidation of 7 m MEA in the HTOR apparatus. 60 to 130 mmol/kg of total HEGly was observed in multiple MEA pilot plant campaigns.

At 120 °C, HEGly thermally degrades at a rate of $1.5 \pm 0.6 \times 10^{-7}$ s^{-1}, 8.8 times faster than MEA. At 150 °C, the thermal degradation rate is $5.7 \pm 0.6 \times 10^{-7}$ s^{-1}. The activation energy of HEGly thermal decomposition is 60 ± 20 kJ/mol. The presence of HEGly does not affect the thermal degradation of MEA.

A new inhibitor, Inhibitor 8 (Inh 8), was tested to determine its ability to reduce the oxidation of piperazine (PZ) by hydrogen peroxide. Inh 8 is expected to behave similarly to Inh A, which has previously been tested at the pilot scale at the SRP facility. Inh 8 can also be recovered from reclaimer waste, potentially decreasing cost. The presence of Inh 8 significantly reduced the accumulation of aldehydes, ethylenediamine, and 1-methylpiperazine in a sample of 5 m PZ reacted with ~100 mmol/kg of hydrogen peroxide and then heated to 150 °C for 21.5 hours.

Introduction

Amine solvents used in post-combustion CO_2 capture degrade via a combination of thermal degradation in the stripper and oxidation by the flue gas in the absorber, which typically contains between 5 and 12 vol % O_2. Dissolved oxygen can react to form peroxides and free radical carriers, which can be carried over to the heated stripper to further oxidize the amine. The most representative method of determining the rate of amine loss and types of products formed is a cyclic system combining the effects of both oxidation and high-temperature thermal degradation. This can only be accomplished in a bench-scale cyclic degradation apparatus or in a pilot plant.

Secondary amines, such as piperazine (PZ), can react with NO_2 absorbed from the flue gas to produce carcinogenic nitrosamines. Primary amines, such as monoethanolamine (MEA), do not form stable nitrosamines on their own. However, secondary amines can accumulate as the result of degradation of MEA. The amino acid N-hydroxyethyl-glycine (HEGly) (Figure 1) has been shown to be one of the most significant secondary amines to accumulate in MEA pilot plant

samples. HEGly can form a stable nitrosamine via reaction with nitrite. HEGly can react with MEA to form the amide N-(2-hydroxyethyl)-2-(2-hydroxyethylamino)-acetamide (HEHEAA), which can potentially ring-close to form 4-(2-hydroxyethyl)-piperzin-2-one (HEPO) (da Silva, 2012).

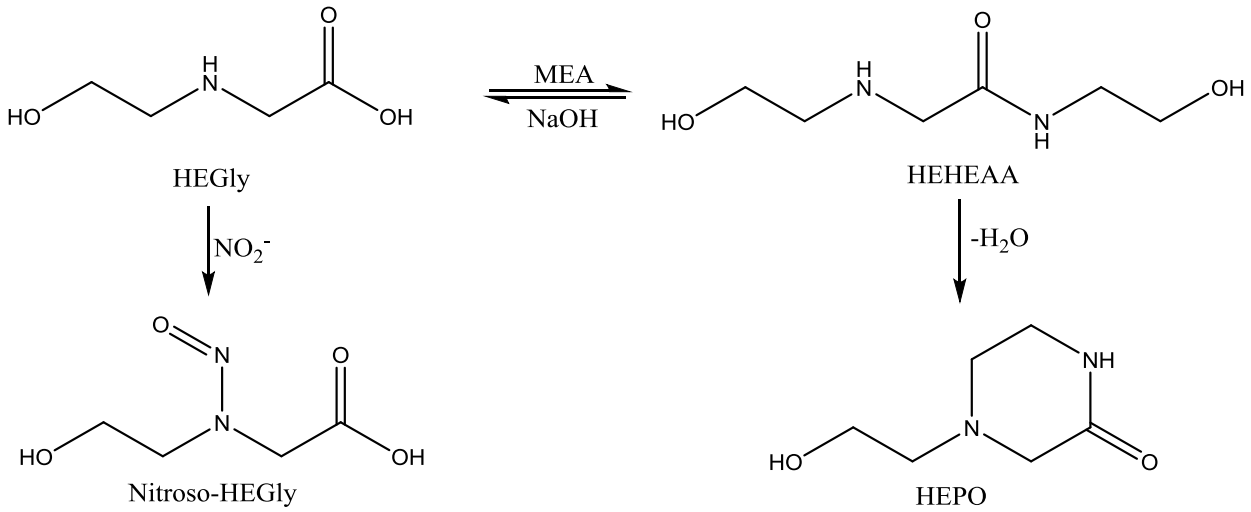

Figure 1: Reaction of N-hydroxyethyl-glycine (HEGly) with MEA to form the HEGly amide (HEHEAA) and N-hydroxyethyl-piperazinone (HEPO) or with nitrite to form nitroso-HEGly

Experimental Methods

Oxidation of Piperazine with Hydrogen Peroxide

In a 40 mL vial, 0.1 mL of 30 wt % hydrogen peroxide (H_2O_2) was added drop-wise to 10 mL of 5 m PZ (α = 0.30 mol CO_2/mol alkalinity) to oxidize ~100 mmol/kg of amine. After allowing 30 minutes for the reaction mixture to mix thoroughly, 4 mL was placed in a sealed thermal cylinder and heated to 150 °C for 24 hours.

Analytical Methods

All analytical methods have been described in previous quarterly reports (Rochelle et al., 2014) and in Freeman (2011).

Total Amino Acids Method

The method for quantifying total HEGly" is identical to the method used to determine total heat stable salts. The concentrated sample is mixed in a 1:1 volumetric ratio with 5 N NaOH and allowed to sit for 24 hours at room temperature to hydrolyze amides back to their constituent amines and free acids. The sample is then diluted by a factor of at least 50x by weight before analysis by the normal AA-HPLC method. The amount of HEGly and other amino acids quantified by this method is the total HEGly amount, representing both free HEGly and the amide.

Safety

Concentrated hydrogen peroxide is an aggressive oxidizer and corrosive to human skin. It can react violently with reducing agents. It can also exothermically decompose into water and oxygen gas, posing a potential flammability risk depending on conditions. Oxidation of amines by hydrogen peroxide may also produce ammonia. All experiments with hydrogen peroxide are conducted in a ventilated fume hood, in vials with sufficient headspace to allow for foaming caused by the decomposition reaction. Reactions between amines and peroxides are done in an aqueous environment to reduce the flammability risk. Concentrated (30 wt %) hydrogen peroxide is stored in a refrigerated space. Exposure to light is minimized. As always when in lab, full PPE consisting of lab coat, safety glasses, latex gloves, long pants, and closed-toe shoes are worn at all times.

Results

Management of N-Hydroxyethyl-glycine (HEGly) in MEA

Accumulation of HEGly and Total HEGly in Cyclic Oxidation of MEA

The accumulation of HEGly in an experiment conducted in the HTOR cyclic oxidation apparatus was reported in the last quarterly report (Rochelle et al., 2014). However, when the samples were treated with NaOH and run again through the AA-HPLC method, the observed HEGly peak was substantially larger, indicating the presence of amides of HEGly that had previously been unquantified. Free HEGly represented around 60% of the total HEGly accumulated during the experiment (Figure 2). The total HEGly accumulated was two times greater than total formate. However, total formate increased linearly while the HEGly accumulation rate decreased over time, indicating that HEGly is less stable and will eventually reach a steady state where the accumulation and degradation rates are balanced.

The amide of HEGly and MEA, N-(2-hydroxyethyl)-2-(2-hydroxyethylamino)-acetamide (HEHEAA), is the primary amide formed. HEHEAA contains an unhindered secondary amine and may be capable of forming a stable nitrosamine.

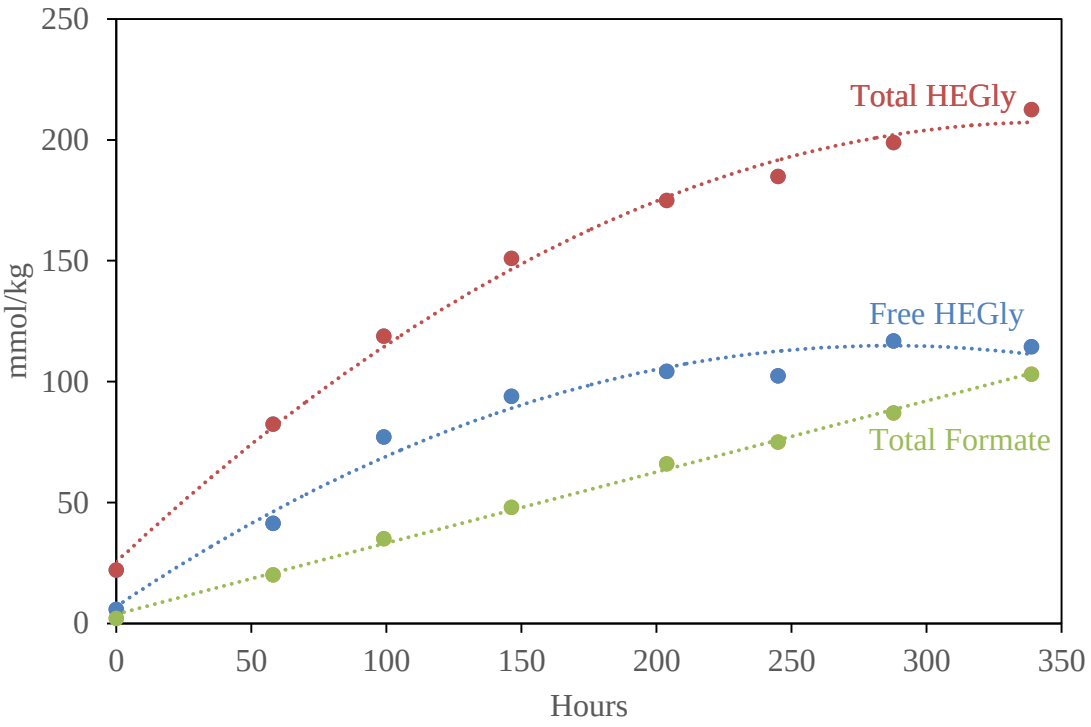

Figure 2: Accumulation of total HEGly, free HEGly, and total formate in HTOR6 (7 m MEA, 7.5 SLPM 2% CO_2 in air, 0.2 L/min cycling from 55 to 120 °C, total inventory 1.5 L) (Total formate results from Voice (2013)).

HEGly has been positively quantified in samples from 5 different pilot plants and two bench-scale cyclic degradation apparatuses (Table 1). Interestingly, HEGly has only been observed in these tests, not in bench-scale low-temperature oxidation experiments or in high-temperature thermal degradation experiments, indicating that both an oxidative environment and high temperature are required to produce HEGly. The values from the Esbjerg and Tiller plants and SDR apparatus as reported in literature were determined using LC-MS (da Silva, 2012). It is unknown whether these values represent free HEGly or include the HEGly amide.

Table 1: Accumulation of free and total HEGly in previous MEA pilot plant campaigns and bench-scale cyclic degradation apparatuses (Esbjerg and Tiller results from da Silva (2012), SDR from Einbu (2013))

Plant (p) or Apparatus (a)	HEGly mmol/kg	Total HEGly mmol/kg	HEPO mmol/kg	Total Formate mmol/kg
HTOR (a)	114.4	212.5		103
SRP (p)	77.3	120.4		20.2
NCCC (p)	79.7	130.6		38.1
OCTAVIUS (p)	26.2	55.7		22
Esbjerg (p)	45– 60		15	25– 30
Tiller (p)	~60		100– 140	15– 25
SDR (a)	~80		~80	~40

The ratio of free to total HEGly in the cyclic oxidation and pilot plant samples was 0.6 ± 0.1.

Thermal Degradation of HEGly

A synthetic mixture of 350 mmol/kg HEGly in 7 m MEA was prepared by reaction of sodium chloroacetate with MEA. The procedure for this synthesis was given in the last quarterly report (Rochelle et al, 2014). Samples were placed in sealed thermal cylinders in ovens at 120 °C and 150 °C, and periodically removed over a week. Control samples of clean 7 m MEA were run in parallel to this experiment.

The results are shown in Figure 3. Assuming a first-order kinetic decay model, total HEGly thermally degrades at a rate of $1.5x10^{-7} \pm 0.6x10^{-7}$ s^{-1} at 120 °C, 8.8 times faster than MEA at the same temperature, and $5.7x10^{-7} \pm 0.6x10^{-7}$ s^{-1} at 150 °C, giving an activation energy of 62 kJ/mol. For comparison, the activation energy of MEA is 110 to 160 kJ/mol depending on loading (Davis, 2009). While HEGly thermally degrades significantly faster than MEA, the effect of temperature is not as strong.

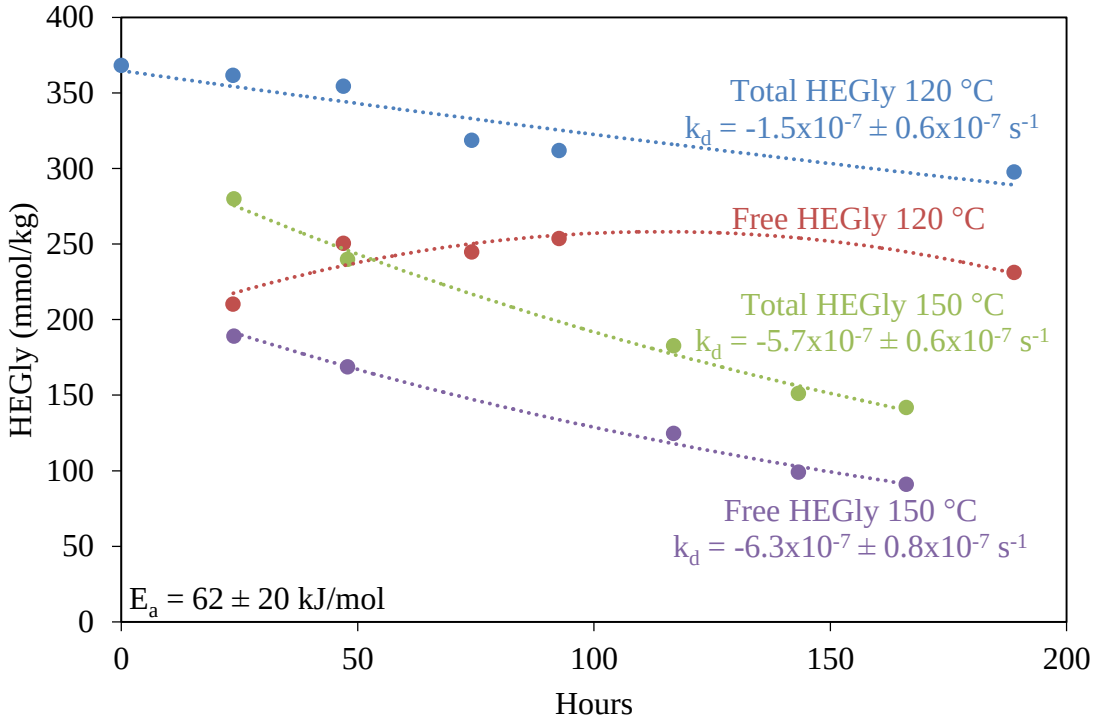

Figure 3: Thermal degradation of 350 mmol/kg HEGly in 7 m MEA (0.26 mol CO_2/mol alkalinity) at 120 °C and 150 °C

Figure 4 shows the thermal degradation of MEA in the 7 m MEA with 350 mmol/kg HEGly samples compared to clean 7 m MEA control samples. The rate of thermal degradation is not significantly different from the control, indicating that the presence of HEGly has no effect on the thermal degradation of MEA. The control samples are also not significantly different from what has previously been observed in MEA thermal degradation experiments, which determined the rate of MEA thermal degradation to be $2.81x10^{-8}$ s^{-1} at 121 °C (Davis, 2009).

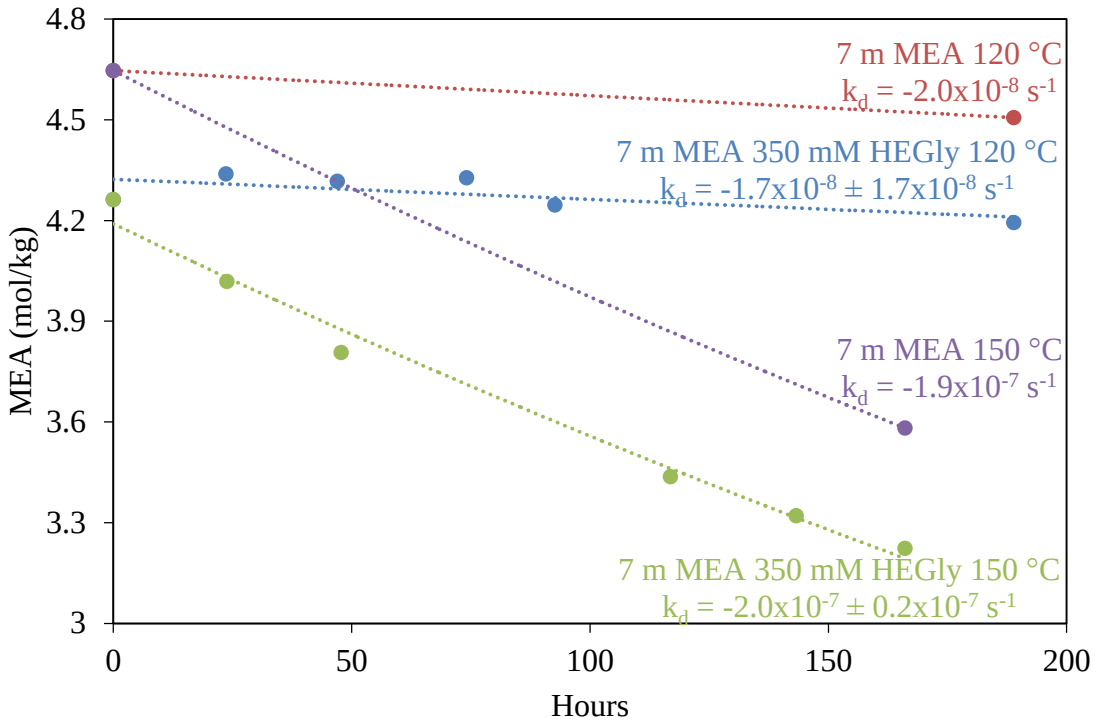

Figure 4: Thermal degradation of 7 m MEA (0.26 mol CO_2/mol alkalinity) at 120 °C and 150 °C with and without the addition of 350 mmol/kg HEGly

Inhibition of PZ oxidation

A preliminary experiment to determine the effectiveness of a proposed oxidation inhibitor, Inhibitor 8 (Inh 8), was conducted by reacting hydrogen peroxide with samples of 5 m PZ with and without Inh 8 present. A portion of the samples were then put in thermal cylinders and heated to 150 °C for 21.5 hours. The results are shown in Table 2. Based on the accumulation of degradation products, the most heavily oxidized sample was the one with hydrogen peroxide and without Inh 8 after heating. This was the only sample in which a significant accumulation of 2-piperazinol (2-PZOH), ethylenediamine (EDA) and 1-methyl-piperazine (1-MPZ) was observed.

Table 2: Accumulation of total aldehydes (C=O), 2-piperazinol (2-PZOH), total formate, ethylenediamine (EDA), and 1-methyl-PZ (1MPZ) in samples of 5 m PZ (α = 0.30 mol CO_2/mol alkalinity) with and without the addition of Inh 8 and H_2O_2 before and after thermal degradation at 150 °C for 21.5 hours

		Room temp *mmol/kg*		After 21.5 hours @ 150 °C *mmol/kg*				
	Sample	Total C=O	2-PZOH	Total C=O	2-PZOH	Total Formate	EDA	1MPZ
1	5 m PZ			12.2	0.3	0.3	1.2	
2	5 m PZ + 85 mmol/kg Inh 8	3.8		45.3	0.3	0.1	1.0	0.1
3	5 m PZ + 87 mmol/kg H_2O_2	69.2	0.5	141.9	5.7	2.7	19.5	5.3
4	5 m PZ+ 85 mmol/kg Inh 8 + 73 mmol/kg H_2O_2	28.4	0.2	91.2	0.6	2.1	0.9	0.3

Conclusions

- The MEA degradation product N-hydroxyethyl-glycine (HEGly) will react to form a reversible amide with MEA. In degraded pilot plant and bench-scale oxidized MEA samples, the ratio of free HEGly to total HEGly (free + amide) was typically 60 ± 10%.
- 212 mmol/kg of total HEGly accumulated in a cyclic oxidation of 7 m MEA in the HTOR apparatus. Approximately 60–130 mmol/kg of total HEGly was observed in multiple MEA pilot plant campaigns.
- At 120 °C, HEGly thermally degrades at a rate of $1.5 \pm 0.6 \times 10^{-7}$ s^{-1}, 8.8 times faster than MEA. At 150 °C, the thermal degradation rate is $5.7 \pm 0.6 \times 10^{-7}$ s^{-1}. The activation energy of HEGly thermal decomposition is 60 ± 20 kJ/mol.
- The presence of 350 mmol/kg total HEGly does not affect the thermal degradation of 7 m MEA.
- The presence of Inh 8 significantly reduced the accumulation of aldehydes, ethylenediamine, and 1-methylpiperazine in a sample of 5 m PZ reacted with ~100 mmol/kg of hydrogen peroxide and then heated to 150 °C for 21.5 hours.

Future Work

- Analysis of pilot plant samples from:
  - NCCC (Wilsonville, AL) using 30 wt % MEA;
  - Trona (CA) using 20 wt % MEA and a reclaimer apparatus;
  - Neumann Systems Group, Inc. (Colorado Springs, CO) using PZ.
- HTOR:

    - Test the effectiveness of Inh 8 and N_2 sparging to remove dissolved oxygen and reduce the oxidation rate of 5 m PZ;
    - Addition of an electrical resistance corrosion probe to measure the corrosion rate of PZ at 150 °C and MEA at 120 °C;
    - Determine oxidation rate of an MDEA/PZ blend.
- SRP reclaimer apparatus: A new atmospheric-pressure thermal reclaimer apparatus has been fabricated at the SRP facility. It is capable of reclaiming 0.1 gpm of solvent (~one 55 gallon drum per day). It will be used to:
    - Reclaim SRP and Tarong PZ solvent inventories;
        - Maximize amine recovery;
        - Determine fate of nitrosamines, aldehydes, and metals;
    - Test recoverability of Inh 8 from reclaimer sludge solution;
- Complete paper and poster presentation for GHGT-12 in October, 2014.

References

da Silva EF, Lepaumier H, Grimstveldt A, Vevelstad SJ, Einbu A, Vernstad K, Svendsen HF, Zahlsen K. "Understanding 2-Ethanolamine Degradation in Post-Combustion CO_2 Capture." *Ind Eng Chem Res*. 2012;51:13329–13338.

Davis JD. *Thermal Degradation of Aqueous Amines Used for Carbon Dioxide Capture*. The University of Texas at Austin. Ph. D. Dissertation. 2009.

Einbu A, da Silva EF, Haugen G, Grimstveldt A, Lauritsen KG, Zahlsen K, Vassbotn T. "A new test rig for studies of degradation of CO_2 absorption solvents at process conditions; comparison of test rig results and pilot plant data for degradation of MEA." *Energy Proc*. 2013;37:717–726.

Freeman SA. *Thermal Degradation and Oxidation of Aqueous Piperazine for Carbon Dioxide Capture*. The University of Texas at Austin. Ph.D. Dissertation. 2011.

Rochelle GT et al. "CO_2 Capture by Aqueous Absorption, First Quarterly Progress Report 2014." Texas Carbon Management Program. The University of Texas at Austin. 2014.

Voice AK. *Amine Oxidation in Carbon Dioxide Capture by Aqueous Scrubbing*. The University of Texas at Austin. Ph.D. Dissertation. 2013.

Appendix A: High Gas Flow (HGF) and High Temperature Oxidation Apparatus (HTOR) Standard Operating Procedures

Safety

The HGF/HTOR apparatus presents several safety challenges during operation. It is constantly circulating solvent from an oxidative reactor, where it is vigorously sparged with air and CO_2, through a cross exchanger and into a trim heater, which operates at up to 160 °C and 200 psig (14 bar), in a high-temperature silicon oil bath. Thus there is significant risk of injury if there is a leak or spill in the system. The solvent will also be producing volatile compounds, such as ammonia and the amine itself, when in operation. In order to mitigate these risks, the entire apparatus, with the exception of the FTIR, is housed in a fume hood with the sash closed to the minimum opening required to maintain airflow. The FTIR exhaust is vented back to the same fume hood. The high-pressure section is constructed entirely from Swagelok 316 stainless steel equipment rated for high-pressure, high-temperature operation, and a pressure relief valve is used to prevent the section from exceeding the design pressure limitations. Liquid solvent samples can be taken from a low-temperature, low-pressure line either before or after the oxidation reactor, and are drawn out through a rubber septa using a syringe and needle. Safety glasses, gloves, and a lab coat should be worn at all times when working with the apparatus.

HGF Startup SOP

1. Turn on the nitrogen purge on the FTIR by opening the needle valve by the fume hood.

2. Turn on the FTIR by flipping the black switch on the instrument.

3. Turn on the heater for the heated pump and umbilical line. Do not turn on the pump motor. The umbilical line must be connected to the pump with a power cord and thermocouple for the pump to control the umbilical temperature.

4. Allow the pump, umbilical, and FTIR to reach 180 °C. For the FTIR, this can take several hours.

5. While waiting for the FTIR to warm up, clean the umbilical by flowing DI water through the line and into a bucket. **Be sure that the line is not connected to the FTIR when you do this. Any liquid entering the FTIR will destroy the instrument.**

6. After the water exiting the lines is clear, turn the water off and use air to blow the residual water out of the line. Be sure that the residual water has been removed and that the temperature has returned to 180 °C before using the line to flow gas into the FTIR.

7. Reconnect the heated umbilical line to the tube exiting the condenser on the HGF apparatus.

8. Plug in the heating mantle around the line exiting the condenser. This mantle is used to preheat gas leaving the condenser and vaporize any entrained liquid. **Be sure that the mantle is wrapped *loosely* around the tube. The mantle will get very hot very quickly; do not touch it when it is plugged in.**

9. After the temperature of the FTIR has stabilized, verify that the interferrogram (IFG) center is below 2600. If the IFG center is not below 2600, wait several more hours, periodically observing if the IFG center is decreasing or stable. If the IFG center is not stable or if it is above 2600 there may be a problem with the instrument. Call Mark Nelson (Gasmet USA) at 512.331.0073.

10. Once the FTIR has warmed up and the IFG center is stable, connect a tube from the nitrogen supply at the fume hood to the heated pump inlet and flow nitrogen at 2–5 L/min into the FTIR.

11. Wait 30 minutes and then check that the background is stable by taking several 1 minute samples. The instrument is ready to be zeroed when the peaks for water and CO_2 are reduced to noise in the baseline.

12. When the background has stabilized, set the measurement time to 5 minutes and take a background scan (the background scan time will be 10 minutes).

13. While the FTIR, pump, and heated line are warming up, load 350 mL of amine solution into the reactor. **Be sure that the black valve at the bottom of the reactor is closed before adding liquid to the reactor. If it is not amine will drain into the saturator and cause a mess.**

14. Turn on the oil pump to heat the reactor and set the temperature as desired.

15. Turn on the two saturator pumps, the saturator bath heater (30 °C), and the condenser chiller (25 °C). Verify that the water makeup pump is pumping water into the saturator and that the level control pump is pumping water out of the saturator.

16. Open the valve at the bottom of the gas-liquid separator in the water collection system.

17. Open the valves on the fume hood to allow air and CO_2 to flow into the system. Set the mass flow controllers at the desired values. Gas will now be flowing into the saturator and out of the gas liquid separator.

18. If the agitator is in use, turn it on to accelerate heat transfer from the oil jacket into the amine solution.

19. Once the FTIR has been properly zeroed, the heated pump and umbilical line are at 180 °C, and the amine liquid has reached the desired temperature, the experiment is ready to start.

20. Half-way close the valve at the bottom of the gas liquid separator to the point where the gas velocity audibly accelerates. This provides pressure to the drain line and ensures that no amine liquid will drain from the reactor.

21. Open the black drain valve at the bottom of the reactor to allow gas to flow into the system.

22. Fully close the valve at the bottom of the gas liquid separator to divert the entire gas flow to the reactor.

23. Turn on the motor on the heated pump to provide gas flow to the FTIR.

24. Begin measuring at the desired sampling interval.

25. Close all doors to the fume hood to provide protection in the event of a pressure failure.

26. After starting the experiment, verify that the water content in the gas leaving the reactor at steady state is 3.41–3.43%. If the saturator bath is at 30 °C, this will ensure no net water loss from the system.

27. Verify that makeup water pump rate is sufficient to keep the saturator filled. After several hours of operation, open the black valve on the saturator and observe that a small amount of water drains out.

28. Verify that the saturator is working by observing a small amount of condensate on the clear gas line leading to the reactor.

29. Verify that the gas rate leaving the reactor is greater than the rate of gas being pumped to the FTIR by submerging the excess gas tube (on the T after the condenser) in a water-filled beaker and observing bubbles.

HTOR Startup SOP

1. Follow steps 1–17 in the HGF startup SOP, with the exception that in step 13 one liter of amine solution should be added to the HGF reactor and additional amine will be added as it is pumped to the other parts of the system. The total inventory is approximately 1.5 L.

2. Open the priming valve after the trim cooler and before the backpressure valve to allow gas to exit the high pressure part of the system.

3. Turn on the HGF reactor level control pump (peristaltic pump) to begin pumping amine into the bubble removal vessel.

4. Turn on the high pressure metering pump to pump liquid from the bubble removal vessel into the high pressure part of the system. Add amine to the HGF reactor as needed and do not allow the bubble removal vessel to be completely empty, as this would introduce air into the system.

5. When the amine is observed in the trim cooler outlet close the priming valve to prevent amine from coming out. Continue pumping amine with the high pressure pump to pressurize the system. **Be sure that the valve on the return line for amine entering the HGF reactor is open. Failure to open this valve can result in over-pressuring the system.**

6. **Be sure that the backpressure valve is set so that the system pressure does not exceed 250 psig. Higher pressures will destroy the heat exchangers which are expensive and time consuming to replace.**

7. The total inventory of the solution can be observed by the height of liquid in the bubble removal vessel. The height should be such that the liquid level is above the liquid inlet, but does not completely fill the vessel. Mark the level on the bubble removal vessel before starting the experiment.

8. Once the liquid has reached the desired pressure and the inventory has been adjusted turn on both of the high temperature heaters and the trim cooler. The high temperature heaters should be set at the desired amine temperature leaving the trim heater plus 3.3 °C. The trim cooler should be set at the temperature of the HGF reactor plus 4–8°C.

9. Proceed with steps 19–29 in the HGF procedure. The agitator cannot be used with high temperature cycling because it interferes with level control in the HGF reactor.

HGF and HTOR Shutdown SOP

1. Turn off the motor on the heated pump to provide gas flow to the FTIR.

2. Stop recording FTIR measurements.

3. (HTOR ONLY) Turn off the high temperature heaters and trim cooler.

4. (HTOR ONLY) Continue solvent circulation until all temperatures have dropped below 80 °C. Then turn off the high pressure metering pump and HGF level control pump to cease circulation.

5. Half-way open the valve at the bottom of the gas liquid separator to the point where the gas velocity audibly accelerates. This provides pressure to the drain line and ensures that no amine liquid will drain from the reactor.

6. Close the black drain valve at the bottom of the reactor to stop gas to flow into the system.

7. Fully open the valve at the bottom of the gas liquid separator.

8. Close the valves on the fume hood to allow air and CO_2 to flow into the system. Turn off the mass flow controllers.

9. Turn off the two saturator pumps, the saturator bath heater, and the condenser chiller.

10. Turn off the HGF oil pump to heat the reactor.

11. Turn off the heater for the FTIR heated pump and umbilical line.

Nitrosation Rates for Amines, Amino Acids, and Imidazoles

Quarterly Report for April 1 – June 30, 2014

by Nathan Fine

Supported by the Texas Carbon Management Program

McKetta Department of Chemical Engineering

The University of Texas at Austin

July 31, 2014

Abstract

This quarter, nitrosation rates were measured for a range of amines, amino acids, and imidazoles at dilute conditions. Solutions were heated between 120 °C and 165 °C with total experimental time lasting between 6 hours and 7 days. All screening was done in 0.1 m solutions at $\alpha \approx 0.3$ to minimize the activity effects associated with high ionic strength. Amines and amino acids with primary functionality nitrosate the slowest with propanolamine (PA), isopropanolamine (IPA), and β-alanine (β-Ala) showing no initial nitrosation. Ethanolamine (MEA) and glycine (Gly) nitrosated, but at much slower rates than the compounds with secondary nitrogen functionality. It is therefore likely that primary amine solvents will be poor nitrite scavengers. All secondary amines and amino acids nitrosate rapidly, so formation of the stable secondary nitrosamine will be favored in amine blends. Despite having a relatively low pH at reaction conditions, both imidazole (Im) and 2-ethylimidazole (2-EIm) react slowly and so will not nitrosate competitively in blends. The third order nitrosation rate increases as the nitrogen becomes more basic due to the increase in basicity of the amine carbamate. Thus in amine blends, the most basic secondary amine will nitrosate the fastest.

Nitrosamine Accumulation in Amine Scrubbing

Figure 1 gives a proposed sequence of processes that determine nitrosamine accumulation in amine scrubbing. Flue gas containing NO_x enters a polishing scrubber where a fraction (α) of the NO_2 can be removed via reaction with sulfite or tertiary amine. The remaining NO_x then enters the absorber where a portion of the NO_2 (β) can be absorbed into the amine solution as nitrite. The NO can also form nitrosamines in the absorber (γ) via reaction with amine radicals formed in the liquid reaction boundary layer. The rest of the NO_x will vent from the absorber along with the scrubbed flue gas. A fraction of amine oxidation (ε) also yields nitrite in amine solvents that are not oxidatively stable. Nitrite from NO_x absorption and amine oxidation will then travel to the stripper where it can nitrosate a secondary amine with a yield of δ. The yield is determined by the concentration of secondary amines in the solvent and their relative nitrosation rates as compared to the primary amine solvent. After nitrosation, the nitrosamine will thermally decompose in the stripper sump according to a pseudo-first-order nitrosamine decomposition rate

constant (k_{str}). In many amine scrubbing systems, a slipstream (x_{recl}) of the solvent is passed through a distillation reclaimer to remove any nonvolatile impurities. Nitrosamines will be removed from the scrubber based on the volatility (H_{NNO}) and the thermal decomposition rate in the reclaimer (k_{Recl}). Finally, nitrosamines will exit the amine scrubber through gaseous emissions or accidental spills (x_{spill}). This report will focus on the nitrosation rates of a range of amines under stripper conditions, which can be used to determine the yield of stable secondary nitrosamines (δ).

Nitrosation Rates for Primary and Secondary Amines

Sample Preparation and Analysis

Previously, nitrosation rates were measured at industrial conditions using approximately 3–8 m amine with α between 0.2 and 0.4 (Goldman et al., 2013). However, nitrosation rate screening was done using very low solvent concentrations for several reasons. Nitrosation rates can be on the same order of magnitude as thermal decomposition of the amines. Amine thermal decomposition is usually second order in amine concentration while nitrosation rates are first order in amine. Consequently, decreasing amine concentration should favor nitrosation over thermal decomposition. The strong ionic environment for concentrated amine solutions can convolute concentration-based screening kinetics since the activity of amine species can vary widely. Using a low and constant ionic strength of approximately 0.06 M, the activities were relatively constant across all experiments, which allowed direct comparison between amines. Screening was done with amines that could thermally decompose and form unknown nitrosamines. Lowering the concentration of nitrite in solution inherently decreases the risk of exposure to dangerous nitrosamines.

Nitrosation has been shown to be carbamate-catalyzed, so amine solutions were loaded with CO_2. To minimize bicarbonate formation in solution, CO_2 loading was limited to $\alpha = 0.3$. Since all amines and amino acids screened are carbamate formers, the CO_2 was assumed to speciate to the carbamate. The concentration of CO_2 in the 50 mL of solution prepared for each experiment was approximately 0.03 M, which equates to only 0.066 g CO_2. The small mass was too difficult to determine gravimetrically, so first CO_2 was sparged directly into distilled de-ionized water. The amine and nitrite were then added to the CO_2 loaded water and pipetted into the thermal cylinders. Amine loading was measured with undiluted samples using the total inorganic carbon method previously described (Freeman, 2011). The pH of solution was measured at room temperature using a potentiometric pH probe (Hilliard, 2008).

The thermal cylinders were heated at 120–165 °C for experiment times ranging from 6 hours to 7 days. Cylinders were removed periodically and the solutions were analyzed directly for nitrite using anion chromatography (Fine et al., 2014). For secondary amines and some primary amines, nitrite disappearance was first order in nitrite. The nitrite concentration was linearized and regressed to yield a pseudo-first-order rate constant (Equations 1 & 2). The third-order rate constant was determined using the solution pH at experimental conditions and carbamate concentration (Equation 3). Solutions are buffered by the amine, so the pH at experimental conditions was calculated by correcting for the change in amine pK_a from room temperature to the reaction temperature (Equations 4 & 5).

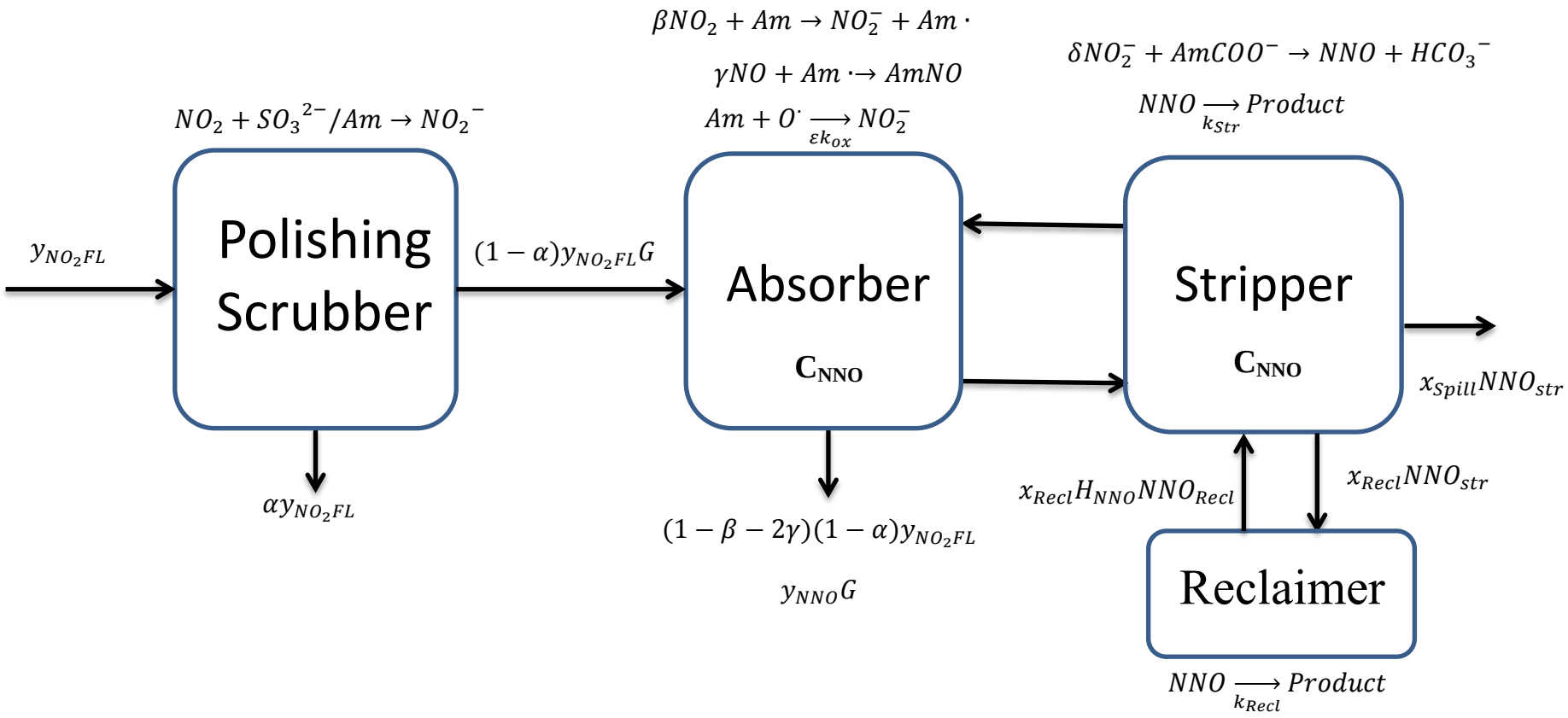

Figure 1: Nitrosamine Accumulation Mechanisms in Amine Scrubbing

$$\frac{d[NO_2^-]}{dt} = -k_{obs}[NO_2^-] \quad (1)$$

$$\ln[NO_2^-] = \ln[NO_2^-{}_i] - k_{obs}t \quad (2)$$

$$k_3 = \frac{k_{obs}}{10^{-pH_{exp}}[CO_2\ absorbed]} \quad (3)$$

$$pH_{exp} = pH_{RT} - (pK_{a\,RT} - pK_{a\,exp}) \quad (4)$$

$$pK_{a\,exp} = pK_{a\,RT} - \log\left(e^{\frac{-\Delta H_{Diss}}{R}*\left(\frac{1}{T_{exp}}-\frac{1}{T_{RT}}\right)}\right) \quad (5)$$

Each amine was nitrosated at two temperatures; the two k_3 values were then used to find the activation energy using the Arrhenius equation (Equation 6).

$$ln\left(\frac{k_{3\,T1}}{k_{3\,T2}}\right) = \frac{-E_a}{R} * \left(\frac{1}{T_1} - \frac{1}{T_2}\right) \quad (6)$$

Results

Table 1 gives the compounds used for nitrosation screening along with their structures and enthalpies of proton dissociation; Table 2 summarizes all of the observed pseudo-first-order nitrosation screening rates along with the third-order rate constants and activation energies.

Table 1: Nitrosation Screening Compounds

Amine	CAS #	Structure	ΔH_{Diss} (kJ/mol)
β-Alanine (β-Ala)	107-95-9	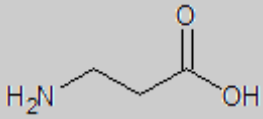	44.5*
Glycine (Gly)	54-40-6	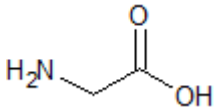	44.2+
Ethanolamine (MEA)	141-43-5	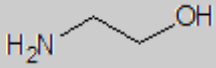	50.2+
Propanolamine (PA)	156-87-6	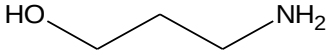	45oo
Isopropanolamine (IPA)	78-96-6	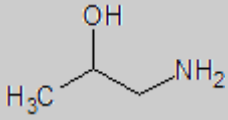	45oo

Methylaminoethanol (MAE)	109-83-1	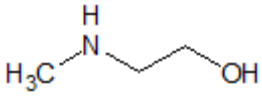	44.4[+]
Ethylaminoethanol (EAE)	110-73-6	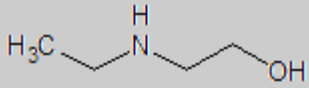	45[oo]
Diethanolamine (DEA)	111-42-2	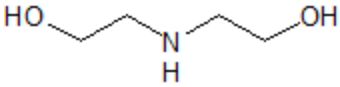	42.1[+]
Diisopropanolamine (DIPA)	110-97-4	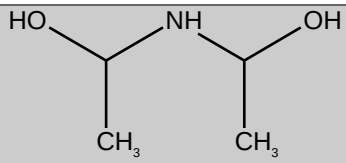	34.8[**]
L-Proline (Pro)	147-85-3	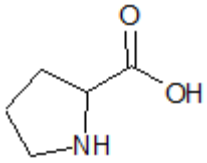	43.2[o]
Sarcosine (Sar)	107-97-1	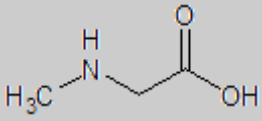	40.5[++]
Imidazole (Im)	288-32-4	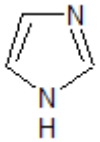	36.6[+]
2-Ethylimidazole (2-EIm)	1072-62-4	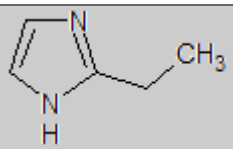	36.6[oo]

[*](Tsurko et al., 2014); [+] (Goldberg et al., 2002); [**](Blauwhoff et al., 1981); [++](Grzybowski et al., 1958) [o](Sorenson et al., 2003) [oo]Default values

Table 2: Nitrosation Rates in 0.1 M Amines, Amino Acids, and Imidazoles

#	Amine	α	pH_{exp}	T (K)	k_{obs} ($s^{-1}*10^6$)	$k_{3\ 135\ C}$ ($M^{-1}\ s^{-1}$)	Ea (kJ/mol)
Primary							
1	β-Ala	0.36	8.1	408	<2	N/A	N/A
2		0.36	7.9	423	<2		
3	Gly	0.29	8.0	408	5.2±0.7	18000	40
4		0.29	7.8	423	12±2		
5	MEA	0.28	7.6	408	4.4±0.1	6600	50
6		0.28	7.2	438	34±5		

7	PA	0.23	8.7	408	<2	N/A	N/A
8		0.23	8.3	438	<2		
9	IPA	0.23	8.1	408	<2	N/A	N/A
10		0.23	7.7	438	<2		
Secondary							
11	MAE	0.25	8.7	393	4±0.2	180000	70
12		0.25	8.5	408	14±0.2		
13	EAE	0.27	8.4	408	4.5±0.3	39700	50
14		0.27	8.0	438	19±2.2		
15	DEA	0.28	7.5	408	14±0.7	16000	50
16		0.28	7.3	423	30±3		
17	DIPA	0.21	8.1	408	16±2	94000	50
18		0.21	7.9	423	42±6		
19	Pro	0.30	8.6	408	7.6±1.4	102000	40
20		0.30	8.4	423	18.5±1.6		
21	Sar	0.35	7.8	408	7.9±0.4	21000	90
22		0.35	7.6	423	33±2		
Imidazoles							
23	Im	0.25	6.7	408	4.5±0.1	940	50
24		0.25	6.5	423	11.5±0.7		
25	2-EIm	0.25	6.1	408	5.1±0.4	240	60
26		0.25	5.9	423	13.2±3.4		

Nitrosation Mechanism

Carbamate-catalyzed nitrosation is theorized to follow the mechanism in Figure 2 with step 4 as the rate-limiting step. The pK_a of the amino group in step 3 is much greater than the pH of solution due to the neighboring negative charge; thus step 3 equilibrates far to the right. Using the pseudo-steady-state approximation, the rate law can be written as Equation 7. The concentration of amine carbamic acid can be determined from the pH and pK_a (Equations 8 & 9). Generally, the presence of the amine carbamic acid (AmCOOH) is neglected because the amine buffer is much more basic than the carbamate group. However, as temperatures approach desorber conditions, the pK_a of the amine drops substantially, lowering the pH and possibly allowing a small quantity of AmCOOH to form.

$$\frac{d[NO_2^-]}{dt} = -k_2[AmCOOH][NO_2^-] \quad (7)$$

$$[AmCOOH] = K_{a\ AmCOO^-}[AmCOO^-]_{Free}10^{-pH} \approx K_{a\ AmCOO^-}[AmCOO^-]_{Tot}a_{H^+} \quad (8)$$

$$\frac{d[NO_2^-]}{dt} = -k^\circ K_{a\ AmCOO^-}[AmCOO^-]a_{H^+}[NO_2^-] \quad (9)$$

The mechanism fits the empirical rate law (Goldman et al., 2013; Fine et al., 2014) and corroborates theoretical results (Lv et al., 2009). There is exceedingly limited data on carbamic acid stability since it is unimportant at absorber conditions. The pK_a of MEA carbamate at 30 °C has been measured as 7.5 (McCann et al., 2009), but there is no data for temperature dependence so it is impossible to calculate $K_{a\ AmCOO^-}$ at desorber conditions.

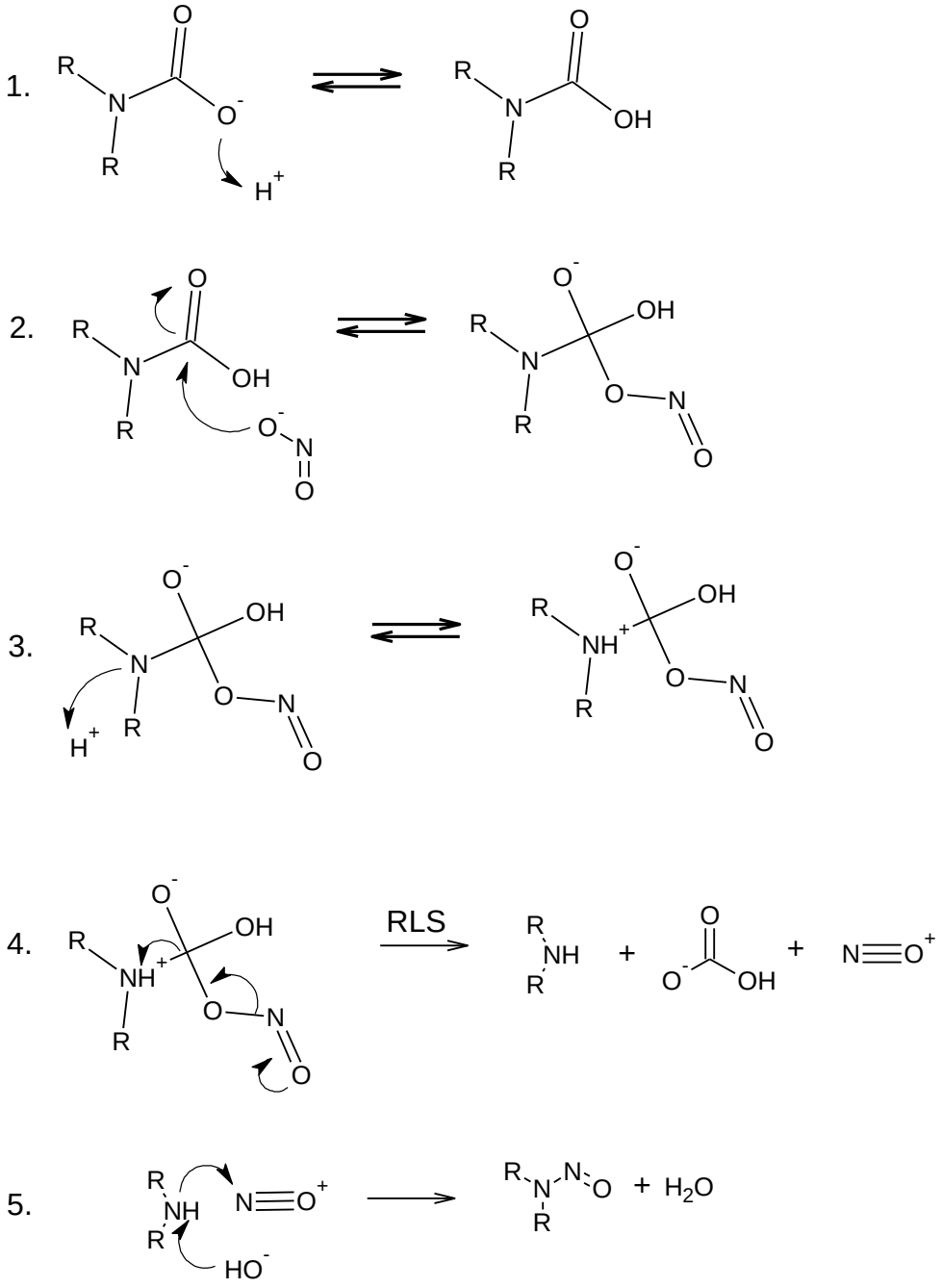

Figure 2: Nitrosation Mechanism

Effect of Amine Order

The yield of stable secondary nitrosamines in amine solutions depends on the nitrosation rates of secondary amines compared to other nitrosating species. Previously, tertiary amines and heavily hindered amines that do not form carbamates were shown not to nitrosate competitively with piperazine (Fine et al., 2014). MEA nitrosated competitively with DEA, 2-hydroxyethyl glycine (HeGly), and hydroxyethyl-ethylenediamine (HEEDA), but reacted 3–9 times slower than the secondary amines. Of all the primary amines and amino acids screened, only MEA and glycine had measurable nitrosation rates (Experiments 1–10), and these rates were much slower than those of the secondary amines, most likely due to the reaction occurring in step 4 of the nitrosation mechanism (Figure 1). The rate-limiting step depends on the elimination of the bicarbonate and nitrosonium cation from the intermediate species. In effect, the carbamate catalyzes the reaction by adding steric hindrance around the amino group, creating a better leaving group for the nitrosonium cation. The strength of the leaving group depends on the instability of the intermediate. With primary amines, the amino group is bonded to two hydrogens, releasing some of the steric hindrance and strengthening the bond between the amine and the carbamate leaving group. In contrast, secondary amines are under severe steric stress in step 4, and the breakup of the intermediate species is much more rapid. The effect is that secondary amines will likely react much faster than primary amines in all solvents. Therefore, the small amounts of secondary amines in primary amine solvents may dominate nitrosation more than previously hypothesized. It is highly advised that all promising primary amine solvents are screened for nitrosation rates so that accurate nitrosamine yields can be determined early on.

Effect of pK_a on Nitrosation of Secondary Nitrogens

For secondary nitrogens the third-order rate constant varies over three orders of magnitude even though it is hypothesized that all compounds go through the same mechanism. The large variance is not due to differences in steric hindrance, but rather differences in the $pK_{a\ AmCOO^-}$. Figure 2 shows how k_3 varies with the pH of solution for all experiments containing secondary nitrogens (Experiments 11–26). Since the amines buffer the solution at approximately the same loading, the pH is indicative of the pK_a of the amine. Counterintuitively, the more basic amines have larger k_3 values so that all observed rate constants are within an order of magnitude. It is likely that the pK_a of the carbamate tracks with the pK_a of the amine, which causes the concentration of AmCOOH to remain relatively constant for all experiments. However, in blends where the nitrosating amine does not buffer the solution, the pK_a of the reactive AmCOOH will be decoupled from the pH. Since the concentration of AmCOOH increases with the pK_a of the carbamate, which should increase with the pK_a of the amine, secondary amines with higher basicity should nitrosate faster. DIPA is an outlier on Figure 2 with a nitrosation rate constant approximately 5 times greater than amines and amino acids with similar pK_a values. This is most likely due to additional steric hindrance on the amino group from the isopropanol arms, which weakens the bond between DIPA and the leaving group.

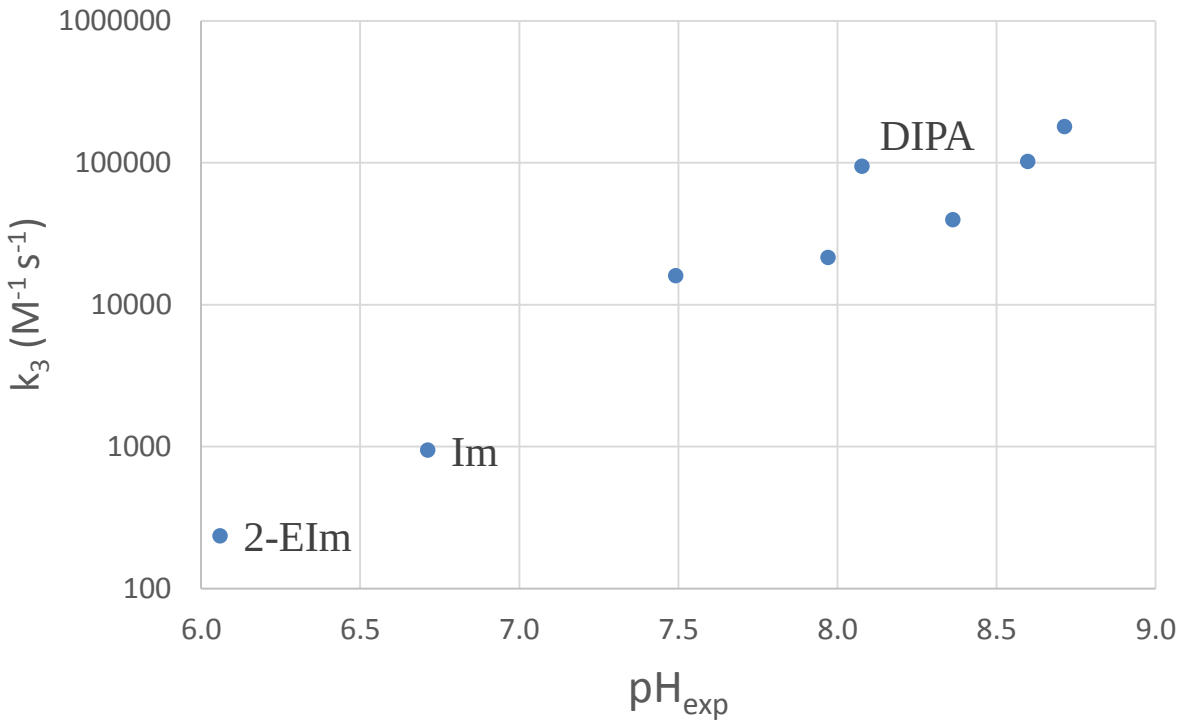

Figure 2: Nitrosation rate dependence on pH at 135 °C

(Experiments 12, 13, 15, 17, 19, 21, 23, 25)

Safety

As with any screening experiment, most of these experiments were done with a range of chemicals which had no previous nitrosation data. All experiments were done with dilute solutions to minimize the degree of exposure, and all nitrosamines were limited to less than 2 mmol/kg. All cylinders were opened in a properly ventilated fume hood, and solutions were capped and stored in amber vials. The samples were clearly labeled and stored in a designated space to avoid any exposure to other experimentalists.

Conclusions

- Nitrosation screening was completed for a range of primary and secondary amines, amino acids, and imidazoles.
- Screening was done in 0.1 M solutions with $\alpha \approx 0.3$
- Primary amines and amino acids nitrosate very slowly; propanolamine, β-Alanine, and isopropanolamine showed no initial nitrosation. Glycine and ethanolamine showed very slow nitrosation rates.
- Secondary amines nitrosated rapidly with more basic amines having higher third-order rate constants.
- Imidazoles have low third-order rate constants due to their low pK_a, but follow the general kinetic trend of secondary amines.

Future Work

- Model NO_x absorption in amine scrubbing.
- Measure NO_x absorption in sulfite scrubbing.
- Measure sulfite oxidation in the presence of NO_x.

References

Goldman MJ, Fine NA, Rochelle GT. "Kinetics of N-nitrosopiperazine formation from nitrite and piperazine in CO_2 capture." *Environ Sci Technol*. 2013;47(7):3528–3534.

Freeman SA. *Thermal degradation and oxidation of aqueous piperazine for carbon dioxide capture*. The University of Texas at Austin. Ph.D. Dissertation. 2011:100–102.

Hilliard MD. *A Predictive Thermodynamic Model for an Aqueous Blend of Potassium Carbonate, Piperazine, and Monoethanolamine for Carbon Dioxide*. The University of Texas at Austin. Ph.D. Dissertation. 2008.

Fine NA, Goldman MJ, Rochelle GT. "Nitrosamine Formation in Amine Scrubbing at Desorber Temperature." *Environ Sci Technol*. 2014. doi:10.1021/es501484w.

Tsurko EN, Kuchtenko YS. "Thermodynamics of the dissociation processes of beta-alanine in ethanol–water mixtures at temperatures from 293.15K to 318.15K." *J Mol Liq*. 2014;189:95–99. doi:10.1016/j.molliq.2013.03.023.

Goldberg RN, Kishore N, Lennen RM. "Thermodynamic Quantities for the Ionization Reactions of Buffers." *J Phys Chem Ref Data*. 2002;31(2):231–370.

Blauwhoff PM, Bos M. "Dissociation Constants of Diethanolamine and Diisopropanolamine in an Aqueous 1.00 M Potassium Chloride Solution." *J Chem Eng Data*. 1981;26(1):7–8. doi:10.1021/je00023a004.

Grzybowski AK, Datta SP. "The second acid dissociations of glycine, saircosine and n-dimethylglycine." *Trans Faraday Soc*. 1958:1188–1194.

Sorenson E, Price J, McRae B, Woolley E. "Thermodynamics of proton dissociations from aqueous l-proline: apparent molar volumes and apparent molar heat capacities of the protonated cationic, zwitterionic, and deprotonated anionic forms at temperatures from 278.15K to 393.15K and at the pressure 0.35 MPa" *J Chem Thermodyn*. 2003;35(3):529–553. doi:10.1016/S0021-9614(02)00375-0.

Lv C-L, Liu YD, Zhong R-G."Theoretical investigation of N-nitrosodimethylamine formation from dimethylamine nitrosation catalyzed by carbonyl compounds." *J Phys Chem A*. 2009;113(4):713–718. doi:10.1021/jp8061674.

McCann N, Phan D, Wang X, Conway W, Burns R, Attalla M et al. "Kinetics and mechanism of carbamate formation from CO_2(aq), carbonate species, and monoethanolamine in aqueous solution." *J Phys Chem A*. 2009;113(17):5022–5029. doi:10.1021/jp810564z.

Ion Exchange for Metals Removal from Amine Solutions

Quarterly Report for April 1 – June 30, 2014

by Kent Fischer

Supported by the Texas Carbon Management Program

McKetta Department of Chemical Engineering

The University of Texas at Austin

July 31, 2014

Abstract

Several column experiments were conducted to determine the viability of two ion exchange resins for metals removal from aqueous amine solutions. The two resins performed well in an initial screening test eluting piperazine (PZ) from a pilot plant solution. The experiment was repeated, both with the same pilot plant solution and with a pilot plant solution which had already undergone an initial metals removal step. This yielded column metal removal data for low and high initial metal concentration PZ pilot plant solutions.

Introduction

Ion exchange chromatography

Ion exchange involves the exchange of ions between an aqueous solution and a solid resin. In cation exchange, metal ions exchange with hydrogen ions on the resin. Because metal ions have a higher affinity for the resin than hydrogen ions, metal is immobilized in the resin as the solution passes through. This is shown in Equation 1, where M represents a metal, and R represents the resin.

$$M_{aq}^{+} + OH_{aq}^{-} + HR_s \rightarrow MR_s + H_2O_l \quad (1)$$

Ion exchange resins operate similarly to adsorption agents, but their selectivity is higher and they are optimized for removal from liquids. This yields an optimal bead size for mass transfer which also allows fluid flow through a column.

Experimental Methods

Screening of metals removal agents in column with PP2 PZ

Several glass columns were procured, each 10 inches long with a ½ inch inner diameter. Each of the columns was filled with a different ion exchange resin or adsorption agent and then plugged at the bottom with glass wool and closed with a septum at one end. A hole was cut in the septum to allow fluid to flow out (Figure 1). Four columns were assembled, each with a different adsorption agent or resin. The results of the screening tests are briefly summarized below in Table 1.

Table 1: Screening test results

	Result	Reason
Basic Alumina	Fail	Low flow due to powdered agent
Dowex Mac-3	Fail	Low flow due to significant resin swelling
Amberlite IRC 748i	Pass	
Amberlite IRC 747	Pass	

The first column used powdered basic alumina. Flow through this column was very slow, with only one "bed volume" (mass solution/mass bed) able to pass through the agent with gravity driven flow over 24 hours. Metals removal occurred in this resin, but the low flow rate through the resin makes it unsuited for column-type experiments. Bed volume is used in quotation marks because the units used here are mass/mass instead of the customary volume/volume.

The second agent tested was Dowex Mac-3 cation exchange resin. Only half a "bed volume" of resin passed through before serious swelling of the resin occurred, preventing additional flow. This indicates that the resin may be poorly suited for use with amine solutions.

Two Amberlite IRC resins were tested. These resins are strong cation exchange resins used for metal removal from electroplating wastes and chlor-alkali brines. These applications suggest resin stability in harsh conditions as well as selectivity for metals. These properties make these resins a promising choise for metals removal from amine solutions. The resins were obtained from Dow chemical and were used in the Na^+ form. The properties of these resins are given below in Table 2.

Amberlite IRC 748i is a divinylbenzene/styrene copolymer with an aminodiacetic chelating functionality. It was tested and showed good flow properties and metals removal. Amine was run through the column at about 5–8 "bed vol"/hr. Up to 2 "bed volumes" were tested in the screening run, with moderate metals removal.

Amberlite IRC 747 is a divinylbenzene/styrene copolymer with an aminophosphonic chelating functionality. It showed good flow properties and metals removal. Amine flow was about 5–8 "bed vol"/hr. 2.4 "bed volumes" were tested in the screening run.

Table 2: Properties of Ion Exchange Resins

	Amberlite IRC748i	Amberlite IRC747	
Max Op. Temp.	90	80	°C
Total Exchange Capacity, min.	1.35	1.75	eq/L
Water Retention Capacity	60-65	64-69	%
Uniformity Coefficient	1.7	1.8	eq/G
Harmonic mean size	0.5-0.65	0.520-0.660	mm
Fines content	< 0.300 1.0% max	<0.300 2.0% max	mm

Coarse beads	>1.100 5.0% max	>1.000 5.0% max	mm
Physical forms	beige beads	beige beads	

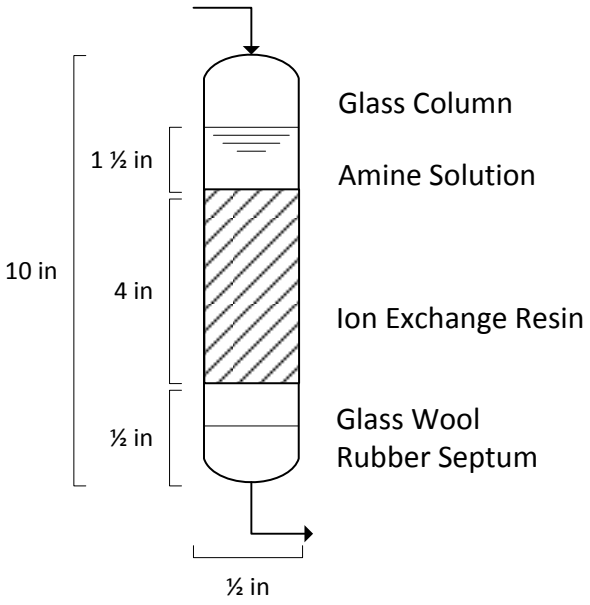

Figure 1: Metals removal column

Preparation of amines used in column experiments

Pilot plant 2 PZ was fully characterized by Paul Nielsen, and his results are given below as the "PP2 Lit" value for reference. There is some deviation between our analyzed values for PZ and metals, especially Fe.

A large amount of the PP2 PZ was put through an initial metals removal step before being run through the columns. This was done to lower the initial metals concentration so the solution would be more representative of a less degraded amine solution.

Previous experiments showed that basic alumina powder was an effective metals removal agent. About 115 g of basic alumina were added to an Erlenmeyer flask with 500 g of PZ from PP2. A large stirbar was added and the solution was stirred for 24 hours and then gravity filtered over a period of 4 days. The alumina 1 sample was then taken. The PZ was massed and weighed 393 grams, a loss of 22% of the initial sample. 116 g of alumina was added and the solution was left to stir for 48 hours. The gravity filtration of the second solution took place over 5 days. The mass of PZ solvent remaining was 284 grams, a loss of 44% for the entire removal process. The alumina 2 sample represents this final solution. This solution was eluted through ion exchange resins in the high resolution column experiments as a "low metals" PZ solution. Table 3 gives the metals and amine concentrations for the solution before and after this metal removal step.

Table 3: Preparation of "Low-Metals" Piperazine (mmol/kg solution)

	Ca	Co	Cr	Fe	Mg	Mn	Mo	Ni	Se	Piperazine
PP2 PZ	0.21	0.08	1.98	0.45	0.50	0.15	0.21	1.70	0.15	4134
PP2 Lit*	-	-	2.21	1.13	-	-	-	1.86	-	3546
Alumina 1	0.00	0.07	1.11	0.17	0.00	0.00	0.21	1.65	0.07	4169
Alumina 2	-0.01	0.07	0.54	0.12	0.00	0.00	0.18	1.52	0.06	4230

*(Nielsen, 2012)

High resolution column metal removal experiments

Column metal removal experiments were repeated using the Amberlite IRC748i and Amberlite IRC747 resins that passed the screening test. Experiments were conducted with both PP2 PZ and "low metals" PZ prepared above. Fresh resin was used for each experiment, and each run passed about 2.6 "bed volumes" through the column. Column preparation and running was identical to the screening tests. Aliquots of about 2 mL were collected throughout the run, massed, and then analyzed by ICP.

Results

Screening of metals removal agents in column with PP2 PZ

Both resins accomplished moderate removal, with high metal removal at the beginning and lower removal at the end. It appeared that the metal removal at the end was constant, and the column had not yet reached breakthrough. A summary of the metals removal is given for the final aliquot of amine from each column in the screening test in Table 4. Removals were similar, with complete removal of Mn, Ca, and Mg. Moderate removal was accomplished of Fe and Cr. Minor removal of all other metals occurred. The resins differed appreciably in their affinity for Ni. IRC748i showed much greater selectivity for Ni than IRC747. Figures 2 and 3 show the removal of metals by Amberlite IRC748i for major and minor metals. These graphs represent the same amine solution, but they were split into two graphs for better legibility. Figures 4 and 5 show the removal of metals by Amberlite IRC747 for major and minor metals.

Table 4: Metal removal from last aliquot of amine in screening test (%)

Resin	"Bed Volumes"	Ca	Co	Cr	Fe	Mg	Mn	Mo	Ni	Se
IRC748i	2.0	97.7	22.7	9.7	45.7	100.3	99.3	4.6	29.3	11.8
IRC747	2.4	97.6	13.6	8.7	55.5	99.3	97.6	2.1	7.3	5.4

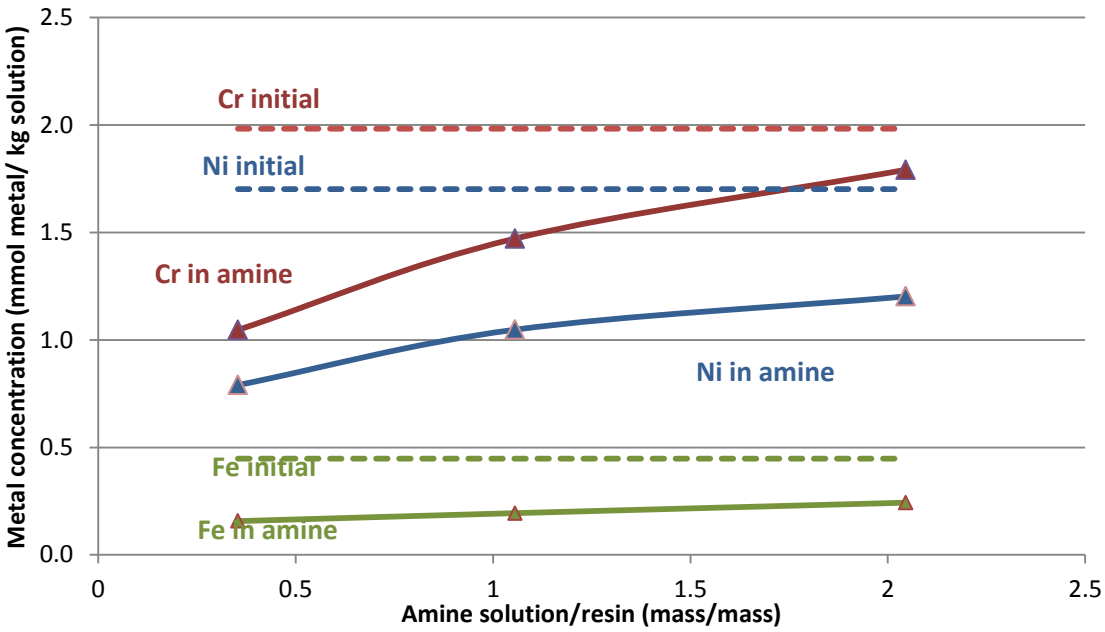

Figure 2: Amberlite IRC748i, major metals

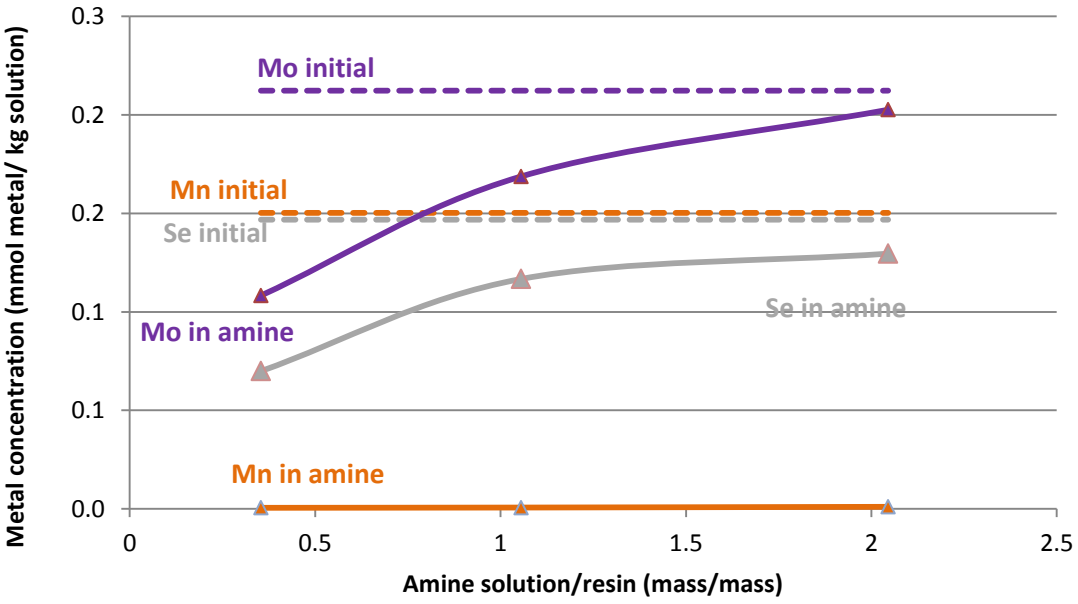

Figure 3: Amberlite IRC748i, minor metals

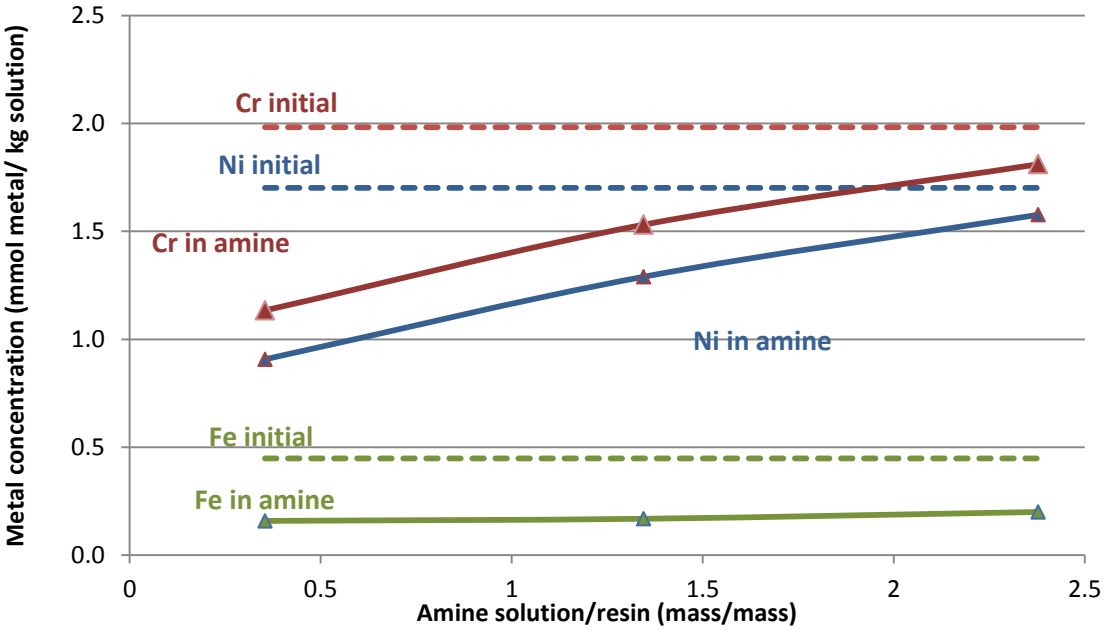

Figure 4: Amberlite IRC747, major metals

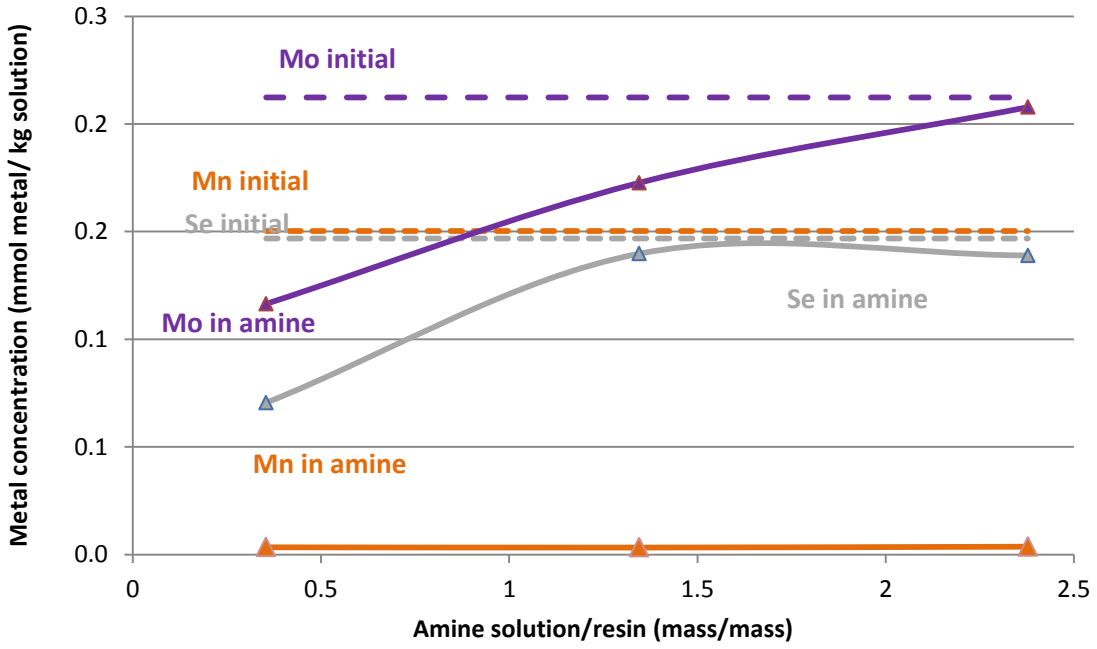

Figure 5: Amberlite IRC747, minor metals

High resolution column metal removal experiments

Results were similar to the screening tests, with both resins accomplishing moderate removal, with high metal removal at the beginning and lower metal removal at the end. A summary of the metals removal is given for the final aliquot of amine for each column in Table 5. No removal is given for several metals, because they were not present in the low metals PZ solvent run through the column. Some values are negative, but this was only seen for metals with relatively low concentrations and is probably due to error. Removal for the high metals PZ is similar to the screening tests, with complete removal of Mn, Ca, and Mg. Moderate removal was accomplished of Fe and Cr. Minor removal of all other metals occurred. Metal removal was apparently still occurring after 2.6 "bed volumes" in both high metal cases.

Although some initial metals removal occurred in early aliquots in the low initial metals PZ, most metals returned to their inlet concentrations by the time 2.6 "bed volumes" had passed through the column. The notable exception is nickel in the IRC748i resin, which was still showing metal removal in the last aliquot. This experiment seems to indicate that metals removal cannot be accomplished below a certain level with these resins. This is troubling because a successful metals removal scheme would need to remove metals to levels much lower than these.

Figures 6 and 7 show the removal of metals by Amberlite IRC748i for major and minor metals for the high initial metals PZ. Figures 8 and 9 show the removal by Amberlite IRC748i for major and minor metals for the low initial metals PZ. Figures 10 and 11 show the removal by Amberlite IRC747 for major and minor metals for the high initial metals PZ. Figures 12 and 13 show the removal by Amberlite IRC747 for major and minor metals for the low initial metals PZ.

Table 5: Metal removal in last aliquot of amine in high resolution column experiments (%)

	"Bed Volumes"	Ca	Co	Cr	Fe	Mg	Mn	Mo	Ni	Se
IRC748i high metals	2.6	104.7	19.0	11.4	59.0	100.2	98.6	3.3	31.4	-2.7
IRC748i low metals	2.6	-	18.9	-0.3	-2.5	-	-	-9.1	16.7	-
IRC747 high metals	2.7	99.9	21.7	17.4	73.4	98.3	97.7	8.4	15.4	36.8
IRC747 low metals	2.7	-	8.6	7.7	4.0	-	-	-3.5	-0.9	-

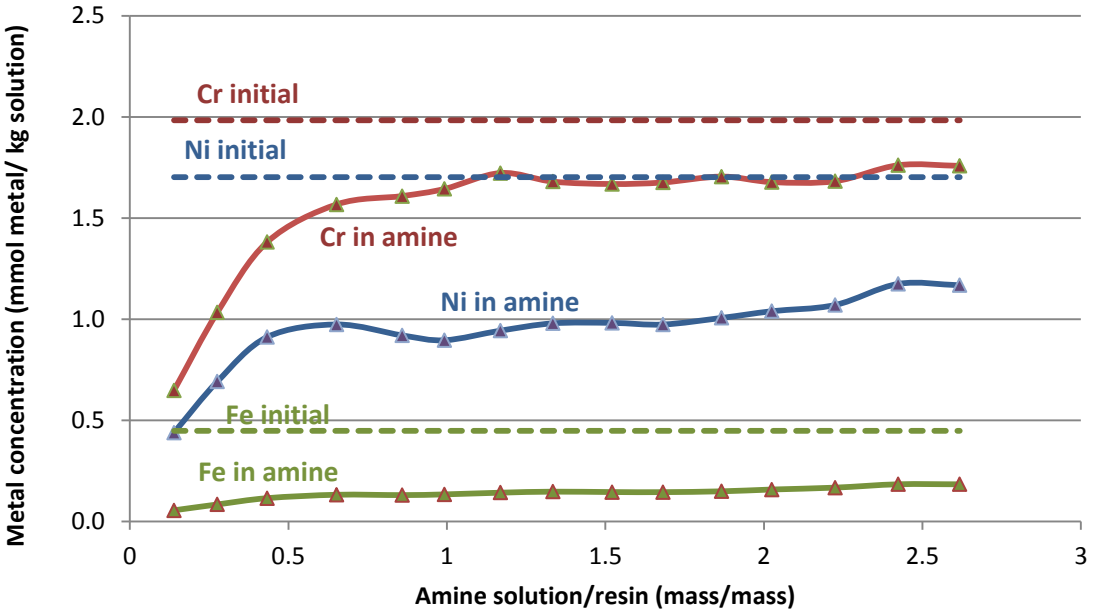

Figure 6: Amberlite IRC748i, high initial concentrations, major metals

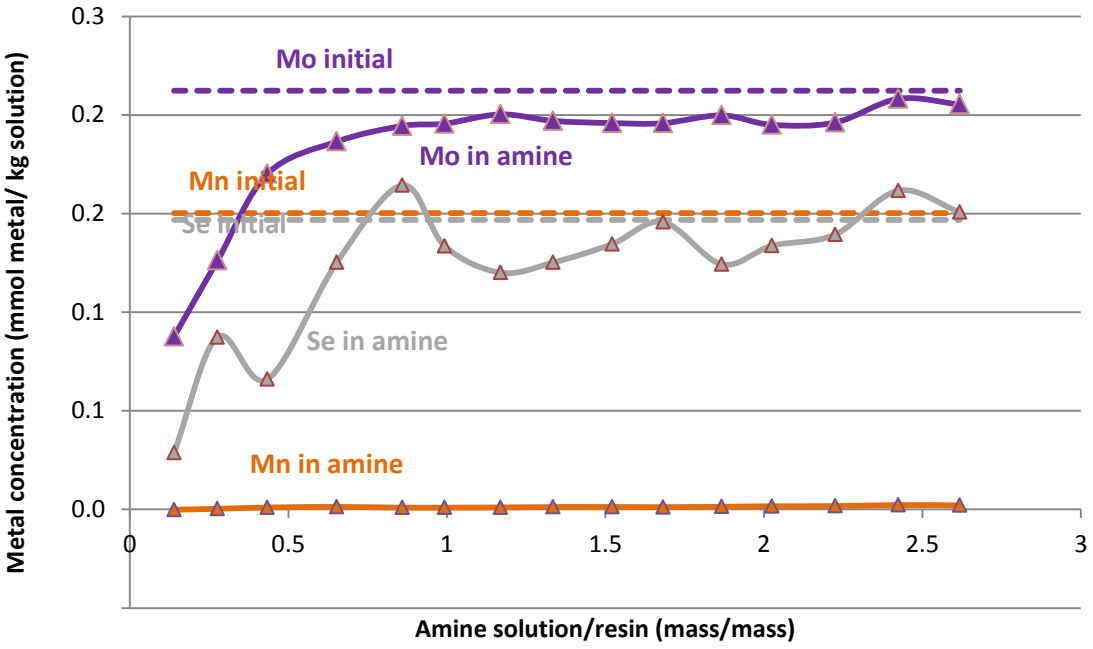

Figure 7: Amberlite IRC748i, high initial concentrations, minor metals

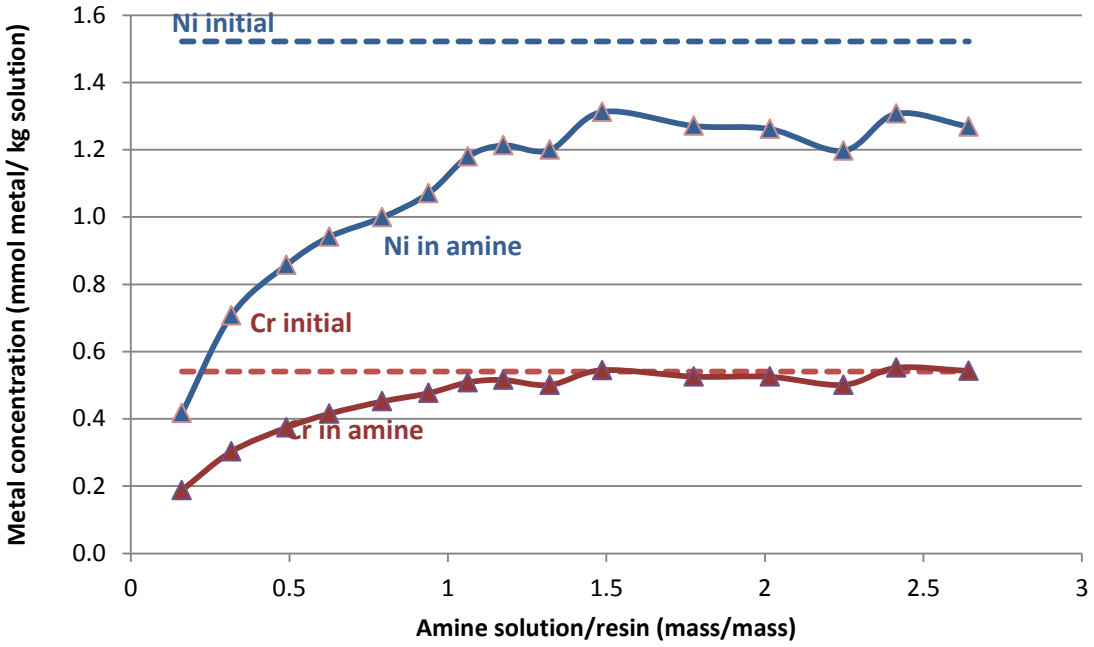

Figure 8: Amberlite IRC748i, low initial concentrations, major metals

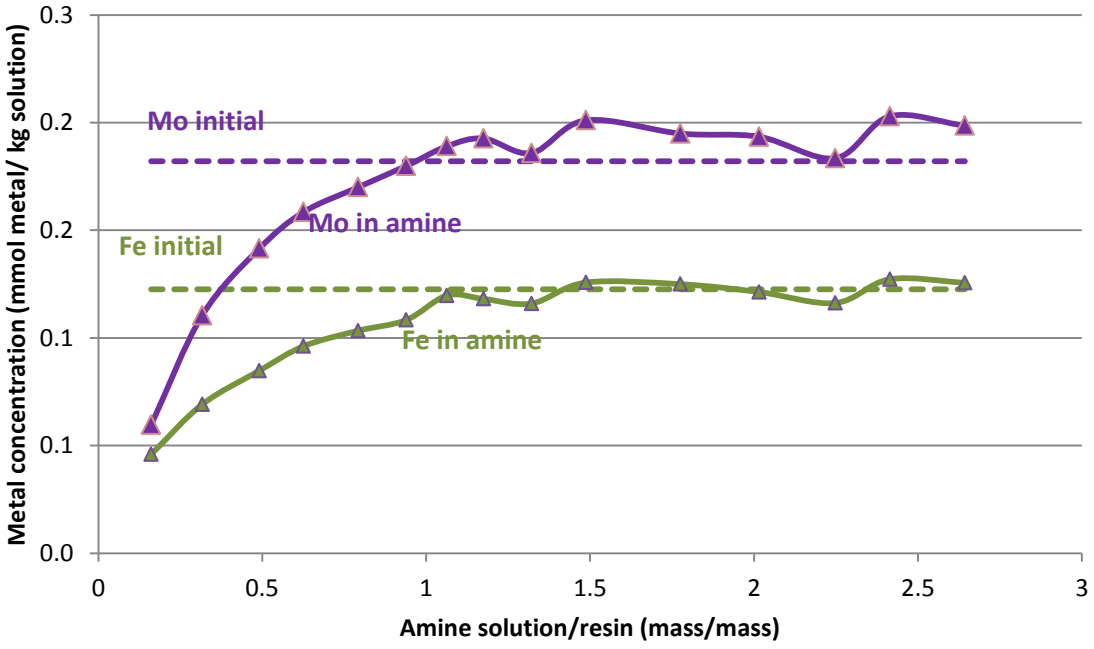

Figure 9: Amberlite IRC748i, low initial concentrations, minor metals

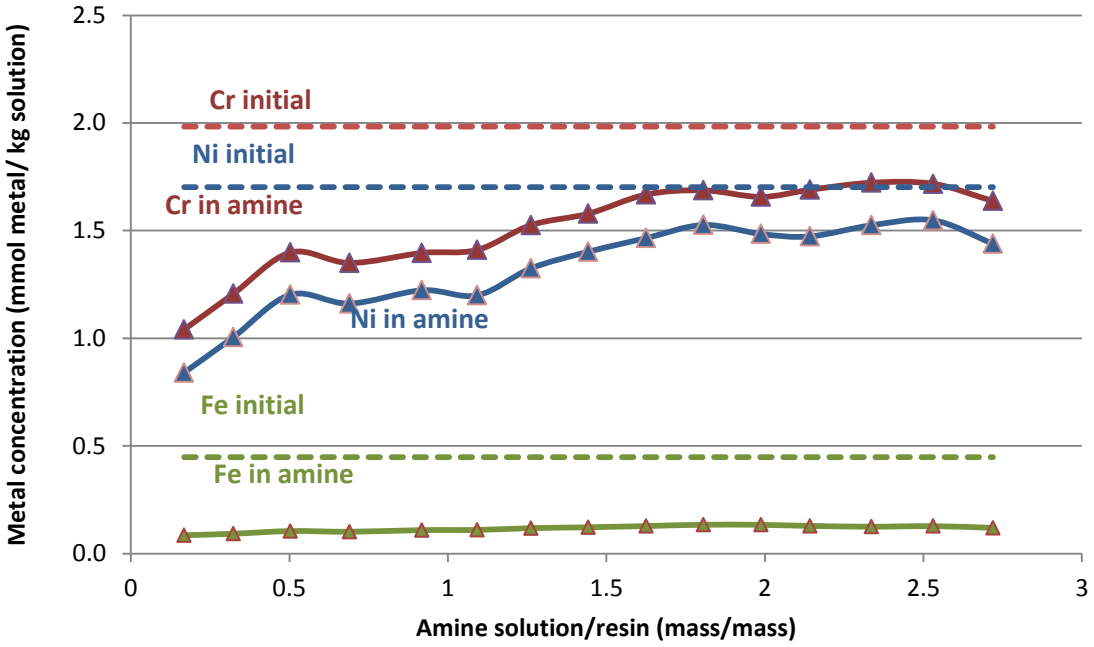

Figure 10: Amberlite IRC747, high initial concentration, major metals

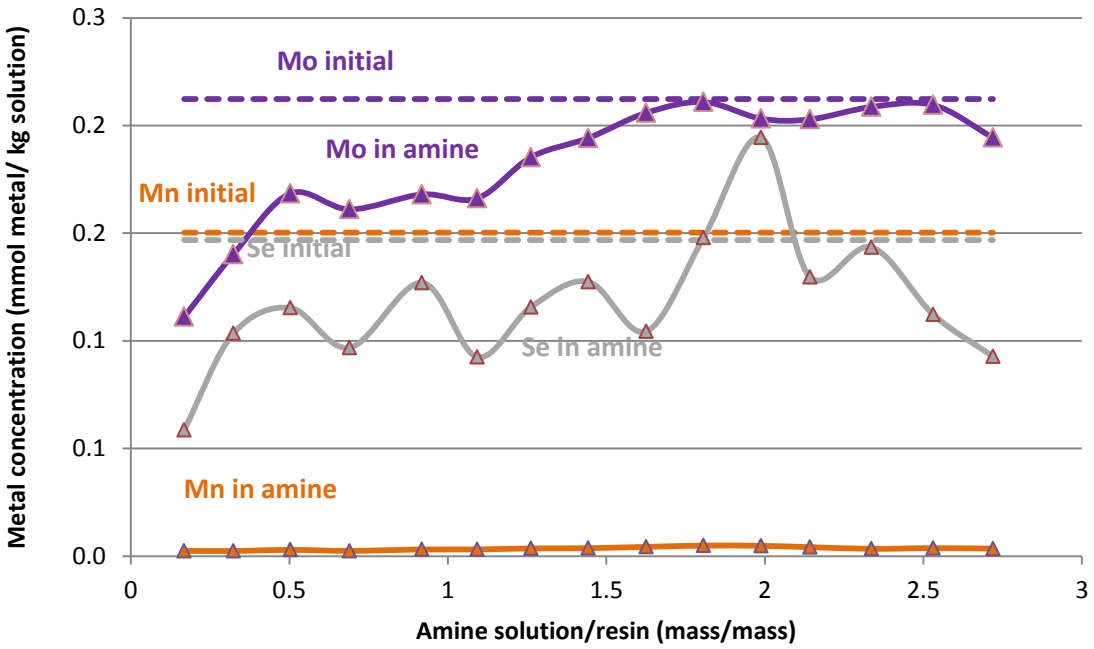

Figure 11: Amberlite IRC, high initial concentration, minor metals

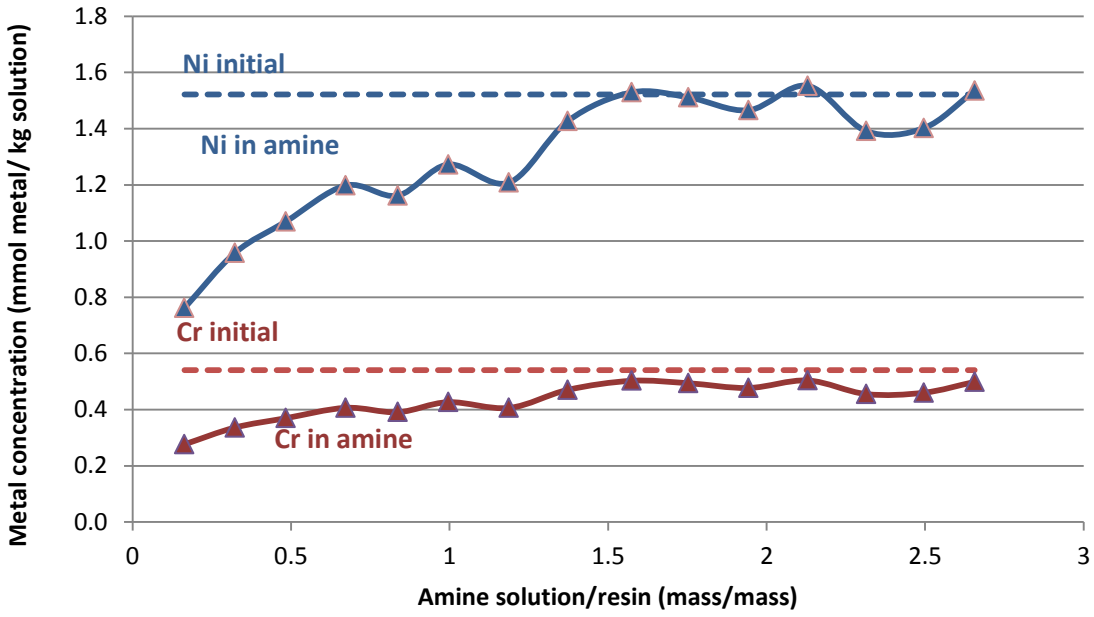

Figure 12: Amberlite IRC747, low initial concentrations, major metals

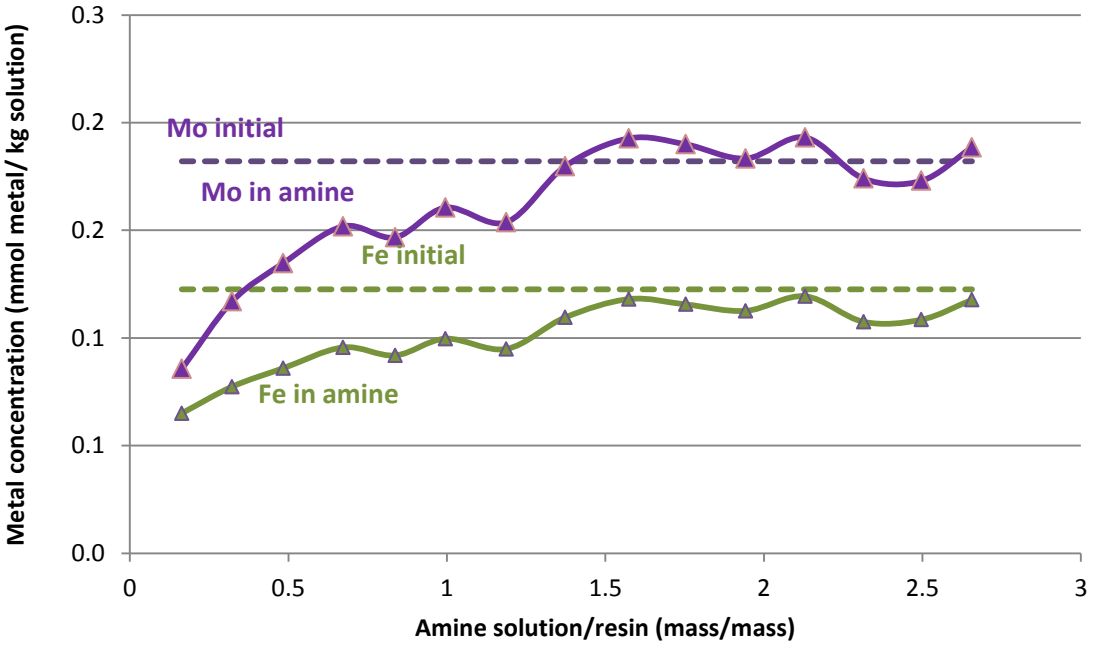

Figure 13: Amberlite IRC747, low initial concentrations, minor metals

Analytical Methods

ICP OES

All metals analysis was done by inductively coupled plasma optical emission spectroscopy using a Varian 710-ES instrument run in axial configuration. Wavelengths analyzed are given in Table 6. Results for each wavelength were averaged with other wavelengths for the same ion.

Table 6: Wavelengths Analyzed in ICP OES analysis (nm)

Ca	Ca	Ca	Co	Co	Co	Cr	Cr	Cr
393.366	396.847	422.673	228.615	230.786	238.892	205.560	206.158	267.716
Fe	Fe	Fe	Mg	Mg	Mg	Mn	Mn	Mn
234.350	238.204	259.940	279.553	280.270	285.213	257.610	259.372	260.568
Mo	Mo	Mo	Ni	Ni	Ni	Se	Se	Se
202.032	203.846	204.598	216.555	221.648	231.604	185.457	196.026	203.985

Cation Chromatography

The concentrations of PZ in Table 3 were determined using cation chromatography on a Dionex ICS2100 instrument. The solution was diluted to 10,000X and then eluted with methanesulfonic acid mixed with water. The eluent followed a gradient starting at 5.5 mM and ending at 38.5 mM methanesulfonic acid. The samples were eluted over an IonPac GC 17 guard column followed by an IonPac CS 17 analytical column. These columns contain ethylvinylbenzene cross-linked with 55% divinylbenzene resin.

Conclusions

Ion exchange resins Amberlite 748i and Amberlite 747 showed complete Ca, Mg, and Mn removal from a pilot plant solution with initial metal concentrations of 0.2, 0.5, and 0.2 mM/kg sol.

Amberlite 748i removed Fe, Cr, and Ni from a pilot plant solution down to levels of 0.18, 1.75, and 1.16 mM/kg sol, representing 59, 11, and 31% removal, respectively. However, from an amine solution with lower initial concentrations of metals, removal was much lower.

Amberlite 747 removed Fe, Cr, and Ni from a pilot plant solution down to levels of 0.12, 1.6, and 1.4 mM/kg sol, representing 73, 17, 15% removal. However, from an amine solution with lower initial concentrations of metals, removal was much lower.

The amine was run through the column faster than suggested by the manufacturer. It is hoped that future experiments will show that longer contacting time with the column improves the removal of metals, especially at lower concentrations.

Safety

Regeneration of ion exchange resins is accomplished by running a dilute solution of acid through the columns. This is usually accomplished with dilute H_2SO_4. Care must be taken to avoid the use of concentrated acids as they can react with the ion exchange resin, causing decomposition of the matrix immobilizing the ion exchange agent. This can cause damage to the column and release of vapor, which could cause an acid spill. Nitric acid in particular is a powerful oxidizer,

and it should not be used for resin regeneration due to the higher risk of resin damage. Care must be taken to wear personal protective equipment including safety glasses, a lab coat, and gloves while handling concentrated acids.

Future Work

These resin experiments were conducted at a rate of about 5–8 "bed volumes" per hour. The manufacturer recommends a bed rate of 2–4 bed volumes per hour. The column experiments will be repeated at this slower rate with the hope of improving metals removal.

References

Nielsen PT, Li L, Rochelle GT. "Piperazine degradation in pilot plants." *Energy Proc.* 2013;37:1912–1923.